22nd Numerical Towing Tank Symposium

29 September – 1 October 2019

Tomar/Portugal

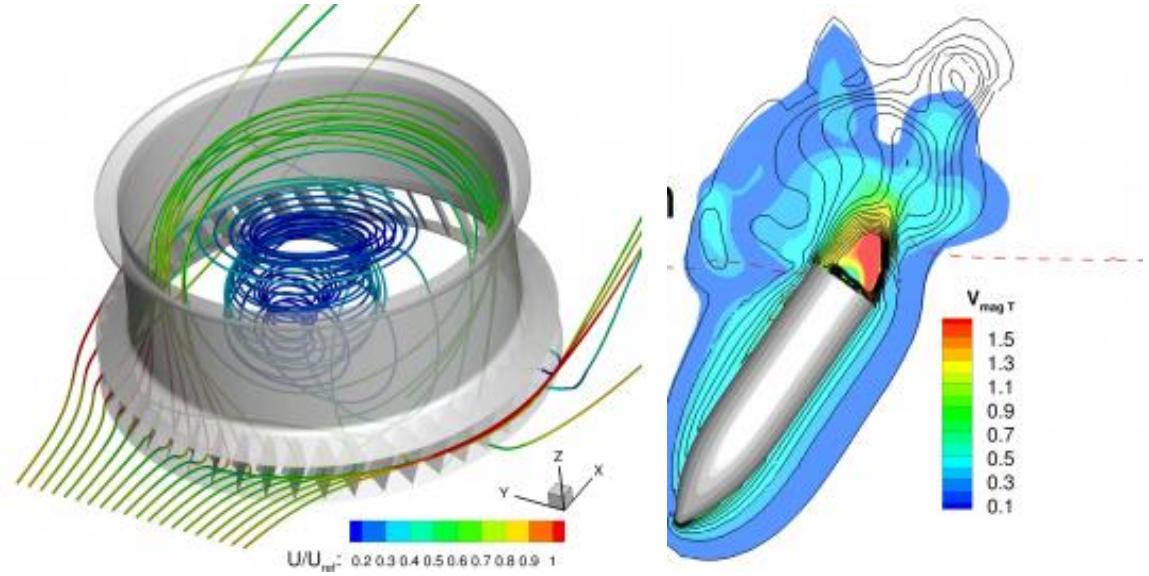

Luis Eca (Ed.)

Sponsored by

Numeca

www.numeca.com

WavEC

Offshore Renewables

www.wavec.org

Index of Papers

Pierre Le Bihan, Benoit Mallol, Charles Hirsch
Investigations and Guidelines for Maneuvering Simulations

Sebastien Lemaire, Guilherme Vaz, Stephen Turnock
On the Need for Higher Order Interpolation with Overset Grid Methods

Nicholas McCaw, Stephen Turnock
The Use of BEMT and a Transient Timoshenko Beam to Obtain Vibration Properties of Propeller Blades Under Manoeuvering Conditions

João Muralha, Luís Eça, Christiaan Klaij
Assessing ReFRESCO Compressible Single Phase Flow Solver Numerical Robustness

Kunihide Ohashi
Comparison of Wall Function Model with Low-Reynolds Number Model under Roughness Effect Condition at Actual Ship Scale

Andreas Peters, Udo Lantermann, Ould el Moctar
Numerical Prediction of Cavitation Damage for the Flow through a Nozzle Using a Multi-Scale Euler-Lagrange Method

Margot Remaud, P-M Guilcher, J.-B. Leroux, J.-M. Laurens
Design of Ducted Propellers

Ronald A. Remmerswaal, Arthur Veldman
Towards numerical simulation of wave impacts in an LNG tank

Rui Lopes, Luís Eça, Guilherme Vaz
Turbulence Decay Corrections for Transitional Flow Calculations

Ginevra Rubino, Michel Visonneau
Towards the Modeling of Laminar to Turbulence Transition for Incompressible Flows

Ahmed Sherif, Michel Visonneau, Ganbo Deng, Luís Eça
eXtended Discontinuous Galerkin (X-DG) method for a bi-material elliptic problem

Keun Woo Shin, Poul Andersen
CFD Study on Propeller-Induced Pressure Pulses in Cavitating Flows

Takuya Tachikawa, Nobuhiro Hasuike, Keita Fujiyama
CFD simulation of propeller noise

Ghalib Taimuri, Tommi Mikkola, Jerzy Matusiak, Pentti Kujala, Spyros Hirdaris
The Influence of Hydrodynamic Assumptions on Ship Maneuvering

Auke van der Ploeg
Anderson-Accelerated Convergence for Incompressible Navier-Stokes Equations

Michel Visonneau, Emmanuel Guilmineau, Ginevra Rubino
Performance of turbulence closures for vortex interaction physics over military aircraft

Michał Wawrzusiszyn, Radosław Kołodziej, Sebastian Bielicki
Numerical analysis of the container vessel's self-propulsion at different rudder deflection angles

Chiara Wielgosz, Rafael Golf, Artur K. Lidtke, Guilherme Vaz, Ould el Moctar
Numerical and Experimental Study on the Duisburg-Test-Case (DTC) Propeller

Kyung-Kyu Yang, Yoo-Chul Kim, Kwang-Soo Kim, Jin Kim, Bo Woo Nam, Min-Guk Seo
Numerical Study on Wave Drift Force of Advancing Ship in Bow Seas

Dissecting the aerodynamics of *Morpho* butterly flight using various turbulence models

Dario Amadori, Jaap Windt, Camille Le Roy, Florian Muijres

September 15, 2019

1 Introduction and main objective

Morpho butterflies are among the largest flying insects, boasting a wing that can reach 20 centimetres in span. Such characteristic allows these butterflies to perform flying techniques that are common in birds but not in insects, like the gliding and flap-gliding flight style. During flap-gliding, *Morpho* butterlies fly at speeds of approximately 1.5 m s^{-1}, and thus the wings operate at Reynolds numbers of the order of 10^4. At this transitional Reynolds number regime, aerodynamic performance of a wing is notoriously difficult to estimate, as turbulence state is difficult to determine *a priori* (Spedding et al. [2008]). Here, we model the aerodynamics of gliding *Morpho* butterflies using different turbulence models with the aim at understanding which ones can give more realistic and reliable results.

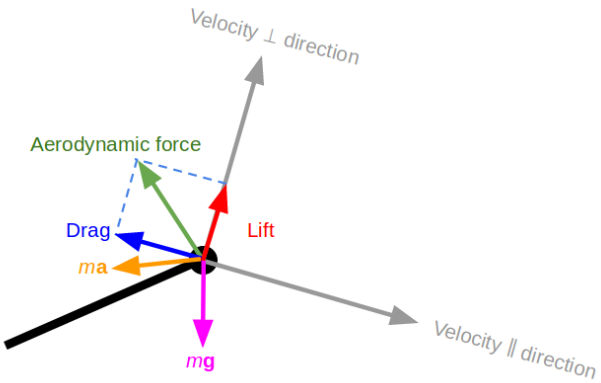

Fig. 1: Free body diagram of a gliding butterfly, including vectors normal and parallel to the flight direction, body acceleration vector and vectors of all external force acting on the animal. The animal is depicted as a lolly-pop whereby the circle is the head. The total aerodynamic force consists of lift and drag components, whereby drag is parallel to the velocity vector. Applying Newton's second law of motion to this system, lift and drag can be estimated from the acceleration and weight vectors (Eq. 1).

2 Kinematics and morphology of a flap-gliding *Morpho* butterfly

The experimental data used for validating our numerical simulations is a glide section of a flap-gliding flight of a *Morpho cisseis* butterfly. The flight was filmed in semi-field conditions with a stereoscopic high-speed camera system, recording at 240 frames per second. Throughout the stereoscopic video, we tracked the position of head, tail, and left and right wingtips, using a manual tracking program. Based on the head location data, we estimated the velocity (**v**) and acceleration (**a**) of the animal throughout the glide (Figure 2 (a)); by combining the wing orientation data with the velocity data, we determined the angle-of-attack of both wings throughout the gliding flight (Figure 2 (b)).

Butterfly wings consist of a front and hind wing, that are most of the time pressed against each other, and thus effectively operate as a single wing. Each wing consists of a flexible membrane (~0.1 mm thick) supported by stiffeners (~1mm thick). These stiffeners, called wing vanes, are mostly allocated near the leading edge. The wing surface is covered by scales that give colour to the wing, but also produce roughness on the wing surface. The wing of a *Morpho cisseis* butterfly has an average width of 7.5 cm and a mean chord length of 5.2 cm.

3 Inverse dynamics model of a gliding butterfly

Based on the accelerations of the butterfly throughout its gliding flight, we used rigid-body inverse dynamics modelling to estimate the aerodynamic lift **L** and drag **D** acting on the animal (Figure 1). By assuming zero wind conditions, we determined the aerodynamic force ($\mathbf{F}_{\text{aero}}$) acting on the animal using Newton's second law of motion as

$$\mathbf{F}_{\text{aero}} = -m\mathbf{g} + m\mathbf{a}, \tag{1}$$

where m is the mass of the butterfly and **g** is the gravitational acceleration. The next step consists in pulling the drag and lift vectors out of the $\mathbf{F}_{\text{aero}}$ vector. The drag is defined as the aerodynamic force component in the free-stream airflow direction, and is thus calculated as (Figure 2 (c))

$$\mathbf{D} = < \hat{\mathbf{v}}, \mathbf{F}_{\text{aero}} > \hat{\mathbf{v}}, \tag{2}$$

where $\hat{\mathbf{v}}$ the normalised velocity field vector and $< \hat{\mathbf{v}}, \mathbf{F}_{\text{aero}} >$ is the scalar product of $\hat{\mathbf{v}}$ and $\mathbf{F}_{aero}$. Note that this will lead to negative values for drag. The lift was estimated as the difference between the total aerodynamic force and drag as (Figure 2 (d))

$$\mathbf{L} = \mathbf{F}_{\text{aero}} - \mathbf{D}. \tag{3}$$

Finally, based on these results, the lift-to-drag ratio (L/D) throughout the glide phase was determined (Figure 2 (e)).

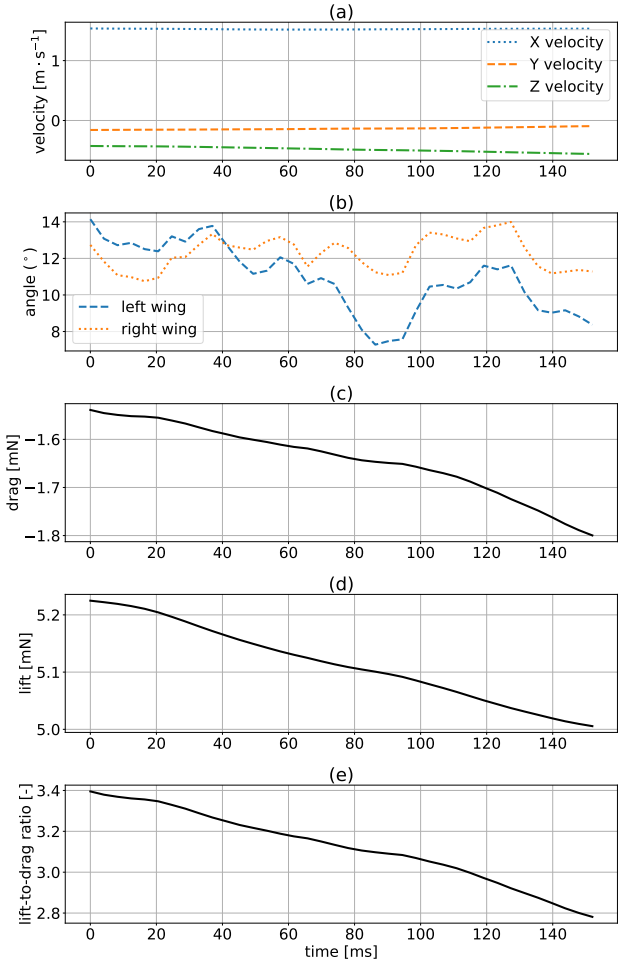

Fig. 2: Experimental kinematics data of the gliding phase in a flap-gliding flight of a *Morpho cisseis* butterfly, determined using stereoscopic high-speed videography and inverse dynamics modelling (Section 3). The parameters shown are the temporal dynamics of flight velocity (a), angle of attack of the left and right wings (b), drag force (c), lift force (d), lift-to-drag ratio (e).

4 Numerical simulation setup

For the numerical simulations, we modelled a single *Morpho* butterfly wing in gliding conditions, whereby the wing root was positioned at a symmetry plane (Figure 3). The wing model consisted of a 1 mm thick rigid smooth flat plate operating at the average angle of attack (10.91°) and average flight speed (1.61m/s) of the digitised gliding flight (Figure 2 (a), (b)). The wing outline was accurately traced from a museum specimen of a *Morpho cisseis* butterfly; the front and hind wing were rigidly connected matching the position that was observed to be used by this specie during gliding flight. The edges of the wing were rounded with 0.5*mm* radius, except for the edge lying on the symmetry plane, which was sharply cut.

The domain of the numerical simulations consisted of a $2 \times 1 \times 2$ metres box, with the hinge of the wing positioned in the origin, which raises in the middle of the xz plane. An inflow condition directed in the $-x$ direction was set on the boundary plane $x = 1$ and a symmetry condition was set on the boundary plane $y = 0$. All the other external surfaces were defined by a zero-pressure condition and the wing was defined by a no-slip condition.

In order to perform a study on the uncertainty due to spatial discretization, for each case four unstructured grids with different refinement were used (Table 1). The time step was set to 0.8 ms; with this value, the mean flow needs more than 50 time steps to sweep the length of the wing.

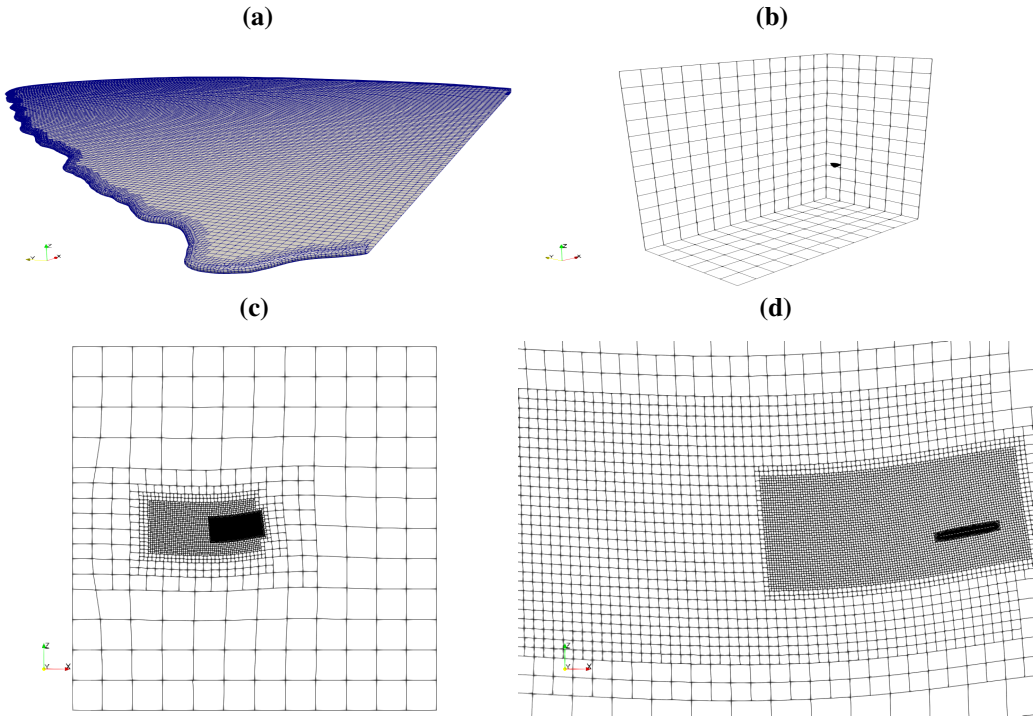

Fig. 3: The mesh topology used for the simulations. (a) the wing surface mesh; (b) the complete computational domain with in its centre the wing surface mesh from (a); (c) the complete symmetry plane, with two box refinements around the wing; (d) zoomed in view of the refinement boxes around the wing, whereby the wing is positioned in the finest cell box.

For this study, we selected five different numerical setups to test, using the following turbulence models: Spalart-Allmaras, SST $\kappa - \omega$, SST $\kappa - \omega$ with $\gamma - \mathrm{Re}_\theta$ transition modelling (with two different inlet conditions: $\nu_t/\nu = 2.5$ and $\nu_t/\nu = 10$) and PANS.

The SST $\kappa - \omega$ model was chosen because it tends to provide relatively precise results, particularly in aerodynamic applications (Menter [1993]); since previous studies suggested that insect flight is characterised by unsteadiness of the flow (Sane [2003]), the steady results obtained with this setup left some doubts. For this reason, we believed that, thanks to its origin and field of application, the Spalart-Allmaras model was as a valid alternative turbulent model to check if any differences would have arisen (Spalart and Allmaras [1992]). Moreover, since it was not possible to state *a priori* if and how turbulence would have been developed, we added to the SST $\kappa - \omega$ model the $\gamma - \mathrm{Re}_\theta$ equations to investigate this topic. Since, following Menter et al. [2004], the latter provided to be sensitive to the inlet conditions imposed, two configurations of the $\gamma - \mathrm{Re}_\theta$ model where set to further investigate this aspect (see validation examples in Langtry and Menter [2005]). Finally, PANS model was chosen as a final attempt to further study this case and to better catch the effects of turbulence. The latter simulations are still in progress and will need further refinements both in time and space to provide reliable data.

5 Results

To test our different numerical cases, we compared the lift, drag and lift-to-drag ratio from the numerical simulations with those estimated from the glide kinematics (Figure 7). The error bars in Figure 7 represent the uncertainties due to spatial discretisation for drag, lift and lift-to-drag ratio for each numerical simulation, which are estimated following the procedure explained in Eça and Hoekstra [2014]. All the uncertainties lie in between 2% and 12%; the estimation is not studied yet for the PANS simulations and not given for the experimental data.

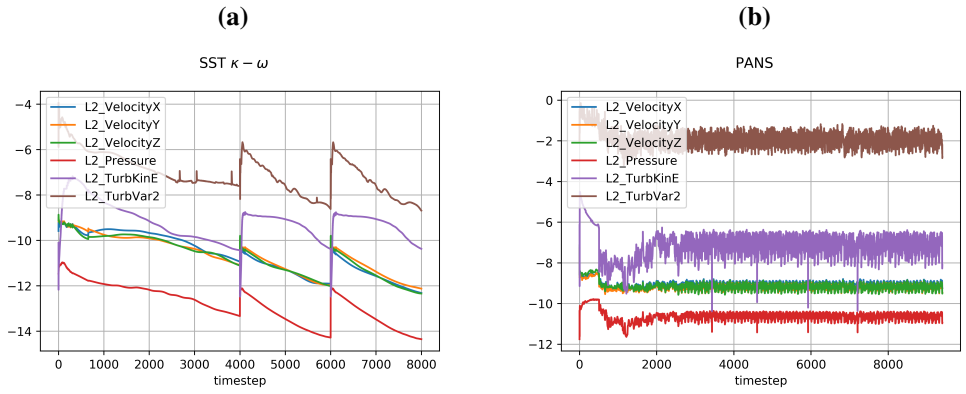

Fig. 4: (a) L_2 norm residuals for the SST κ – omega model with the finest grid, in logarithmic scale; on the x axis the number of time steps. The Spalart-Allmaras and SST $\kappa - \omega$ with $\gamma - \mathrm{Re}_\theta$ transition model have a very similar residuals trend; (b) L_2 norm residuals for the finest grid PANS simulation, in logarithmic scale; on the x axis the number of iterations.

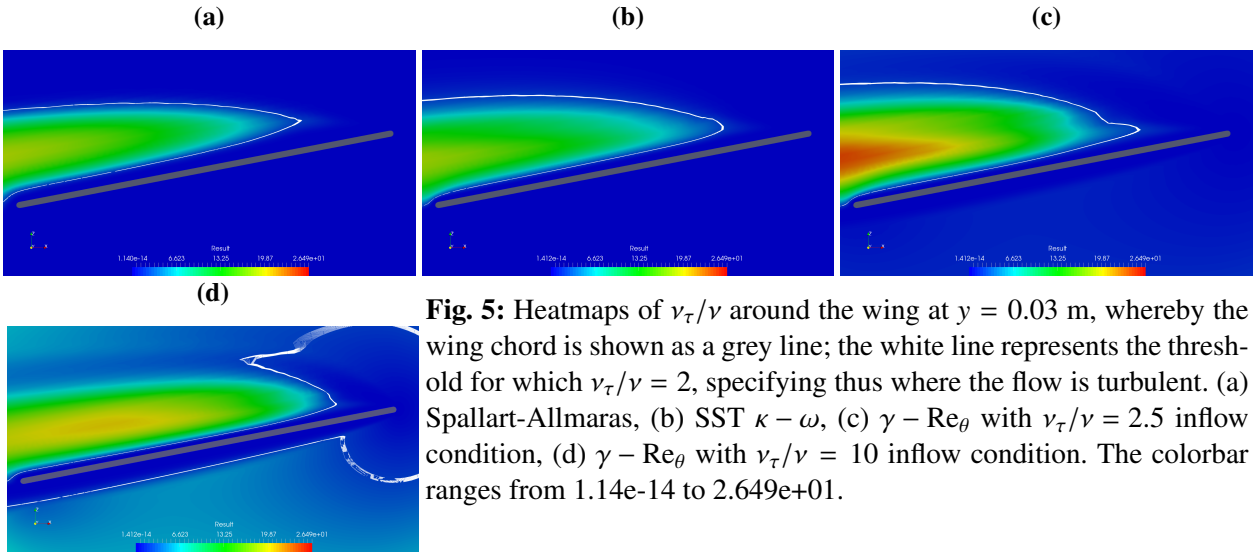

Fig. 5: Heatmaps of ν_τ/ν around the wing at $y = 0.03$ m, whereby the wing chord is shown as a grey line; the white line represents the threshold for which $\nu_\tau/\nu = 2$, specifying thus where the flow is turbulent. (a) Spallart-Allmaras, (b) SST $\kappa - \omega$, (c) $\gamma - \mathrm{Re}_\theta$ with $\nu_\tau/\nu = 2.5$ inflow condition, (d) $\gamma - \mathrm{Re}_\theta$ with $\nu_\tau/\nu = 10$ inflow condition. The colorbar ranges from 1.14e-14 to 2.649e+01.

The SST $\kappa - \omega$, Spalart-Allmaras and SST $\kappa - \omega$ $\gamma - Re_\theta$ simulations converge to a steady flow solution, with L_2-norm residuals reaching values of the order of 10^{-9} (Figure 4a). Due to computational cost restrictions, PANS simulations were run with higher tolerance on the residuals (Figure 4b).

The $\kappa - \omega$, Spallart-Allmaras and $\gamma - Re_\theta$ with both $\nu_\tau/\nu = 10$ and $\nu_\tau/\nu = 2.5$ inflow have a steady flow as result. The PANS simulations lead to unsteady flow configurations, with the first three levels of refinement reaching a periodic state (Figure 8).

Table 1: Number of cells of the four grids used for each turbulence model.

1lev	1,157,340
2lev	3,785,147
3lev	8,406,881
4lev	15,738,960

6 Discussion

Our comparison of aerodynamic forces between the experiment and simulations (Figure 7) shows that all numerical simulations predict larger (in magnitude) drag, lift and lift-to-drag ratio. This systematic offset between experiments and simulations could come from the presence of air currents during the recorded flight, which we assumed to be zero. The experiments were performed in semi-field conditions, so air currents could not be fully controlled, and because butterflies have exceptionally low wing loading small air currents can have a large effect on their flight.

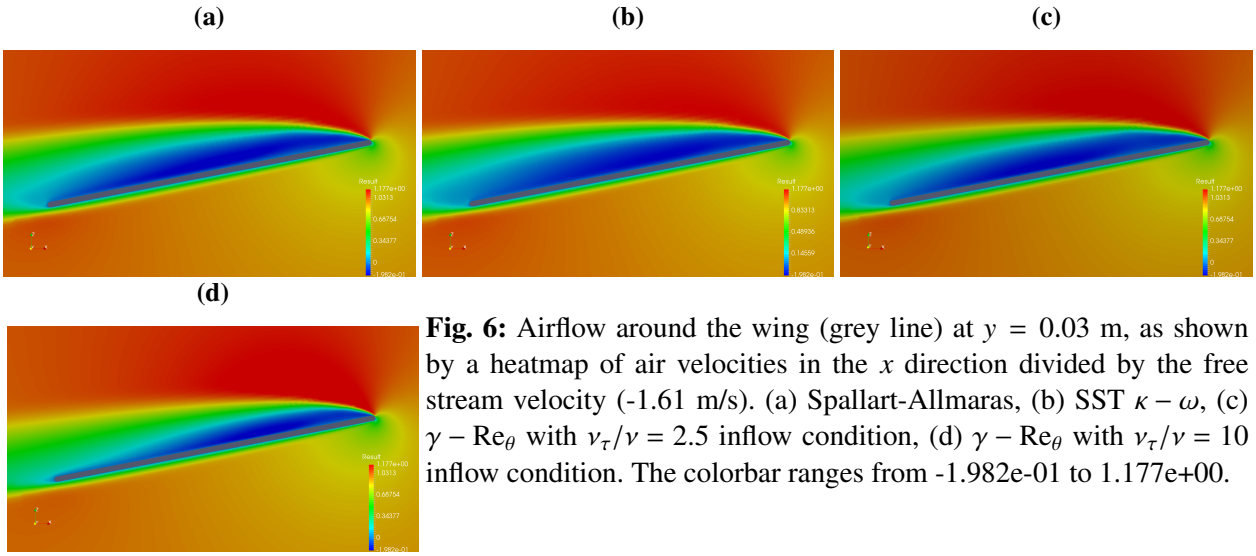

Fig. 6: Airflow around the wing (grey line) at $y = 0.03$ m, as shown by a heatmap of air velocities in the x direction divided by the free stream velocity (-1.61 m/s). (a) Spallart-Allmaras, (b) SST $\kappa - \omega$, (c) $\gamma - \mathrm{Re}_\theta$ with $\nu_\tau/\nu = 2.5$ inflow condition, (d) $\gamma - \mathrm{Re}_\theta$ with $\nu_\tau/\nu = 10$ inflow condition. The colorbar ranges from -1.982e-01 to 1.177e+00.

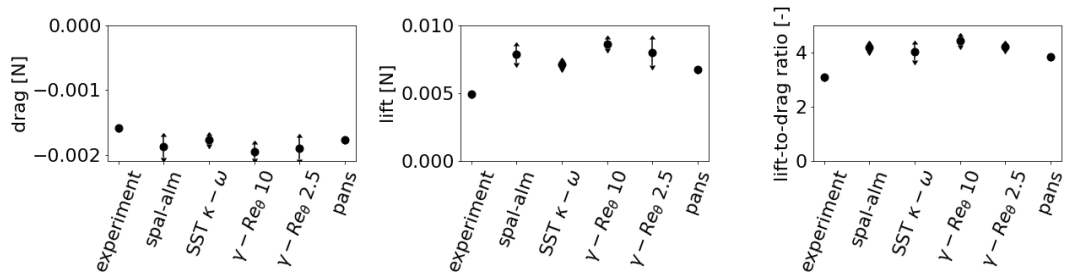

Fig. 7: Drag, lift and lift-to-drag ratio of experiments and numerical simulations. The values are taken from the finest grid setups and the error bars represent numerical uncertainty due to spatial discretisation. For experimental results the uncertainty is not give and for PANS is not computed yet.

We performed the SST $\kappa - \omega$ $\gamma - \mathrm{Re}_\theta$ simulations to test whether modelling of the transition to turbulent flow has a strong effect on the resultant aerodynamic forces on the wing. The results show that the transitional model gives values lying close the SST $\kappa - \omega$ without transition modelling ones (Figure 7), stating that the transitional model has a small impact on the results. Besides, Figure 5 corroborates such conclusion, since it shows that transition to turbulence takes place at almost the same point, roughly at 1/4 chord length for all the four setups. This is also confirmed by the velocity field, visible in Figure 6, which is characterised by separation on the leading edge followed by a separation bubble that sweeps the whole chord length and develops further in the wake.

PANS simulations were run with $\mathrm{f_k} = 0.2$ and are the only ones to catch unsteadiness in the flow. The oscillations are mild though, ranging to a maximum of 3.5% of the mean values. It is important to underline that in PANS simulations, and in particular for a quite low $\mathrm{f_k}$ as 0.2, a conspicuous amount of turbulence is expected to be resolved. Therefore it is physically unlikely to obtain a smooth periodic solution: this suggests that the first three grids are inappropriate for the model, whilst the finest one could be the first one to provide plausible data. Since the size of the finest grid used is already significant, it is not within the means of this work to accomplish a full study with this model, which would result in heavy computational costs and efforts; therefore, PANS results reported here have to be considered as preliminary.

7 Conclusions

The present work shows a general schedule to approach the study of the airflow surrounding the wings of *Morpho* butterflies using computational fluid dynamics. Moreover, it provides a mathematical model for computing

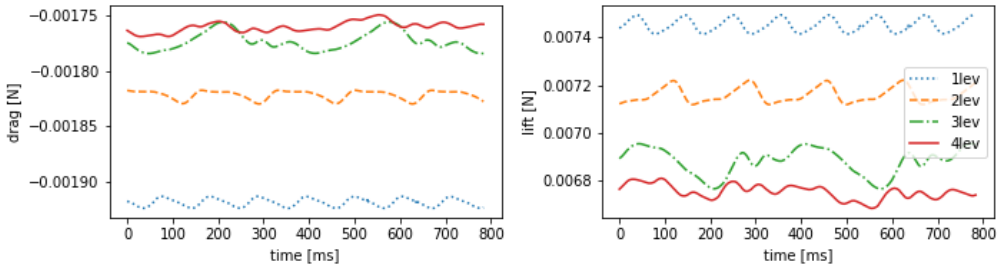

Fig. 8: Oscillatory aerodynamic forces for PANS simulations. Note that the coarser grids (1lev, 2lev, 3lev) provide periodical solutions, whilst the finest (4lev) provides a non periodical one.

the aerodynamic forces acting on a butterfly during gliding flight.

This study shows that, despite the strong assumptions and approximations made due to the limited tools available to study such delicate, small and light insects, numerical experiments can give results lying in the range of values indicated by experimental data.

The many different turbulence models used reveal concrete difficulties in catching the unsteady phenomena that experiments and previous literature suggest are taking place. Besides, $\kappa - \omega$ based models offer results that differ from each other by quantities that are consistently smaller than the ones between the experimental data and the numerical experiments themselves, stating how few the changes brought by transition modelling are. PANS simulations provide an interesting alternative surely capable to catch more detailed characteristics of the flow, even though this comes at a significant cost, which is perhaps unjustified considering the present setup, hypothesis, assumptions and uncertainties in the experimental data.

References

L. Eça and M. Hoekstra. A procedure for the estimation of the numerical uncertainty of CFD calculations based on grid refinement studies. *Journal of Computational Physics*, 262:104–130, 2014. ISSN 00219991. doi: 10.1016/j.jcp.2014.01.006. URL http://dx.doi.org/10.1016/j.jcp.2014.01.006.

R. B. Langtry and F. R. Menter. Transition Modeling for General CFD Application in Aeronautics. *43rd AIAA Aerospace Sciences Meeting and Exhibition*, pages 1–14, 2005.

F. R. Menter. Zonal Two Equation k-ω , Turbulence Models for Aerodynamic Flows . Florian R. Menter E. *24th Fluid Dynamics Conference July 6-9, 1993 / Orlando, Florida*, 1993.

F. R. Menter, R. B. Langtry, S. R. Likki, Y. B. Suzen, P. G. Huang, and S. VoÌlker. A Correlation-Based Transition Model Using Local Variables: Part I â Model Formulation. *Volume 4: Turbo Expo 2004*, (July):57–67, 2004. doi: 10.1115/GT2004-53452. URL http://proceedings.asmedigitalcollection.asme.org/proceeding.aspx?articleid=1638705.

S. P. Sane. The aerodynamics of insect flight. *Journal of Experimental Biology*, 206(23):4191–4208, 2003. ISSN 0022-0949. doi: 10.1242/jeb.00663. URL http://jeb.biologists.org/cgi/doi/10.1242/jeb.00663.

P. R. Spalart and S. R. Allmaras. A One-Equatlon Turbulence for Aerodynamic Flows. *30th Aerospace Sciences Meeting and Exhibit*, 1992.

G. R. Spedding, A. H. Hedenström, J. McArthur, and M. Rosén. The implications of low-speed fixed-wing aerofoil measurements on the analysis and performance of flapping bird wings. *Journal of Experimental Biology*, 211(2):215–223, 2008. ISSN 00220949. doi: 10.1242/jeb.007823.

Effect of Cavitation on the Structure of Tip Leakage Vortex in an Axial Water-Jet Pump

Mohammad Hossein Arabnejad*, Arash Eslamdoost*, Urban Svennberg† and Rickard E. Bensow*

*Chalmers University of Technology, Gothenburg, Sweden, † Kongsberg Maritime Sweden AB, Kristinehamn, Sweden

mohammad.h.arabnejad@chalmers.se.

1 Introduction

Water-jet propulsion systems with axial pumps are mostly used in high-speed vessels and vessels designed for shallow water operations. To achieve high performance in these systems, the pump often operates in cavitating conditions. One type of cavitation in water-jet pumps is cavitation occurring in Tip Leakage Vortex (TLV), a vortex formed due to a leakage flow in the gap region between the tip of a rotating impeller blade and the stationary shroud casing. As the formation of cavitating TLVs is associated with a higher risk of erosion near the blade tip and higher level of vibration and noise [1, 2], it is of interest to understand the structure of TLV and how it is affected by cavitation.

Experimental methods have been used to study TLV in water jet pumps. Wu et al. [3, 4] and Miorini et al. [5] investigated the flow structures and turbulence of TLV formed in an axial water jet pump using Particle Image Velocimetry (PIV) measurements. They showed that TLV originates from vortical structures shed from the blade tip. These structures wrap around each other and form the core of the TLV. As the main vortex migrates in the blade passage, it becomes stronger due to the entrainment of vortical structures. Tan et al. [6, 7] showed that cavitation can incept in the form of bubble cavitation at the core of the TLV. They also showed that by lowering cavitation number, sheet cavitation with unsteady closure line can appear on the suction side of the rotor blade.

In addition to experimental methods, a few number of numerical studies have been devoted to studying the non-cavitating and cavitating TLV in water-jet pumps. For example, Zhang et al. [8, 9] examined the structure of non-cavitating and cavitating TLVs at different flow rates and cavitation numbers. All of these numerical studies used Reynolds Averaged Navier Stokes (RANS) approach, which requires an ad-hoc modification to be able to predict the correct cavitation dynamics [10]. Furthermore, experimental studies by Wu et al. [4] have shown that the flow in the TLV is anisotropic and is controlled by several interacting shear layers. Capturing the dynamics of these shear layers and the correct behavior of non-cavitating and cavitating TLV requires a scale-resolving approach, such as Large Eddy Simulation (LES). In this study, the flow in an axial water-jet pump, AxWJ-2 [11], is studied using an LES approach. The simulations are performed for both non-cavitating and cavitating conditions and the predicted performance and cavitation patterns are compared with the experimental data by Tan et al. [7]. Then, the numerical results are used to study the effect of cavitation on the structure of the TLV.

2 Numerical Set-up

In this study, a modified version of the interPhaseChangeFoam solver from the OpenFOAM-2.2.x framework [12] is used to obtain the numerical results. The turbulence modeling is achieved using LES where a low-pass filter is applied to the governing equations. This filtering results in the sub-grid-scale terms in the momentum equations which are, here, modeled using the wall-adapting local eddy-viscosity (WALE) model proposed by Nicoud and Ducros [13]. For cavitating simulation, the cavitation dynamics is captured by Transport Equation Modelling (TEM), where a transport equation for the liquid volume fraction, α^l, is solved. This equation has source terms accounting for vaporization and condensation, which are modeled using Schnerr-Sauer cavitation model [14].

In this paper, the AxWJ-2 axial water-jet pump [11] from the Johns Hopkins University is selected for the simulations. A sketch of this pump and a summary of its relevant data are given respectively in Fig. 1 and Table 1.

Table 1: Summary of relevant data for AxWJ-2 axial water-jet pump

D_1	305.2 mm
D_2	213.4 mm
D_{rotor}	303.8 mm
Number of rotor blades n_R	6
Number of stator blades n_S	8
Nominal tip clearance h	0.7 mm
Angular speed of the rotor Ω	900 RPM

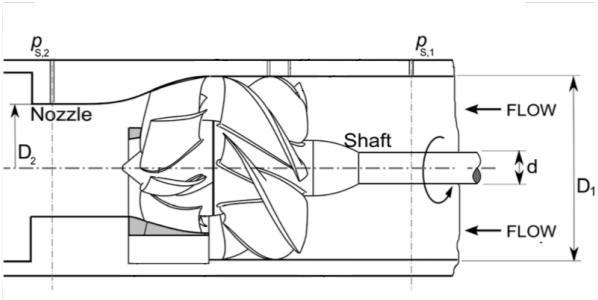

Fig. 1: Sketch of the AxWJ-2 axial water-jet pump [7]

Fig. 2a shows the computational domain used in this study. The computational domain is extended $10D_1$ upstream and downstream of the pump to reduce the interaction between the flow in the pump and the inlet and outlet boundary conditions. The domain is divided into three regions, inlet_pipe, rotor, and stator_outlet_pipe. Cyclic AMI interfaces are used for the boundaries between these regions. For the inlet_pipe, a fully structure grid is used. The mesh topology in the rotor region is shown in Fig. 2b. The mesh is divided into two regions with different types of mesh. The regions near the rotor blades, the hub, and the shroud are discretized with a structured hexahedral mesh, and the region in the middle of the passage is discretized with an unstructured mesh. To increase the mesh resolution in the tip leakage region, the resolution of this region for one blade is refined locally using refineHexMesh utility in OpenFOAM. The size of the refinement region relative to the radius of the pump is shown in Fig. 2b.

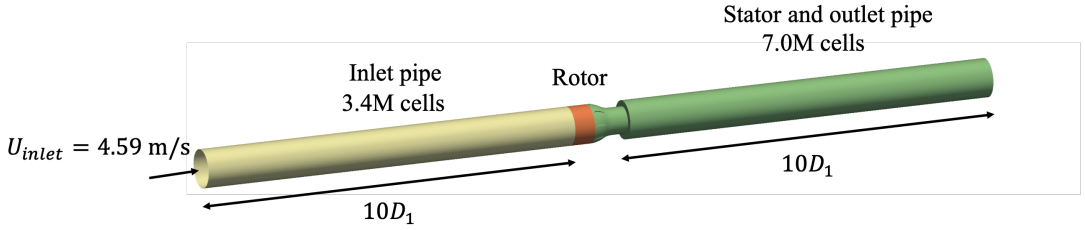

(a)

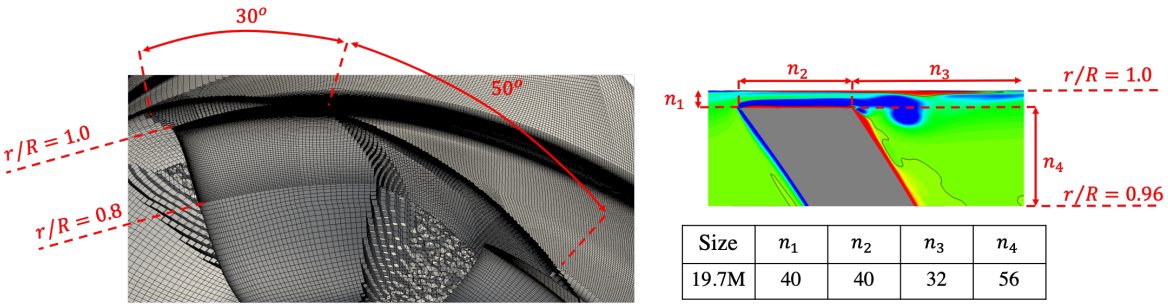

Size	n_1	n_2	n_3	n_4
19.7M	40	40	32	56

(b)

Fig. 2: a) Computational domain used in this paper, b) Mesh topology in the rotor region

3 Results

In the first part of the results, the predicted performance and cavitation pattern in the numerical simulation are compared with the experimental data by Tan et al. [7]. These authors reported the pump performance by two non-dimensional numbers, flow coefficient, φ, and head rise coefficient, ψ, which are defined as,

$$\varphi = \frac{Q}{nD_1^3}\ ,\ \psi = \frac{p_{s,2} - p_{s,1} + \frac{\rho}{2}\left[\left(\frac{Q}{A_2}\right)^2 - \left(\frac{Q}{A_1}\right)^2\right]}{\rho n^2 D_1^2}, \tag{1}$$

where Q is the volumetric flow rate in m^3/s and n is the shaft rotation speed in revolutions per seconds, and $p_{s,1}$, $p_{s,2}$, A_1, and A_2 are, respectively, the static pressures near the casing wall and the flow cross sections at location 1 and location 2, shown in Fig. 1. In this paper, we studied the pump at the flow coefficient, $\varphi = 0.75$. At this flow rate, the experimentally measured head rise coefficient, $\psi_{Exp.}$ is equal to 2.46. In table 2, the performance of the pump predicted by numerical simulations is compared with the experimental data. This comparison shows a good agreement between the predicted head-rise coefficient and experimentally measured one. It can also be concluded from table 2 that the effect of cavitation on the predicted performance at the cavitating condition studied here ($\sigma = 0.162$) is insignificant. This is expected as this condition is far away from the the cavitation breakdown according to Tan et al. [7].

Table 2: Performance of the pump predicted by numerical simulations

Simulations	σ	M_p	M_v	$M_{tot.}$	$\psi_{num.}/\psi_{exp.}$
Non Cavitating	∞	57.8	0.65	58.5	0.999
Cavitating	0.162	60.8	0.65	61.5	0.993

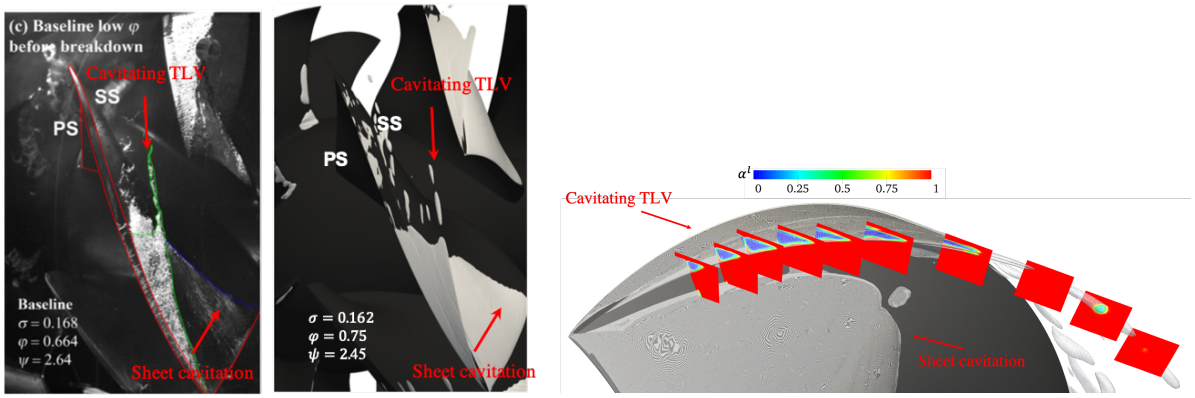

(a) HSV **(b)** Cavitating simulation

Fig. 3: Cavitating regions in a) High Speed Visualization (HSV) by Tan et al. [7] and b) Cavitating simulation (Cavitating regions are shows by an iso-surface of liquid volume fraction, α^l)

Fig. 3 shows the cavitation pattern captured by numerical simulation and the one in the experimental high speed visualization (HSV) by Tan et al. [7]. In the experiment, two main cavitating regions can be seen, sheet cavity formed on the suction side of the blade and the cavitating TLV. Comparison between numerical results and HSV shows that these cavitating region can be captured very well with the numerical simulation. From the distribution of liquid volume fraction on meridional planes in Fig. 3b, it can be seen that the cavitating TLV becomes thinner as it travels in the passage and that some cavitating vortices are detached from the trailing edge of the cavitating TLV. There is a also gap between cavitating TLV and sheet cavitation which indicates that the pressure in this region is higher than vapour pressure. This high pressure is due to the collision between the flow rotating around the cavitating TLV and the suction side of the blade. It can also be noted that the closure region of the sheet cavitation is unsteady and a vapour structure can be detached from the closure region due to this unsteadiness. Being able to capture this detachment is important as it has been shown in the previous studies that the detached cavity structures are associated with high risk of cavitation erosion [15].

In order to compare the structure of non-cavitating and cavitating TLV in the numerical simulations, the averaged tangential vorticity fields on several meridional planes are shown in Fig. 4. Three regions with high vorticity generation can be seen in the non-cavitating simulation. These regions are denoted by A, B, and C in Fig. 4a. Similar tangential vorticity distribution has been observed by Wu et al. [4] who showed that the high vorticity value in regions A, B, and C are, respectively, due to the shear layer between the reverse flow exiting the tip gap and the flow inside the passage, the boundary layer separation in the tip leakage flow near the rotor casing, and the core of the TLV. It can be seen in Fig. 4a that as

the main core of TLV (region C in Fig. 4a) develops in the passage, it detaches from the shear layer at the edge of the blade and the tangential vorticity in its centre decays. Comparison between Fig. 4a and 4b shows that the structure of the cavitating TLV is quite different from the non-cavitating one. In the first seven planes where cavitation exists according to Fig. 3b, a high value of vorticity occurs at the interface of the cavitating region instead of the centre of the cavitating TLV. No sign of the boundary layer detachment can be seen in these planes. However, in the last three planes, where a cavitating vortex is detached from the trailing edge of the cavitating TLV, the distribution of the averaged tangential vorticity is similar to the one in the non-cavitating TLV. In this region, the high value of tangential vorticity occurs in the detached vortex (region C in Fig. 4b) and the boundary layer detaches from the casing (region B in Fig. 4b). Similar to the non-cavitating TLV, the decay of tangential vorticity can be seen when the detached vortex travels in the passage.

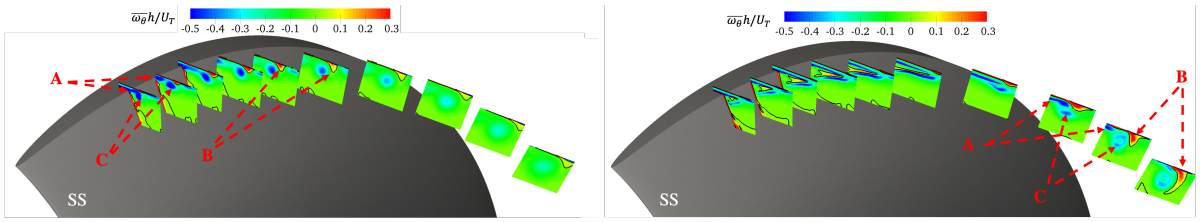

(a) $\sigma = \infty$ **(b)** $\sigma = 0.162$

Fig. 4: Comparison between the averaged tangential vorticity field on several meridional planes in non-cavitating and cavitating simulations (ω_θ: tangential vorticity, U_T: tangential velocity of the blade tip, h: tip gap height).

Fig. 5a and 5b show the distribution of averaged tangential velocity on several meridional planes in non-cavitating and cavitating simulations. In Fig. 5a, it can be seen that as the non-cavitating TLV travels downstream, the averaged tangential velocity increases around the centre of vortex. This increase occurs in the planes where averaged tangential vorticity in the core of the TLV decays (region B) in Fig. 4a. Wu et al. [4] postulated that both the increase in tangential velocity and the decay of tangential vorticity are due to the bursting of the TLV core. To confirm this, Fig. 5c shows an iso-surface of the Q criteria colored by the instantaneous tangential velocity in the non-cavitating simulation. It can be seen that the centre-line of the TLV is almost a straight line in the first five meridional planes and the tangential velocity is small around the TLV. As the vortex becomes unstable and its centre-line deviates from the straight line, spots with a high value of tangential velocity can be seen around the vortex. These spots, marked as region A in Fig. 5c, occur at the planes where the increase in average tangential velocity and the decay of tangential vorticity can be seen. Fig. 5b shows the averaged tangential velocity in the cavitating simulation. It can be seen that the tangential velocity in the cavitating region of TLV (first five planes in Fig. 5b) is high which means that the cavitating region rotates with the blade rotational speed. This is different from the non-cavitating TLV where the averaged tangential velocity is low in the first five planes in Fig. 5a. In the last three planes in Fig. 5b, where a cavitating vortex is detached from the edge of the cavitating TLV, the average tangential velocity is low around the core of cavitating vortex and it increases as the vortex travels in the passage which is similar to non-cavitating TLV. Fig. 5d shows an iso-surface of the Q criteria colored by the instantaneous tangential velocity in cavitating simulation. No vortical structure can be seen in the cavitating part of TLV and spots with high tangential velocity can seen when the centre-line of the cavitating vortex in the last three planes deviates from a straight line.

4 Conclusions

In this paper, we present LES results of non-cavitating and cavitating flows in an axial water-jet pump with the aim to study the effect of cavitation on the TLV. First, we compare the predicted performance and cavitation patterns with the experimental data by Tan et al. [7] and this comparison shows a very good agreement. Then, we investigate the structure of non-cavitating and cavitating TLVs by analyzing numerical results. Our results show that the structure of TLV is highly affected by the presence of cavitation. In the cavitating TLV, the high value of vorticity mostly occurs at the interface of the cavitating

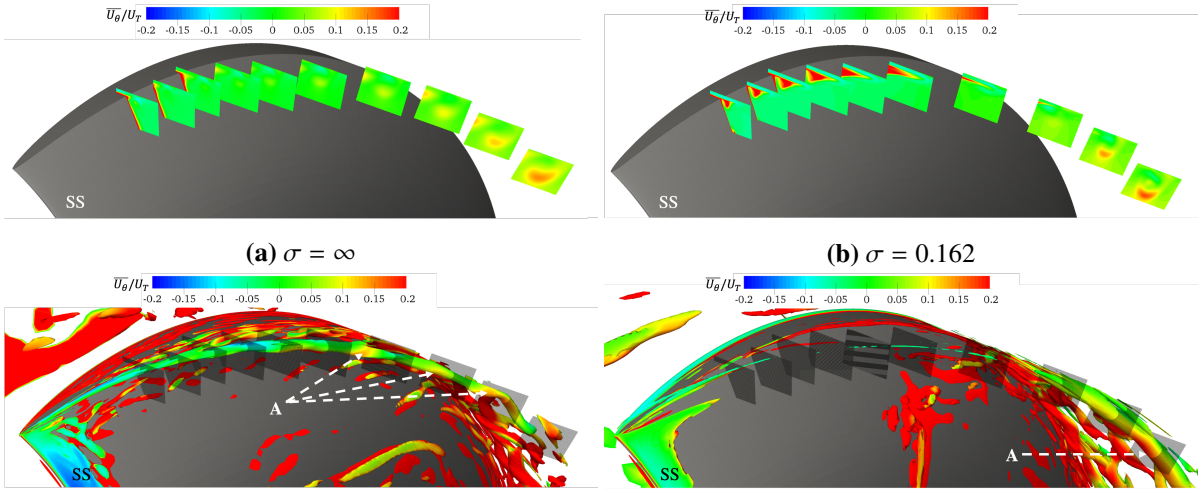

(a) $\sigma = \infty$ **(b)** $\sigma = 0.162$

(c) $\sigma = \infty$ **(d)** $\sigma = 0.162$

Fig. 5: Comparison between the normalized averaged tangential velocity and iso-surface of Q criteria colored by instantaneous tangential velocity in non-cavitating and cavitating simulations (U_θ: tangential velocity, U_T: tangential velocity of the blade tip)

region while in the non-cavitating TLV, a high value of vorticity can be seen in three regions, the shear layer between the reverse flow exiting the tip gap and the flow inside the passage, the boundary layer separation in the tip leakage flow near the rotor casing, and the core of the TLV. Furthermore, our cavitating simulations show that a cavitating vortex is detached from the trailing edge of the cavitating TLV. As this vortex travels in the passage, the averaged tangential vorticity in the vortex decays and the average tangential vorticity increases. Similar phenomena can be seen in the non-cavitating TLV and it is shown that these phenomena are due to the bursting of the vortex.

Acknowledgements

Financial support for this work has been provided by Kongsberg Maritime through the University Technology Centre in Computational Hydrodynamics hosted at the Division of Marine Technology, Department of Mechanics and Maritime Sciences at Chalmers. The simulations were performed on resources at Chalmers Centre for Computational Science and Engineering (C3SE) provided by the Swedish National Infrastructure for Computing (SNIC).

References

R. Laborde, P. Chantrel, and M. Mory, "Tip clearance and tip vortex cavitation in an axial flow pump," *Journal of Fluids Engineering*, vol. 119, no. 3, pp. 680–685, 1997.

F. Avellan, "Introduction to cavitation in hydraulic machinery," in *The 6th International Conference on Hydraulic Machinery and Hydrodynamics, Timisoara, Romania*, 2004, pp. 21–22.

H. Wu, D. Tan, R. Miorini, and J. Katz, "Three-dimensional flow structures and associated turbulence in the tip region of a waterjet pump rotor blade," *Experiments in Fluids*, vol. 51, no. 6, pp. 1721–1737, 2011.

H. Wu, R. L. Miorini, D. Tan, and J. Katz, "Turbulence within the tip-leakage vortex of an axial waterjet pump," *AIAA Journal*, vol. 50, no. 11, pp. 2574–2587, 2012.

R. Miorini, H. Wu, and J. Katz, "The internal structure of the tip leakage vortex within the rotor of an axial waterjet pump," *Journal of Turbomachinery*, vol. 134, no. 3, p. 031018, 2012.

D. Tan, R. Miorini, J. Keller, and J. Katz, "Flow visualization using cavitation within blade passage of an axial waterjet pump rotor," in *ASME 2012 Fluids Engineering Division Summer Meeting collo-*

cated with the ASME 2012 Heat Transfer Summer Conference and the ASME 2012 10th International Conference on Nanochannels, Microchannels, and Minichannels. American Society of Mechanical Engineers, 2012, pp. 395–404.

D. Tan, Y. Li, I. Wilkes, E. Vagnoni, R. Miorini, and J. Katz, "Experimental investigation of the role of large scale cavitating vortical structures in performance breakdown of an axial waterjet pump," *Journal of Fluids Engineering*, vol. 137, no. 11, p. 111301, 2015.

D. Zhang, W. Shi, B. van Esch, L. Shi, and M. Dubuisson, "Numerical and experimental investigation of tip leakage vortex trajectory and dynamics in an axial flow pump," *Computers & fluids*, vol. 112, pp. 61–71, 2015.

D. Zhang, W. Shi, D. Pan, and M. Dubuisson, "Numerical and experimental investigation of tip leakage vortex cavitation patterns and mechanisms in an axial flow pump," *Journal of Fluids Engineering*, vol. 137, no. 12, p. 121103, 2015.

O. Coutier-Delgosha, R. Fortes-Patella, and J. Reboud, "Evaluation of the turbulence model influence on the numerical simulations of unsteady cavitation," *Journal of Fluids Engineering*, vol. 125, no. 1, pp. 38–45, 2003.

T. Michael, S. Schroeder, and A. Becnel, "Design of the ONR AxWJ-2 axial flow water jet pump," Hydromechanics Department Report No. NSWCCD-50TR-2008/066., Tech. Rep., 2008.

H. Weller, G. Tabor, H. Jasak, and C. Fureby, "A tensorial approach to computational continuum mechanics using object-oriented techniques," *Computers in physics*, vol. 12, no. 6, pp. 620–631, 1998.

F. Nicoud and F. Ducros, "Subgrid-scale stress modelling based on the square of the velocity gradient tensor," *Flow, turbulence and Combustion*, vol. 62, no. 3, pp. 183–200, 1999.

J. Sauer, "Instationär kavitierende strömungen-ein neues modell, basierend auf front capturing (vof) und blasendynamik," *Diss., Uni Karlsruhe*, 2000.

M. Arabnejad, A. Amini, R. Bensow, and M. Farhat, "Experimental and numerical investigation of the cavitating flows over a modified NACA0009 foil," in *The 10th International Symposium on Cavitation (CAV2018), Baltimore, Maryland, USA*, 2018.

2D Numerical Simulations of Human Underwater Undulatory Swimming

Dorian A. G. Audot, Joseph Banks, Dominic Hudson
University of Southampton, UK
d.a.g.audot@soton.ac.uk

1 Introduction

In the highly competitive world of elite swimming, underwater phases became predominant in the recent decades (Veiga and Roig, 2016, Veiga et al., 2016). It all started in the late 80s when backstroke swimmers would spend more than half of their races underwater. Later on, swimmers like Michael Phelps proved that doing well and consistently underwater was a huge advantage. In modern swimming, performing well underwater became an indispensable skill to pretend to higher positions. It provides such an advantage that the regulations limit the distance swum underwater (FINA, 2017).
In three out of the four strokes, swimmers perform Underwater Undulatory Swimming (UUS). This technique tries to copy the way of motion of cetaceans. It consists in propagating a wave-like motion along the body, from the tip of the fingers to the toes. This wave amplifies as it goes down along the body and displaces the water surrounding the athlete downstream. The water is pushed down and thrust is produced (Pacholak et al., 2014).
Being underwater helps reducing wave drag (Vennell et al., 2006). It is known to be one of the greatest factor of resistance to swimming. Hence, executing this technique deep enough allow swimmers to maintain greater velocities than their surface swimming and optimize the overspeed phase (obtained from a push on the wall or a dive). For this reason, UUS has been a major focus of research studies in swimming science since late 90s.
The complexity of the motion, its physics and the implication of human swimmers (repeatability, fatigue, non unique body shapes or techniques, ...) makes both experiments and simulations tedious. Experiments are extremely hard to assess as it is difficult to evaluate a swimmer's ability to adapt a stroke he has practiced for years to a requested change (frequency, amplitude, ...). Logically, computational methods seem to be the most convenient way to study UUS.
The most complete simulations feasible at the moment are undoubtedly 3D unsteady simulations (Pacholak et al., 2014). However, they have an important computational cost. This cost dissuades doing studies that would require a great number of simulations (e.g : optimization studies). Thus, would it be possible to reduce our exigencies to have the best simulation and opt for a much simpler model? That would greatly help exploring even more aspects of the UUS performance. Consequently, developing such a tool to perform quick viable simulations seems like a necessity.
LilyPad (Weymouth, 2015b) is a 2D Implicit Large Eddy Simulation (ILES) CFD solver developed to compute fast simulations by using simple high speed methods. LilyPad is written on Processing (Foundation Processing, 2001). Its purpose is solving simple fluid structure interactions problems on Uniform Cartesian Grids using a Boundary Data Immersion Method (BDIM).
Our idea is to realize a simple modeling of a swimmer performing UUS using LilyPad's fast simulations. The goal would be to quickly obtain interesting trends or results to help understand what are the key factors of performance in UUS.

2 Methods

This section describes the methodology we have followed to implement a model of an undulating swimmer in LilyPad. This includes how we defined the kinematics of the swimmer, how we modeled the body and a quick overview of how the simulation is solved and configured.
We assumed that the motion of UUS is almost strictly two-dimensional (in the sagittal plane) and that the distances between consecutive joints along a swimmer's body are constant. These two hypothesizes are not strong but are necessary. They introduce some errors since it is neglecting the natural internal rotation of a swimmer during UUS and the possible extension of the joints during the motion. However, the most important aspect of such simulations is to capture the global physics of the motion and we do not expect

these assumptions to excessively alter the results.
Thus, the UUS kinematics can be defined by the vertical position of seven joints along a swimmer's body and the distance separating these. These joints are the following: fingertips, wrists, shoulders, hips, knees, ankles and toe-tips. We can easily obtain the coordinates of these points through the digitization of recordings of swimmers performing UUS (Fig. 2.b). The vertical position is then fitted with a simple sine function (see Eq. 1). An example of such a fit is provided in Fig. 1.

$$y_i(t) = A_i.cos(2\pi f.t + C_i) + D_i \tag{1}$$

Here, y_i is the function of the time t representing the vertical position of the i^{th} joint of the body, A_i is the amplitude, f is the frequency, C_i is the phase shift of the wave at that position of the body and D_i is the mean vertical position of that joint. Approximating the joints' kinematics with a sine function is viable according to Gavilan et al., 2006. They used Fourier Transformation to study the contribution of the Harmonics of the body-wave. It appeared that the fundamental (first harmonic) contributes to more than 90% of the power production of the motion.
Regarding how our fitting curves seem to be capturing the raw kinematic data of every joint (see Fig. 1), we consider that this sine approximation is completely acceptable.
Because the kinematics are defined by seven joints, there are necessarily six segments linking them :

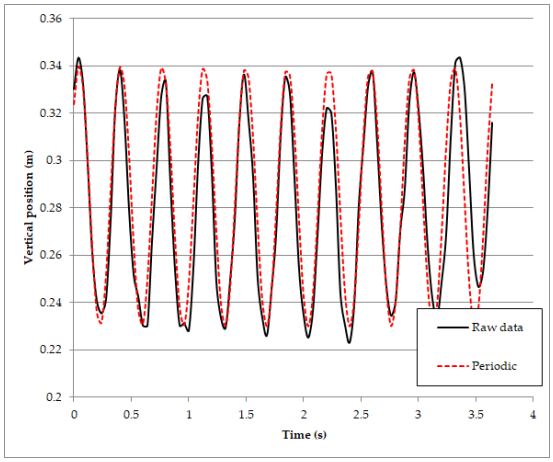

Fig. 1: Periodic sine function fit on the raw vertical position of the toes of a swimmer

hands, arms (elbows are considered to not bend and have a limited impact on thrust production), trunk, thighs, shanks and feet. Each segment is defined by its length and the thicknesses of the two joints it is linking. The simplest body shape model to avoid overlapping, to be able to pilot each segment independently and that would look like a swimmer was a succession of deformed hexagons (see Fig. 2.a). The horizontal position of the hands is fixed and the joints' horizontal coordinates are calculated accordingly to the vertical position and the segments' lengths.
The mesh is based on a Uniform Cartesian Grid (the distance separating a cell to its neighboring cells in the four directions is the same and constant for every cell of the mesh). We chose a squared domain with a side-length of $8m$. This decision was taken arbitrary as it would allow us to observe enough wake behind the swimmer and have enough stream ahead of it while the mesh size reasonable (see Table 1). The length of a human swimmer in streamline position with its arms extended above the head is about $2.5m$ (see Fig 2.b to have a streamline position example). The resolution of the grid is defined by x. As the number of cells along the longitudinal direction n has to be calculated using the following calculation $n = 2^x$.
The convergence study showed that the pressure forces were converging for $x \geq 9$. Table 1 shows the cell size, the approximate number of cells along the modeled swimmer ($\approx 2.5m$) and the total number of cells in the mesh corresponding to x value. For computational cost purposes, we obviously chose $x = 9$ for our studies.
LilyPad uses a BDIM to solve the fluid-body interaction on the grid. The complete theory of this method

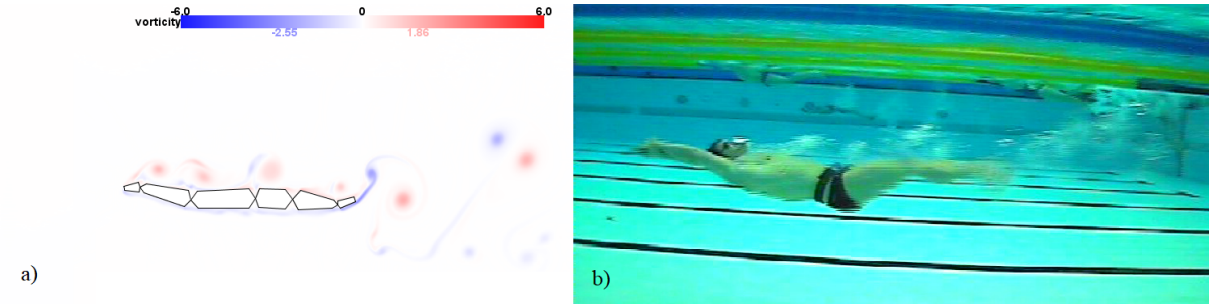

Fig. 2: a) Snapshot of the vorticity of our simulation during the down-kick phase. b) Snapshot of the video footage recording an elite swimmer performing UUS

Table 1: Resolution of the mesh and its size regarding values of x

x	Cell length (mm)	Number of cells along the model swimmer	Total number of cells in the mesh
9	15.7	160	262,144
10	7.82	320	1,048,576
11	3.91	640	4,194,304

is explained in Maertens, Audrey P. and Weymouth, Gabriel D., 2015. The flow is resolved using ILES because of its performances and to get rid of the modelling of sub-grid turbulences (which do not really have a physical meaning in two dimensions). The two different schemes that are implemented are a flux-limited QUICK or a Semi-Lagrangian convection scheme (Weymouth, 2015a). Our simulations are computed using the QUICK scheme.
The time stepping is calculated internally by LilyPad in order to optimize the computational time of the simulations. The repeatability is excellent and successive simulations using the same conditions give exactly the same results.
Now that the methodology has been presented, we are going to discuss about the validations and some preliminary results to estimate the viability of this method.

3 Validation

The simulations being 2D, we do not expect to obtain precise values of the forces, having a good order of magnitude is enough. Thus, the validation's goal is to check if the code captures correctly the physics of the unsteady motion.
The numerical validation is done by two means : verifying the evolution of the drag with parameter sweeps (frequency, inflow velocity and amplitude) and verifying the maintained swimming speed of a swimmer in the simulation (regarding its measured velocity).
We gathered kinematics from an international elite swimmer (previously world record holder) performing UUS in a backstroke position (see Fig 2.b). He was told to push from the wall and perform a maximum velocity trial. His speed is acquired using a built-in device which consists in a rotating sensor (sampling frequency of $250Hz$) linked to a reel of fishing string. The string is attached to the swimmer's hips using a belt-like system and his instantaneous velocity is obtained (Fig. 3). On the trace of the velocity we can clearly observe successive acceleration and deceleration phases. Two successive acceleration peaks correspond to the up-kick and the down-kick. Here, the up-kick is having greater performance (as the swimmer is on the back). Determining the timing between consecutive up-kick velocity peaks gives us the swimming frequency of the undulation. According to the velocity trace, the kicking frequency of that swimmer is $2.76Hz$. The average velocity, once the global deceleration has settled (after $2s$ on Fig. 3) is $1.86m.s^{-1}$.
The kinematics input in the code are obtained from a video footage of the trial discussed previously (see

Fig. 2.b.). The segments lengths is measured on the swimmer and the sine approximation to fit the raw data is done.
We ran a simulation with the kinematics and frequency chosen to correspond to the video trial's values.

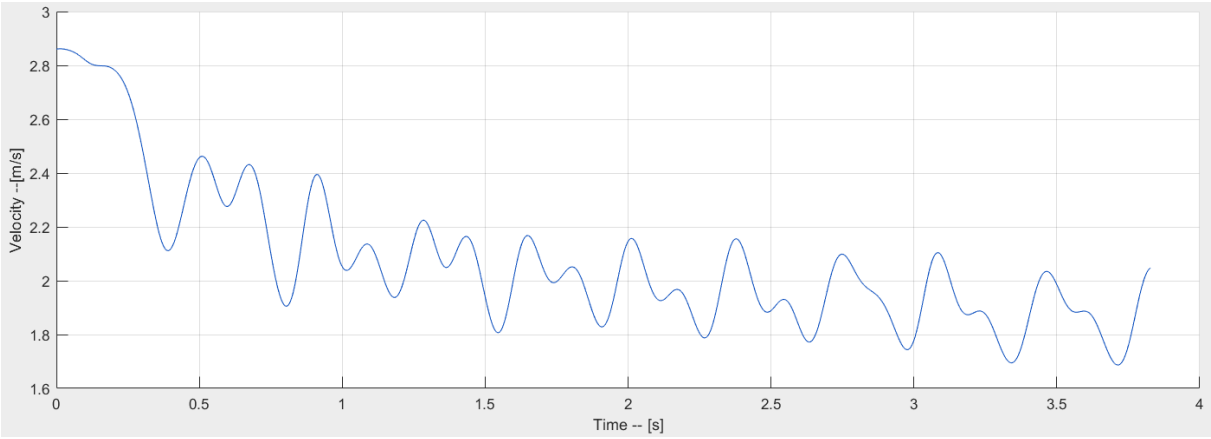

Fig. 3: Trace of the instantaneous velocity of the swimmer recorded using a built-in device

The resolution of the mesh is chosen as $x = 9$. We match the inflow velocity to have an average drag coefficient over a few cycles, from 9^{th} till 14^{th}, of 0. This resulted in a maintained UUS simulated speed of $1.87 m.s^{-1}$. That value is extremely close to the actual swimmer's speed and comforts us in the idea that such simulations can be viable. Different sets of kinematics will be used for further validation as one case might not be enough.
With the kinematics gathered, we realized three parameter sweeps to check how the output of the simulations is affected. The idea of these preliminary studies is to vary only one parameter and keep all the others constant. The way the forces evolve gives us a verification that the unsteady physics of UUS are well captured.
The three tests we did gave the following results:

- Velocity sweep : we varied the inflow velocity of the simulation around the natural maintained swimming speed. When the velocity increases, the mean drag coefficient (from the 9^{th} to the 14^{th} cycle) decreases and, reciprocally, when the velocity decreases, the average drag coefficient increases. A positive average drag coefficient means that the swimmer is giving, overall, more energy to the flow. Hence, if it is positive, the swimmer should be going faster and similarly, if the value is negative, the swimmer should be slowed down by the flow.

- Frequency sweep : we varied the kicking frequency of the swimmer. His performance decreased when kicking slower and increased when kicking faster.

- Amplitude sweep : by using a coefficient to reduce all the vertical amplitudes of every joints (by the same amount), we observed that the maintained swimming speed was reduced and that the more we reduced the amplitude the poorer were the performances.

These results comforted us in the fact that such simulations could be used to study UUS. This method could eventually help us identify different key factors of UUS performance.
The next section will describe the development perspectives for the method, and gives some example of studies that could be carried on in the near future.

4 Next Steps

Even though the results are really encouraging, further validations will be required. We will study different set of kinematic data (of different swimmers?) and verify the hierarchy of the simulated maintained velocity swimming speed between these different strokes while also checking if they correspond to the

measured velocities. Making sure that a stroke having a slower recorded velocity than another faster stroke, also reaches a slower velocity in the simulation.
Moreover, we will have to establish how much does the 2D affect the flow and the forces applied on the swimmer. This aspect of the simulation needs to be explored as we do know that it affects the flow representation and the forces (Taira and Colonius, 2009, Lei et al., 2001 and Mittal and Balachandar, 1995) but, no studies considered looking at how much it altered the forces on such unsteady simulations. Extending the exact same model in the third dimension would allow the turbulence to happen and eventually help dampen smaller flow structures and thus changing the forces applied on the body. Comparing the output of the 2D and the extended 2D simulations could give us an idea of how much the forced 2D turbulence is impacting our computations.
Next, I will present a succession of studies that could be led later using the same method:

- A calculation of the hydrodynamic efficiency (von Loebbecke et al., 2009b) could be easily added and would help to quickly assess the hydrodynamic cost of different techniques.
- Doing a velocity sweep for techniques of different amplitudes in overspeed situation to study the trade off between thrust production and drag.
- It is possible to study the repartition and the direction of the pressure forces along the body. Similarly to von Loebbecke et al., 2009a and Nakashima, 2009 it would be interesting to look at how these two parameters are affected by a change of technique.
- Studying the relevance of the Strouhal number St on UUS. The Strouhal number is a dimensionless number describing oscillating flow oftenly used to describe fish locomotion (Zhu et al., 2002) and used in many other underwater swimming studies (Colomina et al., 2003). We would realize different simulations having the exact same St value. We now know that this number is not likely to describe the hydrodynamic efficiency (von Loebbecke et al., 2009b, Shimojo et al., 2014, Yamakawa et al., 2017). But, can that number help understand the flow mechanism in the wake? Could it describe the propulsion mechanism?

Developing such a method for numerical simulations of UUS could be an asset as such studies, that require a lot of simulations, would be doable. Hopefully, using this method would broaden the spectrum of things we know about swimming science.

References

Colomina, R. A., Pardillo, S., and Gavilán, A. (2003). Usefulness of the strouhal number in evaluating human underwater undulatory swimming. *IXth international symposium on biomechanics and medicine in swimming*.

FINA (2017). FINA Swimming Rules Part 3.

Foundation Processing (2001). Processing. https://www.processing.org/.

Gavilan, A., Arellano, R., and Sanders, R. (2006). Underwater Undulatory Swimming: Study of Frequency, Amplitude and Phase Characteristics of the 'Body Wave'. *Biomechanics and Medicine in Swimming X, 35-37Biomechanics and Medicine in Swimming X, 35-37*.

Lei, C., Cheng, L., and Kavanagh, K. (2001). Spanwise length effects on three-dimensional modelling of flow over a circular cylinder. *Computer methods in applied mechanics and engineering*, 190:2909–2923.

Maertens, Audrey P. and Weymouth, Gabriel D. (2015). Accurate Cartesian-grid simulations of near-body flows at intermediate Reynolds numbers. *Computer Methods in Applied Mechanics and Engineering*.

Mittal, R. and Balachandar, S. (1995). Effect of three-dimensionality on the lift and drag of nominally two-dimensional cylinders. *Physics of Fluids*, 7(8):1841–1865.

Nakashima, M. (2009). Simulation analysis of the effect of trunk undulation on swimming performance in underwater dolphin kick of human. *Journal of Biomechanical Science and Engineering*.

Pacholak, S., Hochstein, S., Rudert, A., and Brücker, C. (2014). Unsteady flow phenomena in human undulatory swimming: a numerical approach. *Sports Biomechanics*.

Shimojo, H., Sengoku, Y., Miyoshi, T., Tsubakimoto, S., and Takagi, H. (2014). Effect of imposing changes in kick frequency on kinematics during undulatory underwater swimming at maximal effort in male swimmers. *Human Movement Science*.

Taira, K. and Colonius, T. (2009). Three-dimensional flows around low-aspect-ratio flat-plate wings at low Reynolds numbers. *Journal of Fluid Mechanics*, 623:187–207.

Veiga, S. and Roig, A. (2016). Underwater and surface strategies of 200 m world level swimmers. *Journal of Sports Sciences*.

Veiga, S., Roig, A., and Gómez-Ruano, M. A. (2016). Do faster swimmers spend longer underwater than slower swimmers at World Championships? *European Journal of Sport Science*.

Vennell, R., Pease, D., and Wilson, B. (2006). Wave drag on human swimmers. *Journal of Biomechanics*.

von Loebbecke, A., Mittal, R., Fish, F., and Mark, R. (2009a). A comparison of the kinematics of the dolphin kick in humans and cetaceans. *Human Movement Science*.

von Loebbecke, A., Mittal, R., Fish, F., and Mark, R. (2009b). Propulsive Efficiency of the Underwater Dolphin Kick in Humans. *Journal of Biomechanical Engineering*.

Weymouth, G. D. (2015a). Lily Pad: Towards Real-time Interactive Computational Fluid Dynamics.

Weymouth, G. D. (2015b). Real-time two-dimensional fluid dynamics simulations in Processing. https://github.com/weymouth/lily-pad.

Yamakawa, K. K., Shimojo, H., Takagi, H., Tsubakimoto, S., and Sengoku, Y. (2017). Effect of increased kick frequency on propelling efficiency and muscular co-activation during underwater dolphin kick. *Human Movement Science*.

Zhu, Q., Wolfgang, M. J., Yue, D. K., and Triantafyllou, M. S. (2002). Three-dimensional flow structures and vorticity control in fish-like swimming. *Journal of Fluid Mechanics*.

Propeller Performance Prediction in an Artificially Generated Wake Field Using RANSE

João Baltazar*, Bart Schuiling†, and Douwe Rijpkema†
*IST Universidade de Lisboa, Portugal, †MARIN, Wageningen/the Netherlands
joao.baltazar@tecnico.ulisboa.pt

1 Introduction

Marine propellers usually operate behind a ship and are subject to a non-uniform inflow field due to the ship's boundary layer and wake system. This flow field is responsible for unsteady loads on the blades and often for the occurrence of unsteady cavitation phenomena, which are important in the analysis of shaft vibrations and pressure fluctuations.

RANSE (Reynolds-Averaged Navier-Stokes Equations) solvers are becoming a widely used tool for the modelling of the unsteady flow around propellers operating behind a ship. However, RANSE solvers are also associated with large computational requirements. Mikkelsen et al. (2007) introduced a method using body-forces for the generation of the ship wake field. These body-forces were combined with RANSE for the prediction of the propeller performance without the presence of the ship hull, reducing substantially the computational cost. A similar method was implemented by Shin et al. (2011) for unsteady cavitation simulations. These results have shown the feasibility of the method for the generation of a desired ship hull wake and prediction of the blade-load variations.

The aim of the present paper is to present a method for an accurate prediction of the propeller unsteady performance in an artificial wake field using RANSE in a cost-effective way. The propeller performance predictions in this artificial wake field are compared to the predictions in behind the ship. The paper is organised as follows: the major features of the numerical method are presented in Section 2; the test case and numerical set-up are described in Section 3; the numerical results are shown in Section 4; in Section 5 the main conclusions are drawn.

2 Numerical method

For the flow simulations, the RANSE (continuity and momentum equations) are solved using the ReFRESCO code (www.refresco.org). For turbulence closure, the $k-\omega$ SST turbulence model is chosen, Menter et al. (2003). A finite-volume discretisation technique with cell-centred collocated variables is used for solving the equations, and a pressure-correction equation based on the SIMPLE algorithm is used to ensure mass conservation. Time integration is performed implicitly with a second-order backward scheme. At each implicit time step, the non-linear system for velocity and pressure is linearised with Picard's method and a segregated approach is adopted for the solution of all transport equations. For the convective flux terms, a second-order scheme (QUICK) is applied for the momentum equations, and a first-order upwind scheme is applied for the turbulence model equations.

Body-forces are added to the momentum equation to generate the wake field. Based on the Rankine-Froude momentum theory and considering a uniform inflow velocity along the x direction, in this case equal to the ship velocity V_S, the local body-force $F_{x,y,z}$ on the actuator disc for an intended wake field $V_{w_{x,y,z}}$ may be written as

$$\begin{aligned} F_x &= -1/2\rho\,(V_S - V_{w_x})\,(V_S + V_{w_x})\,\frac{\Delta A}{\Delta V} \\ F_y &= 1/2\rho\,(V_S + V_{w_x})\,V_{w_y}\,\frac{\Delta A}{\Delta V} \\ F_z &= 1/2\rho\,(V_S + V_{w_x})\,V_{w_z}\,\frac{\Delta A}{\Delta V} \end{aligned} \quad , \tag{1}$$

where ΔA is the cell area perpendicular to the axial direction and ΔV is the cell volume. We note that the minus sign represents the deceleration of the flow in the x direction, simulating the bare hull wake field.

Due to the strong interaction between the axial and the transversal flows, the body-forces are calibrated iteratively by adjusting the wake velocity components:

$$\begin{aligned} F_x^{(i)} &= -1/2\rho\left(V_S - V_{w_x}^{(i)}\right)\left(V_S + V_{w_x}^{(i)}\right)\frac{1}{\Delta V^{1/3}} \\ F_y^{(i)} &= 1/2\rho\left(V_S + V_{w_x}^{(0)}\right)V_{w_y}^{(i)}\frac{1}{\Delta V^{1/3}} \qquad , \; i = 1, 2, \ldots, \\ F_z^{(i)} &= 1/2\rho\left(V_S + V_{w_x}^{(0)}\right)V_{w_z}^{(i)}\frac{1}{\Delta V^{1/3}} \end{aligned} \tag{2}$$

with

$$V_{w_{x,y,z}}^{(i)} = V_{w_{x,y,z}}^{(0)} - \beta\left(V_{w_{x,y,z}}^{(i-1)} - V_{w_{x,y,z}}^{(0)}\right), \tag{3}$$

where the cell area and volume are assumed proportional to h^2 and h^3 respectively, with h as the typical cell size, $V_{w_{x,y,z}}^{(0)}$ represents the intended wake field and β is a relaxation factor assumed equal to 0.5. In the present work, the body-forces are applied one propeller diameter upstream of the propeller plane.

3 Test case and numerical set-up

The KRISO Container Ship (KCS) is considered in the present study. For this ship there is an extensive experimental data set available, which has been used in the comparisons with contemporary CFD codes used in hydrodynamics, see for instance, Larsson et al. (2014). The KCS is a single screw container ship built only as a model with a scale ratio of 31.5994. It has a length between prependiculars of $L_{pp} = 7.2786$m, with a draft of 0.3418m and wetted surface of 9.4379m^2. It was equipped with a five blade right-handed propeller with a diameter of 0.25m. The propeller has a mean pitch-diameter ratio of 0.95, a blade-area ratio of 0.8 and a skew angle of 24 degrees at the tip.

The simulation of the viscous flow around KCS with operating propeller behind is first considered. The calculation is carried out with fixed free-surface, at a ship speed of 2.196m/s and an imposed propeller rotation rate of 9.75rpm. The corresponding Reynolds and Froude numbers based on the length between perpendiculars are 1.4×10^7 and 0.26, respectively. A rectangular computational domain is considered. The size of the computational domain is $3L_{pp}$ at upstream, $6L_{pp}$ at downstream, and $4L_{pp}$ in both transverse and vertical directions. At the propeller region, a sliding block is defined to implement the effect of propeller rotation. The total length and radius of the propeller domain are $0.325D$ and $0.55D$, respectively, where D is the propeller diameter. The inlet is located at $0.15D$ in front of the propeller plane and the outlet is at $0.175D$ behind it. For the generation of the grids, the grid meshing tool HEXPRESS (www.numeca.com), which uses an unstructured grid approach with hanging nodes for refinement, is considered for the hull domain. For the propeller domain, a multi-block structured grid is generated using the grid meshing package GridPro (www.gridpro.com). The grid sizes are 18.4M and 2.9M cells for the hull domain and the propeller domain, respectively. For the prediction of the nominal wake field, a bare hull simulation with the same fixed free-surface is made. A similar grid in comparison with the KCS with operating propeller is generated, keeping the computational domain dimensions. In this case the grid size is 18.8M cells. A comparison of the grids used in the simulations around the KCS with and without propeller is shown in Fig. 1.

For the simulation of the nominal wake field, an iterative calibration of the body-forces is made. Calculations are carried out without the propeller geometry (hub only) in a cylindrical domain with a length of $5D$ in all directions. The grid is generated using the grid meshing tool HEXPRESS and consists in 3.2M cells. For the prediction of the propeller performance in behind conditions using the artificial generated wake field, a similar computational domain is defined. In this case, the propeller region is defined as a separate sliding block, and the same propeller grid as used in the KCS calculations with operating propeller is considered. A comparison of the grids used in the simulations with and without propeller, here referred as open-water conditions, is shown in Fig. 2.

In this study, a fine boundary layer resolution is applied for all grids to obtain $y^+ \sim 1$. The boundary conditions remained fixed for all calculations: no-slip and impermeability conditions are applied at the propeller, hub and hull; at the inlet the ship velocity, an turbulence intensity of 1% and an eddy-viscosity

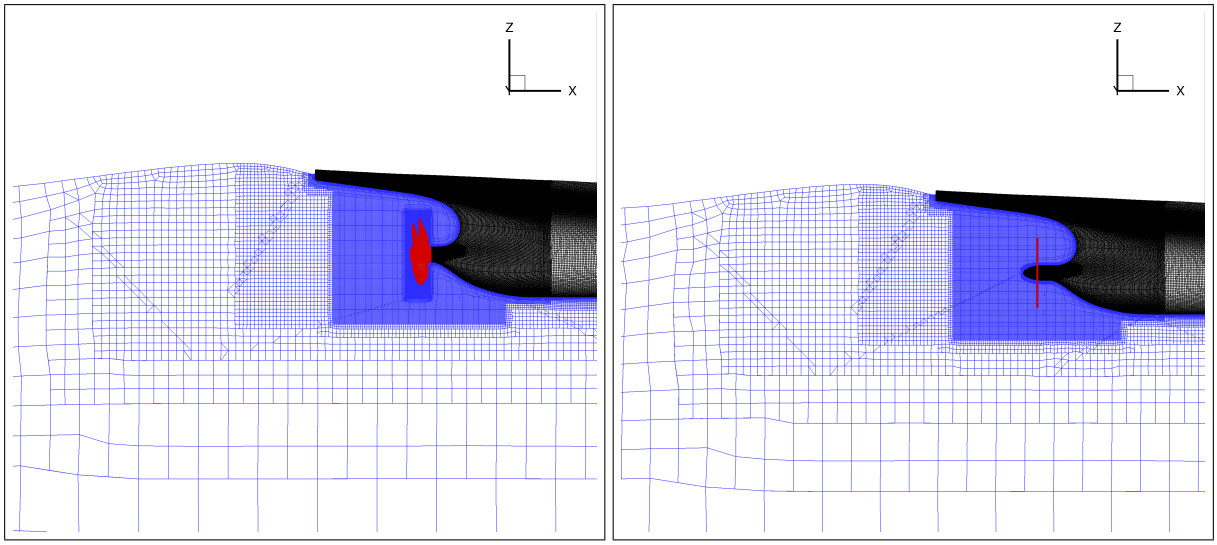

Fig. 1: Overview of the grids for the propeller simulations in behind condition (left) and bare hull simulations (right). The red line in the right figure represents the wake field extraction location.

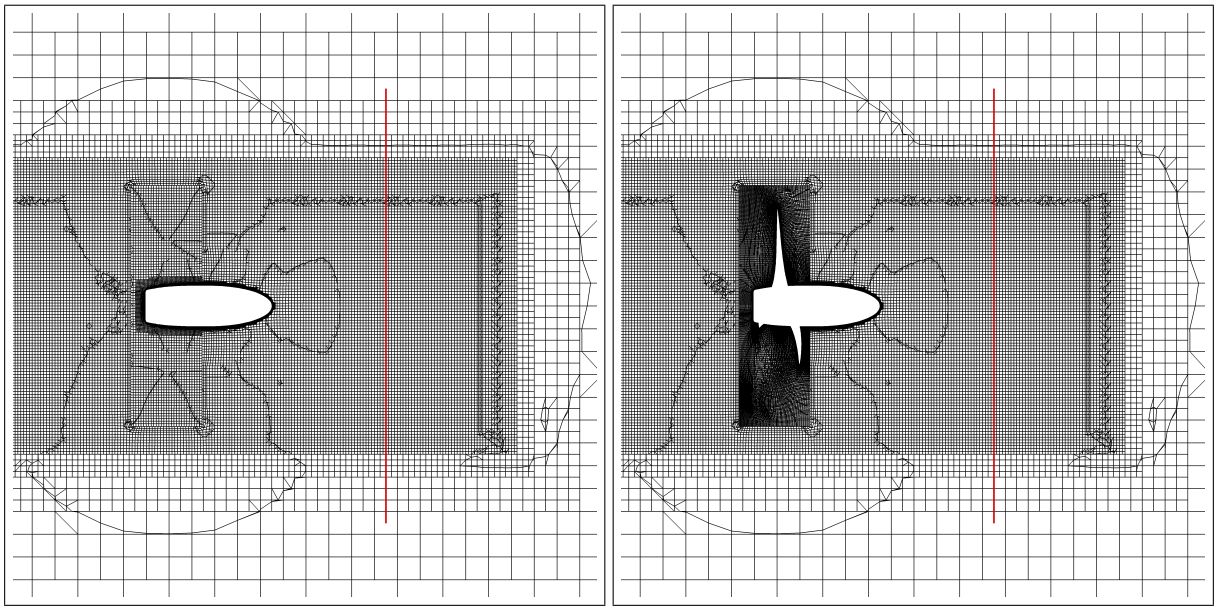

Fig. 2: Overview of the grids for the generation of the wake field (left) and propeller simulations without hull (right). The red line represents the body-forces location.

ratio of $\mu_t/\mu = 1$ are prescribed; for the open-water outlet boundary, a zero downstream gradient is assumed for all flow variables; for the hull free-surface and side boundaries zero normal derivatives are applied to the velocity and to the turbulence quantities, whereas the normal velocity is set equal to zero; finally, a constant pressure equal to the undisturbed flow pressure is considered for the hull outlet and bottom boundaries, and the open-water outer boundary.

4 Results

Results are presented and analysed for the four RANSE simulations in this section. The propeller operating conditions are defined by a single non-dimensional parameter: the advance coefficient $J = V_S/(nD)$, where $n = \Omega/(2\pi)$ is the rate of revolution. The general performance characteristics of the propeller are defined by the thrust coefficient $K_T = T/(\rho n^2 D^4)$, and the torque coefficient $K_Q = Q/(\rho n^2 D^5)$, where T is the thrust, Q the torque and ρ the fluid density.

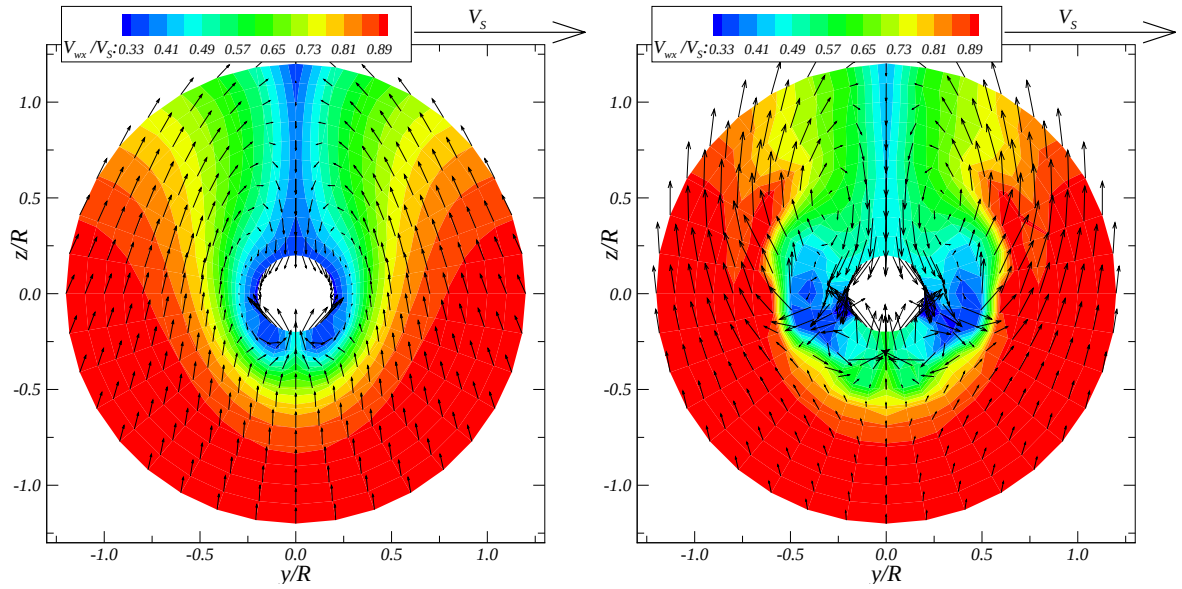

Fig. 3: Predicted nominal wake field from bare hull simulation (left) and generated wake field using calibrated body-forces (right). R denotes the propeller radius.

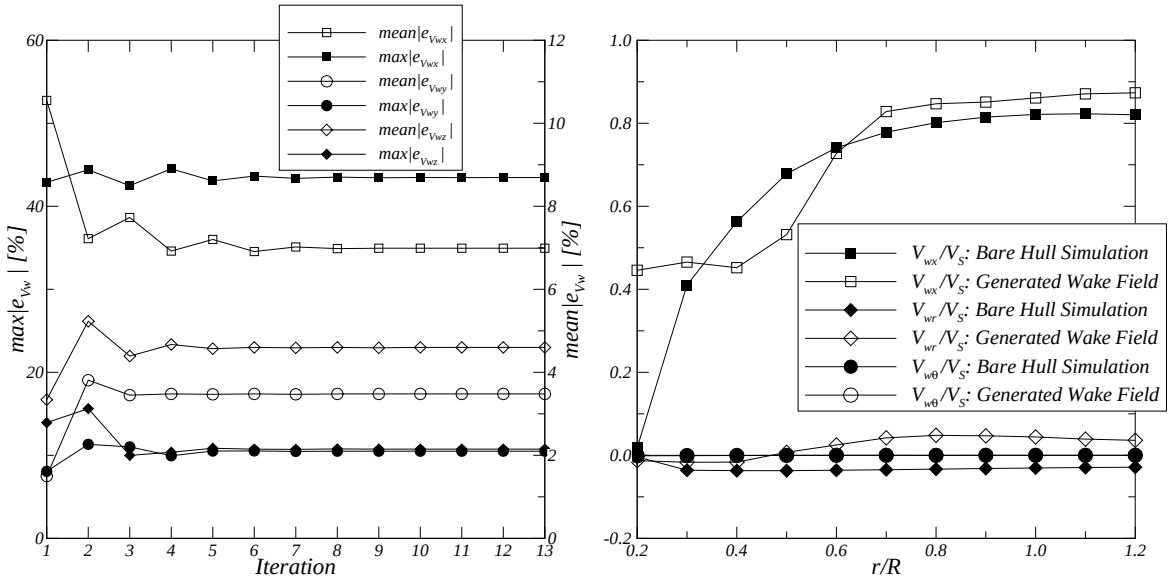

Fig. 4: Convergence history of the mean and maximum differences between the generated wake field using body-forces and the predicted nominal wake field in respect to the ship velocity (left). Comparison of the circumferential average wake fields (right).

4.1 Wake field generation

From the bare hull simulation, the nominal wake field is obtained. The wake velocities are extracted from discrete points in the propeller plane with an angular resolution of 10 degrees at 11 radial sections. For the iterative solution of the transport equations, maximum normalised residuals around 10^{-1} and 10^{-4} are obtained for the velocities and pressure, respectively. The predicted nominal wake field is presented in Fig. 3-(left), where a wake peak is observed near the 12 o'clock position (corresponding to azimuthal position of 0 degrees). From the open-water simulations without propeller, an artificial wake field is generated using iteratively calibrated body-forces. The obtained wake field is shown in Fig. 3-(right). In this case, iterative convergence below 10^{-6} is obtained for all flow quantities. From the comparison with the nominal wake field, a weaker peak is predicted and larger transversal velocities are observed at the inner radii. Note that these two cases correspond to steady computations.

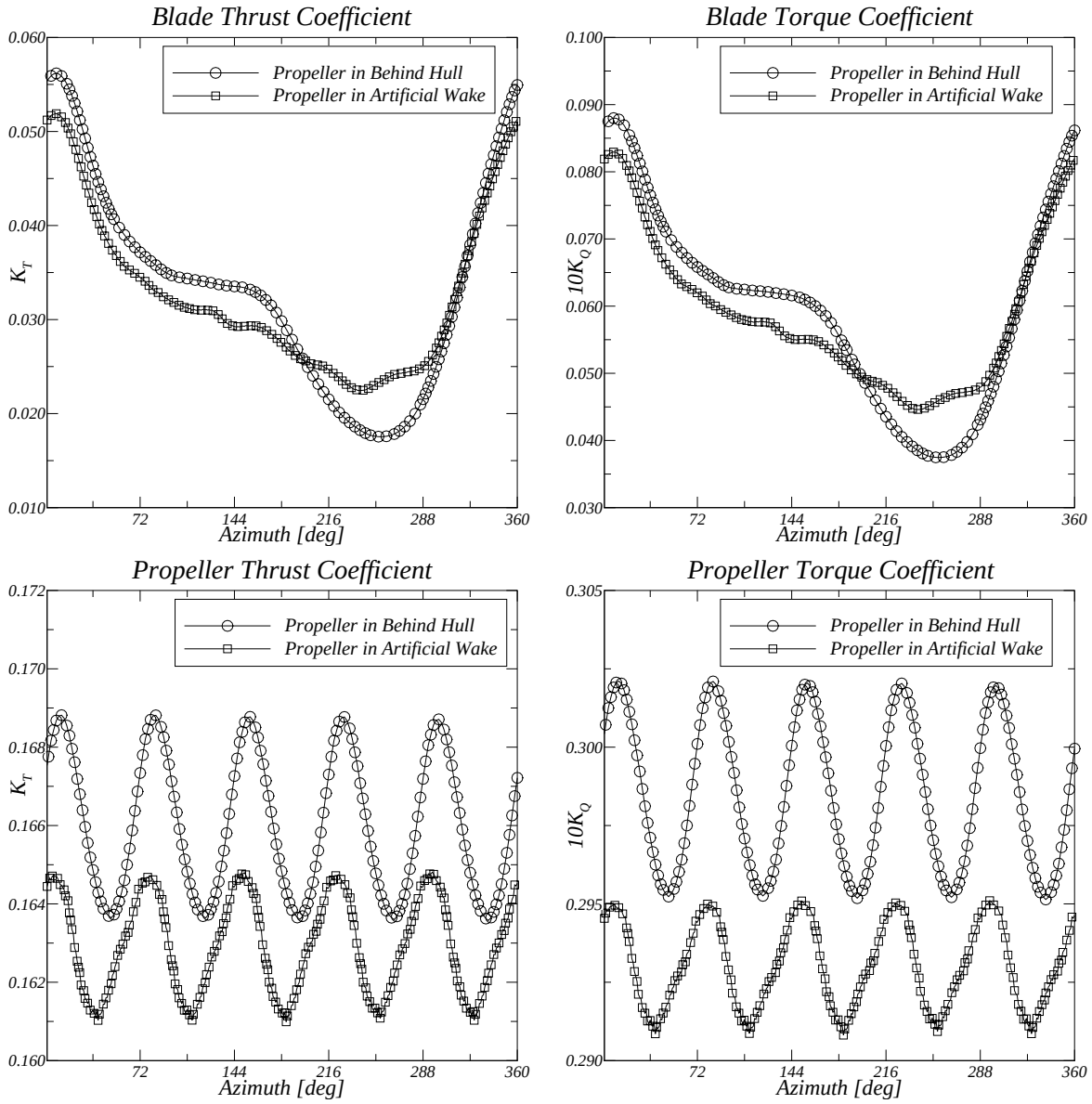

Fig. 5: Thrust (left) and torque (right) fluctuations for a single blade (top) and the propeller (bottom) during one revolution.

The convergence history of the mean and maximum differences between the generated wake field using body-forces and the predicted nominal wake field, in respect to the ship velocity, is presented in Fig. 4-(left). Stagnation of the mean and maximum differences is obtained after 8 iterations. Mean differences of 7% are obtained for the axial velocity. The transversal velocities present lower mean differences in the range of $3-5\%$. For the maximum differences, large values are obtained at the inner radii near the azimuthal positions of 110 and 250 degrees. The axial velocity present a maximum difference around 43%, whereas for the transversal velocities the maximum differences are of the order of 10%. The comparison of the cylindrical components for the circumferential average wake fields is shown in Fig. 4-(right). Significant differences at the inner radii are observed between the axial components.

4.2 Propeller in behind condition

The unsteady simulations of the KCS propeller operating behind hull and in an artificially generated wake field are presented and the performance predictions compared. For the propeller simulations operating in behind hull condition, the time step is tuned to obtain an angular step of 2 degrees. In this calculations, average and maximum Courant numbers around 0.78 and 106 are obtained, respectively. For the iterative

Table 1: Mean, first and second harmonic amplitudes of the blade frequency for the total thrust and torque coefficients.

	Behind Hull		Artificial Wake	
n	$K_T^{(n)}$	$10K_Q^{(n)}$	$K_T^{(n)}$	$10K_Q^{(n)}$
0	0.1660	0.2985	0.1630	0.2930
1	0.0025	0.0034	0.0017	0.0019
2	0.0002	0.0002	0.0002	0.0003

solution, 50 iterations are considered for each time step, leading to a maximum normalised residual around 10^{-1} for the velocitites and pressure. For the propeller simulations in the artificially generated wake field, an angular step of 1 degree is considered. The corresponding time step led to the average and maximum Courant numbers around 0.88 and 33, respectively. In this case, 100 iterations are considered for the iterative solution of the transport equations, where a maximum normalised residual below 10^{-2} is obtained for the velocities and pressure.

Figure 5 shows the thrust and torque fluctuations for a single blade and the propeller during one revolution. For the single blade force coefficients, the comparison shows that the thrust and torque fluctuations due to the wake peak are well captured by the computations in the artificial wake. In this case, the largest differences are observed near the azimuthal position of 252 degrees. Differences are also visible in the propeller thrust and torque coefficients. The mean $K_{T,Q}^{(0)}$, first $K_{T,Q}^{(1)}$ and second harmonic $K_{T,Q}^{(2)}$ amplitudes of the blade frequency for the total thrust and torque coefficients are presented in Table 1. The definitions are:

$$K_{T,Q}(\theta) = K_{T,Q}^{(0)} + K_{T,Q}^{(1)} \sin\left(K\theta + \phi^{(1)}\right) + K_{T,Q}^{(2)} \sin\left(2K\theta + \phi^{(2)}\right), \tag{4}$$

where θ is the azimuthal position, K the number of propeller blades and $\phi^{(1,2)}$ the phase angles. The comparison shows that lower mean and first harmonic amplitudes are obtained in the propeller simulations with the artificial generated wake. Negligible values are obtained for the second harmonic amplitude. The relative differences for the mean total thrust and torque coefficients are equal to -1.8%.

5 Conclusion

A method for the prediction of the propeller unsteady performance in a artificially generated wake field using body-forces is presented. This method offers an alternative to the full RANS approach. The two approaches are compared and the main reasons for the differences in the propeller performance prediction are attributed to the artificially generated wake field used in the propeller computations without hull. In this work, the nominal wake field obtained from the bare hull simulation is considered, which may contribute for the under-prediction of the thrust and torque, since the interaction between the propeller and the nominal wake field is neglected. In addition, the artificial wake field generated from iteratively calibrated body-forces present differences higher than 10% in respect to the ship velocity at the inner radii. These differences are attributed to the strong interaction between the axial and transversal wake flows. Alternative boundary conditions combined with body-forces will be considered for future work to improve the replication of the nominal wake field. Nevertheless, minor differences in the order of 1.8% are obtained for the mean propeller thrust and torque coefficients between the two approaches.

References

L. Larsson, F. Stern, M. Visonneau (eds.) (2014). *Numerical Ship Hydrodynamics: An Assessment of the Gothenburg 2010 Workshop*. Springer.

F.R. Menter, M. Kuntz, and R. Langtry (2003). Ten years of industrial experience with the SST turbulence model. *Proceedings of the Fourth International Symposium on Turbulence, Heat and Mass Transfer*, **4**, 625–632.

R. Mikkelsen, P. Andersen, J.N. Sorensen (2007). Modeling of behind condition wake flow in RANS computation on a conventional and high skew propeller. 10th Numerical Towing Tank Symposium, Hamburg, Germany.

K.W. Shin, P. Andersen, R. Mikkelsen (2011). Cavitation simulation on conventional and highly-skewed propellers in the behind-hull condition. Second International Symposium on Marine Propulsors, smp'11, Hamburg, Germany.

Numerical simulation of bi-stable ventilated flows around surface-piercing hydrofoils

Moran Charlou, Jeroen Wackers*
LHEEA, Ecole Centrale de Nantes/CNRS UMR 6298, Nantes/France
*jeroen.wackers@ec-nantes.fr

1 Introduction

Ventilation is a physical phenomenon in which air is entrained in a low pressure region below the free surface on a hydrofoil or a propeller. It is known to cause substantial drops of performance – lift for a hydrofoil or thrust for a propeller. Ventilation can be used to good advantage, like for drag reduction, but is most often unwanted.

On a surface-piercing lifting hydrofoil at high enough Froude numbers, two flow regimes exist: wetted when water completely covers both sides of the foil, and ventilated when a pocket of air covers a major part of the suction side. A wetted flow usually provides the best lift, whereas ventilation raises the pressure on the suction side and thus lowers the lift. The flow is in general wetted for low angles of attack and ventilated at high angles. However there is a range of angles in between, where both flow regimes exist and are stable. In this bi-stable region, a perturbation can brutally change the flow regime from wetted to ventilated and conversely. Harwood et al. (2014, 2016), in accordance with previous research, identified two conditions on the wetted flow which are required for the existence of a ventilated flow:

- A zone of low pressure, i.e. pressure lower than the atmospheric pressure, so a pressure gradient can entrain air towards the suction side,
- A separated flow on the suction side, i.e. a recirculation bubble.

These two conditions are necessary for stable ventilation, but not sufficient for the spontaneous transition to ventilated flow, since this requires the air to break through the attached flow with atmospheric pressure at the free surface. This explains why both flows can be stable under the same conditions. Fig. 1 shows an example for a vertical hydrofoil at an angle of attack (yaw) of 12.5°. The wetted flow validates the conditions above and the ventilated flow shows a 33% drop in lift compared to the wetted flow.

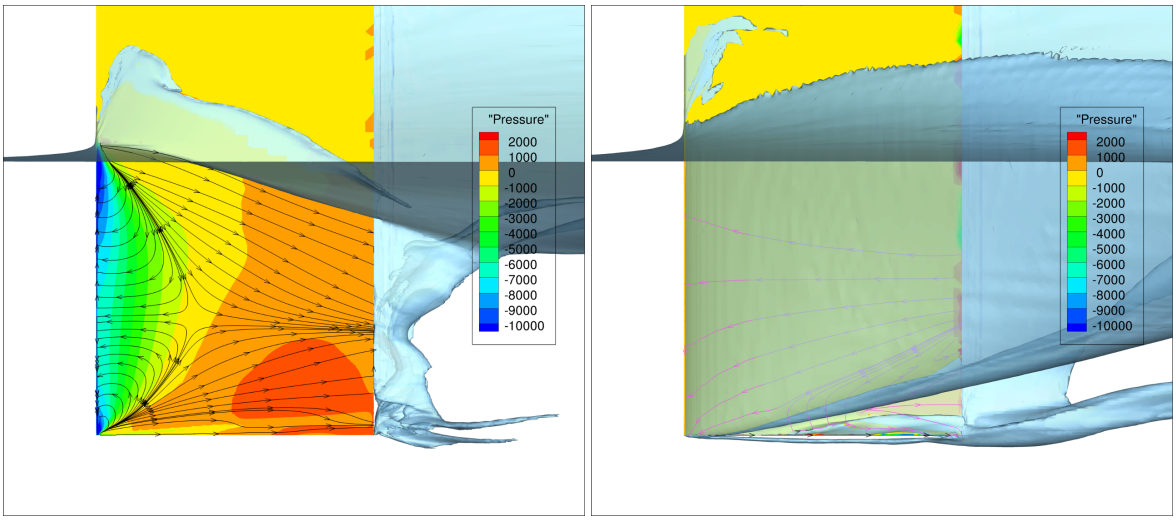

(a) Wetted (b) Ventilated

Fig. 1: Two flow regimes are stable at $\alpha = 12.5°$ and $Fn_h = 2.5$ (pressure, wall streamlines and free surface in a side view of the suction side).

Assessing the risk of ventilation in a bi-stable region through numerical simulation requires first, that the simulation should accurately represent the spontaneous or forced transition from wetted to ventilated flow. And second, when ventilation occurs it must remain stable even in the lower part of the bi-stable range for the angle of attack. The goal of this paper is to investigate these two conditions.

2 Test case

The test case is a vertical surface-piercing hydrofoil as studied in Harwood et al. (2014, 2016), and the present study varies the angle of attack α for a fixed immersion-based Froude number $Fn_h = 2.5$. In the experiments, for α between 2.5° and 15°, wetted flow was established naturally but ventilated flow could be obtained through a perturbation by a blast of air at the leading edge. However the required intensity of such a perturbation is uncertain. The present study instead focuses on natural transition by increasing α in steps of 2.5° through the bi-stable region until spontaneous ventilation occurs, and then decreasing it until the flow re-attaches to the foil, thus moving along a hysteretic cycle (Fig. 2a). The experiments were conducted in a towing tank at fixed α for each run, while the carriage was accelerated from zero to the target Fn_h for that run. If a hysteretic cycle occured, it was therefore along Fn_h and not α.

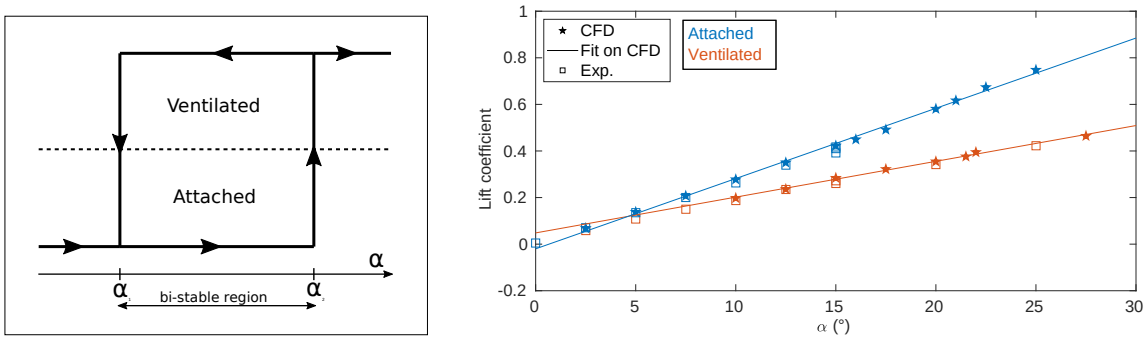

(a) Hysteretic cycle

(b) Lift coefficient: CFD *vs* Exp. from Harwood et al. (2016)

Fig. 2: Schematic representation of the hysteretic cycle and variation of the lift coefficient

The foil is symmetrical, has a chord $c = 0.279m$ with an ogival fore-body, a rectangular aft-body and a blunt trailing edge. The immersion depth is $h = c$. The computational domain is $6.7m$ wide with the foil centered, $4.05m$ high with $3.05m$ water depth and $9m$ long with the foil at 3m from the front.

The RANS solver used in this study is ISIS-CFD, a two-fluid solver developed by Ecole Centrale de Nantes/CNRS and part of NUMECA International's simulation suite FINE™/Marine. The water surface is represented with a water–air mixture surface capturing model using compressive discretisations, see Queutey and Visonneau (2007). Turbulence is solved with the $k-\omega\ SST$ (Menter) model. Adaptive grid refinement is used with a combined free-surface and pressure/velocity Hessian criterion, described in Wackers et al. (2017). The Hessian threshold is set at $0.05m$ ($\approx 0.18c$), the target cell size normal to the free surface is $c/100$ and the minimum cell size is $c/500$. The initial mesh is only refined around the foil. The flow is solved using a 1st-order accurate time-marching algorithm with a time step of $c/100U_\infty$, during which the refinement procedure is called every 20 steps. The size of the refined meshes goes from around 4M cells for a ventilated case to 9M cells for a wetted case.

Two methods were applied to start the computations: (a) increasing the speed of the foil from zero to reach the desired Fn_h, with α fixed, and (b) changing α at fixed speed (and Fn_h) from a previous computation. Method (a) was used to start computations from scratch, while method (b) was used to move along the hysteretic cycle in α.

Fig. 2b shows the lateral forces (lift) obtained in the hysteretic cycle, compared with the experimental data. These confirm that both the wetted and the ventilated states are predicted correctly. The transitions between the two flows are not indicated: these are discussed in the next sections.

3 Transition to a ventilated state

For the flow to transition from a wetted to a ventilated state, a path needs to open up between the surface and the recirculation bubble, through which air can flow. In the present case, the main air path runs down the leading edge to the low pressure peak in the bubble (Fig. 3). However, in the wetted state (Fig. 1a) this path is blocked by the attached flow at ambient pressure along the free surface. To obtain ventilation, this surface seal must be breached.

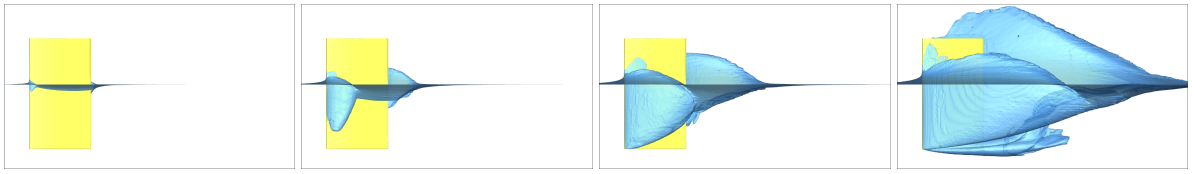

(a) $t \approx 0.10s$, $Fn_h \approx 1.2$ (b) $t \approx 0.17s$, $Fn_h \approx 1.9$ (c) $t \approx 0.24s$, $Fn_h \approx 2.4$ (d) $t \approx 0.37s$, $Fn_h = 2.5$

Fig. 3: Spontaneous ventilation inception at $\alpha = 21.5°$. The acceleration phase is 0.304s long.

In the experiments, spontaneous ventilation inception (above $\alpha = 15°$) is attributed to bubbles of air and turbulent vortex cores breaking the free surface at the leading edge. Such flows cannot be simulated with the present free-surface discretisation and RANS turbulence model, so the inception mechanism for the simulations is the full separation of the flow at the top of the leading edge (Fig. 3).

The simulations show that apart from the flow model, ventilation inception depends strongly on the path to the steady state. When increasing α at fixed $Fn_h = 2.5$ (method (b)), spontaneous ventilation occurs at 27.5°, when unsteady fluctuations of the wake start reaching the foil (Fig. 4). However, spontaneous ventilation occurs at angles as low as 12.5°, as opposed to 15° in the experiments, when accelerating slowly from zero speed like in Fig. 3 (method (a)). The reason for the difference between the two methods is that at Fn_h below 2.5, the wave behind the leading edge is shorter but steeper. This means that ventilation inception occurs more easily than at higher speeds. Thus, the inception takes place during the slow acceleration, after which the flow remains in the ventilated state until $Fn_h = 2.5$ is reached.

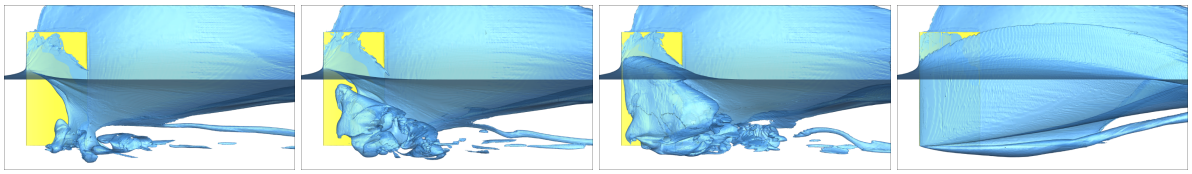

(a) $t \approx 0.24s$ (b) $t \approx 0.37s$ (c) $t \approx 0.44s$ (d) $t \approx 1.45s$

Fig. 4: Spontaneous ventilation inception when α increases from 25° to 27.5° at constant $Fn_h = 2.5$. The rotation phase is 0.202s long.

Thus, since ventilation transition depends more on *unsteady* – either transient or turbulent – phenomena than on the final steady flow conditions, we conclude that there is little practical interest in the investigation of spontaneous ventilation inception. Nature is rife with perturbations of all types, so the actual ventilation would never appear under the same circumstances as in simulation. It is more relevant to numerically evaluate the risk of ventilation occuring than to simulate actual transitions.

To assess the risk of ventilation in a given configuration, we recommend to simulate a big disturbance of the wetted flow, e.g. a sideways acceleration, sufficient to trigger at least a transient ventilated state. The stability of this ventilated flow after the disturbance has stopped determines if the configuration belongs to a bi-stable region. The stability of the wetted flow – i.e. how difficult it is to trigger ventilation – gives an insight into the likeliness of ventilation occuring in practice.

4 Stability of the ventilated state

Contrary to the inception, it is essential to simulate correctly the stability of the ventilated state, i.e. if it spontaneously returns to a wetted state or not. Otherwise, a bi-stable state may be incorrectly considered as free of ventilation risk. This requires the study of ventilation elimination.

In the experiments, elimination occurs when lowering Fn_h at fixed α. In that case, the ventilation pocket gradually closes from below, with a re-entrant jet on the foil surface rising steeper and steeper until it flows back to the leading edge and closes the ventilated pocket. However when lowering α at fixed Fn_h during simulations, ventilation elimination occurs at around 8°, as opposed to the 2.5° suggested by Harwood et al. (2016). With Fn_h staying at 2.5, the re-entrant jet remains on the lower side of the foil.

Instead of the ventilation pocket closing from below, the crest of water at the top of the pocket slowly hits the suction side and collapses, closing the air pocket and cutting off the air inflow. Without the inflow, the flow of air into the wake can no longer be sustained. Some air remains for some time in the recirculation zone, but ends up being chased out, leading to a wetted state (Fig. 5).

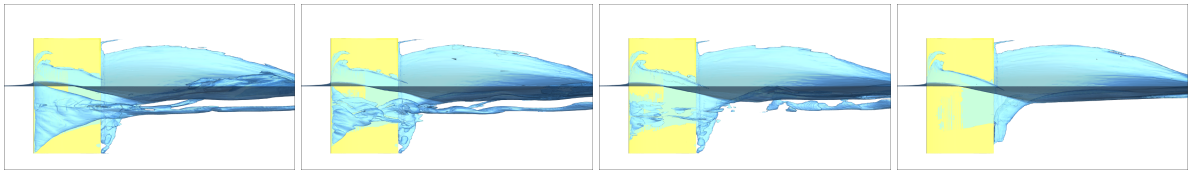

(a) $t \approx 1.51s$ (b) $t \approx 1.61s$ (c) $t \approx 1.71s$ (d) $t \approx 2.18s$

Fig. 5: Ventilation elimination at $\alpha = 7.5°$. $\alpha = 10°$ at $t = 0$, the rotation to 7.5° is done over 0.101s. A thin layer of air on the suction side is eliminated slowly because the speed is zero on the foil's surface.

To fully understand how the water crest collapses and closes the air pocket, the pressure and velocity in the air pocket are considered (Fig. 6). The top of the water crest over the pocket breaks and creates a bridge to the suction side of the foil. This zone of low water volume fraction prevents air from entering the pocket, further decreasing the naturally lower pressure in the air pocket, which in turn generates high velocities towards the inside of the pocket, pulling the water crest towards the foil. This vicious cycle ends up closing the air pocket from the top. Such a blocking effect might not occur if the breaking of the water crest was represented with drops of water instead of a diffuse low water fraction, making this specific issue inherent in the surface-capturing formulation used.

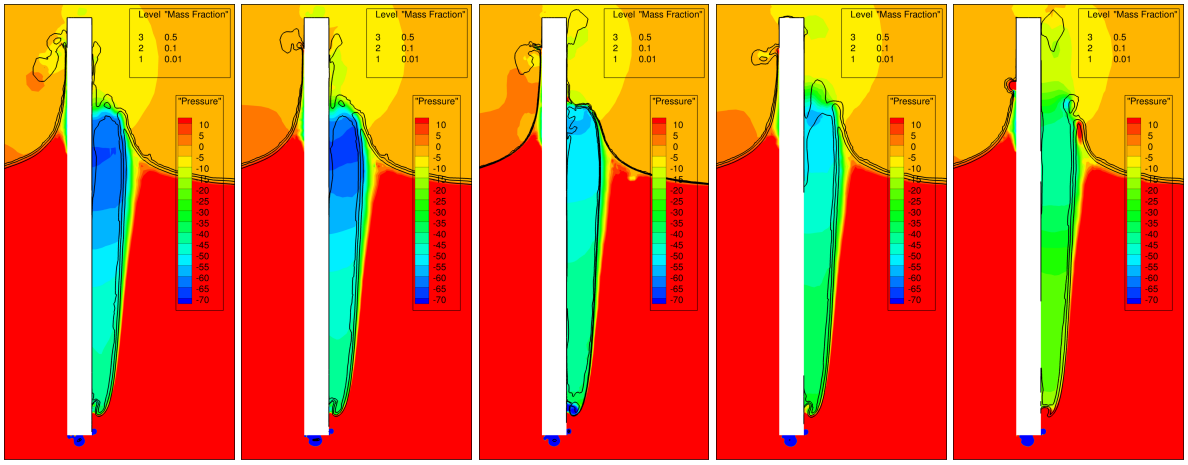

(a) Base parameters (b) Smaller time step, $\Delta t \approx$ 1.69e-4s (c) Refined free surface criterion (d) Surface tension $\sigma = 0.07N/m^{-1}$ (e) Surface tension $\sigma = 0.7N/m^{-1}$

Fig. 6: Slice of the ventilated pocket at $x = 0$ (mid-chord) for $\alpha = 10°$ and different numerical parameters. The pressure gradient introduced by the diffusion of low water fraction is responsible for the collapse of the air pocket.

Several attempt have been carried out to solve this problem. Because the compressiveness of the volume fraction scheme used in ISIS-CFD (Queutey and Visonneau (2007)) is sensitive to the local Courant number, the time step has been reduced. However as Fig. 6b shows, even though the local Courant number is divided by 4, that does not change the diffusion of the water fraction at the crest. Increasing the mesh refinement at the free surface in order to get a finer representation of the water-air interface reduces the induced pressure gradient – at the cost of computational speed – but does not remove the low volume fraction bridge (Fig. 6c). Finally, a surface tension model, based on Brackbill et al. (1992) but with the surface tension included in the pressure gradient, removed the bridge when using a surface tension 10 times higher than in reality (Fig. 6e). However, this changes some other features of the flow and intro-

duces additional numerical problems (e.g. unstable forces created by non-physical pressures on the foil). Using the actual air-water surface tension $\sigma = 0.07N.m{-}1$ (Fig. 6d) yields similar results to refining the free surface (Fig. 6c) in terms of the pressure gradient, while reducing the amount of water arriving on the foil surface significantly.

As a follow-up, the rotation from 10° to 7.5° was repeated with the actual air-water surface tension. While the flow without surface tension reattaches (Fig. 7a, see also Fig. 5), the surface tension model maintains a stable ventilated state (Fig. 7b). However, the rotation rate to 7.5° was reduced for this computation and it was later found out that a sufficiently slow rotation rate on its own is enough to prevent the flow from reattaching (Fig. 7c). But in this last computation a sheet of water is present on the foil, which is removed by the surface tension model. This may be an indication that the surface tension reduces the risk of reattachment.

Thus, while the motion history of the foil must once again be taken into account, the two tests indicate that the physical and numerical modelling of the water crest is a factor in the ventilation elimination. However, only the simulation with an artificially high surface tension (Fig. 6e) produces the straight crest which is observed in images from the experiments. Also, the irregular surface pressure in Fig. 7b is problematic. These are indications that the current surface tension model is ill adapted for the diffused low volume fractions that appear in the wave crest. A more detailed study of the surface tension and surface-capturing models for this flow is planned for future work.

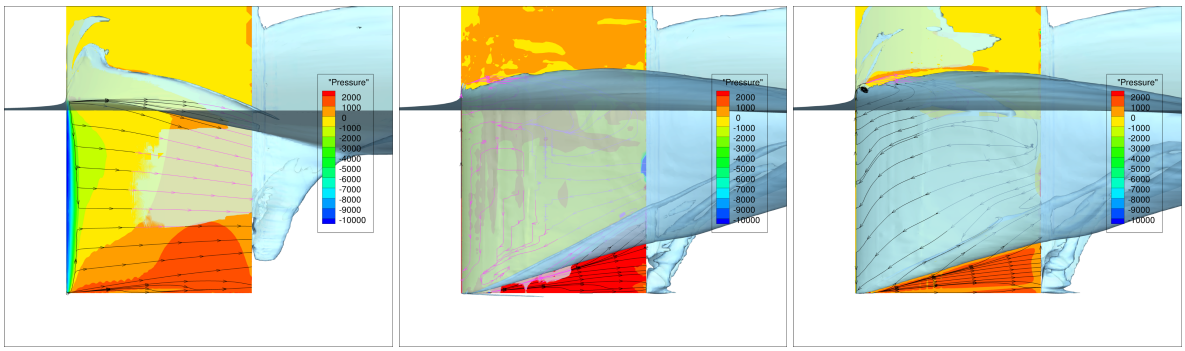

(a) Without surface tension, rotation over 0.101s

(b) With surface tension, rotation over 0.304s

(c) Without surface tension, rotation over 0.405s

Fig. 7: Both adding a surface tension model and slowing the rotation rate (coming from 10°) prevents the flow from rewetting at $\alpha = 7.5°$.

5 Conclusion

This paper studies the inception and stability of ventilation in bi-stable conditions. It is shown that spontaneous inception depends on the path to the steady state. Therefore, it is more relevant to provoke ventilation by artificial perturbation and to consider its stability, than to simulate spontaneous inception. At low angles of attack, the simulated ventilation is eliminated by a wave crest breaking and closing the ventilation pocket from the top. The tests show that this behaviour depends on the detailed physical and numerical modelling of the water sheet which forms the edge of the ventilating pocket.

Acknowledgements

This work was granted access to the HPC resources of the IDRIS computing centre under the allocation 2018/2019-A0052A01308 made by GENCI (Grand Equipement National de Calcul Intensif).

References

J.U. Brackbill, D.B. Kothe, and C. Zemach (1992). A continuum method for modeling surface tension. *J Comp Phys*, 100(2):335–354.

C.M. Harwood, Y.L. Young, and S.L. Ceccio (2016). Ventilated cavities on a surface-piercing hydrofoil at moderate Froude numbers: Cavity formation, elimination and stability. *J Fluid Mech*, 800:5–56.

C.M. Harwood, K.A. Brucker, F.M. Montero, Y.L. Young, and S.L. Ceccio (2014). Experimental and numerical investigation of ventilation inception and washout mechanisms of a surface-piercing hydrofoil. Proceedings of the 30th Symposium on Naval Hydrodynamics, Hobart, Australia.

P. Queutey and M. Visonneau (2007). An interface capturing method for free-surface hydrodynamic flows. *Comp Fluids*, 36(9):1481–1510.

J. Wackers, G. Deng, E. Guilmineau, A. Leroyer, P. Queutey, M. Visonneau, A. Palmieri, and A. Liverani (2017). Can adaptive grid refinement produce grid-independent solutions for incompressible flows? *J Comp Phys*, 334:364–380

Simulation of the Dynamics of Spar-type Floating Offshore Wind Turbine in the ANSYS Aqwa Environment Extended by the Coefficients of Viscosity Forces Determined on the Basis of RANSE-CFD Analysis

Ewelina Ciba*, Paweł Dymarski*
*GDANSK UNIVERSITY OF TECHNOLOGY Gdansk/ Poland
ewelina.ciba@pg.edu.pl

1 Introduction

In recent years, there has been a significant increase in interest in platforms for offshore wind turbines. The transfer of wind energy to sea areas is justified for various reasons. Higher and more stable than on land, wind speeds that are not supported by buildings or green areas allow the installation of more powerful turbines. The size of turbine wings, which in marine conditions may be larger than land-based, also allows for high performance of installed turbines. Lack of public favor for turbines installed near inhabited areas is another factor decisive for displacing them from the mainland.
Offshore wind energy is a new and rapidly developing issue. Innovative solutions are tested, especially in the area of solutions where the turbine platform is a floating object. The authors, as part of their previous work, analyzed three basic types of platforms: Jack-up, Tension Leg Platfrom and Spar. The last concept, the Spar type platform, designed for deep water reservoirs (60-70 m), was decided to be modified and developed. The presented materials contain the results together with a detailed description of the dynamics simulations of the discussed platform. The discussed simulations were carried out in the ANSYS Aqwa environment, using hybrid methods combining fast calculation methods with boundary elements, extended by interaction of fluid viscosity with a resistance coefficient determined on the basis of simulations performed with RANSE CFD methods. The work discusses the Ansys Aqwa environment, and then presents the platform's geometry, its mass properties, boundary conditions as well as the method of obtaining resistance coefficients.

2 Ansys Aqwa

ANSYS Aqwa provides an engineering toolset for the investigation of the effects of wave, wind and current on floating and fixed offshore and marine structures, including: spars; floating production, storage, and offloading (FPSO) systems; semi-submersibles; tension leg platforms (TLPs); ships; renewable energy systems and breakwater design.
The calculations in ANSYS Aqwa are divided into two main parts, in the first (Aqwa Hydrodynamic Diffraction) calculations of hydrostatics and frequency characteristics are performed, which are the basis for the temporal responses of the object under wave conditions (regular or irregular) calculated in the second part (Aqwa Hydrodynamic Response) with additional wind and / or current operation.
In the Aqwa program, he applied a three-dimensional theory of radiation / diffraction and / or the Morison equation in regular waves in the frequency domain.
Elements with non-cylindrical shapes, as well as cylinders with dimensions beyond the possible application of the Morison equation, are modeled in Aqwa using surface panels for which a three-dimensional radiation theory is applied. This theory, however, does not take into account the forces associated with the viscosity of the fluid, therefore, determine the resistance factors of the object for the main directions of motion and give them in matrix form. Similarly, in the case of loading the part of the aquatic platform with the action of wind. Aqwa models the wind velocity distribution according to the spectrum chosen by the user (here Ochi), but calculates the forces based on the integrated pressure over the surface, only determines the force based on the instant wind speed, direction, current position of the platform and the corresponding factor previously given by the user to the program in tabular form.
For modeling anchors aqwa distinguishes 4 basic types: Linear Elastic, Nonlinear Polynomial, Nonlinear Steel Wire and Nonlinear Catenary, allowing to reflect the nature of the anchorage depending on the complexity of the tested model. In the analyzed case, the Nonlinear Polinomial was the best model.

In the case of constructions for which calculations made using the Morisson equation are correct, the rope being the axis of the structure is introduced into the program and defines its cross-section. In other cases, the geometry should be introduced in the form of the surface model, therefore the mass, position of the center of gravity and moments of inertia are not calculated by the program, but are asked by the user.

3 Geometry and mass properties of the platform

The Spar platform type discussed in this presentation was called the three-column spar, unlike the cell spar type analyzed earlier by the authors. The name three-column, of course, refers to the three displacement columns connecting the ballast part of the structure (closed in the lower case) with the free side supporting the column on which the wind turbine is installed. The visualization of the structure is shown in Figure 1

Mass properties are presented in tab. 1

Table 1 Mass propeties

Mass	M [t]	Center of gravity	X_G[m]	Y_G[m]	Z_G[m]	Moment of inertia	I_{xx} [kg m^2]	I_{YY} [kg m^2]	I_{ZZ} [kg m^2]
	8 178		0	0	-30.62		1.18E+10	1.18E+10	3.85E+08

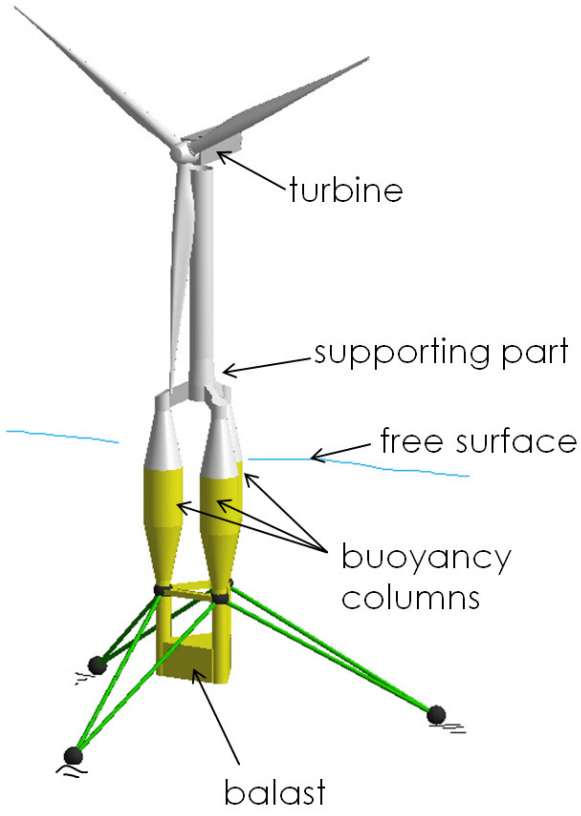

Fig. 1 Geometry

4 Hydro and aerodynamic coefficients

As mentioned in the introduction, the calculation methods used in the Ansys Aqwa software require an expansion with an appropriate ratio. For basic shapes, they can be derived from the literature Sarpkaya (2010), and for complex shapes, model or numerical calculations are performed using the RANSE-CFD codes. The second approach is described here.

The coefficients of resistance allowing to determine the share of forces related to the viscosity of the fluid generated on the object subjected to the action of sea waves were determined based on the Morisson Eq. (1)

$$F(t) = \frac{\pi}{4}\rho C_M D^2 \cdot \dot{u}(t) + \frac{1}{2}\rho C_D D \cdot u(t)|u(t)| \tag{1}$$

Where: ρ [kg m^-3] – density of water, D[m] – diameter of cylinder, u[m s^-1] – velocity of water, C_M-coefficient of inertia forces, C_D- coefficient of drag forces

From this equation it follows that if an object is settled in an oscillatory flow, there will be changes in such moments when the whole is heard will form a component of forces related to inertia (u (t) = 0) and resistance forces (du / dt = 0) On the basis of the obtained values of forces (exemplary shown in Fig. 2), the average coefficient of resistance was determined. The method of determining the Morrison equation coefficients is described in detail in the paper Dymarski et al. (2016)

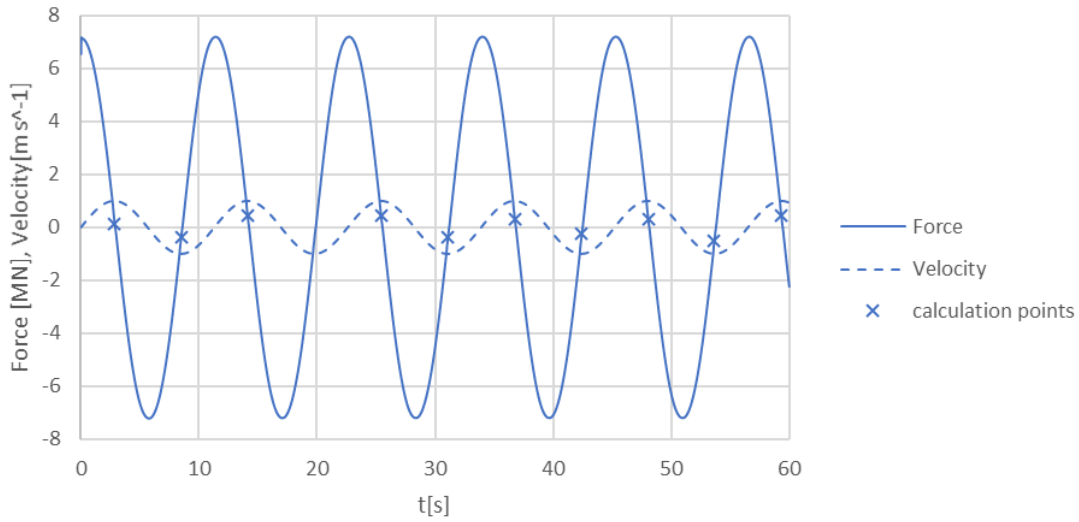

Fig. 2 The force acting on the structure placed in the oscillatory flow at the set speed

The forces caused by the action of wind on the platform's overhead part and on the turbine wings were also modeled using the appropriate coefficient. Similarly to coefficients of hydrodynamic forces, also in this case both model and numerical calculations can be used. These are traditional resistance tests, that is, the object is subjected to the action of a uniform speed velocity and the resulting force is determined. The coefficients obtained allow us to model a windmill under storm conditions, with the turbine turned off (zero moment on the wings)

4 Load

The irregular wave was adopted in the form of Jonswap spectrum, with the parameters given in tab. 2 and the distribution shown in Fig. 3

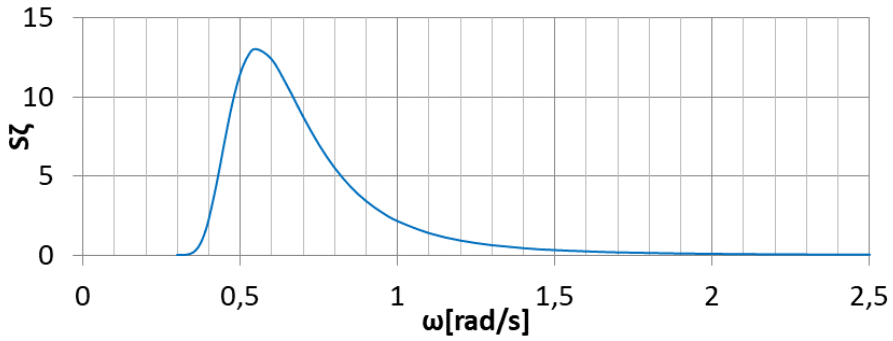

Fig. 3 50-years storm spectrum

Table 2 50-years storm parameters

Significant height H_s[m]	9.01
Peak period T_p[s]	11.3
Factor γ[-]	4.12

The impact of wind was modeled with the help of Ochi and Shin Spectrum with a velocity of v = 29.1 m / s at a height of 10 m.

4 Results and Conclusions

As a result of the calculations platform movements were obtained at all six degrees of freedom during the hour simulation. Fig. 4 (translation) and Fig. 5 (rotation)

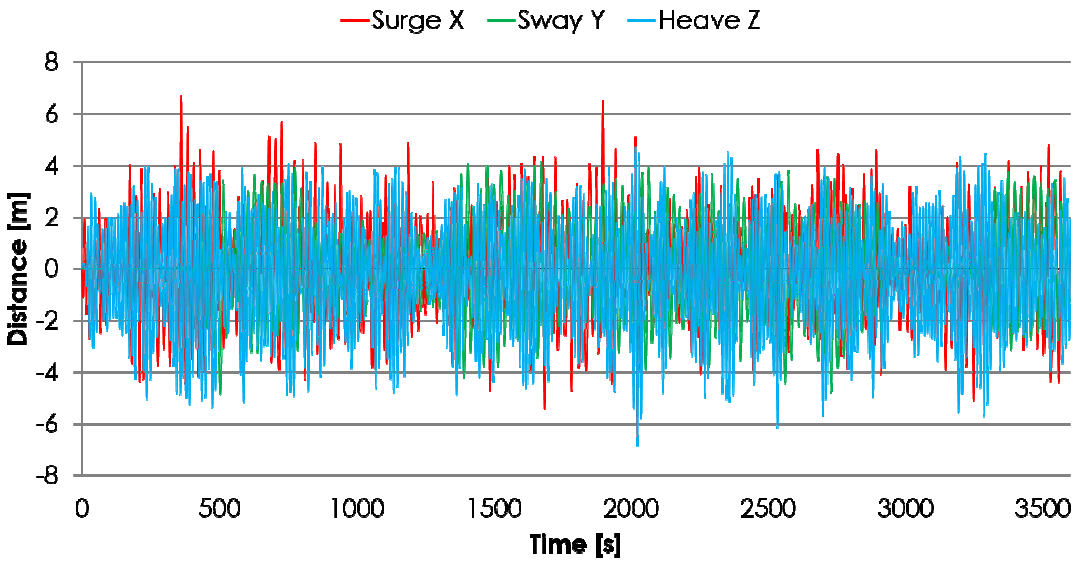

Fig. 4 Translation of platform

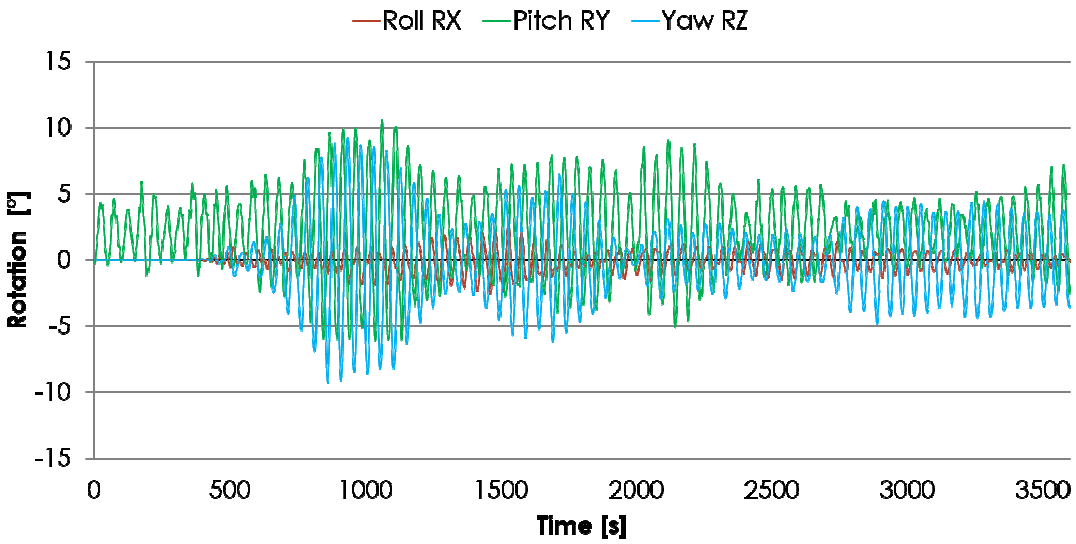

Fig. 5 Rotation of platform

On the basis of which the mean and maximum values were drawn, which are shown in Figs. 6

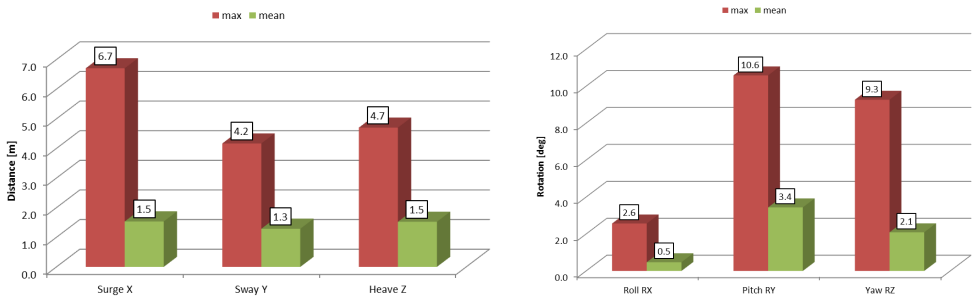

Fig. 6 Max and mean translation, rotation

The forces appearing in the ties were also checked to locate the highest value. Fig. 7.

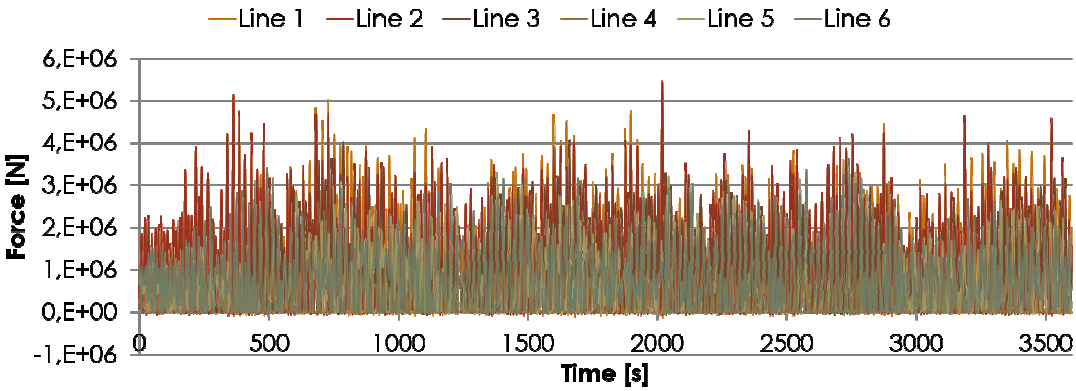

Fig. 7 Force on line

On the basis of the results presented, the following conclusions can be drawn. The results of calculations for the designed structure are optimistic. Displacement, though significant, does not

exceed the assumed values. The stresses in the ropes are twice smaller than the ones assumed, and thus the classification requirements will be met. ANSYS aqwa software allows you to quickly convert the behavior of the platform in different environmental conditions, but the process of data preparation is quite laborious.

As part of further work, model tests are planned to validate calculations

References

Dymarski P., Ciba E., Marcinkowski T(2016).: *Effective method for determining enviromental loads on supporting structures for offshore wind turbines.* Polish Maritime Research No 1(89) 2016 Vol. 23; pp. 52-60

Turgut Sarpkaya (2010) Wave Forces on Offshore Structures,. Cambridge University Press, Cambridge

Towards a Fast Fitting Method for 3D Free Surface Flow

Toon Demeester[*], **E. Harald van Brummelen**[†], **Joris Degroote**[*,‡]
[*]Ghent University, Belgium
[†]Eindhoven University of Technology, the Netherlands
[‡]Flanders Make, Belgium
toon.demeester@ugent.be

1 Introduction

An important application where steady free surface flows appear is the calculation of the steady resistance of a ship. Often these flows are solved using a capturing method to represent the free surface, e.g. the volume-of-fluid method (Hirt and Nichols, 1981) or the level-set method (Sussman et al., 1994). A time-stepping scheme is usually employed to reach the steady state solution. This is inefficient, as transient phenomena at the free surface may take a large number of time-steps to disappear (van Brummelen et al., 2001).

The goal of this ongoing research is to develop a fast, steady iterative method to solve the steady free surface problem. The free surface is represented with a fitting technique, meaning that it lies along a deformable domain boundary. This has the additional advantage that the free surface can be accurately represented by a relatively low number of grid points (in contrast to capturing methods). The air phase is not taken into account, as its influence on the water phase is negligible due to its much lower density. For convenience of use, it is required that the new method can be used with a general purpose black-box flow solver.

Currently a 2D version of this method has been completed and its capabilities demonstrated: it gives good results and converges in a low number of iterations (Demeester et al.,). It is based on quasi-Newton iterations, where a surrogate model of the flow solver is used to approximate the Jacobian and a rank-one update is performed in each iteration except the first one. The first step in extending this method to 3D cases, is to construct a surrogate model for these flows. A strategy to construct the surrogate is outlined in this paper, and the performance of the resulting surrogate is tested.

2 2D steady free surface method

A short overview of the 2D steady free surface method is given here, for details see Demeester et al., . The steady free surface problem can be reduced to a root-finding problem: find the free surface height $\boldsymbol{z}$ so that the free surface pressure $\boldsymbol{p} = \mathscr{F}(\boldsymbol{z}) = 0$. $\mathscr{F}$ is a (black-box) flow solver in which the free surface boundary is implemented as a free-slip wall. It takes a vector $\boldsymbol{z} \in \mathbb{R}^{n\times 1}$ containing the discretized free surface height as input, and returns a vector $\boldsymbol{p} \in \mathbb{R}^{n\times 1}$ containing the discretized free surface pressure as output.

This root-finding problem is solved iteratively with a quasi-Newton method:

$$\boldsymbol{J}\,\Delta\boldsymbol{z}^j = -\boldsymbol{p}^j \tag{1}$$

with superscript j the iteration's index and $\Delta\boldsymbol{z}^j = \boldsymbol{z}^{j+1} - \boldsymbol{z}^j$. The approximate Jacobian $\boldsymbol{J}$ of the flow solver $\mathcal{F}$ consists of two parts: a full-rank surrogate model $\boldsymbol{J}_{\text{sur}}$ and a low-rank least-squares approximation $\boldsymbol{J}_{\text{LS}}$ based on input-output pairs of $\mathcal{F}$ of previous iterations. The least-squares approximation is based on the IQN-ILS algorithm used in partitioned fluid-structure interaction (Degroote et al., 2009). $\boldsymbol{J}_{\text{sur}}$ and $\boldsymbol{J}_{\text{LS}}$ are combined in such a way that there is no overlap between them.

A surrogate model $\boldsymbol{J}_{\text{sur}}$ is required, which gives a relation between perturbations of the free surface height and pressure: $\boldsymbol{J}_{\text{sur}}\,\Delta\boldsymbol{z} = \Delta\boldsymbol{p}$. For this purpose, a perturbation analysis in the Fourier domain was performed analytically on a basic free surface flow (Demeester et al., 2018). The result was a relation between sinusoidal perturbations of the free surface height and pressure ($z_k(x) \sim p_k(x) \sim \sin(kx + \theta)$):

$$L(k) \cdot z_k(x) = p_k(x) \qquad \text{with} \qquad L(k) = \rho g \left(\text{Fr}^2 \frac{kh}{\tanh kh} - 1 \right) \tag{2}$$

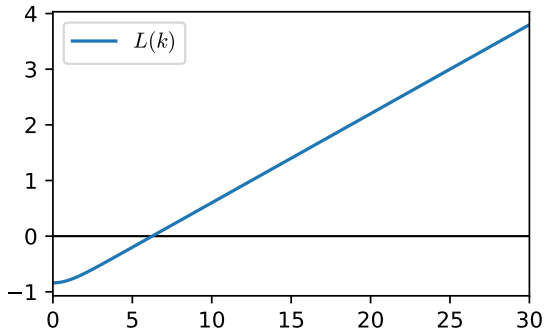

Fig. 1: Factor $L(k)$ from Eq. (2) for Fr = 0.4, $\rho = g = h = 1$.

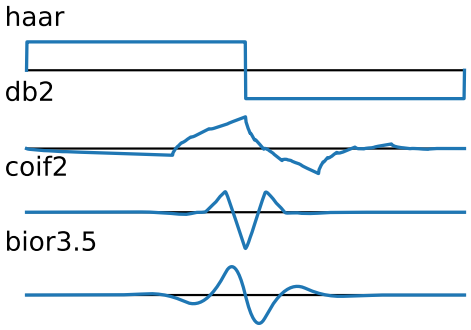

Fig. 2: Some examples of mother wavelets, from top to bottom: Haar, Daubechies 2, Coiflets 2, Biorthogonal 3.5 (see also PyWavelets, 2019).

with k the wavenumber, ρ the density, g the gravitational acceleration, h the depth of the flow, $\mathrm{Fr} = U/\sqrt{gh}$ and U the average velocity of the flow.

If both $\boldsymbol{z}$ and $\boldsymbol{p}$ were transformed to the frequency domain (with the Discrete Fourier Transform, DFT), a surrogate model based on Eq. 2 would be a diagonal matrix. Getting $\boldsymbol{J}_{\text{sur}}$ in the spatial domain takes more effort: two methods based on the Fourier decomposition were proposed. Demeester et al., describes a $\boldsymbol{J}_{\text{sur}}$ for uniform free surface grids based on orthogonal projectors while Demeester et al., 2019 describes a $\boldsymbol{J}_{\text{sur}}$ for stretched free surface grids based on the convolution theorem.

Fig. 1 plots L from Eq. (2) as a function of k, for subcritical flow conditions (Fr < 1). The curve of L has a zero at a certain wavenumber. This is the steady gravity wave, which has a phase velocity equal (opposite) to the flow velocity and therefore appears to be stationary. This wave can appear with arbitrary amplitude and phase in the solution, so that the steady free surface problem has infinite solutions. Correspondingly, the surrogate model becomes singular. In order to find a unique free surface solution, additional conditions are added which force the free surface to be flat at the flow inlet. These extra equations are solved simultaneously with Eq. (1) for $\Delta \boldsymbol{z}^j$ using a least-squares solver.

3 Switching to the wavelet domain

For extending the current method to 3D free surface flows, the first requirement is a new surrogate model which describes perturbations of a 3D free surface. This adds two difficulties: new physics (effects perpendicular to the flow direction, see Sec. 3.3) and an additional dimension. The latter is a problem if a surrogate would be constructed in the same way as for 2D flows: due to the much larger number of unknowns at the free surface, it would be very expensive to construct the surrogate model and perform matrix operations on it. This can be seen as follows: imagine a free surface with r grid points in each direction. For a 2D flow, this would give $\boldsymbol{z} \in \mathbb{R}^{r\times 1}$ and $\boldsymbol{J} \in \mathbb{R}^{r\times r}$. For a 3D flow, this would give $\boldsymbol{z} \in \mathbb{R}^{r^2\times 1}$ and $\boldsymbol{J} \in \mathbb{R}^{r^2\times r^2}$. Matrix calculations for a 2D case on a fine mesh (e.g. $r = 1000$) pose no problems, but would be infeasible for a 3D case, even for coarser meshes. A different approach is required.

Waves are typically very smooth for steady free surface flows: it should be possible to make good approximations of the free surface height and pressure using m smooth basis functions, with m much smaller than the number of free surface grid points n.

The Fourier basis may seem the obvious choice: it uses sines of varying wavenumber to represent signals, it can be calculated efficiently with the FFT (complexity $O(n \log n)$) and the high wavenumber components can be removed to get a low-dimensional representation. However, the Fourier basis has a serious disadvantage: its base signals correspond to a single wavenumber and are consequently not at all localized in space. As a consequence, local phenomena like a single standing wave are hard to represent and problems occur at the boundaries of the domain. If a discontinuity is present between boundary values, high frequency components appear. When the $n - m$ highest modes are removed, an oscillation appears in the reconstructed low-order signal due to the Gibbs phenomenon. As an alternative to the

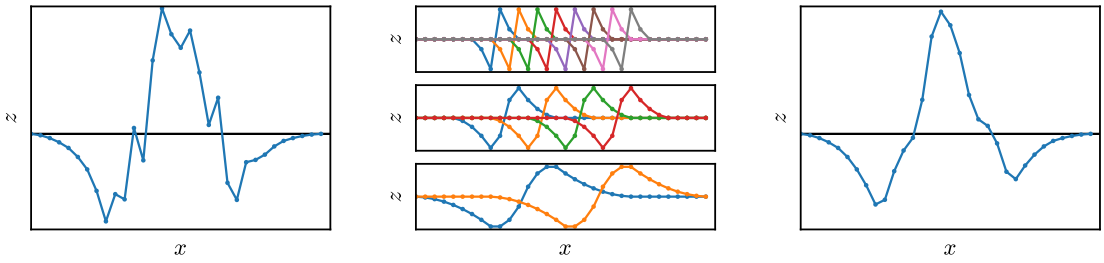

(a) Original signal z. (b) Wavelet basis signals. (c) Low-dimensional signal z_{low}.

Fig. 3: Making a low-dimensional approximation of a signal z by decomposing it into the Biorthogonal 3.1 wavelet basis and removing the smallest scale.

Fourier basis, a wavelet basis is chosen.

3.1 The Discrete Wavelet Transform

For a thorough mathematical description of wavelets, the reader is referred to the reference book by Mallat, 2008, here only the relevant concepts are explained qualitatively. Wavelets are "small waves", which are localized in both the spatial and wavenumber domains. This makes wavelets very suitable for describing local phenomena, e.g. in image compression.[1] The Discrete Wavelet Transform (DWT) can be computed very efficiently using cascaded filter banks, giving a complexity of $O(n)$. An orthogonal wavelet basis can be formed by translating and dilating a single well-chosen *mother wavelet*.[2] The choice of mother wavelet depends on the application, as they can have very different properties. Some examples are given in Fig. 2.

Fig. 3 gives an example of the 1D DWT to explain which basis signals are removed to reduce the number of free surface variables. In Fig. 3a an arbitrary signal z is shown. Calculating the DWT of z means that z is decomposed with respect to the basis signals shown in Fig. 3b. These are discretized versions of the dilated and translated mother wavelet. Three *scales* are used here: the basis signals of scale 0 are shown at the top, those of scale 1 in the center and those of scale 2 at the bottom. By dilating the mother wavelet each time with a factor 2, the basis signals of different scales will correspond to different frequency-bands. The coefficients of z with respect to the basis vectors of scale 0 are collected in a vector $\boldsymbol{Z}_0 \in \mathbb{R}^{8\times1}$. Analogously the coefficients corresponding to scale 1 and scale 2 are collected in respectively $\boldsymbol{Z}_1 \in \mathbb{R}^{4\times1}$ and $\boldsymbol{Z}_2 \in \mathbb{R}^{2\times1}$. The vector $\boldsymbol{Z} = [\boldsymbol{Z}_0 \quad \boldsymbol{Z}_1 \quad \boldsymbol{Z}_2]^T$ is then the DWT of z. The coefficients of the smallest scales can be set to zero to get a low-dimensional approximation of z. In this example $\boldsymbol{Z}_{low} = [\boldsymbol{0} \quad \boldsymbol{Z}_1 \quad \boldsymbol{Z}_2]^T$ for which the inverse DWT is z_{low}, shown in Fig. 3c. Note that only three scales are used here and that boundary effects are not taken into account.

3.2 A wavelet-based surrogate

The DWT is introduced in the quasi-Newton iterations to solve the steady free surface problem. For a non-uniform free surface grid, the pressure $\boldsymbol{p}^j$ is first interpolated to a uniform grid. The DWT is then calculated, giving the array of coefficients $\boldsymbol{P}^j = [\boldsymbol{P}^j_0 \; \boldsymbol{P}^j_1 \; \cdots]^T$. The s smallest scales are then removed, reducing the number of variables from n to m. This also eliminates most interpolation errors, as these are mainly present in the small scales (high wavenumbers). The low-dimensional pressure in the wavelet domain $[\boldsymbol{P}^j_s \; \boldsymbol{P}^j_{s+1} \; \cdots]^T$ is then used in the quasi-Newton equation of Eq. (1), which is solved for the new

[1] The well-known JPEG format uses the Discrete Cosine Transform (closely related to the Discrete Fourier Transform) for lossy image compression. The newer JPEG 2000 format instead uses the Discrete Wavelet Transform. It was developed to improve compression performance, but never became widely adopted. https://blog.ansi.org/2018/07/why-jpeg-2000-never-used-standard-iso-iec/

[2] In fact, wavelets cannot form a complete (bi)orthogonal basis: a wavelet always has average value 0, i.e. it corresponds to a frequency band which does not include $k = 0$. The smallest wavelet scale corresponds to the grid size, the largest wavelet scale depends on the number of scales used in the DWT. To capture all wavenumbers between 0 and the largest wavelet scale, a *scaling function* is introduced. These are very similar to wavelets, but have a non-zero average. A dilated and translated mother wavelet in combination with a translated scaling function, can give a complete (bi)orthogonal basis.

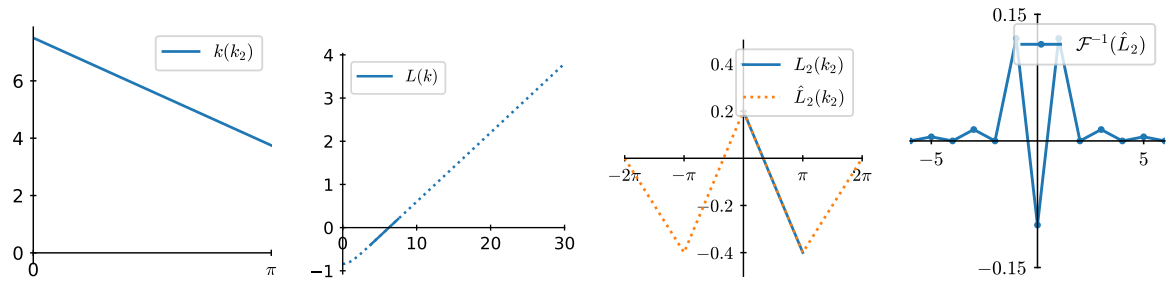

(a) (b) (c) (d)

Fig. 4: Example of steps to construct $\boldsymbol{J}_{\text{sur}}$ for scale $s = 2$.

free surface height $[\boldsymbol{Z}_s^{j+1}\ \boldsymbol{Z}_{s+1}^{j+1}\ \cdots]^T$. The resulting array is padded with zeros, transformed back with the inverse DWT and interpolated to the original grid to get $\boldsymbol{z}^{j+1}$.

As the quasi-Newton equation is now solved in the wavelet domain for a 3D surface, as opposed to in the spatial domain for 2D, the surrogate model $\boldsymbol{J}_{\text{sur}}$ must be adapted to this low-dimensional basis (no adaption is required for the least-squares approximation $\boldsymbol{J}_{\text{LS}}$). The detailed construction of the surrogate model does not fit in the scope of this paper, but an overview of the required steps is given, accompanied by an example in Fig 4. Construction of the 3D surrogate follows the same procedure, but is even more cumbersome to describe.

1. The Biorthogonal 3.5 wavelet basis is used, see Fig. 2. This wavelet is smooth, odd, compact in the spatial domain and well localized in the wavenumber domain. The basis signals are not orthogonal, but using the DWT and inverse DWT, signals have a unique decomposition and reconstruction in this basis.

2. Eq. (2) describes the behavior of sinusoidal perturbations of $\boldsymbol{z}$ with wavenumber k. On the other hand, in the wavelet domain there may be sinusoidal perturbations of $\boldsymbol{Z}_s$ with wavenumber k_s. It has been observed that each sinusoid with wavenumber k_s in the wavelet domain, corresponds approximately to a sinusoid with wavenumber k in the spatial domain. As a consequence, for each scale a function $L_s(k_s)$ can be derived from $L(k)$. This $L_s(k_s)$ relates sinusoidal perturbations $\boldsymbol{Z}_s$ and $\boldsymbol{P}_s$. In Fig. 4a the relation $k(k_s)$ is shown for scale $s = 2$ of a case corresponding to Fig. 4b. In that picture, $L(k)$ is shown with the range of wavenumbers corresponding to scale 2 emphasized. From the curves in Figs. 4a and 4b follows $L_2(k_2)$ in Fig. 4c.

3. In theory, with $\mathcal{F}$ the DFT operator, $\boldsymbol{P}_s$ can be calculated for an arbitrary $\boldsymbol{Z}_s$ by making a detour through the Fourier domain: $\boldsymbol{P}_s = \mathcal{F}^{-1}(L_s \cdot \mathcal{F}(\boldsymbol{Z}_s))$. However, going through the Fourier domain is not very practical. Instead, it is possible to replace the multiplication in the Fourier domain by a convolution in the wavelet domain, using the convolution theorem: $\mathcal{F}^{-1}(L_s \cdot \mathcal{F}(\boldsymbol{Z}_s)) \sim \mathcal{F}^{-1}(L_s) * \boldsymbol{Z}_s$. The left and right hand sides are equal up to a constant factor which depends on the definition of the applied DFT.

4. The inverse transform of L_s is not known. However, each wavelet scale corresponds to only a small band of wavenumbers k, so that all L_s are close to linear functions of k_s. Replacing L_s by a linear approximation $\hat{L}_s$, the inverse Fourier transform can be calculated analytically. $\mathcal{F}^{-1}(\hat{L}_s)$ damps out with $1/x^2$, so a good approximation can be made using only the 7 or 11 central points. Fig. 4c shows the linear approximation $\hat{L}_2(k_2)$ and Fig. 4d its inverse DFT, restricted to 11 points.

5. The discrete convolution $\mathcal{F}^{-1}(\hat{L}_s) * \boldsymbol{Z}_s$ can be seen as a window $\mathcal{F}^{-1}(\hat{L}_s)$ moving over the signal $\boldsymbol{Z}_s$. This process can be described by a matrix product $\boldsymbol{J}_s \cdot \boldsymbol{Z}_s$ where the window is inserted in each row of $\boldsymbol{J}_s$, centered around the diagonal.

6. This process must be done for each wavelet scale which was not set to zero. The individual matrices $\boldsymbol{J}_s$ are put in one big matrix $\boldsymbol{J}_{\text{sur}} \in \mathbb{R}^{m \times m}$.

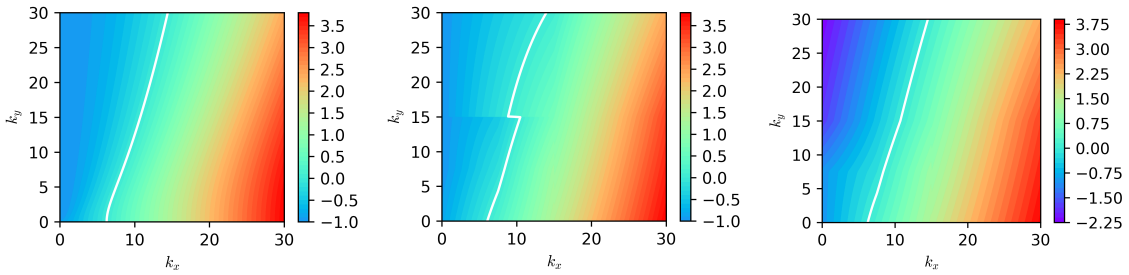

(a) $L(\boldsymbol{k})$ (b) $\hat{L}(\boldsymbol{k})$ (c) $\hat{L}^*(\boldsymbol{k})$

Fig. 5: The function $L(\boldsymbol{k})$ as defined in Eq. (3) for Fr $= 0.4, \rho = g = h = 1$. Two approximations used in constructing $\boldsymbol{J}_{\text{sur}}$ are also shown. The zero-contours are shown in white.

3.3 Testing the new surrogate model

In the last step before the surrogate model can be constructed, the relation of Eq. (2) between perturbations of the free surface height and pressure must be extended to 3D flows. Sinusoidal perturbations now have components in the flow direction (k_x) and perpendicular to the flow direction (k_y). Two notations are introduced to make the equations more compact: $\boldsymbol{k} = (k_x, k_y)$ and $k^2 = k_x^2 + k_y^2$. For a sinusoidal height perturbation $z_{\boldsymbol{k}}(x, y) \sim \sin(k_x x + k_y y + \theta)$, the linearized Euler equations can be solved (with suitable boundary conditions), yielding the relation:

$$L(\boldsymbol{k}) \cdot z_{\boldsymbol{k}}(x, y) = p_{\boldsymbol{k}}(x, y) \qquad \text{with} \qquad L(\boldsymbol{k}) = \rho g \left(\text{Fr}^2 \frac{k_x^2}{k^2} \frac{kh}{\tanh kh} - 1 \right) \tag{3}$$

Notice that for $k_y \to 0$, Eq. (3) reduces to Eq. (2). An example of this relation is plotted in Fig. 5a.

The 3D surrogate model is tested as follows: a height perturbation $\boldsymbol{z} = \sin(k_x \boldsymbol{x} + k_y \boldsymbol{y} + \theta)$ is transformed to the wavelet domain, the small scales are omitted, then it is converted to a pressure using $\boldsymbol{J}_{\text{sur}}$ and finally transformed back to the spatial domain. The obtained pressure $\boldsymbol{p}$ can be compared to the theoretically correct pressure $L(\boldsymbol{k}) \cdot \boldsymbol{z}$. This process is illustrated in Fig. 6 for $\boldsymbol{k} = (3, 5)$. The original domain has $n = 250\,000$ free surface grid points, which is reduced to $m = 7747$ coefficients in the wavelet domain by removing the 3 smallest scales.

From Fig. 6c, the effective factor $L_{sur}(\boldsymbol{k})$ obtained using the surrogate model can be estimated. This should be as close as possible to the correct factor $L(\boldsymbol{k})$. An interesting way of comparing L and L_{sur} for a given test, is by looking at the *amplification factor* $\mu = \boldsymbol{z}^{j+1}/\boldsymbol{z}^j$. This factor expresses how an error component $\boldsymbol{z}$ will converge/diverge, if only the surrogate model $\boldsymbol{J}_{\text{sur}}$ is used as approximate Jacobian in Eq. (1). It can be shown that $\mu = 1 - L/L_{sur}$. In theory, iterations will converge for a certain error mode $\boldsymbol{z}$ when $|\mu| < 1$ for that mode. The amplification factor is calculated for a whole range of values of $\boldsymbol{k}$ and the result is shown in Fig. 7a.

In the region where L is close to zero, the result is not good. The reason can be found in Fig. 5b: the approximation $\hat{L}$ which is used for constructing $\boldsymbol{J}_{\text{sur}}$ is not everywhere a good approximation of L, due to the important non-linearity in L at small k_x. In order to get a better amplification factor, a different approximation of L is made. The original $\hat{L}$ is a bi-linear interpolation from a number of sampled points of L. A new approximation $\hat{L}^*$ (see Fig. 5c) is obtained by adapting the values in some of these points so that there is a better correspondence between the zero-lines in L and $\hat{L}^*$. As a consequence, the difference between L and $\hat{L}^*$ may be larger than between L and $\hat{L}$ in places, but overall μ is much better as can be seen in Fig. 7b.

4 Conclusion

In this paper, wavelets were used to make a low-dimensional approximation of smooth signals. Furthermore, for biorthogonal wavelets a relation was found between the frequency content of a signal in the spatial domain and in the wavelet domain. Using this relation, it is possible to construct surrogate models to approximate the behavior of 2D and 3D steady free surface flows. In 2D the surrogate model

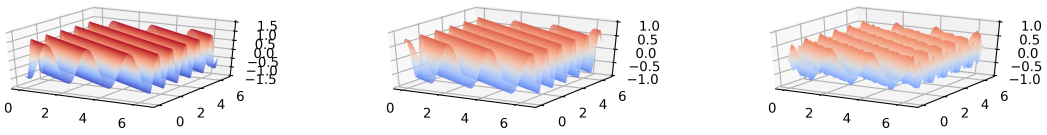

(a) Height z. (b) Correct pressure $L(\boldsymbol{k}) \cdot z$. (c) Predicted pressure $\boldsymbol{J}_{\text{sur}} \cdot z$.

Fig. 6: Testing the surrogate model for a wave with $k = (3, 5)$.

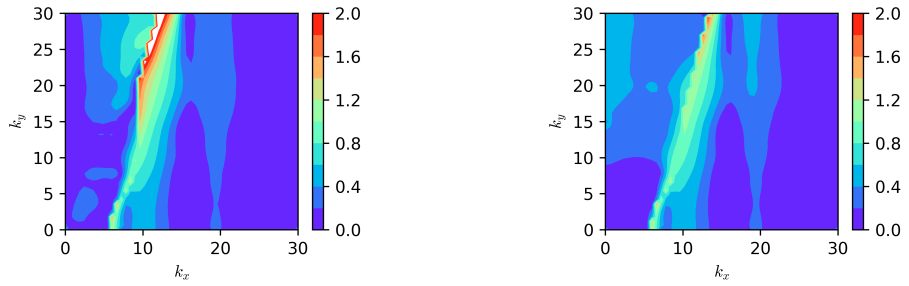

(a) Based on original $\hat{L}(\boldsymbol{k})$. (b) Based on adapted $\hat{L}^*(\boldsymbol{k})$.

Fig. 7: $|\mu(\boldsymbol{k})|$, the absolute value of the amplification factor.

performed very well when solving steady free surface flow with a quasi-Newton method (not discussed in the paper). For 3D, some first tests were done to check the validity of the surrogate model.

In the near future, more extensive testing of the 3D surrogate model will be done, by applying it to non-sinusoidal signals and comparing the result to CFD simulations. When the surrogate model performs satisfactorily, it will be used to extend the 2D steady free surface method to 3D.

References

Degroote, J., Bathe, K.-J., and Vierendeels, J. (2009). Performance of a new partitioned procedure versus a monolithic procedure in fluid–structure interaction. *Computers & Structures*, 87(11):793–801.

Demeester, T., Degroote, J., and Vierendeels, J. (2018). Stability analysis of a partitioned iterative method for steady free surface flow. *Journal of Computational Physics*, 354:387–392.

Demeester, T., van Brummelen, E. H., and Degroote, J. An efficient quasi-Newton method for 2D steady free surface flow. Manuscript submitted for publication.

Demeester, T., van Brummelen, E. H., and Degroote, J. (2019). Extension of a fast method for 2D steady free surface flow to stretched surface grids. In *Proceedings of the 8th International Conference on Computational Methods in Marine Engineering*.

Hirt, C. W. and Nichols, B. D. (1981). Volume of fluid (VOF) method for the dynamics of free boundaries. *Journal of Computational Physics*, 39(1):201–225.

Mallat, S. (2008). *A Wavelet Tour of Signal Processing: The Sparse Way*. Academic Press.

PyWavelets (2019). Wavelet browser. `http://wavelets.pybytes.com/`. Accessed: 05-09-2019.

Sussman, M., Smereka, P., and Osher, S. (1994). A level set approach for computing solutions to incompressible two-phase flow. *Journal of Computational Physics*, 114(1):146–159.

van Brummelen, E. H., Raven, H. C., and Koren, B. (2001). Efficient numerical solution of steady free-surface Navier–Stokes flow. *Journal of Computational Physics*, 174(1):120–137.

Development of a Mesh Refinement Process for the Prediction of Propeller Tip Vortex Cavitation

Ronan Doherty, James Alderton and William Batten
QinetiQ, Haslar Maritime Technology Park, Gosport, United Kingdom
rldoherty@qinetiq.com

1 Introduction

Cavitation occurs when the fluid pressure drops below the local vapour pressure and is often an inevitable phenomenon for hydro machinery. It can have a detrimental impact on power and performance and is therefore a major limiting factor in the design of marine propulsors. The low pressure core of a strong propeller tip vortex can initiate tip vortex cavitation, which can lead to excessive noise and vibration, as well as causing erosion to the propulsor and surrounding structures. Of particular importance is the noise signature associated with the inception of a tip vortex cavity, which can pose a significant threat to ocean wildlife, particularly to marine mammals which rely on sound for communication. Development of accurate and reliable techniques for the numerical prediction of tip vortex cavitation has therefore become an area of growing interest in recent years, as has been the assessment of the application of commercial CFD codes to cavitating propeller flows.

From the relevant literature it can be seen that prediction of the tip vortex cavity depends strongly on the mesh resolution within the vortex region (Szantyr *et al.* 2011, Fujiyama *et al.*, 2011). Mesh refinement approaches have thus far focused on fixed volumetric refinements behind the propeller tip, requiring *a priori* knowledge of the flow field, and a mesh refinement cell size of $D_{Prop}/1000$ has been employed to resolve part of the tip vortex cavity (Yilmaz, 2017). Given the computationally demanding requirements on the mesh, and the current limitations of the cavitation models, it is noted that there are still difficulties in numerically predicting the full extent of the downstream tip vortex cavity when using commercial CFD codes (Usta *et al.*, 2018). In order to predict the conditions for the onset of cavitation for full scale vessels, a reliable scaling law to scale from model tests to full scale propellers for cavitation inception is required. Deriving a suitable scaling law for cavitation inception using CFD has also been an area of interest within cavitation research (Hsiao *et al.*, 2008, Shen *et al.*, 2009).

The aim of this study was to develop a mesh refinement process for the numerical prediction of tip vortex cavitation, using the commercial CFD package STAR-CCM+. Given the strong dependence on the mesh resolution within the areas of interest, this study focuses on mesh refinement, and the use of field functions for adaptive meshing are investigated. The process should be able to capture the minimum pressure within the tip vortex core and should be applicable to different types of hydrodynamic propulsors, at both model and full scale. Additionally, to limit pre-processing time, an overly manual process should be avoided and it should therefore be easily automated. It is also hoped that the mesh refinement process can be used to investigate the effect of scaling on tip vortex cavitation inception.

2 Development of the Mesh Refinement Process

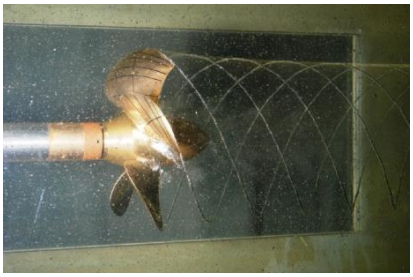

Fig. 1: Still from case 2.3.2.

Propeller diameter, D_{Prop}	0.25m
Advance Ratio, J	1.269
Cavitation number, σ_n	1.424
Density, ρ	997.59 kg/m^3
Dynamic viscosity, μ	9.4472E-04 Pa.s
Inlet velocity	7.93 m/s
Outlet pressure	30516.47 Pa
Propeller RPM	1500

Table 1: PPTC case 2.3.2 conditions.

The Potsdam Propeller Test Case (PPTC) is a 5-bladed model scale propeller which has been experimented on in both cavitating and non-cavitating conditions by the SVA Potsdam Model Basin.

The results were released as part of the 2011 Symposium on Marine Propulsors (smp'11) as validation data to aid the development of numerical methods for calculation of the performance of marine propulsors (Barkmann *et al.*, 2011). Case 2.3.2 from the cavitating experiments was chosen as an ideal case for the development of the refinement process, since in this case tip vortex cavitation visibly occurs, as can be seen in Fig. 1. The flow conditions for this case are shown in Table 1.

The flow solver used was STAR-CCM+ 13.04.011, and the simulations were run in steady state conditions with a single water phase. The rotation of the propeller was modelled using a rotating reference frame. The RANS (Reynolds Averaged Navier Stokes) K-Omega SST turbulence model was used with an all y+ wall treatment. A single blade passage was modelled using periodic boundaries, as the blades were assumed to be identical, and a polyhedral mesh was used for the propeller blade passage. The computational domain and the single blade passage boundaries are shown in Figs. 2 and 3, respectively.

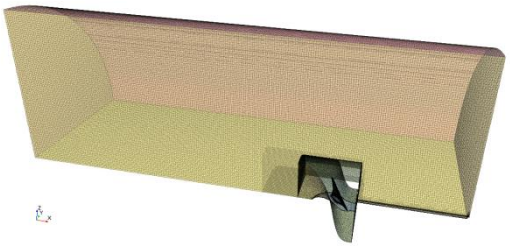

Fig. 2: Full computational domain.

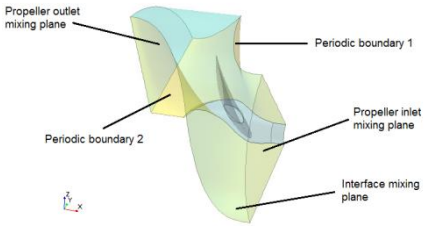

Fig. 3: Single blade passage boundary conditions.

The mesh refinement table method was investigated by firstly obtaining an initial converged solution on a coarse mesh and then defining a mesh refinement x,y,z, position table based on field function criteria. This table is then used to define cell sizes, and the domain is re-meshed before continuing the simulation. However, this method was deemed unsuitable, as the tables do not partition well on multiple cluster cores. The resulting mesh contained large cell volume gradients and poor quality cells, and this led to poor convergence of the solution.

As a result, an alternative method was explored; threshold part volumetric refinement. As before, an initial converged solution is obtained on a coarse mesh and from this solution threshold parts are defined based on field functions of interest. These threshold parts are saved as STL files and imported into the simulation, and the surface is then wrapped using the surface wrapper tool to ensure a closed volume. The wrapped surface can then be used to define volumetric refinements. The simulation continues on the refined mesh until convergence is achieved, and the refinements are repeated iteratively, reducing the refinement cell sizes on each iteration, until convergence of the minimum vortex pressure is achieved. This method has numerous advantages over the mesh refinement table method as thresholds of scalars are easy to construct and export, the volumetric refinements will efficiently mesh in parallel and the resulting mesh is of good quality since volumetric growth rates can be utilised.

a) Helicity, threshold value = 1000 m/s^2

b) Tangential vorticity, threshold value = 300 s^{-1}

c) Threshold value = vapour pressure

Fig. 4: Thresholds of the assessed field functions.

Once the initial solution had been run on the initial coarse mesh, multiple field functions were assessed to determine which of these could effectively delineate the tip vortex region, and to determine what threshold values should be used. To ensure that the refinements would only be applied to the blade tip, the field functions were filtered so as to only be defined within the region 0.8<radial

co-ordinate/propeller radius<1.1. The field functions assessed were helicity, tangential vorticity and absolute pressure, which are shown in Fig. 4. From the assessment, it was decided that a two-tier refinement strategy would be employed, with refinements applied to the region with tangential vorticity > $300s^{-1}$, and a finer refinement applied to the region below the vapour pressure, P < 2771Pa. The volumetric refinement cell sizes were reduced by 25% on each iteration, and the volumetric refinements for iterations two, four and six are shown in Figs. 5 and 6. It can be seen that as the mesh is refined, the absolute pressure volumetric refinement region grows, indicating that the tip vortex is being resolved further downstream as the mesh is refined. Fig. 7 shows the pressure coefficient and the mesh within the tip vortex, just downstream of the blade. It is observed that as the mesh is refined, the vortex core pressure decreases, since the tip vortex is better resolved.

Fig. 5: Tangential vorticity volumetric threshold refinements for iterations two, four and six. Cell sizes are $D_{Prop}/320$, $D_{Prop}/640$ and $D_{Prop}/960$, respectively.

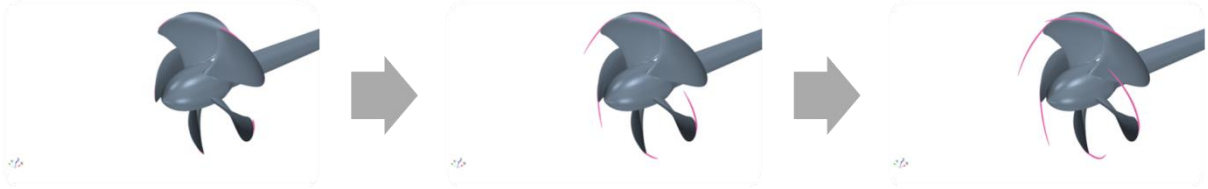

Fig. 6: Absolute pressure volumetric threshold refinements for iterations two, four and six. Cell sizes are $D_{Prop}/640$, $D_{Prop}/1280$ and $D_{Prop}/2880$, respectively.

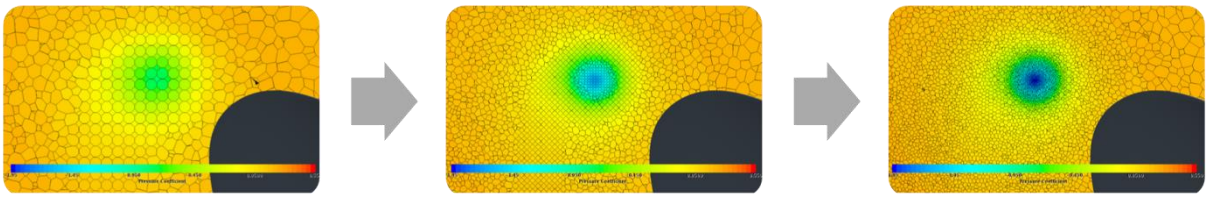

Fig. 7: The refined mesh and pressure coefficient within the tip vortex for iterations two, four and six.

Fig. 8 shows the convergence of the total volume of cells below vapour pressure, throughout the refinement process. Annotations R1 to R6 denote the mesh refinement iterations. Fig. 9 shows the vortex core pressure coefficient at two locations downstream of the propeller, and the minimum pressure coefficient within the vortex, Cp_{min}. Vortex monitor locations 1 and 2 lie on the plane which intersects the propeller centre line and lies parallel to the x- and z-axes, with vortex location 2 lying one full propeller tip vortex rotation downstream. From Fig. 8, convergence of the volume below vapour pressure is achieved by the fifth tip vortex mesh refinement, R5. Fig. 9 shows that convergence is achieved for the vortex core pressure coefficients at locations 1 and 2.

From the experimental data, a thrust coefficient, K_T, of 0.2450 was obtained for the non-cavitating open water case, and a value of 0.2064 for the cavitating case. For the most refined mesh, R6, a K_T value of 0.2458 was calculated. Since cavitation was not modelled in the CFD, this value is compared to the non-cavitating experiment, and a difference of 0.33% is obtained. Monitoring K_T throughout the refinements, it was observed that the tip vortex refinements did not have a significant impact.

3 Application of the Mesh Refinement Process to Scaled-Up Propellers

The refinement process was applied to two scaled up PPTC cases, representative of a medium scale and a full scale propeller. The propeller diameter was scaled up by a factor of six and fifteen to yield the medium and full scale propeller diameters, respectively. The simulation conditions were obtained

by ensuring cavitation number and advance ratio similarity, and are shown in Table 2. The fluid properties of the two larger propellers are representative of seawater at 15 degrees.

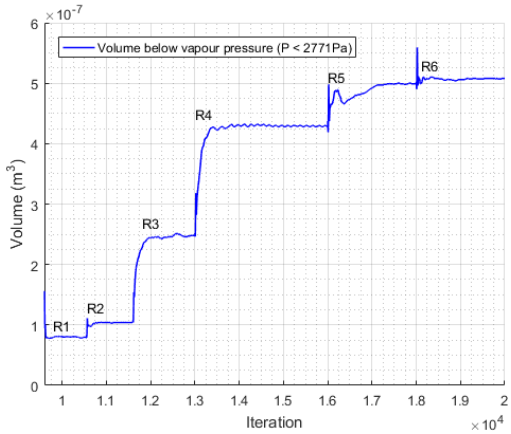

Fig. 8: Monitor of volume below vapour pressure.

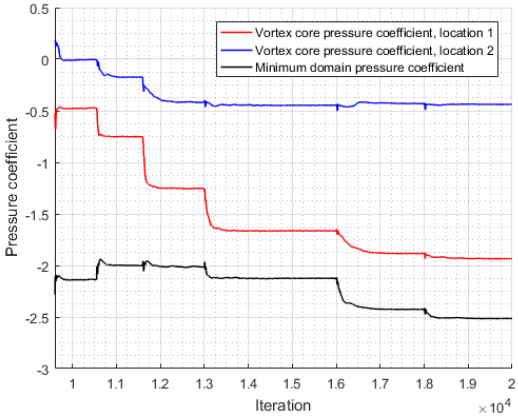

Fig. 9: Monitors of the vortex core pressure coefficients at two locations downstream of the blade, and the minimum domain Cp.

Table 2: Scaled up propeller dimensions and flow conditions.

	Model Scale	**Medium Scale**	**Full Scale**
D_{Prop} (m)	0.25	1.5	3.75
ρ (kg/m^3)	997.59	1025.07	1025.07
μ (Pa.s)	9.4472E-04	1.1030E-03	1.1030E-03
U_∞ (m/s)	7.93	9.774	13.376
P_{Out} (Pa)	30516.47	46085.23	83880.19
RPM	1500	308.14	168.67

It was found that the tangential vorticity threshold value could be non-dimensionalised using the propeller diameter and the inlet velocity, whilst maintaining the same relative refinement volume at all scales. A normalised tangential vorticity threshold value of 9.5 was employed in all cases. The absolute pressure threshold remained the same for all cases, as the fluid vapour pressure was assumed to be unchanged. Figs. 10 and 11 show the monitored values throughout the refinement process for the Full scale propeller.

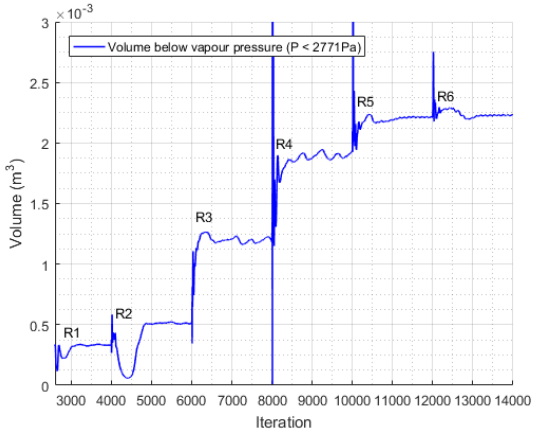

Fig. 10: Monitor of volume below vapour pressure for the full scale propeller.

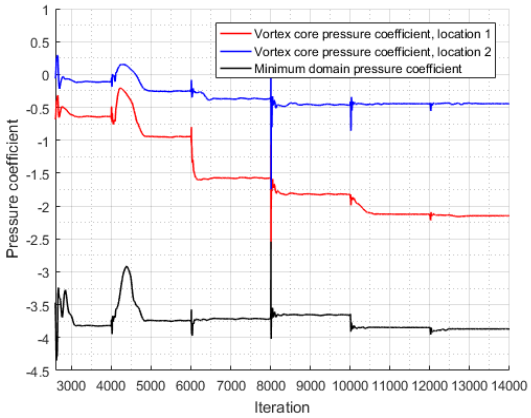

Fig. 11: Monitors of the vortex core pressure coefficients at two locations downstream of the blade, and the minimum domain Cp.

The convergence behaviour remains more or less unchanged when compared to the model scale convergence (Figs. 8 and 9) however it can be seen that the converged pressure coefficient values are lower for the full scale propeller. To further investigate these differences, the pressure coefficient was

plotted through the tip vortex at location 1 for both the model and full scale propellers, and these are shown in Figs. 12 and 13. The distance from the vortex centre has been normalised by propeller diameter in each case.

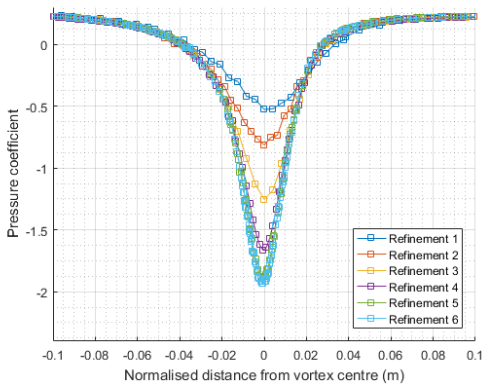

Fig. 12: Plot of Cp across the model scale vortex core.

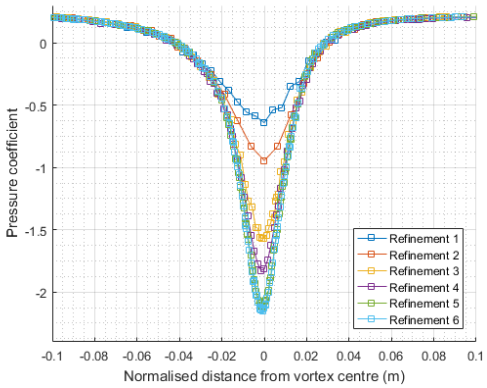

Fig. 13: Plot of Cp across the full scale vortex core.

These Figures show that the vortex core pressures have converged by R6 as there is very little change between the R5 & R6 mesh plots. It is observed that the free stream pressure coefficient is the same in both cases, which is expected as both were run at the same cavitation number, and the relative size of the vortex core remains the same. As observed in Fig. 11, the minimum pressure coefficient is lower for the full scale propeller.

4 Cavitation inception scaling

As the refinement process has been applied to different propeller scales, a cavitation inception scaling law can be investigated. Assuming the cavitation inception number is $-Cp_{min}$, a scaling law can be defined according to Eq. 1.

$$\frac{\sigma_{i,2}}{\sigma_{i,1}} = \frac{-Cp_{min,2}}{-Cp_{min,1}} = \left(\frac{Re_2}{Re_1}\right)^{\gamma} \tag{1}$$

There have been numerous studies investigating the appropriate scaling parameter, γ, that should be used, and these can be compared to that found using the refinement process. The classical constant for γ was calculated by McCormick for a hydrofoil tip vortex, and was found to be 0.4 (McCormick, 1962). However, recent studies have shown that this value is applicable only to the laminar flow regime, and that γ should increase with Reynolds number, R_e. Eq. 2 shows a relation for γ based on turbulent boundary layer theory, which is dependent on R_e (Shen *et al.*, 2009).

$$\gamma = \frac{5.16log\left(\frac{logRe_2}{logRe_1}\right)}{log\left(\frac{Re_2}{Re_1}\right)} \tag{2}$$

Table 3 shows R_e and the tip vortex Cp_{min} obtained from the refinement process for the three propeller scales and Table 4 shows the γ value obtained from the refinement process and from Eq. 2.

Table 3: Re and tip vortex Cp_{min} for the three propeller scales.

	Model Scale	**Medium Scale**	**Full Scale**
R_e	1.745×10^6	18.91×10^6	38.87×10^6
Tip Cp_{min}	-2.514	-3.510	-3.869

It can be seen that the values obtained from the refinement process are much lower than the classical value of 0.4, as the flow within the propeller tip vortex at this R_e range is highly turbulent. The γ values obtained from the refinement process are also lower than those predicted by Eq. 2. However, the trend is the same, indicating that the refinement process results capture the R_e dependency of the scaling law. Hsiao *et al.* (2008) performed a CFD study on small, medium and large scaled propellers,

representing R_e numbers of 2.09×10^6, 4.19×10^6 and 8.38×10^6, using both RANS and DNS (Direct Numerical Simulation) approaches. Values for γ of 0.33 and 0.15 were obtained for the scaling of small to medium and medium to large scales, respectively, using RANS. The DNS simulations yielded lower Cp_{min} values, and γ values of 0.22 and 0.11 were obtained. These results also display a general trend for γ to decrease as R_e increases. As the refinement process simulations were performed at larger R_e, the values obtained by the refinement process are not unreasonable when compared to the higher R_e scaling values obtained by Hsiao *et al.* of 0.15 (RANS) and 0.11 (DNS). It must be noted that only single phase simulations have been run in this study, and there is evidence that γ is adjusted back closer to the classical value of 0.4 when nuclei effects are modelled, provided that a statistical cavitation inception criterion is used and is not too stringent (Hsiao et al. 2008.)

Table 4: Comparison between the CFD obtained scaling law and Shen's scaling law (Eq. 2.)

R_{e1}	R_{e2}	R_e Ratio	CFD γ	Shen's γ
18.91×10^6	38.87×10^6	2.055	0.135	0.302
1.745×10^6	18.91×10^6	10.836	0.140	0.332
1.745×10^6	38.87×10^6	22.267	0.139	0.325

7 Conclusions

A mesh refinement process for the prediction of tip vortex cavitation has been developed and applied to both the model scale PPTC and scaled up propellers. The process achieved convergence of the minimum vortex core pressures, Cp_{min}, for RANS simulations at the three propeller scales to which it was applied. A cell size of $D_{Prop}/2880$ was required within the tip vortex core for a converged Cp_{min} for all scales. It was also found that the tangential vorticity field function threshold could be non-dimensionalised to achieve the same relative refinement volume at all scales. The converged Cp_{min} values obtained by the refinement process reduced as the scale and R_e increased, which allowed for a prediction of the cavitation inception scaling parameter, γ. The scaling parameter obtained from the refinement process grew smaller with increasing R_e, which is in agreement with recent analytical and numerical studies. In the future, the refinement process should be applied to higher fidelity simulation methods such as DES (Detached Eddy Simulation), and the effect of modelling multiphase cavitation on the refinement process and on the predicted cavitation inception scaling parameter should also be investigated.

Acknowledgements

The authors acknowledge the UK MoD for supporting the research and development through the Maritime Strategic Capability Agreement.

References

U. Barkmann, H-J. Heinke and L. Lubke. "Potsdam Propeller Test Case (PPTC) Description", Second International Symposium on Marine Propellers smp'11, Hamburg, Germany, June 2011.

K. Fujiyama, C.H. Kim and D. Hitomi. "Performance and Cavitation Evaluation of Marine Propeller using Numerical Simulations". Second International Symposium on Marine Propulsors (smp'11), Hamburg, Germany, 2011.

C.-T. Hsiao and G. L. Chahine. "Scaling of Tip Vortex Cavitation Inception for a Marine Open Propeller". 27th Symposium on Naval Hydrodynamics, Seoul, Korea, 5-10 October 2008.

B.W. McCormick, "On Cavitation Produced by a Vortex Trailing from a Lifting Surface". *ASME Journal of Basic Engineering*, vol 84, pp. 369-379, 1962.

Y.T. Shen, S. Jessup, S. Gowing, "Tip Vortex Cavitation Inception Scaling for High Reynolds Number Applications". *Journal of Fluids Engineering*, vol. 131(7), 2009.

J. Szantyr, P. Flaszynski, K. Tesch, W. Suchecki and A. Alabrudzinski. "An Experimental and Numerical Study of Tip Vortex Cavitation". *Polish Maritime Research*, vol.18, pp. 14-22, 2011.

O. Usta and E. Korkut, "A study for cavitating flow analysis using DES model". *Ocean Engineering*, vol. 160, pp. 397-411, 2018.

N. Yilmaz , M. Khorasanchi and M. Altar, "An Investigation into Computational Modelling of Cavitation in a Propeller's Slipstream", Fifth International Symposium on Marine Propulsion (smp'17), Espoo, Finland, 2017.

Parametric analysis of the three-column spar platform for 6MW offshore wind turbine

Paweł Dymarski, Ewelina Ciba
Gdansk University of Technology, Gdansk/Poland
pawdymar@pg.edu.pl

1 Introduction

The dynamic development of the offshore wind energy sector in such countries as UK, Germany, Denmark, Netherlands means that shallow water areas are exhausted (with a depth of 40-50m), therefore wind farm projects at a depth of 50m+ are considered. In 2017, the first floating (deep water) mini-farm "Hywind" was launched off the coast of Scotland.

The "Hywind Scotland" farm is located on a 105 m deep water reservoir. The draft of a single platform is 78 meters. The anchoring system is of catenary type - steel chains are attached to suction piles. Each pile is about 15 meters high.

The main aim of this work was to develop an innovative concept of a three-column spar floating platform for a 6MW wind turbine for Polish Exclusive Economic Zone for 65m+ moderate water depth reservoirs. The key issues related to the use of floating platforms as supporting structures are the stability of platforms and the dynamic behavior of these platforms on the wave.

The authors present the stability analysis of the platform for various sizes of cylindrical buoyancy tanks and using different types of ballast. The authors investigated the influence of these parameters on the trim angle of the platform due to the thrust load on the turbine. Based on the results of parametric analysis and based on specific stability criteria, geometrical models of selected variants were created.

For these solutions, a preliminary analysis of platform dynamics was carried out in the conditions of a 50-year storm. Based on calculations of platform on the wave (using a simplified model), the amplitudes of platform motions, the maximum values of tendons tensions resulting from environmental forces were determined.

2 General types of floating wind turbines

Floating offshore wind turbines can be divided into three types due to the method of obtaining stability: tension leg platforms (mooring lines stabilized platforms), semisubmersible platforms (buoyancy stabilized platforms) and spar platforms (ballast stabilized platforms).

Spar platforms are also divided into the following concepts [1]:

- *"Classic" spar* - the hull of the platform is a cylinder, in the lower part there is a ballast, the upper, usually larger, part of the cylinder is empty,
- *truss spar* - the hull of the platform consists of two separate parts: a large buoyancy tank (at the top) and a small ballast tank located at the bottom of the platform. The tanks are connected by a lattice structure with a height of about half of the platform's draft.
- *Cell spar* - the hull is made up of seven cylinders (usually with the same diameter), three cylinders are significantly longer than the others, they keep the ballast tank in the bottom of the platform.

In this work, the third of the types of floating platforms has been developed. The concept of the three-column spar platform is presented in Fig. 1. The platform consists of three columns with a larger diameter around the waterline and a smaller one in the more submerged part. Cylindrical parts are connected with each other by conical elements. Cylinders are connected to each other at the top (above the water line) where there is a "deck" to which the tower is mounted and at the bottom where the ballast tank is located. The additional connection is located at the height of the attachment points of the tendons, this connection is to align the distribution of forces between the columns due to the reaction force from the anchoring system.

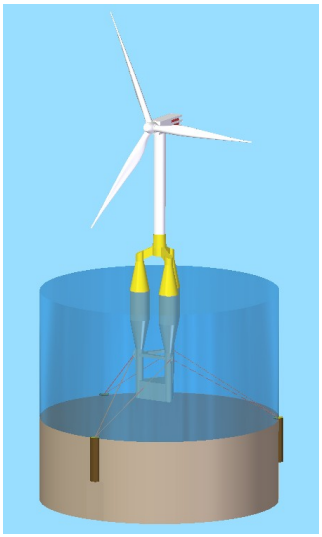

Fig. 1 Three-column spar concept

3 Parametric analysis of static stability

The main goal of the parametric analysis is to assess the static stability of the platform as a function of the two parameters:

- the diameter of the upper cylinders D_{tank} (change of buoyancy),
- the density of the ballast $\rho_{ballast}$, which is placed in the "triangular" bottom tank.The range of the upper cylinder diameter is: D_{tank} = 10 – 12 m, however, the assumed range of ballast density is: $\rho_{ballast}$ = 2600 – 4600 kg/m^3.

The lower value of ballast density corresponds to the density of concrete, while the upper value of the ballast density is close to the density of iron ore.

Static stability analysis of the platform consisted in calculating the trim angle due to the aerodynamic thrust force on the turbine. The desired value of the trim angle is the smallest value. It was assumed, however, that the trim with a value of θ=6˚is acceptable. The maximum static thrust on the turbine is T = 800kN [2, 3]. The value of thrust includes the impact of wind on the platform's tower.

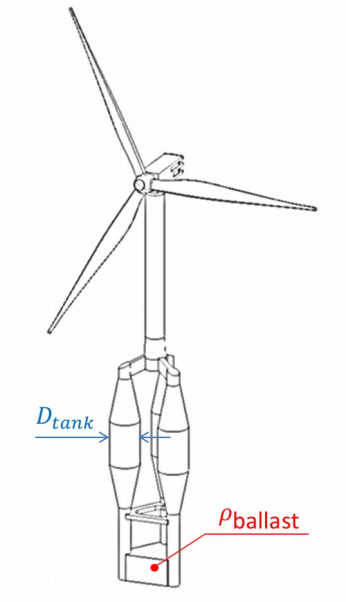

Fig. 2 Parameters D_{tank} and $\rho_{ballast}$

The graph (Fig. 4) show the obtained trim angles θ on the effects of the static thrust force T=800kN for a given range of parameters D_{tank} and $\rho_{ballast}$. On the basis of obtained values of the trim angle as a function of parameters D_{tank} and $\rho_{ballast}$, the area of feasible solutions was determined due to the trim θ caused by the thrust force.

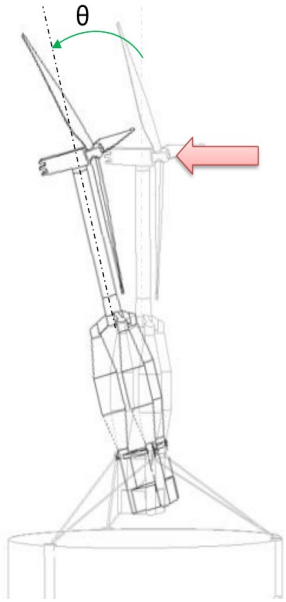

Fig. 3 Trim angle due to thrust force.

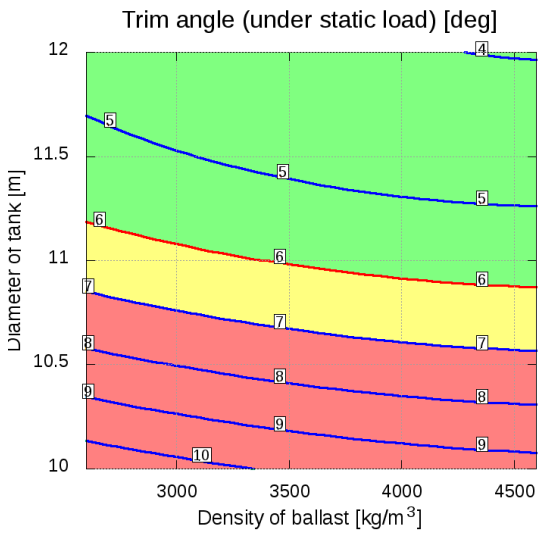

Fig. 4 Trim angle as a function of parameters D_{tank} and $\rho_{ballast}$. Green colour indicates the area of permissible parameters based on the limit line of the trim angle θ_c=6 ˚.

4 Analysis of platform dynamics

The second goal of the parametric analysis is to evaluate the amplitudes of platform movements in the function of the these parameters.

It is particularly important to analyse the heave and pitch motion of the platform. Minimizing horizontal movements (heave) is important due to the limited depth of the basin, the platform can not hit the bottom of the sea. Vertical accelerations, on the other hand, increase the loads from the mass of the structure.

4.1 Hydro-meteorological condition

The analysis of the movement of the platform subjected to wind, wave and sea currents was made for survival conditions [4]:

- Significant wave height: H_s=9m, peak period: T_p=11.3s, speed of sea current U_{curr} =0.45m/s
- Mean wind speed at the height of 10 meters: $U_{w,H=10m}$ = 29.1m/s.

The above weather conditions correspond to the conditions of a 50-year storm (recommended by classification societies [5]). The turbine is turned off.

The wave spectrum was approximated using JONSWAP formula, however the non-stationary character of wind speed was modelled using Ochi-Shin spectrum [6].

In order to disturb the symmetry of external forces, it was assumed that the wind direction is deviated from the wave direction by 10 degrees. This approach results in the fact that the platform is moving in six degrees of freedom, which allows to observe additional (often negative) effects.

4.2 Computational model

The computational model is based on the generalized Morison equation. The structure - consisting mainly of cylindrical elements - has been divided into segments. For each segment, forces are calculated using local velocity and water acceleration values as well as local velocity and acceleration of a given part of the structure. The thrust force on the turbine is calculated based on the thrust coefficient (which is constant for given conditions).

The vector of hydrodynamic force on the i-th cylindical segment is calculated using the formula [7, 8]:

$$\boldsymbol{F}_i = \frac{1}{2} C_D \rho A_{p,i} \left| \boldsymbol{u}_{n,i} - \dot{\boldsymbol{x}}_{n,i} \right| \left(\boldsymbol{u}_{n,i} - \dot{\boldsymbol{x}}_{n,i} \right) + \rho V_{b,i} \left(1 + C_A \right) \dot{\boldsymbol{u}}_{n,i} - \rho V_{b,i} C_A \ddot{\boldsymbol{x}}_{n,i} \quad , \tag{1}$$

where C_D – drag coefficient in the direction normal to the cyliner axis; ρ – water density; $A_{p,i}$ – projection of the segment surface onto the direction normal to the cylinder axis; $\boldsymbol{u}_{n,i}$, $\dot{\boldsymbol{u}}_{n,i}$ - water velocity and acceleration component normal to the cylinder axis, $V_{b,i}$ - segment volume, C_A – added mass coefficient, $\dot{\boldsymbol{x}}_{n,i}$, $\ddot{\boldsymbol{x}}_{n,i}$ – component of velocity and acceleration of the segment normal to the cylinder axisin.
The thrust force on the turbine is calculated from the following formula:

$$T = C_T \frac{1}{2} \rho_{air} A_T \left| u_w - u_t \right| \left(u_w - u_t \right) \quad , \tag{2}$$

where C_T – thrust coefficient of rotor, A_T – area of the rotor disk, ρ_{air} – air density, u_w – wind speed, u_t – the speed of the turbine hub.
The forces of the anchoring system are determined based on the characteristics of force F_t - elongation ε_t of tendons [9]. The actual tendon characteristics are shown in Fig. 5, for the purposes of the calculations the characteristics described in the 5th degree polynomial were adopted. Platform movement is calculated in six degrees of freedom with the assumption that the structure is rigid.
The breaking force of the rope is $F_{breaking}$=12 MN.

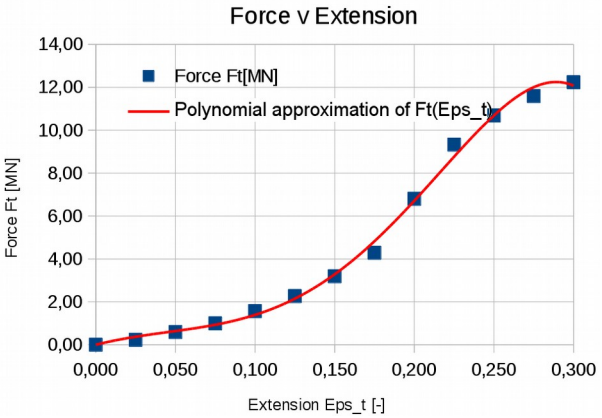

Fig. 5 Polynomial characteristics F_t vs ε_t of tendons. Rope: "*VIKING BRAIDLINE Nylon*", D_{rope}=240mm

4.3 Computation results

As the results of the wave motion calculations of the platform, we obtain graphs: surge, sway and heave motion as a function of time (Fig. 6 a). The horizontal acceleration of the nacelle, which is the main cause of the tower load is shown in Fig. 6 b), angular motions are shown in Fig. 6 c) and force in the ropes of the anchoring system are shown in Fig. 6 d). The results relate to the case: D_{tank} = 11m, $\rho_{ballast}$ = 3600 kg/m^3.

On the basis of the results of calculations in the time domain, diagrams of maximum values of heave amplitude, amplitude of nacelle acceleration, pitch and values of maximum forces in the tendons were created (Fig. 7 a, b, c, d). These diagrams were prepared in the field of D_{tank} and $\rho_{ballast}$ parameters.The area of acceptable values (of a given quantity) is marked with green, yellow indicates values at a critical level, which, however, can still be considered as acceptable. The areas in which the given values exceed the critical values are marked in red.

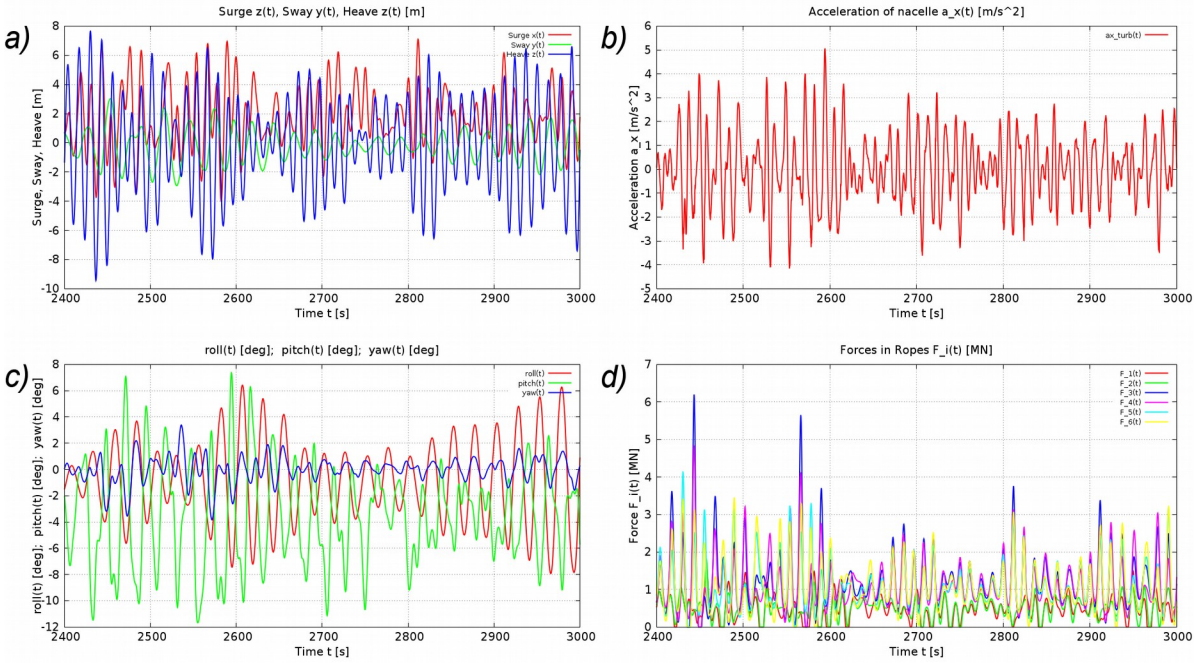

Fig. 6 a) Linear motions: surge (red), sway (green), heave (blue); b) linear, horizontal accelerations of nacelle Forces in ropes; c) Angular motions: roll (red), pitch (green), yaw (blue); d) Forces in ropes. The graphs show results for 600 seconds. The total simulation time is 3 hours (10800 seconds)

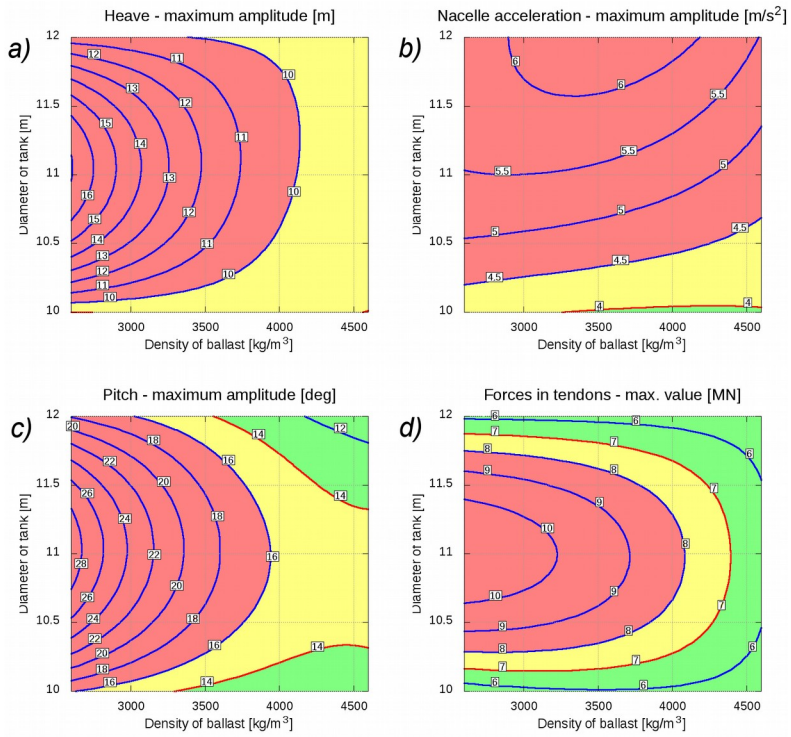

Fig. 7 Diagrams of maximum values recorded during a simulation lasting 3 hours: **a)** heave amplitude; **b)** acceleration amplitude; **c)** pitch amplitude; **d)** the maximum values of forces in the tendons

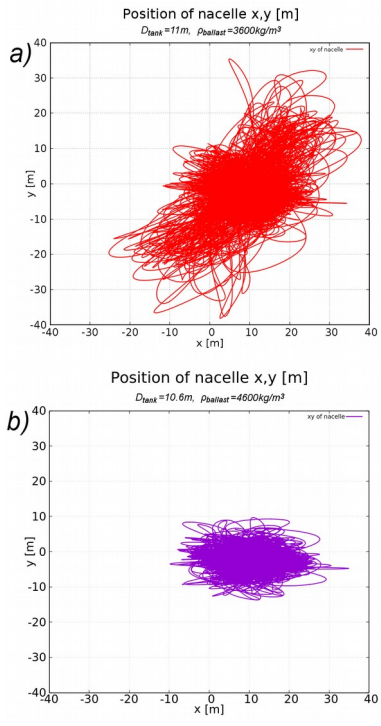

Fig. 8 Path of nacelle *x,y* (top view): **a)** variant from the middle of parametric area: D_{tank}=11m, $\rho_{ballast}$=3600kg/m^3; **b)** Acceptable solution D_{tank}=10.6m, $\rho_{ballast}$=4600kg/m^3

4 Conclusions and comments

- Based on the hydrostatic analysis for the design wind conditions, the trim angle θ was determined as a function of D_{tank} and $\rho_{ballast}$ parameters (Fig. 4). The chart shows that as the diameter of the displacement tanks D_{tank} increases, the trim angle decreases, which for the given range of parameters is between 4 and 10.5 degrees. It is noteworthy that a change in ballast density ρ_{ballas} (and a change in ballast tank size) has little effect on the trim angle achieved.
- The analysis of the calculations results of platform dynamics on the wave shows that the biggest problem are the large values of horizontal acceleration of the nacelle, which are the main reason for the bending moments of the platform's central column (tower). Assuming that the limit value of horizontal acceleration is $a_{x,nacelle,c}$=4.0 m/s^2 (Fig. 7 b), we obtain an area of permissible values that does not coincide with the area of the permissible trim angle, Fig. 4 (see item above). There is no acceptable solution.
- Loosening the criterion of maximum horizontal accelerations in such a way that we assume a critical value of $a_{x,nacelle,c}$=4.5 m/s^2 with a simultaneous increase of the minimum (critical) trim angle to the value of θ_c=7° will cause that the area of solutions acceptable in the small surroundings of the point D_{tank}=10.6 m, $\rho_{ballast}$=4600 kg/m^3 will appear. Fig. 8 shows the comparison between path (trajectory) of nacelle for case D_{tank}=11m, $\rho_{ballast}$=3600kg/m^3 (the middle of parametric area) and path of nacelle motion for the acceptable solution. The smaller the size of the "cloud", the better the conditions for turbine operation
- The authors' experience shows that the amplitudes of movements predicted using CFD, as well as the predicted amplitudes based on model tests are smaller than the amplitudes of motions obtained using a model based on the Morison equation. Probably the real area of acceptable solutions is larger than obtained in this paper.

Acknowledgement

This research was supported by The Polish National Centre for Research and Development (NCBR) under the project “WIND-TU-PLA” ERA-NET MARTEC II (Agreement No. MARTECII/1/2014).

References

[1] Moo-Hyun Kim (2012). SPAR Platforms. Technology and Analysis Methods. American Society of Civil Engineers

[2] Jonkman J., Butterfield S., Musial W., Scott G. (2009). Definition of a 5-MW Reference Wind Turbine for Offshore System Development. National Renewable Energy Laboratory, Technical Report NREL/TP-500-38060 February 2009

[3] Kooijman H.J.T., Lindenburg C., Winkelaar D., van der Hooft E.L. (2003). DOWEC 6 MW PRE-DESIGN. Aero-elastic modelling of the DOWEC 6 MW pre-design in PHATAS. Report DOWEC-F1W2-HJK-01-046/9 (public version). September 2003

[4] Dymarski P., Ciba E., Marcinkowski T. (2016). Effective method for determining environmental loads on supporting structures for offshore wind turbines. Polish Maritime Research 23(1(89)), 52-60. https://doi.org/10.1515/pomr-2016-0008

[5] DNVGL-ST-0437 (November 2016) Loads and site conditions for wind turbines

[6] Feikema G.J.,Withers J.E.W. (1991). The Effect of Wind Spectra on the Low-Frequency Motions of a Moored Tanker in Survival Condition. 23rd Annual Offshore Technology Conference in Houston, Texas. May 6-9, 1991

[7] Sarpkaya T. (2010) Wave Forces on Offshore Structures. Cambridge University Press, New York, 2010

[8] Żywicki J., Dymarski P., Ciba E., Dymarski C. (2017). Design of Structure of Tension Leg Platform for 6 MW Offshore Wind Turbine Based On Fem Analysis. Polish Maritime Research 24(s1), 230-241. https://doi.org/10.1515/pomr-2017-0043

[9] BRIDON. Fibre Rope Catalogue

RANS simulations for the turbulent uniform and channel flow using HDG for incompressible flow

Hashim Elzaabalawy[*,†], **Ganbo Deng**[*], **Luís Eça**[†], **and Michel Visonneau**[*]
[*]ECN/CNRS, LHEEA, Nantes/France
[†]IST, Department of Mechanical Engineering, Lisbon/Portugal
hashim.elzaabalawy@ec-nantes.fr

1 Introduction

All the industrial flow solvers dedicated to high Reynolds turbulent flows for industrial configurations are based on a formally second order accurate temporal and spatial discretization. There is a strong need for more accurate discretization approaches in many fields like computational acoustics or Large Eddy simulation which are still out of reach of systematic industrial studies. During the last ten years, several numerical methodologies have emerged, mainly for compressible flows, which look promising in terms of accuracy, computational cost and numerical robustness. A few of them concerned with incompressible flows which need very specific developments that will be the topic of this extended abstract. Numerous attempts were made to achieve high-order accurate unsteady INS solvers. However, plenty of them fails to satisfy conservation laws. Mass, momentum, and energy conservation are essential for the robustness of the method when solving the unsteady INS. Laminar flow and flows that typically have Reynolds numbers below 10^4 are not affected greatly by the lack of conservation. However, for high Reynolds numbers, i.e. turbulent flows, conservation laws must be satisfied in the numerical method to have a stable one. In order to satisfy the conservation laws numerically, the approximate velocity must be exactly divergence-free to have an energy-stable and momentum conserving method. A proposed method was developed that uses the same idea of approximation spaces mentioned in Rhebergen and Wells (2018), but with different penalization. In addition, the approximation spaces were modified so that the method can be applied for quadrilateral and hexahedral meshes.

2 Going to High-Order

It is accustomed among the CFD practitioners that high-order methods are the ones having the order of accuracy of 3 or more. The capabilities of using high-order methods are vast. Although, high-order methods can result in better accuracy, they are computationally less expensive than low-order methods. This statement is true for simple smooth problems, i.e. the Poisson equation and can easily be proven. However, is this statement true for INS on the industrial scale?
Before answering this question, the complexity added when solving the INS needs to be emphasized. The difficulty is mainly due to the incompressibility constraint and turbulence modeling. In the next section, how the high-order method can deal with the turbulent INS is briefly presented.

3 Numerical method

Hybrid Discontinuous Galerkin (HDG) provides a high-order, compact, and conservative discretization method. The hybridization offers a convenient platform to satisfy the divergence-free condition in an high-order framework, additionaly it reduces the overall operator size by reducing the number of DOF (Degrees of Freedom). However, not all HDG methods compute exact divergence-free velocity fields. Often, a post-processing operator is applied to acquire a divergence-free velocity field. Rhebergen and Wells (2018) provided a simple and efficient solution to impose the divergence-free condition using hybridization without the need of a post-processing operator to obtain an H(div)-conforming and pointwise divergence-free approximate velocity field on triangular meshes. This is achieved by carefully defining the approximation spaces of the velocity, pressure, trace velocity, and trace pressure. Most of the developed HDG methods for INS use the cell mean pressure instead of the trace pressure variable. The method has been modified so it would work with turbulent flows for quadrilateral elements. The INS equation

can be written in the conservative form as,

$$\frac{\partial \boldsymbol{u}}{\partial t} + \nabla (\boldsymbol{u} \otimes \boldsymbol{u}) = -\nabla p + \nu \nabla^2 \boldsymbol{u} + s \tag{1}$$

$$\nabla \cdot \boldsymbol{u} = 0 \tag{2}$$

Just for simplicity, we assume all Dirichlet boundary with u_D defined at the boundaries. If u_D satisfies the solvability condition, then the pressure is unique up to a constant.
The bounded domain Ω is in $\mathbb{R}^d$ with boundary $\partial\Omega = \partial\Omega_D$, $d = 1, 2,$ or 3 is the physical space dimension, and $\boldsymbol{n}$ is the outward unit normal to the boundary of Ω. The domain Ω is approximated by K number of non-overlapping elements and each element has its faces F. Introducing the broken spaces $V_h(\mathcal{T})$ and $W_h(\mathcal{T})$ associated with triangulation $\mathcal{T} = \{K\}$ in Ω which are the spaces for the approximate solution. The broken spaces $\bar{V}_h(\mathcal{F})$ and $\bar{W}_h(\mathcal{F})$ associated with faces $\mathcal{F} = \{F\}$ in $\partial\Omega$ which are the spaces for the trace variable. The approximation spaces are defined as follows,

$$V_h := \left\{ \phi_h \in [L^2(\mathcal{T})]^d \ , \ \phi_h \in [\mathcal{P}_N(K)]^d \ \forall K \in \mathcal{T} \right\}, \tag{3}$$

$$\bar{V}_h := \left\{ \bar{\phi}_h \in [L^2(\mathcal{F})]^d \ , \ \bar{\phi}_h \in [\mathcal{P}_N(F)]^d \ \forall F \in \mathcal{F} \right\}, \tag{4}$$

$$W_h := \left\{ \xi_h \in L^2(\mathcal{T}) \ , \ \xi_h \in \nabla \cdot [\mathcal{P}_N(K)]^d \ \forall K \in \mathcal{T} \right\} \tag{5}$$

$$\bar{W}_h := \left\{ \bar{\xi}_h \in L^2(\mathcal{F}) \ , \ \bar{\xi}_h \in \mathcal{P}_N(F) \ \ \forall F \in \mathcal{F} \right\}. \tag{6}$$

These are the vector spaces presented in Rhebergen and Wells (2018) with a modification for the definition of the space W_h, such that the method would be exactly point wise-divergence free for any element shape. The approximate solution and trace variables are defined as follow, $u_h \in V_h$, $\bar{u}_h \in \bar{V}_h$, $p_h \in W_h$, and $\bar{p}_h \in \bar{W}_h$.
Velocity u_h is of a degree N defined on the elements, pressure p_h is of a degree same as $\nabla \cdot u_h$ defined on the elements, trace velocity $\bar{u}_h$ components and trace pressure $\bar{p}_h$ are of a degree N defined on the facets. It can be proven that the choice of this special approximation space for p_h would automatically satisfy the divergence-free condition in the approximate spaces,

$$\nabla \cdot u_h = 0$$

As the divergence-free condition represents the pressure equation. In other words, the algorithm searches for p_h which satisfies this equation. Since the approximate spaces were designed to force $\nabla \cdot u_h \in W_h$ and $p_h \in W_h$, therefore u_h will be exactly point-wise divergence-free. With this formulation the pressure acts as a Lagrange multiplier to ensure that $\nabla \cdot u = 0$ in the approximate space. Also, the LBB condition is satisfied due to the reduced space for pressure approximation. The trace pressure $\bar{p}_h$ has a different role by acting as a Lagrange multiplier to force the normal velocity continuity at the faces, $u_h \cdot n = \bar{u}_h \cdot n$. These two conditions can be written as,

$$\int_K u_h \cdot \nabla \xi_h \, dx - \int_{\partial K} u_h \cdot n \xi_h \, ds = 0 \quad \forall \xi_h \in W_h, \tag{7}$$

$$\int_{\partial K} u_h \cdot n \bar{\xi}_h \, ds - \int_{\partial K} \bar{u}_h \cdot n \bar{\xi}_h \, ds = 0 \quad \forall \bar{\xi}_h \in \bar{W}_h, \tag{8}$$

After satisfying the mass continuity, a new variable $\boldsymbol{q}$ is defined to make the diffusion term suitable for HDG,

$$\frac{\partial \boldsymbol{u}}{\partial t} + \nabla \boldsymbol{f} = -\nabla p + \nu \nabla \boldsymbol{q} + s \tag{9}$$

$$\boldsymbol{q} - \nabla \boldsymbol{u} = 0 \tag{10}$$

$$\boldsymbol{f} = \boldsymbol{u} \otimes \boldsymbol{u} \tag{11}$$

In which the trace variable $\bar{q}_h$ is defined in terms of the velocity as,

$$n \cdot (\bar{q}_h - q_h) = \tau (\bar{u}_h - u_h) \tag{12}$$

where τ is a penalty parameter to ensure stability. For the sake of brevity, HDG discretization is applied on the viscous, pressure, and advection terms to reach the final discretized form.

4 Turbulence Model

Another challenge that faces the high-order accurate INS is the turbulence modeling. For industrial applications at high Reynolds numbers, RANS is the most convenient method to simulate turbulence in terms of computational time. Unfortunately, RANS has the largest modeling error. Hybrid LES/RANS provides a solution that compromises between computational time and modeling accuracy, but yet involves RANS modeling. It can be agreed upon that RANS is indispensable in the meantime for industrial applications. For that reason, the high-order accurate INS solver needs to be capable of solving the RANS equations. To solve the linear eddy viscosity RANS, a turbulence model is required to acquire the eddy viscosity. The $k-\omega$ model includes two convection-diffusion equations with source terms. However, they form a stiff operator due to their non-linearity. Furthermore, the k profile near the wall has very high gradients and ω goes to infinity at the wall, this adds more complexity. Due to the non-linearity and the huge gradients, oscillations appear near the high gradient zone. These oscillations result in negative quantities for k and ω. Physically, these quantities can never be negative. With the change of sign, production and dissipation terms are reversed, thus leading to a solution blowup. What even makes this worse is that oscillations increase as Reynolds numbers increase or as the polynomial order increases. Which makes high Reynolds number flows very challenging to model with high-order methods. Nonetheless, in this extended abstract attempts were made to solve the turbulence equations using HDG. There are different types of $k-\omega$ models, and the Wilcox 1998 model is chosen to start with.

5 Uniform flow test case

Although the uniform flow test case is a simple test, it can be a useful test case to check the divergence-free condition. Additionally, the turbulence model can be tested, as the analytical solution is expressed by Spalart and Rumsey (2007). The computational domain is a rectangle and inlet velocity is applied from the left boundary, which is equal to 1 in the x-direction and 0 in the y-direction. Symmetry boundary condition is applied at the bottom edge and outflow at the right and top edges. First, to show the importance of using divergence-free methods, the conventional HDG is compared with the developed point-wise divergence-free HDG for quadrilaterals. The contour of the divergence of velocity is plotted for the two methods at different viscosities using 4^{th} order HDG. These results were plotted after 6 linear iterations for the steady state INS.

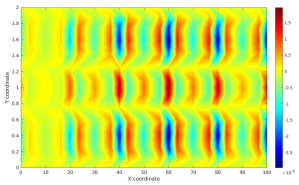

Fig. 1: $\nu = 10^{-2}$

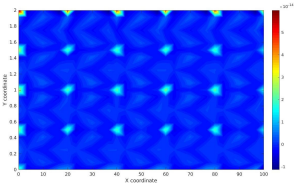

Fig. 2: Div-free $\nu = 10^{-2}$

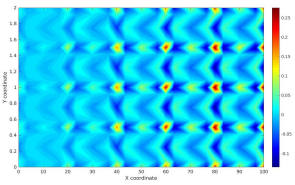

Fig. 3: $\nu = 10^{-9}$

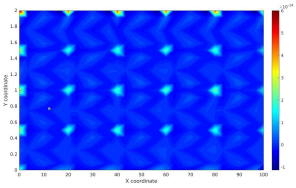

Fig. 4: Div-free $\nu = 10^{-9}$

It can be clearly seen that divergence increases as viscosity decreases in the conventional HDG method. While the point-wise divergence-free HDG always maintains a divergence-free velocity field upto the machine precision for any viscosity. In the steady case for low Reynolds numbers, this divergence in the velocity can be somehow accepted, however in transient cases the blow up is definite for long duration simulations. The divergence-free HDG is then coupled with the $k-\omega$ turbulence model. The values of k and ω are specified at the inlet. It is expected to for the turbulence variables to decay in the x-direction. The results obtained are plotted for $\nu = 10^{-6}$ at different and polynomials degrees and stretching near the inlet using quad meshes.

The polynomial degree of 2, 4, 6, and 10 with 23, 24, 21, and 22 DOF respectively in the x-direction are used. In the first case, the stretching was not enough to obtain stable solutions for higher order cases as shown in Fig. 5. While for the larger stretching, the results were stable even for the 10^{th} order approximation. For equally spaced elements in x, only the 2^{nd} order was stable, and the solution exhibits an undershoot that gives negative turbulence values. Apart from the shortcomings regarding stability, the

accuracy increases as the order increases as it can be shown in the Fig. 5,6,7. An important finding from these results is that, order-refinement increases the accuracy but upto a certain limit then it results in negative turbulence quantities then it blows up.

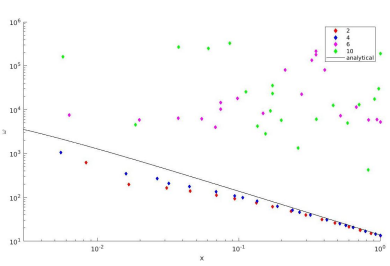

Fig. 5: ω on a less stretched mesh

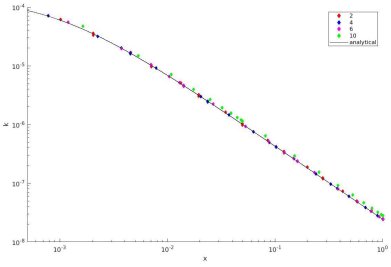

Fig. 6: k on a stretched mesh

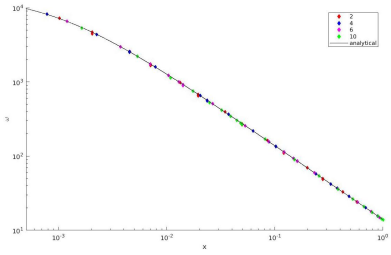

Fig. 7: ω on a stretched mesh

6 Channel flow test case

To understand the behavior of high-order RANS near the boundary layer in fully turbulent flows, the channel flow test case is chosen. Periodic boundary conditions are applied in the flow direction for all the variables, while no-slip wall boundary condition is applied on the other direction. A constant source term is added to the momentum equation as a pressure gradient to induce a flow. By keeping the source term as a constant, various mesh sizes are used for code verification.
The solutions are compared to the classical finite volume solution, where $y+$ and the DOF are kept the same. The solution of the finite volume on a very fine grid is used as a reference solution to compare the FV and 3$^{\text{rd}}$ order HDG. Tests were made at $Re = 2 \times 10^6$ with 40, 60, and 120 DOF in the y-direction. The corresponding $y+$ is 1.6, 0.85, and 0.36 respectively. While the second nearest element to the wall is located at $y_{elem}+$ of 5.7, 3.1, and 1.3 respectively. The near wall analytical solution for ω is used as a boundary condition for the second nearest element to the wall,

$$\omega = \frac{6\nu}{\beta_o y_{wall}^2} \quad \text{as} \quad y_{wall} \to 0 \tag{13}$$

Results are shown for the lower half of the channel with a half-height of 1 using structured triangular meshes. The value of the penalty parameters τ, τ_k, and τ_ω are set to $\frac{Re}{200}$.
It can be seen that HDG predicts better profiles for the velocity, k, and ω near the wall. However, the values of k at the channel centerline are always less than the FV and the reference solution. At the very coarse mesh in Fig. 12 the oscillations near the curve maximum is visible. In Fig. 11, HDG gives a much better result than the FV for the whole velocity profile. It is observed that lower $y+$ values are needed as the Reynolds number increases. The observations were nearly the same for higher Reynolds number. An overshoot of k near the maximum value is also noticed in Fig. 12. It is noted that the reference values is only considered as the best possible result for FV at finner meshes not the overall best results. In addition, the HDG solution does not match the FV solution on the very fine mesh as shown in Fig. 20-22.

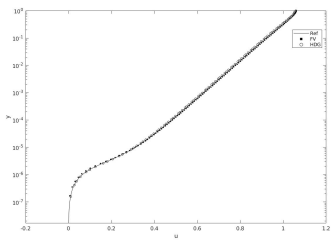

Fig. 8: u at $Re = 2 \times 10^8$ with 120 DOFs at $y+ = 0.29$

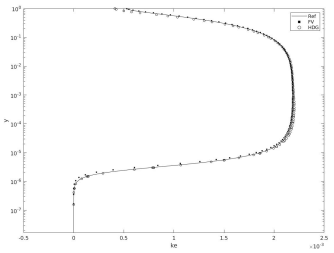

Fig. 9: k at $Re = 2 \times 10^8$ with 120 DOFs at $y+ = 0.29$

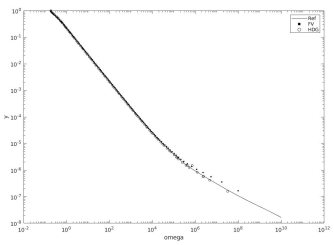

Fig. 10: ω at $Re = 2 \times 10^8$ with 120 DOFs at $y+ = 0.29$

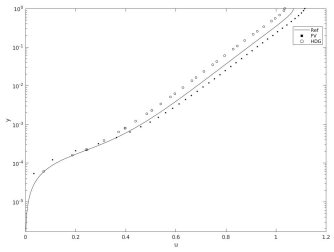

Fig. 11: u at $Re = 2\times10^6$ with 40 DOFs at $y+ = 1.6$

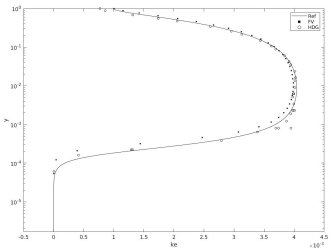

Fig. 12: k at $Re = 2\times10^6$ with 40 DOFs at $y+ = 1.6$

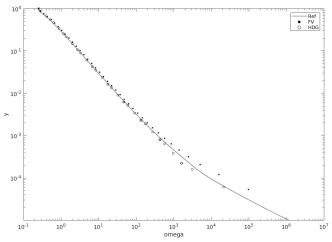

Fig. 13: ω at $Re = 2\times10^6$ 40 120 DOFs at $y+ = 1.6$

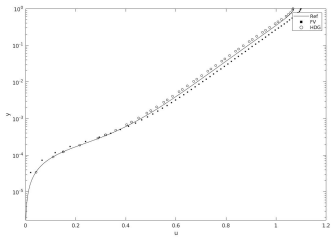

Fig. 14: u at $Re = 2\times10^6$ with 60 DOFs at $y+ = 0.85$

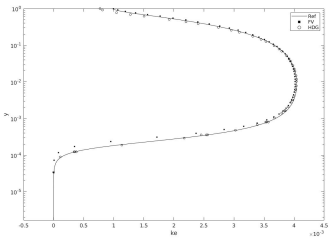

Fig. 15: k at $Re = 2\times10^6$ with 60 DOFs at $y+ = 0.85$

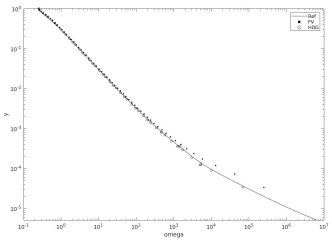

Fig. 16: ω at $Re = 2\times10^6$ with 60 DOFs at $y+ = 0.85$

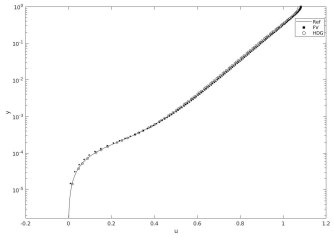

Fig. 17: u at $Re = 2\times10^6$ with 120 DOFs at $y+ = 0.36$

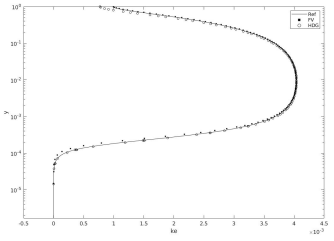

Fig. 18: k at $Re = 2\times10^6$ with 120 DOFs at $y+ = 0.36$

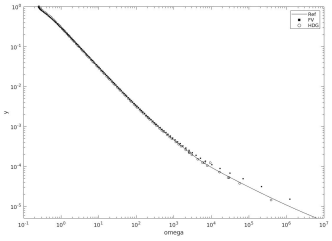

Fig. 19: ω at $Re = 2\times10^6$ with 120 DOFs at $y+ = 0.36$

For the velocity, there is a considerable difference between the FV and DG solutions in the velocity near the centerline of the channel. A similar difference is observed in Fig. 21 for k. While the largest difference in ω is near the wall as shown in Fig 22. At the moment, the exact reason why the FV solution does not match the DG solution at the very fine is not clear. Nevertheless, it is suggested that this mismatch is due to the different treatment of the boundary condition for ω at the wall.

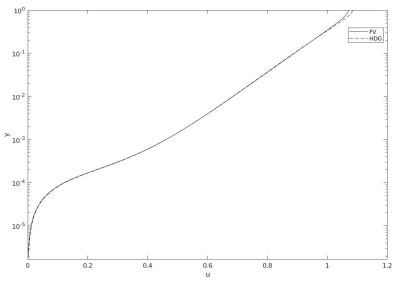

Fig. 20: u plot for HDG vs FV on a very fine grid at $Re = 2\times10^6$

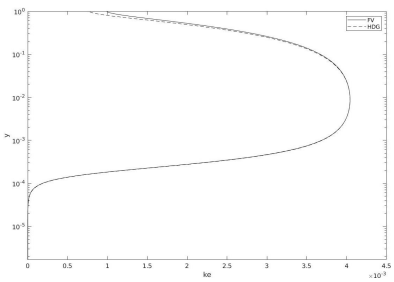

Fig. 21: k plot for HDG vs FV on a very fine grid at $Re = 2\times10^6$

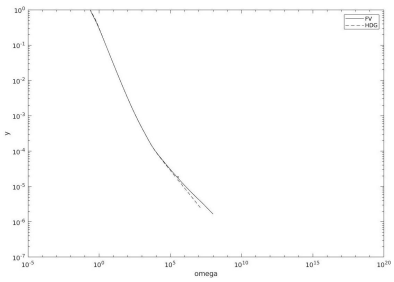

Fig. 22: ω plot for HDG vs FV on a very fine grid at $Re = 2\times10^6$

At this range of high Reynolds numbers, verification exercise is more useful than validation for such test case. The velocity and turbulence quantities are computed at different meshes to perform a grid re-

finement study. Then the results are fitted to a power series in order to estimate the convergence rate. The number of elements in y changed from 30 to 300, this corresponds to $y+$ values of 0.85 to 0.10 and $y_{elem}+$ values of 3.1 to 0.37 respectively. The mean and maximum velocity, maximum k, min ω, and shear stress at the wall are chosen to estimate their convergence rates. Expected convergence rates were obtained which is roughly equal $N+1$ for all variables except the shear stress. The shear stress convergence is not monotonic, possibly due to the near wall oscillations for the mesh with 30 elements in y.
Negative values of k are observed near the wall with some oscillations, however as these values are restricted to the viscous sublayer, their effect are negligible. Unfortunately, if these negitive values appeared in the rest of the domain, they obstruct the convergence. To solve this problem, a generalization of limiting negative k values to zeros and taking the absolute values of ω is proposed to fit the high-order method. During the simulation it was noticed that, as long as the the cell averaged values of the turbulence quantities are positive, the convergence can be guaranteed. Thus, a scaling limiter is applied to preserve the value of the cell average of the element with eliminating the negative values. The scaling limiter is defined in the paper by Zhang and Shu (2010), is applied to limit k and $\frac{1}{\omega}$.

7 Conclusion

The challenges of achieving an industrial high-order incompressible RANS $k-\omega$ solver can be clarified in this report. Fundamentally, an algorithm which is capable of calculating a point-wise exactly divergence-free velocity that can be used for hexahedral and tetrahedral is essential. The method presented in this report has this feature without the need of post-prepossessing operators or unclear penalization. However, the reduced element proposed needs to be optimized. In addition, a study on improving the penalty parameter would be useful at high Reynolds numbers as increasing the penalty parameter for the whole domain increases the conditioning number of the global matrix. Moreover, the global operator lost its symmetry with the introduction of turbulence. For that reason, efficient preconditioners are strongly required for these kinds of problems in order to compete with the finite volume solvers. The channel flow test case gives an indication that high-order RANS solvers have the ability to outperform the finite volume solvers in terms of accuracy per degrees of freedom. Yet, the computational time would be less for the finite volume solvers for the current implementations.

With the introduction of the scaling limiter, the $k-\omega$ equations can be solved using high-order methods. Nevertheless, it is not clear what should be done if the average mean values of the turbulence quantities fail to have positive values. The implicit treatment of the negative source terms may solve this problem. In order to fully test this method, test cases other the 2D channel and uniform flow should be used.

High-order RANS for INS is promising and with some more adjustments, high-order INS solvers can compete with the FV solvers in terms of robustness.

Acknowledgements

This work is done with the funding of SEED Erasmus Mundus Joint Doctorate. We thank Sonia Fernández-Méndez and Jeroen Wackers for their efforts and recommendations.

References

Rhebergen, S., & Wells, G. N. (2018). A hybridizable discontinuous Galerkin method for the Navier?Stokes equations with pointwise divergence-free velocity field. Journal of Scientific Computing, 76(3), 1484-1501.

Wilcox, D. C. (1998). Turbulence modeling for CFD (Vol. 2, pp. 172-180). La Canada, CA: DCW industries.

Spalart, P. R., & Rumsey, C. L. (2007). Effective inflow conditions for turbulence models in aerodynamic calculations. AIAA journal, 45(10), 2544-2553.

Zhang, X., & Shu, C. W. (2010). On maximum-principle-satisfying high order schemes for scalar conservation laws. Journal of Computational Physics, 229(9), 3091-3120.

Unsteady RANS simulation of a flow past a free-surface piercing circular cylinder

Maïté Gouin[*], Adrien Doradoux[*], and Ronan Le Creurer[†]
[*] SIREHNA, Bouguenais/France, [†]Naval Group, Lorient/France
maite.gouin@sirehna.com

1 Introduction

The stealth of submarines is one of the main performance criteria. One important indiscretion source is due to wakes generated by submarine masts when operating at periscope depth. In this work we are interested in the wake generated by a cylindrical mast with a circular cross-section.
The flow around a circular cylinder is characterized by the development of complex free-surface deformations. For submarine cylindrical masts, typical Reynolds numbers are around 10^5 to 10^6 - falling into the critical to supercritical region - and thus making difficult the correct prediction of the drag coefficient [1]. Indeed, in this region, the drag coefficient is decreasing suddenly while increasing the Re number. When dealing with submarine masts, Froude numbers are around 1 to 4, leading to some characteristic behaviours, depending on the Froude numbers [2]. Thus, the numerical modelling of such flows is quite challenging and it has been for a long time a subject of theoretical and analytical research in the naval hydrodynamic field.
Both experimental works ([2][3][4]) and numerical studies (described hereafter) have been conducted to solve this complex problem. First of all, for the case of single phase flows, in [5] the authors compared URANS and DES turbulence modelling at $Re = 9.3\,10^4$ and $Re = 5.5\,10^5$ without correctly reproducing the drag coefficient drop. In [6] the authors performed single phase LES simulations in the subcritical to supercritical regimes and obtained the expected drag coefficient drop. Other authors consider a cylinder piercing a free surface ([7][8][9]). In [7] LES simulations were conducted for different Re and Fr numbers with constant ratio Re/Fr, showing the quite correct prediction of the drag coefficient and of the free-surface deformation. The authors in [9] used a RANS modelling of the turbulence and found that RANS studies are accurate enough to capture the free surface elevation.
A RANS modelling approach appears to be sufficient (to correctly reproduce the free surface elevation) and is thus adopted. The interesting quantities are mainly the free-surface deformation in front of the cylinder (bow wave height) and behind the cylinder (trough depth), as well as the cylinder wake. The forces exerted on the cylinder are also of great interest.

2 Numerical method

2.1 Method

A numerical approach using the open source finite volume computational fluid dynamics (CFD) package OpenFOAM v17.12 [10] is used to simulate the incompressible flow past a vertical circular cylinder piercing the free-surface. The URANS simulations use the interFoam solver with a kω-SST turbulence modelling. Turbulence parameters are chosen according to [11]. The PISO algorithm is used with an adjusted time step leading to a Courant number lower than 1 (leading to time steps around $1e10^{-4}$). A target of y+=0.5 is used so that no wall function is employed. The air-water interface is tracked using a Volume Of Fluid (VOF) method with interface recompression.

2.2 Numerical domain

The numerical domain is constructed as follows: in the horizontal plane, it contains 25D upstream, 60D downstream and 50D in the transverse direction. Moreover, for Froude number higher than 2, an extrusion zone is used at the outlet of the domain to damp the created wake. In the vertical direction, it contains 10 cylinder diameters below the free-surface and 5 diameters above. Simulations are run for 2Tref, where Tref = (25+1+60)D/U is the time taken by the flow to cross the domain.

2.3 Mesh

The mesh is generated with the inbuilt OpenFOAM meshing software blockMesh. A boundary layer mesh with y+=0.5 is used along with a fine discretization around the cylinder, as presented in Fig. 1. A

mesh convergence has been performed on the first case (Re=234000 and Fr=0.84) to ensure that the main quantities (Cd, bow wave height and trough depth) have converged while refining in the z-direction (assuming that the refinement in the x-direction and y-direction is sufficient). For this case (Re=234000 and Fr=0.84), the mesh consists of 12M of cells.

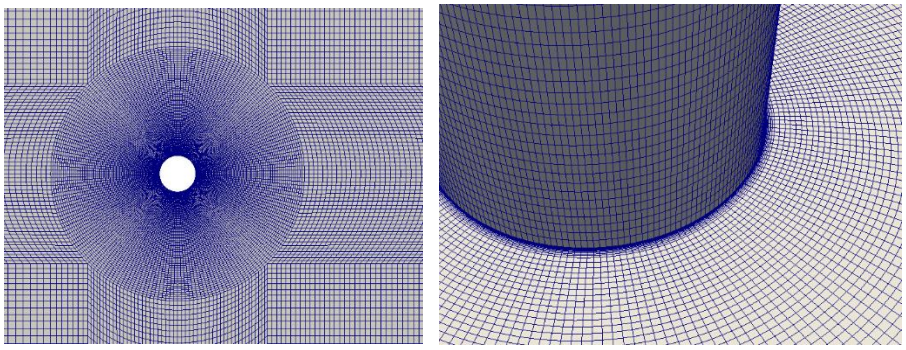

Fig. 1 : Mesh of the computational domain for Re=234000 and Fr=0.84.

2.4 Computed cases

Four operating conditions have been simulated: the case with D=0.2m and V=2.3kts (leading to Re=234000 and Fr=0.8). This case is compared to the experimental data of [2] and the numerical results of [7]. A second case with a higher Froude number Fr=2 and the same Reynolds number Re=234000 is then computed to investigate the effect of a higher Froude number. Then, the effect of a higher Reynolds number is performed with Re=458000 and Fr=0.84. Finally, the effect of a higher velocity on the free-surface deformation with the same diameter as the first case is computed: D=0.2m and V=6kts (Re=614000 and Fr=2.21).

3 Results

3.1 Re=234000 and Fr=0.84 – Validation case

A first simulation is carried out with Re=234000 - Fr=0.84. This first simulation aims at validating the method. The free-surface deformation on the whole domain and close to the mast is presented in Fig. 2 and Fig 3. A good agreement is found with the numerical results of [7]. A synthetic comparison with experimental result [2] and numerical simulation [7] is given in Table 1. The bow wave in front of the cylinder is well reproduced as well as the Kelvin wake angle. The trough depth behind the cylinder is slightly overestimated in our simulation. For this case, free-surface results are in good agreement with the available data.

The mean drag coefficient is also given in Table 1. The OpenFOAM simulation slightly over-predicts the mean drag coefficient compared to the LES simulations of [7]. Moreover, compared to the experimental data of [2], the drag coefficient is much smaller than the biphasic value (1.05). In order to go deeper, the vertical profile of the Cd coefficient is given in Fig 3 and compared to experimental data of [2] and LES simulation of Koo et al. [7]. Our simulation gives a reasonably good prediction of the drag coefficient far from the free surface but does not reproduce the drag coefficient bump close to the free surface, maybe due to the RANS method used. We can observe that the LES simulations of Koo et al. [7] gives a better prediction of the drag coefficient close to the air-water interface.

Table 1 : Results for Re=234000 and Fr=0.84. FS: free-surface. SP: single phase.

Re=234000 Fr=0.84	**Theory**	**Chaplin et Teigen [2]**	**Koo et al. (2014)** [7]	**Simulation**
Bow wave height (/D)	0.35 (Bernoulli)	0.35	0.33	0.34
Trough depth (/D)	0.20 (empirical [12])	0.2	0.24	0.24
Kelvin wake angle	19.5	18-19	18-19	18-19
Cd	-	1.05 FS and 0.75 SP	0.72	0.64
St	-	0.2 Schewe (1983) [13]	0.21	0.26

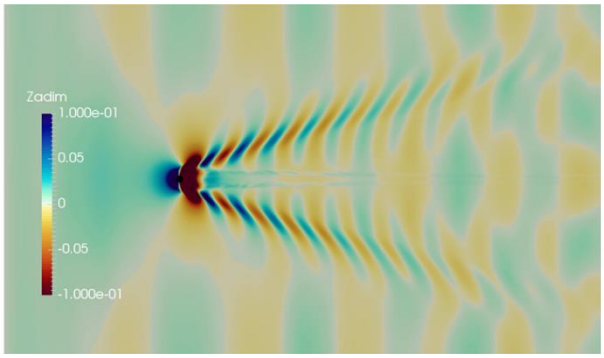

Fig. 2: Free surface elevation (from above). Re=234000 and Fr=0.84.

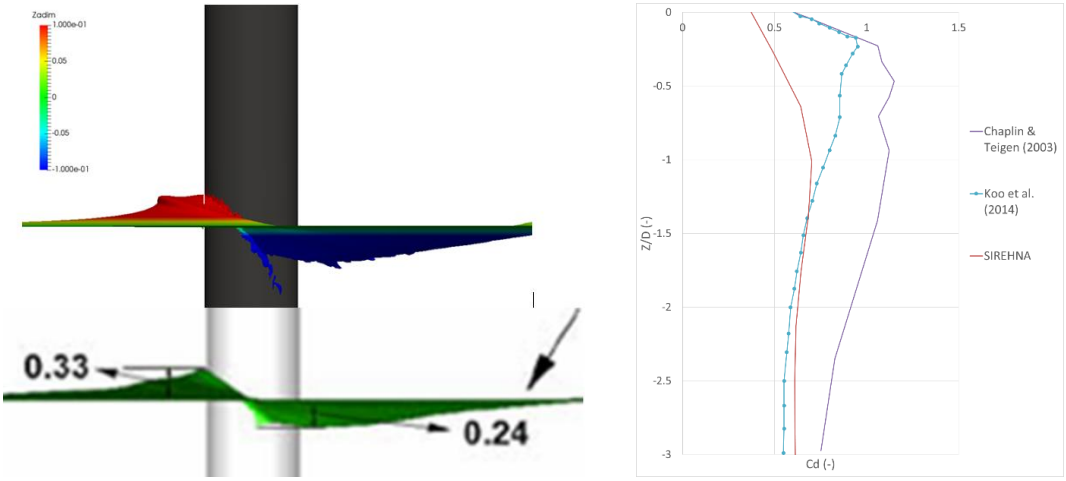

Fig 3: Re=234000 and Fr=0.84. Left: Free surface elevation close to the mast (Above: our result. Below: Results from [7]). Right: Vertical profile of the drag coefficient. Purple: experimental data from [2]. Blue: LES simulation from [7]. Red: Our simulation.

3.2 Re=234000 and Fr=2

This second case investigates the effect of a higher Froude number and the ability of the method to correctly reproduce the main free-surface and force parameters.

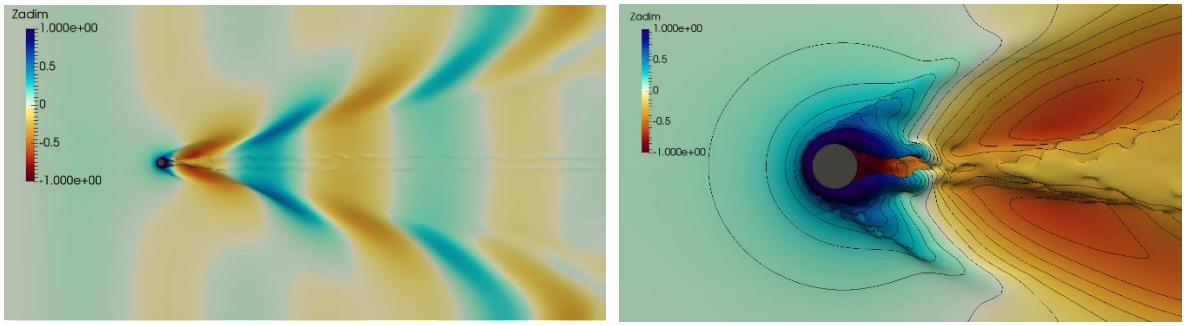

Fig 4: Free surface elevation (from above). Re=234000 and Fr=2.

Table 2: Results for Re=234000 and Fr=2. SP: single phase.

Re=234000 Fr=2	Reference	Simulation
Bow wave height (/D)	2.0 (Bernoulli) and 1.8 (exp [14])	1.6
Trough depth (/D)	1.14 (anal. [12])	1.3
Kelvin wake angle	< 19°	17°
Cd	SP: 0.9	0.55
St	-	0.24

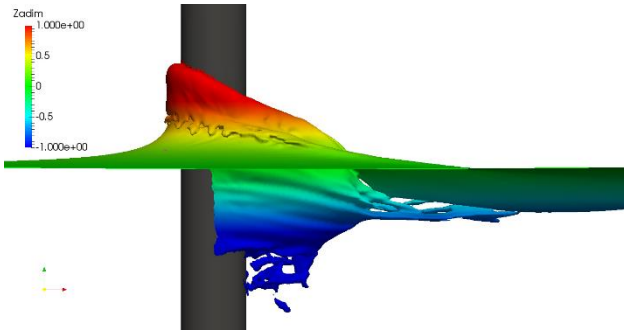

Fig 5: Free surface elevation close to the mast. Re=234000 and Fr=2.

3.3 Re=458000 and Fr=0.84

This third case investigates the effect of a higher Reynolds number. Results are compared to numerical simulations performed by Koo et al.[7].

The free surface elevation is presented on Fig 6 and characteristics parameters are given in Table 3. The free surface elevation is similar to the case Re=234000 and the same Froude number Fr=0.84. Bow wave height and trough depth given by the simulation are very similar to the LES results of Koo et al. [7] (see Fig 7).

Table 3: Results for Re=458000 and Fr=0.84.

	Reference	**Simulation**	**Koo et al. (2014)** [7]
Bow wave height (/D)	0.35 (Bernoulli)	0.35	0.35
Trough depth (/D)	0.2 (anal. [12])	0.25	0.246
Kelvin wavelength (/D)	4.43	4.8	4.35
Cd	0.2 (infinite)	0.56	
St	0.4/0.5	0.39	

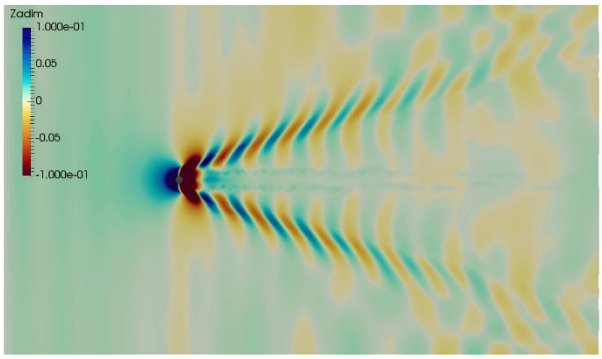

Fig 6: Free surface elevation. Re=458000 and Fr=0.84.

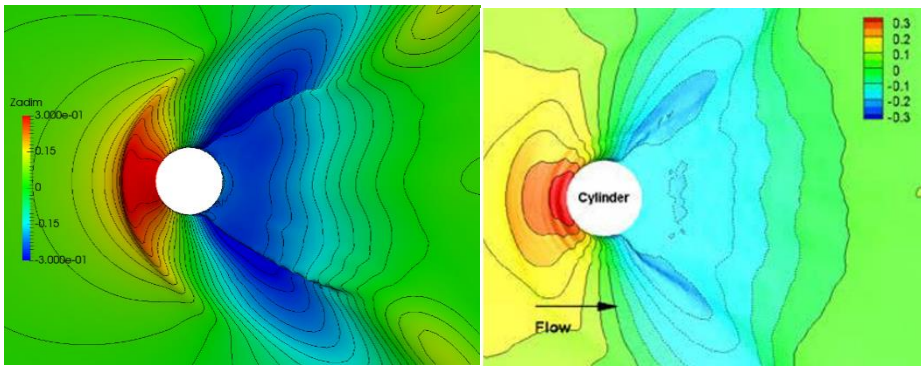

Fig 7: Free surface elevation. Re=458000 and Fr=0.84. Left: OpenFOAM. Right: Results from Koo et al. [7].

3.4 Re=614000 and Fr=2.21

A last simulation is performed with Re=614000 and Fr=2.21 to investigate the effect of a higher mast speed with the same diameter as the first case (D=0.2m). The mesh contains 18 M of cells. The free-surface deformation over the whole domain and close to the mast is presented in Fig 8. The bow wave in front of the cylinder is well reproduced (cf Table 4). The trough depth behind the cylinder is underestimated in our simulation, but it has been reported that it can depart from the analytical formula given in [12] for high values of Re and Fr [2].

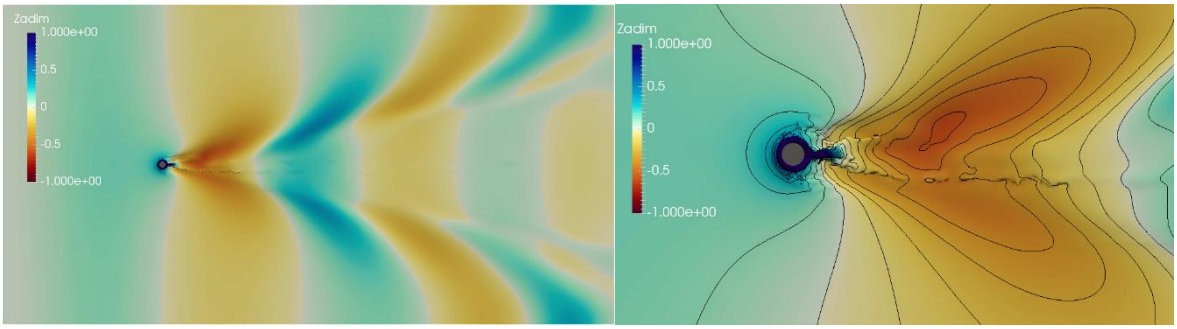

Fig 8: Free surface elevation (from above). Re=614000 and Fr=2.21.

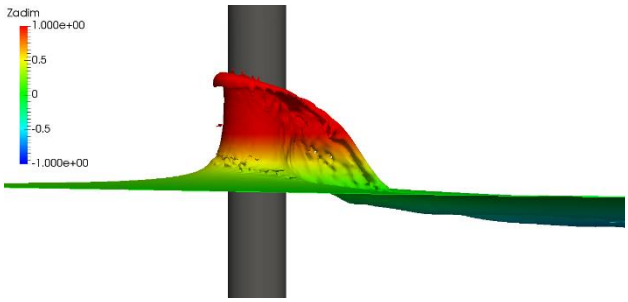

Fig 9: Free surface elevation close to the mast. Re=614000 and Fr=2.21.

Table 4: Results for Re=614000 and Fr=2.21.

	Reference	**Simulation**
Bow wave height (/D)	2.44 (Bernoulli)	2.06
Trough depth (/D)	1.4 (anal. [12])	0.63
Kelvin wake angle	< 19°	16°
Cd		0.56
St		0.24

3.5 CPU time

All computed cases were run on 8 nodes, each node having 20 cores. The summary of CPU time for 10 computed time-steps on 160 cores is reported in Table 5.

Table 5: Summary of CPU time and mesh size.

Computed case	**CPU time for 10 time steps (s)**	**Mesh size (M=millions of cells)**
Re=234000 Fr=0.84	1.9	12 M
Re=234000 Fr=2	4.3	17 M
Re=458000 Fr=0.84	2.7	14.3 M
Re=614000 Fr=2.21	4.2	18.4 M

Thus it appears that the CPU time per timestep is almost linear with the total number of cells. However, the total CPU time depends on both the number of cells and the ratio Re/Fr (as the time step decreases while increasing the Froude number).

4 Conclusion and perspectives

The numerical simulation of a circular mast piercing the free-surface has been presented for different Reynolds and Froude numbers. The main conclusions regarding the physical aspects are the following:

- The free-surface parameters are correctly reproduced by the numerical method (in terms of bow wave height, trough depth (see Fig. 10) and wake),
- The correct modelling of the forces acting on the cylinder is still a challenging task.

Thus the use of a URANS method with a kw-SST model appears to be sufficient to correctly reproduce the free-surface deformation, but the correct modelling of the forces exerted on the cylinder needs more investigation.

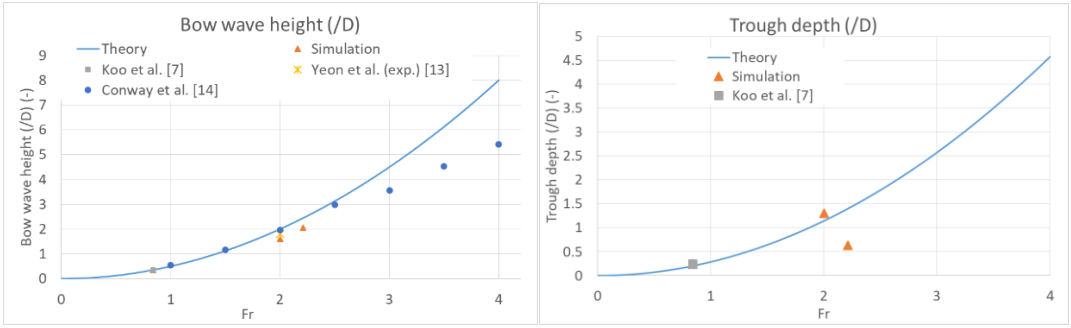

Fig 10: Bow wave height and through depth with increasing Froude number.

References

[1] E. Achenbach, Influence of surface roughness of the cross-flow around a circular cylinder, J. Fluid Mech. 46 (1971) pp321-335.

[2] J.R. Chaplin, P. Teigen, Steady flow past a vertical surface-piercing circular cylinder, Journal of Fluids and Structure 18, 2003, pp271-285.

[3] AST Conway, D. Ranmuthugala, J.R. Binns, M. Renilson, Journal of Engineering for the maritime environment, 2017, pp1-13. The effect of geometry on the surface waves generated by vertical surface-piercing cylinders with a horizontal velocity.

[4] M. Inoue, N. Bara, Y. Himeno, Journal of the Kansai Society of Naval Architects, Japan 220, 1993, pp57-64. Experimental and numerical study of viscous flow field around an advancing vertical circular cylinder piercing a free-surface.

[5] G. Vaz, C. Mabilat, R. van der Wal, P. Gallagher, Proceedings of OMAE, June 10-15, 2007, San Diego, California, USA. Viscous flow around computations on smooth cylinders: A detailed numerical study with validation.

[6] S M Yeon, J. Wang, F. Stern, Applied Ocean Research 59, 2016, pp 663-675. Large Eddy Simulation of the flow past a circular cylinder at sub to super-critical Reynolds numbers.

[7] B. Koo, J. Yang, S.M. Yeon, F. Stern, Int. Journal Arch. Ocean Eng. 6, 2014, pp529-561. Reynolds and Froude number effect on the flow past an interface-piercing circular cylinder.

[8] T. Kawamura, S. Mayer, A. Garapon, L. Sorensen, Journal of Fluid Engineering, ASME, 2002. Large Eddy Simulation of a flow past a free surface piercing circular cylinder.

[9] X. Xiao, T. Tezdogan, A. Incecik, Techno-Ocean (2016), pp618-623. Numerical study on wave run-up height and depression depth around a vertical circular cylinder at various Froude numbers.

[10] H.G. Weller, G. Tabor, H. Jasak, C. Fureby, A tensorial approach to computational continuum mechanics using object-oriented technics, Computers in Physics 12(6), 1998

[11] F.R. Menter, AIAA Journal, 32 (8): 1598–1605, 1994. Two-Equation Eddy-Viscosity Turbulence Models for Engineering Applications.

[12] A.D. Hay, Princeton Univ., 1947, Princeton. Flow about semi-submerged cylinders of finite length.

[13] S M Yeon, J. Wang, F. Stern, Applied Ocean Research 59, 2016, pp 663-675. Large Eddy Simulation of the flow past a circular cylinder at sub to super-critical Reynolds numbers.

[14] AST Conway, D. Ranmuthugala, J.R. Binns, M. Renilson, Journal of Engineering for the maritime environment, 2017, pp1-13. The effect of geometry on the surface waves generated by vertical surface-piercing cylinders with a horizontal velocity.

Numerical Investigation of a General Cargo Vessel Wake in Waves

Mohsen Irannezhad, Arash Eslamdoost, and Rickard E. Bensow
Chalmers University of Technology, Gothenburg/Sweden
mohsen.irannezhad@chalmers.se

1 Introduction

Since calm water is rather an exception at an actual sea, optimizing propulsive efficiency of ships operating in more realistic environmental conditions than calm water has been gaining more attention recently. The effects of waves on propeller performance have been investigated by different researchers such as Taskar et al. (2016) who studied different influencing factors in terms of cavitation, pressure pulses and efficiency on propeller performance of KVLCC2. Since excessive wake variation in waves may have a significant impact on the propeller performance, it is important to study dynamics of the wake field for ships operating in waves.

Although the propeller designers consider experienced-based margins for propellers operating in waves and off-design conditions, the knowledge of the wake field at different wave conditions for each specific hull could be beneficial in designing more efficient propeller. In this study, a general cargo vessel incorporating a Large Diameter Propeller (LDP) with a very small tip clearance is considered. In an earlier investigation, the authors of the current paper have carried out a study, Irannezhad et. al. (2019), on the propeller emergence risk assessment of the LDP vessel employing a potential flow panel code, SHIPFLOW Motions, as well as a viscous flow solver, STAR-CCM+. The aim of this paper is to first validate the LDP vessel computed heave and pitch motions as well as its resistance due to regular head waves in model scale against the experimental data, then to analyze the time-varying wake field and compare it in different wave conditions in the viscous flow solver. The propeller is not modeled in the simulations.

2 Vessel geometry and conditions

An overview of the LDP vessel geometry with a tunnel-shaped aft design meant to accommodate an LDP is shown in Fig. 1 together with the ship-fixed coordinate system at the vessel Center Of Gravity (COG). A simple shaft connects the vessel bare hull to an appended asymmetric rudder. Although the LDP is not modeled in the simulations, its conceptual geometry is represented in Fig. 1. A point probe at the position of the LDP blade tip near the propeller/hull clearance is specified in order to characterize the propeller emergence in the absence of propeller in the simulations. The LDP vessel main particulars in model-scale, its speed as well as the corresponding Froude number are listed in Table 1.

Table 1: The model-scale LDP vessel main particulars and conditions (scale factor = 27).

Particular	≈ Value	Unit	Denotation
L_{pp}	7.95	[m]	Length Between Perpendiculars
LOS	8.11	[m]	Length Overall Submerged
B	0.88	[m]	Breadth at mid-ship
T_A	0.296	[m]	Draft at Aft Perpendicular
T_F	0.296	[m]	Draft at Fore Perpendicular
Δ	1740	[kg]	Mass Displacement
V	0.89	$[\frac{m}{s}]$	Model Speed
Fr	0.10	[-]	Froude Number
Re	7.1E6	[-]	Reynolds Number

Fig. 1: LDP vessel geometry, point probe and ship-fixed coordinate system at COG.

The model-scale LDP vessel appended with a rudder and a shaft, free to heave and pitch operating in fresh water with the density of $\rho = 998.3\ \frac{kg}{m^3}$ is used within the numerical investigations. The simulations are performed in calm water and in the 5^{th} order Stokes regular head waves ($\mu = 180°$) in deep water as listed in Table 2. On the other hand, the LDP vessel model-tests were conducted in free-running self-propulsion mode by Maritime Research Institute Netherlands (MARIN). Fast Fourier Transform (FFT) analysis is used in order to post-process the experimental and numerical data.

Table 2: Environmental conditions of the studied cases.

Case no.	Cond.	$\approx H$ **[m]**	$\approx \lambda$ **[m]**	$\approx \frac{\lambda}{LOS}$ **[-]**	$\approx$ **Steepness** $= \frac{H}{\lambda}$ [-]	$\approx \omega_e\ [\frac{rad}{s}]$	$\approx T_e\ [s]$
1	Calm	-	-	-	-	-	-
2	Wave	0.22	5.57	0.68	0.039	4.33	1.45
3	Wave	0.22	7.27	0.89	0.030	3.68	1.70

The total resistance R_T in self-propulsion model tests is estimated based on the mean measured thrust $\bar{T}$ and the given calm water thrust deduction factor of $t_d = 0.159$ at Froude number 0.10 , see Eq. 1. It is assumed that the thrust deduction factor in waves is equal to that of calm water, t_d.

$$R_T = (1 - t_d) \times \bar{T}. \tag{1}$$

3 Numerical modeling

The CFD simulations are performed using an URANS approach. A second order spacial discretization scheme is used. In order to simulate the vessel motions, the Dynamic Fluid Body Interaction (DFBI) module is used. The DFBI Rotation and Translation model is used in order to enable the RANS solver to compute the vessel motions from the exciting fluid forces and moments as well as the gravity force. The Planar Motion Carriage mechanism is used within the DFBI Rotation and Translation model, in order to simulate the hull free to heave and pitch (2 degrees of freedom) while it is translating with a prescribed constant speed (ship forward speed V) in the longitudinal direction in the earth-fixed co-ordinate system. In order to achieve a robust simulation setup for wave propagation in STAR-CCM+, the best practice provided by Peric' (2017) is complied. The aim is to minimize the wave propagation simulation issues, such as amplitude reduction and period change during propagation, disturbances (wiggles) on the free-surface and reflection at boundaries. The Volume of Fluid (VOF) multiphase model is used as the free-surface capturing technique. The High-Resolution Interface Capturing (HRIC) scheme by Muzaferija and Peric' (1999) is used in VOF simulations to maintain a sharp interface between the incompressible fluid phases.

Mesh generation was performed using the automatic mesh generation tool in STAR-CCM+. The trimmed hexahedral meshes with local refinements near the free-surface as well as near the hull together with prism layers along the hull surface are used. Overset method consisting a moving overset region and a stationary background region with specific treatment of cell sizes near the overlapping region is used to discretize the computational domain. The prism layers are placed in such a way that the non-dimensional wall distance y^+ remains above 30 over the major part of the hull surface during the simulation, hence

wall functions utilization. An overview of the background mesh is shown in Fig. 2 in which the applied boundary conditions is also given. The pressure outlet boundary condition for simulation in calm water is moved from the top boundary to the outlet boundary. Due to the asymmetric geometry of the rudder, no symmetry plane is considered and both side boundaries are given as velocity inlets. For simulations in waves, the wave forcing capability is applied to all of the vertical boundaries in order to force the solution of the discretized Navier-Stokes equations towards the theoretical 5^{th} order Stokes wave solution over a distance equal to Length Overall Submerged (LOS) from the boundaries. For simulation in calm water, the wave damping capability is used in all of the vertical boundaries in order to minimize the wave reflection from the boundaries. The Standard Low-Re $k-\varepsilon$ turbulence model and the Realizable $k-\varepsilon$ turbulence model together with all y^+ wall treatment are used for simulations in waves and calm water respectively. An implicit unsteady solver with a second order temporal discretizational scheme (time-step of 0.003 s) for simulation in waves and a first order temporal discretizational scheme (time-step of 0.02 s) for simulation in calm water is used. The chosen time-step also fulfills the ITTC (2011) recommended criteria of at least 100 time-steps per encountered wave period. Last but not least, ten and forty maximum number of inner iterations for each unsteady time-step is considered in simulations in waves and calm water respectively.

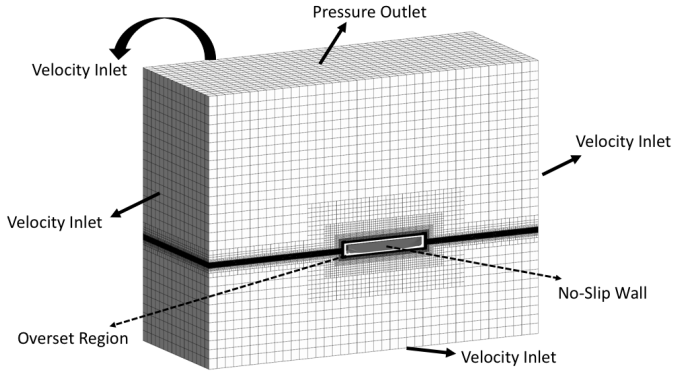

Fig. 2: An overview of the background mesh and the applied boundary conditions.

Table 3: Number of cells in each region.

Cond.	Background	Overset	Total
Calm	5.8 M	2.3 M	8.1 M
Wave	13.5 M	4.1 M	17.6 M

4 Resistance and motions validation

Due to a very small Froude number, the dynamic sinkage and trim as well as the wave making resistance in calm water attain very small values. The self-propelled model test sinkage, trim and total resistance are -0.003 [m], 0.017 [deg] and 15.8 [N], respectively, while the CFD results are -0.002 [m], 0.114 [deg] and 14.6 [N]. Positive sinkage and heave (R3) defined as COG moves upward and positive trim and pitch (R5) are defined as bow moves downward. The 0^{th} harmonic amplitudes of motions in simulations in waves are approximately similar and relatively small. Nevertheless, the 1^{st} harmonic amplitudes of heave and pitch motions, shown in Fig. 3, are the dominating components while higher order components are close to zero. The large amplitude heave response in Case 2 might be due to the near heave resonance conditions. The deviation errors of the 1^{st} harmonic amplitudes of motions and the 0^{th} harmonic amplitudes of resistance from the experimental data are presented on top of each bar in Fig. 3e and 3f. In general, a good agreement is seen between CFD and EFD data.

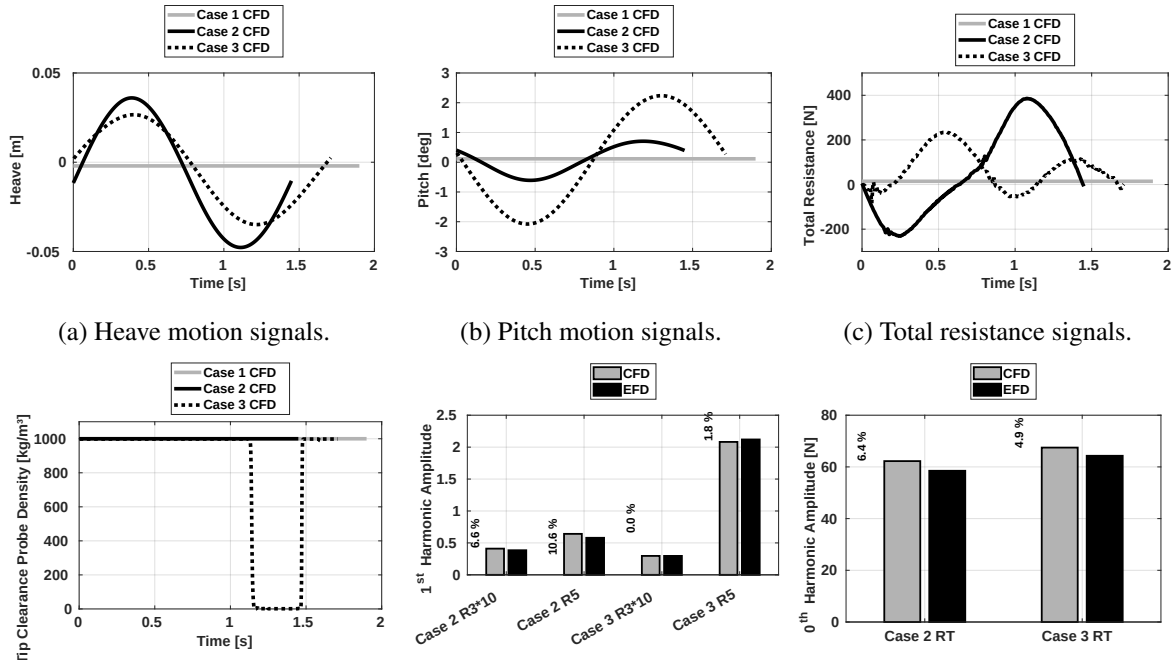

(a) Heave motion signals. (b) Pitch motion signals. (c) Total resistance signals.

(d) Probe density monitor. (e) Motions harmonic amplitudes. (f) Mean total resistance.

Fig. 3: The LDP vessel responses during one encountered wave period.

5 Propeller wake investigations

In this section the nominal wake variation in waves and in calm water is investigated for the LDP vessel. The wake has been studied on a virtual disk located at the propeller center and it is moving with the hull during the motion responses. The disk radius is equal to the propeller radius ≈ 0.13 m. The propeller disk is divided into 11 surfaces in radial direction, with the first surface starts at the shaft edge to a radius of $\Delta r_1 = 0.03m$ and the remaining 10 surfaces with the radius steps of $\Delta r_{2...11} = 0.01m$ to the propeller tip. The disk surface centers are also derived. The mean value of the surface averaged axial and radial velocity components during one encountered wave period is shown in the Fig. 7b and 7c at each surface center radius. The surface averaged calm water wake fraction as well as the surface averaged wake fraction variation during one encounter wave period for simulations in waves are shown in Fig. 7a. Significant wake variation in waves in comparison to calm water wake is seen. The computed values of the mean surface averaged wake fraction for Case 2 and Case 3 are approximately similar to the calm water value; however, a different distribution of the axial an radial velocity components are observed, see Fig. 7b and 7c. The sudden change of wake fraction in Case 3 between 1.12 s and 1.47 s is due to the propeller emergence shown in Fig. 3d. Strong correlation between the pitch motion and the wake field dynamics is seen. The wake fraction is at its minimum (meaning that the inflow velocity into the propeller disk is close to free stream velocity) when the pitch motion is close to zero and the hull stern is just about to move downwards into the water. On the other hand, the wake fraction is at its maximum when the pitch motion is zero but the hull stern moving upwards out of water. The non-dimensional axial velocity contour in the shaft direction as well as the transverse velocity vectors for the simulation in calm water is shown in Fig. 4. Moreover, the non-dimensional axial velocity contours and the transverse velocity vectors for three time instances of the lowest, the mean level and the highest surface averaged wake fraction for simulations in waves are shown in Fig. 5 and Fig. 6. The bilge vortex found by the same Q-criterion are shown in Fig. 8. The bilge vortices in waves show interesting dynamics in comparison to calm water. They become stronger by increasing wave length. The position where the bilge vortices hit the propeller disk in calm water is more and less stationary, while they considerably move up and down in the disk when the waves are present. The other interesting phenomenon in waves is the existence of the secondary vortex system which is caused by the propeller shaft and enters the propeller disk.

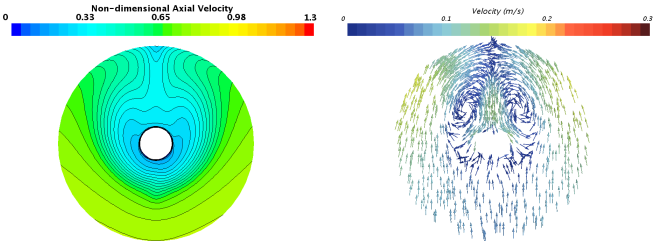

(a) Non-dim. axial contour. (b) Transverse vectors.

Fig. 4: Velocity components on the propeller disk in calm water (Case 1).

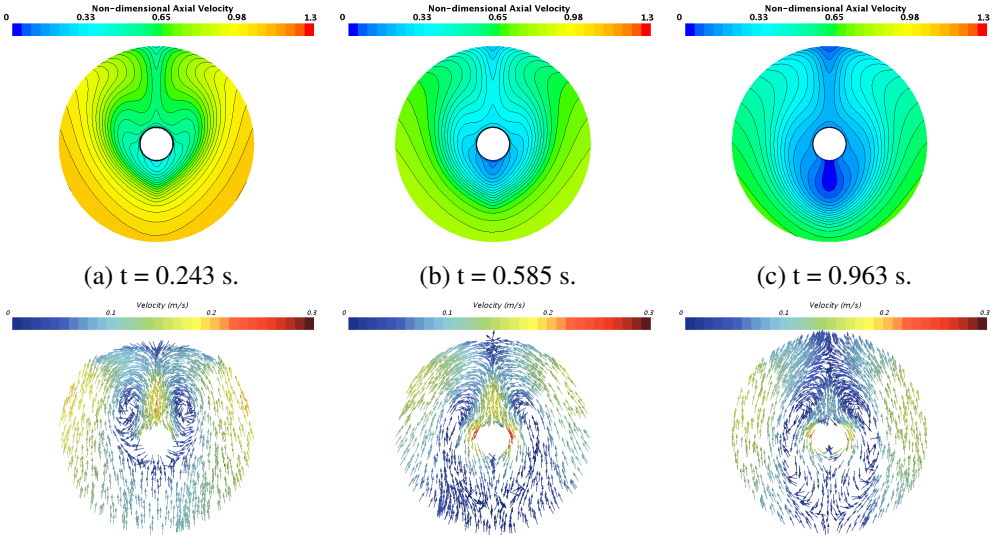

(a) t = 0.243 s. (b) t = 0.585 s. (c) t = 0.963 s.

(d) t = 0.243 s. (e) t = 0.585 s. (f) t = 0.963 s.

Fig. 5: Non-dimensional axial velocity contours and transverse velocity vectors for Case 2 at three time instances; wake trough (a & d), mean wake (b & e) and wake peak (c & f).

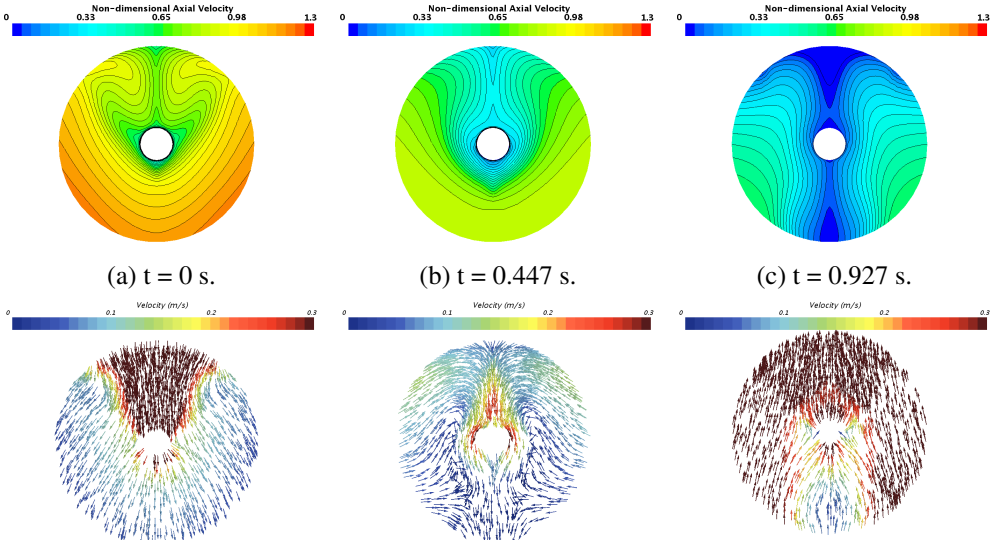

(a) t = 0 s. (b) t = 0.447 s. (c) t = 0.927 s.

(d) t = 0 s. (e) t = 0.447 s. (f) t = 0.927 s.

Fig. 6: Non-dimensional axial velocity contours and transverse velocity vectors for Case 3 at three time instances; wake trough (a & d), mean wake (b & e) and wake peak (c & f).

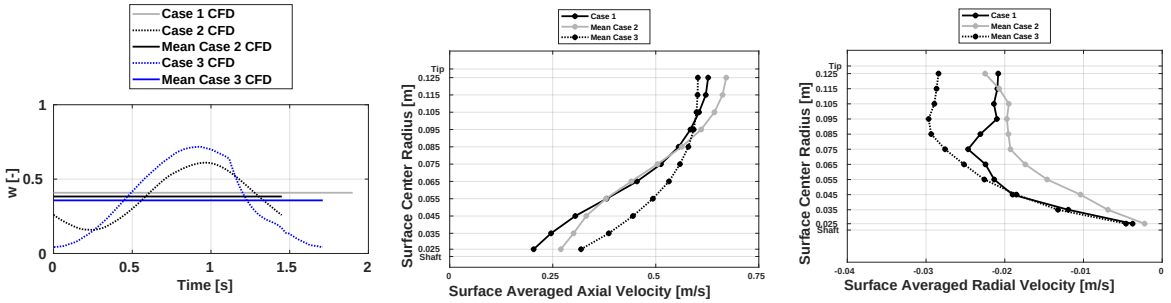

(a) Wake change. (b) Axial velocity. (c) Radial velocity.

Fig. 7: Variation of wake (a) and the mean surface averaged velocity components (b) and (c).

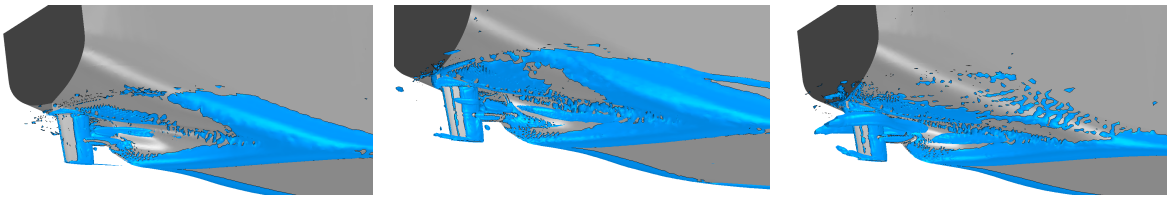

(a) Case 1. (b) Case 2 at t = 0.243 s. (c) Case 3 at time = 0 s.

Fig. 8: The bilge vortex found by Q-criterion = 7.5.

6 Conclusion

This is an ongoing research and so far we have managed to set up a robust method for capturing the dynamics of a ship wake field. The future plan is to investigate the correlation between the ship motions and the wake dynamics more in detail. As a complementary approach to what we have carried out so far, we plan to study the isolated effects from the waves as well as the ship motions on the flow into propeller.

Acknowledgements

This research is funded by The Swedish Transport Administration through LIGHTHOUSE (Swedish Maritime Competence Center). The simulations were performed on resources at Chalmers Centre for Computational Science and Engineering (C3SE) as well as National Supercomputer Center at Linköping University (NSC) provided by the Swedish National Infrastructure for Computing (SNIC). The Maritime Research Institute Netherlands (MARIN) is acknowledged for providing the experimental data.

References

B. Taskar, S. Steen, R.E. Bensow, and B. Schröder (2016). Effect of Waves on Cavitation and Pressure Pulses. *Journal of Applied Ocean Research*, **60**, 61–74.

M. Irannezhad, A. Eslamdoost and R.E. Bensow (2019). Numerical Investigation of a large diameter propeller Emergence Risk for a Vessel in waves. Proceedings of the 8th International Conference on Computational Methods in Marine Engineering (MARINE 2019), Gothenburg, Sweden.

M. Peric' (2017). Best Practices for Simulations With Waves. Presentation at STAR Global Conference, Berlin, Germany.

Muzaferija, S and Peric', M. Computation of free surface flows using interface-tracking and interface-capturing methods. *In Nonlinear water wave interaction*, pp. 59–100, Southampton: WIP Press, (1999).

International Towing Tank Conference (ITTC). Practical Guidelines for Ship CFD Applications. In: *Proceedings of the* 26th *ITTC*, (2011).

Simulation of plunging breaking waves induced by a submerged bump

Qiu Jin, Dominic Hudson, Pandeli Temarel

Fluid Structure Interactions group, Faculty of Engineering and Physical Sciences,
University of Southampton
Southampton, UK

1. Introduction

Plunging wave breaking is one of the most violent phenomena in air-water interface interactions, producing strong turbulence with large amounts of air bubbles, sprays, jets and water droplets. Wave breaking phenomena are easily observed in ship bow and stern waves and they are one of the main sources of underwater noise and white-water wake. However, the process of plunging wave-breaking is not well understood and there are few studies that provide a detailed quantitative description of breaking waves. It is therefore important to investigate the conditions under which breaking appears and the interactions of air and water. This paper investigates a plunging breaking wave generated by a shallowly submerged bump positioned in a uniform flow.

Laboratory experiments provide a highly powerful investigative tool. Early experimental fluid dynamics (EFD) focus on qualitative descriptions of wave geometric properties[1], jet generation and air entrainment[2]. With the development of new measurement techniques, more recent EFD studies provide detailed velocity and turbulence data. A good example is represented by [3] in which a detailed and complete analysis of a plunging breaking wave is provided. However, even with recent sophisticated and highly resolved measuring techniques, it is not always possible to achieve a complete description of phenomena in highly aerated conditions [4].

In computational fluid dynamics (CFD) investigations, non-linear potential flow boundary integral methods or boundary element methods are widely used to predict the occurrence of breaking allowing studies of large computational domains [5]. Only the beginning of the non-linear wave deformation is captured in these models as they are unable to predict beyond the onset of wave breaking or merging. Recently, the Reynold's averaged Navier-Stokes equations have been solved to simulate the two-phase flow with surface capturing methods to describe the motion of the free-surface. Although having limitations, two-phase solvers allow a detailed investigation of the complex flow generated by the breaking of free surface waves. Wang et al. [6] identified three repeated plunging events with a Cartesian Grid, immersed boundary coupled Level Set and Volume of Fluid (CLSVOF) CFD method. Iafrati [4] numerically simulated the energy dissipation mechanisms in the breaking process of third-order Stokes waves with a Navier-Stokes solver combined with a Level Set method. Lubin [7] investigated the generation and evolution of aerated vortex filaments in plunging breaking waves.

This paper uses a two-phase flow solver in the open source RANS solver OpenFOAM to study the wave breaking process and the velocity fields generated by a shallowly submerged bump. The two-phase flow solver is first validated through comparison with experiments. The computational domain and boundaries are designed following the experiments conducted in [3]. The free surface evolution, wave breaking process and velocity fields are investigated around and downstream of the bump. The simulations are carried out using the standard RANS k-ω SST turbulence model with

an algebraic Volume of Fluid (AVOF) technique for the interface capturing.

2. Numerical methods

2.1. Governing equations

In the present work, a standard two-phase solver, interFoam, in the Open source platform OpenFOAM is used to simulate plunging breaking waves. Reynolds averaged Navier-Stokes equations are used to represent the motions of these two incompressible, isothermal and immiscible fluids. The governing equations, including mass and momentum conservation are expressed as:

$$\nabla \cdot \mathbf{U} = 0 \tag{1}$$

$$\frac{\partial \rho \mathbf{U}}{\partial t} + \nabla \cdot \left(\rho\left(\mathbf{U} - \mathbf{U_g}\right)\mathbf{U}\right) = -\nabla p_d - \mathbf{g} \cdot \mathbf{h} \nabla \rho + \nabla \cdot \left(\mu_{eff} \nabla \mathbf{U}\right) + (\nabla \mathbf{U}) \cdot \nabla \mu_{eff} + \mathbf{f}_\sigma \tag{2}$$

Where $\mathbf{U}$ is the fluid velocity and $\mathbf{U_g}$ is the grid velocity, ρ is the mixture density of the fluid, $p_d = p - \rho \mathbf{g} \cdot \mathbf{h}$ is the dynamic pressure which is obtained by subtracting the hydrostatic component from the total pressure, $\mathbf{g}$ is the gravity acceleration, $\mu_{eff} = \mu + \rho \nu_t$ is effective dynamic viscosity, μ is the dynamic viscosity and ν_t is the turbulence viscosity, f_σ is a surface tension term. For modeling turbulent flow, a standard k-ω Shear Stress Transport (SST) turbulence model is selected to solve the Reynold's stress, where k is the turbulent kinetic energy and ω is the turbulence specific dissipation rate:

$$k = 1.5(I|\mathbf{u}_{ref}|)^2, \tag{3}$$

$$\varepsilon = \frac{k^{0.5}}{C_\mu L}, \tag{4}$$

where *I* is the turbulence intensity, $\mathbf{u}_{ref}$ is the reference velocity, C_μ is a constant equal to 0.09, and L is a reference length scale.

In the present work, a Finite Volume Method (FVM) with structured grids is applied to discretize the computational domain. The PIMPLE (PISO-SIMPLE) algorithm is used for pressure velocity coupling, which is a hybrid of a Pressure Implicit Splitting Operator (PISO) algorithm and a Semi-Implicit Method for Pressure-Linked Equations (SIMPLE) algorithm.

2.2. Free surface

The interFoam solver uses an algebraic VOF (AVOF) to track the interface between air and water in a special algorithm called Multidimensional Universal Limiter for Explicit Solution (MULES). Using a phase indicator function α, the two immiscible fluids are considered as one effective fluid throughout the domain and no interface reconstruction process is applied during the calculation. The indicator α is the volume function, which is defined as the relative proportion of water in each cell. If $\alpha = 1$, the cell is full of water and if $\alpha = 0$, the cell is full of air, and in any other case the cell contains the interface between air and water. The transport equation for the phase indicator is shown as:

$$\frac{\partial \alpha}{\partial t} + \nabla \cdot (\mathbf{U}\alpha) = 0, \tag{5}$$

In MULES, an artificial compression term is added to the conventional transport equation, equation 6, to limit the amount of interface smearing:

$$\frac{\partial \alpha}{\partial t} + \nabla \cdot \left(\rho\left(\mathbf{U} - \mathbf{U_g}\right)\alpha\right) + \nabla \cdot (\mathbf{U_r}(1 - \alpha)\alpha) = 0, \tag{6}$$

where $\mathbf{U_r}$ is the artificial velocity field used to compress the interface and which takes effect only near the interface.

The surface tension plays an important role in plunging breaking waves since the pressure jump mainly depends on the curvature of the free surface. It is therefore necessary to take the surface tension into account to capture the free surface accurately. In the interFoam solver, the surface tension at the air-water interface generates an additional pressure gradient resulting in a force, which is evaluated per unit volume using the continuum surface tension (CSF) model:

$$\mathbf{f}_\sigma = \sigma\kappa\Delta\alpha, \tag{7}$$

where σ is surface tension, σ= 0.072 kg/s^2 in an air water system, κ is the mean curvature of the free surface and is defined as:

$$\kappa = -\nabla \cdot \frac{\nabla\alpha}{|\nabla\alpha|}. \tag{8}$$

3. Computational implementation

The geometry model is built from the bump profile with a height H=0.1143m in the experiment [3]. The origin of the coordinate system is placed at the centre of the bump. The simulations are conducted on a 2D computational domain of x/H= [-52, 44] and z/H= [0, 5]. The entire computational domain and the different boundaries applied at inlet, outlet, bottom, upper are shown in Fig. 1. The front and back boundary conditions are set as empty, since it is a two-dimensional simulation. The three-dimensional simulation with the same parameters as the experiment will be investigated in the future. The inlet velocity imposed at the inlet boundary is fixed with U=0.87 m/s for the water and 0 m/s for the air. The initial free surface elevation is set with a height of 2H, with a uniform velocity field of 0.87 m/s prescribed in the water domain, with the air phase at rest. The corresponding initial Re=$\rho uh/\mu$ = 107503 and Fr=$\rho/\sqrt{gh}$=0.789.

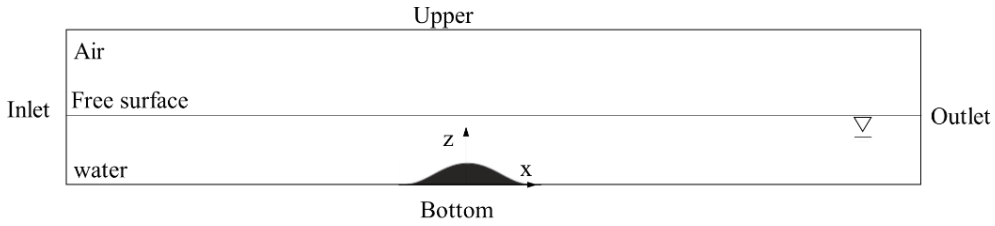

Fig. 1. Computational domain with boundaries.

The meshing of the blocks consists of conformal non-orthogonal structured elements throughout the whole computational domain. A more refined mesh is employed around the bump, the downstream area and free surface compared to the rest of the domain to capture better the near-wall turbulent flow and wave evolution.

Fig. 2. Mesh around the bump.

4. Results and discussion

4.1. Grid independency study

To check the grid independency of the results, three grids are applied in this study, with

consecutively increased (by a factor of 2) sizes from grid one with 154960 cells, to grid two with 348660 cells and grid three, 657984 cells. The maximum Courant number, Co, equals 0.5 in all these three cases. The wave profiles for the three grids are shown in Fig. 3. The overall structures of the interface obtained on the three grids are very similar. The jet tip is slightly sharper on the finest grid since a finer grid can capture more details of the free surface with higher grid resolution. In order to capture more detailed wave evolution and the velocity field, the finest mesh is chosen here for better understanding of the process of the plunging breaking waves.

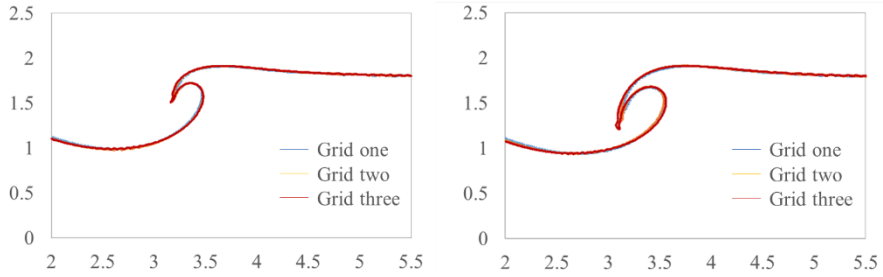

Fig. 3. Wave profiles with three different grids.

4.2. Wave breaking process

The plunging wave breaking process has been characterized in the previous studies (see [3]) by four major phases including steep wave formation, jet formation and overturning, splash-up and air entrainment. The major events of the plunging wave breaking are shown in Fig. 4 including instantaneous wave profiles from both experiments and CFD simulations. t_b is a reference time at which the wave reaches its maximum height [3], which is chosen as the initial time to compare the EFD and CFD results. The time instances do not match between the CFD and EFD due to differences in the initial conditions.

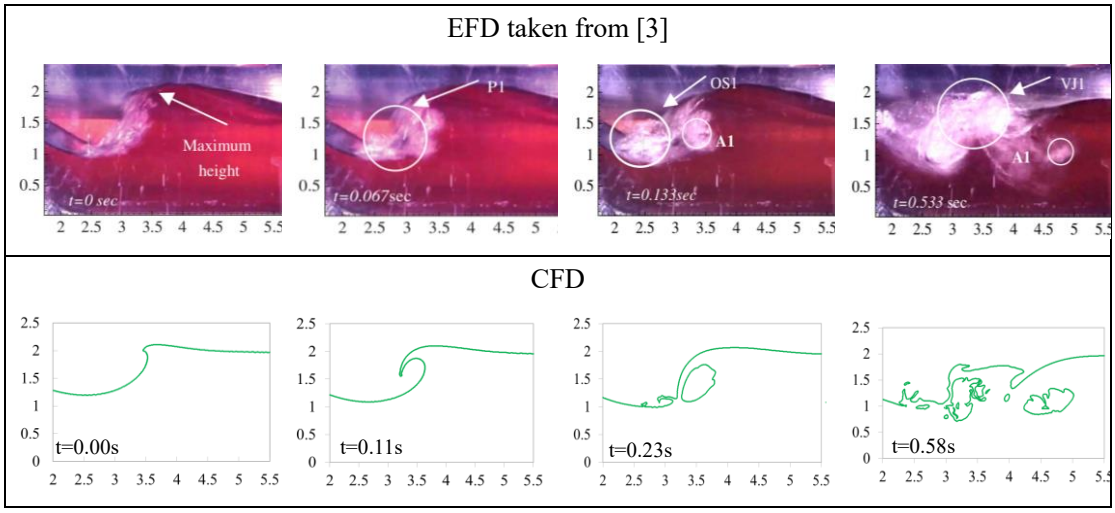

Fig. 4. Instantaneous free surface profiles of the wave breaking process.

At time t=0.0s, the wave crest becomes steepest when it reaches its maximum height and starts to overturn. The location and the wave profiles match quite well. At time t=0.11s, a jet of water is projected forward into a characteristic overturning motion. At time t=0.23s, the first plunge occurs when the overturning jet impinges onto the free surface of the tough. With the overturning jet, a large amount of air below the jet is entrapped which forms a big air bubble. Although the EFD and

CFD bubbles are located at almost the same place, the size of the air bubble is almost 2 times larger than the EFD results. Once the jet tip touches the trough surface, splash-up initiates and develops at the location where the jet impacts. As shown in both EFD and CFD plot, an oblique splash-up is generated towards the upstream direction with a spray region. The splash-up intensified and a vertical jet can be clearly observed in the CFD profiles and reaches its maximum height at t=0.58s. Severe bubble shape deformations can be seen at t=0.58s compared to t=0.23s in the CFD plot as the initially entrapped air bubble moves downstream. It is interesting to observed that the air bubble after the plunging collapsed in EFD but remains the same size in CFD. This may be because of 3D instability, which may contribute to the breaking of the air bubble. 3D simulations with same computational set-up will be investigated in the future.

4.3. Velocity field

Fig. 5 shows the EFD horizontal velocity, U, contours and the CFD U contours, respectively at the time steps that correspond to the wave breaking process in Fig. 4. For CFD results, air and water are presented separately, for clarification of the two-phase flow. All contour plots are presented in the same dimensional form.

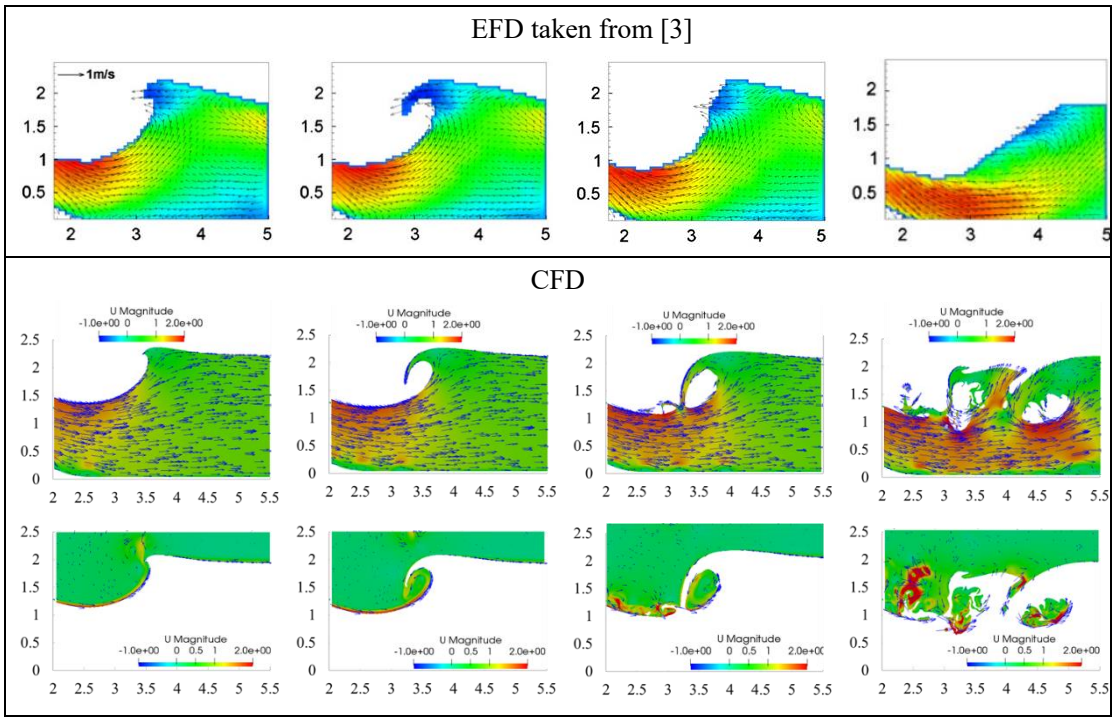

Fig. 5. Velocity fields of the wave breaking process.

The uniform inlet flow was accelerated by the bump and generated plunging breaking waves downstream of the bump. The velocity of the main region of air remains at zero but is increased close to the free surface. During the whole wave breaking process, the velocity in the back side is very high near the free-surface and then gradually decreased along the flow direction. At t=0s, a positive U region extends towards downstream of the bump and is reduced in the region where the steep wave crest is formed. At t=0.11s, a negative U region initiates in the wave crest and intensifies after the overturning jet. The region of bubbly flow increases after the wave crest plunges into the wave trough. The velocity data are not available in these regions through EFD. More detailed resolutions of splashing and vertical jet and bubble entrainment events in the wave breaking process

can be found in CFD simulations. At t=0.23s and t=0.58s, after the overturning jet hits the trough surface, strong air flows are induced with a series of vortices in both air and water.

5. Conclusion

A two-phase flow solver is applied for the simulation of the plunging breaking waves observed behind a shallowly submerged bump in a uniform flow. A standard k-ωSST turbulence model incorporated with the interface capturing algebraic Volume of Fluid (AVOF) method is adopted to captures the interface of air and water and the turbulent flow downstream of the bump.

Satisfactory agreement is observed between the numerical results and experimental data in the process of the plunging wave breaking. The major wave breaking events are revealed by CFD simulations and validated by EFD observations, including maximum wave height, first plunge, splash up and the air entrainment. The algebraic Volume of Fluid method with a k-ω SST turbulence model predicts successfully the formation of the plunging breaking wave and the measured velocity profiles.

For the plunging breaking wave, further investigation will focus on the detailed investigation of turbulent flow below the plunging breaking waves and its effect on the resulting waves. 3D simulation will be designed to investigate the instabilities in the third dimension which may contribute to the observed breaking of air bubbles.

The physics of the formation and break-up of the bubble or water jet is a complex multiphase flow problem. Since the interface is modelled by the AVOF capturing method, the air bubbles or water droplets are unable to be captured when the scale is smaller than the grid spacing. A finer mesh will be designed to get a better understanding of the plunging breaking waves. Besides of the gridding problems, unphysical tearing of the free surface tends to occur due to a large density jumps between the air and the water across the free surface. A physical-based smoothing procedure is required to resemble the viscous boundary layer near the free-surface.

6. References

[1] P. Bonmarin, “Geometric properties of deep-water breaking waves,” *J. Fluid Mesh*., vol. 209, no. 1952, 1989.

[2] H. Chanson and L. Jaw-Fang, “Plunging jet characteristics of plunging breakers,” *Coast. Eng*., vol. 31, no. 1–4, pp. 125–141, 1997.

[3] D. Kang, S. Ghosh, G. Reins, B. Koo, Z. Wang, and F. Stern, “Impulsive plunging wave breaking downstream of a bump in a shallow water flume-Part I: Experimental observations,” *J. Fluids Struct.*, vol. 32, pp. 104–120, 2012.

[4] A. Iafrati, “Energy dissipation mechanisms in wave breaking processes: Spilling and highly aerated plunging breaking events,” *J. Geophys. Res*., vol. 116, pp. 1–22, 2011.

[5] A. Babanin, D. Chalikov, I. Young and I. Savelyev, “Numerical and laboratory investigation of breaking of steep two-dimensional waves in deep water,” *J. Fluid Mesh.*, vol. 644, pp. 433–463, 2010.

[6] Z. Wang, J. Yang, B. Koo, and F. Stern, “A coupled level set and volume-of-fluid method for sharp interface simulation of plunging breaking waves,” *Int. J. Multiph. Flow*, vol. 35, no. 3, pp. 227–246, 2009.

[7] P. Lubin and S. Glockner, “Numerical simulations of three-dimensional plunging breaking waves : generation and evolution of aerated vortex filaments,” *J. Fluid Mesh*., vol. 767, pp. 364–393, 2015.

Parameter Uncertainty Quantification applied to the Duisburg Propeller Test Case

Eduardo T. Katsuno[*‡], Artur K. Lidtke[*], Bülent Düz[*], Douwe Rijpkema[*] and Guilherme Vaz[*†§]
[*]MARIN - Maritime Research Institute Netherlands, [‡] USP - University of São Paulo, Brazil, [†]WavEC - Offshore Renewables, Portugal, [§] ISMT, University of Duisburg-Essen, Duisburg/Germany
eduardo.katsuno@usp.br

1 Introduction

At model-scale conditions (diameter-based Reynolds number below 10^6), laminar-to-turbulent transition plays an important role on the performance of a propeller. While at these Reynolds numbers turbulent transition and its effects on the flow are difficult to simulate, current state-of-the-art transition models (Menter et al. (2004)) provide viable means to do so. Previous studies on these new methods (Eça et al. (2016), Baltazar et al. (2018), Lopes et al. (2018)) show that, as in reality, the results are sensitive to the inlet turbulence intensity and its decay upstream of the propeller plane. In the aforementioned studies, numerical uncertainties were reported to have been small. Therefore, it is expected that variability of the user-specified inflow conditions will have a dominant effect on the solution.

To better understand the associated uncertainty of model-scale open-water propeller performance predictions, Uncertainty Quantification (UQ) methods are employed in this work. Given a prescribed range of input uncertainties reflecting typical ranges found in test facilities and RANS simulation setups, a laminar-turbulent transition model is used in CFD simulations of the Duisburg Propeller Test Case. This paper then aims to use the results in order to quantify the parameter uncertainty and obtain the output-variable's Cumulative Distribution Function (CDF), confidence interval and the Sobol indices of each input variable. Together, these quantities are used to suggest suitable ways of achieving accurate and repeatable predictions of propeller performance at intermediate Reynolds numbers.

2 Methods

In a sampling-based variance decomposition, a function, which is assumed to be a black box, is evaluated typically a large times and, based on its input values and its response through the output value, variance can be obtained, allowing to estimate the parameter uncertainty. However, one of the main drawbacks of this approach is that the quality of parameter uncertainty values is related on how many samples N_i of function f are evaluated on. This approach might become infeasible with CFD, depending on the case studied.

An alternative approach proposed in this work is to use an approximate function $\tilde{f}$ as a surrogate model, which has a considerably lower computational cost, as schematically represented in Fig. 1. In this approach, some points N need to be sampled from CFD solution and used to construct the surrogate model. This yields a response surface approximation $\tilde{f}$ which may be used for sampling thousands of N_i points.

Subsequently $\tilde{f}$ is obtained, it is possible to perform the Uncertainty Quantification. Given the input uncertainties $\mathbf{x}$, each with its Probability Density Function (PDF), the sampler uses the surrogate model $\tilde{f}$ to obtain the output uncertainties and Sobol indices (explained in the next section).

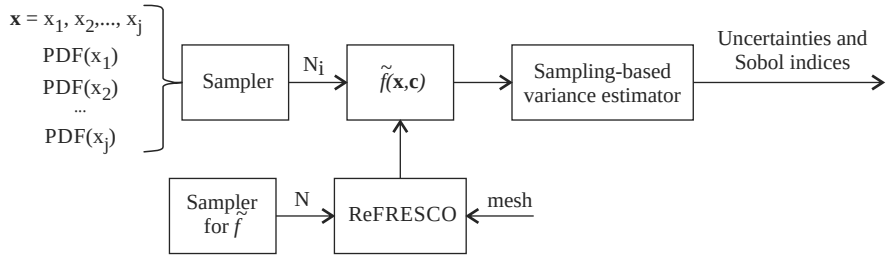

Fig. 1: Algorithm proposed in this work to perform Uncertainty Quantification in a sampling-based approach with CFD.

3 Sobol indices

Sobol indices of an output variable y_m associated with an input variable i denote the variance of the output, assuming the variable i is known (i.e., without uncertainty), divided by the variance of the output y_m, as expressed in Eq. (1). Therefore, a larger value of S_i means that the uncertainty in the input variable i has a larger effect on the variance of the output. Higher-order interaction index S_{i+j} has a similar meaning: variance decomposition by the interaction of the inputs i and j divided by the variance of the output. The sum of all Sobol indices, including the high-order terms, is equals to one. The total-order Sobol index ST_i is the sum of all Sobol indices which contains the input variable i, Eq. (1).

$$S_i = \frac{V_{x_i}\left(E_{\mathbf{x}\setminus x_i}\left(y_m|x_i\right)\right)}{V\left(y_m\right)} \qquad ST_i = \sum_{i\subset k} S_k \tag{1}$$

More detail about Sobol indices and their estimation are given by Saltelli et al. (2010).

4 Surrogate model

The basic idea behind an estimator is to sample a number of points through CFD simulations, feed the results to a regression model, thereby correlating the input and output values. The sampled points are chosen based on a Latin Hypercube Sampling (LHS). The mathematical operation used to create the surface response is linear interpolation between three nearest points when it is possible to create a concave surface. Extrapolation of order zero is used in other regions. This is done to avoid overshooting of results and ensure that the value is bounded within the range of simulated values. Figure 2 shows an example function estimator that considers a case with two inputs, shown on the x and y axes, and one output, plotted on the $z = Cf$ axis.

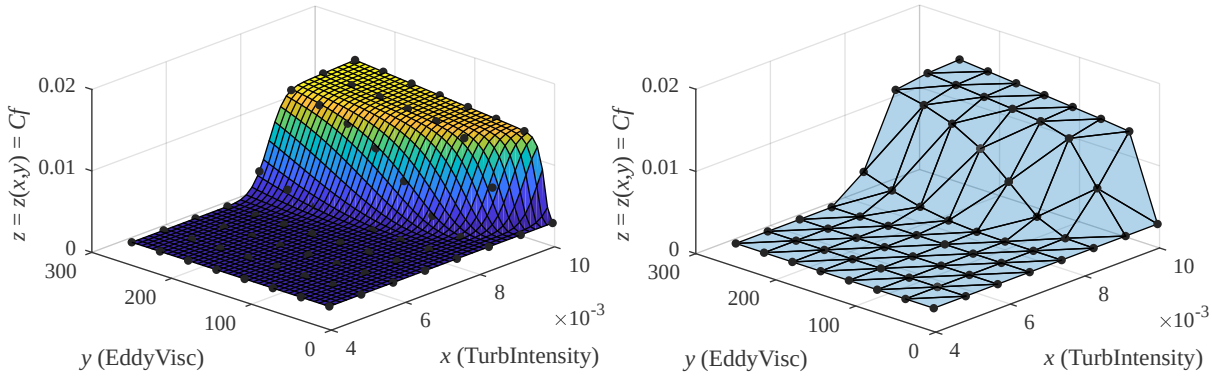

Fig. 2: Schema of function estimator: true response and sampled points (marked as black dots) from CFD results (left) and the surrogate model based on linear interpolation (right).

One drawback of using few points is the excessive use of extrapolation. To avoid it, sampling points are added on the edge of input variable range, yielding a so-called Shell Distribution sampling approach. Figure 3 shows an example of the use of Shell Distribution, LHS distribution and the combined distribution, assuming two inputs x_1 and x_2 characterised by triangular distributions bounded in [0; 1]. Shell Distribution also includes a point with the expected value of input variables, which may be interpreted as the mean input to the CFD simulation.

5 Duisburg Propeller Test Case - DPTC

This study is carried out with the propeller of the Duisburg Propeller Test-Case (DPTC) model P1570 of Ship Model Basin Potsdam (SVA). Pictures of DPTC and its CAD representation are shown in Fig. 4. Numerical and experimental studies with DPTC are presented in details in Wielgosz et al. (2019).

The chosen operating condition is close to the maximum efficiency point, $J = 0.8$, resulting in Reynolds number based on diameter of $Re_D = 2.43 \times 10^5$.

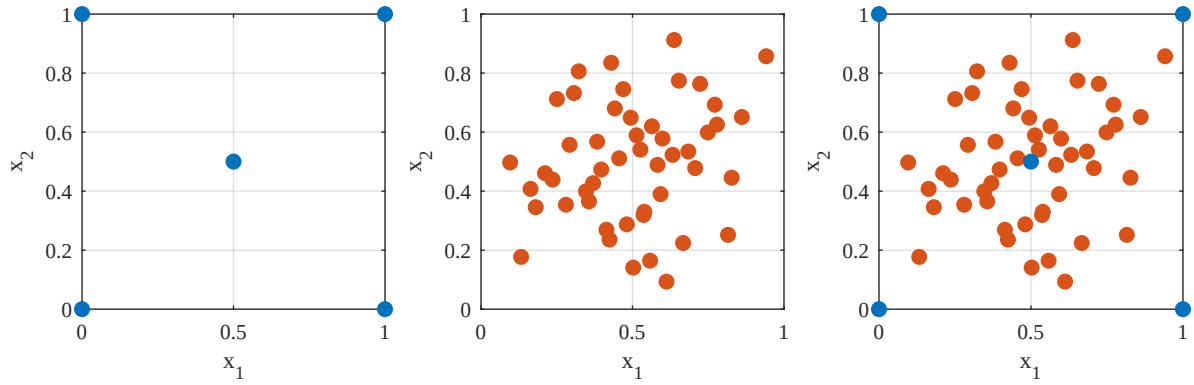

Fig. 3: Shell distribution (left); LHS distribution (center); and combined LHS+Shell distribution (right)

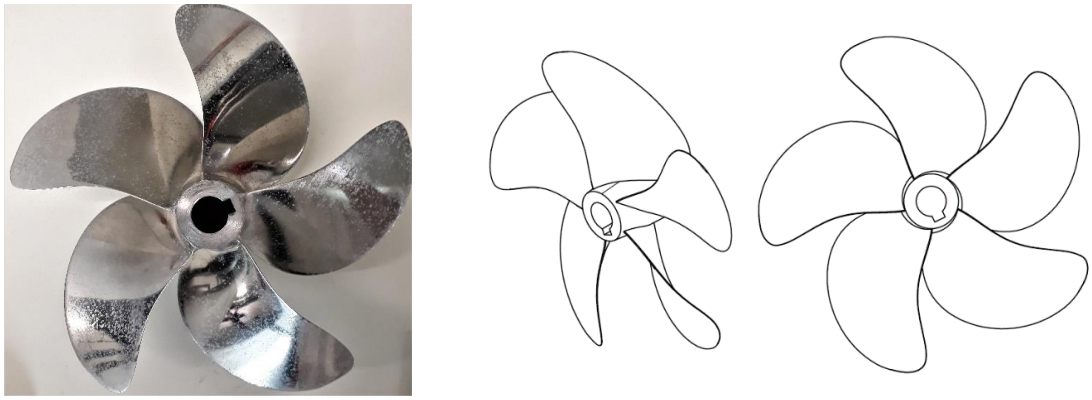
Fig. 4: Duisburg Propeller Test Case P1570. Figures extracted from Wielgosz et al. (2019)

6 Mesh topology

Two regions are used: a cylinder, which contains the rotating propeller, and a cylindrical grid, which represent the stationary part of the cavitation tunnel. The stator mesh is kept the same in all simulations and includes 1.1 million cells. For rotor region, five topologically identical grids with varying refinement levels were used. These varied between 5.2 and 31.2 million cells. Fig. 5 shows the five meshes and the gradation of element size on the blade surface.

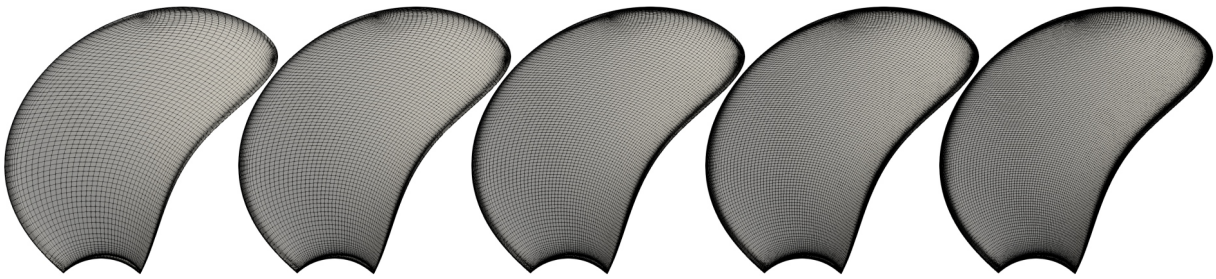
Fig. 5: Mesh elements on the blade.

7 Numerical Setup

Simulations are conducted using ReFRESCO (www.refresco.org), a community-based open-usage/open-source CFD code designed for marine applications, Vaz et al. (2009). Governing equations are discretised using a finite-volume approach and pressure-velocity coupling is solved using the SIMPLE algorithm. For momentum transport equations, `LIMITED QUICK` is used for the convective fluxes. $k-\omega$ SST 2003 turbulence model (Menter et al. (2003)) is used in conjunction with the $\gamma - \tilde{R}e_{\theta_t}$ transition model (Langtry and Menter (2009)). This model was Verified and Validated in Eça et al. (2016). Convective

fluxes of the turbulence equations are discretised with 1^{st} order upwind scheme. All diffusive fluxes are 2^{nd} order and the calculations are steady and in the Absolute-reference Frame Model (AFM).

8 Input Uncertainties and Analysed Outputs

Uncertainties of three input variables are considered: `powerTurbIntensity`, `powerEddyVisc` and `pDpx2FreezeTurb`.

Variable `powerTurbIntensity` is related exponentially to turbulence intensity at the inlet, Tu = 10^`powerTurbIntensity`. The PDF of this variable is assumed to be a uniform distribution. The lower bound is -3.301, which corresponds of $Tu = 0.0005$, smaller than the Selig's wind tunnel, which reportedly has a mean $Tu = 0.0007$ for highest Reynolds number test (Williamson et al. (2012)). The upper bound is -1.0, which corresponds of $Tu = 0.1$, chosen based on the mean value of Tu in rivers (McQuivey (1973)). Although the variable is uniformly distributed, the effect on Tu is exponential, which resembles a log-uniform distribution.

Variable `powerEddyVisc` is related exponentially to eddy viscosity ratio at the inlet, μ_t/μ = 10^`powerEddyVisc`. The PDF of this variable is assumed to be a uniform distribution. The lower bound is -1.301, which corresponds to $\mu_t/\mu = 0.05$. This value is chosen because it is half of lowest value used in Eça et al. (2016). The upper bound is 3.0, corresponding to $\mu_t/\mu = 1000$, twice of highest value used in Baltazar et al. (2018).

Variable `pDpx2freezeTurb` is not a boundary condition, but a parameter to artificially freeze the transport equation of turbulent kinetic energy, expressed in terms of a fraction of the propeller diameter. The PDF of this variable is assumed to be a uniform distribution, varying from 0.0 to 1.0.

It should be noted that the chosen input ranges can be considered conservative, since they are larger than values expected in most realistic scenarios, as well as extreme values reported in the literature. Therefore, it is expected that the computed parameter uncertainty will be considerable.

The analysed outputs correspond to typical open-water performance indicators, namely thrust coefficient K_T, torque coefficient K_Q, torque coefficient due to shear forces only $K_{Q,\,s}$ and hydrodynamic efficiency η_0. These are expressed as:

$$K_T = \frac{T}{\rho n^2 D_p^4}, \qquad K_Q = \frac{Q}{\rho n^2 D_p^5}, \qquad K_{Q,\,s} = \frac{Q_s}{\rho n^2 D_p^5}, \qquad \eta_0 = \frac{J}{2\pi}\frac{K_T}{K_Q}, \tag{2}$$

in which n is the rotation rate, D_p the propeller diameter, and $J = v_a/(nD_p)$ is the advance ratio based on free-stream velocity, v_a.

9 Results: Effect of CFD Sampling

To verify if the number of samples is sufficient to represent the surrogate model, three levels of sampling density are compared. All of them include a number of LHS samples plus 9 samples from the Shell distribution. This sensitivity study was carried out on the medium density grid. Figure 6 shows the CDFs of various responses for three sample sizes. The output values are divided by the mean value of output, showing the x axis in terms of percentage deviation from the mean value.

There is little variation in the CDFs of responses when increasing the number of samples from 29 to 49, indicating that 49 samples are sufficient to correctly represent the function estimator. Furthermore, because the studied input uncertainties were chosen to primarily affect the transition model behaviour, it was expected that the transition location, and consequently the viscous components of the predicted forces and moments, would see the largest response. Presented results indicate that among the analysed outputs, thrust coefficient experiences the smallest variation due to input uncertainties. Since this quantity is mainly influenced by the pressure distribution around the blade and not the shear forces, this trend is consistent with the aforementioned expectations. On the other hand, the shear stress distribution has a higher contribution to the torque than to the thrust and has been predicted to be the most affected by the variation of the inlet conditions, as evident form its largest uncertainty.

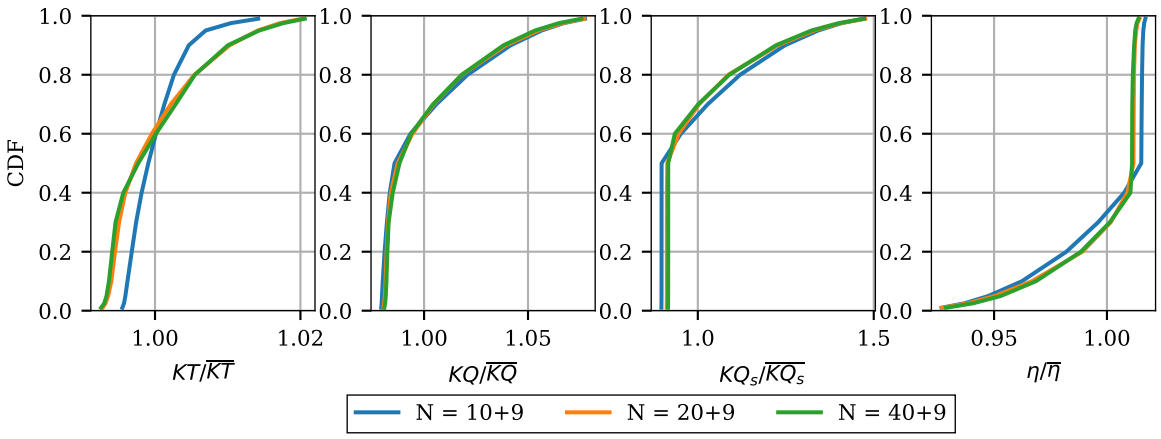

Fig. 6: Cumulative Density Function (CDF) of each output divided by the output expected value $E[Y]$ as a function of the number of elements N used to construct the respective surrogate models.

10 Results: Grid sensitivity study

Input uncertainty analysis was carried out for grids of varying densities, described in Sec. 6, using 49 sampling points. Key results of the analysis are the 95% confidence intervals of the outputs, as well as the associated Sobol indices. These are depicted in Figures 7 and 8 for the thrust and torque coefficients, respectively. For the latter, only the shear force contribution is considered. Left parts of the figures show bars in which the bottom and top represent the bounds of the 95% confidence interval coloured proportionally to each Sobol index. On the right-hand side of the figures, Total-order Sobol indices are shown on an absolute scale, alongside the individual values shown using colour bars. At each mesh refinement h/h(finest) the vertical bars are offset slightly for readability, knowing that where one Sobol contribution ends the next one starts. Subscripts 1, 2 and 3 refer to input variables `powerTurbIntensity`, `powerEddyVisc`, and `pDpx2FreezeTurb`, respectively.

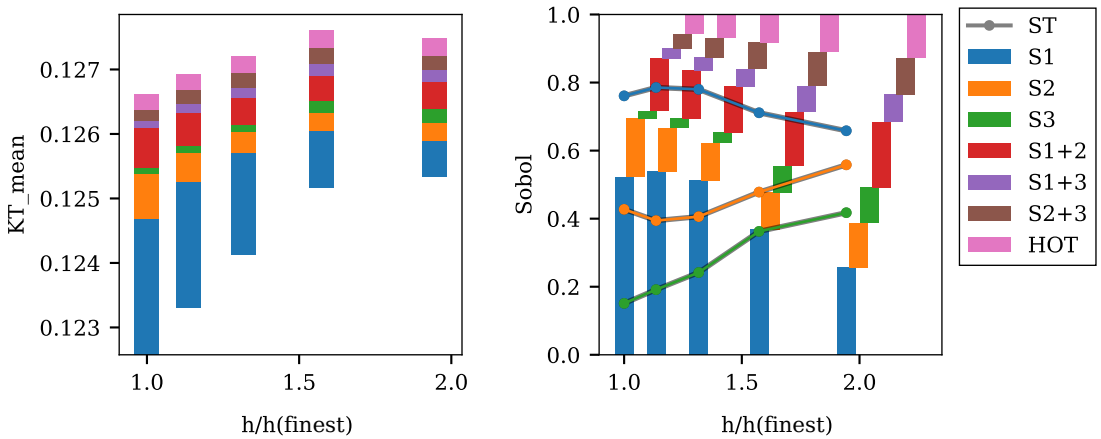

Fig. 7: Thrust Coefficient KT - 95% Confidence Interval (left) and Sobol Indices with the Total-Sobol contribution (right) for each mesh refinement. HOT indicates S1+2+3.

The results show that the confidence intervals change considerably with the mesh density for the K_T output but remains almost constant for the shear component of the torque coefficient $K_{Q,\,s}$ case. As discussed before, K_T is less affected by the parameter uncertainty, so the result may be explained by a higher influence of the discretisation uncertainty. On the other hand, $K_{Q,\,s}$ is more sensitive to parameter uncertainty, making the relative effect of the discretisation uncertainty less pronounced.

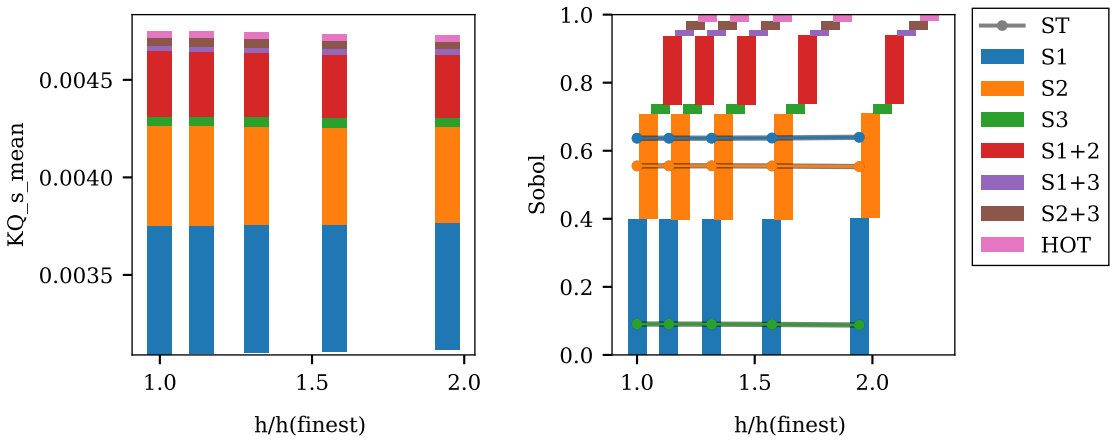

Fig. 8: Torque Coefficient of Shear Stress contribution only KQ_s - 95% Confidence Interval (left) and Sobol Indices with the Total-Sobol contribution (right) for each mesh refinement. HOT indicates S1+2+3.

11 Conclusions

Using a surrogate model instead of direct sampling through CFD runs has been shown to be an effective approach for performing uncertainty quantification analysis of CFD simulations.

The results also showed that, depending on the analysed output, there is a considerable co-dependence between parametric and discretisation uncertainties. In the future, it is considered important to couple the uncertainty of the inputs and the grid refinement studies to obtain a combined uncertainty, taking into account the combined effect of both sets of parameters and their covariance.

The input variables chosen for this test case were focused mainly to understand the transition effect due to uncertainties on the boundary conditions. The proposed model can be used for other similar applications, including other input uncertainties. For example, based on experimental uncertainties to determine the advance velocity or rotation rate on a cavitation tunnel, the presented method can be used to estimate the impact of these uncertainties on the main indicators of open-water propeller performance.

References

J. Baltazar, D. Rijpkema, J. Falcão de Campos (2018). On the use of the Gamma-ReTheta transition model for the prediction of the propeller performance at model-scale. *Ocean Engineering*, **170**(August), 6-19.

L. Eça, R. Lopes, G. Vaz, J. Baltazar and D. R. Rijpkema (2016). Validation Exercises of Mathematical Models for the Prediction of Transitional Flows. Proceedings of 31st Symposium on Naval Hydrodynamics, Monterey, Canada.

R. B. Langtry and F. R. Menter (2009). Correlation-based transition modeling for unstructured parallelized computational fluid dynamics codes. *AIAA Journal*, **47**(12), 2894-2906.

R. Lopes, L. Eça, G. Vaz (2018). Assessment of RANS Transition Models. Proceedings of 21st NuTTS, Italy

R. S. McQuivey (1973). Summary of Turbulence Data from Rivers, Conveyance Channels, and Laboratory Flumes: Turbulence in Water. US Government Printing Office.

F. R. Menter, M. Kuntz and R. Langtry (2003). Ten Years of Industrial Experience with the SST Turbulence Model Turbulence heat and mass transfer. *Turbulence, Heat and Mass Transfer*, **4**, 625-632.

F. R. Menter, R. B. Langtry, S. R. Likki, Y. B. Suzen, P. G. Huang and S. Vo'Ilker, S. (2004). A Correlation-Based Transition Model Using Local Variables: Part I - Model Formulation. *ASME Turbo Expo*, **128**, 57-67.

A. Saltelli, P. Annoni, I. Azzini, F. Campolongo, M. Ratto, and S. Tarantola (2010). Variance based sensitivity analysis of model output. Design and estimator for the total sensitivity index. *Computer Physics Communications*, **181**(2), 259-270.

G. Vaz, F. Jaouen, and M. Hoekstra (2009). Free-Surface Viscous Flow Computations: Validation of URANS Code. Polar and Arctic Sciences and Technology; CFD and VIV, pages 425-437.

C. Wielgosz, R. Golf, A. K. Lidtke, G. Vaz and O. Moctar (2019). Numerical and experimental study on the Duisburg Propeller Test Case. Proceedings of 22nd NuTTS, Tomar, Portugal.

G. A. Williamson, B. D. McGranahan, B. A. Broughton, R. W. Deters, J. B. Brandt and M. S. Selig (2012). Summary of Low-Speed Airfoil Data : Volume 5. PhD thesis, University of Illinois at Urbana-Champaign.

Investigations for CFD Based Form Factor Methods

Kadir Burak Korkmaz* †**, Sofia Werner**†**, and Rickard Bensow***
*Chalmers University of Technology, Gothenburg/Sweden, †SSPA Sweden AB, Gothenburg/Sweden
korkmaz@chalmers.se

1 Introduction

Performance prediction of full-scale ship is one of the most important tasks in the design stage. Depending on the design phase, required accuracy of the prediction varies as well as the prediction methods. Often towing tank tests are carried out at the last stage of the design process. The procedures of the towing tank tests are regulated by the International Towing Tank Committee (ITTC) and the prediction is based on the 1978 ITTC Performance Prediction Method. The form factor concept was adopted by this method as described by Hughes (1954), where the viscous resistance is expressed in relation to the 'ITTC 57 model-ship correlation line' as shown in the Eq. (1).

$$C_V = (1 + k)\, C_F. \tag{1}$$

The concept of Hughes (1954) and the determination method of Prohaska (1966) of form factor have been questioned and investigated for many decades. By analyzing the geosim test data, García-Gómez (2000), Toki (2008) and Van et al. (2011) demonstrated the scale effects on form factor. Additionally, CFD studies presented by Raven et al. (2009) and Wang et al. (2015) supported the existence of substantial scale effects on form factor. The main cause of the scale effects has been found to be the 'ITTC 57 model-ship correlation line' rather than the original hypothesis of Hughes (1954) which suggested that form factor is independent of the Reynolds number. As explained by Raven et al. (2009), scale effects on the form factor depends on several aspects:

1. The assumption that the form factor is not dependent on the Reynolds number. As Raven et al. (2009) and Wang et al. (2015) presented, viscous resistance was nearly proportional for bare hull when modern friction lines, i.e. Grigson (1999) and Katsui (2005), or numerical friction of the same turbulence model is used for extrapolation.

2. The friction line used for the extrapolation method

3. If form factor is determined by CFD, choice of turbulence model might play a significant role

Additionally, when the growing disposition to leave the Prohaska's method of form factor determination and growing confidence in numerical resistance calculations considered, CFD might be able to provide a new method of form factor determination, which can increase the accuracy of the full-scale resistance predictions.

In this study, the form factor concept has been investigated by analyzing the results obtained from the simulations performed on KVLCC2 and KCS hulls. Grid dependence studies, sensitivity analysis of loading conditions and varying grid setups have been performed with SHIPFLOW code. Extrapolation of viscous resistance to full scale has been performed with ITTC57 line and numerical friction lines.

2 Flow Solver, Computational Domain, Grid Generation

Two of the flow solvers and the structured grid generator of SHIPFLOW 6.3 has been used for this study. Potential flow solver, XPAN, is used for obtaining sinkage and trim for the bare hull. Viscous flow is solved with the XCHAP module which solves the Reynolds Averaged Navier-Stokes equations with a finite volume method. XCHAP is a steady state solver which requires structured grids but overlapping grids can be used to introduce refinement regions or appendages.

Viscous flow computations for all cases were carried as double model. The computational domain consists of six boundaries. The distance between inlet and fore-perpendicular (FP) is $0.5L_{PP}$. Outlet plane is located at $0.8L_{PP}$ behind the aft-perpendicular and the radius of the cylindrical outer boundary is $3L_{PP}$ in order to eliminate the blockage effect as much as possible. EASM and $k-\omega$ SST turbulence

models have been used for this study. All simulations performed as wall resolved, i.e. no wall functions used. The computational conditions are presented in Table 1.

Table 1: Computational conditions for the KVLCC2 and KCS hulls

Ship	L (m)	Scale	T (m)	S/L^2	Speed	Rn model	Rn ship	Vm (m/s)	Vs (kts)
KLVCC2 with rudder	320	58	20.8	0.2682	Low	4.1×10^6	1.80×10^9	0.88	13
					Design	4.9×10^6	2.14×10^9	1.05	15.5
KCS with rudder	230	31.6	10.8	0.1803	Low	7.33×10^6	1.39×10^9	1.281	14
					Design	1.26×10^7	2.39×10^9	2.196	24

3 Grid Dependence Study

Grid dependence studies have been performed for KVLCC2 and KCS hulls at two speeds and two grid configurations (with rudder and without rudder). Each grid dependence study has been performed with 5 geometrically similar grids. The finest grid is named as g1 while the coarsest grid denoted as g5. Considering the sensitivity of frictional resistance coefficient to the first layer thickness as highlighted in Korkmaz et al. (2019), average y^+ values are kept below the recommended value of 0.4 which was observed from the flat plate simulations.

All CFD calculations have been performed in double precision in order to eliminate the round-off errors. The iterative uncertainties have been determined from the standard deviation of the force in percent of the average force over the last 10% iterations. Iterative uncertainty for C_F and C_{PV} was kept below 0.01% and 0.15% for all simulations in model scale. Hence, it is assumed that the numerical errors are dominated by the discretization errors and both iterative errors and round-off errors are neglected.

There has been issues with the grids of the KCS hull around and behind the bulb. Close inspection has shown that the first layer thickness was varying irregularly due to difficulties of grid generation around the large protruding bulb at the forebody. Unfortunately, the issue hasn't been resolved completely but only a slight improvement was possible. The grid dependence analysis has shown that the calculated resistance components varied unexpectedly due to the meshing issue. Even though the variations were very limited (for example maximum variation of C_V is approximately 0.4% between 5 geometrically similar grids), it still caused rather high numerical uncertainties in bare hull cases. On the other hand, when the KCS hull is appended with rudder, numerical uncertainties are dropped significantly as presented in Table 2. In contrast to KCS hull, the simulations with KVLCC2 indicates similar uncertainty levels for different speed, turbulence model and existence of the rudder. The $k-\omega$ SST model gave slightly lower uncertainties compared to EASM. As it was the case for the KCS hull, existence of rudder reduced the uncertainties. The numerical uncertainties for KVLCC2 with rudder are presented in Table 2. Below 1% uncertainty was only achieved when the rudder was included in the simulations.

Table 2: Numerical uncertainties of KVLCC2 and KCS hulls, both with rudder and EASM turbulence model

KVLCC2						**KCS**					
$U_{SN}\%S$	g1	g2	g3	g4	g5	$U_{SN}\%S$	g1	g2	g3	g4	g5
C_F	1,3%	1,7%	2,3%	3,2%	4,8%	C_F	1,7%	1,8%	2,3%	3,0%	4,5%
C_{PV}	0,5%	1,6%	0,9%	1,2%	3,1%	C_{PV}	14,0%	17,0%	19,1%	24,7%	34,1%
C_V	0,8%	1,0%	1,0%	1,3%	1,4%	C_V	0,20 %	0,31 %	0,34 %	0,65 %	0,48 %

The first cell size have been varied with KCS and KVLCC2 hulls. The calculated C_F and C_V varies only marginally with the first cell size variation. It is significant to note that the maximum difference of C_F is around 0.1% at KCS hull case. The grid density of KCS hull g1 corresponds to g5 of the numerical flat plate investigations explained in Korkmaz et al. (2019). Such y+ variation caused 0.5% difference in C_F which is significantly larger than of the hull. Therefore it can be concluded that the effect of y^+ variation with a hull from is smaller than the flat plate case.

4 Sensitivity of form factor for varying loading conditions (different draughts and trims)

The loading condition varies during the operation of the ship. Typically, design and ballast loading conditions are tested in towing tanks. However, sea trials are often performed in ballast condition and sea trial at design condition is calculated via an extrapolation. Since the extrapolation is based on the model tests, it is critical to have the correct form factors. Due to the modern forebody designs or bows with bulbs, Prohaska method for obtaining the form factor at ballast condition is often not easy because of the significant wave patterns even at low Froude numbers. The same issue is also common at the design or other loading conditions. Therefore, CFD based form factor has potential improve the form factor determination. In this case, the first question is whether to perform the double model simulation with dynamic sinkage and trim or draught and trim at rest. The loading condition variation has also been suggested by Raven et al. (2009) as a solution to the large protruding bulbs for CFD based methods since the flow is accelerated or in some cases separated around the bulb. It is suggested that if the bulb the submerged more by trimming the hull (bow down) this issue can be prevented. The other issue of the form factor determination is the large submerged transoms which causes large separations behind the ship wake. It is worth to remember that the assumption of Hughes (1954) that form factor is the same in model and full scale is only valid if there is no flow separation. In order to reduce or eliminate the effect of a large submerged transom, the loading condition can be altered with reduced draught.

The loading condition (sinkage&trim) variation has been applied to KVLCC2 and KCS hulls. The form factor has been calculated based on the ITTC57 line and full scale viscous resistance (C_{V_S}) is calculated using the Eq. (1). As presented in Table 3, KVLCC2 and KCS hulls differ 0.24% and 0.10% in C_{V_S} between dynamic sinkage&trim and the draught&trim at rest for the design speed of each hull. This difference is significantly smaller for the lower speeds since the dynamic sinkage and trim is smaller compared to higher speeds. The trim variation is also applied to both hull forms in a way that the draught at the aft perpendicular is equal to the draught at rest (the pivot point) and the hull is trimmed bow up (- sign) or bow down (+ sign). The variation of C_{V_S} due to trim is shown as percentage with respect to the draught&trim at rest and presented in Table 3. Both hull forms indicated that form factor would increase when the hull is trimmed bow down (bow is submerged more) and vice versa for the bow down condition. Having in mind the slight variation in the grids between the trimmed hulls compared to dynamic sinkage and trim, it should be noted that the variation in C_{V_S} due to trim is smaller than the numerical uncertainties of each hull presented in Table 2.

Table 3: Form factor and viscous resistance variations as a result of different loading condition variation with EASM model, g2 with rudder at model scale design speed

KVLCC2					KCS			
Trim	Sinkage	k	C_{V_S}		Trim	Sinkage	k	C_{V_S}
dynamic	dynamic	0,230	0,24 %		dynamic	dynamic	0,106	0,10 %
0°	rest	0,227	ref.		0°	rest	0,105	ref.
0°	-2.5%	0,222	-0,37 %		0°	-2.5%	0,106	0,11 %
0°	2.5%	0,233	0,48 %		0°	2.5%	0,099	-0,55 %
0,25°	rest	0,233	0,46 %		0,25°	rest	0,107	0,19 %
-0,25°	rest	0,221	-0,49 %		-0,25°	rest	0,104	-0,04 %

Increasing the sinkage (with zero trim) for the KVLCC2 hull raises the form factor as expected since the transom is submerged even more compared to the original draught. Similarly, the form factor is decreasing with decreasing draught for the KVLCC2 hull. However, KCS hull indicated opposite trends for the sinkage variation compared to KCS hull. It should be noted that the transom of the KCS hull is not submerged even when the draught is increased 2.5%. On the other hand, the large part of the stern overhang is submerged when the draught is increased since buttocks are rather flat (a common feature for the container ships). As a result of large change in the submerged part of the aftbody due to increased draught, the C_{V_S} change is rather larger than other loading variations applied to the KCS hull.

5 Sensitivity of form factor for varying grid distributions

In addition to the grid dependence studies, several other grid setups have also been tested. The aim of this analysis is to determine the best grid distribution but also to figure out which grid distribution is not acceptable for the purpose of form factor determination. For this exercise, *g2* and *g5* of the grid dependence study has been selected as a starting point. The number of cells and longitudinal grid distribution of g2 has been selected based on the previous experiences. The coarsest grid g5 has only 1.69×10^6 cells. The new grid distributions are created by decreasing the number of cells in one region at a time and keeping all other regions the same. The flow domain and hull is divided into different regions longitudinally as can be seen in Figure 1. In Table 4, each grid is distinguished by it's parent grid (g2 or g5) and the modified region where the number of cells are changed. As an example, g2 grid with coarse bow and medium bow modification has 1/3 (35 cells) and 2/3 (70 cells) of number of cells in longitudinal direction at the bow region (see Figure 1) compared to original g2 grid (105 cells), respectively.

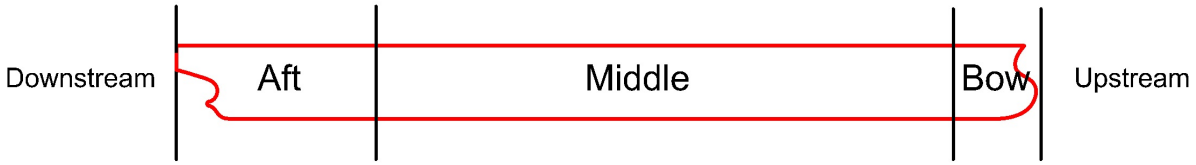

Fig. 1: Longitudinal divisions for grid generation

In Table 4, calculated form factors based ITTC57 line and extrapolated C_{V_S} values of KVLCC2 are presented for EASM and $k-\omega$ SST turbulence models. The coarsest grid with original grid distribution, g5, provides remarkably close C_{V_S} prediction (0.53% smaller) compared to g2 grid. As expected, the grids based on the parent grid of g2 is much less sensitive than g5. However, grids with coarser aft modification is more sensitive than coarser bow. The from factor obtained from the coarse aft grid based on the g5 is abnormally high for both turbulence models. It should be noted that this grid has only 20 cells in the longitudinal direction from aft shoulder to transom. The absolute values of C_{V_S} values are different but the relative changes between the grids are almost the same for both turbulence models.

Table 4: Grid variation, rudder appended at model scale design speed

Parent grid	Modification	Cells	EASM		$k-\omega$ SST	
			k	C_{V_S}	k	C_{V_S}
g2	Original	$8{,}39\times10^6$	0,227	ref.	0,245	ref.
g2	Coarse Bow	$7{,}66\times10^6$	0,233	0,49 %	0,251	0,45 %
g2	Medium Bow	$8{,}02\times10^6$	0,228	0,07 %	0,248	0,18 %
g2	Coarse Aft	$7{,}66\times10^6$	0,236	0,76 %	0,254	0,70 %
g2	Medium Aft	$8{,}02\times10^6$	0,228	0,07 %	0,248	0,18 %
g5	Original	$1{,}69\times10^6$	0,220	-0,53 %	0,240	-0,47 %
g5	Coarse Bow	$1{,}55\times10^6$	0,233	0,49 %	0,250	0,36 %
g5	Medium Bow	$1{,}62\times10^6$	0,223	-0,34 %	0,241	-0,34 %
g5	Coarse Aft	$1{,}55\times10^6$	0,318	7,42 %	0,337	7,32 %
g5	Medium Aft	$1{,}62\times10^6$	0,223	-0,34 %	0,241	-0,34 %

6 Speed dependency of form factor

The scale effects on the form factor has been previously mentioned. In this section, scale effects have been demonstrated by varying the speed of the KVLCC2 and KCS hulls. Since the simulations are performed as double model, the form factors obtained from different speeds should be the same since form factor should be independent of the Reynolds number. The form factor and the full scale viscous resistance (extrapolated) figures are presented in Table 5 and Table 6 for KCS and KVLCC2, respectively. The

same grid density, g2, were used and both hulls are appended with rudders. The form factor and the C_{V_S} values are calculated using both ITTC57 line and numerical friction lines of the corresponding turbulence model used for the calculations. The numerical friction lines for EASM and $k-\omega$ SST turbulence model were derived using SHIPFLOW and used for this study as recommended in Korkmaz et al. (2019). As can be seen in Table 5 and Table 6, the form factors based on the ITTC57 line differs significantly with the varying speed for both hulls and turbulence models. However, when the numerical friction lines are applied, form factors are almost the same at different speeds for the same turbulence model. The form factors differ for the different turbulence models because calculated C_{V_M} is different and also the numerical friction line for EASM and $k-\omega$ SST models are different when numerical friction line is used. However, the difference between extrapolated C_{V_S} values from different turbulent models are significantly smaller when numerical friction lines are applied instead of the ITTC57 line. In Table 7, results of the full scale simulations are presented for the KCS hull. It should be noted that when ITTC57 line is used, extrapolated C_{V_S} values are significantly smaller compared to computed C_{V_S} values.

Table 5: Calculated form factor and extrapolated C_{V_M} values of KCS with rudder

		ITTC57 line			numerical friction line		
Turbulence model	Speed	k	C_{V_S}(14kts)	C_{V_S}(24kts)	k	C_{V_S}(14kts)	C_{V_S}(24kts)
EASM	design	0,106	1,626E-03	1,524E-03	0,169	1,740E-03	1,644E-03
EASM	low	0,088	1,600E-03	1,499E-03	0,169	1,740E-03	1,643E-03
kwsst	design	0,132	1,664E-03	1,559E-03	0,159	1,754E-03	1,649E-03
kwsst	low	0,117	1,642E-03	1,539E-03	0,158	1,753E-03	1,648E-03

Table 6: Calculated form factor and extrapolated C_{V_M} values of KVLCC2 with rudder

		ITTC57 line			numerical friction line		
Turbulence model	Speed	k	C_{V_S}(13kts)	C_{V_S}(15.5kts)	k	C_{V_S}(13kts)	C_{V_S}(15.5kts)
EASM	design	0,230	1,752E-03	1,717E-03	0,340	1,940E-03	1,905E-03
EASM	low	0,219	1,737E-03	1,701E-03	0,337	1,936E-03	1,901E-03
kwsst	design	0,249	1,779E-03	1,743E-03	0,308	1,923E-03	1,885E-03
kwsst	low	0,238	1,764E-03	1,728E-03	0,304	1,917E-03	1,880E-03

Table 7: Full scale simulations of KCS

speed	EASM	kwsst
C_{V_S}(14kts)	1.747E-03	1.772E-03
C_{V_S}(24kts)	1.603E-03	1.665E-03

7 Conclusions

In this study, CFD based form factor determination method have been investigated by analyzing the calculations performed on KVLCC2 and KCS hulls. The following observations have been made:

- Grid dependence studies indicated that numerical uncertainties around 1% is achievable with KVLCC2 hull regardless of existence of rudder and the choice of turbulence model (EASM and $k-\omega$ SST). On the other hand, there has been meshing issues with KCS at the forebody due to large protruding bulb. The numerical uncertainties around 1% was only possible when the rudder appended to the KCS hull.

- Frictional resistance component was less sensitive to the first layer thickness with KCS and KVLCC2 hulls compared to flat plate simulations.

- The loading condition (sinkage&trim) variation had limited effect on the calculated form factor for both KCS and KVLCC2 hulls. The difference in the extrapolated C_{V_S} values due to varying sinkage&trim were often smaller than the numerical uncertainties.

- Different grid density distributions have been simulated in order to find out which grid density is acceptable and which grids should be avoided. The sensitivity of form factor to the grid density at the aft body is bigger than the forebody. It can be argued that unless the grid resolution at the aftbody is very coarse, sensitivity of form factor to the grid resolution at the other parts of the hull is rather low.

- The scale effects on form factor have been one of the most important discussion topic. It has been showed that when ITTC57 line is used, the scale effects are in-avoidable. However, when the numerical friction line that of the same CFD code and same turbulence model is applied scale effects are reduced significantly. The computations with EASM turbulence model with the numerical friction line of the same turbulence model eliminated the scale effects almost completely.

- The EASM and $k-\omega$ SST turbulence models gives different form factors regardless of the friction line used. However, when the numerical friction line is used, the variation of the extrapolated C_{V_S} values between turbulence models are reduced compared to ITTC57 line.

- The C_{V_S} obtained from the full scale simulations with KCS is significantly closer to the extrapolated C_{V_S} when the numerical friction lines are used.

Acknowledgements

This project has been funded by *Vinnova* and the computational resources were provided by the Chalmers Center for Computational Science and Engineering (C3SE).

References

A. García-Gómez (2000). On the Form Factor Scale Effect. *Ocean Engineering*, **Vol. 26**, p.97-109.

C. W. Prohaska (1966). A Simple Method for the Evaluation of the Form Factor and Low Speed Wave Resistance. *Proceeding of 11th ITTC*.

C.W.B. Grigson (1999). A planar algorithm and its use in analysing hull resistance. *Trans. RINA*, **Vol. 142** p.76-115.

G. Hughes (1954). Friction and Form Resistance in Turbulent Flow, and a Proposed Formulation for Use in Model and Ship Correlation. *Trans. RINA*, **Vol. 96**, p.314-376.

H. C. Raven, A. van der Ploeg, A.R. Starke and L. Eça (2009). Towards a CFD-based prediction of ship performance — progress in predicting full-scale resistance and scale effects. *International Journal of Maritime Engineering*, **Vol. 135**.

K.B. Korkmaz, S. Werner, R. Bensow (2019). *Numerical Friction Lines For CFD Based Form Factor Determination. VIII International Conference on Computational Methods in Marine Engineering (Marine 2019).*

L. Eça and M. Hoekstra (2014). A Procedure for the Estimation of the Numerical Uncertainty of CFD Calculations Based on Grid Refinement Studies. *Journal of Computational Physics*, **Vol. 262** p.104-130.

N. Toki (2008). Investigation on Correlation Lines through the Analyses of Geosim Model Test Results. *Journal of the Japan Society of Naval Architects and Ocean Engineers*, **Vol. 8**, p.71-79.

Proceedings of the 8th ITTC (1957).

S.-H. Van, H. Ahn, Y.-Y Lee, C. Kim, S. Hwang, J. Kim, K.-S Kim, and I.-R Park (2011). Resistance Characteristics and Form Factor Evaluation for Geosim Models of KVLCC2 and KCS. *Advanced Model Measurement Technology for EU Maritime Industry*.

T. Katsui, H. Asai, Y. Himeno and Y. Tahara, (2005). The Proposal of a New Friction Line. *Fifth Osaka Colloquium on Advanced CFD Applications to Ship Flow and Hull Form Design, Osaka, Japan*.

Z.-z. Wang, Y. Xiong, L.-p Shi and Z,-h Liu (2015). A Numerical Flat Plate Friction Line and Its Application. *Journal of Hydrodynamics*, **Vol. 23**(3) p.383-393.

Numerical Simulation of Dynamic Behaviour of an Azimuth Thruster in Seaways

Vladimir Krasilnikov[1] **and Nabila Berchiche**[2]
[1]SINTEF Ocean, Trondheim/Norway, [2]formerly SINTEF Ocean
vladimir.krasilnikov@sintef.no

1 Introduction

Operations performed by offshore vessels become increasingly demanding. The recent trend to exploit more exposed sea regions, which we witness in wind energy and aquaculture sectors, means that propulsors installed on such vessels would frequently operate under off-design conditions that may involve large oblique flow angles, ventilation, waves, wave induced ship motions, extreme manoeuvres and impact of slipstream from a neighbouring thruster. The said phenomena are linked to mechanical failures in gears and bearings of azimuth thrusters. They may also result in loss of thrust that can compromise vessel manoeuvring and station keeping performance. Ventilation is identified as one of the most severe phenomena responsible for harmful unsteady load oscillations. Over the last decade a considerable amount of experimental, and more recently, numerical research has been conducted on this topic. In this paper we study numerically the performance of a pushing ducted thruster in regular waves and under the influence of wave-induced planar motions.

2 Impact of ventilation on propulsor performance

According to experimental studies in (Koushan, 2006), the onset of developed ventilation is associated with a sudden drop of thrust and torque and increase of blade load oscillations. For a ducted thruster in bollard operation, at the fixed submergence H/Dp=0.5 (where H is the submergence and Dp is the propeller diameter), without waves, the duct loses about 95% of its thrust, while propeller loses about 80% of its thrust. These figures correlate very well with the magnitudes of thrust losses predicted from CFD analyses carried out on the same propulsor in (Berchiche et al, 2018). Both the measurements and calculations show that blade thrust oscillations increase rapidly already at submergence H/Dp=0.8÷0.7, i.e. when the ventilation event first occurs. The critical submergence and ventilation inception mechanism are shown to be different under the conditions of light loading and heavy loading of propulsor (Berchiche et al, 2018). At light loading such as in transit, fully ventilated condition develops suddenly, in the form of a pocket-like deformation of free surface. At heavy loading such as in bollard or trawling, ventilation reveals an inception stage where a vortex develops from the free surface toward the propulsor, and it serves as an air transport way. There are also distinctly different pictures of air entrainment by propeller blades inside the duct. In regular waves, a sudden drop of thrust occurs at a certain critical advance coefficient, which depends on propulsor loading and submergence (Koushan et al, 2009). In the sub-critical range, the effect of wave height is significant. Maximum thrust losses are registered during the passage of wave troughs where the largest amount of ventilation is found. Blade load amplitudes reach maximum when wave crests pass the propulsor, but the averaged blade thrust at that time is lowest, and vice versa when wave troughs pass. This gives an indication of the influence of wave-induced orbital velocities. Some extreme events such as local peak loads are also registered (Dang et al, 2013). It is hypothesized that these are associated with the collapse of large air pockets.

3 Numerical approach

For the numerical investigation of a generic azimuth ducted thruster whose configuration is detailed in (Koushan, 2006), (Berchiche et al, 2018), an unsteady RANS method of the commercial CFD code STAR-CCM+ (version 12.04) is employed. In order to resolve the interaction between the rotating propeller and stationary components of propulsor such as pod and duct, the mesh region surrounding propeller is separated from the outer fluid (see Fig. 1), and during the solution it participates in rotational motion around propeller shaft axis. The sliding mesh interfaces are applied between the propeller region and outer fluid region. The implicit unsteady solution is performed with a 1st order temporal discretization scheme and the time step corresponding to 1 degree of propeller rotation. Keeping the time step sufficiently small is essential for both the solution stability and accuracy of prediction of unsteady blade loads. The flow is assumed fully turbulent, and the SST k-ω model with "All Y+" near-wall modelling algorithm is used for turbulence closure. The two-phase fluid is considered using the Eulerian Multiphase Mixture model with the VOF method. The High-Resolution Interface Capturing (HRIC) scheme is used for tracking the water-air interface. The default settings of the HRIC scheme in STAR-CCM+ are adopted (2nd order convection scheme, sharpening factor 0.0, angle factor 0.5, CFL_l=0.5, CFL_u=1.0). No phase interaction and phase change are allowed in the solution, so that cavitation is not modelled in the problems with free surface, even though it would develop in a realistic flow, under simulated conditions. For modelling regular waves, a 5th order VOF Wave model is used with wave height, wave period, wave velocity and wave direction specified. The waves are assumed to arrive on the propulsor from ahead and their speed equals to the speed of advance of propulsor. The 2nd order discretization scheme is used in the VOF method.

A large rectangular computation domain (X×Y×Z=200Dp×200Dp×40Dp) is used in the present model to accommodate a sufficient number of wave lengths in the simulations of propulsor in regular waves, and to avoid the influence of boundaries in oblique flow calculation. With the domain of this size, no additional treatment of wave setup is usually required, unless the simulated waves are very long. In the latter scenarios, wave forcing at the outlet boundary is recommended. For modelling the general case that may involve wave-induced planar motions of propulsor and propulsor azimuthing, the two different approaches were investigated – the moving mesh method and overset mesh method. The moving mesh setup contains the two regions – the stationary fluid region and rotating (sliding mesh) propeller region. In the case of forced propulsor motion, the whole region of stationary fluid participates in that motion. In the overset mesh setup, we add one more region – the overset region that surrounds the propulsor and moves according to the user defined motion. In this method, the background fluid region is always stationary, while propeller region is rotating, as before, with respect to the outer (overset) region. The mesh refinement patterns are very similar in the two methods. Some illustrations of mesh refinement are shown in Fig. 1 and 2.

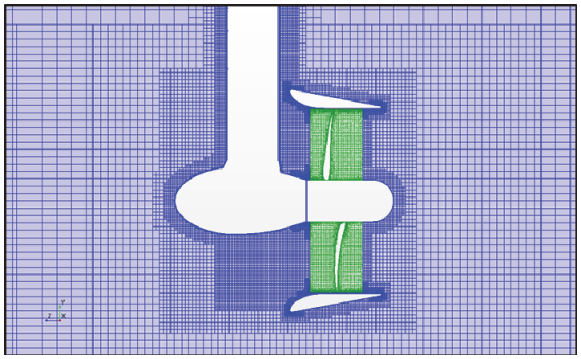

Fig.1: Mesh refinement around propulsor.

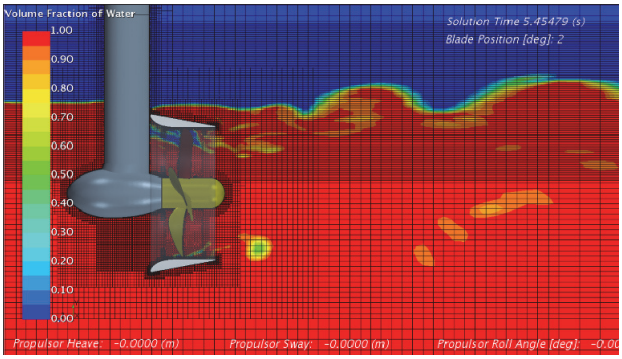

Fig.2: Mesh refinement near free surface.

The important areas that require mesh refinement are the region around propulsor (cell size 1% of Dp), wake area downstream of the strut (cell size 0.5% of Dp), duct leading and trailing edges, propeller blade tip clearance (cell size 0.25% of Dp), as well as leading and trailing edges of propeller blades (cell size 0.125% of Dp). In presence of waves, 40-50 cells per wave height and 120-160 cells per wave length are recommended for this type of simulations due to strong deformations of free surface, resulting from the interaction between the waves and propulsor and ventilation phenomenon. With the above mesh refinement settings, the total cell count is about 17-18 mil in the problems with initially calm free surface, and about 23-25 mil in the problems with regular waves.

There are different ways to simulate a desired motion of propulsor in STAR-CCM+. The forced planar motions can be set up using the general DFBI Rotation and Translation method with the Planar Motion Carriage option. Within this option, the model "General Planar Motion" is available, where one can prescribe a three-component motion either in the roll plane (heave, sway, roll), or in the pitch plane (heave, surge, pitch), or in the yaw plane (surge, sway, yaw). The alternative to DFBI method is to use the mesh motion method, where the same scenarios can be set as forced translational and rotational motions through the velocity equations, using motion managed coordinate systems.

The results of test calculations with the two motion modelling approaches (moving mesh and overset mesh) and the two motion setup methods (DFBI and mesh motion) are discussed below. Table 1 presents a comparison between the measured and computed characteristics of propulsor operating at the advance coefficient J=0.3 (J=V/n/Dp) in straight flow, without free surface.

Table 1: Comparison of integral propulsor characteristics obtained with different calculation methods. (J=0.3, straight flow, no free surface)

	KTP	KTD	KTG	KTTOT	KQP
EXP	0.3170	0.1830	-0.0490	0.4510	0.0570
Moving mesh / Mesh motion	0.3039	0.1736	-0.0353	0.4421	0.0572
Overset Mesh / Mesh motion	0.3039	0.1737	-0.0354	0.4422	0.0572
Moving mesh / DFBI	0.3011	0.1732	-0.0358	0.4386	0.0571
Overset Mesh / DFBI	0.3009	0.1734	-0.0356	0.4387	0.0570

A good agreement between the solutions obtained with different motion formulations is observed. The computed values also correlate well with the experimental data. The solutions using the DFBI formulation with superposed rotation of propeller region show a slightly lower propeller thrust (about -1.0%) than the solutions using the mesh motion formulation. In the second test case, the propulsor was subject to forced heave motion with the amplitude of 0.5Dp and frequency of 1.1Hz (1/10 of propeller rotation frequency), at the same J=0.3. Fig. 3 and 4 illustrate a comparison between the two mesh motion solutions, according to the DFBI method.

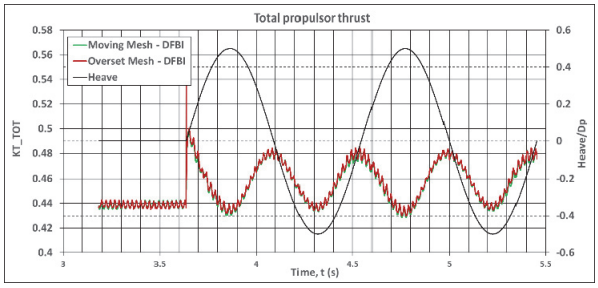

Fig.3: Computed oscillations of total propulsor thrust during heave.

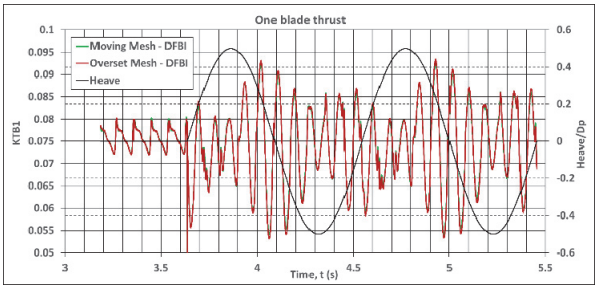

Fig.4: Computed oscillations of single blade thrust during heave.

It can be seen that the moving mesh method and overset mesh method bring nearly identical results. The overset mesh method takes about 1.5 longer time per time step than the moving mesh method due to the update of overset interfaces, in addition to the update of sliding interfaces of propeller region. For further studies in the present work, the moving mesh approach with the DFBI method was employed.

3 Propulsor dynamics in regular waves

The numerical analyses of propulsor in regular waves were performed for the range of wave height (1.0m, 2.5m and 3.0m) and the range of wave period (4s, 8s and 10s), at the transit (J=0.6) and bollard (J=0.0) operation conditions. The simulations were divided into the two groups – the scenarios without ventilation and with ventilation, which were achieved by varying propulsor submergence. The propulsor position with respect to the level of calm free surface was assumed fixed. In the ventilation free conditions at transit, the total thrust of propulsor shows a certain dependency on wave height and period, as illustrated in Fig. 5. For the lowest waves of 1m height, there is no significant dependency of thrust on wave period, while the thrust value is reduced for about 1% compared to the case without waves, at the same submergence. For higher waves, propulsor thrust decreases with the decrease of wave period, and in 3m waves with the period of 4s thrust loss of 5% is predicted. The main contribution to the thrust loss comes from the reduction of duct thrust, which is caused by changes in pressure distribution over the exterior side of the duct under the influence of passing waves.

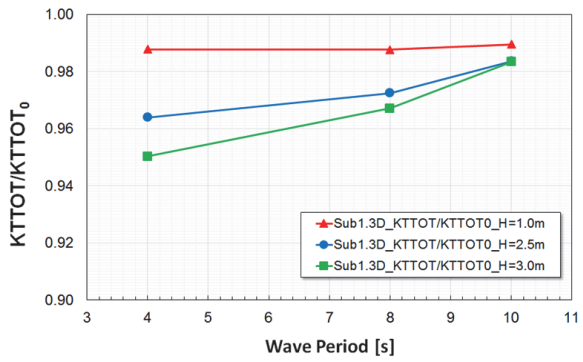

Fig.5: Influence of wave height and period on total propulsor thrust. Transit, J=0.6, H/Dp=1.3, no ventilation. $KTTOT_0$ is the reference value at the same submergence without waves.

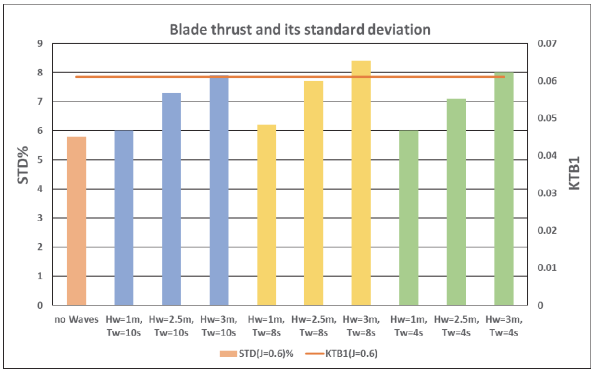

Fig.6: Influence of wave height and period on the amplitude of single blade thrust. Transit, J=0.6, H/Dp=1.3, no ventilation. STD shows standard deviation from mean values.

The averaged value of blade thrust is little affected by the wave period and wave height. However, for the given wave period, the amplitudes of blade thrust oscillations increase with the increase of wave height, as shown in Fig. 6. During bollard operation, at submergences where ventilation does not occur, the influence of regular waves does not result in significant reduction of thrust, while single blade thrust demonstrates similar trends with the variation of wave height and period.

The onset of ventilation event on propulsor in regular waves depends on propulsor loading, submergence and wave parameters. Its impact on total propulsor thrust in transit operation is illustrated in Fig. 7. In longer waves with periods 10s and 8s, intermittent ventilation is found whose cycles occur only for a certain period of time during the passage of wave troughs. The thrust losses amount 2% and 5%, respectively. In shorter waves with period 4s, ventilation is a continuous event, and it results in thrust losses of about 16%. While in longer waves there is dependency of thrust loss on wave height, it is not evident in shortest waves.

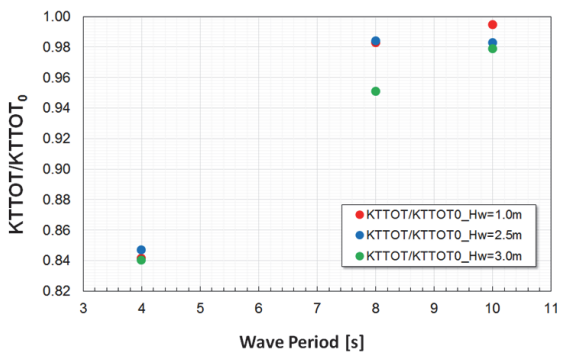

Fig. 7: Thrust losses on propulsor in transit operation in regular waves with ventilation. J=0.6, H/Dp=1.0. $KTTOT_0$ is the reference value at the same submergence without waves.

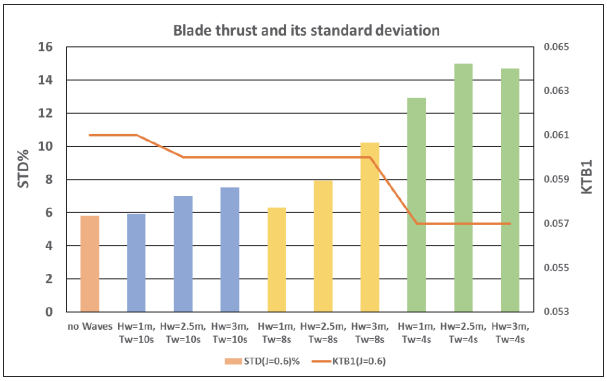

Fig. 8: Influence of wave height and period on the amplitude of single blade thrust with ventilation. Transit, J=0.6, H/Dp=1.0. STD shows standard deviation from mean values.

Fig. 8 illustrates the influence of ventilation on the amplitudes of single blade thrust, for the same conditions. It can be seen that, while the averaged value of blade thrust shows only minor changes, the amplitudes of blade thrust oscillation increase considerably when ventilation occurs. The said increase is especially pronounced in short waves, Tw=4s. The time histories of blade thrust and duct thrust are presented for the case of 3m waves of different periods in Fig. 9 and 10, respectively.

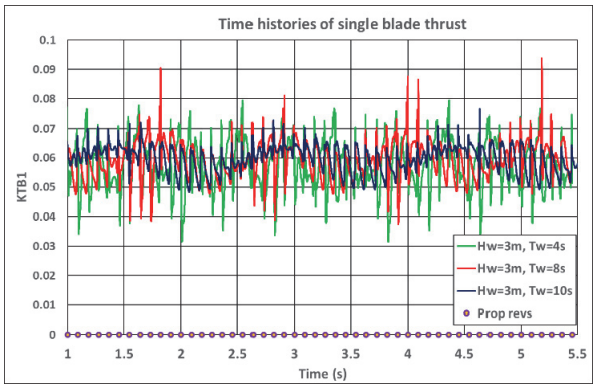

Fig. 9: Time histories of single blade thrust during transit operation in 3m regular waves with the occurrence of ventilation. J=0.6, H/Dp=1.0.

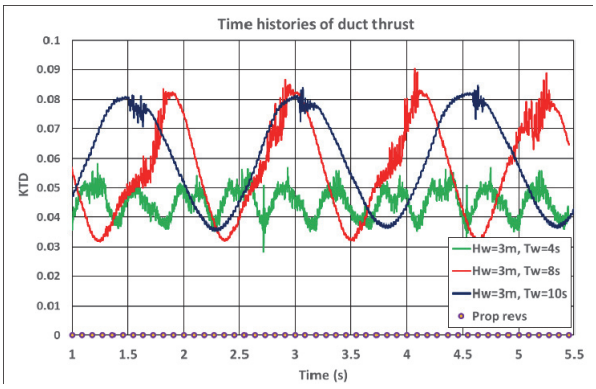

Fig. 10: Time histories of duct thrust during transit operation in 3m regular waves with the occurrence of ventilation. J=0.6, H/Dp=1.0.

In the waves of 10s period, where only a very short ventilation event is found, both the duct thrust and blade thrust show a sinusoidal pattern. Their values increase when the wave trough is approaching. After the brief ventilation event, which is marked by "spikes" in the duct thrust curve, the thrust values begin to decrease, reaching their minima when the crest arrives. Blade thrust oscillations are higher after the passage of wave trough. In the waves of 8s period, the approach of wave trough is marked by the ventilation on the duct, and eventually on propeller. It is noticed in blade thrust history from a rapid increase of oscillation amplitudes. The largest load gradients correspond to the instances when the blade enters the air pockets. The last phase of ventilation, right after the trough passage, is marked by sudden local peaks of blade loads, which are caused by the collapse of air pocket inside the duct. At these instances, the full amplitude of blade thrust oscillation may reach 75% of averaged value. In shortest waves of 4s period, ventilation is a continuous event. The duct thrust is reduced significantly, since the upper part of the duct is always affected by air fraction. The blade thrust

reveals large oscillations with the amplitude about 50% of averaged values, as the blade goes through the air pocket that stays in the upper part of propeller disk.

The development of ventilation on propulsor in regular waves reveals distinct differences between the conditions of light loading operation and heavy loading operation. As one can see from Fig. 11, in the case of transit, for a given wave height ventilation starts earlier in shorter waves, while in bollard it starts earlier in longer waves. This result is explained by the different ventilation inception mechanisms at light loading and heavy loading. In regular waves, the important factor is the exposure time of propulsor to passing wave troughs. Free surface pockets that lead to propulsor ventilation at light loading tend to become more stable in shorter waves, so that the ventilation condition is easier to establish. On the contrary, at heavy loading the vortices which develop from free surface along the strut and which conduct air to propulsor tend to become more stable in longer waves. A more in-depth discussion about the mentioned phenomena can be found in (Krasilnikov et al, 2019).

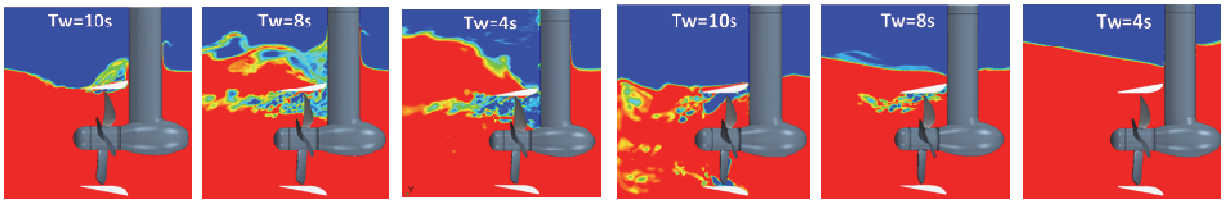

a) Transit, J=0.6, H/Dp=1.0 b) Bollard, J=0.0, H/Dp=1.1

Fig. 11: Ventilation extent on propulsor in regular waves of 3m height with different periods. Transit and bollard operation conditions.

4 Propulsor dynamics at forced planar motions

In the present study the focus was on low speed operation. The cases of trawling (J=0.3) and bollard (J=0.0) were considered, firstly, without the influence of free surface. Simulation scenarios included separate heave, sway and roll motions as well as their combination. The parameters of propulsor motions were derived from the calculation of RAOs at the location of propeller center for a typical offshore vessel, operating in regular waves with the height of 2.5m and period of 8s. The heave and sway motions had approximately the same phase, while roll motion had a phase shift of about -20 deg with respect to heave and sway. With the given conditions, propeller performed about 29 revolutions during one complete propulsor oscillation. Three propulsor oscillations were simulated and the results were sampled from the last two oscillations. The time histories of total propulsor thrust at different planar motions are presented in Fig. 12 and 13, for the cases of trawling and bollard operation, respectively. At trawling, the propulsor thrust experiences largest oscillations during the combined motion. The major contribution comes from the duct thrust variation due to the heave motion component. In addition to large low frequency oscillations directly related to propulsor motion, there are also found high frequency oscillations caused by the interaction of propeller blades with the domains of separated flow behind the pod housing. In the case of combined motion, the changes in loads on propulsor components are not the result of simple addition of changes experienced separately during heave, sway and roll. This gives one an indication that hydrodynamic interaction between the motion components is important. When propeller is moving upwards and passes the position of zero heave, the duct thrust reaches its maximum, and hence the propeller experiences highest flow acceleration by the duct. It results in the occurrence of pressure side cavitation on propeller blades, which is not present when propulsor operates at the same advance coefficient at a fixed position. Unlike trawling operation, in bollard the sway motion and combined motion show comparable amplitudes of oscillations at the motion frequency. The variation of duct thrust and propeller thrust due to sway are the major contributors.

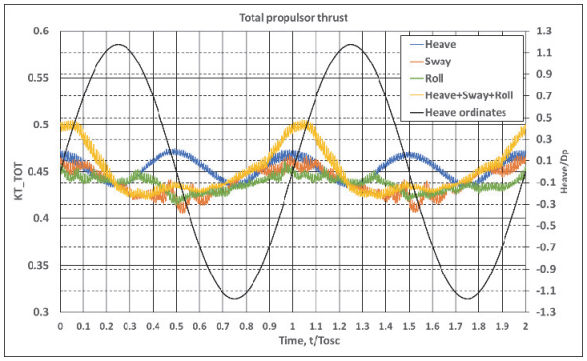

Fig. 12: Time histories of total propulsor thrust at different planar motions. Trawling, J=0.3.

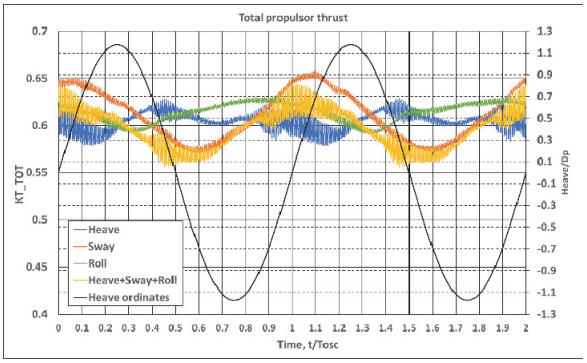

Fig. 13: Time histories of total propulsor thrust at different planar motions. Bollard, J=0.0.

The oscillations at blade passing frequency are still caused by heave, and they reveal larger amplitudes than those at trawling. This is the result of flow separation on the interior side of the duct, which does not develop when propulsor is moving with some, while low speed, but which takes place at zero speed due to very large angles of attack experienced by the duct sections during heave. This separation phenomenon also results in increase of blade loading and cavitation extents on propeller blades when they pass through the separation zone. In general, cavitation is more severe during bollard. In addition to propeller blades, it is also found on the duct leading edge, and it reveals a more dynamic behaviour.

5 Conclusions

CFD provides a useful framework for the quantification of thrust losses and dynamic loads on propulsors operating in seaways, as well for a better understanding of physical mechanisms underlying these phenomena, their dependency on propulsor loading, operation conditions and scale. The onset of ventilation in regular waves depends on propulsor loading, submergence and wave parameters. Ventilation may develop in intermittent form, or in stable form that exists continuously. It is the continuous ventilation that results in largest thrust losses. However, intermittent form may be the cause of strong oscillations of blade thrust, with amplitudes reaching, under some conditions, 75% of mean value. Different ventilation inception mechanisms at light and heavy propulsor loading, and influence of exposure time to passing wave troughs determine different dependencies of ventilation intensity on wave period observed in transit operation and at bollard. Hydrodynamic interaction between the components of forced propulsor motion plays an important role in the resulting changes in propulsor forces and their oscillations. The combined motion (heave+sway+roll) reveals generally larger force oscillations compared to individual motion components.

References

Berchiche, N., Krasilnikov, V.I., and Koushan, K. (2018), "Numerical Analysis of Azimuth Propulsor Performance in Seaways: Influence of Oblique Inflow and Free Surface." Journal of Marine Science and Engineering, 2018, 6, 37; doi:10.3390/jmse6020037.

Dang, J., Koning, J., Brouwer, J. and de Jong, J. (2013), "Dynamic Loads on Mechanical Azimuth Thrusters." Proceedings of the PROADS2013, CECO, Changwon City, Korea, October 20-25.

Koushan, K. (2006b), “Dynamics of Propeller Blade and Duct Loadings on Ventilated Ducted Thrusters Operating at Zero Speed.” Proceedings of T-POD06 - 2nd International Conference on Technological Advances in Podded Propulsion, Brest, France.

Krasilnikov, V.I., Berchiche, N., and Koushan, K. (2019), "Thrust Losses and Dynamic Loads on a Ducted Pushing Thruster in Regular Waves.", Proceedings of the 6th International Symposium on Marine Propulsors SMP'19, Rome, Italy, May.

Acquisition of Maneuvring Characteristics of Ships using RANS CFD

Marin Lauber, Pandeli Temarel
Fluid Structure Interctions, University of Southampton, Southampton
M.Lauber@soton.ac.uk

1 Introduction

Numerical predictions of ship manoeuvring have been performed for some time (Oldfield et al. (2016), He et al. (2016), Zou et al. (2010), Kim et al. (2015)). However, the approach undertaken can drastically vary among authors. In addition, commercial computational fluid dynamics (CFD) software allow for a wide range of turbulence models, mesh topologies, free-surface treatments, etc. This yields non-trivial choices and can lead to noticeable differences in the results. In this paper, we investigate the numerical aspects of ship manoeuvring by replicating captive model tests for a benchmark model (KVLCC2) while performing a large range of numerical investigations.

The objectives of this study are:

i) to determine the manoeuvring coefficients of the model by replicating captive model tests (static and dynamic),

ii) to conduct a proper verification of the results, both for temporal and spatial discretization errors,

iii) to conduct a proper validation of the results using experimental data,

iv) to investigate the influence of the turbulence model, mesh and other numerical aspects on the resulting coefficients.

2 Approach

A 1:110 scaled bare model of the KVLCC2 was used in this study. The maneuvring coefficients were obtained by simulating static drift and planar motion mechanism in pure sway and yaw using a Reynolds-Averaged Navier-Stoke (RANS) finite-volume software (Star-CCM$^+$).

Static drift simulations were undertaken at a Froude number (Fr) of 0.142 and drift angles (β) range of $\pm 16°$, in steps of 4°. The domain used extends $5.5L_{PP}$, $2.5L_{PP}$ and $1.2L_{PP}$ in the longitudinal, transverse and vertical direction, respectively. An unstructured hexahedral mesh with local refinements in way of the free-surface, kelvin wake, viscous wake and hull boundary layer was used as standard, see figure 1. To reduce mesh size, wall functions were used to model the boundary layer, with a target non-dimensional wall distance (y^+) of 30. This resulted in a cells count of 3.4M for the standard mesh. The boundary conditions are set to the standard velocity inlet and pressure outlet, while all domain walls are set to the free-slip condition. No-slip boundary conditions are imposed on the hull of the model. The shear stress transport version of the k-ω turbulence model was used to close the RANS equations. The standard volume of fluid (VOF) approach, coupled with a high-resolution interface capturing scheme, was used to capture the free-surface. All degrees of freedom of the the model were constrained to simplify computations. A second-order upwind scheme was used to discretize the convective term and it was integrated in time using a second-order backward differentiating scheme. The *SIMPLE* scheme is used to solve the resulting system of coupled algebraic equations. A time step (Δt) of 0.05 second was chosen based on the *CFL* condition, with 10 inner-iterations. The resulting sway force and yaw moment were obtained by averaging the instantaneous values over a period of 10 seconds once the L_2 norm in the pressure change on the hull reached 10^{-4}. Typical simulations required around 80 seconds of physical time to reach the desired level of convergence.

On top of the previous cases, additional investigations were performed at a $Fr = 0.142$ and a drift angle $\beta = 8°$ to determine the temporal and spatial discretization errors, following the Verification & Validation procedure proposed by Stern et al. (2001). The spatial uncertainties were determined using

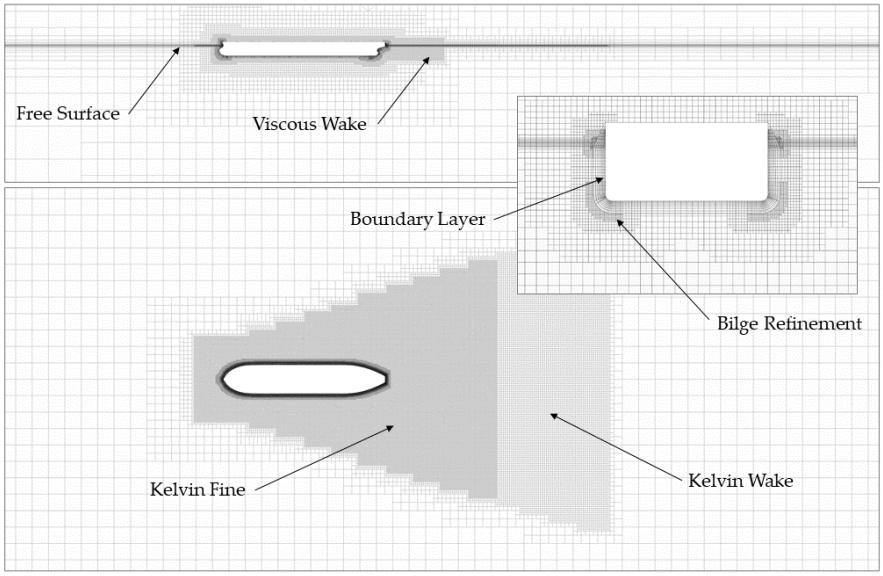

Fig. 1: Standard mesh used for the static drift simulation ($\beta = 0$, $Fr = 0.142$) together with details of the refinements around the model.

Richardson extrapolation (Celik et al. (2008)). The L_2 norm defined earlier was used to quantify the iterative uncertainty, following Eça and Hoekstra (2016). In this regard, a coarser and finer mesh with 2M and 6.3M cells were used. The temporal discretization was not altered for the spatial discretization study. The temporal discretization study was carried out by varying the time-step between 0.025 and 0.1 second, with the number of inner-iterations adjusted to achieve a global iteration count identical between the three cases. To conclude the static drift case, two turbulence models, the Realizable k-ϵ and the Spalart-Allmaras, as well as the double-body approach (no free-surface) were compared. Those simulations used the standard mesh described above, with the exception of the double-body approach that used a different mesh and numerical algorithm (steady simulation).

Planar motion mechanism (PMM) simulations were performed following a similar approach. The motion was achieved using an overset mesh with a total of 6.5M cells. Similar mesh topology to the static drift case was used, with the addition of the overset domain. The coupling between the overset and the background mesh was obtained using linear interpolation. No source or flux correction terms were applied. Both PMM in pure sway and yaw were simulated for oscillatory periods of 6 and 12 seconds. A time-step of 0.005 second was chosen based on the *CFL* condition and motion requirements. This results in a total of 2400 iterations per oscillatory period. Twenty inner-iterations were used within each time-step. Motion for the pure yaw case was imposed so that the centreline of the model was kept tangent to its path at all time. The yaw angle varies as

$$\psi(t) \approx \tan^{-1}\left(\frac{-y_0\omega}{U}\right)\cos(\omega t) = \psi_0\cos(\omega t), \tag{1}$$

where U is the forward speed of the model, y_0 is the sway amplitude and ω is the motion frequency. Simulations are initialized with a straight tow (no motion), until the solution has settled, before imposing the motion. This prevents generating non-physical free-surface oscillations that otherwise travel in the domain and pollute the solution. The manoeuvring coefficients were obtained by an RMS minimization of the error between the measured force/moment and its corresponding Taylor series expansion obtained from the equations of motion, see Oldfield et al. (2016). The same procedure as in the static case was followed for the spatial discretization errors, however, here the manoeuvring coefficients and not the force measured were compared. Turbulence sensitivity was investigated with the Realizable k-ϵ turbulence model. A PMM test in pure sway with an oscillatory period of 12 seconds was chosen for those investigations. The double-body approach was not investigated.

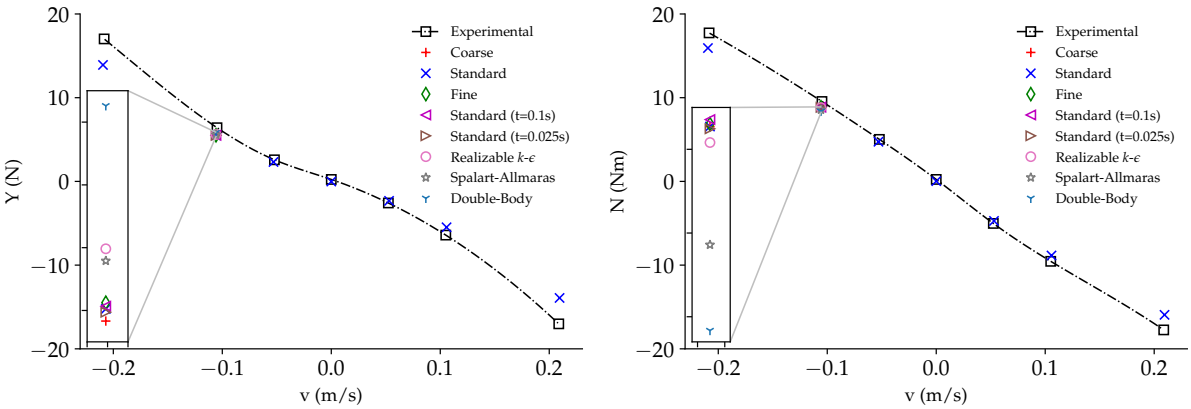

(a) Detail magnification: 75×

(b) Detail magnification: 50×

Fig. 2: Sway force (a) and yaw moment (b) from the static drift simulations against experimental data.

3 Results

The sway force as a function of the drift velocity ($v \equiv -U\sin(\beta)$), is presented on figure 2a. The results for the different spatial and temporal discretizations as well as the different modelling strategies for the chosen test case are also presented. The investigations on the different turbulence models used the same temporal and spatial discretization as the standard case, which was first validated using the procedure described previously. For small drift angles, the agreement with the experimental data is good. For larger drift angles, it can be observed that the agreement deteriorates. The different discretizations, both temporal and spatial, result in very similar values of the sway force. Despite having different formulations, the two additional turbulence models are in good agreement. The largest differences are obtained when the free-surface is omitted. Figure 2b shows the yaw moment as a function of the sway velocity. The yaw moment prediction follows a similar trend as the sway force but under-predicting for the double-body case instead of over-predicting it as in the sway force.

Monotonic convergence is found for the two variables measured (Y, N), with discretization uncertainties of the order of one percent for the standard mesh. Iteration uncertainties were typically lower than the discretization uncertainties by an order of magnitude of two, which allowed to safely neglect them. This results in validation uncertainties of $2.75\%D$ and $0.56\%D$ for the sway force and yaw moment, respectively. The corresponding errors are $14.19\%D$ and $7.25\%D$, so that the results are not validated for the configuration considered ($Fr = 0.142, \beta = 8°$). Comparison on local flow quantities (viscous wake and wave profile) with experimental data show excellent agreement, see figure 3. In the viscous wake, the numerical simulations are able to capture the typical hook-shaped flow structure, and an excellent agreement is obtained in terms of the wave profile along the hull (see figure 3b). It should be noted that despite showing good agreement with the sway force and yaw moment predicted using other models, the Spalart-Allmaras model largely under-predicted the shear stresses on the fore part of the model.

The manoeuvring coefficients are obtained by measuring the slope of the curve shown in figure 2 at the origin. Results are presented in table 1 together with three different sets of experimental data. The first set was obtained from the experimental data presented on figure 2. The yaw moment shows a better agreement with all of the experimental data compared to the sway force.

The results from the PMM simulations are presented in table 2. Coefficients with a subscript v or $\dot{v}$ were obtained from PMM in pure sway whereas the ones with r or $\dot{r}$ were obtained from PMM in pure yaw. In pure sway, the agreement with both sets of experimental results is acceptable. The captured differences are of the same order as the static drift simulation ones. Better agreement is obtained for the larger motion period. Velocity dependent coefficients are shown to agree better with the experimental data, this being more pronounced for the smallest motion period. An acceptable agreement is also noted with the MOERI experimental data, despite being at a different motion period and model scale.

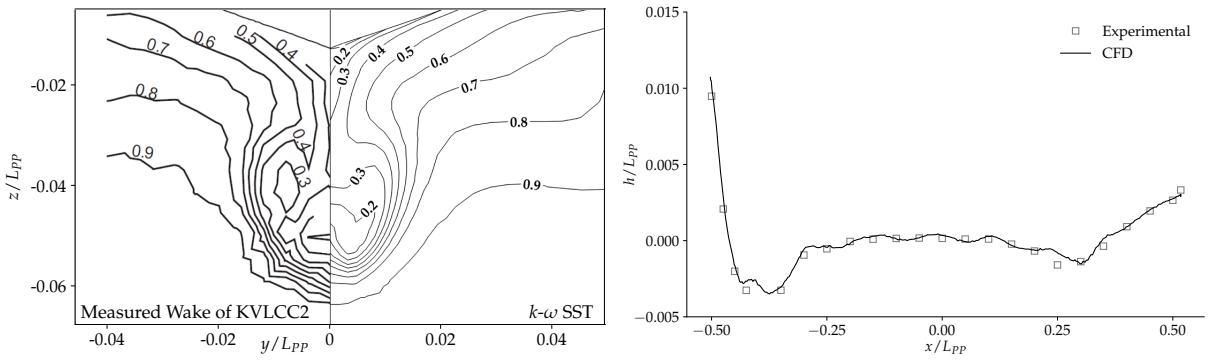

(a) (b)

Fig. 3: Nominal wake (a) and wave profile along model (b) from numerical simulation and experimental measurements (Kume et al. (2006), Kim et al. (2001)).

The different mesh sizes and the turbulence model considered showed an excellent agreement with the baseline simulations (not shown here), with differences in the order of one percent. Iterative uncertainties is found to reach 10^{-3} at the end of each inner-iteration loop, this allows to safely neglect them. Oscillatory convergence is found for all coefficients but $\tilde{N}'_{\dot{v}}$. As a result, Richardson extrapolation cannot be used to estimate the discretization error. This oscillatory behaviour could be due to the limitation of the method used, and not represent an actual oscillation in the convergence of the results, as also noted by Carrica et al. (2016). Despite not being able to rigorously validate the results, we can consider the agreement with experimental data as acceptable for the pure sway case.

The pure yaw motion case has proven to be more challenging to simulate than the pure sway case. This is because of the highly non-linear behaviour of pure yaw compared to pure sway, as documented in Kim et al. (2015). Such different behaviours are also reflected by the poor agreement with the experimental data obtained. Again, angular velocity dependent coefficients are in much better agreement than angular acceleration dependent coefficients. Issues with the post-processing of the experimental data for the pure yaw case at a period of 6 seconds did not allow oscillatory coefficients to be extracted.

4 Concluding Remarks

To conclude this investigation, the following recommendations can be drawn; static drift simulations have shown to yield good results for small drift angles, with the different methods used all being very close, for larger drift angles the agreement deteriorates. This is probably due to the unsteadiness of the flow becoming important and the RANS strategy not being able to capture all the details of the flow. Temporal discretization errors were found to be small, the only noticeable difference in the three time-step was how well the free-surface was captured (not presented here). It can thus be noted that for static drift simulations, at small drift angles, the choice of numerical method does not play a key role in the computation of the coefficients, and all the focus should be on the quality of the mesh to capture all the relevant flow structures. If computational power is an issue, the double-body approach can be considered without too much loss of accuracy, and with a reduction in computation time by a factor of 100.

For planar motion mechanism simulations, similar recommendations can be made for the pure sway

Table 1: Manoeuvring coefficients from static drift simulations against experimental data.

Coefficient	Present (CFD)	NMRI (EFD) (SIMMAN (2014))	MOERI (EFD) (He et al. (2016))	Kume et al. (2006) (EFD)
Y'_v (ϵ %D)[a]	-0.01362	-0.01535 (-11.27)	-0.01619 ((-15.87)	-0.01838 (-25.89)
N'_v (ϵ %D)	-0.00954	-0.01027 (-7.11)	-0.00875 (9.03)	-0.01064 (-10.34)

[a] ϵ defined as the relative error between numerical simulations and experimental results.

Table 2: Manoeuvring coefficients from PMM simulations against experimental data. The tilde above each coefficient emphasises their frequency-dependence.

Coefficient	Present (CFD)		NMRI (EFD)		MOERI (EFD)
	Period: 12 s	6 s	12 s	6 s	10 s
$\tilde{Y}'_v$ (ϵ %D)[a]	-0.01367	-0.01438	-0.01519 (-10.00)	-0.01638 (-12.21)	-0.01619 (-15.56)
$\tilde{Y}'_{\dot{v}}$ (ϵ %D)	-0.01419	-0.01470	-0.01439 (-1.39)	-0.01868 (-21.31)	-0.015104 (-6.05)
$\tilde{N}'_v$ (ϵ %D)	-0.00998	-0.01076	-0.01070 (-6.72)	-0.01318 (-18.36)	-0.00875 (14.05)
$\tilde{N}'_{\dot{v}}$ (ϵ %D)	-0.00046	-0.00042	-0.00051 (-9.80)	-0.00076 (-44.76)	-0.00078 (-41.02)
$\tilde{Y}'_r$ (ϵ %D)	0.00286	0.00269	0.00430 (-33.48)	[b]	0.00472 (-39.41)
$\tilde{Y}'_{\dot{r}}$ (ϵ %D)	-0.00056	-0.00051	-0.00312 (-82.05)	[b]	-0.00142 (-60.56)
$\tilde{N}'_r$ (ϵ %D)	-0.00213	-0.00246	-0.00252 (-15.47)	[b]	-0.00311 (-31.51)
$\tilde{N}'_{\dot{r}}$ (ϵ %D)	-0.00067	-0.00101	-0.00113 (-40.70)	[b]	-0.00080 (-16.25)

[a] ϵ defined as the relative error between numerical simulations and experimental results.
[b] Raw experimental data is problematic.

case, however, this time proper initialisation of the solution is necessary. This only needs to be done once, and the resulting initialised field can be used to start all required cases. In the pure yaw case, more investigations are required, the coefficients obtained do not agree well with experimental data. This arise from much more non-linearities and unsteadiness in the flow generated by this motion. This seems to be a general issue in manoeuvring simulations (Kim et al. (2015)). The method used to derive the oscillatory coefficients is believed to be a better representation than computing the coefficients at a single point.

5 Acknowledgements

The author would like to thanks Prof. Pandeli Temarel for his help during the conduction of this master project as well as Mr. Bernat Font Garcia and Dr. Gabriel Weymouth for their useful comments on an early version of this extended abstract.

References

C. Oldfield, M.M. Larmaei, A. Kendrick, K. McTaggart (2015). Prediction of Warship Manoeuvring Coefficients using CFD. *World Maritime Technology Conference*.

F. Stern, R.V. Wilson, H.W. Coleman, E.G. Paterson (2001). Comprehensive approach to verification and validation of CFD simulations-part 1: methodology and procedures. *Journal of Fluid Engineering*, **123**(4), 793–802.

H. Kim, H. Akimoto, H. Islam (2015). Estimation of the hydrodynamic derivatives by RANS simulation of planar motion mechanism test. *Journal of Ocean Engineering*, **108**, 129–139.

I.B. Celik, U. Ghia, P.J. Roache, C.J. Freitas, H. Coleman, P.E. Raad (2008). Procedure for estimation and reporting of uncertainty due to discretization in CFD applications. *Journal of Fluids Engineering*, **130**(7).

K. Kume, J. Hasegawa, Y. Tsukada, J. Fujisawa, R. Fukasawa, M. Hinatsu (2006). Measurements of hydrodynamic forces, surface pressure, and wake for obliquely towed tanker model and uncertainty analysis for CFD validation. *Journal of Marine Science and Technology*, **12**(2), 65–75.

L. Eça, M. Hoekstra. (2006). On the influence of the iterative error in the numerical uncertainty of ship viscous flow calculations. *26th Symposium on Naval Hydrodynamics*, 17–22

L. Zou, L. Larsson, M. Orych (2010). Verification and validation of CFD predictions for a manoeuvring tanker. *Journal of Hydrodynamics, Ser. B*, **22**(5), 438–445.

P.M. Carrica,A. Mofidi, K. Eloot, G. Delefortrie (2016). Direct simulation and experimental study of zigzag maneuver of KCS in shallow water. *Ocean Engineering*, **112**, 117–133.

S. He, P. Kellett, and Z. Yuan, A. Incecik, O. Turan, E. Boulougouris (2016). Manoeuvring prediction based on CFD generated derivatives. *Journal of Hydrodynamics, Ser. B*, **28**(2), 284–292.

SIMMAN (2014). Workshop on Verification and Validation of Ship Manoeuvring Simulation Methods.

W.J. Kim, S.H. Van, D.H. Kim, D (2001). Measurement of flows around modern commercial ship models. *Experiments in fluids*, **31**(5), 567–578

Investigations and Guidelines for Maneuvering Simulations

Pierre Le Bihan, Benoit Mallol, Charles Hirsch

NUMECA International, Brussels/Belgium
benoit.mallol@numeca.be, charles.hirsch@numeca.be

1 Introduction

The ONRT test case for course keeping provides an excellent set of data to validate guidelines as it covers many features that CFD software should have, to perform accurate and robust maneuvering simulations in a relatively short time frame: overset grids, adaptive grid refinements, propellers and rudders motion controllers as well as internal wave generation with specific treatments at the boundaries have been used among interesting other features. Besides, the geometry details reflect the complexity often observed at an industrial level. The objective is to validate guidelines for this interesting case but also make them generic enough to be replicated in different maneuvering conditions.

Fig. 1: ONRT geometry

2 Case description

The ONR Tumblehome model is a preliminary design of a modern surface combatant ship. The ship is fully appended, including skeg and bilge keels. Twin spade rudders, and propellers with shafts and brackets are present in the model. Fig. 1 shows the ship model and Table 1 lists the main characteristics and dimensions of the ship. Free-running course keeping tests, in regular waves were performed at IIHR Hydraulics Wave Basin Facility and the results were reported (Sanada et al., 2013) for the Japan 2015 workshop.

Dimension	Full-scale	IIHR
Scale	1.0	1/49
Lpp[m]	154.0	3.147
Bwl[m]	18.78	0.384
D [m]	14.5	0.266
T [m]	5.494	0.112
Δ [kg]	8.507e6	72.6
Kxx [m²]	-	0.34Bwl
Kyy, Kzz [m²]	-	0.264Lwl

Table 1: Main characteristics of the ship

The simulations include a preliminary self-propulsion study and various heading angles: X =0° (head wave), 45°, 90°, 135° and 180°. Rudders are deflected with the following proportional controller: $\delta(t) = K_p[\psi(t) - \psi_c]$ where δ is rudder angle, ψ is yaw angle, $\psi_c = 0$ is target yaw angle, and proportional gain $K_P = 1$, similarly to the IIHR's experiments. The ship movement is solved with 6 degrees of freedom (DOF) and the propeller revolution rate is determined by a preliminary self-propulsion study with the target approaching speed $U_0 = 1.11\ m/s\ \ (Fr = 0.2)$ in calm water conditions.

To perform these simulations, FINE™/Marine CFD simulation suite is used including HEXPRESS™, an automated fully hexahedral unstructured mesh generator, together with the flow solver ISIS-CFD (developed by the CNRS and the Ecole Centrale de Nantes), a 3D unstructured flow solver able to simulate Euler or Navier-Stokes (laminar or turbulent) flows in a steady or unsteady way.

3 Methodology

3.1 Domains definition and meshing strategy

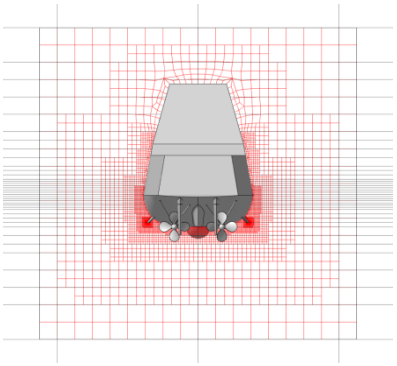

Fig. 2 : Mesh around the ship

The background domain is defined to simulate all the wave directions tested in the IIHR experiments, including following waves. In this configuration, the boat sails faster than the wave propagation speed. To avoid the situation where the ship catches up the wave front, a long enough domain is needed. As such, the size is selected to be the same as the actual IIHR towing tank (40m long, 20m wide). The domain is then considered as a background grid, fixed in the Earth reference frame, and the ship is located in an overlapping grid travelling through the towing tank. Another important benefit of this approach is that the ship's large motions induced by the waves can be handled without mesh deformation for all wave or maneuvering conditions. To make the overset as robust as possible some mesh criteria should be respected to improve the transfer of information at the interpolation location. The cell size ratio between overlapping and background domains should be equal to 1. Since the background domain is fixed, imposing a refinement at every possible location of the ship's grid would result in a too heavy mesh. To work around this issue, the mesh is dynamically refined during the simulation to respect this condition only at the overlapping locations, thanks to FINE™/Marine's adaptive grid refinement (AGR) technique. The AGR with the overset mesh continuity criterion is activated, and the size of the domains is set to get the exact same cell size at the overlapping boundary after this dynamic refinement. A free surface AGR criterion is also activated. The target cell size at the free surface is set to $\frac{L_{PP}}{1024}$, the recommended value for resistance calculation. These settings give 20 cells peak-to-peak, also matching with the ITTC (2011) recommendations for seakeeping simulations. For information, the total number of cells during the simulation with AGR is around 21.4M cells, whereas the mesh would have contained 36M cells with an equivalent static refinement box without AGR. For the ship grid, no initial grid refinement has been created at the free surface: AGR will also take care of it.

Since large relative motions of the appendages are expected and they are quite close to each other, an overset approach is used in the paper. In this case, overset method is not strictly necessary instead of sliding grids for the rudders but it validates this technique in case of strict necessity. In this situation where an overlapping grid is located inside another overlapping grid, a simple distance approach is used by the solver to determine the best interpolation location. That allows the rudder grids to cross the hull surface and simplify the meshing process. The grids are generated using HEXPRESS™ thanks to the grid convergence studies done by d'Aure et al. (2015) on seakeeping case and Zubova et al. (2016) for zigzag case for instance. The different numbers of cells per domain are detailed in Table 2.

Domain	Nb. of cells
Ship	3.7M
Rudders	1.15M
Propellers	2.26M
Background	7.42M
AGR	3.5M
Total	21.4M

Table 2: Cells repartition

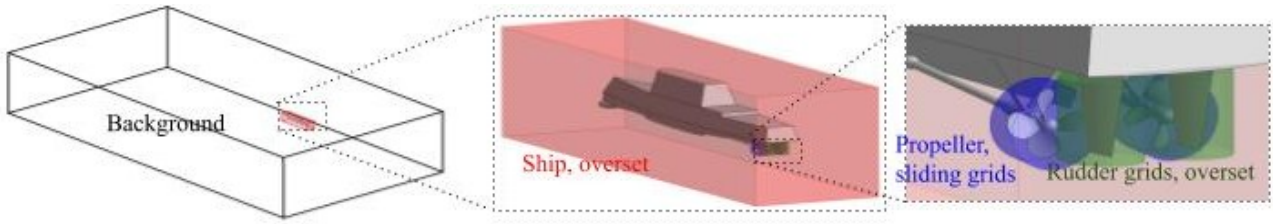

Fig. 3: Domains definition

3.2 Turbulence modeling

Giving the expertise of the CFD marine community with $k-\omega$ (SST Menter) and all the validations performed with FINE™/Marine with this model, it will be used together with wall function. This choice is also justified since DES model is still too costly and Zubova et al. (2017) showed that EASM returns a larger error compared to $k-\omega$ (SST Menter) in ship maneuvering simulations with flow separations.

3.3 Time step selection

The choice of the time step value is of high importance to avoid CPU time penalties. Four main constraints can be identified and Table 3 summarizes the possible values. The time step values for the rudder rate and propeller rotational speed should ensure a Courant number below 0.3 at the interface between domains. Thus the mesh cell size should always be taken into account for the time step value selection. Besides, a rotating frame method (RFM) can be used to calculate the flow inside the rotating sliding grids of the propellers. The flow in each rotating cell is solved using the rotating reference frame equations but it does not account for the relative motion of the adjacent domains of simulation. This method is a steady-state approximation and its usage can be justified since the rudder angles are relatively small and should not be too much impacted by the incoming flow perturbations which are aligned with the rudder position. However, it should not be used in case of zigzag or turning circle simulations. The time step value can then be calculated such that the propeller will perform a complete rotation in 20 time steps. The time step value is 27 times higher with a RFM approach than without. Another approach to model the propeller is the actuator disk. However, the RFM approach doesn't require the performance curve of the propeller, which is required for self-propulsion simulation. This is a great advantage when those curves are not provided. In such a situation, no preliminary computations have to be performed to predict the full open water data.

Criterion	Value [s]
The ships advancing speed	1.42e-2
The rudder rate	2.02e-2
The propeller rotational speed without RFM	2.07e-04
The propeller rotational speed with RFM	5.61e-3
The waves period	1.42e-2

Table 3: Possible time step value

3.4 Wave generation

The wave parameters follow the experimental setup: regular waves with a wavelength equal to ship length ($\lambda = L_{wl}$) and a wave steepness (H / λ) of 0.02. An Internal Wave Generator (IWG) is used to generate the wave directly inside the domain based on additional momentum source terms applied to the Navier-Stokes equations, which is numerically more natural than generating waves at boundaries. To generate the wave field with a reduced computation time, the simulation is made of two different steps. First, an internal wave generator covering the entire domain inflates the waves. Contrary to other methods for initialization, IWG approach initializes not only the volume fraction but the velocity field and pressure field as well. Using this method, waves are initialized everywhere in the domain within one wave period (1,42s). Fig. 4 shows the wave field during the inflating phase at 3 different times. After this initialization, a standard internal wave generator, with a width of 1 wavelength is used near the left border. A 3 wavelength width forced layer zone is set on the opposite side of the towing tank. It imposes the exact wave signal from the IWG to remove any wave reflections from solid bodies or domain boundaries.

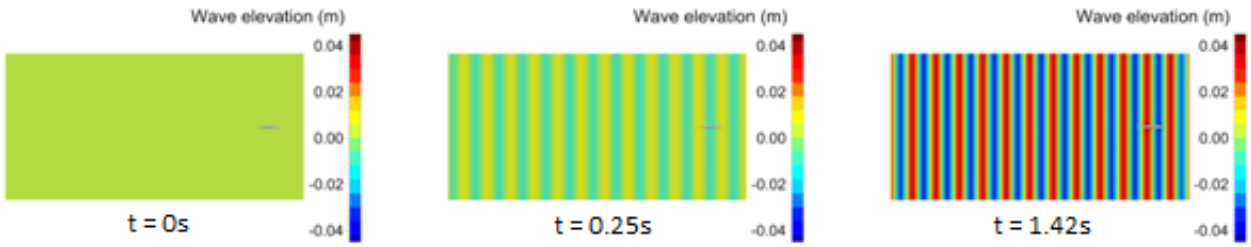

Fig. 4: Wave field at different time of the inflating phase

3.5 Self-propulsion controller

The first simulation is a preliminary self-propulsion study in calm water conditions. The objective is to determine the propeller rotational speed balancing forces when the ship is sailing at $U_0 = 1.11\ m/s$. The FINE™/Marine's code dedicated to self-propulsion study has been extended to handle multi-propeller cases and to control the rudders at the same time in order to keep the desired heading.

This self-propulsion controller cancels the forces projected onto the X-axis by adjusting the propeller rotational speed, with an imposed ship speed. The controller was developed to ensure stability, robustness, and speed, but most of all, to be valid for any kind of configuration. Extensive tests were performed to determine the default parameters allowing the controller to have this general behavior. Hence, the default parameters for the controller were used to study the self-propulsion. For a faster convergence, a first steady acceleration phase is performed. The ship is accelerated up to its target speed U_0 and the propeller to an estimated rotational speed. Herein the value found by Sanada et al. (2013) is taken as an initial value. Only trim and sinkage are solved. In the second phase, the propeller controller is activated and the 5 dof are solved. Although a pure sliding-grid approach might capture more physical phenomena and so return a result closer to the experiments, the objective of this computation is to find the propulsion point for the upcoming free-running simulations. Since the propellers will be modeled using a RFM in those computations, the same model should be used in the self-propulsion study.

4 Results and validation

4.1 Preliminary self-propulsion study

The predicted sinkage and trim (shown in Table 4) agree well with the available experimental data, the error is below 0.2mm for the sinkage and 0.02° for the trim. The self-propulsion controller behaves as expected, forces are balanced.

	CFD	EFD (IIHR)	Difference
n [rad/s]	56.43	56.36	0.07
Sinkage [m]	0.0025	0.0023	0.0002
Pitch [deg]	-0.018	-0.039	0,021

Table 4: Self-propulsion results

Fig. 5 shows the time evolution of the propeller rotational speed. The computed self-propulsion point is achieved for a propeller rotational speed of 56.43 rad/s, compared to the experimental data of 56.36 rad/s. The fact that the propeller revolution rate from experiments almost balances the forces indicates that the flows around the hull, the rudders, and the propeller, as well as their interaction, are well captured. It proves the feasibility of self-propulsion simulation using the present approach and provides a good starting point for the next course keeping simulations.

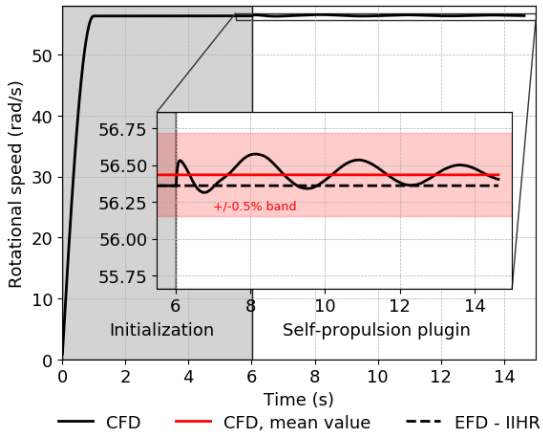

Fig. 5: Time history of propeller's revolution rate

4.2 Course keeping in wave

Fig. 6 shows the motion of the ship with all the wave angles. The solid line represents the computed results and the crosses the experimental data presented by Sanada et al. (2013). They are synchronized with $t = 0$ when the first wave peak reaches the bow. In contrast with the towing tank experiments, the present simulations start, with a wave field initialized everywhere in the domain thanks to the wave inflating method performed at the initialization step. That is the reason why the results are shown after 5 wave periods when both numerical and experimental data have reached this steady oscillating state. That explains the offset in heading angle for $X = 45°$ and $X = 90°$.

For all the wave directions the motions (yaw, pitch and roll) are well predicted. For the cases $X = 0°$, $X = 45°$ and $X = 90°$, the amplitude of motion differs from the experiments by less than 5%. Bigger differences are obtained for the $X = 135°$ and $X = 180°$.

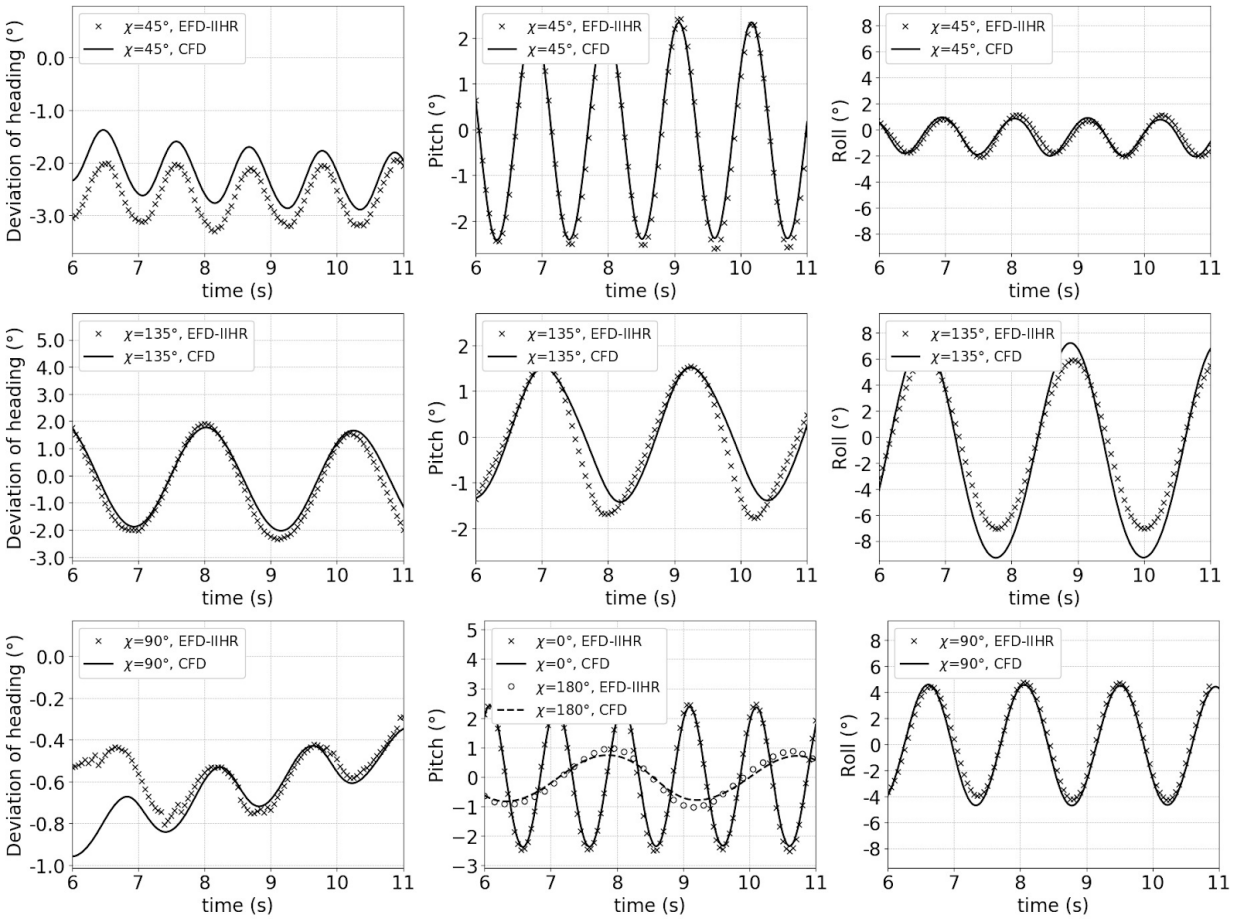

Fig. 6 : Computed ship motion and IIHR's experiments

Fig.7 shows the surge speed for heading and following waves. The global trend is well captured by CFD for the oscillation period and the amplitude especially for following waves. However, the heading wave signal amplitude is different: a sinusoidal signal is obtained in experiments whereas CFD predicts a flat signal at the peak locations. Similar behavior has been reported by other CFD users and remains unexplained for the moment. Wang et al. (2017) suggest that the propeller revolution rate is not kept exactly constant in the experiments. The time history of the propeller speed, thrust and torque from the experiment is not available to confirm this assumption.

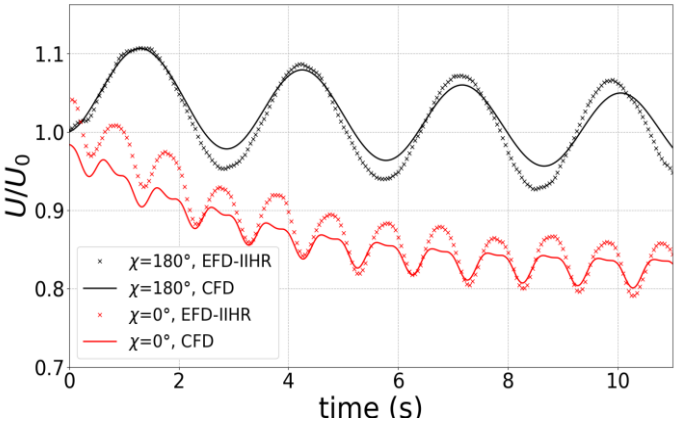

Fig. 7: Time history of surge velocity for 0° and 180° waves

5 Conclusions

Many CFD techniques have been used and validated at the same time to ensure satisfactory maneuvering simulations. For instance, adaptive grid refinement seems to be well indicated to reduce the CPU cost and ensure the best interpolation at any moment of the simulation. The results are accurate for many variables at a reasonable CPU cost. Indeed, the total cost of the simulation for 1 wave angle (including wave initialization) using 240 cores is around 104 clock hours (25×10^3CPU hours). The extension of the self-propulsion controller allows to adapt the propeller's rotational speed and the rudder angles. The RFM method helps to significantly decrease the required CPU time but should not be used for maneuvering conditions such as turning circle and zigzag. Current investigations are also going towards a dynamic time step based on the relative motion of each grid to ensure the proper transfer of information and to accelerate the computation. Structured meshes will also be investigated to make sure forces are always well computed on propellers and rudders at large angles.

References

Y. Sanada, K. Tanimoto, K. Takagi, Y. Toda and F. Stern (2013). Trajectories and Local Flow Field Measurements around ONR Tumblehome in Maneuvering Motion. Ocean Engineering, Vol. 72, pp. 45-65

B. d'Aure, B. Mallol and C. Hirsch (2015). Resistance and seakeeping CFD simulations for the korean container ship. Proceeding of NuTTS 2015, Marstrand, Sweden.

A. Zubova, A. del Toro Llorens, B. Mallol and C. Hirsch (2016). Progress towards CFD guidelines for zig-zag simulation in waves. Proceeding of NuTTS 2016, St. Pierre d'Oleron, France.

A. Zubova, A. del Toro Llorens, B. Mallol and C. Hirsch (2017). Extended CFD Guidelines for Zigzag Simulations in Self-propulsion Conditions at Low Froude Number. Proceeding of NuTTS 2017, Wageningen, The Netherlands.

J. Wang, L. Zou, D. Wan (2017). CFD simulations of free running ship under course keeping control. Ocean Engineering, 141, 450–464

ITTC – Recommended Procedures and Guidelines (2011).

On the Need for Higher Order Interpolation with Overset Grid Methods

Sébastien Lemaire[*†], **Guilherme Vaz**[*‡], **and Stephen Turnock**[†]
[*]MARIN, Wageningen/Netherlands, [‡]WavEC, Lisbon/Portugal,
[†]FSI Group, University of Southampton, Southampton/UK;
sebastien.lemaire@soton.ac.uk

1 Introduction

Overset methods, by overlapping several grids, allow large and arbitrary motion of bodies. First developed for the aerospace industry (Benek et al., 1985), it is now used for a wider range of applications like maritime ones (Carrica et al., 2013). At the fringes of each grid, the coupling is done by interpolating field variables. This interpolation step is key in any overset computations since the choice of the interpolation scheme directly influences the accuracy of the solution and the performance. Most overset implementations done for unstructured CFD codes uses 1st or at most 2nd order interpolation schemes (Gatin et al., 2018, Völkner et al., 2017, Chandar et al., 2018) but higher order interpolation schemes (3rd or 4th) are not often studied (Chandar, 2019). This paper evaluates the use of higher order (higher than 2nd order) interpolation schemes for the overset method by comparing the accuracy of different interpolation schemes on a Poiseuille flow test case, no performance study is however conducted here. The overset implementation used in this study is a coupling between the CFD solver ReFRESCO and the overset library Suggar++ (Noack and Boger, 2009).

The paper is organised as follows: section 2 presents the overset approach and the different interpolation schemes used in this study. Section 3 discusses the robustness of Least Squares interpolation scheme. Section 4 describes the test cases ran for the study as well as the computational setup. Results are presented in section 5 and finally concluding remarks are given in section 6.

2 Overset method and Interpolation

ReFRESCO (`refresco.org`) is a community-based open-usage CFD code for the maritime world. It solves multiphase incompressible flows using the Navier-Stokes equations, complemented with turbulence models, cavitation models and volume-fraction transport equations for different phases. The equations are discretised using a finite-volume approach with cell-centered collocated variables. Like most unstructured solver, ReFRESCO's discretisation is at most 2nd order.

The overset implementation used in this study has been described in Lemaire et al., 2018. It uses the two external libraries Suggar++ and DiRTlib (Noack and Boger, 2009) to compute the domain connectivity information. The domain connectivity information or DCI defines a status for each cell; *Hole* cells are being ignored by the solver, they correspond to cells outside the domain or that are being overlapped by any other mesh. *In* cells are normal domain cells. Finally, between *Hole* and *In* cells as well as at the edge of an overlapping mesh *Fringe* cells are placed. These cells are the ones performing the coupling between the different meshes. Each *Fringe* cell will receive interpolated field data from an other mesh. The interpolation phase is done in two steps: first each *Fringe* cell is assigned several donor cells that belong to the other mesh (a donor cell being a normal *In* cell); then donor cells field data are gathered and the interpolation is performed, the interpolated value is placed at the *Fringe* cell center. In an explicit coupling between meshes, the interpolated value is placed on the right hand side corresponding to each *Fringe* cell (for more details see Lemaire et al., 2018).

Multiple interpolation schemes can be used to perform this coupling, the number of donor cells needed depending on the scheme employed. In this study, three different schemes are tested resulting in an interpolation order between 1 and 4. First, the *inverse distance* scheme, it is a weighted average where the weights are based on the distance between the interpolation location and the donor cell center location. The number of donor cells N can be freely chosen. Equation 1 shows a formal description where ϕ is the field to interpolate, $\tilde{\phi}$ the interpolated function, $\boldsymbol{x_i}$ the i-th donor location, $\boldsymbol{x}$ the interpolation location (cell center of the *Fringe*) and ω_i the weight corresponding to the i-th donor cell.

$$\tilde{\phi}(\boldsymbol{x}) = \frac{\sum_{i=1}^{N} \omega_i \phi(\boldsymbol{x_i})}{\sum_{i=1}^{N} \omega_i}, \qquad \omega_i = \frac{1}{\|\boldsymbol{x} - \boldsymbol{x_i}\|^p}. \tag{1}$$

The *inverse distance* interpolation is a first order scheme that guaranties for the interpolated value to be bounded. It is very often implemented in overset capable solvers like StarCCM+ (Schreck and Peric, 2012), FOAM-extend (Gatin et al., 2018) or FRESCO+ (Völkner et al., 2017).

By using the gradient of the donor cell, a second order scheme can be constructed using only one donor cell. This scheme will be called *nearest cell gradient* in the following:

$$\tilde{\phi}(\boldsymbol{x}) = \phi(\boldsymbol{x_1}) + \nabla\phi(\boldsymbol{x_1}) \cdot (\boldsymbol{x} - \boldsymbol{x_1}). \tag{2}$$

Finally, unlimitedly high order interpolations can be performed using the *least squares* approach in conjunction with polynomial based interpolations. To obtain a n-th order interpolation, an $n-1$-th degree polynomial function is used. The polynomial function is constructed by minimising the square of the errors made on the donor locations (*least squares* approach). In this approach, the number of donor cells used has to be higher or equal to the number of unknown coefficients in the polynomial function. Table 1 shows the minimum number of donor cells depending on the polynomial degree and the dimension of the problem. One should note that a n-th degree polynomial function will lead to an $n+1$ interpolation order. Section 3 discusses the robustness of *least squares* interpolation depending on the number of donor cell used.

Dimension	N (number of donor cells)			
	n (degree)	$n=1$	$n=2$	$n=3$
2D	$\frac{(n+1)(n+2)}{2}$	3	6	10
3D	$\sum_{i=0}^{n} \frac{(i+1)(i+2)}{2}$	4	10	20

Table 1: Minimum number of donor cells N for *least squares* interpolation depending on the dimension of the problem and the degree of the polynomial function used. The resulting interpolation order is $n+1$, with n the degree of the polynomial.

3 Study of Least Squares interpolation robustness

Amongst the interpolation schemes presented in the previous section, the *least squares* approach is the only one that can provide an interpolation order of 3 and higher. Its robustness however depends on the number of donor cells it uses, and this section studies the influence of the number of donor cells used in the interpolation error. Note that increasing the number of donor cells reduces parallel performance due to an increased number of communications.

When using the *least squares* scheme, for a given interpolation order, a minimum number of donor cells is needed. When this minimum is used, the interpolation becomes a pure polynomial interpolation where the interpolated function goes through every donor cell point (the error made on each donor cell is 0). In this section the *least squares* interpolation using a degree two polynomial function (leading to a 3rd order interpolation scheme) is tested in isolation without overset computations. An analytical function (Eq 3) is used as a field data to compute the interpolation on. This function was chosen because it is bounded between -1 and 1, it does not show any oscillation in the $[-1,1]\times[-1,1]$ domain and is constructed with non polynomial functions. Donor points are randomly placed on the $[-1,1]\times[-1,1]$ domain and the interpolation error is measured by performing a *least squares* interpolation close to the donor points average location, which ensures that no extrapolation is performed. For each set of donor point, the interpolation error is measured by taking the difference between the interpolated value and the result of f at the interpolation location.

$$f(x,y) = \sin(-2x) + \cos(\frac{3y}{2}). \tag{3}$$

Figure 1 shows error distributions for various number of donor cells used. On the horizontal axis, the log of the error is displayed. For each plot, 50 000 different sets of donor points were generated and interpolations performed. The median error is marked by the dashed line and C_{mult} is the multiplier coefficient that gives the number of donor N compared to the minimum number of donors (6). Using more donor points tends to reduce the median error here, however this is not a general result since it has been observed that for some

functions f (different from Eq 3) this was not true. When C_{mult} increases, the spreading of the errors higher than the median reduces, which leads to a more robust interpolation since higher errors are less likely to be returned. Using only one more donor than the minimum ($N = 7$) the effect is already visible and no set of donor cells result in errors higher than 10^{-1}.

This test was conducted by placing donor points randomly in space, however, when placing the donor points on a Cartesian grid some interpolations result in infinitely high errors. The reason for this is the alignment of donor points that polynomial based interpolations are sensible to. When using a Cartesian mesh, increasing the number of donor points reduces the number of diverging results. If the minimum number of donor point ($N = 6$) is used, 2.9% of the interpolations result in infinitely high errors, this decreases to 0.3% when using only 1 more donor point ($N = 7$), and goes to 0% at $N = 9$. Fully Cartesian meshes are not often found in complex computations, however locally Cartesian or locally structured meshes with enough cell alignments are more common, and in such situations, using the minimum number of donor cells is not advisable. A C_{mult} of 1.5 was enough to remove any diverging results and gives robust *least squares* interpolations, and therefore this value is used in the following section for overset computations.

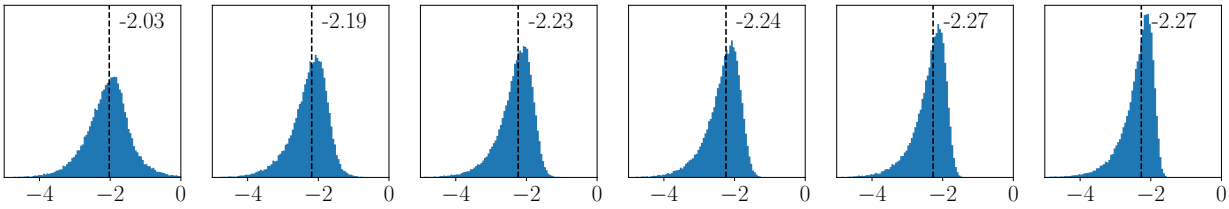

(a) $C_{mult} = 1$ ($N = 6$) (b) $C_{mult} = 1.2$ ($N = 7$) (c) $C_{mult} = 1.3$ ($N = 8$) (d) $C_{mult} = 1.5$ ($N = 9$) (e) $C_{mult} = 2.0$ ($N = 12$) (f) $C_{mult} = 2.7$ ($N = 16$)

Fig. 1: Influence of the number of donor points (N) on the error distribution. Histograms show the log of the errors for a degree two *least squares* interpolations. Plot 1a has a C_{mult} of 1, and it is mathematically equivalent to a Polynomial Interpolation of degree 2.

4 Test case description

For this study, the *inverse distance* scheme, *nearest cell gradient* scheme and *least squares* interpolation using a polynomial function of degree 1, 2 and 3 are used, leading to 1st, 2nd (both *nearest cell gradient* and *least squares 1*), 3rd and 4th order interpolation schemes. The *inverse distance* scheme is using here 4 donor cells, however very similar results were found with either 1 or 10 donor cells. All of the computations were done on a *Poiseuille* flow case using 5 grid assemblies consisting of a background grid and a foreground one, both being 2D Cartesian meshes with a 2:1 ratio (like in Lemaire et al., 2018). The foreground grid is twice smaller in both direction compared to the background grid and is positioned in the center of the background grid and rotated by about 19 degrees. Table 2 shows the different cell counts and Figure 2 shows the grid assembly and cell status as computed by Suggar++. Two layers of *Fringe* cells are used in order to reconstruct gradients properly. Finally, computations done using only the background grid, hence without the overset method, were performed for comparison purposes.

	Background	N_i	Foreground	N_i^f
G1	32x16	512	16x8	128
G2	64x32	2048	32x16	512
G3	128x64	8192	64x32	2048
G4	256x128	32768	128x64	8192
G5	512x256	131072	256x128	32768

Table 2: Details of the Cartesian grids used and cell count (N_i)

The *Poiseuille* flow case is an academic case for which an analytical solution is known but still relevant for maritime applications being a boundary layer problem. The 2D flow is bounded between a top and bottom wall and driven by an axial pressure gradient. The analytical solution is presented in Eq. 4 with L the length of the channel (X direction), and h the distance between the walls.

$$U_x(y) = \frac{Ph^2}{2\mu}\left(1 - \frac{y^2}{h^2}\right) \quad , \quad U_y = 0 \quad , \quad \frac{\partial p}{\partial x} = -P \quad , \quad p(x) = -P(x - L) \quad . \tag{4}$$

In this test case steady computations are performed, and the momentum equation and the pressure correction via the SIMPLE method are solved. The Reynolds number, based on the height of the channel, is $Re_h = 10$. At the inlet, the analytical velocity profile is set and at the outlet the pressure is enforced. The top and bottom of the domain uses non-slip wall boundary conditions. Convergence is ensured by letting the infinity norm of the residual stagnate, that happens below 10^{-14} for all the computations performed. A second order central difference scheme is used for the discretisation of convective and diffusive fluxes.

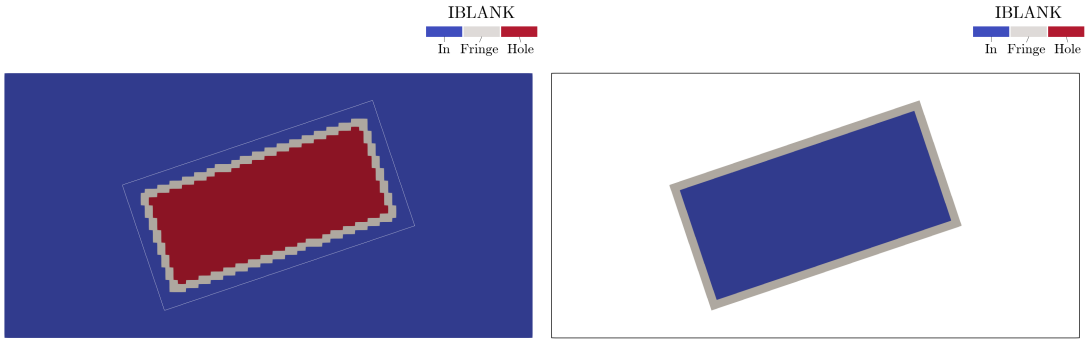

Fig. 2: Cell status computed by Suggar++ for the G3 grid assembly. Two layers of *Fringe* cells are used.

5 Results

Since an analytical solution is known for a Poiseuille flow test case, errors can be evaluated in the entire domain. Figure 3a shows the infinity norm of the error made on the velocity field depending on the grid refinement. Each scheme shows a converging trend, the error levels as well as the convergence order (slope of the curve when refining the grid) however varies between schemes. Computations done with the *inverse distance* scheme resulted in a convergence order of about 0.5, and also yield errors level several orders of magnitude higher than the other schemes. The *nearest cell gradient* scheme results in a convergence order of about 1.5 like the degree 1 *least squares* scheme, with error levels however being lower when using the *nearest cell gradient* scheme. Finally, the two last *least squares* schemes tested (using 2nd and 3rd degree polynomial functions, i.e. 3rd and 4th order schemes) result in the same error levels and a convergence order of 2.0 (the two curves overlapping each others), exactly like the computations done without overset.

The mass imbalance between the inlet and outlet of the domain is also measured in Figure 3b for all scheme and grids. This metric is particularly relevant since it relates to the pressure accuracy in the domain and for unsteady cases mass imbalance can lead to pressure fluctuations. Contrary to the computation done without overset, every scheme introduce some mass imbalance. Once again, the 3rd and 4th order schemes show similar results with the finest grid giving a mass imbalance as low as 1.3×10^{-11}, meaning that there is no gain in using a scheme of interpolation order higher than 3 and that this level of mass imbalance is likely to be negligible. The *inverse distance* scheme is performing closely to the *nearest cell gradient* one here but with a less smooth trend. The *least squares 1* scheme shows a similar slope as the *nearest cell gradient* but with a higher imbalance.

When analysing the error localisation, similar observations can be drawn. Figure 4 shows the log of the error made on the velocity field for the grid assembly G3. Both the foreground and background grid are displayed on a single plot here, only the bottom half of the foreground grid being shown to be able to see the *Fringe* cells of the background grid. Infinitely low errors are present at the inlet of the domain for every computation because the analytical solution is prescribed as a boundary condition. Visible artefacts due to the interpolation in the overlap region are visible for the *inverse distance*, *nearest cell gradient* and *least squares 1* schemes but not for the two higher degree *least squares* computations. Compared to *nearest cell gradient*, the *least squares 1* shows a smoother field close to the *Fringe* cells, partially because it uses more donor cells to perform the interpolation. However, it has a higher maximum but also norm-2 error field.

Finally, the error field for the 3rd and 4th order interpolation schemes are very similar to the computation done without overset. Computing the actual difference between the non overset computation and the 3rd or 4th order *least squares* interpolation on the background grid shows that the maximum difference is bellow $10^{-4.4}$ for the grid G3, which is 1 order of magnitude lower than the difference with the analytical solution.

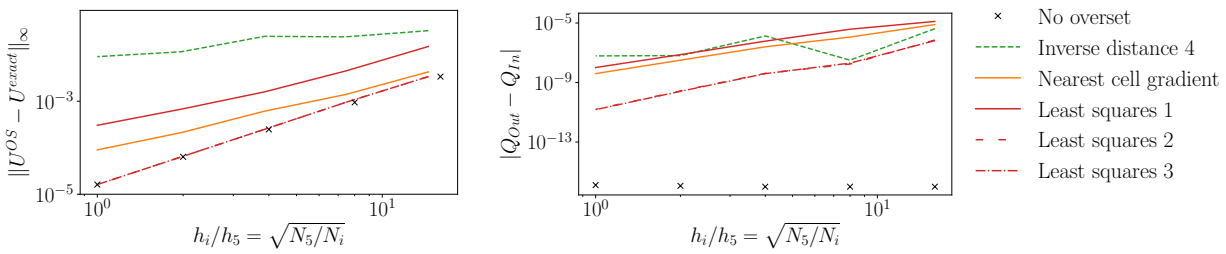

(a) Infinity norm of the error for the velocity field

(b) Mass Imbalance between inlet and outlet

Fig. 3: Infinity norm of the error and mass imbalance against the grid refinement for every scheme tested. The *least squares* 2 and 3 lines are overlapping each other on both plots.

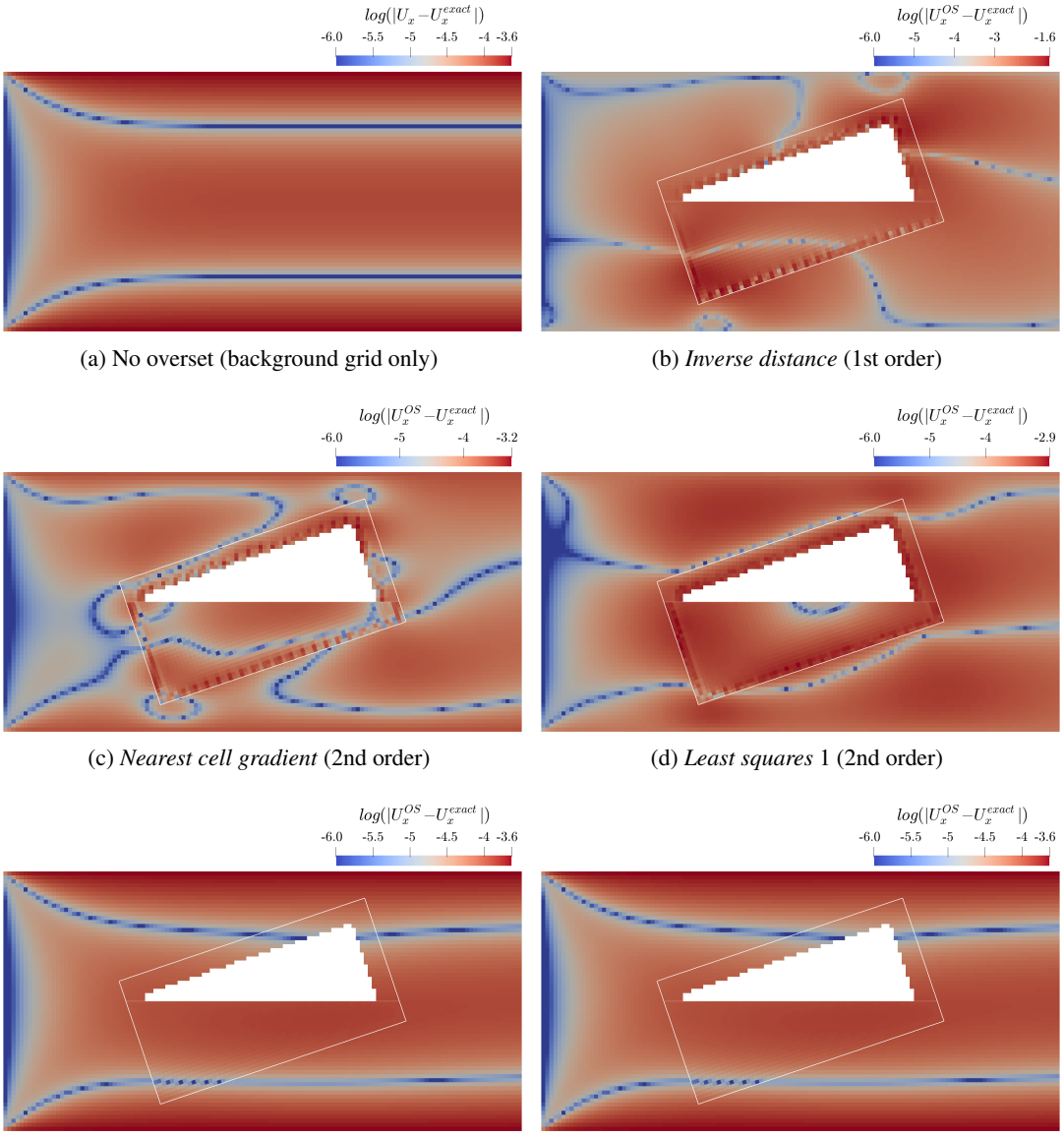

(a) No overset (background grid only)

(b) *Inverse distance* (1st order)

(c) *Nearest cell gradient* (2nd order)

(d) *Least squares* 1 (2nd order)

(e) *Least squares* 2 (3rd order)

(f) *Least squares* 3 (4th order)

Fig. 4: Log of the error for the velocity field computed with the analytical solution for the grid assembly G3. Each plot has its own color bar with the maximum corresponding to the maximum error of the field and a minimum at 10^{-6}. No overset related artefacts are visible for the schemes of order 3 or higher.

6 Concluding remarks

From this study performed on interpolation for overset meshes several conclusions can be drawn. On a CFD solver that uses second order schemes for its discretisation, at least a 3rd order interpolation scheme is needed for the overset coupling in order for the interpolation error to be bellow the transport equation discretisation errors. Moreover, no gain is achieved when using interpolation schemes of order higher than 3 (same mass imbalance and error). Some mass imbalance is introduced with the use of interpolation, it however reduces with the increase of interpolation order and grid refinement. Minimising the mass imbalance is particularly relevant on unsteady cases since it can lead to pressure fluctuations being propagated in the entire domain. In order to perform a 3rd order interpolation, one can use the *least squares* approach. When using locally structured or Cartesian grids however, more donor cells are needed to prevent high errors. The computational cost is however higher when increasing the number of donor cells since the search and the gathering of field data need more parallel communications. On the other hand, the *nearest cell gradient* scheme only needs one donor cell, is a second order scheme and has error levels lower than the *inverse distance* scheme, it should hence be preferred over the later. Future works are now focusing on the performance and parallelisation of the interpolation and donor cell searching methods in order to make 3rd order *least squares* interpolation more affordable.

Acknowledgements

The authors would like to thank Dr. Ralph Noack and Prof. Pablo Carrica for their help with the coupling with Suggar++. This work was supported by the EPSRC Centre for Doctoral Training in Next Generation Computational Modelling (EP/L015382/1). The authors acknowledge the use of the IRIDIS High Performance Computing Facility at the University of Southampton, in the completion of this work.

References

Benek, J., Buning, P. G., and Steger, J. (1985). A 3-D chimera grid embedding technique. In *7th Computational Physics Conference*, page 10, Reston, Virigina. American Institute of Aeronautics and Astronautics.

Carrica, P. M., Ismail, F., Hyman, M., Bhushan, S., and Stern, F. (2013). Turn and zigzag maneuvers of a surface combatant using a URANS approach with dynamic overset grids. *Journal of Marine Science and Technology*, 18(2):166–181.

Chandar, D. D. (2019). On overset interpolation strategies and conservation on unstructured grids in OpenFOAM. *Computer Physics Communications*, pages 1–12.

Chandar, D. D., Boppana, V. B. L., and Kumar, V. (2018). A Comparative Study of Different Overset Grid Solvers Between OpenFOAM, StarCCM+ and Ansys-Fluent. In *AIAA SciTech Forum*, number January, Kissimmee, Florida.

Gatin, I., Vukcevic, V., Jasak, H., and Lalovic, I. (2018). Manoeuvring simulations using the overset grid technology in foam-extend. In *32nd Symposium on Naval Hydrodynamics*, number August, page 10, Hamburg, Germany.

Lemaire, S., Vaz, G., and Turnock, S. R. (2018). Implementation and Verification of an Explicit Overset Grid Method. In *21th Numerical Towing Tank Symposium (NuTTS)*, Cortona, Italy.

Noack, R. W. and Boger, D. A. (2009). Improvements to SUGGAR and DiRTlib for Overset Store Separation Simulations. In *47th AIAA Aerospace Sciences Meeting*, number January, pages 5–9, Orlando, Florida.

Schreck, E. and Peric, M. (2012). Overset Grids in STAR-CCM+: Methodology, Applications and Future Developments. In *STAR Japanese Conference*.

Völkner, S., Brunswig, J., and Rung, T. (2017). Analysis of non-conservative interpolation techniques in overset grid finite-volume methods. *Computers and Fluids*, 148:39–55.

Turbulence Decay Corrections for Transitional Flow Calculations

Rui Lopes[1], **Luís Eça**[1], **and Guilherme Vaz**[2,3]
[1] Instituto Superior Técnico - University of Lisbon,
[2] Maritime Research Institute Netherlands
[3] WavEC - Offshore Renewables
rui.a.lopes@tecnico.ulisboa.pt

1 Introduction

Transitional flow calculations are becoming increasingly common due to the emergence of applications operating at low Reynolds numbers and the appearance of mathematical models focused on modeling transition. From a physical perspective, transition is a complex phenomenon, non-linear and unsteady, in which flow disturbances from the freestream cause the laminar flow in the boundary layer to become unstable and transition to turbulent flow. As a result, the exact location for the transition region is dependent on the characteristics of the freestream flow and its disturbances. From the numerical standpoint, this sensitivity to the freestream conditions is obtained from inlet boundary conditions for turbulence. In calculations using the Reynolds-Averaged Navier-Stokes (RANS) equations, when transition models are not employed, transition is handled by the underlying turbulence model. This leads to transition occurring at too low Reynolds numbers, which originates turbulent flow close to the leading edge of a body, regardless of the specified turbulence quantities at the inlet.

However, when transition modelling is desired, the inlet turbulence quantities have a strong influence on the transition location as shown by Eça et al. (2016). Despite being physically expected, this influence causes difficulties, since the specification of these values becomes a challenge as little information about turbulence is known in order to determine both variables (in the case of two-equation models). Additionally, common two-equation eddy-viscosity models such as the $k-\epsilon$ and $k-\omega$ turbulence models predict a very strong decay of the turbulence variables in the freestream, which is related to the value of the eddy-viscosity at the inlet according to Spalart and Rumsey (2007). Thus it is common to observe that calculations with transition modelling are accompanied by very high values of $\frac{\nu_t}{\nu}$ in order to maintain a 'reasonable' decay of the turbulence intensity.

This means that for practical applications, one must not only know the correct value for the turbulence intensity, but also has to estimate the eddy-viscosity value that will result in the correct evolution of the turbulence intensity along the flow. This situation severely hinders the predictive capability of transition models (Li et al. (2019)), and often results in awkward values for the eddy-viscosity at the inlet, which may become physically questionable.

In this paper, we explore an alternative technique to control the decay of turbulence kinetic energy in the freestream that modifies dissipation in the k and ω transport equations. This modification is calibrated for the flow around a flat-plate and then subsequently tested on the flow around the NACA 0012 airfoil. The mathematical formulation is described in section 2. The test cases and numerical settings are described in sections 3 and 4 while the results are presented and discussed in section 5. Section 6 summarizes the conclusions of this work.

2 Mathematical Models

This study is concerned with the statistically steady flow of a single-phase incompressible Newtonian fluid, solved by the RANS equations. These are obtained by applying time-averaging to the flow properties and to the continuity and momentum equations. A turbulence closure is necessary in order to determine the Reynolds-stress tensor. In this work, we use the two-equation $k-\omega$ Shear-Stress Transport (SST) turbulence model which resorts to the concept of eddy-viscosity in order to close the system. The γ-$\tilde{R}e_{\theta_t}$ model by Langtry and Menter (2009) is used to account for transition modelling.

$k-\omega$ SST model

The two-equation $k-\omega$ SST turbulence model by Menter et al. (2003) solves transport equations for the turbulence kinetic energy k and for the specific turbulence dissipation ω. The model includes a blending

function F_1 that is designed to switch from $k-\omega$ behaviour near the wall to the $k-\epsilon$ equations in the freestream. Model constants and blending functions are given in Menter et al. (2003).

Considering steady, uniform flow aligned with the x axis and neglecting the cross-diffusion term $CD_{k\omega}$, the transport equations of the SST model can be written as:

$$U\frac{dk}{dx} = -\beta^*\omega k \tag{1}$$

$$U\frac{d\omega}{dx} = -\beta\omega^2 \tag{2}$$

where β and β^* are constants. Under these conditions the eddy-viscosity can be obtained from:

$$\nu_t = \frac{k}{\omega} \tag{3}$$

Using dimensionless variables $k^* = k/V_\infty^2$, $\omega^* = \omega * L_{ref}/V_\infty$, $U^* = U/V_\infty$, $x^* = x/L_{ref}$ with $U^* = 1$, the solution to these equations can be written as:

$$k^* = \frac{k^*_{in}}{\left(1+\beta(x^*-x^*_{in})k^*_{in}\left(\frac{\nu}{\nu_t}\right)_{in}Re\right)^{\frac{\beta^*}{\beta}}} \tag{4}$$

$$\omega^* = \frac{\omega^*_{in}}{1+\beta(x^*-x^*_{in})k^*_{in}\left(\frac{\nu}{\nu_t}\right)_{in}Re}. \tag{5}$$

From these equations it can be observed that the decay of ω and k in the freestream along the domain depends on β, β^*, $\left(\frac{\nu}{\nu_t}\right)_{in}$, k^*_{in} and the Reynolds number. These equations explain why high values for the eddy-viscosity ratio are commonly observed in calculations that make use of transition models. The approach presented here follows a different route: instead of controlling the decay through $\left(\frac{\nu}{\nu_t}\right)_{in}$, the constants β and β^* are redefined:

$$\begin{aligned} \beta &= (1-F_{FS})\beta_o + F_{FS}\beta_{FS} \\ \beta^* &= (1-F_{FS})\beta^*_o + F_{FS}\beta^*_{FS}\ , \end{aligned} \tag{6}$$

where β_0 and β^*_0 are the original constants of the SST model and β_{FS}, β^*_{FS} are the new values which will be active in the freestream and will be responsible for controlling the decay:

$$\begin{aligned} \beta_{FS} &= \lambda\beta_o \\ \beta^*_{FS} &= \lambda\beta^*_o\ , \end{aligned} \tag{7}$$

λ is defined in the range $0 < \lambda < 1$. Of course, this modification changes the original calibration of the SST model, and therefore it should only be active in the freestream. Hence, we use the function F_{FS}, which is meant to identify whether a given point in the domain lies in the freestream, in a similar approach to that of Lopes et al. (2017), although the transition model was not used in that study. The F_{FS} function is built using the eddy-viscosity ratio and the vorticity magnitude:

$$F_{FS} = \min\left(F_{FS1}, F_{FS2}\right) \tag{8}$$

$$F_{FS1} = \begin{cases} 1 & , \ \frac{\Omega L}{V_\infty} \le 20 \\ 1-3\xi^2+2\xi^3 & , \ 20 < \frac{\Omega L}{V_\infty} < 50 \\ 0 & , \ \frac{\Omega L}{V_\infty} \ge 50 \end{cases} \quad \text{and} \quad F_{FS2} = \begin{cases} 1 & , \ \frac{\nu_t}{\nu} \le \left(\frac{\nu_t}{\nu}\right)_{in} \\ 1-3\Psi^2+2\Psi^3 & , \ \left(\frac{\nu_t}{\nu}\right)_{in} < \frac{\nu_t}{\nu} < 1.5\left(\frac{\nu_t}{\nu}\right)_{in} \\ 0 & , \ \frac{\nu_t}{\nu} \ge 1.5\left(\frac{\nu_t}{\nu}\right)_{in} \end{cases} . \tag{9}$$

where $\xi = \frac{\frac{\Omega L}{V_\infty}-20}{30}$ and $\Psi = \frac{\frac{\nu_t}{\nu}-\left(\frac{\nu_t}{\nu}\right)_{in}}{0.5\left(\frac{\nu_t}{\nu}\right)_{in}}$. The F_{FS1} auxiliary function based on the vorticity magnitude is built to identify the laminar boundary layer and the near-wall linear sublayer, while the F_{FS2} function

identifies the edge of the turbulent boundary layer. Combined together, these two functions identify the regions of the domain where viscous effects are relevant, i.e., where the turbulence model must be working with its original constants to guarantee that the behaviour of the original model in the laminar and turbulent regions is preserved.

Under the proposed formulation, the decay of turbulence in the freestream is now controlled by the product $\frac{\nu}{\nu_t}\lambda$. Hence, low values of λ can be used to obtain a slow decay instead of decreasing $\frac{\nu}{\nu_t}$ at the inlet.

3 Test Cases

In this work the previous corrections are applied to the two-dimensional steady flows over a flat plate and around the NACA 0012 airfoil. The setup for these cases has been used before by Eça et al. (2016) so it is only briefly mentioned below. The Reynolds number for the flow over the flat plate is $Re_L = 10^7$ (based on the plate length L). The plate extends from $x = 0$ to $x = L$, and the inlet boundary is placed at $x = -0.25L$, while the outlet is located at $x = 1.25L$. The top boundary is $0.25L$ away from the plate. For the flow around the NACA 0012 airfoil the Reynolds number (based on the chord of the airfoil c) is $Re_c = 2.88 \times 10^6$. The top and bottom boundaries are approximately $12c$ away from the airfoil while the inlet and outlet boundaries are placed $12c$ upstream of the leading edge and $23c$ downstream of the trailing edge, respectively.

For both cases the velocity and turbulence variables are specified at the inlet while pressure is extrapolated from the interior. Pressure is fixed at the top boundary for the flat plate flow, and at the outlet for the flow around the airfoil. Zero streamwise derivatives (Neumann conditions) are used for the remaining variables at these boundaries and for the bottom boundary of the airfoil domain as well. Symmetry conditions are applied on the regions upstream and downstream of the plate on the bottom boundary. At the surface of the plate and airfoil, the no-slip condition is enforced and the pressure normal derivative is set to zero. At the wall k is equal to zero, whereas Neumann conditions apply to γ and $\tilde{Re}_{\theta_t}$. ω is specified at the near-wall cell centre according to the near-wall solution (Wilcox (1998)).

4 Numerical Settings

The finite-volume flow solver ReFRESCO (www.refresco.org) is used for all calculations. It uses cell-centered collocated variables and, to ensure mass conservation, a pressure-correction equation based on the SIMPLE algorithm. Second-order schemes are applied to the convective and diffusive terms of all transport equations. Iterative convergence criteria is set so that the L_∞ norm of the normalized residuals of all transport equations must be below 10^{-6} for the flat plate flow and below 10^{-8} for the flow around the NACA 0012 airfoil. The normalized residuals are equivalent to dimensionless variable changes in a simple Jacobi iteration.

The grid used for the flat plate flow has 1024 cells on the surface of the plate and a total of 294, 962 cells while the grid for the flow around the airfoil has 1024 cells on the surface of the airfoil and a total of 391, 168 cells. The maximum dimensionless near-wall cell size, y^+_{max}, is always below 0.5. The grids are illustrated in Figure 1.

5 Results

Flat plate flow

The flat plate test case served as a calibration for the F_{FS} function. At this stage, the goal is to ensure that the sensitivity of the location of the transition region is changed from $\left(\frac{\nu_t}{\nu}\right)_{in}$ to λ. To that end, baseline calculations are performed using a given value for the viscosity ratio at the inlet and setting $\lambda = 1$, which results in the unmodified SST model. Then, a series of calculations using different combinations of $\left(\frac{\nu_t}{\nu}\right)_{in}$ and λ that lead to the same decay (same $\left(\frac{\nu}{\nu_t}\right)_{in}\lambda$) for the freestream turbulence as the baseline calculations are performed. These combinations are shown in Tab. 1: pairs with matching decay type have the same freestream turbulence decay, and should, therefore, lead to a similar location of the transition region.

Figure 2 presents the results obtained for an inlet turbulence intensity of 3%. As expected, combinations of $\frac{\nu_t}{\nu}$ and λ that share the decay type exhibit transition at the same location and matching turbulence

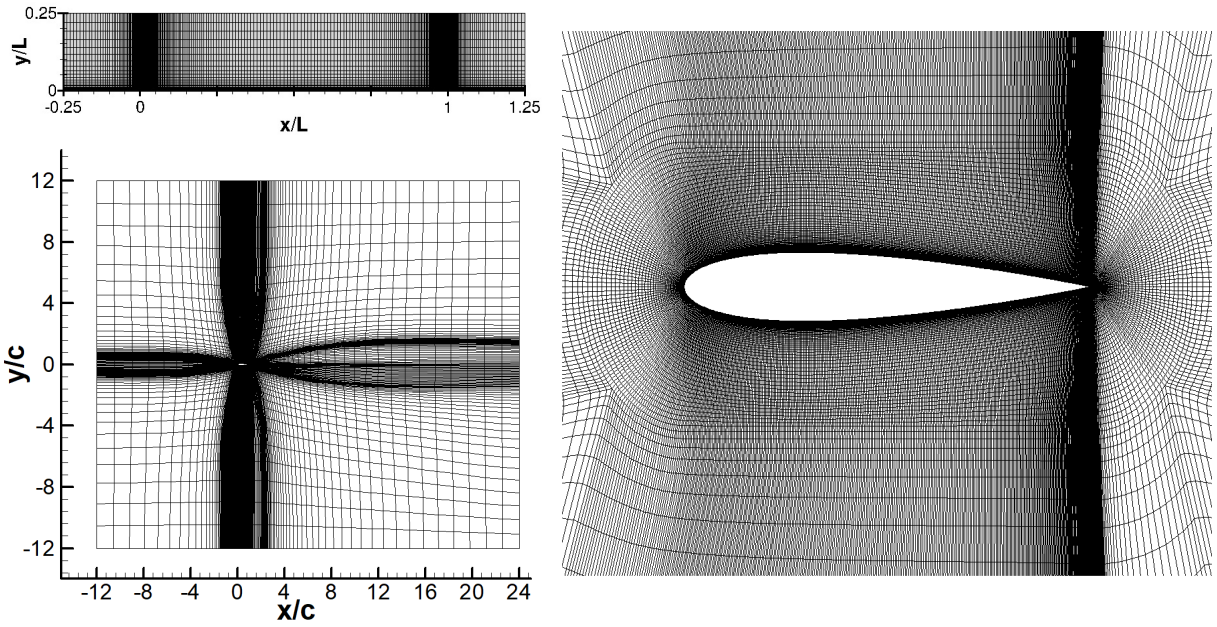

Fig. 1: Illustration of the domain and grids of the two test cases.

Table 1: Combinations used for the flat plate test and corresponding decay type.

$\left(\frac{\nu_t}{\nu}\right)_{in}$	100	10		1			0.1		
λ	1.0	1.0	0.1	1.0	0.1	0.01	0.1	0.01	0.001
Decay type	A	B	A	C	B	A	C	B	A

decay. The only exception occurs for $\frac{\nu_t}{\nu} = 0.1$ and $\lambda = 0.001$, in which a significant deviation for the transition region can be observed. All calculations using the modified dissipation terms show that the solution in both the laminar and turbulent regions was not changed when compared to the baseline calculations, hence the behaviour of the original model is preserved.

A comparison of F_{FS} for two calculations with decay type A is shown in Fig. 3. It is clear that the current formulation for this function makes it dependent on the value of λ, which is not the physically expected behaviour (F_{FS} should be not depend on λ). However, the main challenge of this approach

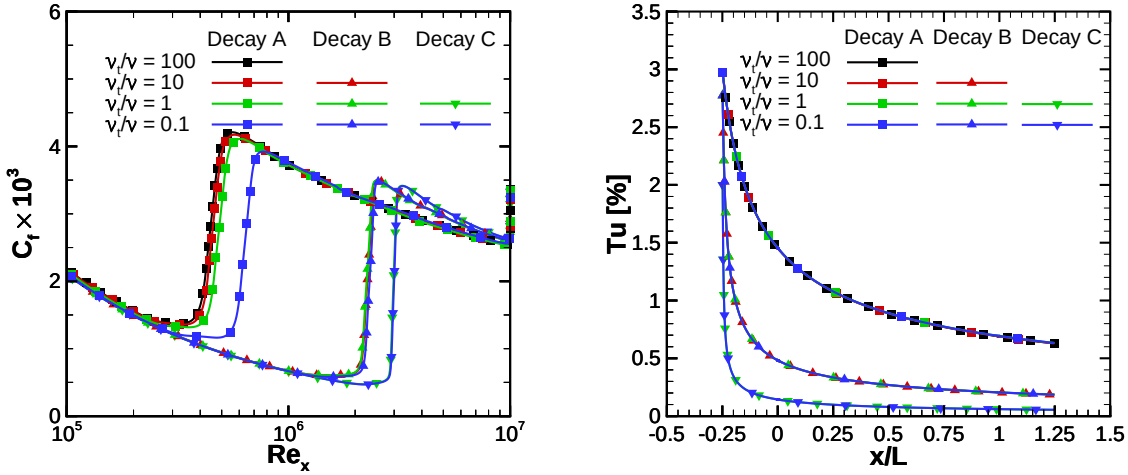

Fig. 2: Local skin friction coefficient C_f along the plate (left) and turbulence intensity Tu along the domain in the freestream (right). Inlet turbulence intensity of 3%.

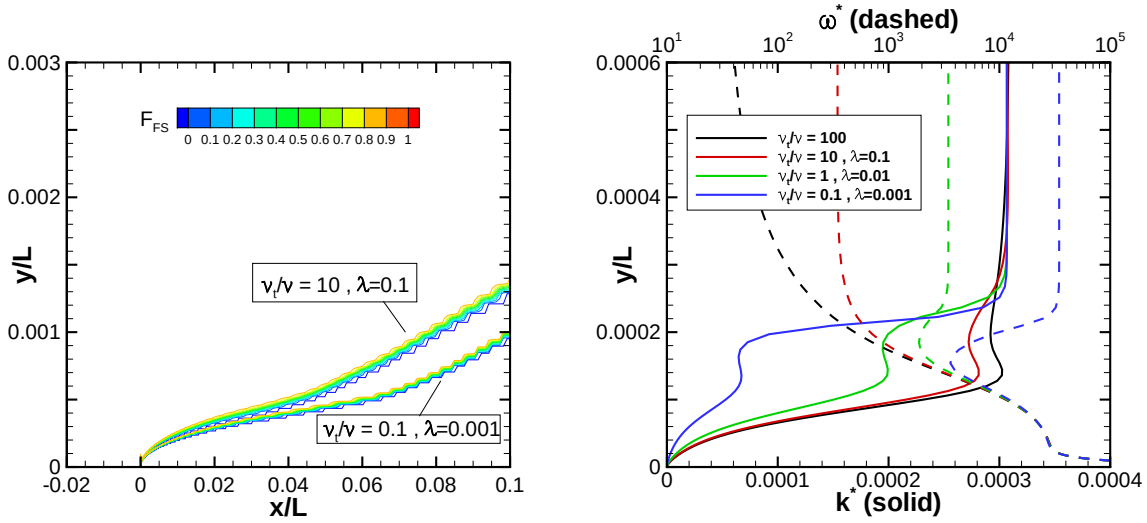

Fig. 3: Comparison of the F_{FS} function in decay type A (left) and k and ω profiles at $x/L = 0.01$ (right).

is illustrated in the right plot of Fig. 3 that depicts the k and ω profiles at $x = 0.01L$, upstream of the critical Reynolds number. The change of λ and $\frac{\nu_t}{\nu}$ leads to a significant difference of the level of ω in the freestream. On the other hand, the four ω profiles are coincident in the boundary-layer region. Therefore, to obtain approximately similar k profiles for different values of λ (the goal of this approach), F_{FS} must start decaying at the same location and decay faster as λ decreases, since freestream ω increases with the decrease of λ. At this stage, the F_{FS} definition is not able to exhibit these properties, especially for $\lambda = 0.001$. Additional calculations were performed for an inlet turbulence intensity of 1%, which led to similar observations. Consequently, they are not shown here.

Flow around the NACA 0012 airfoil

For this case, the combinations for inlet eddy-viscosity and λ are the same as those used for the flat plate case and presented in Tab. 1. However, there is one further addition: the equations of the turbulence model are solved without dissipation terms up to the plane $x/c = -0.5$. This effectively keeps the turbulence variables constant up until the mentioned plane. The goal of this setting is to avoid having the turbulence quantities suffering from a considerable decrease from the inlet up until the leading edge of the airfoil. The results are exhibited in Fig. 4 for an inlet turbulence intensity of 1%.

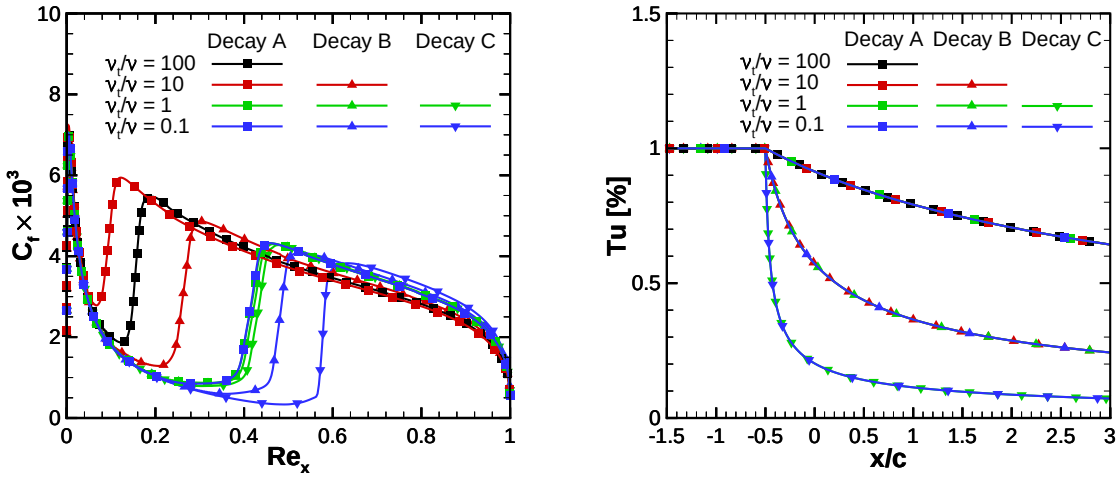

Fig. 4: Local skin friction coefficient C_f on the upper surface of the airfoil (left) and freestream turbulence intensity Tu along part of the domain (right).

Once again the use of the modified dissipation terms causes matching decay of turbulence in the free-

stream. However, unlike the previous case, this is not translated in the same location for the transition region. For decay type A, the calculation with $\frac{\nu_t}{\nu} = 100$ predicts transition to start at around $x/c = 0.16$, while for the case with $\frac{\nu_t}{\nu} = 10$ it starts before $x/c = 0.08$ and after $x/c = 0.25$ for the remaining combinations. The remaining decay types also exhibit highly varying locations for the transition region.

This case involves a more complex flow than the previous one, thus it is to be expected that it is harder to achieve the desired properties of F_{FS} in this case. The results confirm that the success of this approach requires improvements in the formulation of F_{FS}.

6 Conclusions

A modification to the dissipation terms of the $k - \omega$ SST turbulence model is presented in this paper. Its goal is to reduce the influence of the inlet eddy-viscosity in the decay of the turbulence variables in the freestream, allowing for low values to be used when small decay is desired, which is usually the case for transitional flow simulations. In the present approach, the desired decay of freestream k is achieved through the decrease of the constants of the dissipation terms of the k and ω transport equations.

Calculations with the proposed modification were performed, employing the widely used $\gamma - Re_\theta$ transition model, for the flow over a flat plate and the flow around the NACA 0012 airfoil. Different combinations for the inlet turbulence quantities were tested in order to assess whether the proposed modification achieved the desired purpose. The calculations for the flat plate, which were also used for the calibration of some parameters, exhibited promising results. However, the desired properties were not obtained when the freestream constants of the dissipation terms are less than two orders smaller than the standard values. This was further confirmed in the NACA 0012 test case, in which the shortcomings of the current approach became even more evident.

Therefore, further work is required to obtain a robust formulation which is able to keep the behaviour of the original model in the laminar and turbulent regions, while allowing for control of the freestream turbulence decay such that the same decay leads to the same location of the transition region.

Acknowledgements

The first author acknowledges financial support provided by Fundação para a Ciência e Tecnologia through a research grant under the Bolsas de Doutoramento and Pós-Doutoramento 2016 program. Funding from the Dutch Ministry of Economic Affairs is also acknowledged.

References

Eça, L., Lopes, R., Vaz, G., Baltazar, J., and Rijpkema, D. (2016). Validation Exercises of Mathematical Models for the Prediction of Transitional Flows. In *Proceedings of 31st Symposium on Naval Hydrodynamics, 11th-16th September, Berkeley*.

Langtry, R. B. and Menter, F. R. (2009). Correlation-based Transition Modeling for Unstructured Parallelized Computational Fluid Dynamics Codes. *AIAA journal*, 47(12):2894–2906.

Li, D., P., L., and Werner, S. (2019). Transitional flow on model scale propellers and their likely influence on performance prediction. In *Proceedings of* 6^{th} *International Symposium on Marine Propellers, Rome, Italy*.

Lopes, R., Eça, L., and Vaz, G. (2017). On the Decay of Free-stream Turbulence Predicted by Two-equation Eddy-viscosity Models. In *Proceedings of* 20^{th} *NuTTS, Wageningen, The Netherlands*.

Menter, F. R., Kuntz, M., and Langtry, R. (2003). Ten Years of Industrial Experience with the SST Turbulence Model. *Turbulence, Heat and Mass Transfer*, 4(1):625–632.

Spalart, P. R. and Rumsey, C. L. (2007). Effective Inflow Conditions for Turbulence Models in Aerodynamic Calculations. *AIAA Journal*, 45(10):2544–2553.

Wilcox, D. C. (1998). *Turbulence Modeling for CFD, 2nd ed.* DCW Industries.

The use of BEMT and a Transient Timoshenko Beam to Obtain Vibration Properties of Propeller Blades Under Manoeuvring Conditions

Nicholas McCaw*, **Stephen Turnock***
*University Of Southampton, Southampton, United Kingdom
n.mccaw@soton.ac.uk

1 Introduction

Propellers are commonly used as propulsors for ships and maritime submarines. Unsteady propeller blade motions can have a significant impact on the fatigue life of the propeller and shaft line and increase the noise generation. If the motions excite a vibration mode of the propeller the effect can be significantly detrimental to the fatigue life of the propeller and drive train and be a source of noise. The motion of the blade also uplifts broadband noise contributions. Excluding cavitation there are two main causes of propeller hydrodynamic noise; swathing and singing. Swathing is the structural response of the propeller blade caused by the unsteady and non-uniform wake inflow. Singing occurs when a trailing edge vortex sheet is shed from the foil and excites one of the vibration modes of the propeller (Sastry 1982). The structural vibration modal frequencies will typically lock-in the vortex frequency rather than that of the shedding frequency for a rigid structure.

The influence of noise uplift is not only a Naval vessel issue but of growing importance because of increasing attention and evidence of its potential impact on the wider marine environment. Typically, a propeller designer mitigates the possibility of blade motion and associated vibrations by designing to reduce blade unsteady forces for a single design condition. This is typically done by careful choice of blade skew and rake distribution. The possibility of blade vibrations is then normally judged based on experience of full scale tests and a limited finite element modal analysis. Full transient simulations are not normally done however CFD is being performed to predict ship loads during manoeuvrers and different sea states. Predicting if propeller blade vibration is an issue is a complex task: vibrations can be caused by either or both the unsteady inflow and self-induced vibration from vortex shedding from the trailing edge.

Simulation of this phenomenon using large scale coupled simulations have been developed (Lloyd 2013) ,(Domenico 2018) however, typically these are impractical for design purposes due to their high computational cost. For practical design tools, it is desirable to reduce the computational cost as much as possible. This is done by modelling the fluid loading and structural response using well defined models. In this case the fluid loading is modelled using Blade Element Momentum Theory and the structure of the propeller blade is idealized as a Timoshenko beam.

The aim is to present the simulation tools developed to model the fluid structure interaction response of a propeller blade and eventually of use for design assessment of propeller candidates across a range of operating conditions. These include: (1) the model for a time accurate one-dimensional, six degree of freedom Timoshenko beam (2) implement an unsteady wake into a blade element momentum theory code and obtain transient deformation of the propeller blade as it passes through the unsteady wake. This will indicate if the propeller blade natural frequencies are excited by the unsteady wake. For this test case the HMRI propeller was used in the wake of the KVLCC2 hull form (Larsson,2010).

2 Methodology

2.1 1D Timoshenko Beam Model

To model the structural response of the blade Timoshenko (1921) beam theory was used. It takes into account shear deformation and rotational bending making it suitable for low aspect ratio beams. This was chosen as it is computationally cheap and can accurately model the structure with relatively few elements. The theory has been used to model the structure of horizontal axis wind turbines and helicopter blades (Yardimoglu 2003). Full details of the theory of Timoshenko beams can be found in Andersen et al (2008) .

The Timoshenko model is defined as a series of nodes each with six degrees of freedom with the stiffness matrix of the beam model computed using the moment of inertia, the elastic modulus and the

beam geometry. The geometry of the beam is determined by the geometric properties of the propeller blade. The length of the beam is the radius of the propeller subtracting the radius of the hub, the thickness of the beam was determined using the maximum thickness of the blade and the breadth determined by the chord at that section. The code to determine the stiffness matrix is capable of changing the chord and thickness of the beam depending on the chord and thickness distribution along the blade. The beam is modelled as a series of cuboidal sections with the height of the element being 70% of the blade thickness and breadth 70% of blade chord to account for the reduced area of the blade section due to the curvature.

This generates a beam capable of motion in 6 degrees of freedom with similar geometric and physical parameters to the propeller blade. To determine the accuracy of the beam model a 3D FEA model was generated using Ansys v19.2. The Ansys model used one blade of the HMRI with the hub. The Ansys model consists of 20,000 solid 210 elements with care to capture the curvature of the blade using increased refinement at the blade tip, trailing edge and leading edge. Two tests were used to determine the accuracy of the beam model in comparison to the Ansys model, these tests were: comparison of transient response, comparison of modal frequencies.

The damping matrix was determined by determining the damping ratio of the 3D FEA model. Firstly, a transient response is developed in the Ansys model by applying a small velocity to the blade tip. A curve fit was added to the transient response of the 3D Ansys model using damping coefficient γ. The general shape of the damping was matched using $y = e^{-\gamma t}$ and γ is adjusted to determine an accurate damping rate. Once an appropriate damping coefficient was determined, the natural frequencies were used to obtain the mass damping coefficient α and the stiffness matrix damping coefficient β as shown in equation 1.

$$\alpha = \frac{\omega_2}{\omega_1}, \quad \beta = \frac{(1-\alpha)\zeta}{\omega_2 - \alpha\omega_1} \tag{1}$$

where ω_n is the modal frequency of mode n and $\zeta = \frac{\gamma}{\omega_2}$. The damping matrix is then determined using $C = \alpha[M] + \beta[K]$ (Capsoni 2013). Once this damping matrix is determined the transient response of the beam model can be compared to the blade model. The modal frequencies are determined through a simple modal analysis where the modal frequencies and shapes are determined by the eigenvalues and eigenvectors. The static analysis is performed by solving the equation $[K]U = [F]$ where [K] is the stiffness matrix U is the deflection vector and F is force matrix

As the propeller will be operating in water it is important to consider the effects of the surrounding fluid on the response of the structure. The Ansys model was placed in a spherical domain of water, with the domain radius only being slightly larger than that of the propeller. The result of placing the propeller in the domain in water is that is lowered the natural frequencies with dry ω_1 = 1144.3Hz and wet ω_1 = 686Hz . The frequency is changed due to added mass. The added mass is modelled in the beam model by assuming each element to be a ellipse at an angle of attack and using equation 2 as found in Bishop (1979).

$$m_{added} = \frac{\rho_{fluid}}{\pi}(t^2 \cos^2(\beta_{beam}) + c^2 \sin^2(\beta_{beam})) \tag{2}$$

Where ρ_{fluid} is the density of the fluid, t is the thickness of the element, c is the chord and β is the element angle of attack relative to the velocity. Now the stiffness $[K]$, mass $[M]$ and damping matrices $[C]$ have been computed the transient response of the beam can be found. To compute the position of all elements at the next time step the $HHT - \alpha$ method has been implemented.

The Hilber-Hughes-Taylor-α ($HHT - \alpha$) is a generalized method of the $Newark - \beta$ numerical integration method which is an unconditionally stable, implicit scheme. The equation of motion of the beam system is $[M]\ddot{x} + [C]\dot{x} + [K]x = f(t)$. Where x is the displacement of the beam elements and $\dot{x}$ is the time derivative and $f(t)$ is the time dependent forces. Full explanation of the $HHT - \alpha$ method can be found in Hughes (1983). For this case the material properties used was that of stainless steel with Youngs modulus 2.1×10^{11}, Poisson ration $\nu = 0.3$ and density $\rho = 7865 kg/m^3$

To further verify the transient response the Fast Fourier Transformation (FFT) of the transient response is found. From this result it can be seen that the vibration response of the beam model and Ansys

Table 1: Structural Comparison

Ansys Model		
Mode	Frequency (Hz)	Shape
1	1144 .3	Bending
2	2493.3	Torsion
Beam Model		
Mode	Frequency (Hz)	Shape
1	1145.2	Bending
2	3723.5	Bending

Table 2: CFD simulation details

Solver	OpenFoamv1712
Method	RANS
Turbulence model	$k-\omega-SST$
Mesh size	$\sim$ 13.5 million cells
K_T (CFD)	0.138
K_T (BEMT)	0.135
K_T (EFD)	0.1307

model match very well in the bending motion with both having a response frequency of $\sim$ $1100Hz$. However, it can also be seen that the beam model does not capture the torsional response shown at $\sim$ $2493.3Hz$. The results of the modal analysis are shown in Table 1 here it is clear that the beam model fails to capture the torsion mode of the Ansys blade model. This is due to the absence of elements in the chordwise direction as when the mode shape of the 2nd mode of the Ansys model is plotted the blade leading and trailing edge are predominantly excited not the bending axis. To model the torsion it would be advisable to replace the beam model with that of a 2D plate. The model is designed to capture the vibration properties of metallic propellers. The use of composite materials will add further complications due to changes in laminate build up which is not modelled using a Timoshenko beam and therefore require further refinement of the modelling approach.

2.2 Blade Element Momentum Theory

Blade element momentum theory is useful for modelling propeller performance. This method combines momentum theory, where the propeller is modelled as an infinitely thin annulus with a momentum change, and blade element theory where the propeller blades are modelled as a 2D lifting surface. This method is computationally cheap and has proven to be reasonably accurate. The method is well established and a comprehensive overview can be found in Molland et al (2017) and Burril (1955).

The BEMT algorithm was adapted to allow for the inclusion of a wake inflow. The disc annulus is split into both radial components and circumferential components. This allows for a more accurate description of the force distribution along the annulus whilst also keeping the computational cost low. For this study the disc annulus is split into 12 radial sections to account for the data given for the HMRI and 36 circumferential sections allowing for 10^o per section (Badoe 2015).

The BEMT code has been verified using previous codes as benchmark cases. Moreover, a CFD case was run to test the open water results and thrust distribution. The details of the CFD are shown on Table 2.

The BEMT and CFD results had good agreement with thrust shown in Table 2. To accurately verify the thrust distribution along each blade the CFD simulation of the HMRI was split into several radial sections to match with the BEMT sections.

The thrust coefficient against the radial position are compared between the CFD and BEMT thrust results. It can be seen from figure 1a that the thrust from the two methods agree well in parts and are poor in others. The BEMT tends to under-estimate the maximum thrust at position $\frac{r}{R} = 0.6$. Although the overall trend between thrust and radial position is captured well. The overall performance curves using BEMT are compared to the values acheived by experimental data are shown in figure 1b. The curves agree particularly well for efficiency however the BEMT code slightly overestimates the thrust and torque coefficients. This can be improved by appropriately correcting the 2D lift and drag curves using Reynolds number corrections.

2.3 Coupling Algorithm

To find a time dependent solution to the structural response due to the fluid loading the Timoshenko beam and Blade Element Momentum theory codes must be coupled. This can be done in two ways: i) One-way coupling is where the fluid loading is applied directly to the structure to obtain a response as

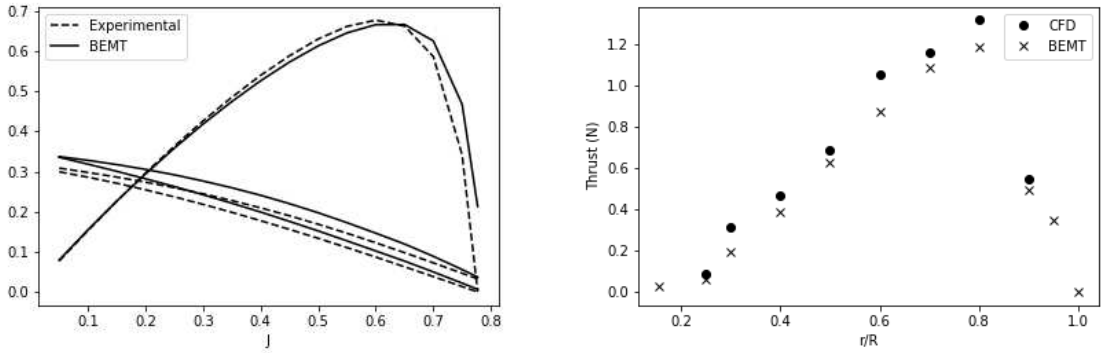

(a) Performance Curves of HMRI Propeller from Experimental and Blade Element Momentum Theory

(b) Comparison between CFD and BEMT for Thrust distribution along the blade

Fig. 1: Propeller performance metrics

done in Benra (2011). ii) two-way coupling where the deformation of the structure is iteratively fed back to the fluid solver. The change in geometry will then change the loading on the blades which will then further change the geometry at every timestep.

In this case the one way coupling is achieved by firstly splitting the BEMT output into 36 sections representing 10^o per fluid time step, this keeps computational cost low but limits the frequency range that can be captured. Using the rotational rate it is a simple calculation to determine the loading on the beam at each time step. The loading for the BEMT is appropriately spread over the FEA grid as the FEA grid is much finer than the BEMT grid. The transient response of the beam is solved using a time step of 0.001s and the loading is changed at each timestep as the beam rotates through the hull wake. To obtain an accurate response a static analysis is performed first to set the initial conditions of the beam bending and deflection. This is to avoid the propeller blade going from unloaded to fully loaded thus creating an impulse force causing the bending frequency of the blade to be excited.

2.4 Simulation of KVLCC2

The KVLCC2 is a hull form used in several validation cases such as the Gothenburg 2010 workshop and the SIMMAN 2020 workshop. There has been extensive experimental data acquired for this hull form therefore making it a strong validation case (Larsson,2010). The simulation has been conducted at model scale with the domain shown in figure 2. The model L_{pp} is 6.8927 m with in inlet velocity of 1.702 m/s resulting in $Fr = 0.142$. This was to coincide with available experimental data. It is important to note that the free surface has not been modelled in this simulation to reduce computational cost. Ideally this will be modelled to ensure accuracy and test its requirements.

3 Results

To understand the deflection of the blade the inflow to the propeller has been taken as the wake from the KVLCC2 hull form. The axial velocity is shown in figure 3b as a contour plot with a quiver plot showing the tangential and radial velocity components when the hull form in the straight ahead position. The flow pattern here is relatively clean with the flow slowing at the north position due to the friction of the hull and increasing towards the free stream velocity the further away from the hull the fluid is . The experimental resistance is approximately 34.02N and the numeric resistance gives a value of 36.6N with a mesh size of 30 million cells. Although this is fairly close there is still a slight error. Moreover, the characteristic bilge vortex 'hook' is not well captured in the CFD simulation. This can be due to many issues such as turbulence model or meshing. The y^+ value in the simulation was not consistently less than one. The y^+ value ranges from 0.6 to 200 so the boundary layer has not been held well throughout the hull form.

The one way coupling technique were used as described previously, however the inflow used was

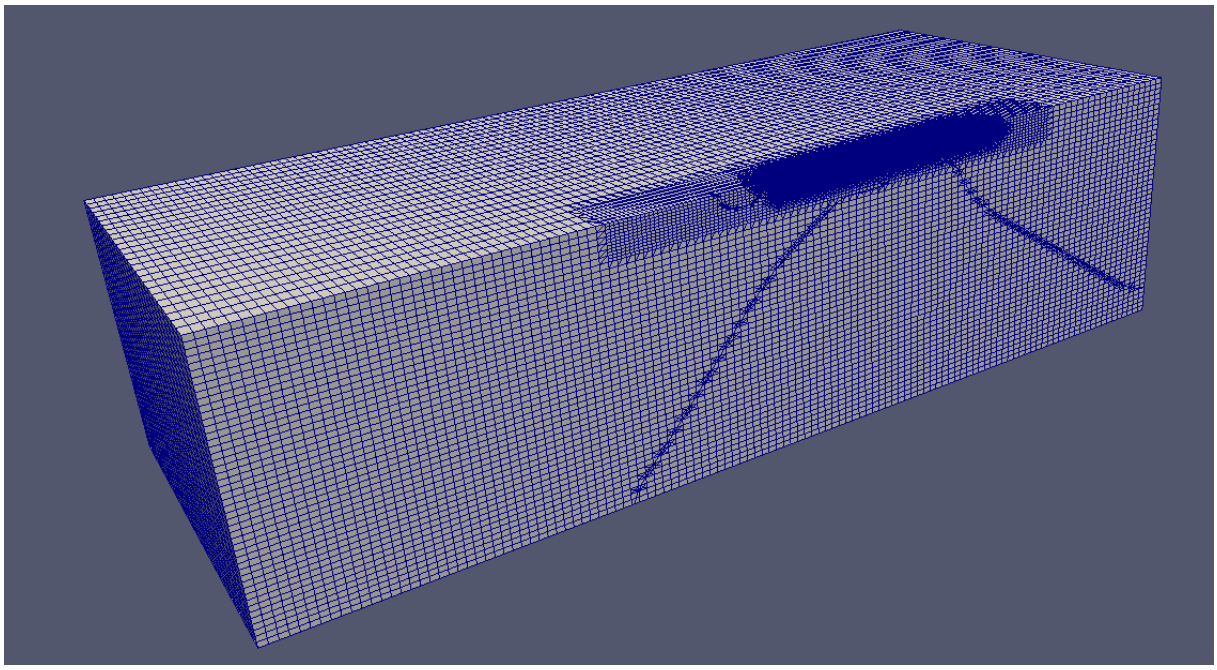

Fig. 2: KVLCC2 Simulation Domain. Note the two lines from the bottom to the hull is a visulisation issue and not due to refinement. Additional mesh refinement occurs at the hull and into the wake.

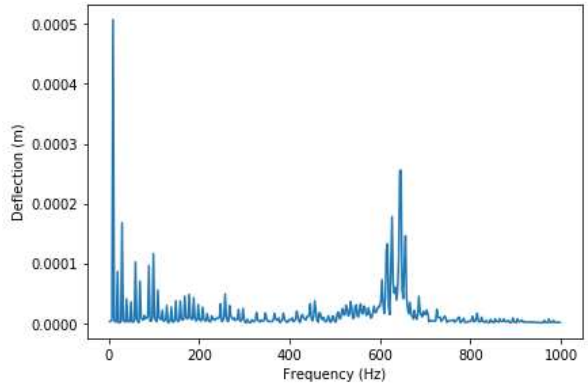

(a) FFT of the response of the beam model to the wake from the KVLCC2 hull form using one-way coupling.

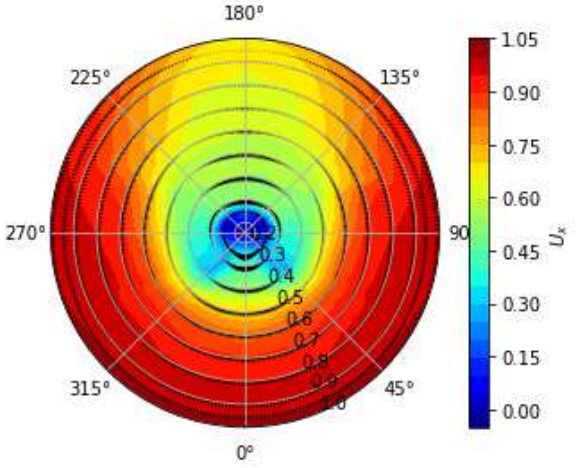

(b) Axial Inflow into propeller from KVLCC2 simulation.

Fig. 3: Propeller vibration properties and wake inflow from KVLCC2

that shown in figure 3b. The FFT of the response of the blade tip is shown in figure 3a.

Several peaks exist at the rotation rate of the propeller which is at 9.9 rps and its multiples. This is expected as the wake is steady and clean hence there will be cyclic loading as the propeller rotates. Another peak occurs at the natural wet frequency of the propeller being excited by the axial bending force. With the tangential velocity included there are many secondary peaks in the frequency distribution. The tangential velocity is modelled in the BEMT code by introducing a second angular momentum source a''. Depending on the wake angular velocity this can cause the blade section to increase or decrease thus changing the propeller performance.

4 Conclusion

The coupling between a transient timoshenko beam and blade element momentum theory has been achieved. Modelling techniques have been demonstrated to effectively model the structural and performance of the propeller. Further work includes: verification and modification of the Beam theory and BEMT to ensure accurate results. Moreover, simulations of ships in manoeuvres will be conducted to be able to apply unsteady wakes into the coupling technique. The use of unsteady wakes would give a far more interesting dynamic response of the propeller blades and is key to move away from the static analysis.

Acknowledgements

The authors acknowledge the ESPRC award reference NGCM 1789206 for supporting the research. The authors also acknowledge the use of the IRIDIS High Performance Computing Facility.

References

Andersen, L., Nielsen, S, 2008, Elastic Beams in Three Dimensions, Aalborg University

Badoe, C. 2015, Design practice for the stern hull of a future twin-skeg ship using a high fidelity numerical approach, Thesis for Doctor of Philosophy, University of Southampton

Benra F K, Hans Josef Dohmen, Ji Pei, Sebastian Schuster, and Bo Wan, 2011, ?A Comparison of One-Way and Two-Way Coupling Methods for Numerical Analysis of Fluid-Structure Interactions,? Journal of Applied Mathematics, vol. 2011, Article ID 853560, 16 pages.

Bishop, R.E.D,1979, Hydorelasticity of Ships, Cambridge University Press

Burril L.C , 1955 , The optimum diameter of marine propellers: A new design approach , Transactions of North East Coast Institution of Engineers and Ship-builders Vol 72 pp 57-82

Capsoni. A, 2013 On damping effects in Timoshenko beams International Journal of Mechanical Sciences, Volume 73, p 27-39

Di Domenico, M. (2018). Fluid structure interaction analysis: vortex shedding induced vibrations. Procedia Structural Integrity

Hoekstra, M,1977, An investigation into the difference between nominal and effective wakes for two twin-screw ships , Educational and Psychological Measurement

Hughes, T.J.R.,1983, Analysis of Transient Algorithms with Particular Reference to Stability Behavior. in Computational Methods for Transient Analysis North-Holland, pp. 67?155.

Kiam Beng Yeo, Rosalam Sabatly, Wen Yee Hau and Cheah Meng Ong, 2014. Effects of Marine Propeller Performance and Parameters Using CFD Method. Journal of Applied Sciences, 14: 3083-3088.

Liaghat, T. Guibault, F. Allenbach, L. Nennemann, B. , 2014 , Two-Way Fluid-Structure Coupling in Vibration and Damping Analysis of an Oscillating Hydrofoil , Volume 4A: Dynamics, Vibration, and Control

Lloyd. (2013). Large eddy simulations of inflow turbulence noise: application to tidal turbines. Thesis University of Southampton.

Molland, A.F., Turnock, S.R., and Hudson D.A., Ship Resistance and Propulsion, Cambridge University Press 2nd Ed(2017)

Sastry, H, 1982, Singing Propellers, Defence Science Journal Volume 32 Issue 1 p 67-73

Timoshenko, S. P., 1921, On the correction factor for shear of the differential equation for transverse vibrations of bars of uniform cross-section, Philosophical Magazine, p. 744.

Yardimoglu, B., 2003, Finite element model for vibration analysis of pre-twisted Timoshenko beam, Journal of Sound and Vibration 273 (2004) 741?754

Assessing ReFRESCO Compressible Single Phase Flow Solver Numerical Robustness

João Muralha*, Luís Eça*, and Christiaan Klaij†
*IST Técnico Lisboa, Lisbon/Portugal, †MARIN Maritime Research Institute Netherlands, Wageningen/The Netherlands
joao.muralha@tecnico.ulisboa.pt

1 Introduction

For must numerical simulations done in naval and offshore applications considering the fluids to be incompressible is a valid and reasonable approximation. Specific phenomena like slamming, sloshing and cavitation may require fluid compressibility to be taken into consideration. The goal of the present development of ReFRESCO is to modify the current flow solver to accurately solve compressible two-phase flows.

The first stage of this development was the introduction of a pressure-based single-phase flow solver. Before continuing ReFRESCO development, it is necessary to check the numerical convergence properties, i.e., the robustness (iterative errors) and order of grid convergence (discretization errors) of the solver. For this purpose, two test cases were used: the two dimensional zero pressure gradient turbulent flat plate and the two dimensional flow over a bump. These test cases were selected from NASA Langley Research Center Turbulence Modeling Resource webpage (Rumsey, 2009).

In the present work, the results, of ReFRESCO single-phase compressible flow solver are also compared to the results from CFL3D and FUN3D, which are available at Rumsey (2009).

2 ReFRESCO Flow Solver

ReFRESCO (`www.refresco.org`) is a CFD code aimed for maritime applications. The equations are discretised using a finite volume approach with cell-centered collocated variables. A face based implementation permits the use of grids with arbitrary cells geometries, as well as the use of grids with hanging nodes. Equations are linearised using Picard's method.

The flow solver used in the present work is a pressure based solver of the compressible Navier-Stokes equations. Mass conservation is ensured by means of a pressure-correction equation based on the SIMPLE algorithm. The pressure-velocity-density used in the derivation of the pressure correction equation is described in Ferziger and Perić (2001) and Muralha et al. (2018). The compressible Navier-Stokes equations require a relation between temperature, density and pressure, that in the present solver is given by the perfect gas equation of state.

2.1 Turbulence modelling in compressible flows

In compressible turbulent flows, density and temperature fluctuations must be taken into account. If the Reynolds average are applied to compressible flows the complexity of the closure approximations would increase in comparison to incompressible flows, for example, a triple correlation involving density and velocities fluctuations appears. The time-averaged equations can be simplified by applying a density-weighted averaging procedure, known as Favre averaging (Wilcox, 1998). It is important to note that this type of averaging procedure only removes the density fluctuations from the averaged equations, i.e., it is a mathematical simplification.

The steady Favre averaged mean conservation equations are:

$$\frac{\partial}{\partial x_i}\left(\overline{\rho}\tilde{u}_i\right) = 0 \tag{1a}$$

$$\frac{\partial}{\partial x_j}\left(\overline{\rho}\tilde{u}_j\tilde{u}_i\right) = -\frac{\partial \overline{p}}{\partial x_i} + \frac{\partial}{\partial x_j}\left[\overline{\tau}_{ij} - \overline{\rho u_j'' u_i''}\right] \tag{1b}$$

$$\frac{\partial \overline{p}}{\partial t} + \frac{\partial}{\partial x_j}\left[\overline{\rho}\tilde{u}_j\left(c_p\tilde{T} + \frac{1}{2}\tilde{u}_i\tilde{u}_i\right) + \tilde{u}_j\frac{1}{2}\overline{\rho u_i'' u_i''}\right] = \frac{\partial}{\partial x_j}\left[-\overline{q_j} - c_p\overline{\rho u_j'' T''} + \overline{\tau_{ij}u_i''} - \frac{1}{2}\overline{\rho u_j'' u_i'' u_i''}\right] + \frac{\partial}{\partial x_j}\left[\tilde{u}_i\left(\overline{\tau}_{ij} - \overline{\rho u_i'' u_j''}\right)\right] \quad (1c)$$

where u_i, ρ, p, T and c_p represent the i$^{\text{th}}$ component of the velocity vector, density, pressure, temperature and specific heat at constant pressure and $\overline{\tau_{ij}}$ and q_j are given by:

$$\overline{\tau}_{ij} = \mu\left(\frac{\partial \tilde{u}_i}{\partial x_j} + \frac{\partial \tilde{u}_j}{\partial x_i}\right) - \frac{2}{3}\mu\frac{\partial \tilde{u}_k}{\partial x_k}\delta_{ij},\ \overline{q}_j = -\kappa\frac{\partial \tilde{T}}{\partial x_j}$$

with μ and κ being the dynamic viscosity, which is calculated by Sutherland's law, and thermal conductivity coefficient. The overline denotes Reynolds average and the tilde represents mass-averaged.

The Favre averaged momentum equations take the same form as the momentum Reynolds averaged equations and require the term $\tau_{ij} = -\overline{\rho u_j'' u_i''}$ to be modelled. This term is modelled using Boussinesq approximation:

$$\tau_{ij} = -\overline{\rho u_j'' u_i''} = \mu_t\left(\frac{\partial \overline{u}_i}{\partial x_j} + \frac{\partial \overline{u}_j}{\partial x_i}\right) - \frac{2}{3}\mu_t\frac{\partial \overline{u}_k}{\partial x_k}\delta_{ij} - \frac{2}{3}\overline{\rho}k\delta_{ij} \quad (2)$$

where $k = (1/2)\,\overline{u_i'' u_i''}$ is the kinetic energy of the fluctuating field and μ_t is the eddy viscosity.

In the energy equation the following terms require modelling:

$$c_p\overline{\rho u_j'' T''} \quad \overline{\tau_{ij}u_i''} \quad -\frac{1}{2}\overline{\rho u_j'' u_i'' u_i''}$$

The turbulent heat flux vector, first term starting from the left, is modelled using Reynolds analogy:

$$c_p\overline{\rho u_j'' T''} = -\frac{\mu_t c_p}{Pr_t}\frac{\partial \tilde{T}}{\partial x_j} \quad (3)$$

where Pr_t is the turbulent Prandtl number that is considered constant, 0.90 for air.

The remaining two terms, molecular diffusion and turbulent transport, are usually ignored, which is a good approximations for flows up to supersonic Mach number range.

Eddy viscosity is calculated using Spalart-Allmaras one equation turbulence model. According to Allmaras et al. (2012), the turbulence model formulation implemented in ReFRESCO is valid for both incompressible and compressible flows, so no significant changes were made.

3 Test Cases

As mentioned in Section 1, the two cases used to test the solver robustness are the steady state flow over a flat plate and over a bump. These test cases are part of NASA Langley Research Center Turbulence Modeling Resource verification case list, that provides information about each test case domain size and boundary conditions. Results for two CFD codes (CFL3D and FUN3D) in sets of geometrically similar grids, as well as the grid sets, are available. For both cases, the flow has an undisturbed Mach number (M_∞) of 0.2 and a temperature (T_∞) of 300K. The fluid is considered to be a perfect gas with specific heat ratio of 1.4 and Prandtl number equal to 0.72. The flow over the flat plate has a Reynolds number based on unit length ($L = 1$ m) equal to 5×10^6, while for the flow over the bump the Reynolds number is 3×10^6.

Figure 1 illustrates the domain of both test cases and indicates the boundary conditions used at each boundary. Form Fig. 1a, it is possible to see that the plate extends from $x = 0$ m to $x = 2$ m, the inlet is situated at $x = -0.3333$ m and the outlet coincides with the end of the plate. The domain used for the flow over a bump is considerably larger than for the flat plate. The inlet and outlet are located 25 meters apart from the beginning and end of the bump and the top boundary is located at $y = 5$ m, giving a domain height 100 times larger than the bump height. Although large, these type of dimensions are typical of compressible flow simulations. The bump starts at $x = 0$ m and ends at $x = 1.5$ m.

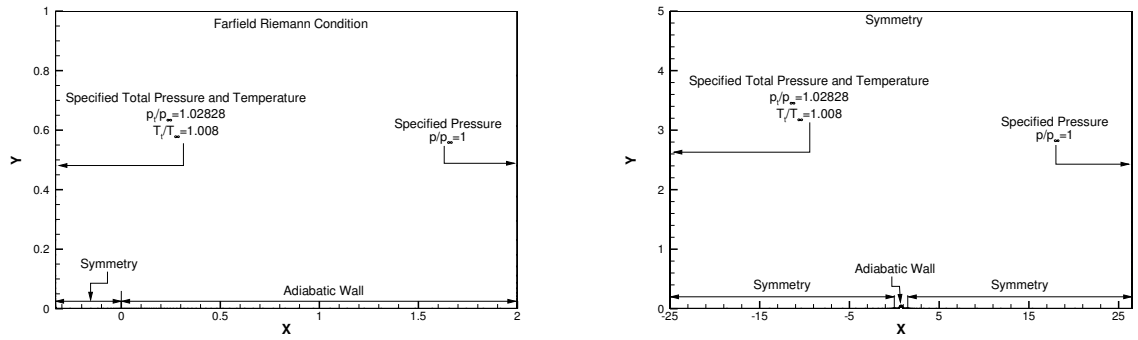

(a) Flat Plate (b) Bump

Fig. 1: Illustrations of the domain and applied boundary conditions used in the simulation of flow over a flat plate (left) and over a bump (right), as specified in the Turbulence Modeling webpage.

For both cases, the inlet flow is considered to be isentropic and total pressure, p_T, and total temperature T_T are specified, as well as the ratio between turbulent kinetic viscosity and the fluid kinetic viscosity ($\nu_{t,\infty}/\nu = 0.214038$). The implementation of the total pressure boundary condition in pressure based solvers is fully described by Ferziger and Perić (2001). At the outlet, pressure is specified and all other quantities are extrapolated from the interior cell, with exception of density. It is calculated based on the specified pressure and on the extrapolated temperature values from the equation of state (Rudy and Strikwerda, 1981). In the flat plate case a far-field Riemann boundary condition is used at the domain top. This boundary condition specifies variables according to one dimensional Riemann invariants of the Euler equations, see Hirsch (1991) for detailed explanation. For all remaining boundaries a symmetry boundary condition is applied.

4 Numerical Settings

The discretisation of the convective and diffusive terms of all transport equations was performed using second order schemes, limited QUICK for the convective term and Gauss theorem for gradient calculation. The simulations were stopped when the L_∞ norm of the normalised residuals of all solved equations were inferior to 10^{-8} for the flow over a flat plate and 10^{-7} for the flow over a bump.

The grids are illustrated in Fig. 2. The number of cells of the grids used in the flat plate case ranges from 816 to 208896, while on the bump case it ranges from 3520 to 901120. The maximum dimensionless near-wall cell size, y^+_{max}, is inferior to 1.15 in the flat plate grids and 0.75 in the bump grids.

For both test cases sets of five geometrically similar grids were used to estimate the numerical uncertainty and the order of grid convergence, p, based on the procedure introduced by Eça and Hoekstra (2014).

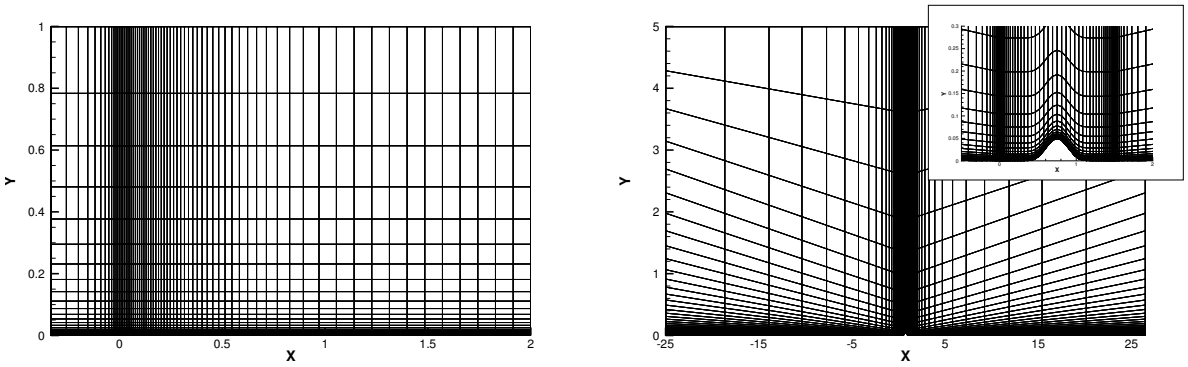

(a) Flat Plate (b) Bump

Fig. 2: Grid topology used in the simulations.

5 Iterative Convergence

Iterative convergence of the flow solver is illustrated in Fig. 3, that presents the L_∞ norm of the normalised residuals as a function of the iteration counter. The data show that the convergence of the momentum and energy equations is noisy. The origin of the noise in the convergence is the inlet boundary condition (specified total pressure and total temperature). In this type of boundary condition velocity, temperature and density are calculated at every iteration to comply with specified values of total pressure and total velocity and the perfect gas model. Figure 4 shows the iterative convergence behaviour for the simulation run using the same grid as in Fig. 3b, but with velocity, temperature and density specified at the inlet boundary. The change in inlet boundary condition will affect the obtained results, but as the domain is relatively large the change in results is small (see Section 6).

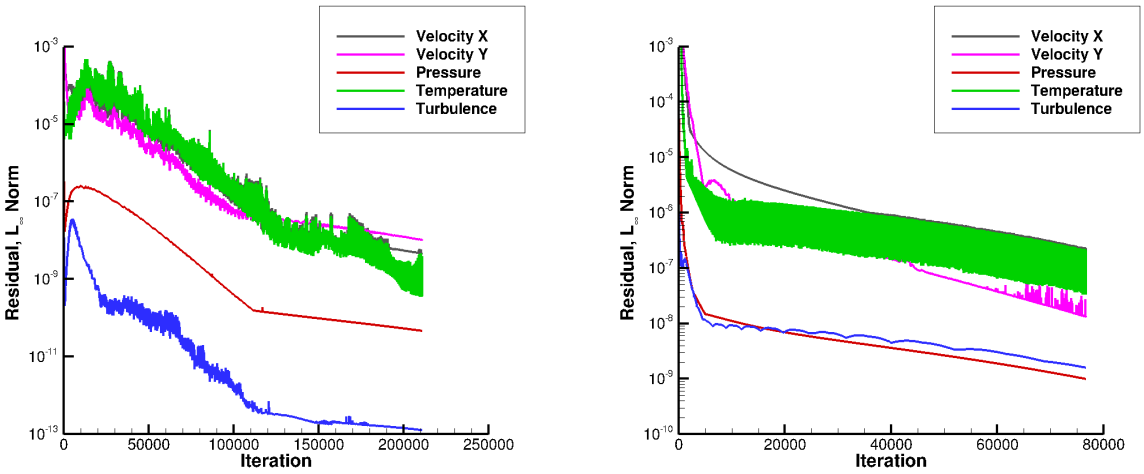

(a) Flat plate, grid with 544×384 cells.

(b) Bump, grid with 352×160 cells.

Fig. 3: Evolution of the L_∞ norm of the residuals for the simulation of flow over a flat plate and over a bump.

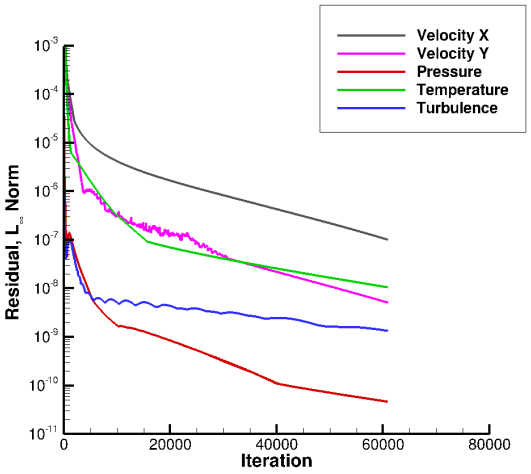

Fig. 4: L_∞ norm of the residuals for the bump case simulated in a grid with 352×160 cells and specifying velocity, temperature and density as inlet boundary conditions.

6 Grid Convergence

The select quantities of interest to determine the grid convergence properties of ReFRESCO include force coefficients (integral quantities) and skin friction coefficient (local quantities). For all the selected quantities, results obtained with CFL3D and FUN3D (density based flow solvers) in the same grids are available at Rumsey (2009). Table 1 compares the friction coefficients obtained in the ReFRESCO simulations (last line) with the results available for CFL3D and FUN3D. The friction coefficient for the

flow over a flat plate is calculated at approximately $x = 0.97$ m and the frictions coefficients for the bump case are calculated at approximately $x = 0.63$ m (upstream from bump peak, $C_{f,u}$), $x = 0.75$ m (bump peak, $C_{f,p}$) and $x = 0.87$ m (downstream from bump peak, $C_{f,d}$). The results obtained for the integral quantities are presented in Table 2. These tables show that ReFRESCO results are in good agreement with those determined by CFL3D and FUN3D.

Table 1: Results obtained using the finest grid for the local quantities of interest.

Code	Flat Plate	Bump		
	$C_{f,x} \times 10^{-3}$	$C_{f,u} \times 10^{-3}$	$C_{f,p} \times 10^{-3}$	$C_{f,d} \times 10^{-3}$
CFL3D	2.7056	5.1852	6.1494	2.6777
FUN3D	2.7054	5.1869	6.1514	2.6808
ReFRESCO (p_T and T_T)	2.7079	5.1931	6.1597	2.6870
ReFRESCO (u, T and ρ)	-	5.2126	6.1614	2.6915

Table 2: Results obtained using the finest grid for the integral quantities of interest.

Code	Flat Plate	Bump			
	$C_D \times 10^{-3}$	$C_D \times 10^{-3}$	$C_{D,v} \times 10^{-3}$	$C_{D,p} \times 10^{-4}$	$C_L \times 10^{-2}$
CFL3D	2.8599	3.5724	3.1907	3.8170	2.4900
FUN3D	2.8525	3.5611	3.1787	3.8231	2.4942
ReFRESCO (p_t and T_t)	2.8621	3.5758	3.1948	3.8102	2.4975
ReFRESCO (u_i, T and ρ)	-	3.5796	3.1992	3.9038	2.4981

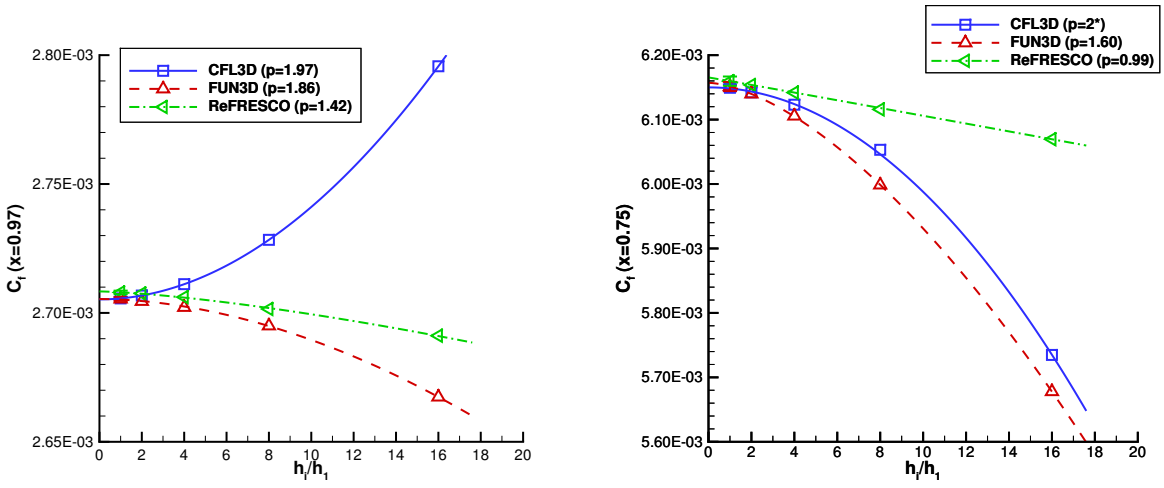

(a) Flat Plate, C_f at location x=0.97

(b) Bump, C_f at bump peak

Fig. 5: Grid convergence of the friction coefficient, C_f, and of the drag coefficient, C_D

Figure 5 illustrates the grid convergence of the friction coefficient for the flat plate (left plot) and bump (right plot) cases. Although second order convergence was achieved for manufactured solutions (laminar flow), for these test cases observed orders of grid convergence are lower than 2, with the bump test case leading to $p = 1$. The turbulence model might be responsible for the reduction of the observed order of grid convergence. As illustrated in Eça et al. (2018), the values of p obtained with the incompressible solver depend on the value of y^+. Nonetheless, the error constant obtained with ReFRESCO is smaller than those derived from the CFL3D and FUN3D data. Therefore, although observed p is larger for CFL3D and FUN3D than for ReFRESCO, the change in the solutions with grid coarsening is smaller for ReFRESCO than for the other two flow solvers.

7 Conclusions

This paper presents a study on the numerical convergence properties of ReFRESCO single phase compressible flow solver. To conduct this analysis two test cases were selected from NASA Langley Research Center Turbulence Modeling Resource webpage (Rumsey, 2009): the flow over a flat plate and over a bump. Iterative convergence properties are illustrated for the two test cases using the L_∞ norm of the normalised residuals. Observed orders of grid convergence are determined for skin friction coefficients (local flow quantities) and force coefficients (integral flow quantities). The selected quantities of interest are compared with the results of two density based solvers (CFL3D and FUN3D) available in the open literature.

Iterative convergence is significantly affected by inlet boundary conditions based on total temperature and total pressure, which originates oscillations in the convergence history and the need to use low under-relaxation parameters. Iterative convergence is improved when velocity, density and temperature are imposed at the inlet. However, such boundary condition requires a location of the inlet boundary sufficiently upstream to impose undisturbed flow conditions. Results obtained for the flow over a bump showed similar results for the two alternatives.

A good agreement between ReFRESCO, CFL3D and FUN3D solutions was obtained, but the observed order of grid convergence obtained with ReFRESCO is lower than that exhibited by the other two solvers. On the other hand, the error constant of the ReFRESCO solution less sensitive to grid coarsening.

As for the tests reported in Muralha et al. (2018) performed with manufactured solutions, the present study suggests that the choice and implementation of the boundary conditions has a decisive influence on the numerical convergence properties of the pressure based compressible flow solver.

Acknowledgements

The authors acknowledge the financial support of Fundação para a Ciência e Tecnologia throught a PhD grant attributed to the first author under the Bolsas de Doutoramento program. This research is also partly funded by the Dutch Ministry of Economic Affairs.

References

Allmaras, S. R., Johnson, F. T., and Spalart, P. R. (2012). Modifications and Clarifications for the Implementation of the Spalart-Allmaras Turbulence Model. In *Seventh International Conference on Computational Fluid Dynamics (ICCFD7)*, pages 1–11.

Eça, L. and Hoekstra, M. (2014). A procedure for the estimation of the numerical uncertainty of CFD calculations based on grid refinement studies. *Journal of Computational Physics*, 262:104–130.

Eça, L., Pereira, F. S., and Vaz, G. (2018). Viscous flow simulations at high Reynolds numbers without wall functions: Is $y^+ \simeq 1$ enough for the near-wall cells? *Computers & Fluids*, 170:157–175.

Ferziger, J. H. and Perić, M. (2001). *Computational Methods for Fluid Dynamics*. Springer-Verlag GmbH, 3rd edition.

Hirsch, C. (1991). *Numerical Computation of Internal and External Flows*, volume 2. John Wiley & Sons Ltd.

Muralha, J., Eça, L., and Klaij, C. (2018). Application of the SIMPLE Algorithm to a Manufactured Subsonic Flow. In *NuTTS*.

Rudy, D. H. and Strikwerda, J. C. (1981). Boundary Conditions for Subsonic Compressible Navier-Stokes Calculations. *Computers & Fluids*, 9(3):327–338.

Rumsey, C. (2009). Turbulence Modelling Resources.

Wilcox, D. C. (1998). *Turbulence Modeling for CFD*. DCW Industries, 2nd edition.

Comparison of Wall Function Model with Low-Reynolds Number Model under Roughness Effect Condition at Actual Ship Scale

Kunihide Ohashi*
*National Maritime Research Institute, Japan
k-ohashi@nmri.go.jp

1 Introduction

The wall function model with a roughness effect is developed and applied to the cases of the two-dimensional(2D) flat plate and flows around the actual ship which has the measured data at the actual sea test. The wall function is composed by a non-dimensionalized roughness height, turbulent kinetic energy and a specific frequency based on the assumption of the local equilibrium. The distributions of the non-dimensionalized velocity based on the non-dimensionalized distance are compared with the curves of the low-Reynolds number model with changing the roughness height and Reynolds number. Additionally, the velocity contours of the wall function method are compared with the results of the low-Reynolds number model and the actual sea test. The applicability of the present method is examined through the detailed comparisons.

2 Computational method

2.1 Base solver

An in-house structured CFD solver (Ohashi et al.(2018)) is employed. The governing equation is 3D RANS equation for incompressible flows. Artificial compressibility approach is used for the velocity-pressure coupling. Spatial discretization is based on a finite-volume method. A cell centered layout is adopted in which flow variables are defined at the centroid of each cell and a control volume is a cell itself. Inviscid fluxes are evaluated by the third-order upwind scheme based on the flux-difference splitting of Roe. The evaluation of viscous fluxes is second-order accurate. The first order Euler implicit scheme is employed for the temporal step. The linear equation system is solved by the symmetric Gauss-Seidel (SGS) method.

The Reynolds stress components are evaluated by one of the linear two equation model, the $k-\omega$ SST model. For free surface treatment, an interface capturing method with a single phase level set approach is employed. The propeller effects are accounted for according to the body forces derived from the propeller model(Ohashi et al.(2018)), which is based on the potential theory.

2.2 Overset grid method

The weight values for the overset grid interpolation are determined by an in-house system(Kobayashi et al.(2016)). The detail of the system can be found on Kobayashi et al.(2016), the summary is described.

1. The priority of the computational grid is set.
2. The cells of a lower priority grid and inside a body is identified (called as in-wall cell in here).
3. Receptors cells which the flow variables have to be interpolated from donor cells are defined. Two cells on a higher priority grid and facing to the outer boundary are set as receptor cells to satisfy the third order discretization of NS solver. Additionally, two cells neighborhood of in-wall cells, the cells of a lower priority grid and inside the domain of a higher priority grid are also set as the receptor cell.
4. The weight values for the overset interpolation are determined by solving the inverse problem based on Ferguson spline interpolation.

Flow variables of the receptor cell are updated when the boundary condition is set. The forces and moments are integrated on the higher priority grid to eliminate the lapped region on body surfaces. At first, the cell face of the lower priority grid is divided into small pieces. Secondly, the small piece is projected to the cell face of the higher priority grid by using the normal vector of the higher priority

face. Then the 2D solid angle is computed and the small piece is decided in or out of the higher priority face. Once the small piece is in the higher priority face, the area ratio of the piece is set to zero. Finally, the area ratio is integrated on the lower priority face, then we have the ratio to integrate the forces and moments on lower priority face.

2.3 Wall function with roughness model

Non-dimensionalized roughness height is defined by using the frictional velocity u_τ and roughness height h_r as follows:

$$h_r^+ = \frac{u_\tau h_r}{\nu} \tag{1}$$

Non-dimensionalized form of Eq.(2) is given as follows:

$$h_r^+ = u_\tau h_r R \tag{2}$$

Shear stress can be obtained by the following equation applying the wall function.

$$\tau_w = c_\mu^{1/4} k_p^{1/2} \frac{\kappa U_p}{ln\left(\frac{Ey^+}{(1+C_s h_r^+)}\right)} \tag{3}$$

where k_p is the turbulent kinetic energy at the first point away from a wall surface, and the second term is based on the correction formula to take into account the roughness effect suggested by Cebeci(Cebeci et al.(1977)). c_μ is 0.09, E=9.8, $\kappa = 0.41$ and $C_s = 0.3$ based on the assumption of the local equilibrium. U_p is the wall parallel component at the first point away from a wall surface.

The boundary condition of the specific frequency ω on a wall surface is determined by the condition of the dissipation rate ϵ as follows;

$$\epsilon = \frac{C_\mu^{3/4} k_p^{3/2}}{\kappa y_p} \tag{4}$$

$$\omega = \frac{\epsilon}{C_\mu k} \tag{5}$$

where y_p is the distance from the wall surface at the first cell center position.

The velocity profile which is proposed by Apsley(Apsley(2007)) is utilized for the comparison.

$$u^+ = y_{v0}^+ + \frac{1}{\kappa} ln\left(\frac{1+\kappa(y^+ - y_v^+)}{1+\kappa(y_{v0}^+ - y_v^+)}\right) \tag{6}$$

$$y_v^+ = \begin{cases} C - \frac{1}{\kappa} ln(\kappa) & C - \frac{1}{\kappa} ln(\kappa) \geq 0 \\ \frac{1}{\kappa}(1 - e^{-\kappa(C - \frac{1}{\kappa} ln(\kappa))}) & C - \frac{1}{\kappa} ln(\kappa) < 0 \end{cases} \tag{7}$$

$$C = 8 - \frac{1}{\kappa} ln(h_R^+ + 3.152) \tag{8}$$

$$y_{v0}^+ = max(y_v^+, 0) \tag{9}$$

2.4 Uncertainty analysis

Uncertainty analysis based on the Richardson extrapolation method with the FS method(Xing et al.(2010)) is performed. The grid discretization uncertainty is evaluated due the steady condition on the present study, and the three systematic grids with the uniform refinement ratio $r_G = \sqrt{2}$ are utilized. Once, the solutions S_3, S_2, S_1 relevant from the coarse grid to fine grid are obtained, the solution changes are defined as $\epsilon_{12} = S_2 - S_1$, $\epsilon_{23} = S_3 - S_2$. The convergence ratio R is $\epsilon_{12}/\epsilon_{23}$, and R takes the monotonic convergence with $0 < \epsilon_{12}/\epsilon_{23} < 1$. The order of accuracy p and the error δ_{RE} are defined as follows:

$$p = \frac{ln(\epsilon_{23}/\epsilon_{12})}{ln(r_G)}, \quad \delta_{RE} = S_1 - S_0 = \frac{\epsilon_{12}}{r_G^p - 1} \tag{10}$$

The uncertainty is estimated by the following equation using the variable $P = p/p_{th}$. Theoretical accuracy p_{th} is assumed as $p_{th} = 2$.

$$U_{SN} = \begin{cases} (2.45 - 0.85P)|\delta_{RE}|, & 0 < P \leq 1 \\ (16.4P - 14.8)|\delta_{RE}|, & P > 1 \end{cases} \tag{11}$$

3 Computational results

3.1 2D Flat plate case

A 2D flat plate case is selected as the fundamental test case. The Reynolds number is set 1.0×10^7 and 1.0×10^9 based on the plate length L as the reference length. Table 1 shows the computational grids with the three resolutions. Fig. 1 shows the computational grid, the boundary conditions and the definitions of directions of the divisions. The distance between the wall surface and the top boundary is 0.1L.

Table 1: Division number of computational grid

Grid	IM×JM
Coarse(G_3)	193×113
Medium(G_2)	273×161
Fine(G_1)	385×225

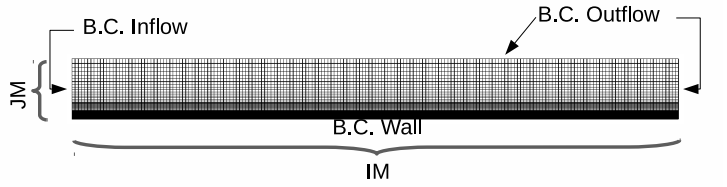

Fig. 1: Computational grid

Table 2 shows the non-dimensionalized distance y^+ and resistance coefficient with changing the minimum spacing on wall at $R = 1.0 \times 10^7$. Although, the resistance coefficient takes higher value at the lower range of y^+, the influence of the minimum spacing on wall is relatively small in the every case with changing the roughness height. The non-dimensionalized distance y^+ is set as 200 hereafter.

Table 2: Resistance coefficient with changing roughness height and minimum spacing on wall ($\times 10^{-3}$, $R = 1.0 \times 10^7$)

y^+	1×10^{-5}	2.5×10^{-5}	5×10^{-5}	7.5×10^{-5}
30	3.034	3.458	3.947	4.323
75	2.985	3.377	3.860	4.216
100	3.061	3.401	3.810	4.134
150	3.026	3.375	3.805	4.147
200	3.061	3.401	3.810	4.134
300	3.128	3.464	3.854	4.155

Table 3 shows the comparison of the resistance coefficient with changing the roughness height from $h_r = 1 \times 10^{-5}$ to $h_r = 7.5 \times 10^{-5}$ and the grid resolutions at the Reynolds number $R = 1.0 \times 10^7$. The roughness height is non-dimensionalized by the plate length L, and the roughness height is selected in the range where the resistance coefficient becomes larger than the value of the smooth surface. Although the uncertainty is resulted in the range from 7% to 17% of the solution of the fine grid, the differences between the three grids are limited within 1%. The results of the wall function indicate from 1% to 3% higher than the result of the low-Reynolds number model(Ohashi(2019)), and the resistance coefficient increases with the roughness height which is similar to the results of the empirical formula.

Table 3: Comparison of resistance coefficient ($\times 10^{-3}$, $R = 1.0 \times 10^7$)

Grid	1×10^{-5}	2.5×10^{-5}	5×10^{-5}	7.5×10^{-5}
Coarse	3.061	3.402	3.810	4.134
Medium	3.072	3.415	3.825	4.152
Fine	3.085	3.429	3.841	4.169
$U_{SN}\%G_1$	7.27	14.52	16.86	16.5
Fine(Low-Re)	3.036	3.295	3.780	4.040
Emp.	2.872	3.350	3.788	4.081

Fig. 2 shows the distribution of u^+ and y^+ with changing the roughness height at the positions $x/L = 0.5$ and $x/L = 0.9$. For the reference, the correlations based on the smooth surface condition and Eq.(6) with the roughness $h_r = 7.5 \times 10^{-6}$ are also shown in Fig. 2. The velocity distributions change at the logarithmic region with the roughness height which is similar to the results of the low-Reynolds number model(Ohashi(2019)), and the first point away from a wall surface locates at $y^+ = 200$ to which is intended.

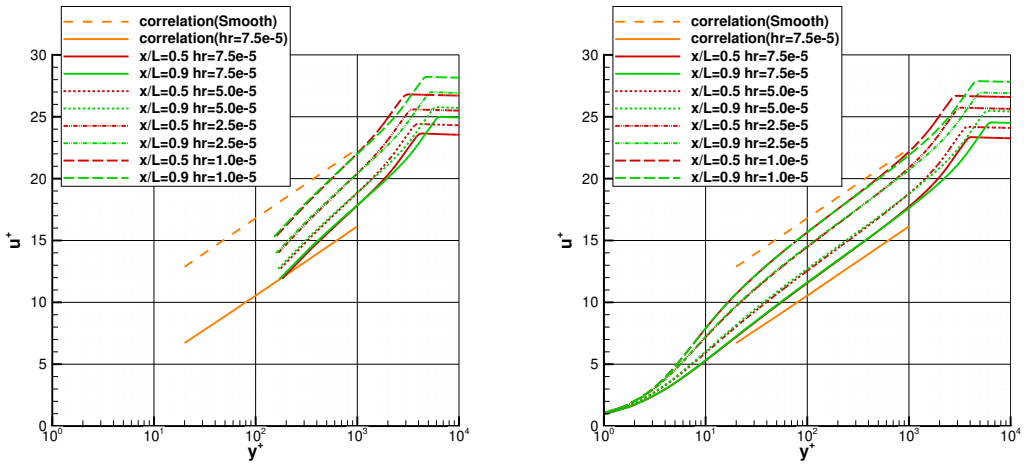

Fig. 2: Comparison of y^+ and u^+ at $R = 1.0 \times 10^7$ (Left: Wall function, Right: Low-Reynolds number model)

Table 4 shows the resistance coefficient with changing the roughness height from $h_r = 1 \times 10^{-7}$ to $h_r = 7.5 \times 10^{-7}$ and the grid resolutions at the Reynolds number $R = 1.0 \times 10^9$. The uncertainty is resulted in the small value which is less than 1%. The difference between the value of the wall function method and the value of the empirical formula is about 2%, and the difference between the value of the wall function method and the value of the low-Reynolds number model results within 5%.

Fig. 3 shows the distribution of u^+ and y^+ with changing the roughness height. The computed results show the similar distribution with the case $R = 1.0 \times 10^7$ excepting the logarithmic region becomes wider

Table 4: Comparison of resistance coefficient ($\times 10^{-3}$, $R = 1.0 \times 10^9$)

Grid	1×10^{-7}	2.5×10^{-7}	5×10^{-7}	7.5×10^{-7}
Coarse	1.513	1.622	1.752	1.853
Medium	1.539	1.652	1.787	1.891
Fine	1.541	1.655	1.790	1.894
$U_{SN}\%G_1$	0.48	0.66	0.52	0.63
Fine(Low-Re)	1.627	1.709	1.845	1.984
Emp.	1.487	1.673	1.837	1.944

than the results of $R = 1.0 \times 10^7$. The first point away from a wall surface with the wall function locates again at $y^+ = 200$, and the distributions take the similar curve with the result of the low-Reynolds number model.

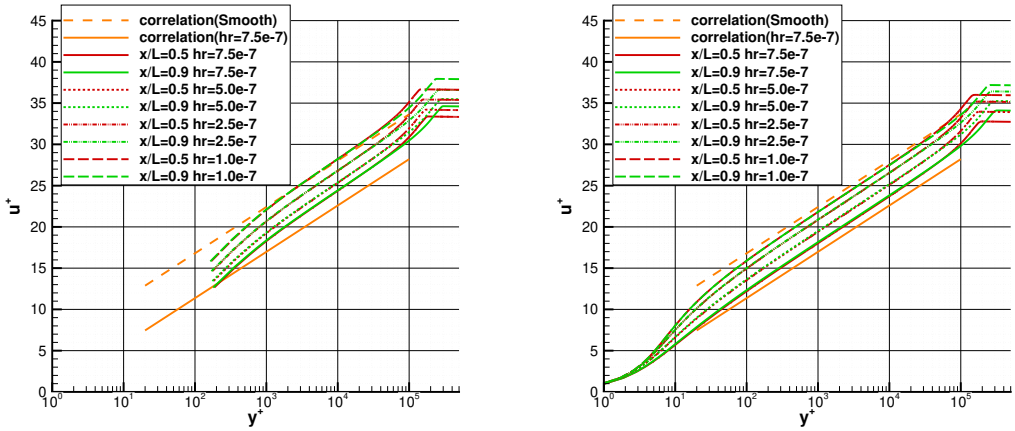

Fig. 3: Comparison of y^+ and u^+ at $R = 1.0 \times 10^9$ (Left: Wall function, Right: Low-Reynolds number model)

Figure 4 shows the distribution of h_r^+ on the flat plate at the condition with $h_r = 7.5 \times 10^{-7}$. h_r^+ takes larger value near the front end of the flat plate, then, the value becomes almost constant value with $h_r^+ = 25$ over the surface.

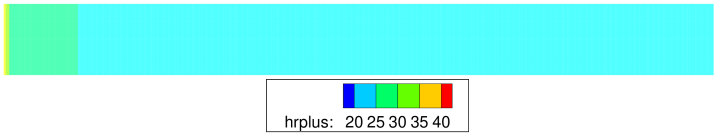

Fig. 4: Non-dimensionalized roughness height on the wall($h_r = 7.5 \times 10^{-7}$, $R = 1.0 \times 10^9$)

3.2 Actual ship scale

The wall function with the roughness effect is applied to the case with the tanker hull(CFD W.S.(1994)) which has the flow measurement data of the actual ship. The computations are carried out on the propulsive condition with the free surface effect. The Reynolds number based on the ship length L is $R = 2.43 \times 10^9$, and the Froude number is $Fn = 0.153$. Propulsive condition is achieved by using the propeller model, and propeller rotational speed and thrust are adjusted to be equal to the resistance of the ship. The roughness value is set $150 \times 10^{-6} m$ based on the ITTC recommended procedure(ITTC R.P. 7.5-02-03-01.4,).

Table 5 shows the division number of computational grids in each direction. The grids are arranged with the priority of the overset interpolation. The computational grid is consisted from the hull grid, the

rudder grid and two rectangular grids including the refinement grid near the aft part of the ship hull and the grid covering the whole domain.

Fig. 5 shows the global view of the computational grids with the boundary conditions and the grids near the aft part of the hull. The minimum spacing on the wall surface is set to $y^+ = 200$.

Table 5: Division number of computational grid

Grid	Coarse IM×JM×KM	Medium IM×JM×KM	Fine IM×JM×KM
Rudder	45×69×35	61×97×49	85×137×69
Refined Rect.	45×33×45	45×33×45	45×33×45
Hull	141×145×41	197×209×57	277×305×81
Rect.	337×89×57	337×89×57	337×89×57

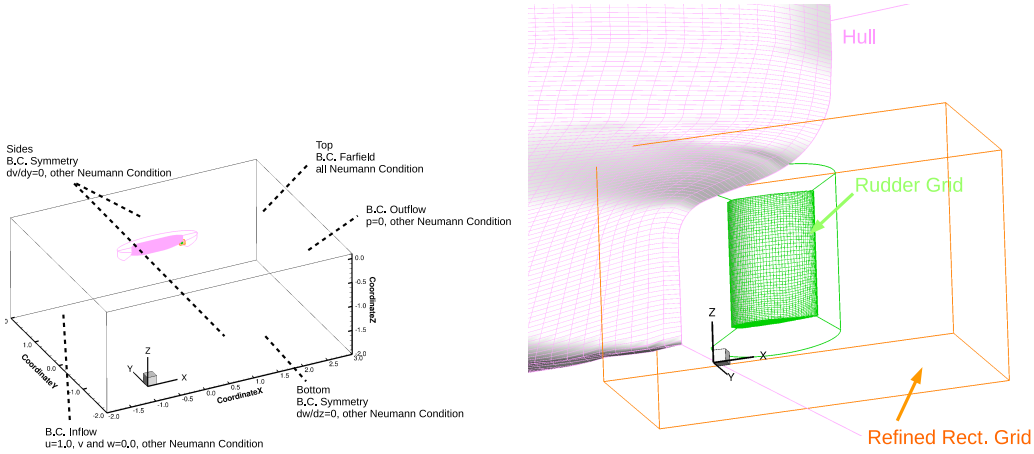

Fig. 5: Computational grid (Left:global view, Right:near aft part of hull)

Fig. 6 shows the comparisons with the measured data of the actual ship. The position is x/L=0.98533 from the fore perpendicular position. The results with the roughness effect show agreement with the measured data, especially, the range $u/U = 0.5 - 0.7$. The differences between the result of the grid resolutions are slightly small. Fig. 7 shows the comparison between the results with the wall function and the data with the low-Reynolds number model(Ohashi(2019)). The difference between the results of the wall function and the low-Reynolds number model is slightly small, and the both results with the roughness effect show good agreement with the measured data of the actual ship.

Finally, figure 8 shows the distribution of the non-dimensionalized roughness height h_r^+ on the body surfaces. h_r^+ takes small value near the fore and stern end, and h_r^+ is distributed on the body surface with the value near 40. The difference between the port and starboard sides is slightly small. The non-dimensionalized roughness height on the rudder surface which is positioned behind the propeller takes higher value than h_r^+ on the hull surface. The difference between the port and starboard sides on the rudder surface can be observed which is affected by the propeller rotational flow. h_r^+ with the wall function show similar distribution of the low-Reynolds number model on the hull surface except the region near the fore and stern ends, and h_r^+ distributions on the rudder surface take similar shapes, and the values of h_r^+ of the wall function are resulted in larger value than the results of the low-Reynolds number model.

4 Conclusion

The wall function including the roughness effect is developed and applied to the cases at the high Reynolds number on the actual ship scale. At first, the present method is applied to the 2D flat plate case with changing the roughness height and Reynolds number. The resistance coefficients of the wall

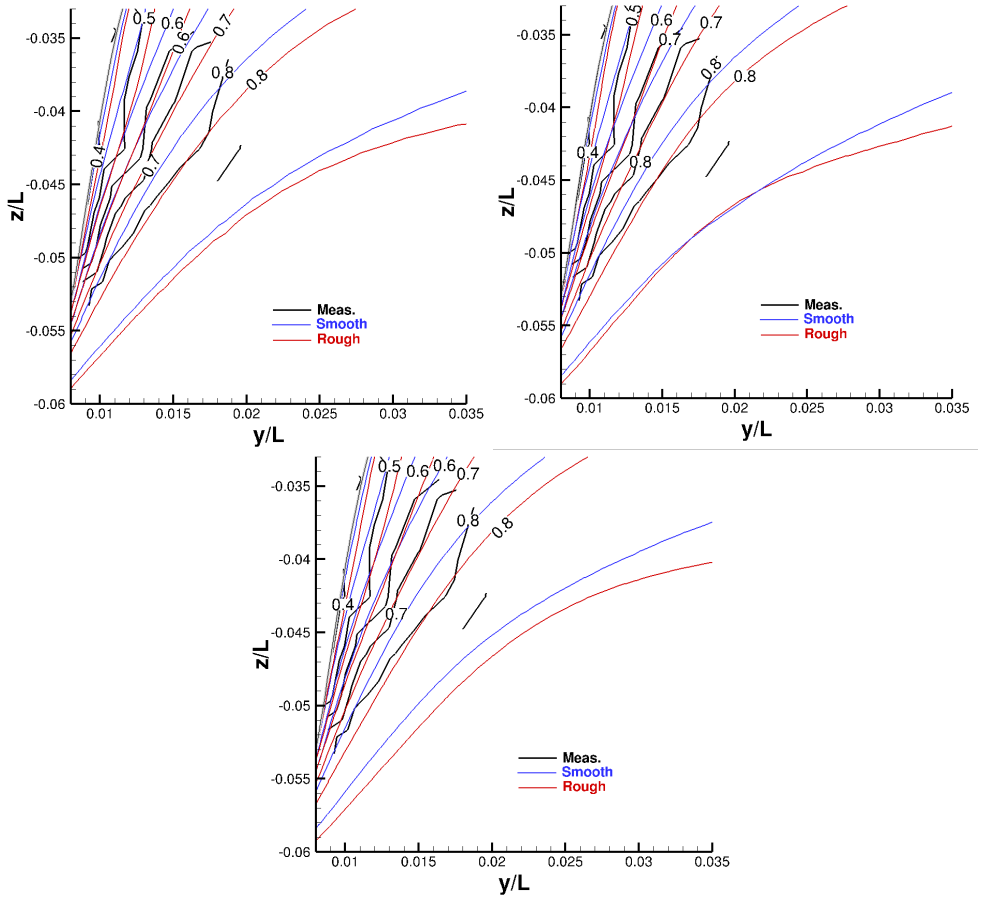

Fig. 6: Axial velocity contour(Top left:Coarse grid, Top right:Medium grid, Bottom:Fine grid)

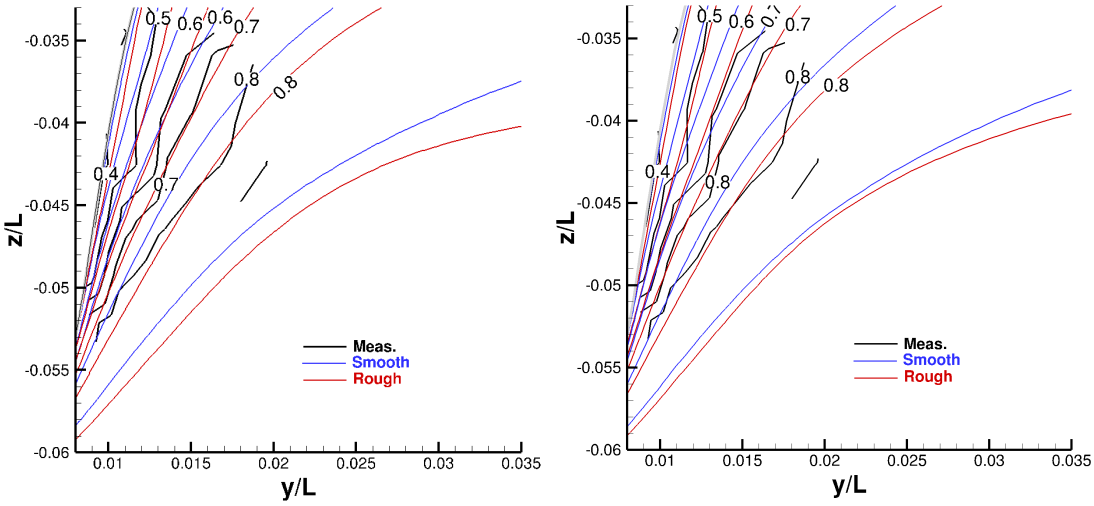

Fig. 7: Axial velocity contour(Left: Wall function, Right: Low-Reynolds number model)

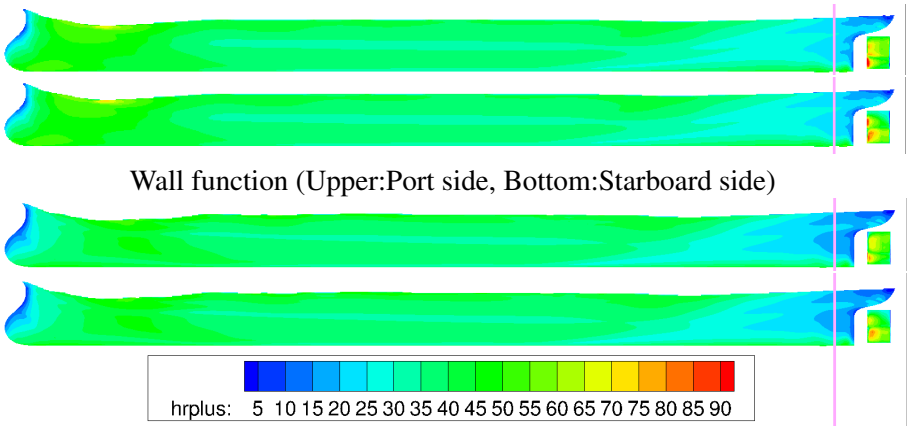

Wall function (Upper:Port side, Bottom:Starboard side)

Low-Reynolds number model (Upper:Port side, Bottom:Starboard side)

Fig. 8: Non-dimensional roughness on the hull and rudder surfaces

function close to the values of the low-Reynolds number model and the empirical formula, and the distributions of the non-dimensional velocity u^+ based on y^+ decrease with the increase of the roughness height and show the similar curves of the low-Reynolds number model. Next, the present wall function method is applied to the flows around the tanker ship, and the velocity distributions with the roughness effect show agreement with the measured data of the actual ship as similar with the results with the low-Reynolds number model.

References

K. Ohashi et al. (2018). Development of a structured overset Navier-Stokes solver including a moving grid with a full multigrid method, JMST.

H. Kobayashi and Y. Kodama. (2016). Developing Spline Based Overset Grid Assembling Approach and Application to Unsteady Flow Around a Moving Body, Journal of Mathematics and System Science 6, pp.339-347.

T. Cebeci and P. Bradshow. (1977). Momentum Transfer in Boundary Layers, Hemisphere Publishing Corporation, Series in Thermal and Fluids Engineering.

D.C. Wilcox. (2006). Turbulence modeling for CFD, Third Edition, DCW Industries.

L. Eça, M. Hoekstra. (2011). Numerical aspects of including wall roughness effects in the SST $k-\omega$ eddy-viscosity turbulence model, Comp. and Fluids, Vol.40, pp.299-314.

A. Hellsten. (1997). Some improvements in Menter's $k-\omega$ SST AIAA-98-2554.

D. Apsley. (2007). CFD calculation turbulent flow with arbitrary wall roughness, Flow Turb. Comb., Vol.78, pp.153-175.

T. Xing, , F. Stern. (2010). Factors of safety for Richardson extrapolation, J. Fluids Eng., Vol.132(6).

A. Mills, X. Hang. (1983). On the skin friction coefficient for a fully rough flat plate, Trans. ASME, J. Fluids Eng., Vol.105, pp.364-365.

K. Ohashi. (2019). Numerical Study of Roughness Model Effect at Actual Ship Scale, ECCOMAS MARINE 2019.

Proc. of CFD Workshop Tokyo 1994.

ITTC recommended procedures and Guidelines 7.5-02-03-01.4, 1978 ITTC Performance Prediction Method.

Numerical Prediction of Cavitation Damage for the Flow through a Nozzle Using a Multi-Scale Euler-Lagrange Method

Andreas Peters, Udo Lantermann, and Ould el Moctar
Institute of Ship Technology, Ocean Engineering and Transport Systems,
University of Duisburg-Essen, Duisburg/Germany
andreas.peters@uni-due.com

1 Introduction

In maritime flows, cavitation occurs around ship appendages such as rudders and propellers. High flow velocities are accompanied by low static pressures in the liquid that cause vapourisation of cavitation bubbles. In regions of higher pressures, the cavitation bubbles collapse and radiate shock waves of high pressure amplitudes that are able to damage material surfaces. As experimental approaches to predict cavitation erosion for ship appendages involve scale effects, numerical methods to predict erosion have received increasing attention within the last years.

Numerical methods to simulate cavitation are mostly characterised by the approach used to treat the vapour phase. While Euler-Euler methods consider both the liquid and the vapour phase as continua, Euler-Lagrange methods assume only the liquid phase to be continuous and the vapour phase to be an accumulation of spherical Lagrangian bubbles. Despite the details gained by a Lagrangian treatment of the vapour phase, Euler-Lagrange approaches demand a high computational effort. To benefit from the efficiency of the Euler-Euler method and still have insight into details using an Euler-Lagrange method, the approaches are combined in a multi-scale method similar to the ones of Vallier (2013) and Lidtke (2017). Large vapour structures are, therein, treated in an Eulerian framework, while small vapour structures are treated as Lagrangian bubbles. Dynamics and motions of each Lagrangian bubble are calculated and used to identify bubble collapses close to solid surfaces that can possibly cause erosion.

2 Multi-Scale Euler-Lagrange Method

In the multi-scale Euler-Lagrange method, large vapour volumes are captured on the Eulerian grid, while small volumes are treated as spherical Lagrangian bubbles. Vapour volumes are transformed between the two frameworks based on their absolute size – the reference radius of a coherent vapour volume – and their size relative to the numerical grid. Vapour volumes are transformed from the Eulerian grid to Lagrangian bubbles when they decrease below these threshold sizes. Lagrangian bubbles are transformed into Eulerian vapour volumes, when they increase over these threshold sizes or merge into Eulerian vapour volumes.

Cavitating flows are simulated based on a RANS approach using the volume of fluid method to capture the interface between phases. To model turbulence, we apply the k-ω-SST model. For cavitation modelling in regions where the Euler-Euler method is used, we apply the model of Sauer and Schnerr (2000). For each spherical Lagrangian cavitation bubble, its dynamics in terms of growth and collapse are calculated from an equation according to Tomita and Shima (1977). The bubble radius, R, is obtained by solution of the following equation:

$$\frac{p_{r=R} - p_\mathrm{l}}{\rho_\mathrm{l}} + \frac{R\dot{p}_{r=R}}{\rho_\mathrm{l} c_\infty} = R\ddot{R}\left[1 - (1+\epsilon_R)\frac{\dot{R}}{c_\infty}\right] + \frac{3}{2}\dot{R}^2\left(\frac{4-\epsilon_R}{3} - \frac{4}{3}\frac{\dot{R}}{c_\infty}\right), \tag{1}$$

where $\dot{R}$ and $\ddot{R}$ are the bubble growth rate and the bubble wall acceleration, respectively. p_l is the pressure in the liquid and ρ_l is the density in the liquid. c_∞ is the speed of sound of liquid water in the far field and $\epsilon_R = 1 - \rho_\mathrm{g}/\rho_\mathrm{l}$ with ρ_g as the density of the gas in the bubble. $p_{r=R}$ is the pressure at the inner bubble wall. A first order approximation of it reads:

$$p_{r=R} = p_\mathrm{v} + p_{\mathrm{g},0}\left(\frac{R_0}{R}\right)^{3\gamma_\mathrm{h}} - \frac{2\sigma}{R} - \epsilon_R\frac{4\mu_\mathrm{l}\dot{R}}{R}, \tag{2}$$

and its time derivative is written as:

$$\dot{p}_{r=R} = -3\gamma_\mathrm{h} p_{\mathrm{g},0}\frac{\dot{R}}{R}\left(\frac{R_0}{R}\right)^{3\gamma_\mathrm{h}} + \frac{2\sigma}{R^2}\dot{R} - \epsilon_R 4\mu_\mathrm{l}\frac{\ddot{R}R - \dot{R}^2}{R^2}. \tag{3}$$

p_v is the vapour pressure, μ_l is the viscosity of the liquid, and γ_h is the ratio of specific heats. During bubble growth, the compressibility of the liquid in Eq. (1) is neglected by assuming $\epsilon_R \to 1$ and $c_\infty \to \infty$.

To calculate bubble motions, we use the Lagrangian equation of motion which reads:

$$m_b \frac{d\vec{u}_b}{dt} = \sum_i \vec{F}_i \, . \tag{4}$$

$\vec{u}_b$ is the velocity of the bubble and $m_b = \rho_b V_b$ is the mass of the bubble. ρ_b is the density of the bubble and the volume of a sphere is $V_b = \frac{4}{3}\pi R^3$. $\vec{F}_i$ are forces acting on the bubble owing to drag, pressure gradient, virtual mass, buoyancy, volume variation, and lift and depend on the behaviour of the bubble relative to the carrier fluid and the bubble's dynamics.

Interactions between Lagrangian bubbles and the liquid phase are considered in form of a two-way coupling that exchanges momentum from the carrier fluid to the bubbles and vice versa and the calculates mixture properties such as density and viscosity of the fluid based on both phase fractions in a control volume.

3 Results

The flow passing through a vertical nozzle was simulated using the multi-scale Euler-Lagrange method. Franc and Riondet (2006) experimentally investigated this case in terms of cavitation-induced erosion. Flow entered the geometry through a vertical cylinder that was connected to a radial channel via a 1 mm radius. A stagnation type flow developed at the bottom of the domain below the vertical cylinder and caused the flow to diverge radially outwards. At the connecting radius, cavitation structures evolved, travelled further downstream, and collapsed in regions of higher pressure. Fig. 1 shows a time instance of Eulerian vapour structures (dark blue) and Lagrangian bubbles (light blue) travelling through the nozzle. Blue to red colours on the bottom and the side boundaries indicate pressures from 0 to 1 bar. Cavitation structures formed close to the radius at the end of the vertical cylinder and detached in form of cavitation clouds owing to vortices in the flow. In the time instance shown, Lagrangian bubbles appear downstream from the larger vapour structures as a result of detachment from or separation of larger vapour volumes as well as collapse processes. Close to the Lagrangian bubble positions shown, collapses of the bubbles were calculated.

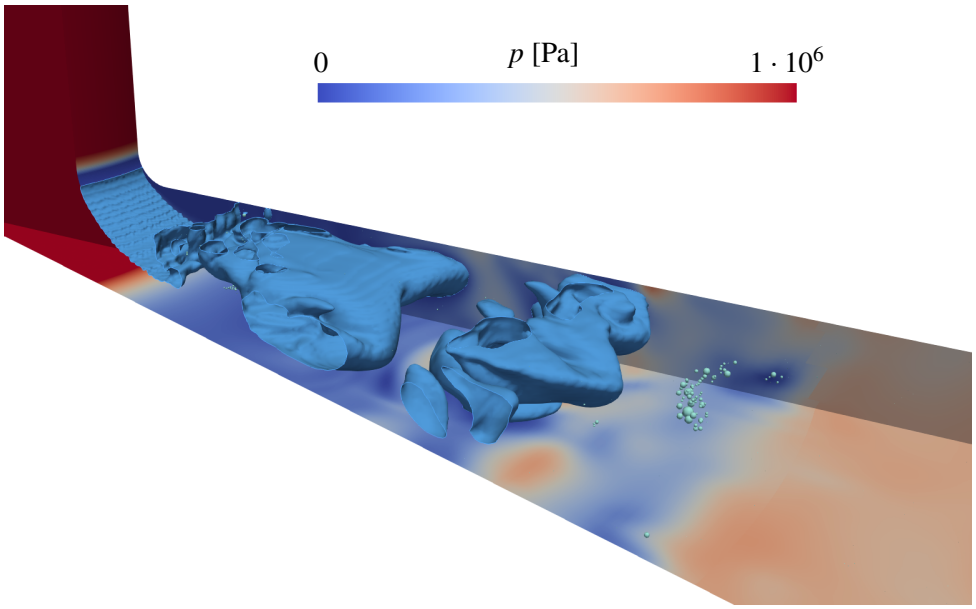

Fig. 1: Perspective side view of Eulerian vapour structures and Lagrangian bubbles in the nozzle

Fig. 2 depicts the predicted areas of erosion on the bottom surface along with positions of Lagrangian bubble collapses. Blue colours on the bottom surface mark regions where the erosion coefficient c_{ero} and

the erosion risk are low; red colours, regions of high erosion risk. c_{ero} was calculated considering the amount of bubble collapses close to the bottom surface and their respective collapse pressures. Spheres indicate collapse positions and are scaled and coloured with their maximum bubble radii, R_{max}, at the beginning of the respective collapse. On these spheres, light grey colours indicate maximum collapse radii of $1 \cdot 10^{-5}$ m; dark grey colours, radii of $1 \cdot 10^{-4}$ m. Within radial distances of 19 to 24 mm from the centre axis of the nozzle, a light green ring marks the area where erosion was measured in experiments of Franc and Riondet (2006). Although, compared to the experimental prediction, bubble collapses were calculated in a larger area, the highest calculated impacts on the bottom surface agreed well with the experimentally measured erosion pattern.

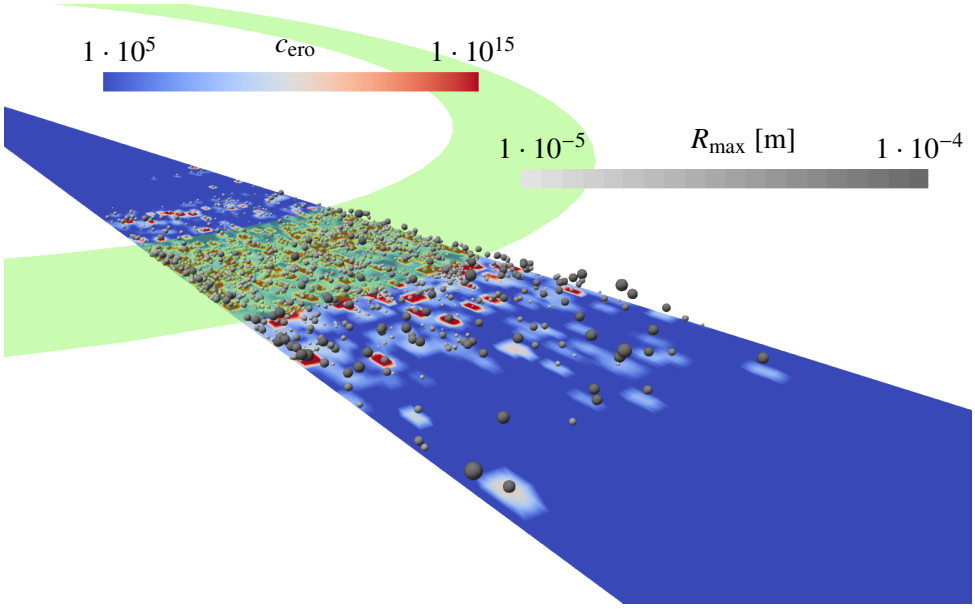

Fig. 2: Erosion prediction on bottom surface and bubble collapses indicated by spheres of maximum radii during respective collapses; green ring marks region where erosion was measured in experiments of Franc and Riondet (2006)

4 Conclusion

The present multi-scale Euler-Lagrange method allows the identification of time instances, positions, bubble radii, and pressures of Lagrangian bubble collapses, while maintaining computational efficiency. Taking into account the behaviour of single cavitation bubbles, more accurate numerical erosion predictions can be performed than for Euler-Euler simulations that neglect single bubble behaviour. The multi-scale method enables to correlate erosion rates with Lagrangian bubble collapse rates and ring-shaped erosion patterns (“pits”) with the radii of Lagrangian bubble collapses.

Acknowledgements

This work was supported by the German Research Foundation (DFG grant EL 611/2-1). The authors gratefully acknowledge the computing time granted by the Center for Computational Sciences and Simulation (CCSS) of the University of Duisburg-Essen and provided on the supercomputer magnitUDE (DFG grants INST 20867/209-1 FUGG, INST 20876/243-1 FUGG) at the Zentrum für Informations- und Mediendienste (ZIM).

References

Franc, J.-P. and Riondet, M. (2006). Incubation Time and Cavitation Erosion Rate of Work-Hardening Materials. In *Proceedings of the 6th International Symposium on Cavitation, CAV2006, Wageningen, Netherlands*.

Lidtke, A. K. (2017). *Predicting Radiated Noise of Marine Propellers Using Acoustic Analogies and Hybrid Eulerian-Lagrangian Cavitation Models*. PhD Thesis, University of Southampton, Southampton, Great Britain.

Sauer, J. and Schnerr, G. H. (2000). Unsteady Cavitating Flow - a New Cavitation Model Based on Modified Front Capturing Method and Bubble Dynamics. In *Proceedings of FEDSM, 4th Fluids Engineering Summer Conference*.

Tomita, Y. and Shima, A. (1977). On the Behavior of a Spherical Bubble and the Impulse Pressure in a Viscous Compressible Liquid. *Bulletin of the JSME*, 20(149):1453–1460.

Vallier, A. (2013). *Simulations of Cavitation – From the Large Vapour Structure to the Small Bubble Dynamics*. PhD Thesis, Lund University, Lund, Sweden.

Design of ducted propellers

M. Remaud, P-M Guilcher, J.-B. Leroux and J.-M. Laurens*
*jean-marc.laurens@ensta-bretagne.fr

Introduction

The paternity of the marine propeller is highly disputed. The Austrian J. Russel in 1828, the Scot R. Wilson the same year, the French F. Sauvage in 1832, the English J. Ericsson in 1836 and several other inventors filed the patent. The legal battles that have accompanied these developments attest to the importance of the industrial challenge. Who is really the inventor? Everyone and no-one. The principle they applied was that of the worm screw illustrated by Leonardo da Vinci's famous engraving. This principle was already known to ancient Egyptians who used it to irrigate fields in the Nile Valley. But the operating principle of a propeller is not the same as a worm screw. The blades arranged around the hub act on the principle of the wing, the theory of which was not developed until the beginning of the 20th century by L. Prandtl. As for a wing, one of the two sides of the blade is in depression while the other is in overpressure and it is this pressure difference that is at the origin of the thrust force. To provide thrust, the propeller is rotated by an engine to which it is connected by the shaft line. Propulsive efficiency is the ratio between the propeller thrust power and the torque power provided by the engine.

The design of the propulsion system and therefore of the propeller consists in obtaining the best possible performance for the operating points corresponding to the vessel. For a ship that makes long crossings this operating point is unique since it almost always operates at the same speed. The propulsion efficiency for these vessels varies between 55 and 75% depending on the quality of the design. In the propulsion chain, the highest loss occurs at the propeller level. Under the best possible conditions, propeller efficiency can hardly exceed 80%.

Many ships do not have a single operating point. Military vessels, for example, because they have to cruise, patrol, monitor and sometimes quickly intervene. The worst off in this area are fishing vessels and especially trawlers. They must travel to and from fishing areas but also fish. The speed is then slow or very slow but the power required is very important because they have to pull the trawl behind them. For the propeller, this is the worst situation because it is extremely loaded; the pressure difference between the back and the belly of the blades is very large. The propeller efficiency can then be catastrophic, even less than 20%. The remaining 80% is wasted stirring water. The increase in the price of diesel fuel, the increasing scarcity of the resource and the environmental footprint no longer make it possible to accept such a waste. Although fuel economy was not the main focus, low performance was a problem. The theory shows that a loaded propeller wastes a lot of energy accelerating the fluid axially and the kinetic energy thus dissipated can easily be estimated; the rest of the loss is due to rotation and friction. An example of percentage of loss versus the thrust loading coefficient (C_{Th}) is shown in Figure 1. The same analysis has been performed changing the geometrical characteristics of the propeller blades, and it appeared that the most sensitive parameter is the maximum camber of the sections. The only way to partially counteract this effect and thus unload the propeller is to transfer part of the thrust to another appendix. This other appendix is the nozzle; a thick ring with a profiled section shape and inside which the propeller is placed. The first nozzle developed by Kort in 1934 was of this type. Since the highly charged propeller strongly accelerates the fluid axially, the pressure is reduced upstream of the propeller. By depressurizing the rounded wall inside the nozzle it is sucked forward creating a pushing force. Thus the nozzle participates in the

thrust and reduces the propeller load. Under these conditions, the ducted propeller pushes more and has a better efficiency. The Dutch Maritime Research Institute has developed a series of results for open and ducted propellers using its test facilities and reported by Kuiper (1992). These results are commonly used to dimension the propellers. In the case of open water propellers, these results allow a first dimensioning before optimizing the geometry of the propeller. For ducted propellers, the tendency is to manufacture the ducted propeller directly based on the results without seeking to optimize it. This is an improvement compared to the propeller alone, but since we know that a trawler on average consumes one tonne of diesel fuel per tonne of fish caught, we should try to improve its performance.

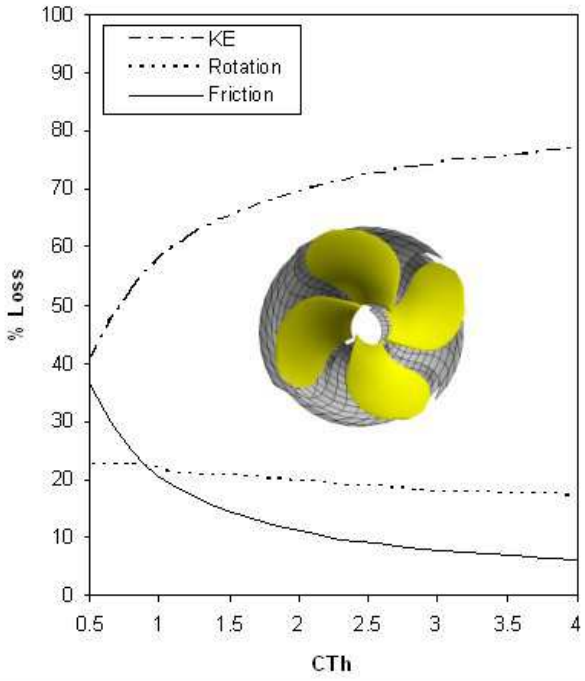

Figure 1 Percentage of loss of energy versus C_{Th} for a bare propeller. The kinetic energy loss (KE) becomes dominant when the thrust loading coefficient, C_{Th}, is important.

The first digital models to simulate ducted propellers date back to the 1960s, but finally there exist very few research projects in this field until recently with the very strong increase in crude oil from 2011 to 2014. The search for efficiency seems to follow the fluctuations of the oil market but research has a much greater inertia than stock markets and therefore solutions do not arrive fast enough and projects are abandoned until the next crisis. Environmental regulations provide a new element that will undoubtedly make it possible to continue research projects in the field of energy saving. Since 1960, the characterization and the design of ducted propellers have been the subjects of ongoing studies. One of the first fundamental papers, written by Morgan (1961), provided a ducted propeller analysis by modelling the duct according to the lifting line theory. In the late 1960s, Van Manen (1970) published an eminent paper on accelerating ducts and Kaplan propellers. Kerwin et al. (1987) published a fundamental analysis of the numerical modelling of ducted propellers . This study aimed to explain the use of potential flow theory in blade, hub, and duct numerical modelling. The panel code generated a complex mesh with helical panels named “extravaganza” by the authors. Subsequently, further research was carried out on this topic by Baltazar and Falcão de Campos (2009), Baltazar et al. (2012), and Laurens et al. (2012). Some research on the duct design demonstrated that ducted propellers are interesting in high loading blade conditions, such as fishing vessels Dasira and Laurens (2014). A recent paper by Gaggero et al. (2017) on the study of ducted propeller characteristics deserves to be

cited. Their study aimed to characterize the flow swallowing in decelerating ducts, and how it influences propeller behaviour. Finally, few studies have been conducted on the characterization of parameters for ducted propeller design. This paper focuses on 3 ducted propellers, using only one rotor type: the Kaplan 4.55. We have very recently published a preliminary characterisation for numerical optimisation of ducted propellers, Remaud et al. (2019). Here we simply want to list the elements we must take into account to determine the optimisation strategy.

Duct section shape, circulation and trailing edge

We read in all handbooks that there are three types of duct: accelerating, decelerating and neutral. A lifting profile induces a circulation clockwise or anti-clockwise according to the direction of the lift. The flow through the duct is accelerated if the lift force is inward and decelerated if the lift force is outward. Although the phenomenon is easily understood, recent and less recent studies sometime ignore it and early numerical studies have to be retrieved like Van Manen and Oosterveld (1966). A ducted water turbine should therefore present a positive flare angle and/or a negative camber, Laurens et al. (2016). Heuristic reasoning provides a simple relationship between the section lift coefficient and the relative average acceleration, Remaud et al. (2019) but the detailed nominal flow is needed for an optimization procedure. Two computing procedures around the duct alone can be used: an axi-symmetric simulation of the real flow using a standard Navier-Stokes solver or a 3D potential flow. For this second procedure, the duct must be considered as a lifting body which imposes the use of the Kutta condition at the trailing edge of its profile and therefore a sharp trailing edge. Baltazar et al. (2009) showed that otherwise, the slightest variation for the position of the Kutta condition severely modifies the results. Both procedures are very fast and velocity profiles such as those presented in Figure 2 within the duct alone are easily obtained.

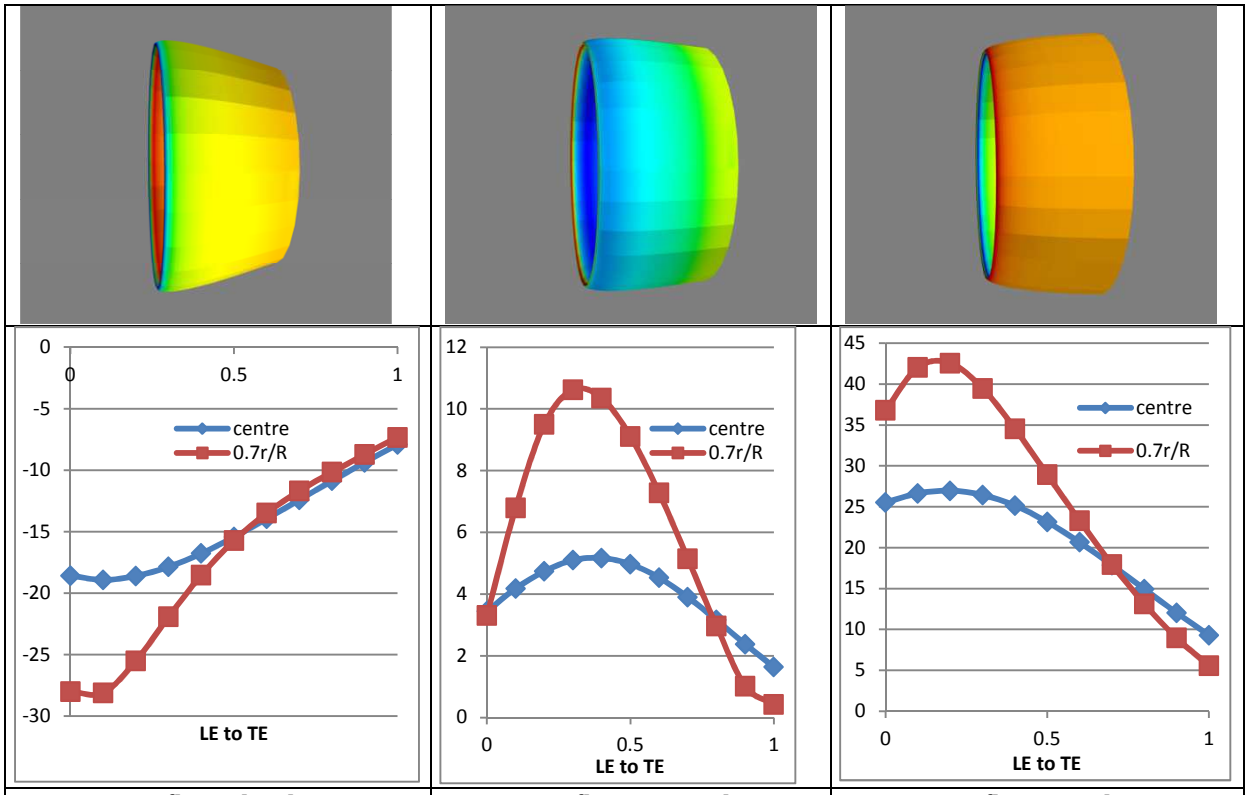

Negative flare: decelerating.	No flare: Neutral	Positive flare: accelerating

Figure 2: Percentage of axial velocity increase for decelerating, neutral and accelerating ducts. The circulation is induced by applying a flare angle to the symmetrical section.

The obtained velocities in the propeller disk are therefore equivalent to the nominal wake measured or computed behind the vessel. But before going any further the axial position of the propeller disk has to be decided.

Position of the rotor and preliminary parametric study

Like the propeller behind the ship, since the rotor accelerates the flow, it modifies the nominal wake. We can use the axi-symmetrical Navier-Stokes procedure combined with an actuator disk representation of the rotor and develop a procedure to obtain the effective wake, Hally and Laurens (1998). It must first be decided where the rotor will be placed axially. The answer may be obtained from the curves of Figure 2 but a preliminary parametric study reported in details in Remaud et al. (2019) showed that the answer is not so obvious. Three parameters of the duct geometry were considered in this study: the duct section thickness, the axial position of the rotor and the gap between the blade's tip and the inner duct. Like Saari (2014), we used the Kaplan 4.55 propeller with P/D=1 and the results are compared with the modified[i] 19A duct. The duct chord is half its diameter.

The configurations reported here are described in Table *1*.

Table 1 Configurations.

Configuration	Profile	Gap/R	Rotor x-position
Reference	19A-sharp	3.10 %	1/3
A	NACA0017	3.10 %	1/3
B	NACA0017	7.00 %	1/3
C	NACA0017	7.00 %	7/12
D	NACA0008	3.10%	1/3
E	NACA0008	7.00%	1/3
F	NACA0008	7.00%	7/12

At this stage, the propeller has not been modified but it should obviously have to be modified in a full design procedure. The complete results are shown in Table 2 and 3.

Table 2 Complete performance predictions for 3 configurations using the NACA0017.

	Reference			Configuration A			Configuration B			Configuration C		
J	KtD	Kt	Eta	KtD	Kt	Eta	KtD	Kt	Eta	KtD	Kt	Eta
0.45	0.035	0.209	0.540	0.035	0.238	0.537	0.037	0.245	0.543	*No results*		
0.5	0.027	0.193	0.576	0.028	0.215	0.575	0.031	0.222	0.583	0.047	0.288	0.624
0.55	0.020	0.177	0.606	0.023	0.191	0.609	0.025	0.198	0.617	0.039	0.259	0.662
0.6	0.014	0.161	0.630	0.018	0.168	0.637	0.019	0.174	0.645	0.031	0.230	0.695
0.65	0.008	0.144	0.647	0.013	0.144	0.656	0.014	0.150	0.666	0.024	0.200	0.721
0.7	0.003	0.126	0.652	0.009	0.120	0.665	0.010	0.126	0.677	0.018	0.171	0.739
0.75	-0.003	0.111	0.641	0.005	0.096	0.659	0.006	0.102	0.673	0.012	0.143	0.747
0.8	-0.006	0.089	0.621	0.002	0.073	0.632	0.003	0.078	0.650	0.007	0.114	0.742
0.85	-0.009	0.070	0.569	0.000	0.049	0.564	0.000	0.054	0.591	0.003	0.086	0.716
0.9	-0.011	0.050	0.470	-0.002	0.024	0.410	-0.002	0.029	0.459	0.000	0.059	0.651

Table 3 Performance predictions for the 3 configurations using NACA0008.

	Reference			Configuration D			Configuration E			Configuration F		
J	KtD	Kt	Eta	KtD	Kt	Eta	KtD	Kt	Eta	KtD	Kt	Eta
0.45	0.035	0.209	0.540	*No results*						0.057	0.273	0.587
0.50	0.027	0.193	0.576	0.025	0.180	0.565	0.036	0.207	0.599	0.056	0.256	0.644
0.55	0.020	0.177	0.606	0.020	0.162	0.598	0.030	0.190	0.636	0.045	0.235	0.681
0.60	0.014	0.161	0.630	0.015	0.144	0.624	0.024	0.172	0.669	0.036	0.213	0.714
0.65	0.008	0.144	0.647	0.011	0.125	0.641	0.019	0.154	0.696	0.029	0.192	0.743
0.70	0.003	0.126	0.652	0.007	0.105	0.648	0.014	0.136	0.715	0.022	0.169	0.766
0.75	-0.003	0.111	0.641	0.004	0.085	0.640	0.010	0.116	0.726	0.016	0.146	0.781
0.80	-0.006	0.089	0.621	0.001	0.065	0.605	0.007	0.097	0.724	0.011	0.123	0.786
0.85	-0.009	0.070	0.569	-0.001	0.043	0.525	0.004	0.076	0.704	0.007	0.100	0.778
0.90	-0.011	0.050	0.470	-0.003	0.020	0.333	0.002	0.055	0.651	0.004	0.077	0.746

The results show that neutral NACA profiles can provide higher performance predictions than the accelerating Kort nozzle 19A. A smaller gap slightly changes the maximum circulation along the propeller blade but does not prevent the tip vortex and the resultant 3D effect. This observation explains why configuration A is not more efficient than configuration B. As expected, the hierarchy of the results is the same as the maximum thickness is changed; however and more surprisingly, the values are slightly higher for the smaller maximum thickness. These results tend to show that not only does reducing the duct section thickness increase the propeller diameter, but it also ensures a better performance.

Conclusion

This preliminary analysis has provided interesting perspectives on improving ducted propeller efficiency and performance predictions. The results of this study showed that a ducted propeller can be made more efficient by changing the geometry of the duct and the position of the rotor and more surprisingly that the ducted propeller can present a higher overall efficiency coefficient than the bare propeller.

In order to develop a complete design procedure to optimize a ducted propeller according to its operational purpose, we must first have a deep understanding of the interaction. The different numerical procedures mentioned here have to be involved and ideally experimental results are needed.

References

Baltazar, J., & Falcao de Campos, J.A.C. (2009). *On the modeling of the flow in ducted propellers with a panel method*. Norway: Trondheim.

Baltazar, J., Falcão de Campos, J. A. C., & Bosschers, J. (2012). Open-water thrust and torque predictions of a ducted propeller system with a panel method. *International Journal of Rotating Machinery 2012*, 474785. doi:10.1155/2012/474785

Coache, S., & Laurens, J. M. (2014). *Trawler duct propeller design: From systematic series to CFD*. In 3rd International Symposium on Fishing Vessel Energy Efficiency.

Dasira, A., & Laurens, J. M. (2014). Energy efficiency analysis of trawlers: Case study on an Indonesian trawler. *Indonesian Scholar Journal 1*(1), 245-250. doi:10.12962/ j23546026.y2014i1.202

Gaggero, S., Villa, D., Tani, G., Viviani, M., & Bertetta, D. (2017). Design of ducted propeller nozzles through a RANSE-based optimization approach. *Ocean Engineering 145*, 444-463. doi:10.1016/j.oceaneng.2017.09.037

Hally D. and Laurens J.-M. (1998), *Numerical simulation of hull-propeller interaction using force fields within Navier-Stokes computations*, Ship Technology Research , Vol.45.

Kerwin, J. E., Kinnas, S. A., Lee, J. T., & Shih, W. Z. (1987). A surface panel method for the hydrodynamic analysis of ducted propellers. *Transaction SNAME 95*, 1-22.

Kuiper, G. (1992). *The Wageningen Propeller series*. Wageningen: Marin Publication.

Laurens, J. M., Deniset F., & Moyne, S. (2012). *A BEM method for the hydrodynamic analysis of fishing boats propulsive systems*. In Second International Symposium on Fishing Vessel Energy Efficiency. Vigo, Spain.

Laurens, J. M., Leroux, J. B., & Coache, S. (2013). *Design and retrofit of the propulsion of trawlers to improve their efficiency*. Spain: A Coruna.

Laurens, J. M., Ait-Mohammed, M., & Tarfaoui, M. (2016). Design of bare and ducted axial marine current turbines. *Renewable Energy, 89*, 181-187.

Morgan, W. B. (1961). *A theory of the ducted propeller with a finite number of blades*. University of California Report, Berkeley, California.

Remaud M., Laurens J.-M., and Guilcher P.-M. (2019). *Preliminary parameter characterization for numerical optimization of ducted propeller*. Maritime Technology and Research doi:10.33175/mtr.2019.183390.

Saari, A. (2014). *Hydrodynamic study on a ducted propeller in a large vessel by time-accurate self-propulsion simulation with Reynolds-Averaged Navier-Stokes-equations*. (Master Thesis). Aalto University, Helsinki, Finland.

Van Manen, J.D. and Oosterveld M.C.W (1966), analysis of ducted-propeller-design, Trans. SNAME vol.74.

Van Manen, J. D. (1970). *Wake adapted ducted propellers*. Wageningen: H. Veenman & Zonen.

[i] Since the potential flow code is used we had to modify trailing edge of the 19a duct section shape as explained in the previous section. The modified section shows a sharp trailing edge but the results are almost identical.

Towards numerical simulation of wave impacts in an LNG tank

Ronald A. Remmerswaal and Arthur E.P. Veldman*
Bernoulli Institute, University of Groningen, The Netherlands
* Corresponding author: a.e.p.veldman@rug.nl

1 Introduction

During the transport of Liquefied Natural Gas (LNG) in LNG carriers sloshing can dangerously interfere with the ship motion through violent breaking-wave impacts with the container walls. The role of free surface instabilities during these impacts is not well understood [Lafeber et al., 2012]; we will study it via computer simulation. Its numerical modeling involves dealing with multi-phase flow, featuring a multitude of jumps (discontinuities) of fluid properties across the interface separating the fluids. The thin shear layers around the interface usually are numerically underresolved and result in unphysical interaction between the two fluids. Such an underresolved layer is numerically better described by a velocity field which has a (contact) discontinuity in the tangential direction.

2 Mathematical model

The equations for *incompressible Euler flow* describe the conservation of mass and momentum in each of the phases $\pi = l, g$ (liquid and gas) in an arbitrary control volume $\omega = \omega^l \cup \omega^g$

$$\frac{\mathrm{d}}{\mathrm{d}t}\int_{\omega^\pi} \rho^\pi \,\mathrm{d}V + \int_{\partial\omega^\pi\setminus I} \rho^\pi u_\eta^\pi \,\mathrm{d}S = 0 \tag{1}$$

$$\frac{\mathrm{d}}{\mathrm{d}t}\int_{\omega^\pi} \rho^\pi \mathbf{u}^\pi \,\mathrm{d}V + \int_{\partial\omega^\pi\setminus I} \rho^\pi \mathbf{u}^\pi u_\eta^\pi \,\mathrm{d}S = -\int_{\partial\omega^\pi} (p^\pi - \rho^\pi \mathbf{g}\cdot\mathbf{x})\boldsymbol{\eta}\,\mathrm{d}S, \tag{2}$$

where $\boldsymbol{\eta}$ denotes the face normal, u_η^π the face normal velocity component, p^π the pressure, $\mathbf{g}$ the gravitational acceleration and ρ^π the density per phase. We consider incompressible flow for which the mass conservation equations result in a volume constraint on the evolution of the interface

$$\frac{\mathrm{d}}{\mathrm{d}t}|\omega^l| + \int_{\partial\omega^l\setminus I} u_\eta^l \,\mathrm{d}S = 0, \quad \text{where } |\omega^\pi| \text{ denotes the volume of } \omega^\pi. \tag{3}$$

The influence of surface tension, relevant in this application, is included via Laplace's law

$$[\![p]\!] := p^g - p^l = -\sigma\kappa. \tag{4}$$

Here κ denotes the interface mean curvature and $[\![p]\!]$ denotes the jump of p over the free surface. We assume immiscible fluids without phase change, and therefore $[\![u_\eta]\!] = \boldsymbol{\eta}\cdot(\mathbf{u}^g - \mathbf{u}^l) = 0$. Together with appropriate boundary conditions on $\mathbf{u}^\pi$ and a contact angle boundary condition on κ, this results in a closed system of equations. Note that this model does not impose any smoothness on the tangential velocity component $u_\tau = \boldsymbol{\tau}\cdot\mathbf{u}$, where $\boldsymbol{\tau}$ denotes the interface tangent.

Addition of the mass conservation equations, when divided by their respective densities, yields

$$\int_{\partial\omega} u_\eta \,\mathrm{d}S = \int_{\partial\omega^l\setminus I} u_\eta^l \,\mathrm{d}S + \int_{\partial\omega^g\setminus I} u_\eta^g \,\mathrm{d}S = 0, \tag{5}$$

thus showing that the mixture velocity field is divergence free. Taking the time derivative of the divergence constraint, substituting the momentum equation and using $[\![u_\eta]\!] = 0$, yields

$$\int_{\partial\omega} \frac{1}{\rho}\,\partial_\eta p \,\mathrm{d}S = -\int_{\partial\omega} \boldsymbol{\eta}\cdot(\mathbf{u}\cdot\nabla)\mathbf{u} \,\mathrm{d}S. \tag{6}$$

We supplement the aforementioned equation with Laplace's law (4), a homogeneous Neumann boundary condition on the pressure along the side walls, and a jump condition on the normal pressure gradient at the interface which is necessary for well-posedness:

$$\left[\!\!\left[\frac{1}{\rho}\,\partial_\eta p\right]\!\!\right] = -\left[\!\!\left[\boldsymbol{\eta}\cdot\frac{D\mathbf{u}}{Dt}\right]\!\!\right]. \tag{7}$$

It follows directly from the strong form of the Euler equations.

3 Numerical model

Notation The cells in the staggered rectilinear (Arakawa C) grid constitute the set C, with faces $\mathcal{F}(c)$ for $c \in C$. A time-dependent subset $\mathcal{F}_I$ of the faces is cut by the interface $I(t) \subset \Omega$; these are split into their liquid and gaseous parts: $f = f^g \cup f^l$. This defines the set $\hat{\mathcal{F}}^\pi$ of all the (possibly cut) faces which are entirely contained in the π-phase; let $\hat{\mathcal{F}} = \hat{\mathcal{F}}^l \cup \hat{\mathcal{F}}^g$(Fig. 1a). The functions defined on C form C^h, with e.g. $p \in C^h : c \mapsto p_c \approx p(\mathbf{x}_c)$, where $\mathbf{x}_c$ is the center of cell c. Similarly, we have the space F^h defined in the center $\mathbf{x}_f$ of the face f with normal $\boldsymbol{\eta}_f$, whereas $\alpha : C \times \mathcal{F} \to \{1, -1\}$ encodes the orientation of the face normals, with $\alpha_{c,f}\boldsymbol{\eta}_f$ pointing outward.

3.1 Momentum equations

In the interior of each of the phases, the momentum equations are discretized using the symmetry-preserving finite-volume method of [Verstappen and Veldman, 2003]. Near the interface we choose to discretize the momentum equations in strong form, thereby sacrificing exact momentum conservation but alleviating difficulties faced with arbitrarily small cells $|c^\pi|(t)$ and non-smooth-in-time face areas $|f^\pi|(t)$. At the interface we use a first-order upwind convection scheme *per phase*, which relies on linear extrapolation of velocities. The interface is represented using the volume fraction field $\bar{\chi} = |c^l|/|c| \in C^h$ as per the Volume-of-Fluid method. Advection of the interface is performed using the Lagrangian-Eulerian Advection Scheme (LEAS) [Zinjala and Banerjee, 2015].

The time integration is performed under a CFL constraint of 0.5 using a second-order accurate explicit method, followed by a pressure correction step

$$\frac{u_f^* - u_f^{(n)}}{\Delta t} = R\left(\frac{3}{2}u_f^{(n)} - \frac{1}{2}u_f^{(n-1)}\right)_f, \quad u_f^{(n+1)} = u_f^* - \frac{\Delta t}{\rho}(Gp)_f, \quad \forall f \in \hat{\mathcal{F}}. \tag{8}$$

Here R denotes the convection and gravity terms, and $G : C^h \to \hat{F}^h$ is the gradient operator.

The pressure implicitly couples the two phases. To make the velocity field divergence free, the Laplace operator is decomposed in a divergence $\bar{D} : \hat{F}^h \to C^h$ and a gradient G:

$$\bar{D}\left(\frac{1}{\rho}Gp\right)_c = \bar{D}\,(u^*)_c\,, \quad \forall c \in C. \tag{9}$$

The gradient G contains the value jump due to capillarity, as well as the jump in the normal derivative.

At the interface the velocity field is discontinuous, and the divergence operator needs to be modified. A finite-difference Ghost Fluid Method (GFM) [Liu et al., 2000] will result in an incompatible discretization of the pressure Poisson problem. As there will be functions $u \in \hat{F}_0^h$, i.e. vanishing at the boundary, which are not solenoidal, hence do not all satisfy a discrete Gauss divergence theorem. A consequence of this incompatibility is that the resulting pressure Poisson equation has no solution.

A finite-volume approach naturally preserves the flux cancellation property which a divergence operator should satisfy, and hence all solutions in $\hat{F}_0^h$ do satisfy a discrete Gauss theorem. We choose the cut-cell method [Udaykumar et al., 1997]. Face apertures $A_f \in F^h$ are computed (from the PLIC reconstruction) as the fraction of the face $f \in \mathcal{F}$ contained in the reference fluid l, so $A_f = |f^l|/|f|$. This gives the divergence operator

$$|c|\bar{D}\,(u)_c = \sum_{f \in \mathcal{F}(c)} \alpha_{c,f}|f|\bar{u}_f, \tag{10}$$

where we define the mixture velocity $\bar{u}_f = A^f u_f^l + (1 - A^f)u_f^g$ (Fig. 1a).

In the interior of the phases we define the gradient G as a standard finite difference operator. Near the interface the gradient needs modification to sharply capture the imposed jumps, as will be described next.

3.2 The Ghost Fluid Method

We consider a finite-difference approximation for the gradient at a face $f \in \mathcal{F}_I$ near the interface. The pressure $p \in C^h$ is defined point-wise according to the liquid indicator $\chi \in C^h$ ($\chi = 1$ in liquid and $\chi = 0$ in gas). Now, consider a face f which connects two nodes $C(f) = \{c, c'\}$ from different phases

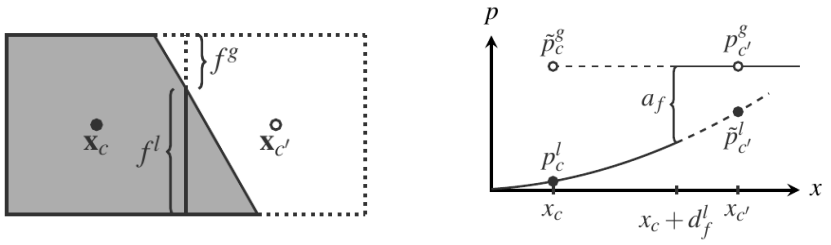

(a) CCM: Each face is split into its liquid and gaseous part $f = f^l \cup f^g$. Shaded region corresponds to the liquid parts c^l, c'^l.

(b) GFM: The pressure values denoted by $\tilde{p}$ are 'ghost' pressures and not actually part of the solution.

Fig. 1: Illustration of the cut-cell method (CCM: left) and the ghost fluid method (GFM: right).

(so $\chi_c \neq \chi_{c'}$). Hence we know the liquid pressure p_c^l on one side of the face and the gas pressure $p_{c'}^g$ on the other side of the face. Also, we can evaluate the value jump $a_f = -\sigma\kappa_f$ (with κ calculated via a generalized local height function [Popinet, 2009]) and gradient jump b_f. The unkown scaled gradients are denoted by g_f^π (Fig. 1b).

The scaled mixture gradients, as per the Ghost Fluid Method [Liu et al., 2000], are then given by

$$\bar{g}_f = \frac{1}{\bar{\rho}_f}(\bar{G}p)_f = \frac{1}{\bar{\rho}_f}(Gp)_f + \frac{\delta_f a_f}{\bar{\rho}_f h_f} - b_f \frac{\hat{\rho}_f}{\bar{\rho}_f}, \tag{11}$$

where $\bar{\rho}_f$, $\hat{\rho}_f$ are average densities depending on the face aperture A_f and the distance to the interface. The difference between the liquid indicators at opposite sides of the face f is denoted by $\delta_f = h_f(G\chi)_f \in \{-1, 0, 1\}$. If the value jump a_f is known at second order accuracy, it follows that the resulting gradient will be at most first order accurate in h_f.

The jump in the pressure gradient occurs only in the component normal to the interface. In [Liu et al., 2000] it is assumed that the jump component tangential to the interface vanishes: $b_f = \alpha_{i_f,f}[\![u_\eta^*]\!]$, where $\alpha_{i_f,f} = \boldsymbol{\eta}_{i_f} \cdot \boldsymbol{\eta}_f$ is the face normal component of the interface normal $\boldsymbol{\eta}_{i_f}$. We refer to this approach as the *'one-dimensional' GFM (1d-GFM)*.

Whenever the interface is not aligned with the face f (hence $|\alpha_{i_f,f}| \neq 1$), the 1d-GFM is inconsistent. A *multi-dimensional GFM (Md-GFM)* has been developed, in which we replace the expression for b_f by a formula which consistently imposes the normal derivative jump condition on the gradient (7). As (7) involves the dot product of the full gradient with the interface normal, for the interpolation to the face f of interface tangential pressure derivatives will be required. The interface configuration, defined by the indicator χ as well as the face apertures $A \in F^h$, defines two types of interface faces where the gradient will be modified:

- If a face f connects two nodes $C(f) = \{c, c'\}$ from different phases (so $\chi_c \neq \chi_{c'}$) we call this an interface normal face $\in \mathcal{F}_{\mathcal{I}_\eta}$ (Fig. 2a).
- On the other hand, if a face f connects two nodes from the same phase, but with a nontrivial aperture (so $A_f \notin \{0, 1\}$) then we call this an interface tangential face $\in \mathcal{F}_{\mathcal{I}_\tau}$ (Fig. 2b).

For the discretization of the gradient operator for an interface normal face we choose two faces $\hat{f}^g \in \hat{\mathcal{F}}^g$, $\hat{f}^l \in \hat{\mathcal{F}}^l$ whose face normals are orthogonal to $\boldsymbol{\eta}_f$. From here we define the jump interpolant as (Fig. 2a)

$$(Ju)_f = \boldsymbol{\eta}_f[\![u_f]\!] + \boldsymbol{\eta}_{\hat{f}^g} u^g_{\hat{f}^g} - \boldsymbol{\eta}_{\hat{f}^l} u^l_{\hat{f}^l}, \tag{12}$$

Using this jump interpolant we can consistently impose (7)

$$\boldsymbol{\eta}_{i_f} \cdot \Big[(Jg)_f - (Ju^*)_f\Big] = 0. \tag{13}$$

Combining (12) and (13), and solving for $[\![g_f]\!]$, yields the jump across the face f

$$b_f^\eta = \frac{\boldsymbol{\eta}_{i_f} \cdot (Ju^*)_f}{\alpha_{i_f,f}} - \frac{\alpha_{i_f,\hat{f}^g}}{\alpha_{i_f,f}} g^g_{\hat{f}^g} + \frac{\alpha_{i_f,\hat{f}^l}}{\alpha_{i_f,f}} g^l_{\hat{f}^l}. \tag{14}$$

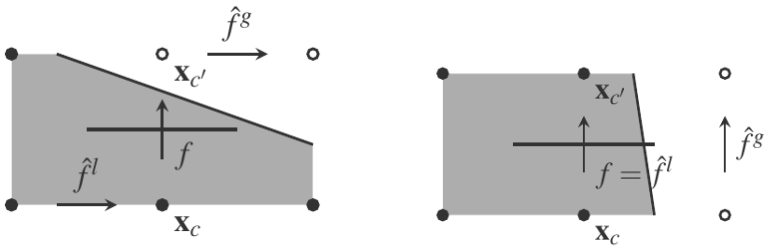

(a) Interface normal face $f \in \mathcal{F}_{I_\eta}$. (b) Interface tangential face $f \in \mathcal{F}_{I_\tau}$.

Fig. 2: Examples of Md-GFM gradient stencils.

The faces $\hat{f}^g, \hat{f}^l$ should be chosen such that the evaluation of the interpolant can be done explicitly, hence $\hat{f}^\pi \notin \hat{\mathcal{F}}_{I_\eta}$. Moreover, the interpolant should result in a compact 6-point stencil for the Md-GFM gradient. Ensuring $|\alpha_{i_f,\hat{f}^\pi}/\alpha_{i_f,f}| \leq 1$ greatly improves the quality of the Md-GFM operator. For faces $f \in \mathcal{F}_{\mathcal{I}_\eta}$ for which this ratio exceeds 1 we interpret the face as an interface tangential face instead.

For an interface tangential face $f \in \mathcal{F}_{\mathcal{I}_\tau}$ we select two faces $\hat{f}^g, \hat{f}^l$ (one of which coincides with f itself) with the same face normal direction but each in a different phase to be used for computing the gradient jump (Fig. 2b). This results in the following gradient jump

$$b_f^\tau = \frac{1}{\rho^g}(Gp)_{\hat{f}^g} - \frac{1}{\rho^l}(Gp)_{\hat{f}^l}. \tag{15}$$

Composition of the CCM divergence operator with the aforementioned modified gradient operator defines our Laplace operator, with a stencil fitting in 3×3. It is no longer self-adjoint but can still be shown to be negative semi-definite with only the constant pressure in the null-space.

4 Verification and validation

4.1 Poisson problem

We first compare our proposed method to the Immersed Interface Method (IIM) [Leveque and Li, 1994] which sharply imposes jump conditions directly on the Laplacian. Hereto, we consider 'Problem 3' as given by [Leveque and Li, 1994] (with $\beta = \rho^{-1}$):

$$\nabla \cdot \left(\frac{1}{\rho}\nabla p\right) = f, \quad \mathbf{x} \in \Omega = (-1, 1)^2. \tag{16}$$

The right-hand side f, the Dirichlet conditions, as well as the jump conditions at the interface correspond with the exact solution $p = \exp(x)\cos(y)$ when $\mathbf{x} \in \Omega^l$, whereas $p = 0$ when $\mathbf{x} \in \Omega^g$. Here Ω^l is the interior of a circle with radius $\frac{1}{2}$ centered at the origin. Note that p is discontinuous and has a jump in the normal as well as tangential derivative.

N	IIM	1d-GFM	Md-GFM
20	4.38×10^{-4}	7.78×10^{-3}	2.67×10^{-3}
40	1.08×10^{-4}	6.48×10^{-3}	6.15×10^{-4}
80	2.78×10^{-5}	6.47×10^{-3}	1.56×10^{-4}
160	7.50×10^{-6}	3.20×10^{-3}	3.36×10^{-5}
320	1.74×10^{-6}	1.49×10^{-3}	9.11×10^{-6}

ρ^g/ρ^l	$\|\frac{1}{\rho}\nabla p - \frac{1}{\rho}Gp^h\|_{L^\infty}$
10^6	3.14×10^{-2}
10^3	3.14×10^{-2}
10^0	3.24×10^{-2}
10^{-3}	2.14×10^{-2}
10^{-6}	2.14×10^{-2}

Table 1: *(Left)* The error $\|p - p^h\|_{L^\infty}$ for the Poisson problem defined by (16) (IIM results from [Leveque and Li, 1994]). *(Right)* Dependence of the scaled gradient error on the density ratio ρ for the Md-GFM.

We first let $\rho^l = \rho^g = 1$ and vary the mesh-width as $h = 2/N$ where $N = 10 \times 2^l$ for $l = 1, \ldots, 5$. The resulting L^∞ errors in the pressure are shown in Table 1a. As expected, the 1d-GFM is first-order accurate, whereas the Md-GFM is second-order accurate, and of comparable accuracy to the IIM. The main advantage of using the Md-GFM is that the Laplace operator itself follows from the *composition* of

a divergence operator and a gradient operator which is required in the context of solving incompressible two-phase problems.

To asses the dependence of the errors on the density ratio we fix the mesh-width $h = 2/80$, and vary the density ratio. The resulting gradient errors are shown in Table 1b. We note that the accuracy of the gradient is independent of the density ratio. Hence the proposed method can be used to accurately simulate near the one-phase limit $\rho^g \to 0$.

4.2 A dambreak problem

The proposed discretization has been implemented in our in-house two-phase Navier-Stokes solver ComFLOW [Wemmenhove et al., 2015]. Local, adaptive mesh refinement is used, as in [Van der Plas, 2017].

A dambreak problem is studied in a rectangle of size $20 \times 12m$ with an elliptic bathymetry of half lengths 18 and $2.8\,m$ whose center lies in the left-hand side bottom corner. Slip boundary conditions are imposed. The liquid density is given by $\rho^l = 10^3\,kg/m^3$, the gas density varies and will always be indicated. Both fluids are initially at rest and separated by the interface profile $y(x) = 7.6 + 3.6\tanh(0.36\,(x - 12.5))$. This will result in a flip-through impact (FTI) [Etienne et al., 2018] in which the wave trough and crest reach the wall at the same time instance, resulting in a violent impact. The gravitational acceleration is $g = -9.81\,m/s^2$ and the surface tension $\sigma = 0.072\,J/m^2$ with static contact angle of 90°.

Our base mesh is uniform with $N_x = 80$ and $N_y = 48$ cells in the x- and y-direction respectively. We consider several levels of mesh refinement, where we refine the mesh near the interface using blocks of size 16×16. The refinement level at the interface $l \in \{2, 3, 4\}$ will always be indicated, the resulting interface mesh-width is given by $h = 2^{-(l+2)}m$.

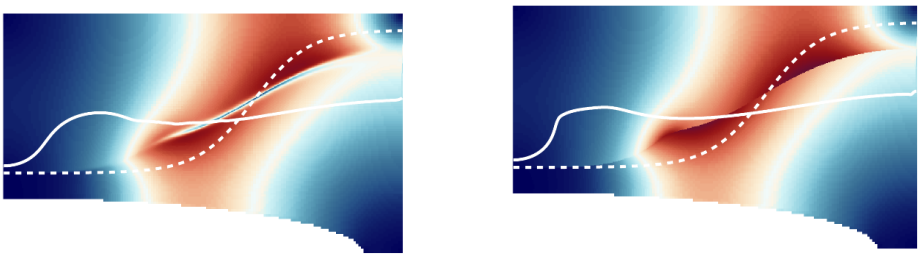

(a) Standard two-phase model. (b) Proposed two-phase model.

Fig. 3: The absolute velocity $|\mathbf{u}|$ at $t = 0.75$. The interface is shown at $t = 0$ and $t = 1.47$.

We first demonstrate the efficacy of the proposed model when compared to the standard two-phase model for $\rho^g = 1$ and $l = 3$. For this case, Fig. 3 shows the resulting absolute velocity as the initial interface profile (dashed) and at a later time $t = 1.47$ (solid). Note that the standard two-phase model has a thin region at the interface in which the velocity transitions from gas to liquid. Our proposed model captures this transition in a discontinuity, which allows the breaking wave to develop properly, as seen by the interface profile at $t = 1.47$.

To show the dependence of the solution on the gas density, we vary it as $\rho^g = 10^{-3}$, 1, 3 and $5\,kg/m^3$. For the latter three cases a reference exists by CADYF [Etienne et al., 2018]. Figure 4(top) shows a fair agreement in terms of the interface profile. The maximum tangential velocity jump increases as the gas density decreases, which may be expected (Fig. 4(bottom)). For larger gas densities, oscillations in the tangential velocity jump can be observed just before impact, suggesting that free surface instabilities are about to develop. Such oscillations are not present for $\rho^g = 10^{-3}$, meaning that we successfully approach the one-phase limit in which no free surface instabilities due to shearing gas flow are present.

5 Conclusion

We presented a discretization approach for capturing contact discontinuities in two-phase flow, with emphasis on the discretization of the pressure Poisson problem. It imposes smoothness of the velocity field *only in the interface normal direction*. A novel combination of our proposed Md-GFM and the CCM

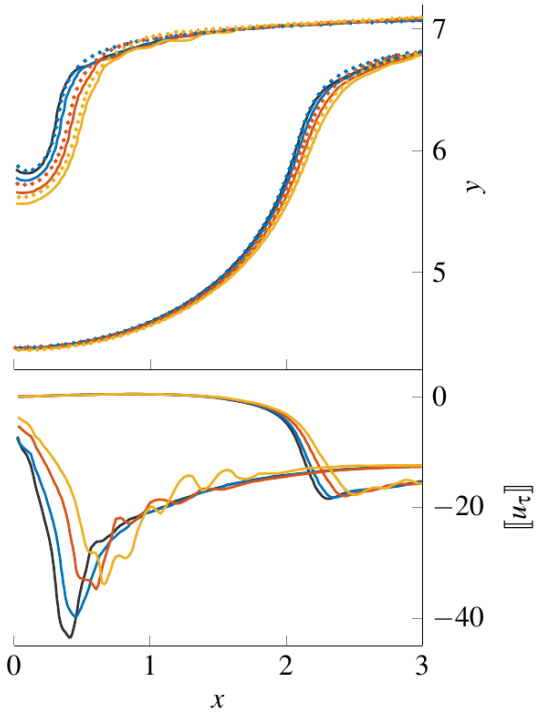

Fig. 4: Interface profiles (top) and velocity discontinuity (bottom) for gas densities $\rho^g = 10^{-3}$ (black), 1 (blue), 3 (red) and $5\,kg/m^3$ (yellow) at $t = 1.47$ and 1.67. The grid-refinement level was $l = 3$. Reference solutions by CADYF (colored markers) [Etienne et al., 2018].

was used to achieve this. We demonstrated that this approach is able to capture contact discontinuities sharply and accurately, even at high density ratios (demonstrated up to 10^{-6}) close to the one-phase limit. After adding the effects of compressibility and viscosity, we want to use this model to study the effects of free surface instabilities in sloshing of LNG and its vapor.

Acknowledgements This work is part of the research programme SLING, which is (partly) financed by the Netherlands Organisation for Scientific Research (NWO).

References

Etienne, S., Scolan, Y.-M., and Brosset, L. (2018). Numerical study of density ratio influence on global wave shapes before impact. In *37th Int. Conf. Ocean, Offshore Arctic Eng.* Paper OMAE2018-78624.

Lafeber, W., Brosset, L., and Bogaert, H. (2012). Comparison of wave impact tests at large and full scale: Results from the Sloshel project. In *22nd Int. Symp. Offshore Polar Eng.*, volume 4, pages 285–299.

Leveque, R. J. and Li, Z. (1994). The immersed interface method for elliptic equations with discontinuous coefficients and singular sources. *SIAM J. Numer. Anal.*, 31(4):1019–1044.

Liu, X.-D., Fedkiw, R. P., and Kang, M. (2000). A boundary condition capturing method for poisson's equation on irregular domains. *J. Comput. Phys.*, 160:151–178.

Popinet, S. (2009). An accurate adaptive solver for surface-tension-driven interfacial flows. *J. Comput. Phys.*, 228(16):5838–5866.

Udaykumar, H. S., Kan, H.-C., Shyy, W., and Tran-Son-Tay, R. (1997). Multiphase dynamics in arbitrary geometries on fixed Cartesian grids. *J. Comput. Phys.*, 137(2):366–405.

Van der Plas, P. (2017). *Local Grid Refinement for Free-Surface Flow Simulations*. PhD thesis, University of Groningen.

Verstappen, R. W. C. P. and Veldman, A. E. P. (2003). Symmetry-preserving discretization of turbulent flow. *J. Comput. Phys.*, 187(1):343–368.

Wemmenhove, R., Luppes, R., Veldman, A. E. P., and Bunnik, T. (2015). Numerical simulation of hydrodynamic have loading by a compressible two-phase flow method. *Comput. Fluids*, 114:218–231.

Zinjala, H. K. and Banerjee, J. (2015). A Lagrangian-Eulerian volume-tracking with linearity-preserving interface reconstruction. *Numer. Heat Transfer, Part B*, 68:459–478.

Towards the Modeling of Laminar to Turbulence Transition for Incompressible Flows

Ginevra Rubino* **and Michel Visonneau***
*ECN/CNRS, Nantes, France †
ginevra.rubino@ec-nantes.fr

1 Introduction

Nowadays, in the context of transition modeling, the CFD community is moving towards the so-called Local-Correlation based Transition Modeling (LCTM) concept. The main idea is to provide a set of generic transport equations built using local informations, based on experimental correlations and coupled with the already existing turbulence models. Within LCTM, the γ model, Menter et al. (2015), is the transition model that we are going to analyze.
The γ model is included in the class of transition models based on the intermittency concept and the use of only local informations to trigger the transition. Within LCTM, it is the only model Galilean invariant. The transport equation for the intermittency γ is:

$$\frac{\partial(\rho\gamma)}{\partial t}+\frac{\partial(\rho u_j\gamma)}{\partial x_j}=\underbrace{F_{\text{onset}}[F_{\text{length}}(\rho S(1-\gamma)\gamma)]}_{P_\gamma}-\underbrace{c_{a2}\rho\Omega\gamma F_{\text{turb}}(c_{e2}\gamma-1)}_{E_\gamma}+\frac{\partial}{\partial x_j}\Big[\Big(\mu+\frac{\mu_t}{\sigma_\gamma}\Big)\frac{\partial\gamma}{\partial x_j}\Big]. \tag{1}$$

E_γ and P_γ are the relaminarization/destruction term and production term, respectively. In the latter, the constant $F_{\text{length}}=100$ determines the magnitude of the production term, while F_{onset} is defined through an empirical correlation and it is meant to activate the production of intermittency inside the boundary layer, when the transition process starts. The definition of the correlation F_{onset} slightly changes according to the transition mechanism. It is based on the relation between the vorticity Reynolds number Re_v and the momentum thickness Re_{θ_c},

$$\frac{Re_V}{2.2Re_{\theta_c}}. \tag{2}$$

Experimentally, indeed, it was observed that transition occurs when $Re_V=\frac{\rho y^2 S}{\mu}$ reaches a critical value inside the boundary layer.
The critical Reynolds number is computed through the correlation $Re_{\theta_c}=f(Tu_L,\lambda_{\theta L})$, which depends on local quantities computed inside the boundary layer:

- the level of turbulence intensity inside the boundary layer is expressed as

$$Tu_L=\min\left(100\frac{\sqrt{2k/3}}{\omega y},100\right); \tag{3}$$

- the pressure gradient parameter λ_θ can be expressed exploiting the incompressibility constraint in 2D as

$$\lambda_\theta=\frac{\rho\theta^2}{\mu}\frac{dU}{dS}=-\frac{\rho\theta^2}{\mu}\frac{dV}{dy}, \tag{4}$$

  where $\frac{dU}{dS}$ is the flow acceleration in the stream-wise direction, at the edge of the boundary layer and $\frac{dV}{dy}$ is the derivative of the wall normal velocity component V in respect of the direction normal to the wall.

For a general geometry, $\frac{dV}{dy}$ can be computed as:

$$\frac{dV}{dy}\equiv\nabla(\mathbf{n}\cdot\mathbf{U})\cdot\mathbf{n}. \tag{5}$$

where $\mathbf{U}$ and $\mathbf{n}$ are the velocity and normal to the wall vectors, respectively.

Coupling with SST turbulence model. In the original $k-\omega$ SST turbulence model, the transport equation for the turbulence kinetic energy k is modified as it follows:

$$\frac{\partial(\rho k)}{\partial t}+\frac{\partial(\rho u_j k)}{\partial x_j}=P'_k+P_k^{\lim}-D'_k+\frac{\partial}{\partial x_j}\Big[\big(\mu+\sigma_k\mu_t\big)\frac{\partial k}{\partial x_j}\Big], \tag{6}$$

where the primary production term P'_k and the destruction term D'_k are redefined as

$$P'_k=\gamma P_k \text{ and } D'_k=\max(\gamma,0.1)\cdot D_k. \tag{7}$$

The term P_k in Eq.(7) is equal to $\mu_t S\Omega$, according to Kato-Launder modification. The additional term of production $P_k^{\lim}$ is added in order to make the transition prediction more reliable when it develops under low turbulence intensities.
Finally, the blending function F_1 is redefined in order to guarantee the use of $k-\omega$ formulation in the near wall region. In the presented work, γ model has been coupled with the 1994 version $k-\omega$ SST from Menter.
We are going to discuss a 2D and a 3D computation. The simulations presented in the following where computed using ISIS-CFD solver for incompressible flows.

2 2D-Flat Plate

With the purpose of evaluating the modeling error, we will present the results around a flat plate for $Re=10^7$ has been run. The inlet turbulence intensity is set to $Tu=0.536609\%$ and three different eddy viscosity ratios $\nu_t/\nu=\{270,280,290\}$ were tested in order to evaluate the input/parameter uncertainties. The simulations were run on a set of five geometrical similar structured O-grids provided by IST.
Multivariate Metrics. Following ASME V&V 20-2009, given a set of n validation points, we define the $n\times n$ covariance matrix $U_{\text{val}}=U_{\text{num}}+U_{\text{d}}+U_{\text{input}}$, whose entrances are the sum of the numerical, experimental and input uncertainties. Computed the comparison error $E=S-D$ (S numerical, D experimental) at each given point, we define the multivariate metric as

$$E_{\text{mv}}=\sqrt{E^T U_{\text{val}}^{-1}E}. \tag{8}$$

Assuming that each estimate of the comparison E and u_{val} is distributed as a Gaussian, we can define a reference value for the multivariate metric $E_{ref}=\sqrt{n+\sqrt{2n}}$.
Through the multivariate metrics we can state that if E_{mv}/E_{ref} is larger than one, it is an indication that the model is not able to reproduce the experimental data within the range of the validation uncertainty at each set point.
Results. In Figures (1) and (2) are presented the C_f and the velocity profile V_x/V at $X/L=0.02035$ (transition region) with the estimated error bars next to the correspondent comparison errors $E(C_f)$ and $E(V_x/V)$. The multivariate metrics are reported in Tables (1) and (2).
In Fig.(1), we plot the skin friction profile all along the flat plate. The main discrepancies between the model and the experimental data are in the transition region: the model predicts higher values of skin friction in the transition region in respect of the experiments. It is interesting that there is no overlapping between the numerical and experimental error bars in this region and this reflects the high multivariate metrics computed in this zone (Table(1)). The source of this high uncertainty is related to the lack of accuracy of the model, but also to the lack of accuracy of the experimental data. In addition, the experimental uncertainty is very low and that could be an additional reason of the error bars non-overlapping. The quantitative discrepancies between the experimental data and the computations in the laminar region are related to the fact that the values of turbulence kinetic energy at the leading edge between computations and experiments do not match, despite the freestream turbulence intensity at the inlet of the computational domain has been tuned in order to have the experimental value of k at the leading edge. Minor differences are observed in the turbulence region.
In general, the numerical uncertainty is the biggest contributor to the matrix U_{val}. Indeed, despite we

obtain reasonable value of the order of accuracy p, which is above 1.6, the numerical uncertainty percentage is high because the meshes are not in the asymptotic range. For this reason, we are planning to run new simulations on a set of finer meshes.
In Fig.(2), the velocity profile V_x/V at $X/L = 0.02035$ in the transition region is plotted. We notice that numerically the production term of turbulence kinetic energy is too strong, slightly accelerating the transition process in the boundary layer. As discussed for the skin friction distribution, the modeling error results to be higher in the transition region in respect of the laminar and turbulence one, as we can observe from the multivariate metrics computed at three different slices in the three different regions reported in Table(2).

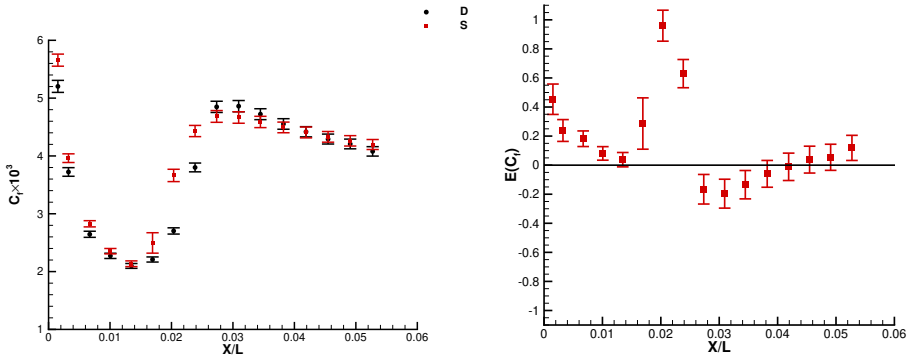

(a) Numerical (S) and Experimental (D) $C_f \times 10^3$ profiles on the flat plate surface.

(b) Comparison error $E(C_f)$.

Fig. 1: Error bars for the Skin Friction C_f.

	Laminar Region	Transition Region	Turbulent Region	Total
E/E_{ref}	2.34	4.03	0.71	2.89

Table 1: Multivariate metric for the skin friction in different regions and all over the flat plate.

	$X/L = 0.01006$	$X/L = 0.02035$	$X/L = 0.05273$
E/E_{ref}	1.58	4.56	1.73

Table 2: Multivariate metric for the velocity profiles at different positions along the flat plate.

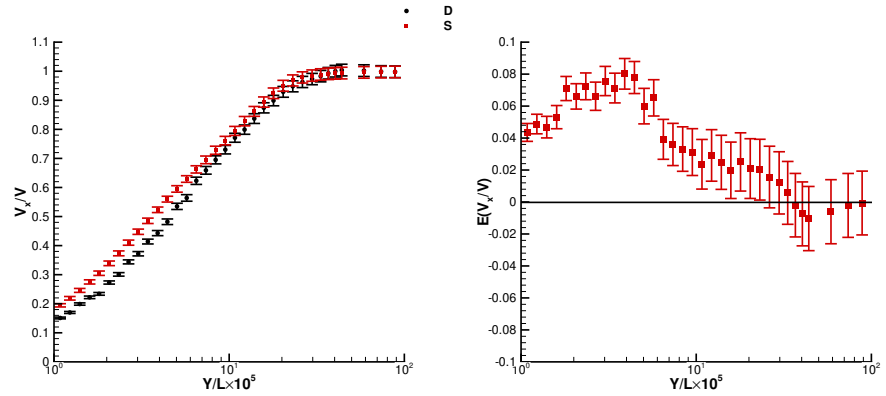

Fig. 2: V_x/V and $E(V_x/V)$ with error bars in the transition region at $X = 0.02035L$.

3 γ Model - Towards 3D

The crossflow effects in the γ model are included through the C1-correlation proposed by Arnal (1984). According to the correlation, the crossflow transition occurs when the following criterion is met:

$$\frac{Re_{\delta^*_{\delta 2t}}}{150 f(H_S)} \geqslant 1, \tag{9}$$

where $Re_{\delta^*_{\delta 2}}$ is the crossflow Reynolds number and $f(H_s)$ is a function of the shape factor.
The C1 criterion is locally formulated and implemented as:

$$T_{\mathrm{C1local}} = \frac{C_{RSF}}{150}(G\Psi Re_V) > 1. \tag{10}$$

Each function in the parenthesis in (10) accounts for a specific effect:

- G accounts for the influence of the pressure gradient, i.e. the shape factor;
- the indicator Ψ is a non-dimensional measure of the local crossflow strength in respect of the streamwise strength and it is defined as:

$$\Psi = \left|\vec{n} \cdot \nabla\left(\frac{\vec{\omega}}{|\vec{\omega}|}\right)\right| y, \tag{11}$$

  with $\vec{n}$ wall normal and $\vec{\omega}$ vorticity. The vorticity $\vec{\omega}$ and its derivatives in the normal direction are used because they are the only physical quantities which describe the 3-dimensionality of the boundary layer;
- Re_V is the local vorticity Reynolds number.

The crossflow transition is then triggered through the onset function

$$F_{\mathrm{onset,CF}} = \min[\max[100(T_{\mathrm{C1local}} - 1), 0], 1]. \tag{12}$$

3.1 6:1 Prolate Spheroid

The model described above was tested on the 6:1 prolate spheroid configuration. We compared two different simulations with the experimental results performed in the low speed wind tunnel at DLR Gottingen, Kreplin et al. (1985). The simulations have run for $\alpha = 15°$, $Re = 6.5 \times 10^6$. Under these conditions Tolmienn-Schlichting transition is observed on the leeward side next to the symmetry plane, while the transition in the middle and windward side is dominated by crossflow instabilities.
We have set to different combinations of values of turbulence intensity and eddy viscosity ratios at the inlet: (1) $Tu = 0.15\%$ and $\frac{\nu_t}{\nu} = 21$, (2) $Tu = 0.5\%$ and $\frac{\nu_t}{\nu} = 250$. The first combination leads to $\omega = 1$ and it represents an unphysical way to reduce the turbulence kinetic energy decay ahead of the leading edge; the second combination mathematically results in a value of k at the leading edge as the one of the experiments. Simulations have been run on half model. The grid, provided by DLR, is unstructured with a total number of nodes $N = 53938$, of which 1253 on the spheroid surface, with $y^+ = 1$.
Results. In Fig.(3) are shown the experimental and the numerical skin friction distributions on the surface for the different inlet conditions. The differences between computations and experiments are huge: none of the computations is able to predict crossflow transition, because the crossflow criterion is never activated in the first cells next to the wall. In both cases, the model is predicting natural transition.
In Fig.(3b) and (4a), we observe the skin friction distribution for $Tu = 0.15\%$ and $\frac{\nu_t}{\nu} = 21$, on two different planes x-z and x-ϕ, where $0° \leqslant \phi \leqslant 180°$. On the leeward side, next to the symmetry plane, transition due to T-S waves occurs at about 10% of the spheroid length, upward in respect of the experiments. Indeed, experimentally, transition occurs along the isoline $C_f = 0.0025$, which are denoted by the black dots in Fig.(4). At about 10% of the spheroid length, we observe the upper side kink, which is less pronounced with respect to the experimental results. This discontinuity is present because of the change on

the transition mechanism, from T-S to crossflow instabilities. However, on the windward side the model does not predict any transition and the flow only transitions as it separates at the trailing edge, where the skin friction lines converge. Also the topology of the skin friction lines is questionable, indeed, because of the high angle of incidence, we were expecting the streamlines on the windward side to converge to the primary separation line upward with respect to what is predicted by the present computations.
In Fig.(3c) and (4b) another scenario is visible for $Tu = 0.5\%$ and $\frac{\nu_t}{\nu} = 250$. It is evident the extreme sensitivity of the model to the inlet parameters: an higher value of turbulence kinetic energy at the inlet results in a faster transition. This is the reason why the flow transitions at about 5% of the length the spheroid. The transition is due to a 2D mechanism, because neither in this case the crossflow criterion is ever activated as it has mentioned before. Nonetheless, this kind of behavior was not expected according to the experiments and it is allegedly due to a excessive numerical production of turbulence kinetic energy inside the boundary layer related to the computation of the velocity derivative normal to the wall.

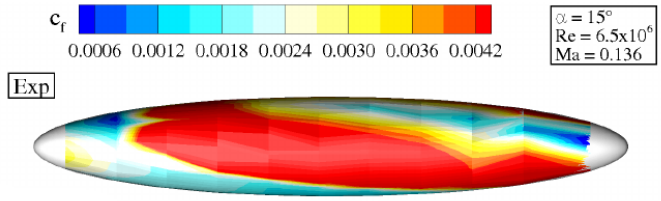

(a) Experimental Results from Grabe et al. (2016).

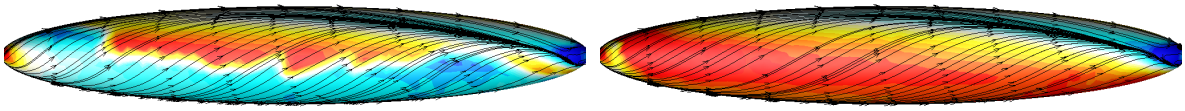

(b) Numerical results for $\frac{\nu_t}{\nu} = 21$ and $Tu = 0.0015$ at the inlet.(c) Numerical results for $\frac{\nu_t}{\nu} = 250$ and $Tu = 0.005$ at the inlet.

Fig. 3: Top views of experimental and numerical results of the crossflow transition around a spheroid for $\alpha = 15°$. Skin-friction lines are added to computations.

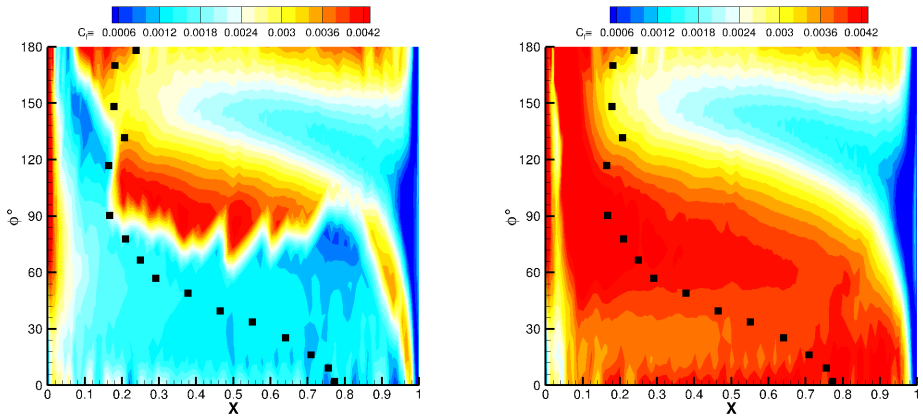

(a) (b)

Fig. 4: Cf distribution in the $x - \phi$ plane for $\frac{\nu_t}{\nu} = 21$ and $Tu = 0.0015$ at the inlet (left) and for $\frac{\nu_t}{\nu} = 250$ and $Tu = 0.005$ at the inlet (right) vs experimental iso$-C_f-$line $C_f = 0.0025$ (black dots).

For what concerns the trigging of crossflow transition, we think that the problem relies on the calculation in Eq.(10) of $\vec{\phi}$, i.e. the derivative of the vorticity vector, in the first layer of cells next to the wall. An extremely accurate calculation of the second derivative of the velocity is here demanded in order to

activate the criterion and to trigger the crossflow transition.
The second derivative of the velocity is calculated through an Hessian function. Each entrance of the Hessian matrix for a generic quantity Q is built through a least square 2nd order accurate interpolation. Although this Hessian calculation has been demonstrated to be efficient far from the wall, it does not ensure an accurate estimation of the second derivate in the first two layers from the wall where transition is occurring.

4 Conclusion

The presented results made possible to discover some deficiencies of the only Galilean invariant model that is at our disposal in literature, the γ model. All the issues that have been discussed in 2D are mainly related to the implementation of the model. Among all, a not accurate calculation of the velocity derivative normal to the wall can result in an excessive production of turbulence kinetic energy inside the boundary layer. This leads both to an over prediction of the skin friction (flat plate results) and to the not accurate prediction of the transition position isoline, as it is the case for the spheroid on the leeward side. It seems that the choice of the the turbulence model for the coupling (Menter (1994) vs Menter (2003)) does not affect the results, however further investigation should be done for the 3D case. Concerning the crossflow implementation, the main issues are related to the calculation of the second derivative of the velocity in the boundary layer. Extreme accuracy is demanded in the first two layers in order to trigger the transition correlation. Nonetheless, it is necessary to estimate first the physical validity of the included crossflow criterion, then, possibly, to find a new method for the calculation of the second derivatives.
In general, γ-model is extremely sensitive to the inlet parameters. The decay of turbulence kinetic energy ahead of the body strongly affects the numerical results, thus a prior tuning of the input parameters is necessary for a successful computation. Nonetheless, the use of non-physical inlet values, such as enormous values of eddy viscosity ratio to control the turbulence decay, is a topic that is worthwhile to discuss.
In the next future, we are planning to implement the $\gamma - Re_\theta$ model both for Tollmien-Schlichting and crossflow transition.

References

Standard for Verification and Validation in Computational Fluid Dynamics and Heat Transfer. ASME, 2009.

C. Grabe, N. Shengyangand and A. Krumbein (2016) . Transition Transport Modeling for the Prediction of Crossflow transition. 34th AIAA Applied Aerodynamics Conference 2016, Washington D.C., USA.

H.P. Kreplin, H. Vollmers and H.U. Meier (1985). Wall Shear Stress Measurements on an Inclined Prolate Spheroid in the DFVLR 3m x 3m Low Speed Wind Tunnel, Gottingen. DFVLR-AVA, Report Ib 22-84 A 33, 1985.

F.R. Menter, P.E. Smirnov, T. Liu and R. Avancha. A One-Equation Local Correlation-Based Transition Model. *Flow Turbulence Combust*, **95**, 583–619.

https://www.sharcnet.ca/Software/Ansys/17.0/en-us/help/cfx_thry/i1067426543678865.html

eXtended Discontinuous Galerkin (X-DG) for bi-material elliptic problem

Ahmed Sherif[*], **Michel Visonneau**[*,†], **Ganbo Deng**[*,†], **and Luís Eça**[‡]
[*]ECN, LHEEA, Nantes/France, [†]CNRS, France, [‡]ULisboa/IST, Lisbon/Portugal
ahmed.sherif@ec-nantes.fr

1 Introduction

The development of high-order accurate numerical schemes for Computational Fluid Dynamics (CFD) applications is getting a considerable attention in the research community Wang et al., 2013, Kroll, 2006. When it comes to research in high-order schemes, the family of Discontinuous Galerkin (DG) Finite Element Method (FEM) is very popular.

The flow around a maneuvering ship is a problem of interest in the field of marine engineering. It involves multi-fluid (air-water) flow all within the limit of incompressibility hypothesis. The simulation of such incompressible flow requires an interface-capturing technique to numerically resolve the position of the air-water-ship interfaces when unfitted meshes are employed. An example of such interface-capturing techniques is the Level-Set method. Some work has been done to incorporate the Level-Set method into a DG framework using the concepts of eXtended FEM (X-FEM) Moës et al., 1999, as for instance the work presented in Utz, 2018 leading to the concept of extended DG (X-DG).

In this report, a first step towards the full development of a solver for laminar incompressible multi-fluid flow is shown. A technique to solve a bi-material elliptic problem is introduced. This could represent the step for solving the pressure equation or the Helmholtz equation of the viscous step in a projection method solver for Incompressible Navier-Stokes (INS) equations as in Karniadakis et al., 1991. This first step is composed of implementing the following:

- X-DG solver for *stationary interface* bi-material elliptic problems using linear elements
- X-DG solver for *stationary interface* bi-material elliptic problems using high-order elements
- X-DG solver for *moving interface* bi-material elliptic problems using high-order elements

where only the first point is discussed in this paper.

2 Problem Statement

Let $\Omega \subset \mathbb{R}^d$ be a bounded domain by a boundary $\partial\Omega$. Ω is divided into two disjoint subdomains

$$\overline{\Omega} = \overline{\Omega_1} \cup \overline{\Omega_2}, \qquad \Omega_1 \cap \Omega_2 = \emptyset$$

with an interface

$$\mathcal{I} = \overline{\Omega_1} \cap \overline{\Omega_2}.$$

A bi-material elliptic problem, whose solution presents a weak discontinuity at the interface, is stated as

$$\begin{cases} -\boldsymbol{\nabla}\cdot(\mu\boldsymbol{\nabla}u) = s & \text{in } \overline{\Omega_1} \cup \overline{\Omega_2}, \\ u = u_D & \text{on } \Gamma_D, \\ -\mu\boldsymbol{\nabla}u \cdot \boldsymbol{n} = g_N & \text{on } \Gamma_N, \\ [\![u\boldsymbol{n}]\!] = \boldsymbol{0} & \text{on } \mathcal{I}, \\ [\![\mu\boldsymbol{\nabla}u \cdot \boldsymbol{n}]\!] = 0 & \text{on } \mathcal{I}. \end{cases} \tag{1}$$

where u is the solution to the problem, μ is a material property that is discontinuous across the interface $\mathcal{I}$ (that is, $\mu = \mu_i$ in Ω_i for $i = 1, 2$), s is a known source term, u_D is a prescribed value of the solution on the Dirchlet boundary Γ_D, and g_N is a prescribed normal flux on the Neumann boundary Γ_N, with $\Gamma_D \cup \Gamma_N = \partial\Omega$. The *jump* operator $[\![\odot]\!]$ is defined as:

$$[\![\odot]\!] := \odot_{left} + \odot_{right}.$$

3 Concepts of eXtended Finite Element Method (X-FEM)

3.1 Enrichment Functions in Cut Elements

In the context of X-FEM Moës et al., 1999, Pommier et al., 2011, in an element K_i cut by an interface $\mathcal{I}$, the standard FE polynomial approximation of the solution is enriched by adding extra terms to the interpolation as follows:

$$u|_{K_i}(\boldsymbol{x}) \approx u^h|_{K_i}(\boldsymbol{x}) = \underbrace{\sum_{j=1}^{\mathtt{n_{en}}} N_j(\boldsymbol{x}) u_j}_{\text{Standard FE}} + \underbrace{\sum_{j=1}^{\mathtt{n_{en}}} H(\boldsymbol{x}) N_j(\boldsymbol{x}) a_j}_{\text{Enrichment}} \quad \in \mathcal{V}^h, \quad \text{if } K_i \cap \mathcal{I} \neq \emptyset.$$

where u_j is the value of the solution u at node j, N_j is the polynomial shape function of order k associated to node j, and $\mathtt{n_{en}}$ is the number of nodes per element. In a cut element, the approximation of the solution is enriched by an enrichment function H that allows for the representation of discontinuities within the element, and a_j are the enrichment nodal coefficients. The type and nature of the enrichment function depends on the type of discontinuity to be modelled Sala Lardies et al., 2012.

3.2 Level-Set Representation

The material interface is represented using Level-Set. Basically, a distance function $\phi(\boldsymbol{x})$ is defined that gives the shortest distance between a point and the interface. Assuming that the interface location is known, then each node i of the mesh is assigned a value ϕ_i that provides the information of how far this node is from the interface. The value of ϕ is zero on the interface, negative on one side, and positive on the other side. Furthermore, this distance function is interpolated within an element K_i using the standard FE shape functions as follows

$$\phi|_{K_i}(\boldsymbol{x}) \approx \phi^h|_{K_i}(\boldsymbol{x}) = \sum_{j=1}^{\mathtt{n_{en}}} N_j(\boldsymbol{x}) \phi_j \tag{2}$$

meaning that the Level-Set function is continuous across the interface.

3.3 Modified Intergration in Cut Elements

One of the main ingredients in X-FEM is the modified integration quadrature in each cut element. For this purpose, it is a must to accurately represent the interface within each cut element. A material interface is generally curved. High-order accurate representation of the interface is crucial for optimal convergence, see Cheng and Fries, 2010, Sala Lardies et al., 2012. However, in this paper, only linear approximation of the interface is adopted as a starting point in the development. Furthermore, only the simple case of an interface cutting through an element is discussed, where an interface cuts an element twice at two different edges, this is referred to as *basic* cut. Dealing with more complex cuts is discussed for instance in Gürkan et al., 2017. Fig. 1 summarizes the process for modifying the integration quadrature within the element and on the edges as well.

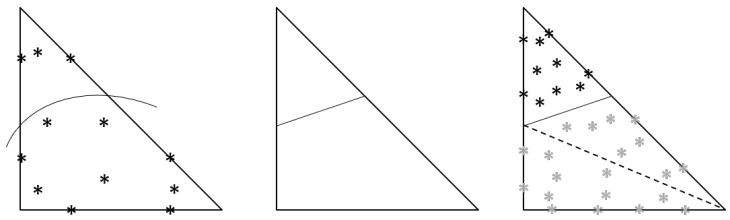

Fig. 1: Element with standard integration points and a curved interface cutting through (left), linear representation of the interface (center), and element with modified quadrature (right). In the right plot, integration points in black are in domain Ω_1 while grey points are in domain Ω_2, which is divided in two sub-domains.

4 Weak Form with no Condition on the Material Interface

The weak form of the bi-material elliptic problem is derived using the concepts discussed in Arnold et al., 2000, Arnold et al., 2002, Hartmann, 2008, where the mixed strong form of the problem is considered and Symmetric Interior Penalty (SIP) approximation for the DG numerical fluxes are employed, see Hesthaven and Warburton, 2007 for further details.

Using the *ridge enrichment* function presented in Moës et al., 2003 which is defined as:

$$H(\boldsymbol{x}) = \sum_i N_i(\boldsymbol{x})|\phi_i| - |\sum_i N_i(\boldsymbol{x})\phi_i| \tag{3}$$

and plotted for a 1D linear element as shown in Fig. 2, results in the following weak form:

$$\begin{aligned}(\boldsymbol{\nabla} v, \mu \boldsymbol{\nabla} u^-)_{K_i} &- \frac{1}{2}\langle \boldsymbol{\nabla} v, \mu(u^- - u^+)\boldsymbol{n}^-\rangle_{\partial K_i \setminus \partial\Omega} - \frac{1}{2}\langle v, \mu(\boldsymbol{\nabla} u^- + \boldsymbol{\nabla} u^+)\cdot \boldsymbol{n}^-\rangle_{\partial K_i \setminus \partial\Omega} \\ &+ \langle v, \mu\tau(u^- - u^+)\rangle_{\partial K_i \setminus \partial\Omega} \\ &- \langle \boldsymbol{\nabla} v, \mu u^- \boldsymbol{n}^-\rangle_{\partial K_i \cap \Gamma_D} - \langle v, \mu \boldsymbol{\nabla} u^- \cdot \boldsymbol{n}^-\rangle_{\partial K_i \cap \Gamma_D} + \langle v, \mu\tau u^-\rangle_{\partial K_i \cap \Gamma_D} \\ &= (v, s)_{K_i} - \langle v, g_N\rangle_{\partial K_i \cap \Gamma_N} - \langle \boldsymbol{\nabla} v, \mu u_D \boldsymbol{n}^-\rangle_{\partial K_i \cap \Gamma_D} + \langle v, \mu\tau u_D\rangle_{\partial K_i \cap \Gamma_D}\end{aligned} \tag{4}$$

where the variables with superscript $^-$ belong to the element K_i while that with superscript $^+$ belong to the adjacent element.

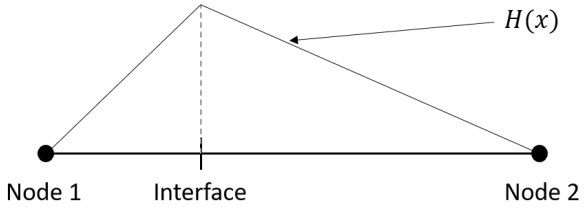

Fig. 2: The *ridge enrichment* function given by Eq. (3) in a 1D linear element.

5 Numerical Example

The bi-material heat problem introduced in Sec. 2 is solved in this section using the eXtended Discontinuous Galerkin (X-DG) method. A problem with known exact solution is presented in Gürkan et al., 2017. In this example a circular interface $\mathcal{I}$ with radius $R = 0.5$ is considered to divide the square domain $\Omega = [-1, 1]^2$ into two to regions, Ω_1 and Ω_2, as shown in Fig. 3. The heat distribution over a plate, which is made of two materials with different thermal conductivities, is computed. The thermal conductivities and the analytical solution are defined by:

$$\mu(\boldsymbol{x}) = \begin{cases} \mu_1 = 100 & \text{in } \Omega_1 \\ \mu_2 = 1 & \text{in } \Omega_2 \end{cases} \qquad u(\boldsymbol{x}) = \begin{cases} \dfrac{1}{\mu_1}(x^2 + y^2)^{5/2} & \text{in } \Omega_1 \\ \dfrac{1}{\mu_2}(x^2 + y^2)^{5/2} + \left(\dfrac{1}{\mu_1} - \dfrac{1}{\mu_2}\right)R^5 & \text{in } \Omega_2 \end{cases}$$

The corresponding source term is $s = -25(x^2 + y^2)^{3/2}$, Dirichlet boundary conditions are set on the boundary. The problem is solved using the X-DG method with linear ($p = 1$) triangular elements. Six meshes are used where the initial mesh is isotropically refined in each refinement. The respective recorded errors in the $\mathcal{L}_2$-norm are shown in Table 1, and the mesh convergence plot is shown in Fig. 4. It is noticed that optimal convergence of order ($p + 1$, i.e. 2) is not achieved, in fact, the plot shows non-monotonic convergence.

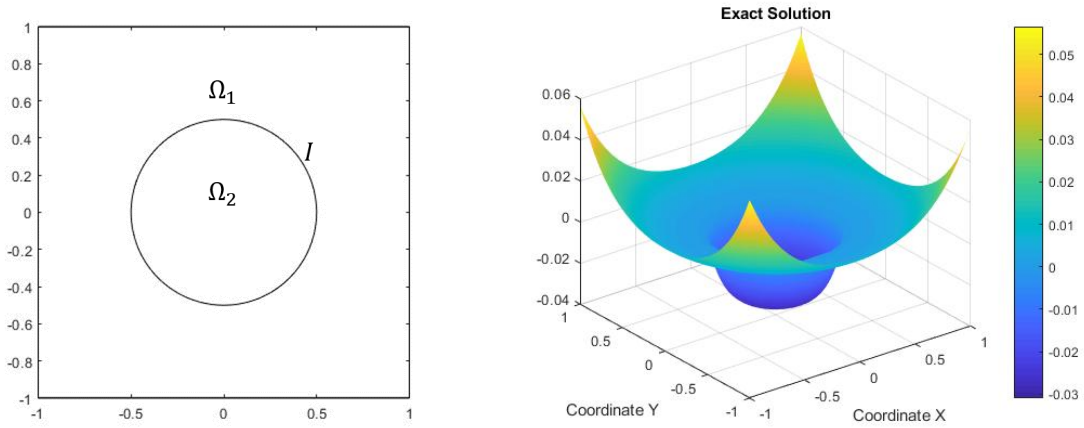

Fig. 3: Square domain with circular interface (left), analytical solution (right).

$\mu_1 = 100, \mu_2 = 1$ - X-DG solver						
Mesh	error $\mathcal{L}_2$-norm	size of the discrete operator	% of cut elements with area ratio > 9	maximum area ratio in cut elements	condition number of the discrete operator	maximum absolute residual $\boldsymbol{AU}_{enr}$-$\boldsymbol{f}$
mesh 1	3.9866	720^2	40%	17 : 1	1.1408e+11	3.4e−13
mesh 2	0.0480	$2,568^2$	29%	108 : 1	4.3237e+08	1.7e−13
mesh 3	0.0142	$10,008^2$	41%	419 : 1	6.1022e+10	1.7e−13
mesh 4	0.0969	$39,288^2$	43%	1,639 : 1	3.2652e+11	2.2e−13
mesh 5	0.0165	$155,496^2$	45%	6,479 : 1	2.3599e+11	2.8e−13
mesh 6	0.0096	$618,216^2$	43%	3,062 : 1	2.2869e+15	2.9e−13

Table 1: Data from the convergence study of the X-DG solver for the bi-material problem with $\mu_1 = 100$ and $\mu_2 = 1$.

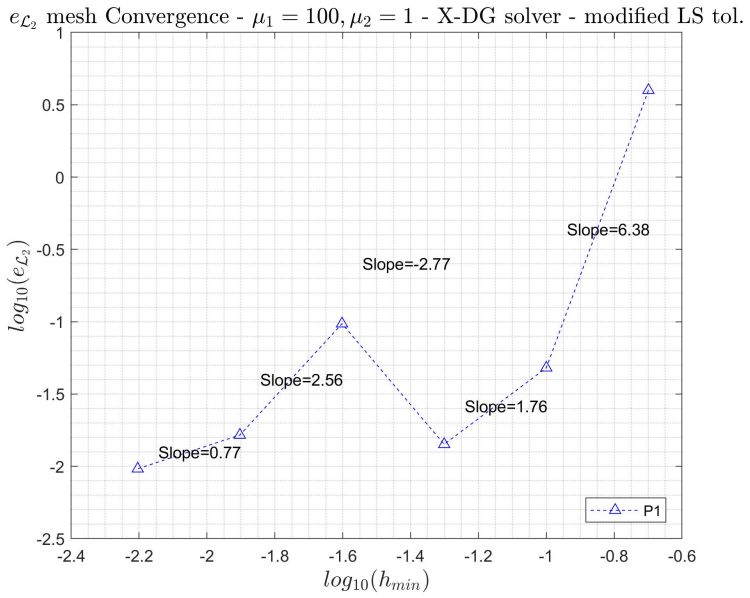

Fig. 4: Convergence plot of the X-DG solver for the bi-material problem with $\mu_1 = 100$ and $\mu_2 = 1$.

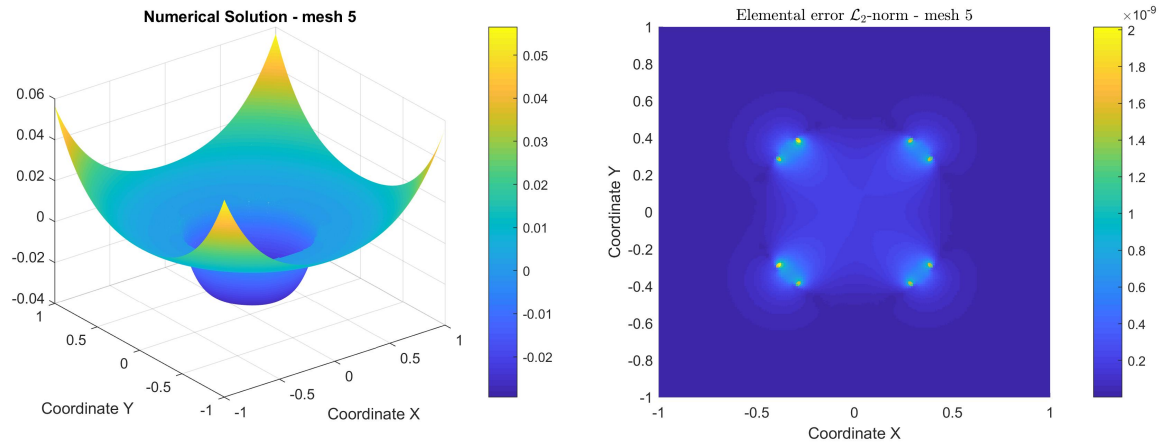

Fig. 5: The numerical solution (left) and the elemental errors $\mathcal{L}_2$-norm (right) for mesh 5.

However, by checking the solution itself and the local elemental errors in $\mathcal{L}_2$-norm, for instance in mesh 5, in Fig. 5, it is noticed that the overall error is dominated by the local errors of some cut elements which are divided by the interface into two regions; one region is very small compared to the other.

To better represent the quality of the cut, we introduce an elemental area ratio, defined as $max(A_1/A_2, A_2/A_1)$; where A_i is the area of the region in domain Ω_i within each cut element. Note that the area ratio is only defined in the cut elements.

A bad-cut is defined as a cut that gives an area ratio greater than 9 Gürkan et al., 2017. For each mesh, the percentage of cut elements with bad-cut situations is recorded in Table 1. These bad-cuts lead to an ill-conditioned discrete operator with very large condition number as recorded in Table 1.

In the literature, for instance in Gürkan et al., 2017, the authors showed optimal convergence using the eXtended Hybridizable DG (X-HDG) for the same problem but they modify the mesh whenever a situation of bad-cut arises. However, as they also reported, this is not a solution, it is just a temporary modification to show that the X-HDG method can converge optimally. To solve this issue of ill-conditioning, further stabilization strategies are used, for instance the strategy based on Nitsche's method Hansbo and Hansbo, 2002. This is going to be the near future work.

6 Conclusions and Near-Future Work

Preliminary results for the bi-material Poisson's problem using X-DG method were shown. The problem was steady, i.e. with stationary material interface. Linear elements were used and the solution was enriched using *ridge enrichment* in the cut elements, i.e. the weak formulation had no interface integrals. The results obtained in the initial tests showed convergence issues because of the situations of bad-cut where the interface divides an element into two regions, one is very small compared to the other.

The near-future work will be:

- Solve the convergence issues resulting from bad-cuts.
- Extend the X-DG solver to accommodate high-order approximation of the solution and the interface, and according to the literature Sala Lardies et al., 2012, this would require the use of *Heaviside enrichment* to recover the optimal convergence.
- Move to problems with moving interface where the interface is described explicitly.
- Move to problems with moving interface where the interface is described implicitly using the Level-Set method.
- Start the implementation for laminar incompressible multi-fluid flow problems.

Acknowledgements

This project is part of Marie Sklodowska-Curie ITN-EJD ProTechTion funded by the European Union Horizon 2020 research and innovation program with grant no. 764636.

References

Arnold, D. N., Brezzi, F., Cockburn, B., and Marini, D. (2000). Discontinuous Galerkin methods for elliptic problems. In *Discontinuous Galerkin Methods*, pages 89–101. Springer.

Arnold, D. N., Brezzi, F., Cockburn, B., and Marini, L. D. (2002). Unified analysis of discontinuous Galerkin methods for elliptic problems. *SIAM journal on numerical analysis*, 39(5):1749–1779.

Cheng, K. W. and Fries, T.-P. (2010). Higher-order XFEM for curved strong and weak discontinuities. *International Journal for Numerical Methods in Engineering*, 82(5):564–590.

Gürkan, C., Kronbichler, M., and Fernández-Méndez, S. (2017). eXtended hybridizable discontinuous Galerkin with Heaviside enrichment for heat bimaterial problems. *Journal of scientific computing*, 72(2):542–567.

Hansbo, A. and Hansbo, P. (2002). An unfitted finite element method, based on Nitsche method, for elliptic interface problems. *Computer methods in applied mechanics and engineering*, 191(47-48):5537–5552.

Hartmann, R. (2008). Numerical analysis of higher order discontinuous Galerkin finite element methods.

Hesthaven, J. S. and Warburton, T. (2007). *Nodal discontinuous Galerkin methods: algorithms, analysis, and applications*. Springer Science & Business Media.

Karniadakis, G. E., Israeli, M., and Orszag, S. A. (1991). High-order splitting methods for the incompressible Navier-Stokes equations. *Journal of computational physics*, 97(2):414–443.

Kroll, N. (2006). ADIGMA: A European project on the development of adaptive higher order variational methods for aerospace applications. In *47th AIAA Aerospace Sciences Meeting including The New Horizons Forum and Aerospace Exposition*, page 176.

Moës, N., Cloirec, M., Cartraud, P., and Remacle, J.-F. (2003). A computational approach to handle complex microstructure geometries. *Computer methods in applied mechanics and engineering*, 192(28-30):3163–3177.

Moës, N., Dolbow, J., and Belytschko, T. (1999). A finite element method for crack growth without remeshing. *International journal for numerical methods in engineering*, 46(1):131–150.

Pommier, S., Gravouil, A., Combescure, A., and Moës, N. (2011). *Extended finite element method for crack propagation*. Wiley Online Library.

Sala Lardies, E., Fernández Méndez, S., and Huerta, A. (2012). Optimally convergent high-order X-FEM for problems with voids and inclusions. In *ECCOMAS 2012: 6th European Congress on Computational Methods in Applied Sciences and Engineering. Programme book of abstracts, September 10-14, 2012, Vienna, Austria*, pages 1–14.

Utz, T. (2018). *Level set methods for high-order unfitted discontinuous Galerkin schemes*. PhD thesis, Technische Universität.

Wang, Z. J., Fidkowski, K., Abgrall, R., Bassi, F., Caraeni, D., Cary, A., Deconinck, H., Hartmann, R., Hillewaert, K., Huynh, H. T., et al. (2013). High-order CFD methods: current status and perspective. *International Journal for Numerical Methods in Fluids*, 72(8):811–845.

CFD Study on Propeller-Induced Pressure Pulses in Cavitating Flows

Keun Woo Shin[*] and Poul Andersen[†]
[*]MAN Energy Solutions, Frederikshavn/Denmark,
[†]Technical University of Denmark (DTU), Kgs. Lyngby/Denmark
keun.shin@man-es.com

1 Introduction

Accurate predictions of propeller-induced pressure pulses in cavitating flows are important, because maximum allowable pressure pulses on the hull surface above the propeller are often specified as a requirement for the propeller design and pressure pulse levels are increased 5 to 15 times in cavitating flows relative to without cavitation (ITTC 1999). CFD made by a viscous flow solver is generally known to show higher accuracy and robustness in predicting cavity extents and pressure pulses than potential flow methods (Perali et al 2016). CFD is heavier in terms of computational effort and CFD predictions can be quantitatively varied depending on the numerical setup and cavitation model. Therefore, it is necessary to develop a CFD setup by validating it against experimental results for reliable predictions in cavity extents and pressure pulses.

In this work, CFD simulations are made on INSEAN E779A propeller in the behind-hull condition by a DES solver with a cavitation model and it is validated against experimental results with respect to cavity extents and pressure pulses. The cavitating flows on the target propeller have been considered for validating CFD methods by a number of research groups (Vaz et al. 2015), because a comprehensive series of cavitation tunnel tests have been conducted with measuring cavity extents, pressure pulses and acoustic noise in the open-water and behind-hull conditions (Pereira et al 2004, Salvatore 2006).

As high-frequency oscillations in the pressure field can be numerically generated by low grid resolutions at the interface of the rotating domain and insufficient iterative convergence, the influences of time-step, number of inner iterations and grid size at the interface of the rotating domain on CFD results are investigated by varying these numerical parameters.

2 CFD setup

A DES solver with the curvature-corrected k-ω SST turbulence model in the commercial CFD software StarCCM+ is adopted for unsteady cavitation simulations. Two-phase flows are modelled by the volume-of-fluid (VOF) method and a generic transport equation for vapor volume fraction α_V. Cavitation is modelled by the interphase mass transfer model of Schnerr & Sauer (2001).

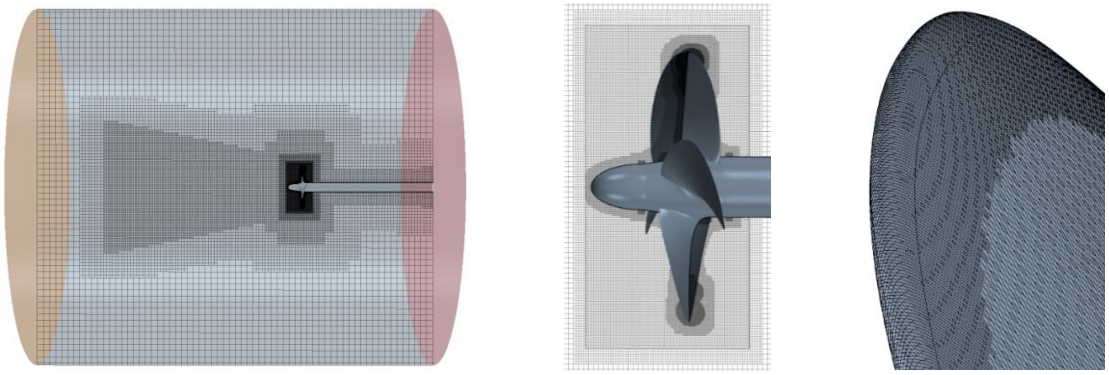

(a) (b) (c)

Fig. 1: (a) Computational domain with the grid on the vertical section, (b) inner rotating domain around the propeller model and (c) surface grid on the blade tip

A trimmed hexahedral grid is generated around the propeller model in a cylindrical fluid domain extending axially 3·D to the inlet, 6·D to the outlet and radially 4·D to the outer wall from the intersection of the shaft axis and the propeller plane, as shown in Fig. 1(a), where D is the model propeller diameter of 227.3 mm. The cross-section area of the computational domain is much larger than that of the cavitation tunnel, so the blockage effect of the cavitation tunnel is neglected in CFD. Instead of simulating the blockage effect, the inflow speed U_O is adjusted to reach the measured thrust in the experiment. The propeller speed is fixed to N = 30.5 rps. Propeller rotations are modelled by the rigid body motion and the sliding grid in a sub-domain around the propeller model, as shown in Fig. 1(b).

The grid size is Δx = 0.2 – 0.5 mm on the blade surface and it is refined to half of Δx at the blade edges, as shown in Fig. 1(c). The grid at the wall boundary has 12 prism layers leading to mostly $y+ \leq 1$. The outer-radius region has a consistent volume grid size of 0.3 – 0.4 mm for resolving cavitating flows better.

While an array of plates are installed to generate hull wake in the upper propeller disk in the cavitation tunnel test, the hull wake measured 0.26·D upstream from the propeller plane is applied to the inlet boundary. The hull wake field is examined by a numerical test in the computational domain excluding the propeller. In Fig. 2, the comparison of the measurement and the wake field of the numerical test shows that the hull wake is well preserved from the inlet to the propeller plane without significant numerical diffusion.

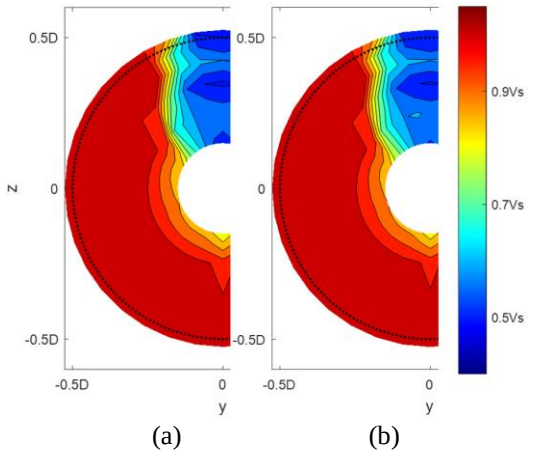

(a) (b)

Fig. 2: Hull wake 0.26·D upstream from the propeller plane without the propeller model – (a) measurements, (b) numerical test

CFD has been validated for fully-wetted and cavitating flows on E779A propeller in the open-water condition (Shin & Andersen 2019) and the validation has shown overestimations of the cavity extent in low cavitation numbers, which are common in other CFD validations made by a number of institutes (Vaz et al. 2015). While a model for transitional flows is included for the open-water condition, it is not included in the current setup for the behind-hull condition.

3 CFD result

CFD is made first at a cavitation number of σ = 10.0 to have the fully-wetted condition, where $\sigma = (P_O – P_V)/(0.5 \cdot \rho \cdot U_{O,Exp}^2)$ and $U_{O,Exp}$ is the inflow speed in the experiment, $U_{O,Exp}$ = 6.22 m/s for the considered advance ratio of J = 0.897. U_O in CFD is iteratively adjusted to reach the measured thrust of K_T = 0.175 within 0.5% deviation. As K_T in CFD at $U_O = U_{O,Exp}$ is 8.3% lower than the measured value, U_O is reduced by 3.2% from $U_{O,Exp}$.

CFD is made at σ = 2.5, which is the lowest cavitation number among those considered in the experiment. The initial simulation is made at a time-step corresponding to $\Delta\theta$ = 0.5° propeller rotation per Δt. CFD is repeated with smaller time-steps of $\Delta\theta$ = 0.25°, 0.125°. A 2nd-order implicit time-stepping scheme is used. CFD is also made with different numbers of inner iterations of N_{Iter} = 5, 10, 20 at $\Delta\theta$ = 0.5°. The surface grid size on the interface of the inner rotating domain is varied in Δx_{Rot} =

2.5, 5, 10, 20 mm to examine the influence of Δx_{Rot} on pressure pulses. Δx_{Rot} = 5 mm is applied to the CFD investigations with varying Δt and N_{Iter}.

3.1 Cavity extent

In Fig. 3, cavity extents in CFD and experimental results are compared. In CFD, cavitation interfaces defined by the iso-surfaces of α_V = 0.1 and 0.5 are in light blue and dark blue, respectively. The blue color at the aft end of the sheet cavity is even darker, as the cavity detached from the blade surface is rolled back by re-entrant jet and so the interface is overlapped. The darker blue part in CFD corresponds to the frothy cavitation at the aft end of the sheet cavity in the experiment.

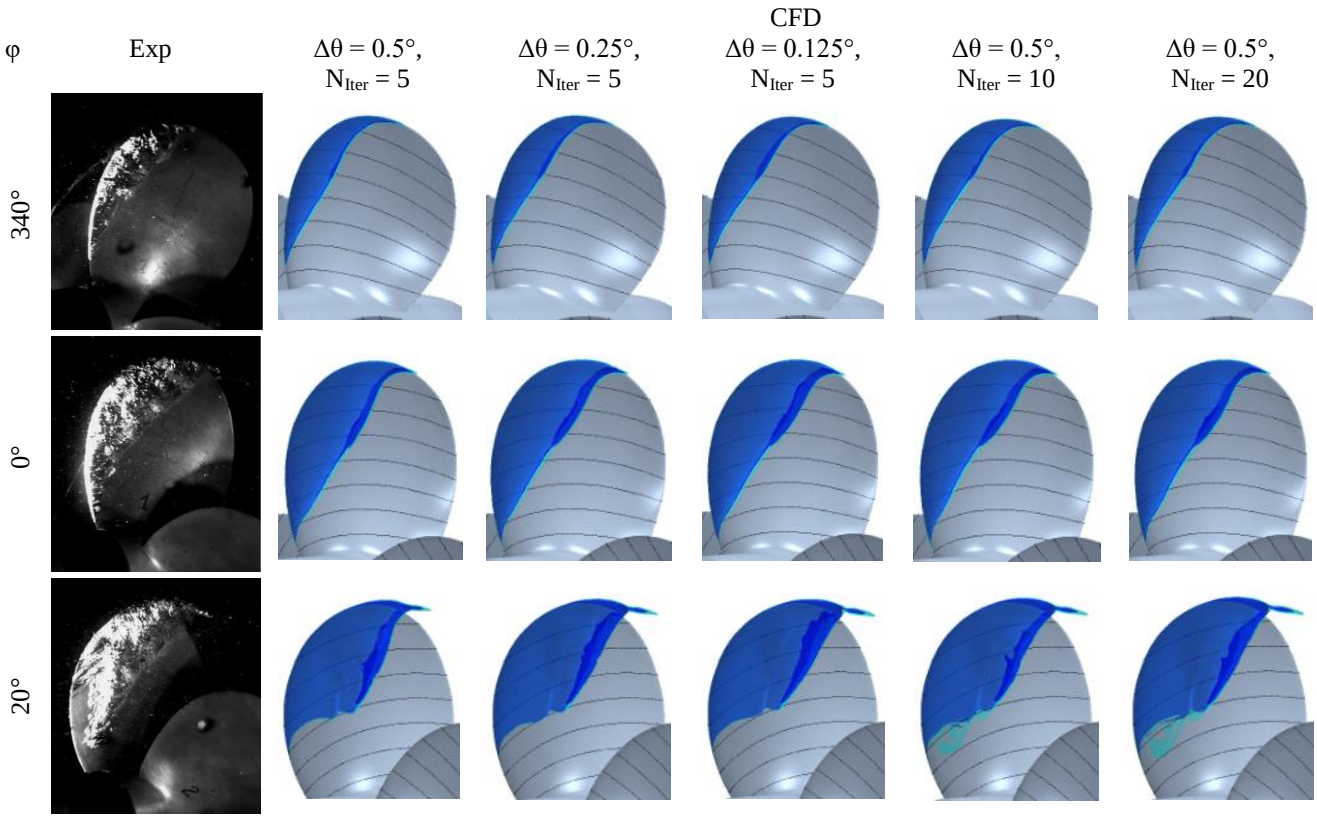

Fig. 3: Cavity extents in the experiment and CFD
(dark blue – α_V = 0.5, light blue – α_V = 0.1)

CFD shows a reasonable agreement in the sheet cavity extent at φ = 340° and 0° with a little underprediction at the outer radii of r/R ≥ 0.8, but the mid-chord cavitation at r/R = 0.45 – 0.7 is not reproduced well at φ = 20° probably due to the fluctuating flows from the wake generator, of which the averaged wake is applied to CFD. The overall sheet cavity is more extended for smaller time-steps and higher numbers of inner iterations. It indicates that the cavity growth is numerically delayed in the initial setup with $\Delta\theta$ = 0.5° and N_{Iter} = 5.

CFD at φ = 20° shows that the sheet cavity at r/R = 0.6 – 0.7 starts from the leading edge regardless of $\Delta\theta$ and N_{Iter}, and scattered cavities with low vapor fractions are formed at r/R = 0.5 – 0.6 for N_{Iter} = 10 and 20. The root mean squared values of normalized residuals for continuity, momentum and turbulence equations are in the order of 10^{-4} – 10^{-6} for N_{Iter} = 5 and those for continuity and momentum equations are reduced to be in the order of 10^{-5} – 10^{-6} for $N_{Iter} \geq 10$.

K_T in the cavitating condition of σ = 2.5 is 1.4% higher than that in the fully-wetted condition. K_T for $\Delta\theta$ = 0.25°, 0.125° and N_{Iter} = 10, 20 is slightly lowered from that in the initial setup, but the

variations are within 0.4%. While the variation of single-blade thrust in Fig. 5(a) shows no noticeable difference except the declining phase, the growing and decaying rates of the cavity are increased for $\Delta\theta \leq 0.25°$ and $N_{Iter} \geq 10$ and so the maximum value of A_{Cav} is increased from 37.5% to 39.6 – 40.3% in Fig. 5(b), where A_{Cav} is the ratio of the surface area under cavity of $\alpha_V \geq 0.1$ to the suction-side blade area.

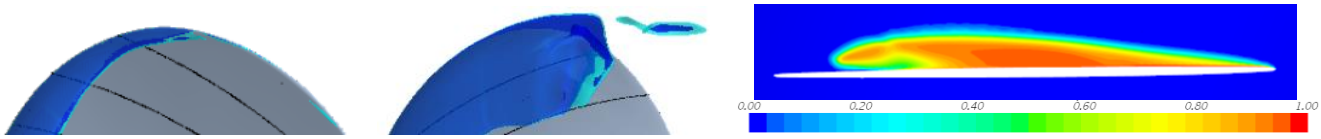

(a) (b) (c)

Fig. 4: Cavity extents at (a) φ = -34° and (b) 42° and (c) α_V at 0.9R section of φ = 15° in CFD

A_{Cav} in CFD is considerably lower than the experimental measurement based on projected areas, firstly because the cavity detached from the surface at the rear part of the sheet cavity is not included in CFD, as shown in Fig. 4(c). The maximum cavity area is shown at $\varphi \approx 15°$, which is later than $\varphi \approx$ -10° showing the maximum $K_{T,1\text{-Blade}}$, as the expansion of the leading-edge cavitation over the chord length takes time. The fluctuations of $K_{T,1\text{-Blade}}$ at φ = -40 – -30° and 30 – 40°, seemingly related to cavitation detachment at the leading edge and trailing edge in Fig. 4(a) & (b), respectively, are alleviated for N_{Iter} = 10 and 20.

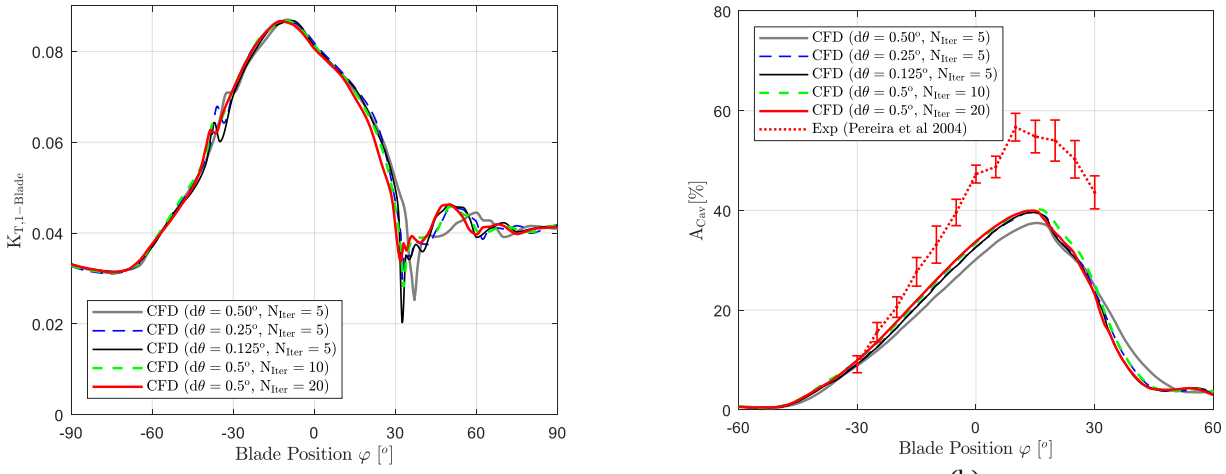

(a) (b)

Fig. 5: (a) Variations of single-blade thrust and (b) cavity area ratio with respect to blade position

3.2 Pressure pulse

In Fig. 6, the comparison of pressure variations on 4 points, which are 0.3 m straightly to the right, above, to the left and below the propeller disk centre (Pereira et al 2004), shows that the peak-to-peak amplitudes on P1 and P4 are overestimated by CFD, whereas the high-frequency fluctuations on P2 are not reproduced and the negative amplitudes on P3 are underestimated. The high-order pressure pulses on P2 can be related to the dynamic behavior of detached cavitation and tip vortex cavitation, which is not simulated well probably due to the insufficient grid refinements and the inflow simplified to averaged axial wake without oscillating vortex shedding. The pressure amplitude is slightly larger and the small fluctuations at peaks and troughs are increased for smaller time-steps and higher numbers of inner-iterations.

In Fig. 7, the pressure pulses at harmonics of the blade passing frequency show that the first-order pressure pulse ΔP_1 is overestimated except P3 and the high-order pressure pulses are underestimated

by CFD. Since pressure variations are probed in the middle of the fluid domain without a wall boundary in CFD, the overestimation of the first-order pressure pulse can be even larger when considering a solid boundary factor of 1.8 – 2.0 (Carlton 2007).

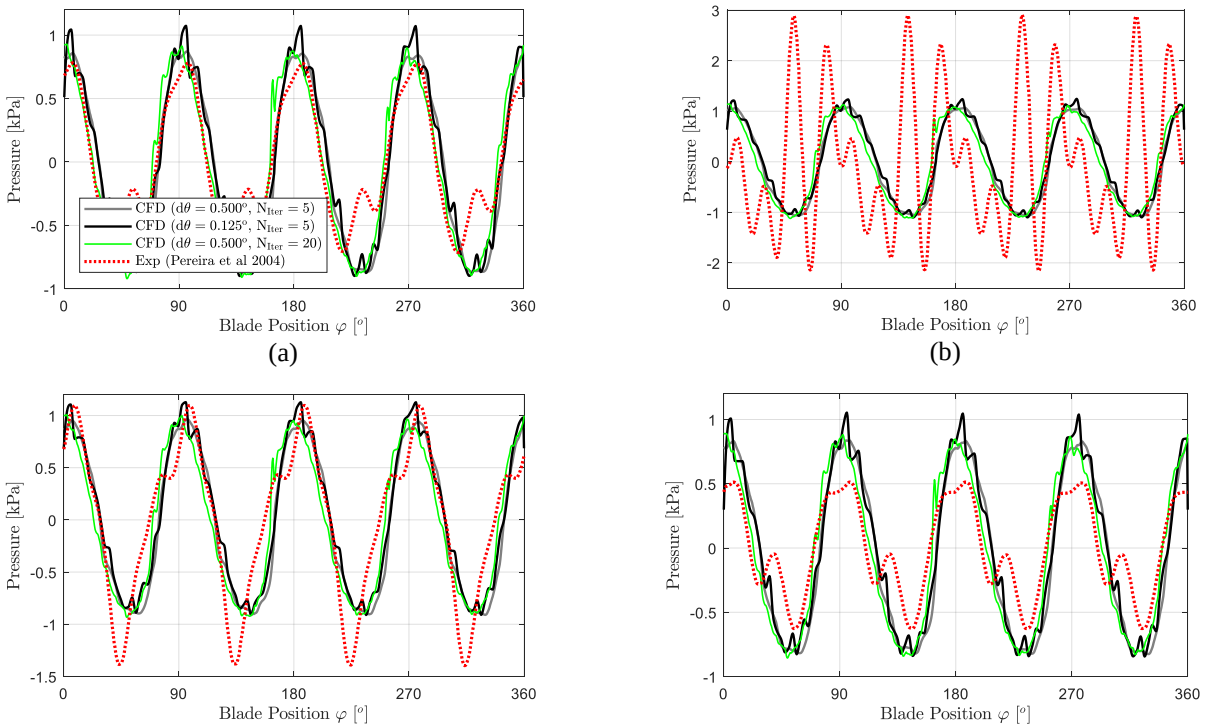

Fig. 6: Variations of pressure on 4 Points – (a) P1, (b) P2, (c) P3, (d) P4

Although P2 is above the upright blade position showing the largest cavitation extent, ΔP_1 on P3 is higher than on P2 in the experiment due to ΔP_3 and ΔP_4 on P2 higher than ΔP_1, whereas ΔP_1 on P2 is the highest among the 4 points in CFD due to the underestimation of high-order pressure pulses.

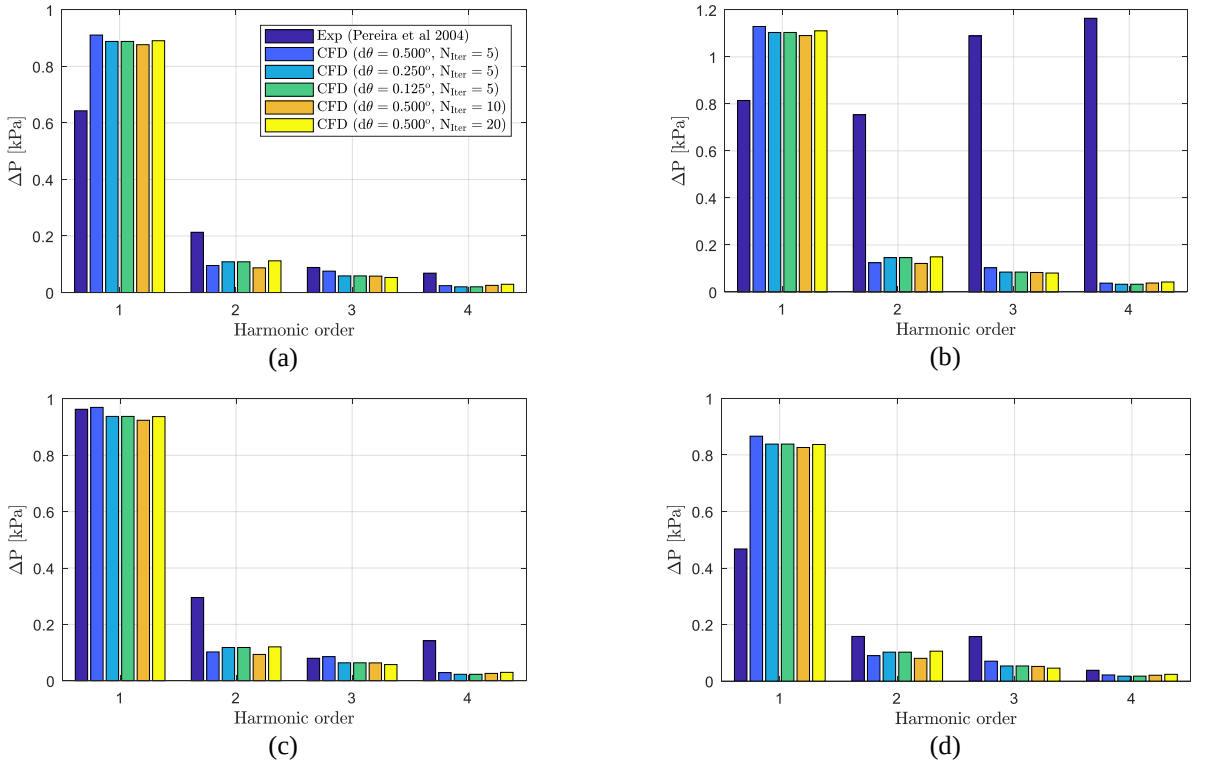

Fig. 7: Pressure pulses at harmonics of the blade passing frequency – (a) P1, (b) P2, (c) P3, (d) P4

While ΔP_1 on P3 is lowered by about 50% on P4 in the experiment, the variation of ΔP_1 at the different points is about 20% in CFD. In CFD, ΔP_1 is lowered by 2 – 5% for $\Delta\theta = 0.25°$, 0.125° and $N_{Iter} = 10$, 20, and ΔP_2 is increased by 14 – 20% for $\Delta\theta = 0.25°$, 0.125° and $N_{Iter} = 20$, compared to the initial setup. Such changes are still much smaller than the deviations from the experimental result.

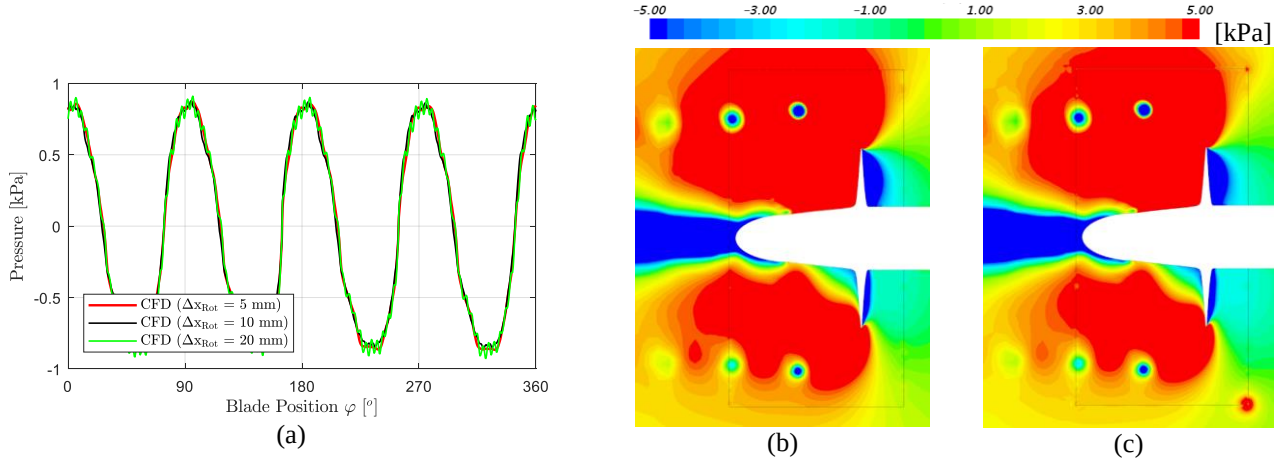

(a) (b) (c)

Fig. 8: (a) Pressure variation on P1 in CFD with different values of Δx_{Rot} and pressure distribution on vertical section – (b) $\Delta x_{Rot} = 5$ mm, (c) $\Delta x_{Rot} = 10$ mm

When Δx_{Rot} is increased to 10 and 20 mm, small oscillations are formed especially at the peaks and troughs of the pressure variation in Fig. 8(a). The pressure fluctuations at the edges of the rotating domain interface are intensified for $\Delta x_{Rot} = 10$ mm in Fig. 8(c), which may cause the numerical oscillations of the pressure variations. As the pressure variation in CFD with $\Delta x_{Rot} = 2.5$ mm does not show significant differences from that with $\Delta x_{Rot} = 5$ mm, $\Delta x_{Rot} \leq 5$ mm seems sufficient for avoiding numerical pressure oscillations from the interface grid of the rotating domain.

4 Conclusion

The extent of sheet cavity can be underestimated by CFD with insufficient time-step sizes and numbers of inner iterations. The number of inner iterations is important for simulating sporadic cavitation with low vapor volume fractions. Sufficient temporal discretization and numbers of inner iterations can contribute to more accurate predictions of high-order pressure pulses by resolving cavitation dynamics better. Numerical pressure fluctuations can be generated by insufficient grid sizes on the interface of the rotating domain.

References

J.S. Carlton (2007). *Marine propellers and propulsion*. Elsevier

ITTC (1999). The specialist committee on cavitatin induced pressure fluctuation: Final report and recommendations to the 22nd ITTC. Proceedings Of the 22nd ITTC, Seoul/Shanghai, Korea/China

P. Perali, T. Lloyd & G. Vaz (2016). Comparison of uRANS and BEM-BEM for propeller pressure pulse prediction: E779A propeller in a cavitation tunnel. Proceedings of 9th NuTTS, St. Pierre d'Oleron, France

F. Pereira, F. Salvatore, F. Di Felice & M. Soave (2004). Experiment Investigation of a cavitating propeller in non-uniform inflow. Proceedings of 25th Symposium on Naval Hydrodynamics, St. John's, Newfoundland, Canada

F. Salvatore (2006). The INSEAN E779A Propeller Dataset. INSEAN Technical Report, Rome: INSEAN

G.H. Schnerr & J. Sauer (2001). Physical and numerical modeling of unsteady cavitation dynamics. Proceedings of 4th International Conference on Multiphase Flow (ICMF2001), New Orleans, LA, USA

K.W. Shin & P. Andersen (2019). CFD analysis of ship propeller thrust breakdown. Proceedings of 6th International Symposium on Marine Propulsors (SMP'19), Rome, Italy

G. Vaz, D. Hally, T. Huuva, N. Bulten, P. Muller, P. Becchi, J.L.R. Herrer, S. Whitworth, R. Mace & A. Korsstrom (2015). Cavitating flow calculations for the E779A propeller in open water and behind conditions. Proceedings of 4th International Symposium on Marine Propulsors (SMP'15), Austin, TX, USA

CFD simulation of propeller noise

Takuya Tachikawa[1], Nobuhiro Hasuike[2], and Keita Fujiyama[3]

[1,2]Nakashima Propeller Co., Ltd., Okayama/Japan, web page: http://www.nakashima.co.jp/
[3]Software Cradle Co., Ltd., Osaka/Japan, web page: https://www.cradle-cfd.com/
E-mail: [1]t-tachikawa@nakashima.co.jp,[2]nobuhiro@nakashima.co.jp, [3]fujiyama@cradle.co.jp

1 Introduction

Propeller cavitation causes under water radiated noise. Low frequency tonal noise is mainly related to the volume variation of the sheet cavitation which is the formation of unity of the cavitation bubbles. On the other hand, the high frequency noise is related to the dynamics of the micro cavity collapse and its rebound after the division. The bubble radius, the ambient pressure and the initial gas contents are dominant factors of the bubble dynamics and its resulted sound pressure.
Recently developed "Multi-process cavitation model" (Tsuda et al.[1], 2015) is considering the basic bubble dynamics like as bubble expansion/shrinkage with bubble-bubble interaction, evaporation/condensation, inception/collapse, coalescence and break-up. "Multi-process cavitation model" provides the distribution of the number density and the bubble radius analytically. By using these information, the radiated sound pressure by each single bubble can be estimated by Rayleigh-Plesset equation with compressibility. In this study, combination of "Multi-process cavitation model" and simple bubble dynamics was discussed.

2 Multi-process cavitation model

The "Multi-process cavitation model" (Tsuda et al.[1], 2015) is constructed based on the moment method. "*i*th moment *Mi* is defined using the size distribution function *f(R, t)*.

$$\boldsymbol{M_i = \int R^i f(R,t)\, dR} \qquad (1)$$

Taking the time derivative for the quantity *Mi*, following relationship is derived.

$$\boldsymbol{\frac{DM_i}{Dt} = iG(\bar{R})M_{i-1} + S_{p,i}(for\ i = 0,1,2,3)} \qquad (2)$$

Where, $f(R,t)$ is size distribution function. $\bar{R}$ is mean radius of bubbles defined as M_1/M_0. $G(\bar{R})$ is expansion and shrinkage speed. $S_{p,i}$ reflects the change of the number of bubbles, which occurs with inception/collapse and break up/coalescence.

$$\boldsymbol{G(\bar{R}) = \frac{d}{dt}\left(\frac{M_1}{M_0}\right)} \qquad (3)$$

$$\boldsymbol{\bar{R} = \frac{M_1}{M_0}} \qquad (4)$$

R_c is critical size. J_s is inception and collapse rate. S_b and S_c are break-up and coalescence rate respectively. $\dot{m}_v$ is evaporation and condensation flux.

Expansion/ Shrinkage — Inception/ Collapse — Coalescence/ Break-up

$$\boldsymbol{\frac{DM_0}{Dt} = J_s + S_b - S_c} \qquad (5)$$

$$\boldsymbol{\frac{DM_1}{Dt} = G(\bar{R})M_0 + R_cJ_s + \bar{R}(S_b - S_c)} \qquad (6)$$

$$\boldsymbol{\frac{DM_2}{Dt} = 2G(\bar{R})M_1 + R_c^2J_s + \overline{R^2}(S_b - S_c)} \qquad (7)$$

$$\boldsymbol{\frac{DM_3}{Dt} = 3G(\bar{R})M_2 + R_c^3J_s + \overline{R^3}(S_b - S_c)} \qquad (8)$$

$$\boldsymbol{\frac{D(\rho_g M_3)}{Dt} \approx \dot{m}_v M_2 M_3 + \rho_g \frac{DM_3}{Dt}} \qquad (9)$$

Evaporation/ Condensation

Void fraction ϕ and Quality Y are derived as followings;

$$\phi = \frac{(4\pi/3)\mathbf{M_3}}{\mathbf{1} + (4\pi/3)\mathbf{M_3}} \quad (10)$$

$$\mathbf{Y} = \frac{(4\pi/3)\rho_g M_3}{\rho_l + (4\pi/3)\rho_g M_3} \quad (11)$$

3 Numerical simulation of cavitation performance

"Multi-process cavitation model" was implemented to commercial solver Software Cradle SC/Flow 2020, which is the navier-stokes solver based on a finite volume method. The coalescence and break-up term were neglected in this study. To simulate the two-phase cavitating flow, the single fluid approach was used. In addition, the mixture density was treated as a compressible flow by using barotropic relation. SST k-ω model was used. In practical view of simulation, CFD simulation neglected the second order derivative of Rayleigh-Plesset equation.

Numerical grids

Seiun-Maru HSP II propeller[2,3] was selected for this study(See Fig. 1). Principal particulars of the ship and the propeller and operating condition are shown in Table 1. Simulation was conducted in model scale. The computational domain was composed of the inner rotational part including the propeller and the outer stationary part including hull. Unsteady propeller simulation in the wake uses the sliding mesh methodology. The numerical mesh was an unstructured grid. Basic meshes were polyhedral and prismatic cells were applied to near the blade surface for resolving the boundary layer. The first layer thickness of the prism layer was set to a non-dimensional wall distance for a wall-bounded flow (y^+ in short) =50. The second order accuracy of the convective term was adapted. The region was the same size as the large cavitation tunnel in NMRI (See Fig. 2). In the experiments, auxiliary equipment called Flow Liner was installed to simulate the full scale ship wake distribution.

The thrust coefficient k_T was adjusted to 0.201 as predefined value by changing the inflow speed.

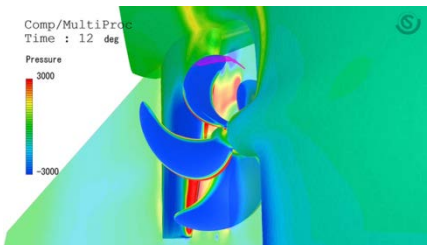

Figure 1: Seiun-Maru HSP II propeller

Table 1 Principal particulars[2,3]

			Ship	Model
Ship length	L_{wl}	m	109	6.687
Propeller diameter	D_p	m	3.6	0.22
Thurst coefficient	k_T	-		0.201
Cavitation number	σ_n	-		2.99
Shaft speed	n	rps	2.72	17.5

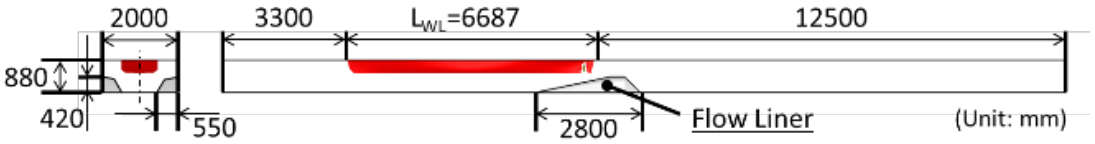

Figure 2: Computational domain

Pressure pulse simulation

The tonal noise up to 100Hz is related with the pressure pulse caused by the whole sheet cavitation dynamics. Therefore, the estimation accuracy of pressure pulse of blade frequency component is important for the prediction of the low frequency noise. The first and the second order blade frequency components of pressure amplitude were compared in Fig. 3. For the first order blade frequency components, "Multi-process cavitation model" (MP) showed better agreement in

comparison with Full cavitation model (FCM)[4]. On the other hand, both cavitation models underestimated the second order blade frequency components.

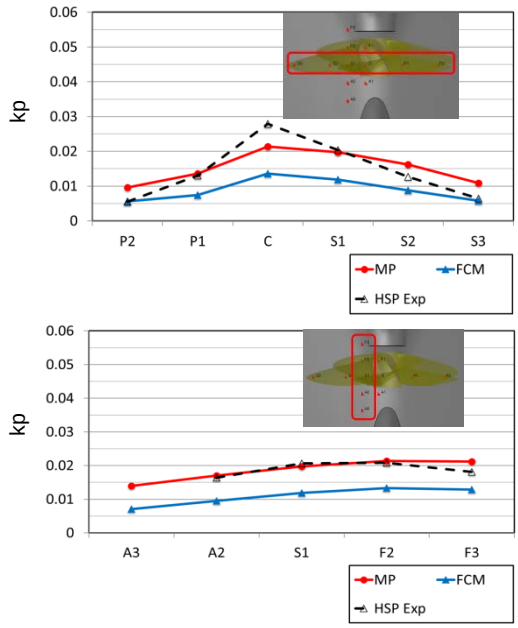

Figure 3: Comparison of the first order component of pressure pulse

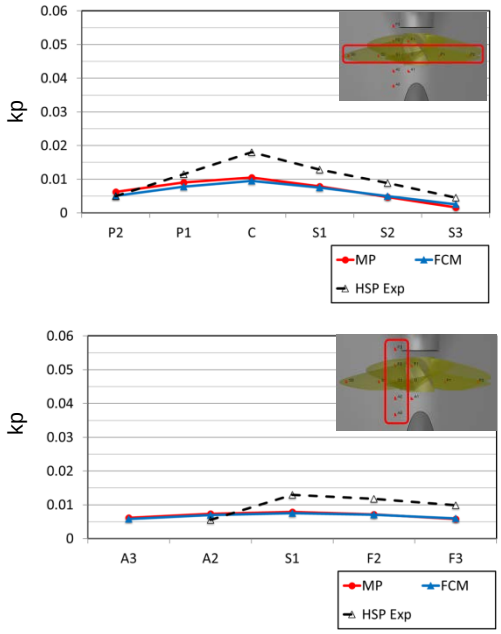

Figure 4: Comparison of the second order component of pressure pulse

Cavitation pattern and distribution of cavitation bubbles

In order to simulate the cavitation noise, estimation accuracy of cavitation volume is important. The cavitation pattern simulated by "Multi-process cavitation model" was compared with experimental results. Fig. 5 shows the comparisons of the cavitation pattern between the experiment and the isosurface of 10% void fraction from the calculations. Calculation result showed good agreement with model experiment.

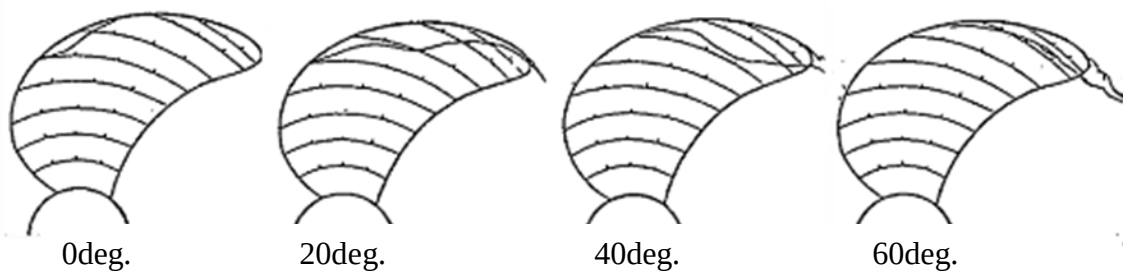

Figure 5(a): Cavitation patterns(Experiment)

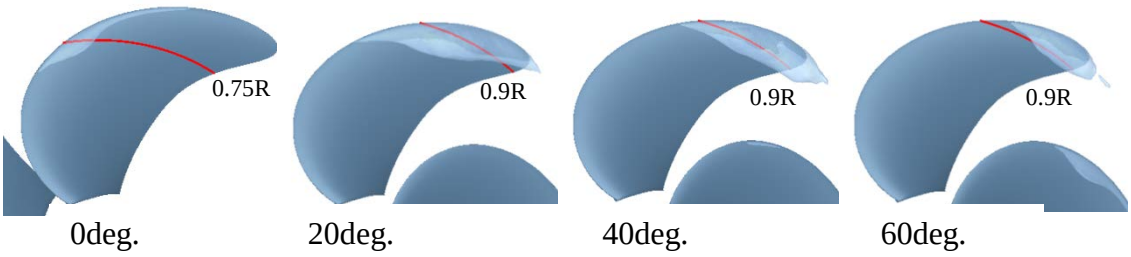

Figure 5(b): Cavitation patterns(MP)

Bubble distribution

Simulated number and radius of bubbles at 45deg. are shown in Fig. 6(a) and (b), which was the blade position with maximum cavity size. The bubble radius increased with expansion of the sheet cavitation. The bubble radius decreased with whole cavity shrinkage. The number of cavitation nuclei

and bubble radius were smaller near the surface of the sheet cavitation. The bubble radius at 0.85R was mainly from 2.5 to 3.0mm. Smaller bubbles are located near the sheet cavity surface. The bubble radius at 0.90R was from 2.5 to 4.0mm. The bubble radius at 0.95R and 0.975R were mainly from 3.5 to 4.5mm.The bubbles in the sheet cavitation grew and moved from leading edge to trailing edge. The bubbles at 0.95R grew more in comparison with those at 0.85R by the lower pressure at the leading edge. On the other hand, the cavitation at 0.975R included the sheet cavitation and the tip vortex cavitation. The tip vortex cavitation was generated near the leading edge and stably maintained along the tip vortex core. The tip vortex cavitation including large bubbles seemed to play an very important role for its high frequency noise, because the large bubbles generates the large sound pressure of the shock wave impulse.

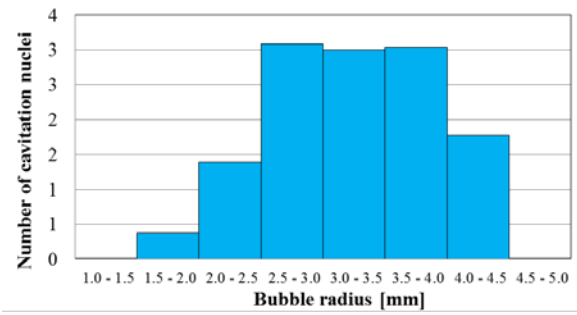

Figure 6(a): Distribution of the number and the radius of the bubbles at 45deg. position

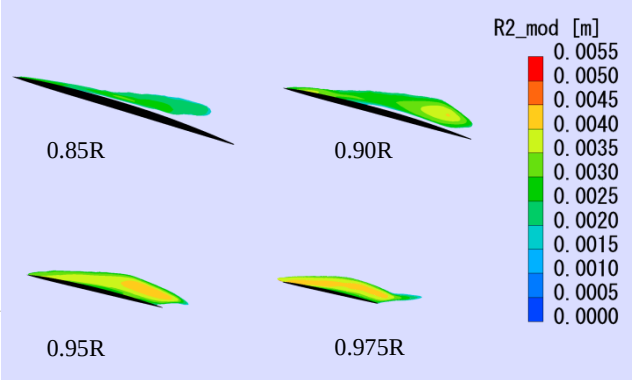

Figure 6(b): Distribution of the bubble radius

Noise prediction

In this study, several noise simulation approaches were studied as practical design tools.

(a) Direct simulation of pressure pulse at receiver position

(b) Brown formula[5](1977)

Brown's formula assumes the relation between cavitation area and the high frequency noise. As estimation of cavitation area by calculation or model experiment is consistent and visible, this kind of approach is attractive for daily use.

$$SPL_{src} = K + \log_{10}\left(BD_p{}^4 n^3 f^{-2}\right) + \log_{10}(A_c/A_D) \qquad (12)$$

Where, SPL_{src} $[dB\ re\ 1\mu Pa/\sqrt{Hz}\ at\ 1m]$ is the sound source level. K is an empirical constant which is used as 163 at the standard propeller case and B is the number of the blades. A_c [m^2] is the area of cavity on the blade, and [m^2] is the area of the blade. A_c/A_D was 0.11, which was decided by referring maximum A_c/A_D from the CFD results with consideration of safety side.

(c) Single bubble dynamics equation(Tomita and Shima et al.[6], 1977)

Single bubble dynamics was solved by Tomita and Shima method which includes the compressibility (Eq. (13)-(15)). The sound pressure by one bubble p_a is derived by Eq. (16). Total sound pressure level was derived by summation of each bubble. This approach was suggested by Kamiirisa et al.[7](2005) and Ando et al.[8](2018). The merit of using bubble dynamics was that time history of the bubble radius and the impulse pressure was easily treated without the problem of the spatial mesh density, although the coupling of the flow field solved by the CFD and the bubble dynamics is one way coupling.

This approach needed an assumption of initial bubble radius and number of the cavitation nuclei. "Multi-process cavitation model" was expected to give theoretical number of the cavitation nuclei and the bubble radius. In this study, the initial radius and the number of bubbles were referred from the number and the radius distribution at 45deg. simulated by "Multi-process cavitation model", which was the blade position with maximum cavity. By this way, the initial dR/dt for Lunge Kutta calculation was approximately treated as zero.

$$R\ddot{R}\left[1-(1+\varepsilon)\frac{\dot{R}}{C_\infty}+\left(-1+\frac{7}{2}\varepsilon-\frac{\varepsilon^2}{5}\right)\frac{\dot{R}^2}{{C_\infty}^2}\right]$$
$$+\frac{3}{2}\dot{R}^2\left[\frac{4-\varepsilon}{3}-\frac{4}{3}\frac{\dot{R}}{C_\infty}+\left(\frac{-4}{3}+4\varepsilon-\frac{43}{30}\varepsilon^2+\frac{\varepsilon^3}{6}\right)\frac{\dot{R}^2}{{C_\infty}^2}\right]$$
$$+\frac{1}{\varepsilon\rho_\infty}\left[p_\infty-p_{2_{r=R}}-\frac{R\dot{p}_{1_{r=R}}}{C_\infty}\right.$$
$$\left.+\frac{1}{{C_\infty}^2}\left\{(1+\varepsilon)R\dot{R}\dot{p}_{1_{r=R}}+\left(p_\infty-p_{1_{r=R}}\right)\left[\left(-2+\frac{7}{2}\varepsilon-\varepsilon^2\right)\dot{R}^2+\frac{3}{2}\frac{p_\infty-p_{1_{r=R}}}{\rho_\infty}\right]\right\}\right]$$
$$=0 \tag{13}$$

$$p_{1_{r=R}}=\frac{-2\sigma}{R}+p_0\left(\frac{R_0}{R}\right)^{3\gamma}+\rho_g\varepsilon\dot{R}^2-\varepsilon\frac{4\mu\dot{R}}{R} \tag{14}$$

$$p_{2_{r=R}}=p_{1_{r=R}}+\frac{\varepsilon}{{C_\infty}^2}\left(\frac{4\mu}{3}+\zeta\right)\left\{\frac{3}{2}\varepsilon(1-\varepsilon)\frac{\dot{R}^3}{R}-\frac{\dot{p}_{1_{r=R}}}{\varepsilon\rho_\infty}+(1-\varepsilon)\frac{\left(p_\infty-p_{1_{r=R}}\right)\dot{R}}{\varepsilon\rho_\infty R}\right\} \tag{15}$$

$$p_a=\frac{\rho_l}{4\pi r}\frac{d^2V}{dt^2} \tag{16}$$

Where, C_∞ is the velocity of the sound in the liquid at infinity. γ is the ratio of the specific heats of gas. ζ is the bulk viscosity of the liquid. μ is the viscosity of the liquid. σ is the surface tension of the liquid. R and R_0 are the radius and the initial radius of the bubble. V is the volume of the bubble. p_0 is the initial gas pressure inside the bubble. p_∞ is the pressure in the liquid at infinity. p_a is the sound pressure at radial distance r from the bubble center. The pressure in the liquid at the bubble wall $p_{ir=R}$ can be written in Eq. (14) and Eq. (15) as the ith approximation. ρ is the density where the subscripts of "g" and "l" denote the gas and the liquid respectively. ε is the ratio defined with the gas density and density at infinity($\varepsilon=1-\rho_g/\rho_\infty$).

Fig. 7 shows the sound receiver positions. The tonal noise is related to the dynamics of the sheet cavitation which is the unity of the bubbles. In this case, the tonal noise can be scaled as the monopole (See Eq. (18)). On the other hand, the higher frequency noise can be treated as the shock wave impulse and scaled by Levkovskii[9](1968) Eq. (19). Where, the subscripts of "m" and "s" denote model and full scale, respectively, and $V=nD_p$.

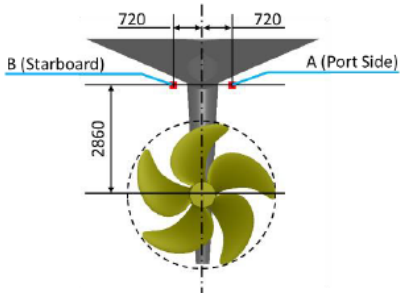

$$\lambda=D_{ps}/D_{pm} \tag{16}$$

$$\frac{f_s}{f_m}=\frac{n_s}{n_m} \tag{17}$$

$$SPL_s-SPL_m=10\log_{10}\left[\lambda^6\cdot\left(\frac{n_s}{n_m}\right)^4\cdot\left(\frac{{r_m}^2}{r_s}\right)\right] \tag{18}$$

$$SPL_s-SPL_m=10\log_{10}\left[\lambda^5\cdot\left(\frac{n_s}{n_m}\right)^2\cdot\left(\frac{{r_m}^2}{r_s}\right)\right] \tag{19}$$

Figure 7: Sound receiver position

Fig. 8(a) and (b) show the computational and experimental results of the sound pressure level on the sound receiver position at B (starboard side). Narrow band estimation results showed clear blade frequency components as tonal noise.

Direct simulation of the pressure pulse at the receiver position showed good agreement with the experimental result around the first to the fourth blade passing frequency range, which was from 10Hz to 100Hz in this case. However, the prediction did not agree with the experimental results over hundreds Hz. CFD simulation neglected the second order derivative of Rayleigh-Plesset equation. The numerical mesh and time step seemed to be still coarse for the collapsing of bubble. These seemed to bring the limitation for the higher frequency noise estimation. The results by the Brown's method showed good agreement between middle hundreds Hz and middle thousands Hz region. Tomita-Shima method combined with the information from "Multi-process cavitation model" showed also good agreement between middle hundreds Hz and middle thousands Hz region. Direct simulation

of pressure pulse at receiver position well predicts the noise level at low frequency.

For higher frequency noise prediction, the Brown's formulae based on the cavitation area derived from CFD are practical as design tool. Tomita-Shima method based on the number and the radius of the bubbles derived by "Multi-process model" seems to be also the good measure.

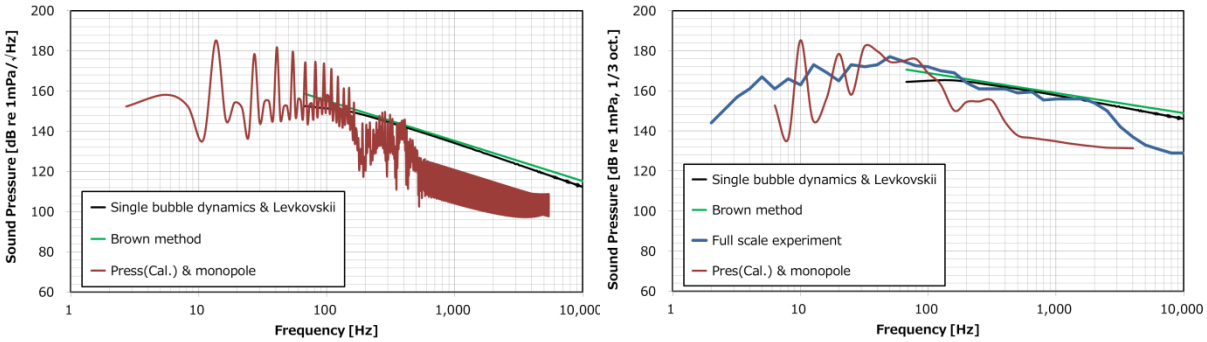

(a) Narrow band (b) 1/3 oct. band

Figure 8: Sound pressure estimation resutlt

4 CONCLUTIONS

In this study, newly developed "Multi-process cavitation model" was adopted for the unsteady cavitation simulation.

1) The unsteady cavitation pattern behind ship condition was well reproduced by the "Multi-process cavitation model".
2) "Multi-process cavitation model" gave distribution of number of cavitation nuclei and bubble radius which was related to higher frequency noise.
3) Direct noise predictions showed good agreement up to 5th blade passing frequency with monopole scaling method. It seems to be difficult to predict the accurate noise level by the direct CFD calculation at over hundreds frequency range noise.
4) Brown's empirical formula or Tomita-Shima method in combination with "Multi process cavitation model" showed good capability for practical estimation at over hundreds frequency range noise.

5 REFERENCES

[1] Tsuda, S. and Watanabe, S., "Application of Multi-Process Cavitation Model for Cavitating Flow in Cold Water and in Liquid Nitrogen around a Hydrofoil", Proc. ASME/JSME/KSME 2015 Joint Fluids Engineering Conf., Paper No. AJKFluids2015-05532.

[2] Gindroz, B.,Hoshino, T. & Pylkkanen, V., "Propeller RANS/Panel Method Workshop, 22nd ITTC Propulsion Committee Propeller RANS/Panel Method Workshop", Grenoble, Apr.1998.

[3] Hoshino,T. , "Experimental Data For Unsteady Panel Calculations And Comparison (Seiun-Maru HSP)", Proceedings of Propeller RANS/Panel Method Workshop, 22nd ITTC Propulsion Committee, Grenoble, Apr.1998.

[4]Singhal A. K., et al., "Mathematical basis and validation of the full cavitation model", Journal of Fluids Eng. 124(3), pp.617-624, 2002

[5] Brown. N.A.,"Cavitation noise problems and solutions", Proc. International Symposium on Shipboard Acoustics, pp.21-38, 1977

[6] Tomita, Y. and Shima, A., "On the Behavior of a Spherical Bubble and the Impulse Pressure in a Viscous Compressible Liquid", Bulletin of the JSME, Vol. 20, No. 149, 1977

[7] Kamiirisa et al., "Development of Prediction Method for Ship Underwater Noise by Bubble Dynamics", Mitsui Engineering & Shipbuilding Co Technical Review No.185, 2005

[8] Ando, S., Kimura, K., Segawa, K., Yamamoto, K., "Study on the Hybrid Method of CFD and Bubble Dynamics for Marine Propeller Cavitation Noise Prediction", Proceedings of the 10th International Symposium on Cavitation (CAV2018), 2018

[9] Levkovskii, Y.L.,"Modelling of cavitation noise", Soviet Physics-Acoustics 13, pp.337–339, 1968

[10] Fujiyama K., "Numerical Simulation of Ship Hull Pressure Fluctuation Induced by Cavitation on Propeller with Capturing the Tip Vortex", Fourth International Symposium on Marine Propulsors SMP'15, 2015

The Influence of Hydrodynamic Assumptions on Ship Maneuvering

Ghalib Taimuri, Tommi Mikkola, Jerzy Matusiak, Pentti Kujala & Spyros Hirdaris
Aalto University, Mechanical Engineering (Marine Technology), Espoo,Finland
ghalib.taimuri@aalto.fi

1 Introduction

We present a preliminary assessment on the influence of the hydrodynamic assumptions associated with ship motions, for vessels maneuvering in calm waters. Three approaches are considered: (a) ***Model 1*** idealising the maneuvering of a ship in 3-dof as per Brix (1993); (b) ***Model 2*** representing the 6-dof hybrid time domain unified seakeeping / maneuvering model of Matusiak (2017); and (c) ***Model 3*** - idealising combined seakeeping and maneuvering nonlinear characteristics in 6-dof by the time domain Green function method of McTaggart (2005). Simulations of turning circle and zig-zag manoeuvers are assessed and compared against available data for two tankers (KVLCC2 & Esso Osaka) and a container ship (DTC). It is concluded that in calm waters simplified models with hydrodynamic derivatives from either RANSE CFD or model tests can be used. However, implementation of well-validated CFD hydrodynamic coefficients may be more economic for the development of practical engineering tools, such as rapid assessment tools accounting for evasiveness in ship crashworthiness (Goerlandt et al. 2012).

2 Hydrodynamic models

Over the years, maneuvering has been associated with open or restricted calm waters (i.e. in sheltered waters or in a harbor). For this reason, traditional maneuvering models assume that external actions relate with constant valued slow motion derivatives applicable at all frequencies of excitation with little or no account of ship dynamics (e.g. forward speed, heading angle, etc.). Seakeeping models assume vessel operations at a speed and heading in regular or random seas in the absence of control plane actions. They assess the influence of parasitic motions or responses of a rigid vessel to waves (e.g. Hirdaris et al., 2016). In combined seakeeping and maneuvering fluid actions that include the influence of hydrodynamic coefficients and wave environmental actions can account for operational scenarios that allow the vessel to respond in various degrees of freedom (e.g. Bailey et al., 2002 and Matusiak, 2017). From the viewpoint of operations and safety of a vessel, combining random seaway and control plane actions may be useful, especially for ships travelling with forward speed in close proximity to fixed or floating structures in severe open waters; or in shallow, restricted waters. In such cases it is possible to superimpose Froude-Krylov, diffraction, radiation and 2nd order mean forces computed from potential flow in maneuvering models that account for the influence of hull, propeller, rudder and drift forces. Hydrodynamic assumptions are from empirical formulae, CFD or model tests. Consequently, the position of the vessel during maneuvers and the associated ship speed data are transfered on seakeeping (Seo and Kim, 2011). This paper compares the following models for fine and full form vessels:

- ***Model 1*** idealises the maneuvering of a ship in calm waters by a 3-dof box-like model based on Brix (1993). The ship origin is in way of still water line and on the symmetry plane, at a distance 'x_G'(mid-ship) from the Centre of Gravity (CoG). The radiation part of the hull forces includes added mass coefficients as per Clarke et al. (1983) and Brix (1993). The mathematical equation is:

$$\begin{aligned} m[\dot{u} - rv - r^2 x_G] &= X_{res} + X_{prop} + X_{rud} + X_{hull} \\ m[\dot{v} + ru + \dot{r}x_G] &= Y_{rud} + Y_{Hull} \\ (I_z + mx_G^2)\dot{r} + m[x_G(\dot{v} + ur)] &= N_{rud} + N_{Hull} \end{aligned} \quad (1)$$

  where : 'm' is the mass of the ship [kg] and 'I_Z' is the yaw moment of inertia; u, v and r, are surge, sway and yaw velocities respectively. Ship resistance, propulsion and rudder forces are represented with subscripts '*res*', '*prop*' and '*rud*' respectively. Subscript '*hull*' denotes hull forces.

- ***Model 2*** presents the 6-dof hybrid time domain unified model of maneuvering in waves introduced by Matusiak (2017). The ship's origin is on a line passing through CoG at still water plane and the vertical z-axis points downwards. The added mass and damping are calculated using strip theory as per Salvesen et al. (1970). Time dependent radiation forces are computed by convolution integral and hydrostatic forces are evaluated by a panel method. The mathematical equation is:

$$
\begin{aligned}
&(m + a_{11})\dot{u} + a_{15}\dot{q} = -mg\sin\theta + X_{res} + X_{prop} + X_{rud} + X_{hull} + (m + a_{22})(rv - qw)\\
&(m + a_{22})\dot{v} + a_{24}\dot{p} + a_{26}\dot{r} = mg\cos\theta\sin\varphi + (m + a_{11})(pw - ru) + Y_{hull} + Y_{rud} + a_{33}pw + a_{35}pq\\
&(m + a_{33})\dot{w} + a_{35}\dot{q}\\
&\qquad = mg\cos\theta\cos\varphi + m(uq - vp) - k_{33} - k_{35} - b_{33}w - b_{35}q + a_{11}uq + a_{15}q^2 - a_{22}vp - a_{26}pr\\
&\qquad - a_{24}p^2\\
&a_{42}\dot{v} + (I_x + a_{44})\dot{p} + a_{46}\dot{r} = (I_y - I_z)qr - Y_{rud}z_{rud} + K_{hull} - k_{44} - k_{42} - k_{46} - b_{44}p + 2\zeta p\omega_{\varphi}\\
&a_{15}\dot{u} + a_{53}\dot{w} + (I_y + a_{55})\dot{q} = (I_y - I_x)pr + X_{rud}x_{rud} - k_{55} - k_{53} - k_{15} - b_{55}r - b_{35}w\\
&a_{62}\dot{v} + a_{64}\dot{p} + (I_z + a_{66})\dot{r} = (I_x - I_y)pq + Y_{rud}x_{rud} + N_{hull}
\end{aligned}
\tag{2}
$$

where: 'a_{ij}' are the added mass coefficients at infinite frequency, 'k_{ij}' is an element of memory function and 'b_{ij}' are damping radiation terms . I_x, I_y, and I_Z are roll, pitch and yaw moment of inertia respectively. Roll (φ), pitch (Θ) and heave velocities are given by p, q and w respectively; ζ *and* ω_{ϕ}, represent the critical damping ratio and angular velocity with respect to roll respectively. The hull x,y and z directional forces are represented by X, Y and Z respectively. The moments around x,y and z axis are denoted by K, M and N respectively. The remaining terms correspond, as applicable, to the same symbols as in Equation (1).

- ***Model 3*** accounts for the combined seakeeping and maneuvering characteristics of a vessel in 6-dof by a time domain green function method accounting for the nonlinearities in real hull form dynamics as per McTaggart (2005). The axis of origin is defined along North-West (X,Y).The direction of the head wave is coming from (North/X) axis (see Table 1a). The origin of the body fixed system is on CoG at a distance from still water line. At first instance hydrodynamic forces and motions are at first estimated in the frequency domain using Green function at zero forward speed. Forward speed effects are in turn implemented as a function of added mass ($[A]$) and damping ($[B]$) as per Salvesen et al. (1970). Time domain results use convolution integral and memory effects of radiation forces are determined from retardation functions embedded in ($[K]$). Incident waves and hydrostatic forces (F_{waves}) are computed non-linearly; diffracted and radiated forces are evaluated linearly and the hydrostatic restoring matrix is denoted as [C]. The subscripts *hull*, *prop*, *res* and *rud* show hydrodynamic, propulsion, hull-resistance and rudder forces respectively. The mathematical equation is :

$$
([M] + [A])\ddot{X} + [B]\dot{X} + [C]X + [K] = F_{hull} + F_{waves} + F_{prop} + F_{res} + F_{rud} \tag{3}
$$

3 Results and Discussion

Hull forces in all models include hydrodynamic derivatives estimated from empirical relations (see Table 2). For example, KVLCC2 deep-water derivatives are selected from model test results reviewed by Aksu and Köse (2017) and for shallow waters from the CFD simulations of Mucha (2017). On the other hand, Esso Osaka derivatives are opted from Kobayashi et al. (2003) model tests. DTC maneuvering coefficients use the CFD model of Kinaci et al. (2019).

Turning circle manoeuvers of KVLCC2 are shown in Figure 1(i). Results for Model 1 based on experimental and empirical derivatives show good agreement. For the same case manoeuvring trajectories produced by Models 2 & 3 deviate from experiments. Having a closer look at Model 2 it appears that the advance, transfer and tactical diameter of the ship lie within the reasonable limits of 12%, 10% and 3% respectively. The reason for these deviations may be due to the differences between the damping terms used by different methods and the coupled effects of heave, pitch and roll. In model tests and CFD models the effect of viscosity may be another term that influences hydrodynamic performance. On the other hand, in Model 3 results deviate significantly in comparison to experimental data and this could be attributed to Inoue et al. (1981) idealisation that assumes no additional surge component that would influence the resistance of the ship while progressing in way of her trajectory (see Table 2). As shown in Figure 1(ii) in a similar fashion to KVLCC2 the turning circle of Esso Osaka is close to the actual trajectory of Model 1. On the other hand, Model 2 PURE trajectory deviates significantly from the MMG and EXP trajectories, while the tactical diameter seems reasonable. It is thought that these differences appear because the higher order surge ($X'_u, X'_{uu}, X'_{uuu}, X'_v, X'_{vvv}$), sway ($Y'_{vv}, Y'_{rr}$) hydrodynamic derivatives and yaw moments (N'_{vv}, N'_{rr}) that are included in the PURE mathematical model presented in Table 2, are not incorporated in the results. This observation is also confirmed by the comparisons of results from Models 1, 2 shown in Figures 2(a),(b). It is thought that 0Model 3 results for Esso Osaka deviate in comparison to experimental data primarily for the same reasons explained for KVLCC2. For the remaining models differences may be attributed to various methods used for the derivation of hydrodynamic derivatives (see Table 2). As presented in Figure 1(iii) the DTC container ship shows satisfactory initial trajectories with Model 1 when empirical and CFD based hydrodynamic derivatives are implemented. This is not the case for Models 2 & 3 that predict adequate trajectories only for the case of CFD hydrodynamic derivatives.

Table 1. Summary of maneuvering and seakeeping Models

(a) Axis of Origin (ψ: heading angle, μ : *wave direction*; OXY : Earth-fixed coordinate system; oxy: body coordinate system).

Model 1	Model 2	Model 3
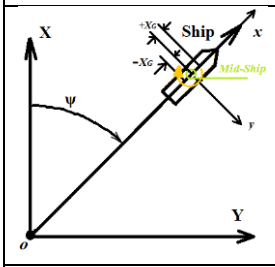	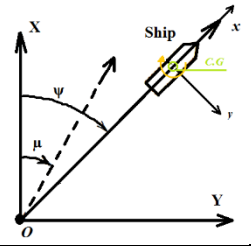	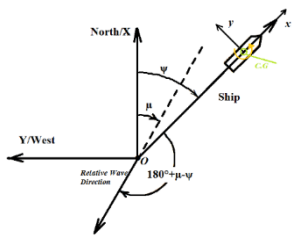

(b) Hull Resistance (X_{res}, F_{res})

$X_{res} = -0.5\rho U^2 S_w C_T/(1-t)$	$F_{res} = -0.5\rho U^2 S_w C_T$

where, X_{res}, F_{res} is hull resistance, U is the initial velocity of vessel, s_w is wetted surface area, C_T is resistance coefficient and 't' is thrust deduction factor.

(c) Propeller Forces (X_{prop}, F_{prop})

$X_{prop} = \rho n^2 D^4 K_T$	$F_{prop} = (1-t)\rho n^2 D^4 K_T$

K_T is the thrust coefficient defined as: $k_{t0} + k_{t1}J + k_{t2}J^2$; where J is the advance number and $k_{t0}, k_{t1}, and\ k_{t2}$quadratic coefficients; 'D' is propeller diameter, 'n' is revolution of propeller (rps) and ρ is density of water.

(d) Rudder Forces $(X_{rud}, Y_{rud}, N_{rud})$

Rudder forces are estimated according to Söding, (1982), Brix, (1993) $X_{rud} = -0.5C_D\rho A_r\left(V_{x,r}^2 + V_{y,r}^2\right)$ $Y_{rud} = 0.5C_L\rho A_r\left(V_{x,r}^2 + V_{y,r}^2\right)[0.6\cos\beta + 0.6\,X_{rud}\sin\beta]\ N_{rud} = x_R Y_{rud}$ where: C_D and C_L are rudder drag and lift coefficients´; A_r is rudder area and $V_{x,r}\ and\ V_{y,r}$ are inflow axial and radial velocity at rudder respectively; β and ρ are drift angle and density of water respectively.	Rudder forces are calculated using Inoue et al., (1981)as : $X_{rud} = -F_N \sin\delta$ $Y_{rud} = -(1+a_H)F_N\cos\delta$ $N_{rud} = -(1+a_H)x_R\ F_N\cos\delta$ where: F_N is rudder normal force; a_H is rudder hull interaction coefficient; x_R is a distance of rudder from CoG and δ is the rudder angle.

Table 2. Hydrodynamic derivatives ($X'_H, Y'_H\ and\ N'_H$ show linear, higher order and coupled, non-dimensional damping forces for surge force X' , sway force $Y'$and yaw moment N')

INOUE (Model 3) - Inoue et al., (1981)

$$Y'_H = Y'_v v' + Y'_{vv} v'|v'| + Y'_{vr} v'|r'| + Y'_r r' + Y'_{rr} r'|r'|$$
$$N'_H = N'_v v' + N'_{vvr} v'^2 r' + N'_{vrr} v' r'^2 + N'_r r' + N'_{rr} r'|r'|$$

MMG (Model 1& Model 2) - Yasukawa and Yoshimura (2015)

$$X'_H = -R'_0 + X'_{vv} v'^2 + X'_{vr} v' r' + X'_{rr} r'^2 + X'_{vvvv} v'^4$$
$$Y'_H = Y'_v v' + Y'_r r' + Y'_{vvv} v'^3 + Y'_{vvr} v'^2 r' + Y'_{vrr} v' r'^2 + Y'_{rrr} r'^3$$
$$N'_H = N'_v v' + N'_{vvr} v'^2 r' + N'_{vvv} v'^3 + N'_r r' + N'_{vrr} v' r'^2 + N'_{rrr} r'^3$$

PURE (Model 1 & Model 2) - Papanikolaou et al.(2016)

$$X'_H = X'_v + X'_{vv} v'|v'| + X'_{vvv} v'^3 + X'_u u' + X'_{uu} u'^2 + X'_{uuu} u'^3$$
$$Y'_H = +Y'_v v' + Y'_{vv} v'|v'| + Y'_{vvv} v'^3 + Y'_r r' + Y'_{rr} r'|r'| + Y'_{rrr} r'^3$$
$$N'_H = +N'_v v' + N'_{vv} v'|v'| + N'_{vvv} v'^3 + N'_r r' + N'_{rr} r'|r'| + N'_{rrr} r'^3$$

EMP (Model-1) [$X'_{vv}, X'_{vvvv}, Y'_{vvv}, Y'_{vvr}, N'_{vvv}$ Yoshimura, Masumoto, (2012), Clarke et al., (1983)], [Y'_v, N'_r, N'_v, Y'_r Clarke et al., (1983)], [Y'_{vv}Kijima, Nakiri, (1990), Inoue et al., (1981)]

$$X'_H = X'_{vv} v'|v'| + +X'_{vvvv} v'^3|v'|$$
$$Y'_H = Y'_v v' + Y'_r r' + Y'_{vv} v'|v'| + Y'_{vvv} v'^3 + Y'_{vvr} v'|v'|r'$$
$$N'_H = N'_v v' + N'_{vvv} v'^3 + N'_r r'$$

The zig-zag manoeuvers of KVLCC2 and Esso Osaka using Models 1 & 3 present satisfactory results in comparison to experimental data (see Figures 2a,b and 3b). Although the equation of PURE hydrodynamic derivatives demonstrated good results for turning circle simulations they seem less adaptable to zig-zag manoeuvres in comparison to other hydrodynamic derivative options available (see Table 2 and Models 1,2 in Figure 3). When Model 2 is used, a shift in the period of zig-zag manoeuvers becomes evident. This could be primarily attributed to the different way of modelling the effects of inertia (e.g. compare Brix, 1993 to McTaggart, 2005) and/or secondarily the effects of scaling. This matter is under further investigation. Hydrodynamic derivatives for the case of the DTC are based on the simulation of pure yawand sway and coupled yaw and sway by CFD (see Kinaci et al., 2019). Figure 2c, suggests that the most important parameter in the prediction of zig-zag manoeuvers at low speed is the 2nd order pure sway velocity force ($Y'_{vv} v'|v'|$). This is because all models presented - apart from the MMG model - take under consideration this action. This seems to lead to escalation in the overshoot angle especially at lower speeds.

For ships operating in shallow waters the forces acting on the hull, rudder and propeller are changed due to the influence of seabed, side walls and quay. As per Raven (2019) the later is believed to increase the viscous resistance of the ship, ultimately affecting the inflow induced forces to the propeller, rudder and hull. To elaborate the influence of such effects, shallow water attributes were added in the numerical code of Model 1 by considering two aspects : (1) the influence of the viscous resistance of the ship in shallow water as a function of the ship draft to sea depth (see Raven, 2019); and (2) the influence of hydrodynamic derivatives by averaging the Ankudinov et al., (1990) and Kijima and Nakiri, (1990) empirical methods. The combination of (1) and (2) is thought to provide better fit in of hydrodynamic derivatives originally derived via regression analysis. Because of lack of openly available data, only comparisons of Esso Osaka and KVLCC2 are presented in Figures 4 & 5 for sea depth / ship draft ratio of 1.2 m. The simulations for KVLCC2 (see Figure 4) utilise the CFD shallow water hydrodynamic derivatives computed of Mucha, (2017). It appears that those give good estimation for turning trajectory and zig-zag manoeuvers. On the other hand, turning circle simulations for Esso Osaka seem reliable when using the EMP and MMG models (see Figure 5). Because of lack of openly available manoeuvring trajectories and associated hydrodynamic derivatives in shallow waters, to conclude on the validity of this method further model tests, open water tests and / or CFD simulations have to be pursued.

(a) Model 1 (b) Model 2 (c) Model 3

(i) KVLCC2 Tanker ship (Speed : 15.5 Knots, Rudder angle : 35^0 portside turn)

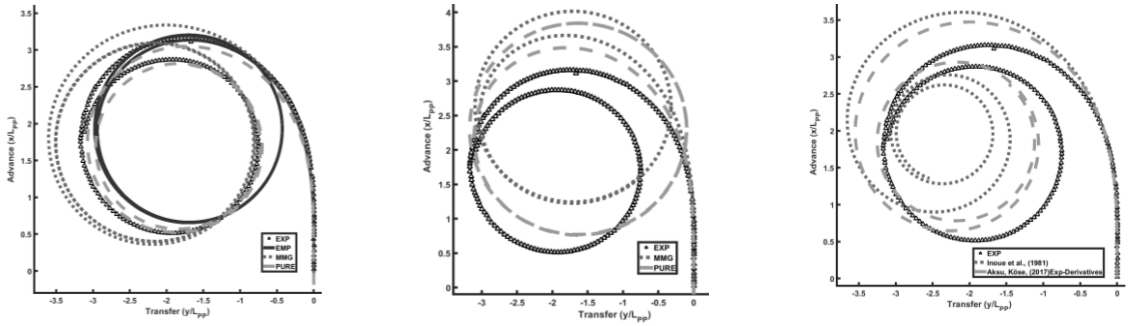

(ii) Esso Osaka Tanker ship (Speed : 10 knots, Rudder angle : 35^0 starboard turn)

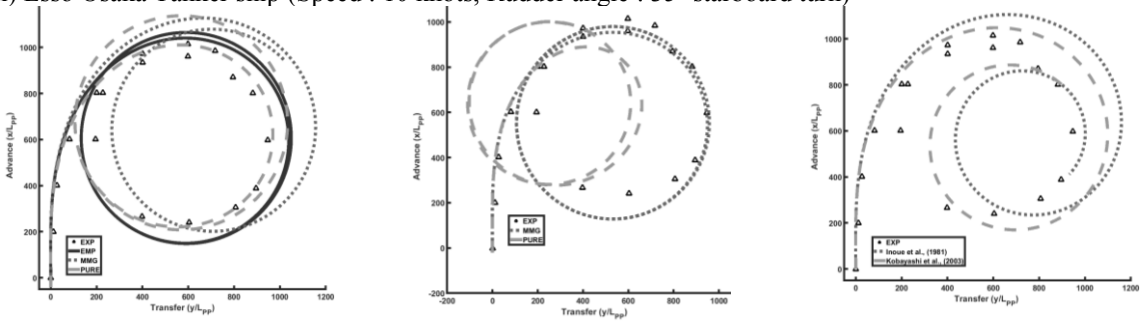

(iii) DTC Container ship (Speed : 6 knots, Rudder angle : 35^0 starboard turn)

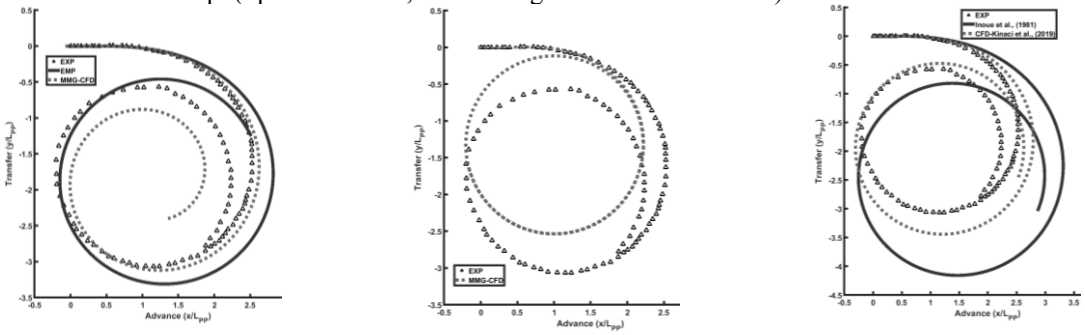

Fig. 1: Deep water turning circle simulations for all ships. (EXP denotes results from model tests; EMP & Inoue et al.,1981 represent the hydrodynamic coefficients of Table 2. For KVLCC2 and Esso Osaka the hydrodynamic derivatives are from Aksu and Köse (2017) and model tests of Kobayashi et al. (2003) respectively. DTC hydrodynamic derivatives are based on CFD by Kinaci et al.,2019).

(a) Esso Osaka (Speed :7.8 knots) (b) KVLCC2 (Speed : 15.5 knots) (c) DTC (Speed : 6 knots)

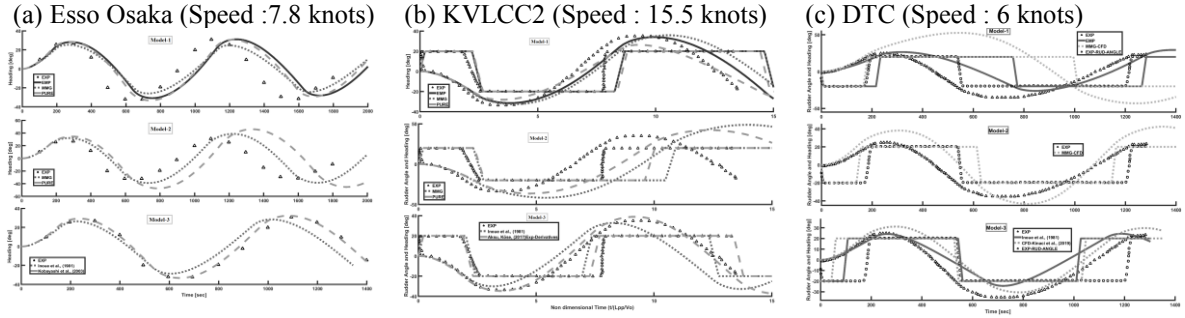

Fig. 2: Comparison of deep water $20^0/20^0$ zig-zag manoeuvres (EXP are model test results; for other hydrodynamic derivatives see Table 2 and Figure 1).

(a) Turning circle

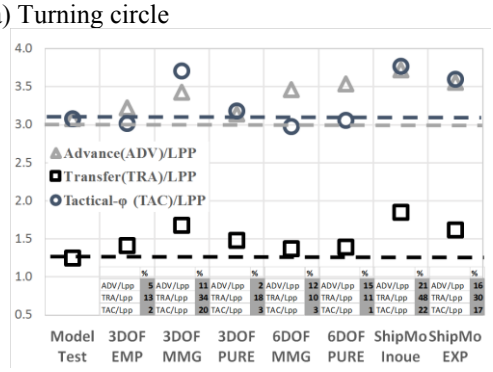

(b) Zig-zag

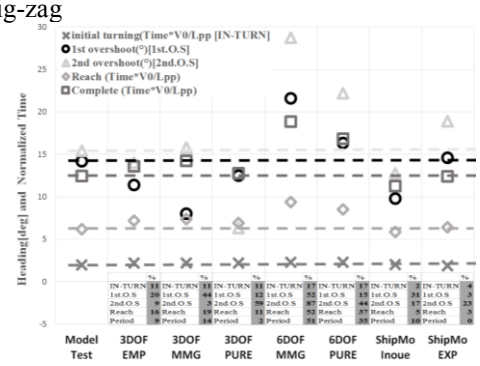

Fig. 3: Parametric study of deep water KVLCC2 manoeuvring simulations (LPP : Length between perpendiculars; V_0 : initial ship speed; for other hydrodynamic derivatives see Table 2 and Figure 1).

(a)Turning circle manouvers Rudder angle : 35^0 portside turn

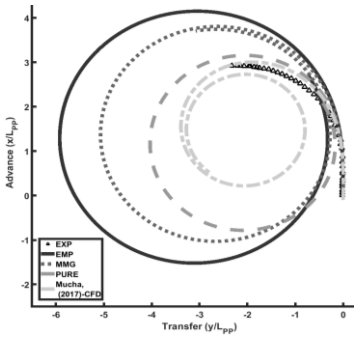

(b) $20^0/5^0$ Zig-zag manouvers

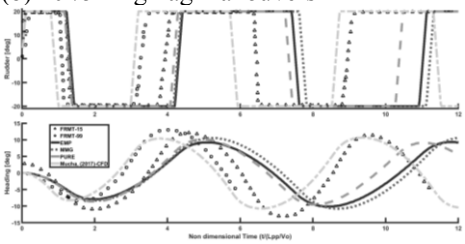

Fig. 4: Shallow water simulations for KVLCC2 using Model 1 at 7.5 Knots (EXP denotes model test results; for other hydrodynamic derivatives see Table 2 – FRMT-15 and FRMT – 99 represent free running model tests from two facilities under http://simman2019.kr .

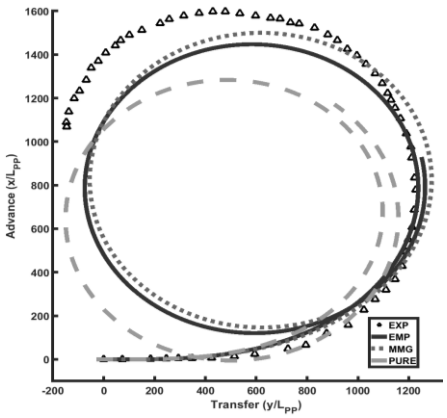

Fig 5: Shallow water manoeuvring simulation for turning circle of Esso Osaka at 7 knots speed and 35° portside turn; EXP denotes results from full-scale trials. For other hydrodynamic derivatives see Table 2. EMP represents empirically evaluated hydrodynamic coefficients, other hydrodynamic derivatives are based on model test which are converted into shallow water using empirical realtion by Ankudinov et al. (1990) and Kijima and Nakiri (1990).

4 Conclusions

- In shallow waters EMP and MMG models were shown to be suitable for Esso Osaka as compared to full-scale data. For KVLCC2 viscous effects in model experiments tend to overestimate full-scale results.
- Pure sway velocity force ($Y'_{vv}v'|v'|$) was shown to be particularly important for zig-zag manoeuvers. Differences in zig-zag test results could be attributed to uncertainties associated with added mass formulations. This could be particularly important in terms of idealising the maneuvering trajectories of vessels with standard propulsion set up (singe screw) as demonstrated in this paper, or more innovative propulsion configurations (e.g. RoPax and passenger vessels with podded or twin-screw propulsion).
- In shallow waters transforming deep-water hydrodynamic coefficients by empirical relations seems to be the traditional practice. However, validated CFD based hydrodynamic derivatives exist in open literature and depending on the case could be practically implemented in numerical codes.
- The 3-dof simplified manoeuvring model (Model 1) appears to give better results. This is encouraging, as our intention is to use this model or a more intelligent derivative of the same including wind effects and roll motions to idealise ship state before possible grounding or collision. In such situations the trajectory and speed are key parameters in terms of rounding up the influence of hydrodynamic actions on dynamic response. Model tests are expensive and the uncertainties associated with the estimation of maneuvering coefficients especially in restricted and / or shallow waters may be significant. In this sense well validated CFD simulations available in open literature could be useful.

References

Aksu, E. & Köse, E. (2017). Evaluation of Mathematical Models for Tankers' Maneuvering Motions, *Journal of ETA Maritime Science,* 5(1):95-109.

Ankudinov, V.K., Miller, E.R., Jakobsen, B.K. & Daggett, L.L. (1990). Maneuvering performance of tug/barge assemblies in restricted waterways, *Proc. of the Intl. Conference on Marine Simulations and Ship Maneuverability (MARSIM),* pp. 311 - 319, Tokyo, Japan, 4-7 June 1990.

Bailey, P.A., Hudson, D.A., Price, W.G. & Temarel, P. (2002). Time simulation of maneuvering and seakeeping assessments using a unified mathematical model, *Trans. of the Royal Inst. of Nav. Archs.,* 144: 27-48.

Brix, J.E. 1993, *Manoeuvring technical manual,* Seehafen Verlag.

Clarke, D.P., Gedling, P. & Hine, G. (1983). *The Application of Manoeuvring Criteria in Hull Design Using Linear Theory*. *In Maritime Archives of the the Royal Inst. of Nav. Archs.,* Report 03-1983.

Goerlandt, F., Ståhlberg, K. & Kujala, P. (2012). Influence of impact scenario models on collision risk analysis, *Ocean Engineering,* 47:74-87.

Hirdaris, S.E., Lee, Y., Mortola, G., Incecik, A., Turan, O., Hong, S.Y., Kim, B.W., Kim, K.H., Bennett, S., Miao, S.H., Temarel, P. (2016). The influence of nonlinearities on the symmetric hydrodynamic response of a 10,000 TEU Container ship, Ocean Engineering, 111:166-178.

Inoue, S., Hirano, M., Kijima, K. & Takashina, J. (1981). A practical calculation method of ship maneuvering motion, *International Shipbuilding Progress,* 28:207-222.

Kijima, K. & Nakiri, Y. (1990). Prediction method of ship manoeuvrability in deep and shallow waters,. *Proceedings of the Intl. Conference, Marine Simulation and Ship Manoeuvrability (MARSIM & ICMS)*, vol. 90, pp. 311-319, Tokyo, Japan, 4-7 June 1990.

Kinaci, O.K., Sukas, O.F. & Bal, S. (2019). A modular mathematical approach to predict the maneuvering ability of the Duisburg test case in regular waves, *Proceedings of the 5th Ship Manoeuvring in Shallow and Confined Water with non-exclusive focus on manoeuvring in waves, wind and current (MASHCON)*, pp. 251-264, 19 - 23 May 2019, Ostend, Belgium.

Kobayashi, H, Blok, J J, Barr, R, Kim, Y S and Nowicki, J. (2003). *Specialist Committee on Esso Osaka: Final Report and Recommendations to the 23rd ITTC,* vol. 2, pp. 581–743.

Matusiak, J. (2017). *Dynamics of a rigid ship,* 2nd Edition, Aalto University Series, Helsinki, Finland.

McTaggart, K. (2005). Simulation of Hydrodynamic Forces and Motions for a Freely Maneuvering Ship in a Seaway, *Defense R&D Canada (DRDC - Atlantic) Technical Memorandum,* TM:2005-071.

Raven, H.C. (2019). Shallow water effects in ship model testing and at full scale, *Technical Report of the Knowledge Centre for Maneuvering in Shallow and Confined Water*, Maritime Technology Division, Ghent University and Flanders Hydraulics Research, Belgium.

Seo, M. & Kim, Y. (2011). Numerical analysis on ship maneuvering coupled with ship motion in waves, *Ocean Engineering,* 38(17-18):1934-1945.

Söding, H. (1982). Prediction of ship steering capabilities, *Schiffstechnik,* 29(1):3-29.

Yoshimura, Y. & Masumoto, Y. (2012). Hydrodynamic database and maneuvering prediction method with medium high-speed merchant ships and fishing vessels, *Proceedings of the Intl. Conference on Marine Simulations and Ship Maneuverability (MARSIM),* pp. 494-503, 23-27 April 2012, Singapore.

Anderson-Accelerated Convergence for Incompressible Navier-Stokes Equations

Auke van der Ploeg
MARIN, Wageningen/Netherlands, a.v.d.ploeg@marin.nl

1 Introduction

We consider iterative solvers for the systems of non-linear equations that need to be solved to compute incompressible flows. To ensure that the computed solution is not spoiled by grid dependence, the grids have to be sufficiently fine, which causes these systems to become large. For instationary flows such systems have to be solved every timestep, and to be sure that the instationary behavior is computed correctly, the time step cannot be chosen too large and at each time step the system of non-linear equations has to be solved sufficiently accurate. As a result, for many cases the computational effort is quite substantial. Therefore, in this paper we study the effectiveness of an acceleration strategy introduced in Anderson, 1965 to reduce the computational effort. In recent years, this strategy has been analyzed in the context of solution methods for fixed point problems, Fang and Saad, 2009. In the sequel of this report, this strategy will be referred to as Anderson Acceleration (AA).

The basic idea is that, if the problem to solve were linear, at each iteration in which AA is applied some of the history is used to optimize the next update of the approximate solution. Therefore, several vectors from previous iterations have to be stored, and frequently updated. This is very similar to the basic idea of the well-known minimal residual method GMRES, Saad and Schultz, 1986 to solve a non-symmetric system of linear equations.

In Pollock et al., 2018, Anderson-accelerated Picard iterations are analyzed for solving incompressible Navier-Stokes equations, and tested by computing the steady, laminar flow in a 2D and a 3D lid-driven cavity. In Pollock et al., 2018 it is shown that Anderson Acceleration can provide a significant, and sometimes dramatic, improvement in the convergence behavior, and it is even proven analytically that, as long as the underlying fixed-point problem satisfies some constraints, AA provides guaranteed improved convergence behavior.

2 DERIVATION AND ALGORITHMS

When solving the discretized, incompressible Navier-Stokes equations, the system of non-linear equations $\mathbf{r}(\mathbf{x}) = \mathbf{0}$ with $\mathbf{r} : \mathbb{R}^{\mathbf{n}} \rightarrow \mathbb{R}^{\mathbf{n}}$, has to be solved. Herein the vector-valued function $\mathbf{r}$ indicates the residual vector that contains the values of the residual for the transport equations. For the results presented in this paper, AA will be used to solve the coupled system of mass and momentum equations arising from a cell-centered discretization. In that case, in three space dimensions $\mathbf{r}$ contains four residual values for each cell center: three components from the momentum equation and the residual of the mass equation:

$$\mathbf{r} \;=\; \left(\mathbf{r_u}, \mathbf{r_v}, \mathbf{r_w}, \mathbf{r_p}\right)^T$$

Hence the vector length n is four times the number of cells. In general, $\mathbf{r}$ will also contain the residuals from other transport equations, like those coming from a turbulence model, or a transport equation for the volume fraction. For time-dependent flows $\mathbf{r}(\mathbf{x}) = \mathbf{0}$ has to be solved at each time step to such an accuracy that the iterative error does not affect the computed instationary behavior.

Suppose that the 'basic' solution technique without AA to solve $\mathbf{r}(\mathbf{x}) = \mathbf{0}$ is denoted by B. This can be a coupled solver as described in Klaij and Vuik, 2013, or a segregated method like 'SIMPLE' or 'SIMPLER'. The basic method constructs a sequence of estimates $\mathbf{x}_k$, $k = 1, 2, \ldots$ of the solution vector, such that $\mathbf{x}_{k+1} = \mathrm{B}(\mathbf{x}_k)$. If AA is applied at the k-th step of the basic solution technique, first an 'optimized' update $\widetilde{\mathbf{x}_k}$ is constructed. Next, $\mathbf{x}_{k+1} = \mathrm{B}(\widetilde{\mathbf{x}_k})$.

To be able to construct $\widetilde{\mathbf{x}_k}$, the residual vectors together with the solution vectors of some previous outer loops have to be stored in memory. Of course, we have to choose a maximum number of such vectors. This number will be denoted by m, and the resulting AA method to accelerate the computation will be denoted by AAm. For ease of presentation, we will first assume that $k > m$. Solving $\mathbf{r}(\mathbf{x}) = \mathbf{0}$ is

equivalent to solving the fixed point problem $\mathbf{x} = \mathbf{g}(\mathbf{x})$ in which the operator $\mathbf{g}$ is defined by

$$\mathbf{g}(\mathbf{y}) = \alpha \mathbf{r}(\mathbf{y}) + \mathbf{y} \qquad \text{for any given vector } \mathbf{y}$$

Herein α is a parameter to be chosen in advance such that $0 < \alpha \leq 1$. In the next subsection, the effect of this parameter will be discussed.

The AAm-algorithm updates the solution vector as

$$\widetilde{\mathbf{x}_k} \;=\; \sum_{i=0}^{m} \theta_i \mathbf{g}(\mathbf{x}_{k-i}) \qquad \text{satisfying the constraint} \qquad \sum_{i=0}^{m} \theta_i = 1. \tag{1}$$

Herein $\mathbf{x}_{k-1}$ indicates the solution vector from the previous outer loop, $\mathbf{x}_{k-2}$ the solution vector from the previous previous outer loop etc. The zero-sum constraint is necessary to guarantee that at a converged stage, at which $\mathbf{x} = \mathbf{x}_{k-i}$ for, $i = 0, .., m$, $\widetilde{\mathbf{x}_k}$ is indeed a solution to the fixed point problem $\mathbf{x} = \mathbf{g}(\mathbf{x})$. From this constraint it follows that $\theta_0 = 1 - \sum_{i=1}^{m} \theta_i$. To ensure that new information is incorporated into $\widetilde{\mathbf{x}_k}$, θ_0 should be positive. From Eq. (1) it follows that

$$\widetilde{\mathbf{x}_k} \;=\; (1 - \sum_{i=1}^{m} \theta_i)\mathbf{g}(\mathbf{x}_k) + \sum_{i=1}^{m} \theta_i \mathbf{g}(\mathbf{x}_{k-i}) \;=\; \mathbf{g}(\mathbf{x}_k) + \sum_{i=1}^{m} \theta_i \left[\mathbf{g}(\mathbf{x}_{k-i}) - \mathbf{g}(\mathbf{x}_k)\right] \tag{2}$$

The question is now how to determine the coefficients $\theta_1, ...\theta_m$. This is done in such a way that

$$\|\mathbf{r}(\widetilde{\mathbf{x}_k})\|_2 \qquad \text{is minimized, if } \mathbf{r} \text{ were linear.} \tag{3}$$

Therefore, we want to express $\mathbf{r}(\widetilde{\mathbf{x}_k})$ as a function of $\theta_1, ...\theta_m$. First, note that, if $\mathbf{r}$ were linear, the operators $\mathbf{r}$ and $\mathbf{g}$ commute:

$$\mathbf{r}(\mathbf{g}(y)) \;=\; \mathbf{r}(\alpha \mathbf{r}(y) + y) \;=\; \alpha \mathbf{r}(\mathbf{r}(y)) + \mathbf{r}(y) \;=\; \mathbf{g}(\mathbf{r}(y)) \qquad \text{for any given vector } \mathbf{y}.$$

From Eq. (2) it follows that $\mathbf{r}(\widetilde{\mathbf{x}_k}) = \mathbf{r}\left(\mathbf{g}(\mathbf{x}_k) + \sum_{i=1}^{m} \theta_i \left[\mathbf{g}(\mathbf{x}_{k-i}) - \mathbf{g}(\mathbf{x}_k)\right]\right)$. From this equation, and the fact that the operators $\mathbf{r}$ and $\mathbf{g}$ commute we obtain, if $\mathbf{r}$ were linear,

$$\mathbf{r}(\widetilde{\mathbf{x}_k}) \;=\; \mathbf{g}\left(\mathbf{r}(\mathbf{x}_k) + \sum_{i=1}^{m} \theta_i \left[\mathbf{r}(\mathbf{x}_{k-i}) - \mathbf{r}(\mathbf{x}_k)\right]\right) \;=\; \mathbf{g}\left(\mathbf{r}(\mathbf{x}_k) - \mathbf{R}\boldsymbol{\theta}\right) \tag{4}$$

in which the i-th column of the $n \times m$ matrix $\mathbf{R}$ consist of $\mathbf{r}(\mathbf{x}_k) - \mathbf{r}(\mathbf{x}_{k-i})$ and the vector $\boldsymbol{\theta} = (\theta_1, ..., \theta_m)^T$. If $\alpha = 0$, $\mathbf{g}$ is the identity operator and in that case Eq. (4) holds as well. From Eq. (3) and Eq. (4) it follows that $\|\mathbf{r}(\mathbf{x}_k) - \mathbf{R}\boldsymbol{\theta}\|_2$ must be minimized, independent of the value of α.

The minimization problem can be solved by first making a QR-decomposition of $\mathbf{R}$: an orthogonal $n \times n$ matrix $\mathbf{Q}$, a permutation matrix $\mathbf{P}$ and an $m_k \times m_k$ upper-triangular matrix $\mathbf{U}$ are made such that the matrix product $\mathbf{RP} = \mathbf{Q}(\mathbf{U}\ \ \mathbf{0})^T$. This is equivalent to $\mathbf{Q}^T\mathbf{RP} \;=\; (\mathbf{U}\ \ \mathbf{0})^T$. The equivalence follows from the fact that since $\mathbf{Q}$ is orthogonal it obeys $\mathbf{Q}^T\mathbf{Q} = \mathbf{I}$. If $\mathbf{R}$ has full rank m_k the matrix $\mathbf{U}$ also has full rank and, therefore, is nonsingular. Applying $\mathbf{Q}^T$ to a vector does not change the length of that vector (think of it as a rotation). In addition, the permutation matrix satisfies $\mathbf{PP}^T = \mathbf{I}$. Therefore, if we denote the residual vector $\mathbf{r}(\mathbf{x}_k)$ simply as $\mathbf{r}$,

$$\min_{\boldsymbol{\theta}} \|\mathbf{r} - \mathbf{R}\boldsymbol{\theta}\|_2 \;=\; \min_{\boldsymbol{\theta}} \left\|\mathbf{Q}^T(\mathbf{r} - \mathbf{R}\boldsymbol{\theta})\right\|_2 \;=\; \min_{\boldsymbol{\theta}} \left\|\mathbf{Q}^T\mathbf{r} - (\mathbf{Q}^T\mathbf{RP})\mathbf{P}^T\boldsymbol{\theta}\right\|_2 \;=\; \min_{\boldsymbol{\theta}} \left\|\mathbf{Q}^T\mathbf{r} - (\mathbf{U}\ \ \mathbf{0})^T\mathbf{P}^T\boldsymbol{\theta}\right\|_2$$

If we put $\mathbf{y} = \mathbf{P}^T\boldsymbol{\theta}$ and partition $\mathbf{Q}^T\mathbf{r}$ as $(\mathbf{r_1}, \mathbf{r_2})^T$ in which $\mathbf{r_1}$ has m_k components, this can be written as

$$\min_{\boldsymbol{\theta}} \|\mathbf{r} - \mathbf{R}\boldsymbol{\theta}\|_2 \;=\; \min_{\mathbf{y}} \left\| \begin{pmatrix} \mathbf{r_1} \\ \mathbf{r_2} \end{pmatrix} - \begin{pmatrix} \mathbf{U} \\ \mathbf{0} \end{pmatrix} \mathbf{y} \right\|_2 \;=\; \min_{\mathbf{y}} \sqrt{\|\mathbf{r_1} - \mathbf{U}\mathbf{y}\|_2^2 + \|\mathbf{r_2}\|_2^2}$$

The solution can be obtained from $\mathbf{Uy} = \mathbf{r_1}$ by back substitution. In our current implementation, the QR-factorization is not yet implemented in parallel: the matrix $\mathbf{R}$ is gathered on the master processor

and on that processor the factorization is performed. Therefore, the timings reported in the next section contain some overhead, which can be reduced in future implementations.

Both the residual vectors and solution vectors of m previous outer loops should be stored in memory. In our implementation, these vectors are shifted: the current residual vector and solution vector are added and, if the resulting number of residual vectors exceeds m, the 'oldest' vectors are deleted.

The AA acceleration can be applied at every step of the iteration, but to reduce the overhead, it is also possible to apply it only every second, third or fourth iteration. If the frequency of application of AA is controlled by the parameter $freq$, the basic iterative method B accelerated by Anderson Acceleration is given by Algorithm 1.

Algorithm 1: **Basic method B accelerated by Anderson Acceleration**:
Given $\mathbf{x}_0$ and $m \geqslant 1$: Set $\mathbf{x}_1 = \mathrm{B}(\mathbf{x}_0)$;
For $k = 1, 2, ...$
IF mod$(k, freq) == 0$ THEN
Set $m_k = \min(m, k)$;
Determine $\boldsymbol{\theta} = (\theta_1, ..., \theta_{m_k})^T$ in such a way that $\|\mathbf{r}(\mathbf{x}_k) - \mathbf{R}\boldsymbol{\theta}\|_2$ is minimized;
IF $\sum_{i=1}^{m_k} \theta_i < 1.0$ THEN
Set $\widetilde{\mathbf{x}_k} = \mathbf{g}(\mathbf{x}_k) + \sum_{i=1}^{m_k} \theta_i \left[\mathbf{g}(\mathbf{x}_{k-i}) - \mathbf{g}(\mathbf{x}_k)\right]$; Set $\mathbf{x}_{k+1} = \mathrm{B}(\widetilde{\mathbf{x}_k})$
ELSE Set $\mathbf{x}_{k+1} = \mathrm{B}(\mathbf{x}_k)$
ELSE Set $\mathbf{x}_{k+1} = \mathrm{B}(\mathbf{x}_k)$

2.1 Effect of the parameter α

As already mentioned in the introduction, in Pollock et al., 2018 it is proven analytically that, as long as the underlying fixed-point problem satisfies some constraints, AA provides guaranteed improved convergence behavior. The main constraint is that the fixed-point operator should be a contraction operator. To be precise, in Pollock et al., 2018 it is proven that if the spectral radius of the Jacobian of the operator $\mathbf{g}$ is below 1, the fixed point iteration $\mathbf{x_{k+1}}$=$\mathbf{g}(\mathbf{x_k})$ is locally convergent.

From $\mathbf{g}(\mathbf{y}) = \alpha\mathbf{r}(\mathbf{y}) + \mathbf{y}$, for any $\mathbf{y}$ it follows that if λ is an eigenvalue of the Jacobian of the operator $\mathbf{r}$, then $1 + \alpha\lambda$ is an eigenvalue of the Jacobian of the operator $\mathbf{g}$. Therefore, the choice of α directly influences the spectral properties of the Jacobian of the fixed-point operator. If all possible values for λ would be real and negative, choosing a positive, small enough value for α would guarantee the fixed-point operator to be a contraction operator. For real-life applications it is hard to guarantee such conditions.

If $\alpha = 0$, the operator $\mathbf{g}$ is simply the identity operator and solving the equation $\mathbf{r}(\mathbf{x})$ is no longer equivalent to solving the fixed point problem $\mathbf{x} = \mathbf{g}(\mathbf{x})$. In that case, if AA is applied at the k-th step of the iteration $\widetilde{\mathbf{x}_k}$ is constructed as

$$\widetilde{\mathbf{x}_k} \;=\; \sum_{i=0}^{m} \theta_i \mathbf{x}_{k-i} \;=\; \mathbf{x}_k + \sum_{i=1}^{m} \theta_i \left[\mathbf{x}_{k-i} - \mathbf{x}_k\right] \qquad \text{again satisfying the constraint} \qquad \sum_{i=0}^{m} \theta_i = 1.$$

So the difference vector $\widetilde{\mathbf{x}_k} - \mathbf{x}_k$ is a combination of m previous difference vectors. Again the coefficients θ_i are determined in such a way that $\|\mathbf{r}(\widetilde{\mathbf{x}_k})\|_2$ is minimized, if $\mathbf{r}$ were linear. Again, from this condition it follows that $\|\mathbf{r}(\mathbf{x}_k) - \mathbf{R}\boldsymbol{\theta}\|_2$ must be minimized. The algorithm is as listed in Algorithm 1, with $\mathbf{g}$ simply replaced by the identity operator.

3 RESULTS

The results described in this section were obtained with the RANS code REFRESCO (www.refresco.org), a community based CFD code for the maritime world. It solves multiphase (unsteady) incompressible viscous flows using the Navier-Stokes equations, complemented with turbulence models, cavitation models and volume-fraction transport equations for different phases. The equations are discretised using a finite-volume approach with cell-centered collocated variables, in strong-conservation form. In REFRESCO, segregated methods like 'SIMPLE' or 'SIMPLER', or a coupled solver as described in

Klaij and Vuik, 2013 can be chosen as 'basic' solution methods. We will first show the results obtained for some relatively easy 2D test cases from the so-called verification Suite of REFRESCO. Next, we will show results for a more difficult 3D test case with a turbulence model.

The verification Suite consists of a set of test cases in which for each case a range of grids of different density is used to establish the order of grid convergence using the method of manufactured solutions, Eça et al., 2012. The exact solution, the 'manufactured solution' and the error are known because the right-hand side is determined by simply substituting this solution in the momentum equations and the continuity equation. For example, in case of a Taylor-vortex, the pressure $p = -\frac{1}{4}(\cos(2\pi x) + \cos(2\pi y))$ and the velocity components are $u = -\cos(\pi x)\sin(\pi y)$ and $v = \sin(\pi x)\cos(\pi y)$. In the 2D-Poiseuille test cases, the pressure $p = 8\mu(2 - x) + 1$ in which $\mu = 0.1$ and the velocity components are $u = 4y(1 - y)$ and $v = 0$. Different types of grids are used, as shown in Fig. 1. For illustration of the type of grid, this figure shows only the coarsest grids. In the numerical experiments descibed below we use strongly refined grids.

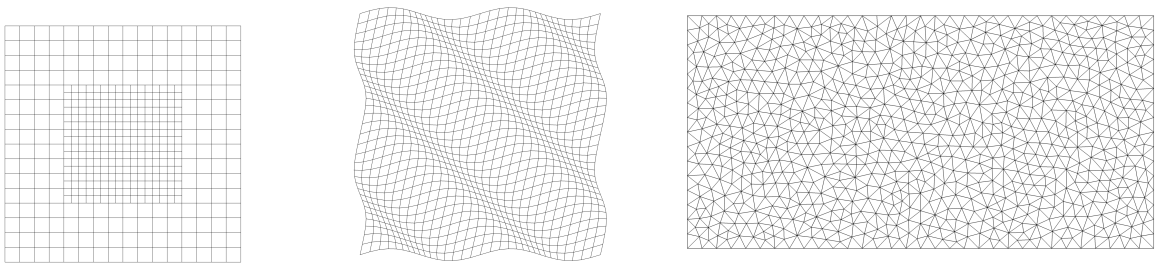

Fig. 1: Examples of grids used in the verification Suite. Left: hgrid. Middle: sgrid. Right: Delauney grid.

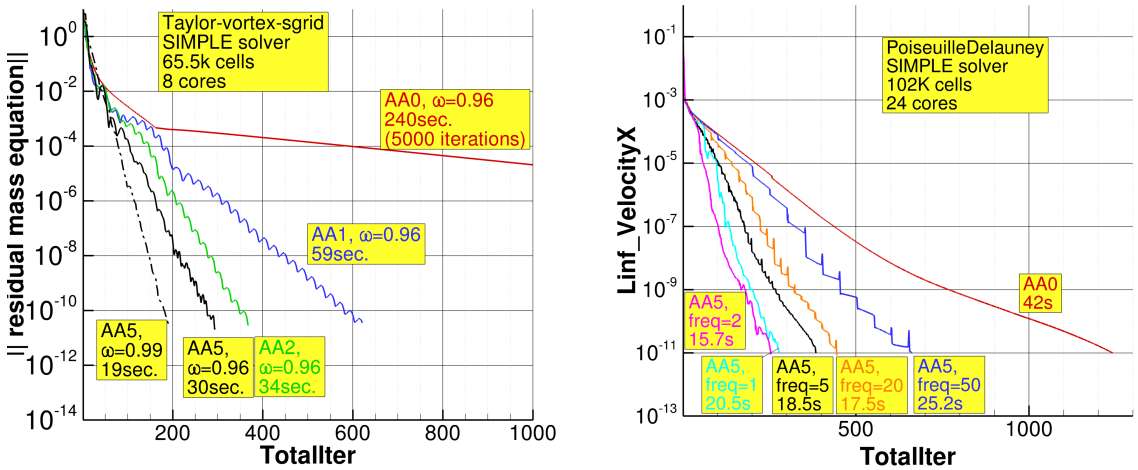

Fig. 2: Left: Effect of AA for two cases from the verification Suite. $\alpha = 1$ in both cases.

The left picture in Fig. 2 shows the results obtained on the s-grid when the manufactured solution is a Taylor-vortex. The text in the box has the same color as the corresponding line, and shows the dimension of the search space m in AAm together with the required wall clock times, using 8 cores and $freq = 1$. Relaxation parameters were determined in such a way that the solution method without AA, indicated by AA0, gives the smallest wall clock time. Anderson Acceleration gives a significant improvement of the convergence behavior and a considerable reduction in computational effort. The parameter m does not have to be chosen large, so the overhead in extra memory usage and cpu time is relatively small. The amount of implicit underrelaxation for the velocity is indicated by ω. For values of ω larger than 0.96, the computation without AA diverges. Only in combination with AA it is possible to choose $\omega = 0.99$, giving superior convergence behavior (dashed black line) and the smallest required wall clock time.

The right picture in Fig. 2 shows results obtained for a Poiseuille flow computed on a Delauney grid. Also on this type of grid Anderson Accelaration can significantly improve the convergence behavior. The wall clock times can be reduced with more the a factor of 2.5 and the choice of $freq$ is not very critical for the required wall clock time.

For the cases from the verification Suite, we obtain similar results with $\alpha = 0$ as with $\alpha = 1$. We illustrate this in Fig. 3 with the case that computes the Poiseuille flow on the hgrid. Again we see that AA strongly improves the convergence behavior and significantly reduces the required wall clock time. For this case, a five-dimensional search space seems to be a good choice. Increasing the dimension of the search space does not further improve the convergence behavior, and the required wall clock time increases due to the extra overhead.

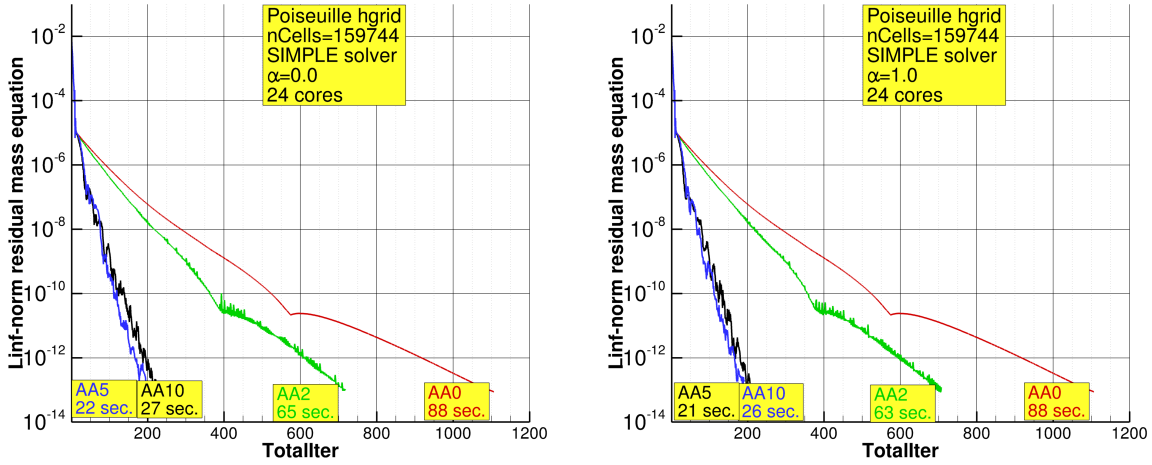

Fig. 3: Effect of α on the convergence behavior for the Poiseuille-hgrid case. Left: $\alpha = 0$. Right: $\alpha = 1$.

To illustrate the effect of AA for a 3D case with turbulence, we compute the flow around the KVLCC2 tanker with undisturbed watersurface at model-scale Reynoldsnumber 4.6E6, including the boundary layer and k-omega turbulence model. We use two grids, a structured mesh generated by Gridpro containing 0.26M cells, and an unstructured mesh with many hanging nodes generated by Hexpress containing 0.18M cells. For this application, use of Anderson Acceleration leads to divergence for all positive values of α. The effect of Anderson Acceleration on the convergence behavior with $\alpha = 0$ is shown in Fig. 4. Again the red lines show the convergence behavior without AA. With $\alpha = 0$, we obtain a reduction in wall clock time, although for this case it is not as strong as shown in the previous section for the easier, 2D test cases without turbulence. A reduction of about 40% can be achieved for the mesh generated by Gridpro, and about 30% for the one generated by Hexpress.

The green and orange lines in the right picture show that AA causes a very irregular convergence behavior at the early stage of the iteration and a severe increase of the maximum norm of the residual of the mass equation. Therefore, the blue line shows the result obtained when AA is not applied at the first 200 steps of the iteration. In that case, the use of AA gives an irregular convergence behavior between iteration number 200 and 400. About the same amount of wall clock time is required as with AA applied from the start. The reason for the irregular convergence behavior is still unknown. A possible reason is that AA is used only for the coupling between the momentum equations and the mass equation, and not for the transport equations of the turbulence model.

4 Conclusions

Anderson Acceleration (AA) can significantly speed up the solution of the systems of non-linear equations as they occur in the computation of incompressible flows. Especially for 2D problems without turbulence, the improvement in convergence rate can be spectacular and a reduction in the required wall clock time of more than one order of magnitude can be obtained. For some applications AA allows to

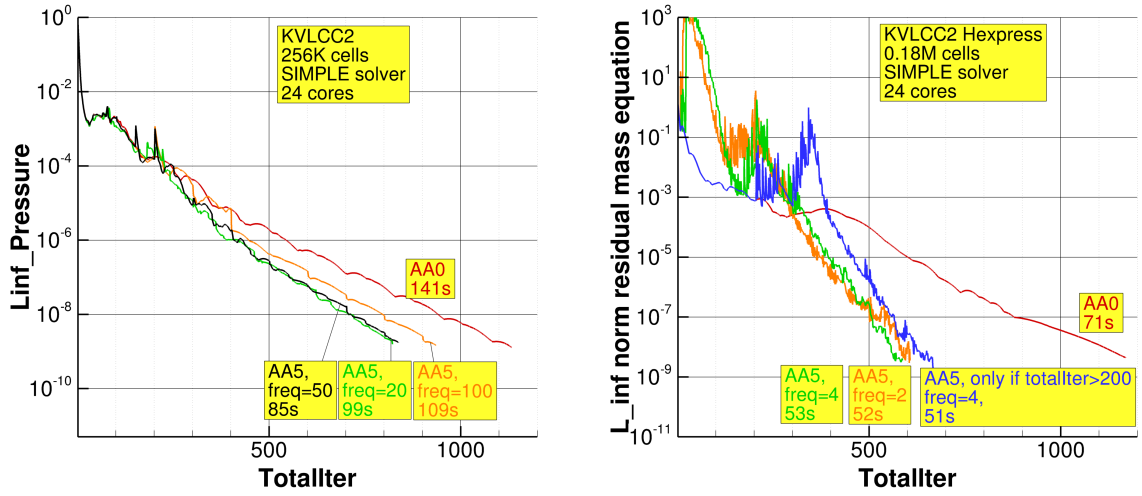

Fig. 4: Effect of AA on the computation of the flow around the KVLCC2 tanker. Left: Gridpro grid. Right: Hexpress grid. $\alpha = 0$ in both cases.

use less implicit underrelaxation, which results in a significant further reduction of the wall clock time.

For more realistic 3D test cases with turbulence, AA also can improve the convergence but the reduction of the wall clock time is not as spectacular. Typically, a reduction of 30% can be achieved when a relatively coarse mesh and up to 24 cores are used. This may be caused by the fact that in the current implementation in REFRESCO, the transport equations of the turbulence model are not yet included in the set of equations that is accelerated by the AA algorithm.

In the current implementation in the CFD-code REFRESCO, the solution of the minimization problem required by the AA algorithm has not yet been parallelized. Parallelization of this step will strongly reduce the overhead of AA. It will become mandatory for very large applications in which the required matrices will not fit in the memory of only one node.

References

Anderson, D. (1965). Iterative Procedures for Nonlinear Integral Equations. *Journal of the Association for Computing Machinery*, 12(4):547–560.

Eça, L., Hoekstra, M., and Vaz, G. (2012). On the use of Method of Manufactured Solutions for Code Verification of RANS solvers based on Eddy-viscosity Models. *ASME V&V Conference, Las Vegas, USA*.

Fang, H. and Saad, Y. (2009). Two classes of multisecant methods for nonlinear acceleration. *Numer. Linear Algebra Appl.*, 16:197–221.

Klaij, C. M. and Vuik, C. (2013). SIMPLE-type preconditioners for cell-centered, colocated finite volume discretization of incompressible Reynolds-averaged Navier-Stokes equations. *International Journal for Numerical Methods in Fluids*, 71(7):830–849.

Pollock, S., Rebholz, L., and Xiao, M. (2018). Anderson-accelerated convergence of Picard iterations for incompressible Navier-Stokes equations.

Saad, Y. and Schultz, M. (1986). A generalized minimal residual algorithm for solving nonsymmetric linear systems. *SIAM J. Sci. Comput.*, 7:856–869.

Walker, H. (2011). Anderson Acceleration: Algorithms and Implementations. Technical Report MS-6-15-50, Worcester Polytechnic Institute Mathematical Sciences Department.

Performance of turbulence closures for vortex interaction physics over military aircraft

Michel Visonneau*, Emmanuel Guilmineau*, and Ginevra Rubino*
*ECN/CNRS, LHEEA, Nantes/France
michel.visonneau@ec-nantes.fr

1 Introduction

Modern air tactics require agile maneuverability capability that includes operations at high angles of attack and sideslip. Military air vehicles routinely develop multiple, close-proximity vortices within required operating conditions. Interactions among these vortices, between the vortices and the vehicle components, and at high speeds, between the vortices and shock waves significantly affect maneuver performance, often with adverse consequences. Current capability to predict these effects with CFD is inadequate, and some aspects of the vortex-interaction flow physics are not well understood. The NATO/AVT-316 collaborative research ahs been built to assess the capability of current CFD methods to predict vortex-interaction effects, extend our understanding of vortex-interaction flow physics for these problems through numerical and physical experimentation. In the framework of this general collaborative effort, this article gives a glimpse of the current studies undertaken by the authors after one year of collaboration.

2 ISIS-CFD at a glance

The solver ISIS-CFD, available as a part of the FINE^{TM}/Marine computing suite distributed by NUMECA Int., is an incompressible unsteady Reynolds-averaged Navier-Stokes (URANS) method mainly devoted to marine hydrodynamics. The method features several sophisticated turbulence models: apart from the classical two-equation k-ϵ and k-ω models, the anisotropic two-equation Explicit Algebraic Reynolds Stress Model (EARSM), as well as Reynolds Stress Transport Models (RSTM), are available, see Deng and Visonneau (1999) and Duvigneau and Visonneau (2003), with or without rotation corrections. All models are available with wall-function or low-Reynolds near wall formulations. Hybrid RANS-LES turbulence models based on Detached Eddy Simulation (DES-SST, IDDES) are also implemented, see Guilmineau et al. (2013), and have been validated on automotive flows characterized by large separations. The solver is based on a finite volume method to build the spatial discretization of the transport equations. The second order accurate unstructured discretization is face-based. While all unknown state variables are cell-centered, the systems of equations used in the implicit time stepping procedure are constructed face by face. Pressure-velocity coupling is enforced through a Rhie & Chow SIMPLE type method. Free-surface flow is simulated with a multi-phase flow approach: the water surface is captured with a conservation equation for the volume fraction of water, discretized with specific compressive discretization schemes, see Queutey and Visonneau (2007). The technique included for the six degrees of freedom simulation of ship motion is described by Leroyer and Visonneau (2005). Many possibilities of grid management are included like morphing, sliding and overlapping grids. Finally, an anisotropic automatic grid refinement procedure has been developed which is controlled by various flow-related criteria, see Wackers et al. (2014). Parallelization is based on domain decomposition using the MPI (Message Passing Interface) protocol.

3 Description of the test case and numerical setup

Airtbus Defence and Space and the Technical University of Munich are in charge of the measurements on a model military aircraft studied in the framework of the Research Technical Group NATO/AVT-316 (Hitzel et al. (2019), Pfnür et al. (2019)). The model is shown in Figure 1. Experiments are conducted in a wind tunnel for a speed of 51.97 m/s, which leads to a Mach number of 0.15, a value for which it is still reasonable to use an incompressible flow solver. Drag, lift, sideslip forces and moments are measured at several angles of attack ranging from 4° to 40° . Up to now, 0° and 5° sideslip angles are considered. PIV measurements are also conducted at 16° and 24° angles of attack without sideslip. Sixteen cross-sections covering the wing have been chosen where the three velocity components, the longitudinal vorticity and

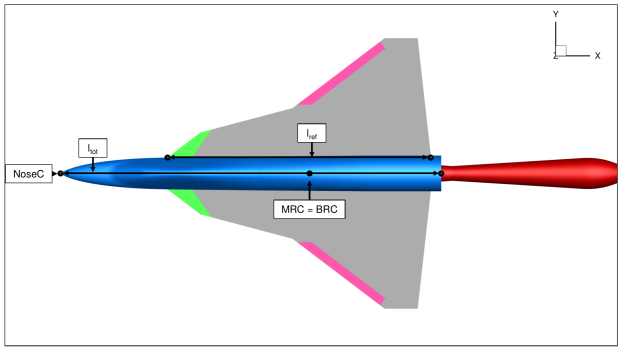

Fig. 1: Main characteristics of the model

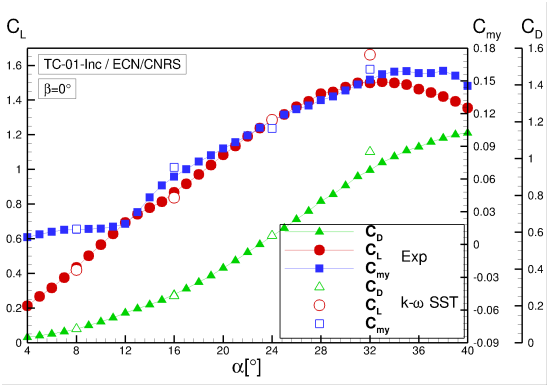

Fig. 2: $k-\omega$ SST - Drag, lift and pitching moment at various angles of attack

the turbulence kinetic energy are measured. Specific refined zones across the core of the vortices have been defined to follow the onset and progression of the various vortices present in the flow configurations of interest.

The computations performed with ISIS-CFD make an intensive use of the automatic mesh refinement procedure based on the Hessian of the flux in order to build a mesh with a controlled high density in the core of the vortices. For instance, some cross-sectional views of the adapted grids are shown in Figure 6 for various turbulence closures.

4 Global analysis at various angles of attack

Figure 2 shows a comparison between the computations of drag, lift and pitch moment and measurements. In these first computations, only the $k-\omega$ SST closure is used. The agreement is very good for almost all incidences but one can notice a degradation of the agreement for higher incidences.

Figure 3 shows the different topologies of the flow over the wing for four angles of incidence (8° , 16° , 24° and 32°). This figure provides a global view of the three-dimensional vortical structures which are created, progress and and interact along the wing. The vortices are represented as isosurfaces of the dimensionless second invariant $Q^* = 50$ and the red surface inside the vortices correspond to the region where a flow reversal is observed. All these computations are performed with $k-\omega$ SST turbulence model. At 8° , no interaction takes place between the two vortices emanating from the wing leading edge and no flow reversal is observed in the core of these vortices. At 16° , the interaction between the two main vortices is observed in the second half of the wing and is accompanied by a flow reversal in the core of the largest vortex. At 24° , a third vortex generated at the fore part of the aircraft, progresses along the fuselage and is suddenly diverted to interact with the two vortical structures already present at lower angles of attack. Flow reversal is observed earlier in the same vortex as previously. At 32° , a fourth vortex progresses close to the one which appeared at 24° . Both vortices are violently diverted away from the fuselage and interact with the aforementioned third vortex. At this angle of attack, flow reversal in the largest vortex appears very close to the leading edge. It is worthwhile to mention that once the flow reversal takes place, no coherent vortical structure can be observed. Moreover, these computations based on a linear isotropic turbulence closure ($k-\omega$ SST without any rotation correction) do not necessarily reflect the true physics of these flows, especially at high angles of attack as indicated, at least, by the degraded agreement with measured forces and moment.

5 Angle of attack 16°

In order to understand the reasons of the deteriorated agreement between measured and computed forces and pitching moment at high angle of attack, it is necessary to proceed to a local analysis of the flow and try to relate global data to local flow characteristics. Since the automatic grid refinement is used, one can consider that the discretisation error is kept unrelatively low in the vortices and their neighborhood. However, nothing is known on the modelling error associated with the turbulence closure. This is the

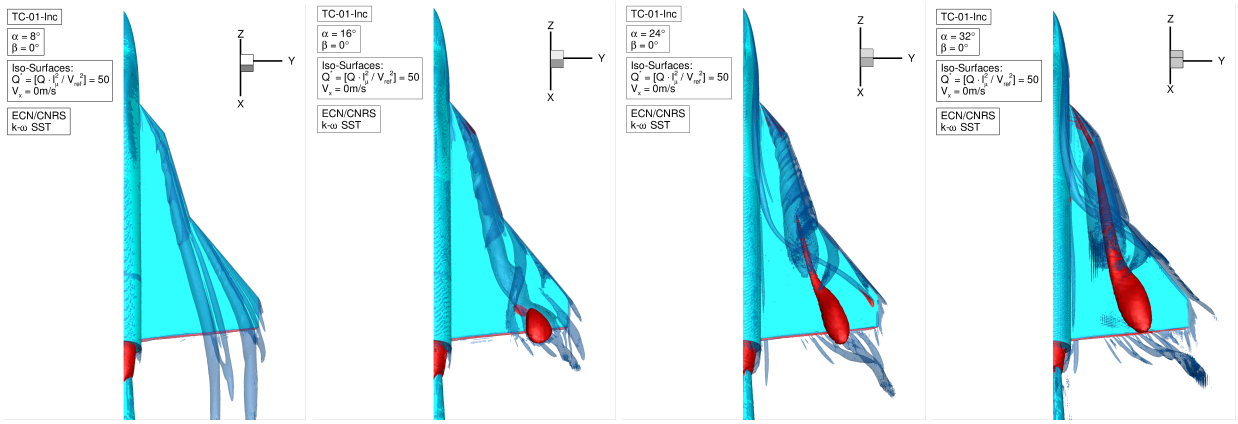

(a) 8° (b) 16° (c) 24° (d) 32°

Fig. 3: $k-\omega$ SST - Main vortical structures at various angles of attack

reason why it has been decided to perform a systematic study of turbulence closures at a selected angle of attack of 16° for which PIV experiments were available. Our objective is to assess/compare the performances of various turbulence closures and make some recommendations. In this study, three models are studied, ranging from the linear isotropic $k-\omega$ SST model Menter (1994), an explicit anisotropic Reynolds stress closures built by the authors in the late 90's Deng and Visonneau (1999) and a recent Reynolds Stress Transport model Cecora et al. (2015). First of all, Table 1 shows a comparison between measured and computed forces and moments for these three turbulence models encompassing most of the available RANS modeling strategies. In this table, S stands for simulation, D for experimental data and $E = S - D[\%D]$ provides the percentage of error with the measured data. One can notice that the best prediction of forces and moment is provided by the RSTM model while the EARSM model developed by ECN/CNRS behaves very well for the forces but is less accurate on the prediction of the pitching moment. The number of cells reached once the adaptive grid process has converged is 36.5M for $k-\omega$ SST, 51.5M for EARSM and 124.6M for SSGLRR RSTM turbulence models over a half-aircraft. Figure 4 shows the three-dimensional vortices represented by Q^*=50 and the location of the flow reversal in the core of vortices for an angle of attack of 16° while Figure 5 shows the wall pressure distribution and the skin-friction lines. The interaction between vortices takes place almost at the same location, independently of the turbulence closures. However, the vortices predicted by SSGLRR are more intense and less diffused. We can observe the influence of the vortex interaction on the shape of the skin friction lines on $k-\omega$ SST and RSTM results but not on the EARSM prediction. RSTM results exhibit a more pronounced convergence, associated with a more intense open separation. Figure 4 shows that flow reversal occurs near the trailing edge with $k-\omega$ SST while no reverse flow is visible with the anisotropic turbulence models. Figure 6 shows the meshes in a cross-section $x/Cr = 0.592$ obtained once the adaptive mesh refinement procedure has converged. The locations and regions of high shear of both vortices of interest are clearly visible on the meshes, which illustrate the remarkable efficiency of such a methodology. For the SSGLRR RSTM model, the adaptive mesh refinement leads to a very dense concentration of points

Table 1: AoA 16° - Forces and moment

α=16°	C_D		C_L		C_{my}	
β=0°	S	E	S	E	S	E
Experiments (D)	0.2620		0.8580		0.0622	
k-ω SST	0.2553	-2.55%	0.8372	-3.59%	0.0707	13.71%
EARSM	0.2627	0.25%	0.8674	-0.11%	0.0524	-15.66%
SSGLRR-ω	0.2639	0.70%	0.8612	-0.82%	0.0651	4.78%

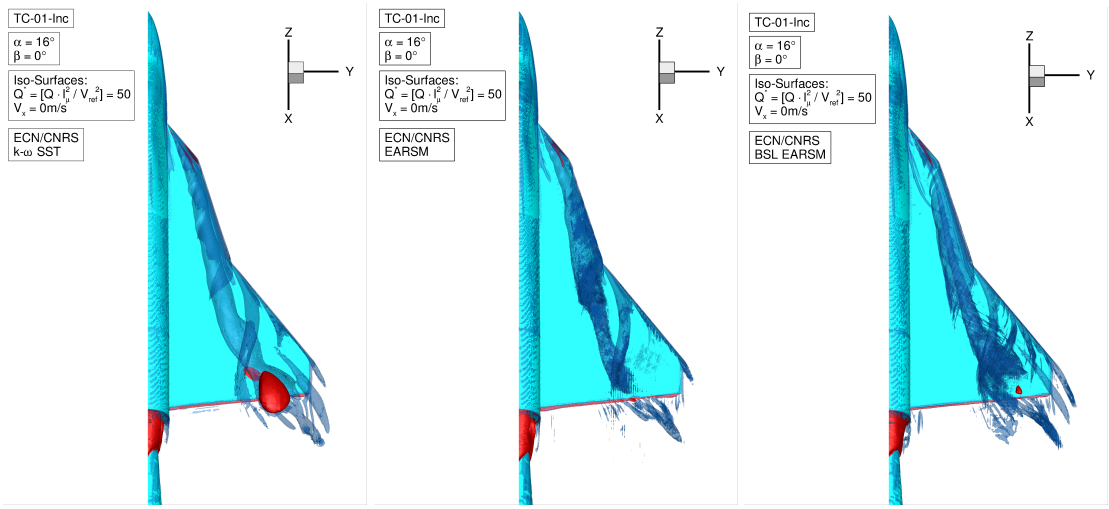

(a) k-ω SST (b) EARSM (c) SSGLRR-ω

Fig. 4: AoA 16° - Influence of the turbulence closure on the main vortical structures characteristics

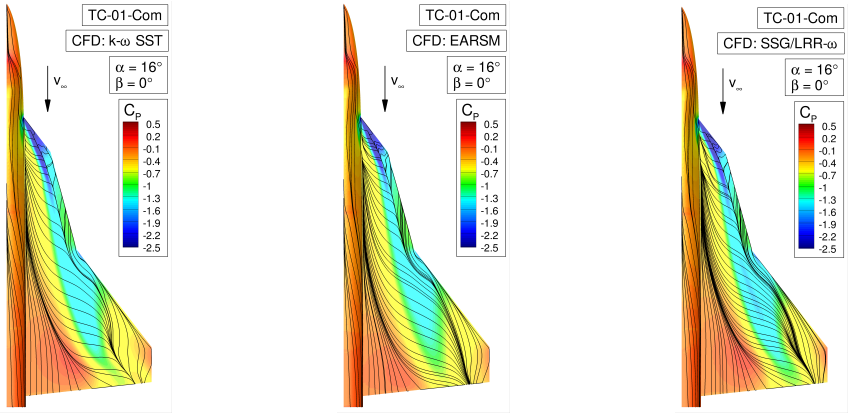

(a) k-ω SST (b) EARSM (c) SSGLRR-ω

Fig. 5: AoA 16° - Influence of the turbulence closure on the wall pressure distribution and friction lines

in the core of the vortices for unclear reasons at the time of writing this paper. Figure 7 to Figure 9 show at the same location, the cross-sectional distributions of U, ω_x, and tke obtained with the same turbulence closures to be compared with TUM PIV measurements. The best overall distribution of U contours is obtained with the SSGLRR RSTM model although the low value of the velocity (blue region) in the core of the first vortex is not captured. EARSM appears to behave better from that standpoint but the size of the region where U is low appears to be overestimated in comparison with measurements. Moreover, the higher velocity region above the previous region, is not captured by EARSM while it is correctly simulated by SSGLRR and to a lesser extent by k-ω SST. Figure 8 shows the cross-sectional distribution of ω_x. It is clear that the magnitude of the longitudinal vorticity is under-estimated by the linear isotropic $k-\omega$ SST model, which is not surprising. On the other hand, SSGLRR RSTM provides a higher longitudinal vorticity in good agreement with the experiments for the second vortex but slightly over-estimated for the first vortex. EARSM seems to behave relatively well as long as one can judge from this global picture. Finally, Figure 9 shows the cross-sectional distribution of the turbulence kinetic energy, tke. This is a very important data to assess the physical consistency of a turbulence model in the core of vortices since it is difficult to get a correct agreement both on the longitudinal vorticity and tke. Very often, the rotation corrections aiming at increasing the longitudinal vorticity cause a local decay of tke in the core of the vortex which is not necessarily in agreement with the measurements (see Visonneau et al. (2018)

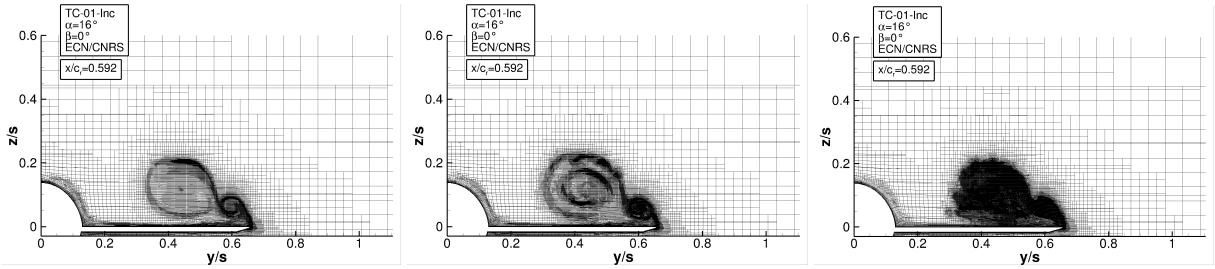

(a) k-ω SST (b) EARSM (c) SSGLRR-ω

Fig. 6: AoA 16° - Local mesh density at $x/c_r = 0.592$

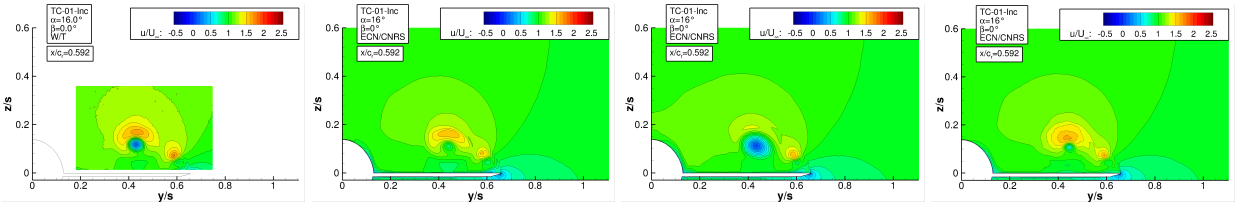

(a) Experiments (b) k-ω SST (c) EARSM (d) SSGLRR-ω

Fig. 7: AoA 16° - Axial velocity at $x/c_r = 0.592$

for an extensive computational study of the local core flow physics of a vortex emanating from the sonar dome of a US Navy frigate at static drift). Although the preliminary TUM measurements of tke should be considered with care, one can observe that the core with a significant tke region is smaller in the experiments than in the simulations. $k-\omega$ SST predicted tke distribution is very homegeneous with a minimum in the core of the vortex, which is not in agreement with TUM measurements. Both EARSM and RSTM predict a higher value of tke in the core of both vortices, with a significantly higher local value for SSGLRR RSTM. Globally, this distribution complies better with the measurements, although the local value of tke appears to be significantly over-estimated. At this stage, it is difficult to go further in the analysis since TUM has to check if the measured tke distribution takes into account enough small flow scales to be considered accurate enough for a detailed turbulence closure assessment. However, it should be mentioned that, contrary to what is observed for U and ω_x in the core of a vortex, tke is a quantity for which very large differences can be observed between different categories of turbulence closures.

6 Conclusion

The flow over a military aircraft at high incidence is very complex and characterized by vortex interaction even if at 16° , the interaction is relatively weak. The preliminary results presented here illustrate a very first attempt to compare several turbulence models on meshes for which the discretization error should not play a prominent role. It leads us to realize how difficult it is to simulate accurately the vortex core flow physics. The onset and progression of vortices appear to be strongly dependent on the turbulence model. Although the most sophisticated turbulence model based on Reynolds Stress Transport Equations appear to provide the most intense vortices, no turbulence model is able to provide a satisfactory agreement on all the experimental data of interest in the core of vortices. A more complete analysis of the flows and additional computations based on hybrid RANS/LES will be presented during the symposium.

Acknowledgements

The computations were performed using HPC resources from GENCI (Grand Equipement National de Calcul Intensif) (Grant-A0042A00129, Grant-A0062A00129), which is gratefully acknowledged. The experimental data were provided in the framework of the NATO-STO task group AVT-316 by Airbus

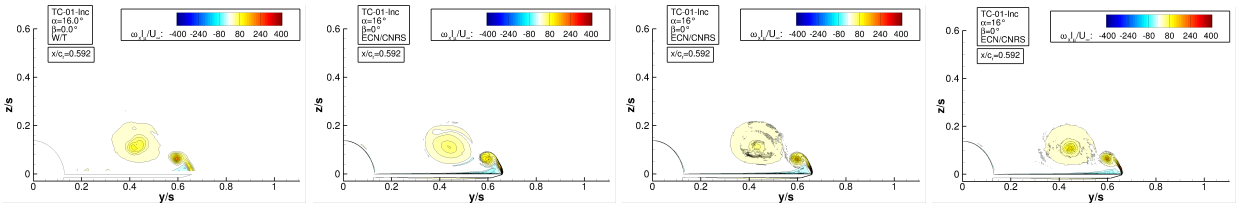

(a) Experiments (b) k-ω SST (c) EARSM (d) SSGLRR-ω

Fig. 8: AoA 16° - Axial vorticity at $x/c_r = 0.592$

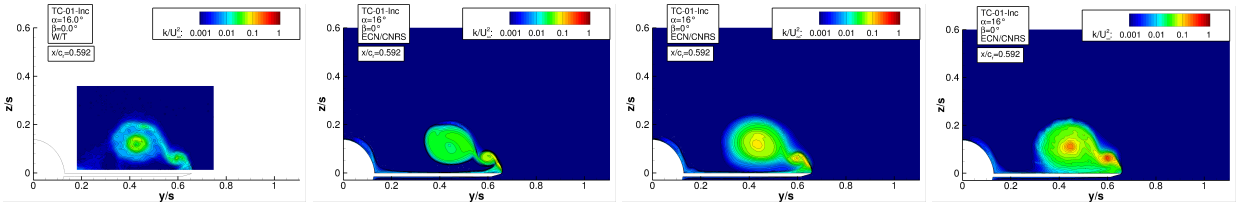

(a) Experiments (b) k-ω SST (c) EARSM (d) SSGLRR-ω

Fig. 9: AoA 16° - Turbulence kinetic energy at $x/c_r = 0.592$

Defence and Space (Aerodynamic Design, TEAGA-TL6) and the University of Munich (Chair of Aerodynamics, (TUM-AER)).

References

G. Deng and M. Visonneau (1999). Comparison of Explicit Algebraic Stress Models and Second-Order Turbulence Closures for Steady Flows around Ships. *Proc. 7th Int. Conf. on Numerical Ship Hydrodynamics*, Nantes, France.

R. Duvigneau and M. Visonneau (2003). On the Role Played by Turbulence Closures in Hull Shape Optimization at Model and Full Scale. *J. Mar. Sci. Technol.*, **8**, 11–25.

E. Guilmineau, O. Chikhaoui, G. Deng and M. Visonneau (2013). Cross Wind Effects on a Simplified Car Model by a DES Approach. *Computers & Fluids*, **78**, 2013, 29–40.

A. Leroyer, and M. Visonneau (2005). Numerical Methods for RANSE Simulations of a Self-Propelled Fish-like Body. *J. Fluid & Structures*, **30-3**, 975–991.

P. Queutey, and M. Visonneau (2007). An Interface Capturing Method for Free-Surface Hydrodynamic Flows. *Computers & Fluids*, **36**, 1481–1510.

J. Wackers, G. Deng, E. Guilmineau, A. Leroyer, P. Queutey, and M. Visonneau (2014). Combined Refinement Criteria for Anisotropic Grid Refinement in Free-Surface Flow Simulation. *Computers & Fluids*, **92**, 209–222.

F. Menter (1994). Two-equation eddy-viscosity turbulence models for engineering applications. *AIAA Journal*, **32-8**, 1598–1605.

R.-D. Cecora, R. Radespiel, B. Eisfeld, B. and A. Probst (2015). Differential Reynolds-Stress Modeling for Aeronautics. *AIAA Journal*, **53-3**, 739–755.

S. Pfnür, C. Breitsamter (2019). Leading-Edge Vortex Interactions at a Generic Multiple Swept-Wing Aircraft Configuration. *Journal of Aircraft (Review number: C035491)*, accepted for publication.

S.M. Hitzel, A. Winkler, A. Hövelmann (2019). Vortex Flow Aerodynamic Challenges in the Design Space for Future Fighter Aircraft. To appear in *New Results in Numerical and Experimental Fluid Mechanics XII*, published by Springer.

M. Visonneau, E. Guilmineau and G. Rubino (2018). Computational Analysis of the Flow around a Surface Combatant at 10° Static Drift and Dynamic Sway Conditions. *Proc. 32nd Symposium on Naval Hydrodynamics*, Hamburg, Germany.

Numerical analysis of the container vessel's self-propulsion at different rudder deflection angles

Michał Wawrzusiszyn[a], Radosław Kołodziej[a, b], Sebastian Bielicki[a]

[a] *Ship Design & Research Centre, CTO S.A, 80-392 Gdańsk, Szczecińska 65, Poland*
[b] *Gdansk University of Technology, 80-233 Gdańsk, Narutowicza 11/12, Poland*
Michal.Wawrzusiszyn@cto.gda.pl, Radoslaw.Kolodziej@cto.gda.pl, Sebastian.Bielicki@cto.gda.pl

1. Introduction

Nowadays, CFD becomes one of the most commonly used research method in ship hydrodynamics, limited to the analyses of hull resistance in calm water. With continuously improving computing power and increasingly more accurate numerical methods it is possible to simulate more complex cases. State of the art CFD tools also enable development of new ways of assessing ship maneuvering performance. This paper presents an attempt on using CFD for evaluation of the coefficients used in the formulation of rudder forces applied in the ship manoeuvring model. These coefficient are normally evaluated in captive tests of the hull with working propeller and rudder deflected at different angles; the paper presents the results of CFD simulation of this kind of experiment. The test case used in the analyses is the well known the KRISO Container Ship (KCS). The computations were carried out at model scale 1:50, for which the reference model test results are available. Comparison of CFD and experimental results is presented.

2. Mathematical model

There are many approaches to decomposition of forces acting on the ship during manoeuvring described in literature. According to MMG standard method [1] they can be presented as sum of following components:

$$X = X_H + X_P + X_R \quad (1)$$
$$Y = Y_H + Y_R \quad (2)$$
$$N = N_H + N_R \quad (3)$$

where:
X, Y, N - Surge force, lateral force, yaw moment
X_H, Y_H, N_H - Surge force, lateral force, yaw moment acting on the hull
X_R, Y_R, N_R - Surge force, lateral force, yaw moment acting on rudder
X_P - Surge force generated by the propeller

Effective rudder forces and moment are expressed as:

$$X_R = -(1 - t_R)F_N \sin\delta \quad (4)$$
$$Y_R = -(1 + a_H)F_N \cos\delta \quad (5)$$
$$N_R = -(x_R + a_H x_H)F_N \cos\delta \quad (6)$$

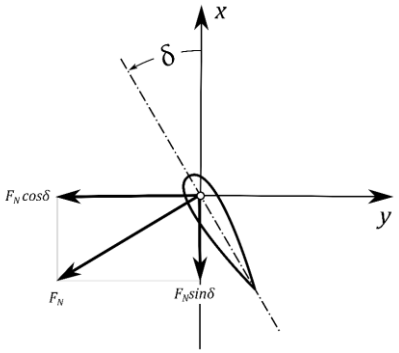

Fig. 1: Coordinate system

where:
F_N - Rudder normal force
t_R - Steering resistance deduction factor
a_H - Rudder force increase factor
x_H - Longitudinal coordinate of point of application
x_R - Longitudinal coordinate of rudder position (~$0.5L_{PP}$)

Mathematical model of maneuvering ship includes certain parameters that are unknown at initial design stage (a_H, x_H and t_R) thus they can be evaluated only by the means of model tests or numerical analyses. The evaluation consists in analysis of forces acting on hull and rudder in vessel moving straight ahead with rudder deflected at certain angles and constant speed, when forces Y_H and N_H on right hand sides of equations (2) and (3) are equal to zero. Forces X_H+X_P are assumed to be constant for considered propeller rate of revolution and vessel speed (constant propeller advance ratio).

3. CFD Simulation

The computations were carried out at model scale 1:50 using the Reynolds Averaged Navier-Stokes Equations (RANSE) method. The CFD method applied is based on previous publications for NuTTS conferences [2][3]. Meshing and flow simulations were conducted with use of Star CCM+ 2019.1. Analyses were done with the use of the Estimating Hull Performance (EHP) module.
As turbulence model the Realizable K-Epsilon (two-layer all-y+ wall treatment) was used. The mean value of y+ on the hull was about 3.2 and below 1.0 in rudder/propeller region. Main particulars of the hull and propeller are presented below.

Fig. 3: Propeller CP572

Propeller CP572	**Value**
Diameter [m]	0.160
Pitch ratio [-]	1.240
Hub ratio [-]	0.333
Expanded area ratio [-]	0.640
Direction of rotation	Left

Main hull particulars	**Unit**	**Value**
Model scale	[-]	1:50
Length b.p.	m	4.600
Length of waterline	m	4.649
Breadth	m	0.644
Draught	m	0.216
Displacement volume	m^3	0.416
Surface wetted area	m^2	3.781
Block coefficient	[-]	0.651
Midship section coefficient	[-]	0.985

Configuration for propulsion analyses is presented in Fig. 4. The flow was computed in the rectangular domain of the following dimensions: [6L; 5L; 2.5L], where L is the hull length. Analyses were divided into three parts:

- Mesh sensitivity study;
- Bare hull computations;
- Appended hull computations with working propeller.

Mesh sensitivity study with bare hull (half domain) was done. The size of mesh was analysed against influence on resistance value. Taking into account almost constant value of resistance for meshes 3, 4 and 5, mesh No. 3 was used for further computations as the optimal compromise providing the mesh-independend solution (see the table below).

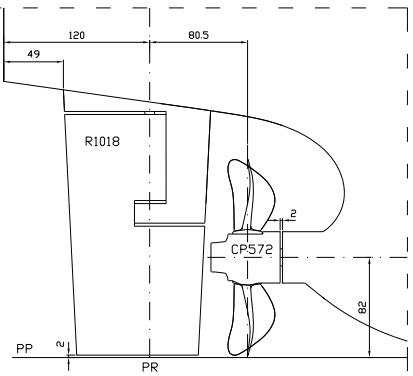

Fig. 4: Propulsion arrangement

No.	**Mesh size [Num. of cells]**	**y+**	**Size of base element [m]**	**Resistance [N]**	**Relative resistance [%]**
1	1 840 000	9.65	1.000	11.226	94.45
2	2 410 000	5.64	0.095	11.310	94.57
3	**3 330 000**	**3.27**	**0.085**	**11.996**	**100.30**
4	4 510 000	3.25	0.750	11.992	100.27
5	7 960 000	2.82	0.600	11.960	100.00

During analyses with propeller the hull was fixed to reduce computation time. The free surface was modelled. Values of hull trim (0.078°) and sinkage (-0.0046m) for propulsion analyses were determined from resistance computations.

Total mesh size for analyses with working propeller was about 8 000 000 cells (see Fig. 5). Seven rudder angels were analysed: 0^0; $\pm10^0$; $\pm20^0$; $\pm35^0$.
For resistance and propulsion computations a constant inlet velocity was set to 1.31m/s. Water density was set to 998.540kg/m^3 and dynamic viscosity was set to 1.0122×10^{-3} Pa-s.

The time step value was changed during computations:
t_s=0.030s – for development of a free surface and resistance stabilisation
t_s=0.001s – when propeller was rotated by 2.94^0 per one time step.

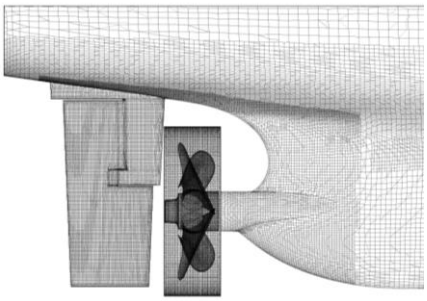

Fig. 5: Mesh presentation

Designed pitch ratio set on propeller geometry was $P/D_{0.7}$=1.24 while in experiment $P/D_{0.7}$=0.80. The constant propeller revolutions n=8.165 [RPS] were set according to propeller thrust value T_P=13.0[N] from model test results, where rudder was not deflected. Simulation of propeller rotation in the domain was solved by using sliding mesh.
Global forces in *i* and *j* direction on rudder and hull were monitored. Moment acting on the entire ship model (rudder, propeller and hull) was measured relative to z-axis located in hull LCB (x=2.23m).

4. Results of CFD analyses

Detailed results of computations are presented in below table and in Figs. 6-7.

Rudder angle δ [deg]	Propeller thrust T_P [N]	Hull resistance R_H [N]	Force X_{FN} [N]	Force Y_{FN} [N]	Force F_N [N]	Force X [N]	Force Y [N]	Moment N [Nm]	U_{Rmean} In front of rudder [m/s]
-35.0	14.54	24.60	-9.62	13.24	-16.36	-10.40	15.85	-34.35	1.289
-20.0	13.37	19.22	-3.95	13.45	-13.99	-6.16	16.15	-35.15	1.336
-10.0	13.05	16.81	-1.47	7.27	-7.41	-4.08	9.20	-19.64	1.351
0.0	13.17	16.12	-0.59	-0.19	0.19	-3.29	0.09	-0.26	1.362
10.0	13.13	16.75	-1.17	-7.59	7.68	-3.96	-9.17	19.48	1.357
20.0	13.55	19.08	-3.50	-13.26	13.66	-5.85	-15.75	33.70	1.344
35.0	14.48	24.06	-8.77	-18.37	20.08	-9.88	-21.68	46.58	1.306

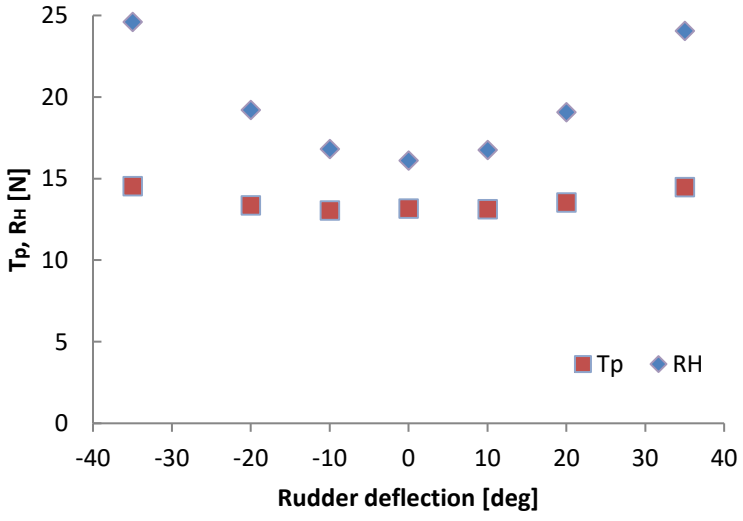

Fig. 6: Thrust and hull resistance comparison for different rudder angles

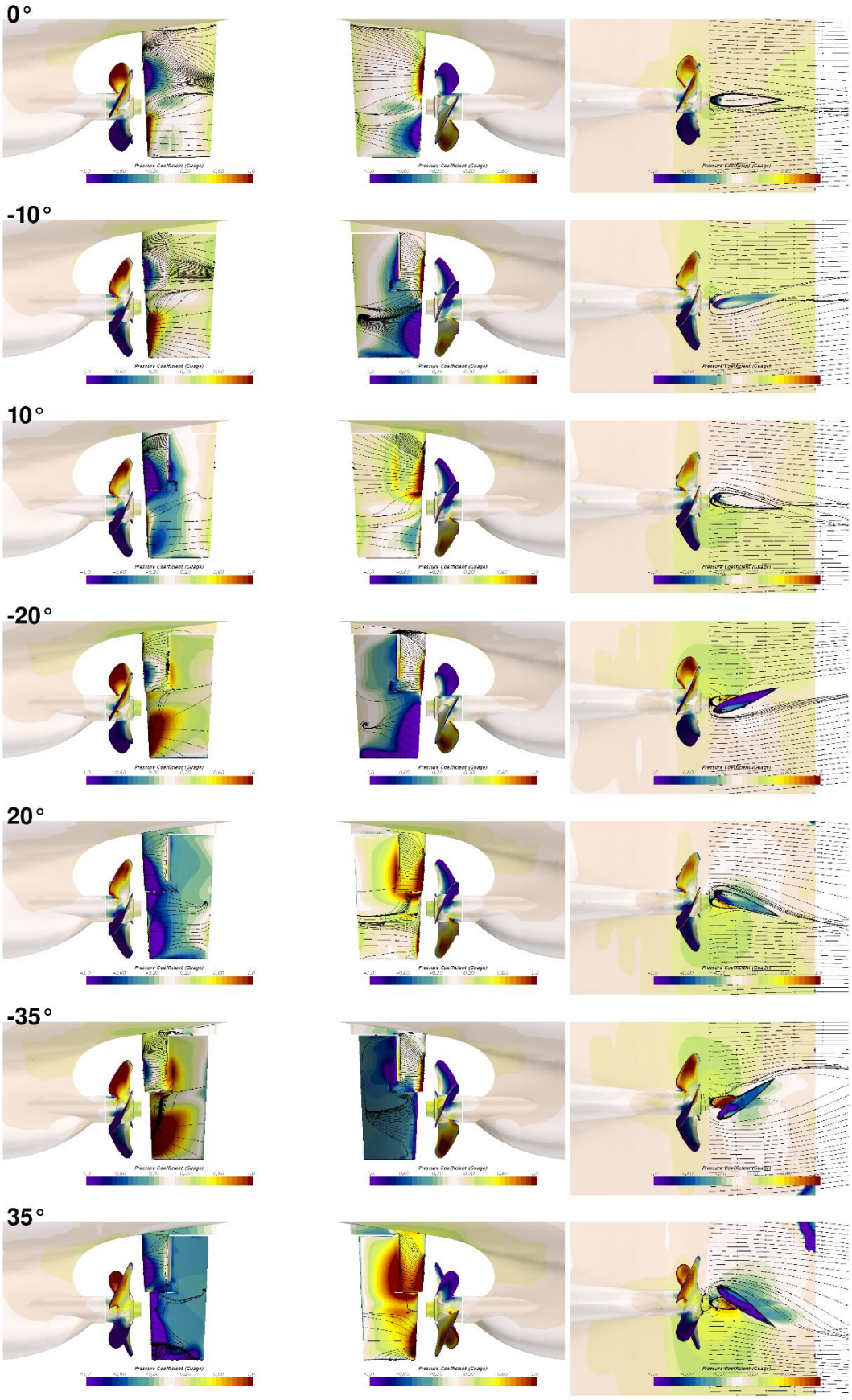

Fig. 7: Comparison of flow and pressure distribution for different rudder angles (left column port side, middle – starboard, right – top view)

During the resistance computations of bare hull the water velocity at propeller disc and rudder position was measured. The mean values were then used to calculate the wake fraction coefficients of propeller w_{P0} and rudder w_{R0} as presented below.

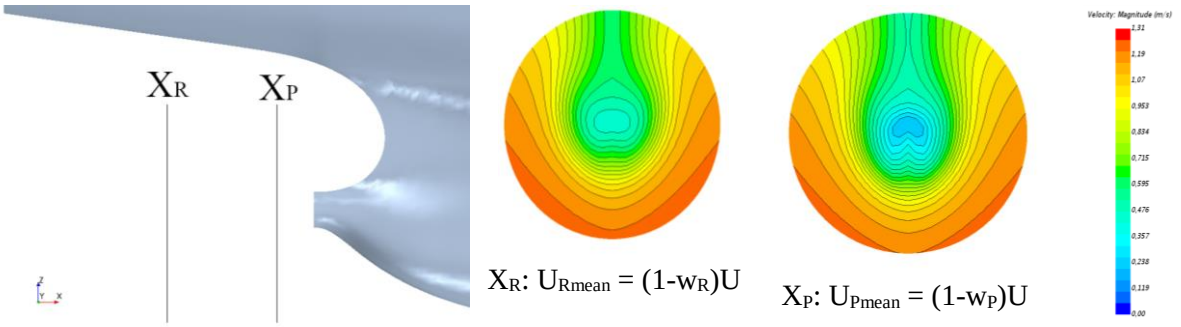

Fig. 8: Wake fraction coefficients

U_{Pmean} in propeller disc [m/s]	U_{Rmean} in front of rudder [m/s]	U [m/s]	w_{P0} propeller wake fraction coeff. [m/s]	w_{R0} rudder wake fraction coeff. [m/s]
0.893	0.954	1.309	0.271	0.319

In order to determine the hydrodynamic coefficients of rudder (t_R, a_H and x_H), forces acting on a hull X_H+X_P, Y_H and moment N_H can be expressed as a function of $F_N\sin\delta$ and $F_N\cos\delta$ [4]. It turns out that their relationship is almost linear for given propeller load, therefore derivatives can be approximated as a constant value (Fig. 8).

The results for -35º rudder deflection were substantially different from other results. It seems it is the consequence of the flow separation. Therefore the data for this particular rudder angle, were not taken into consideration during rudder coefficients calculation.

t_R	a_H	x_H	x_R
0.426	0.262	-0.346	-0.500

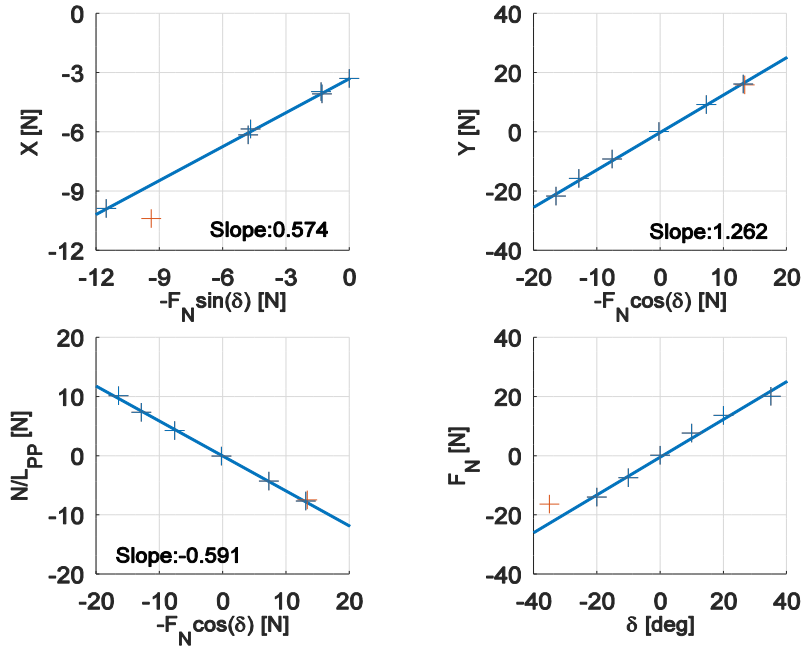

Fig. 8: Rudder coefficients approximation (red cross – points excluded from analyses)

5. Conclusions

- Considerable difference between water flow in rudder section for portside and starboard can be noticed.
- The coefficients resulting from CFD vary substantially from the experimental values. The difference may arise from neglecting in the experiment the force component generated on the rudder horn. Despite the simulations of turning test based on CFD and experimental coefficients show that the sensitivity of the model to the values of these coefficients is rather small the influence of rudder horn forces will be analysed to enhance the approach.

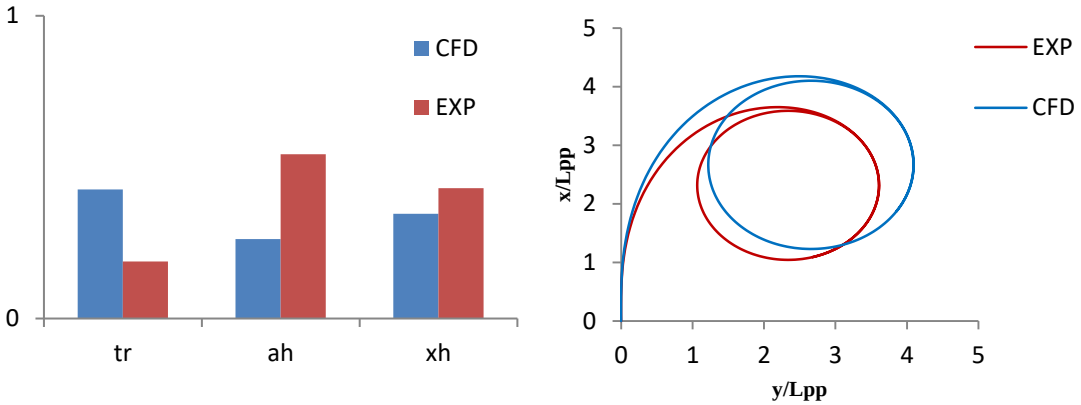

Fig. 9: Comparison of CFD and experimental results (left) and the results of turning simulation based on CFD and experimental input.

6. References

1. Yasukawa Y.Y.H., "*Introduction of MMG standard method for ship maneuvering*", Technol, 2015
2. Wawrzusiszyn M., Kraskowski M., Król P., Bugalski T., (2018). "Experimental and numerical hydrodynamic analysis of propulsion factors on R/V Nawigator XXI with pre-swirl stator device", 21st Numerical Towing Tank Symposium
3. Wawrzusiszyn M., Bugalski T., Hoffmann P., (2015). "Numerical simulations of ship hull-propeller interaction phenomena", 18th Numerical Towing Tank Symposium
4. Bielicki S.: Opracowanie matematycznego manewrowania statku na fali. Część1: identyfikacja charakterystyk kadłuba i opracowanie modelu matematycznego ruchu statku na wodzie spokojnej, Technical Report No. RH-2018/T-104, Gdańsk, December 2018

Numerical and experimental study on the Duisburg Propeller Test Case

Chiara Wielgosz[*,†], **Rafael Golf**[*], **Artur K. Lidtke**[‡], **Guilherme Vaz**[*,‡,§] **and Ould el Moctar**[*]
[*]ISMT, University of Duisburg-Essen, Duisburg/Germany, [†]MARIN Academy, Wageningen/The Netherlands, ‡MARIN, Wageningen/The Netherlands, §WavEC-Offshore Renewables, Lisbon/Portugal
chiara.wielgosz@uni-due.de

1 Introduction

Understanding of cavitation behaviour on marine propellers is of critical importance to ship designers as it dictates several of the operating limits of the propulsor due to onset of increased erosion risk or unacceptable levels of noise and vibration. Consequently, this topic continues to inspire experimental studies aimed at providing a more in-depth understanding of the physical phenomena involved, but also to provide means of validation for numerical models. Unfortunately, many of these studies do not cover the complete spectrum of types of cavitating flows seen in practice on modern ship propellers and do not present uncertainties of the experimental data. Present work aims to address these issues by reporting on a new series of quantitative and qualitative model-scale propeller tests on the Duisburg Propeller Test Case (DPTC). The experimental data is then used to validate Computational Fluid Dynamics (CFD) predictions of open water performance and cavitation patterns and a verification and validation study is carried out.

2 Experimental methodology

The experiments were carried out at the Institute of Marine Technology, Maritime Engineering and Transport Systems (ISMT) in the 'Kavitationstunnel K23'.The tunnel working section has a cross section of 0.3 m x 0.3 m. The propeller is connected to a J19 Kempf & Remmers dynamometer mounted at the end of the rotating shaft. This measuring unit is capable of recording thrust, torque and rotational speed of the propeller; to measure the pressure inside the tunnel, a pressure sensor, positioned at the upstream end of the test section, was used. Velocities were calculated from the recorded value of pressure difference between two sections upstream of the working section. The propeller is the P1570 model of SVA (Report 3733), designed to be representative of those used on contemporary vessels, which was also used on the container ship of the Duisburg Test Case project, el Moctar et al. (2012). The general characteristics and schematic representation of the propeller can be found in Figure 1 and Table 1. Additional details about the experimental study are reported by Golf (2018).

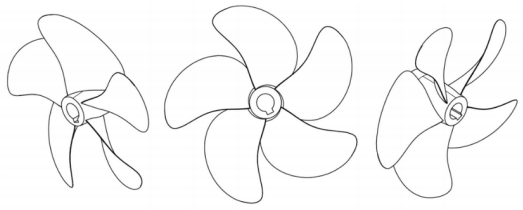

Fig. 1: Schematic representation of the P1570 SVA propeller (Report 3733), (Golf , 2018)

Table 1: Characteristics of the SVA P1570 propeller (Report 3733).

Parameter	Value	Unit
Diameter	0.150	[m]
Chord length at r/R=0.7	0.054	[m]
Effective skew angle	31.970	[deg]
Pitch/Diameter ratio at r/R=0.7	0.800	[-]
Effective area/Disk area ratio	0.800	[-]

2.1 Open water tests

The model was tested in open water inside the cavitation tunnel in wetted conditions over a range of advance coefficients $J = V_A/nD$ (where V_A is the inlet speed, n the propeller rotation rate, and D its diameter) and the open water characteristics were recorded for five different rotational speeds: 720, 1080, 1500, 2000 and 2500 RPM, with corresponding inlet velocities adjusted to maintain a constant advance ratio J range. The highest Reynolds number value for 2000 RPM at the tip of the blades is $Re(R) = 8.18 \cdot 10^5$ (where $Re(R) = R \cdot v_{ref}/\nu$ being R the propeller's radius, $v_{ref} = \sqrt{({V_A}^2 + (2\pi n 0.7R)^2)}$ the relative velocity and ν the kinematic viscosity of water) showing that the flow has a transitional nature. Tests without the propeller installed on the shaft were run for the highest inlet velocity of each

measurement series to record thrust and torque corrections. For what concerns the calculation of the uncertainties, measurements for inlet velocity, rotational speed, thrust T and torque Q were logged every 10 seconds over a 1 minute span for three velocities (low, medium, high) of the open water diagram. Following the measurements, the average of the standard deviation was computed and the uncertainties were assessed through the 'Gaussian error propagation law' (Dinter , 2011) to obtain uncertainties for the thrust coefficient $K_T = T/\rho n^2 D^4$ (with ρ density of water), the torque coefficient $10K_Q = 10Q/\rho n^2 D^5$, the open water efficiency $\eta_O = JK_T/2\pi K_Q$ and the advance ratio J, rare values found in experimental studies. It was observed that lower rotational speed tests were less credible due to the high impact of the velocity uncertainty on the actual measured values of interest.

2.2 Cavitation tests

A systematic cavitation inception study was performed by varying the inlet velocity and the static pressure p_∞ to determine the operational regions where the different cavitation topology could be observed. The rotational speed was kept constant at 2000 RPM. The cavitation structures that have been observed were: hub vortex, single bubble, tip vortex, sheet cavitation, cloud cavitation, pressure side cavitation and supercavitation. In addition, at the advance ratio $J = 0.60$, a study on the reduction of thrust and torque due to the presence of cavitation was carried out. In this case, measurements without the propeller installed on the shaft reported thrust corrections for each pressure step but no torque corrections.

3 Numerical methodology

Simulations were performed using the Computational Fluid Dynamics code ReFRESCO version 2.5.0 (www.refresco.org), developed by MARIN in collaboration with several universities. The code is based on the finite volume, face-based approach, with the flow variables collocated at the cell centers and the equations coupled via a segregated SIMPLE-type algorithm. The wetted and cavitating flow conditions were simulated by solving the RANS equations with the $k - \sqrt{k}L$ model for turbulence by Menter et al. (2006). This has been reported to produce less eddy viscosity than the more commonly used $k - \omega$ SST model, for instance, providing improved convergence (Rijpkema et al. (2015)) and better modelling of cavitation dynamics. Eddy viscosity and turbulence intensity were set at the inlet to reproduce a turbulence intensity of 3%, as observed during the experiments. The convective fluxes were discretised using the second order LIMITED QUICK scheme for the momentum equations and a first order upwind scheme for the turbulence equation. To compute the open water wetted flow propeller performance, steady simulations were performed by using the Absolute Frame of Motion (AFM) approach, where the governing equations are solved with respect to the body-fixed reference system and the flow variables are expressed with respect to the earth-fixed reference system. Cavitation was modelled using a homogeneous mixture-based approach, the source term in the transport equation was based on Sauer and Schnerr (2001) model chosen due to the more realistic results as seen in Vaz et al. (2015), and the equation was discretized with a first order upwind scheme. The cavitating flow simulations were unsteady and the temporal discretisation was obtained by applying a second order implicit three-time-level scheme. Data of the water temperature during the experiments were not methodically registered and standard water properties, computed based on the average temperature recorded during the tests, were used in the simulations.

The numerical domain consisted of two cylindrical sub-domains: an 'internal' one containing the rotating propeller and hub, and an 'external' one representing the cavitation tunnel and containing the non-rotating part of the shaft. The stator domain extended 5 propeller diameters upstream and 10 downstream to reproduce the open water condition avoiding effects of the boundaries, and had a radius of 1.13 diameter to achieve a cross-section area equivalent to the one of the cavitation tunnel in order for the blockage effects present in the experiments to be accounted for. Fixed velocity and turbulent quantities were prescribed at the inlet, while fixed pressure was specified on the part of the outlet extending outside of the propeller slipstream. An outflow boundary condition was used in the middle of the outlet to reduce the effect of boundaries on the jet of the accelerated fluid created by the propeller. The propeller, the hub and the shaft were specified as no-slip walls, the outer wall of the stator as slip-walls and the interfaces between the two sub-domains were treated as sliding interface boundaries with a first order

nearest-cell interpolation method. Six different geometrically similar grids were designed for the rotor using a structured grid generator, while two grids, corresponding to the coarsest and a medium cell densities, were generated for the stator. This decision was taken to allow a higher cell density in the rotor, prioritising the region close to the propeller where more challenging flow phenomena were expected, while saving computational time with a coarser grid for the stator, where the flow is of less interest. The stator grids included 1.1 and 10.6 million cells, while the propeller domains contained between 2.9 and 40.7 million cells. Maximum y^+ of 0.533 was found on the coarsest grid in open water conditions for advance ratio of 0.80.

3.1 Open water simulations

A verification and validation study was carried out for the rotational speed of 2000 RPM. The methodology based on Eça and Hoekstra (2014) was applied, assuming that the leading numerical error was the discretization error and that iterative and round-off errors were negligible in comparison. Round-off errors can be considered negligible since double precision was used, as well as the iterative error since L_{inf} norm residuals were two order of magnitude smaller than the discretization error (Eça and Hoekstra , 2009). After this study, carried out for design J value of 0.80, a grid of medium cell density with a total of 23.8M cells (grid $f0.550$) was chosen to simulate the experimental conditions due to a good compromise between number of cells and quality of the results. Values for L_{inf} norm residuals were required to be lower than 10^{-6} for the convergence to be considered acceptable; when this condition could not be met, due to the presence of flow separation or high loading, a minimum criterion of L_2 norm residuals being two orders of magnitude less than L_{inf} norm residuals was used, with values for L_2 norm residuals not higher than 10^{-5} and checking the location of the cells with the highest residuals.
The validation procedure suggested in ASME (2009) was used to address modeling errors of the thrust coefficient K_T, the torque coefficient $10K_Q$ and the open water efficiency η_O, adopting a 'strong-model' and expanded uncertainties U_{95} with a coverage factor $k = 2$ due to the derivation of the experimental uncertainties u_D from the standard deviation. Three different numerical uncertainties u_{num} (Eça and Hoekstra (2014)) were computed as a function of the flow topology; for the interval of advance ratio $0.28 \leq J \leq 0.68$ the limiting streamlines show separation of the flow and the numerical uncertainties were estimated over the four coarsest grids for a value of advance ratio $J = 0.44$. For the interval $0.72 \leq J \leq 0.92$ separation is not present and the numerical uncertainties obtained for $J = 0.80$ were used. An additional numerical uncertainty is computed for the higher advance coefficient values $0.96 \leq J \leq 1.02$ due to the vicinity to the zero-thrust condition. Numerical uncertainty for this regime was estimated at the advance ratio value of 0.98 using the four coarsest grids.

3.2 Cavitation simulations

Two different operating points were selected for simulating cavitation behaviour. These were differentiated by different cavitation numbers $\sigma_{0.7} = (p_\infty - p_v)/0.5\rho(V_A^2 + (\pi n 0.7D)^2)$ (where p_v is the vapour pressure) and advance coefficients J. These two specific points were chosen due to the evident presence of sheet cavitation (Point 1 with $\sigma_{0.7} = 0.227$ and $J = 0.596$) and tip vortex cavitation (Point 2 with $\sigma_{0.7} = 0.396$ and $J = 0.60$). Simulations were carried out using the medium density grid $f0.550$ and the cavity extent was compared with the available experimental photographs from the experiments. The adopted time step was equal to 0.25° of propeller rotation (Vaz et al. , 2015) and the flow was simulated for five propeller rotations for Point 1 and eight propeller rotations for Point 2 to achieve values for L_2 norm residuals lower than 10^{-4} and L_{inf} norm residuals lower than 10^{-2} for all flow quantities. Higher residual values were accepted due to the more complicated physics present in these simulations.

4 Results

4.1 Open water performance

Comparison between experimental and numerical results for the open water diagram obtained for a propeller rotation rate of 2000 RPM is depicted in Figures 2 and 3, where the percentage difference was calculated applying the formula $\%\ difference = (\phi_{num} - \phi_{exp}) * 100/(\phi_{exp})$ and for clarity values of advance ratios J close to zero-thrust condition were omitted. The comparison shows that, for the interval

of advance ratios J from 0.68 to 0.88 the numerical difference between the two solutions is within 4% of the measured value; for the lower J where higher loading and a leading edge vortex are present, the comparison is worse with the numerical solution over-estimating propeller forces and moments by up to 8% of the experimentally reported value. At advance coefficients above 0.9, the propeller approaches the zero-thrust condition, making a quantitative comparison with the experiments less meaningful. Nevertheless, the overall trend in variation of K_T, $10K_Q$ and η_O is well represented. By interpolating experimental and numerical data to find the value of the advance coefficient J for which the zero-thrust condition is obtained, an acceptable agreement was found, with an experimental advance ratio J equal to 1.015 and the numerical value equal to 1.014. The above comparison does not take into account experimental u_D and numerical u_{num} uncertainties. The verification study asserts that the highest numerical uncertainties are present for the highest range of advance ratios ($0.96 < J < 1.02$), with $u_{num}(K_T) = 1.1\%$, $u_{num}(10K_Q) = 2.9\%$ and $u_{num}(\eta_O) = 2.1\%$ as visible in Table 2. In the case of experimental uncertainties, the highest values for the advance ratio uncertainties were found for 720 RPM with values up to 10%, decreasing with increasing rotational speed to a value of 4% for rotational speed of 2500 RPM. Similar behavior was found for all the other experimental uncertainties, thrust coefficient uncertainties varied from 9% to 1%; for the torque coefficient uncertainty values varied from 3% to 0.4% and for open water efficiency from 8% down to 5%. The validation analysis shows that each studied variable behaves differently; for the thrust coefficient the estimated uncertainty intervals contain values of the modeling error equal to zero from $J = 0.68$ forward, with an over-estimation of the average between experimental and numerical K_T up to 12% and an under-estimation up to 11% (Figure 4a). For the torque coefficient $10K_Q$ (Figure 4b), an over-estimation of the averaged $10K_Q$ up to 9% and an under-estimation up to 9% are visible. In Figure 4c corresponding to the open water efficiency, it is possible to observe that all the derived model uncertainty intervals contain the model error zero-value, with an over-estimation of the efficiency over 13% and an under-estimation up to 8%. For all three variables, the model uncertainties are caused by both experimental and numerical uncertainties roughly of the same magnitude, as visible in Figure 2 where none of the error bars is visibly dominating. Comparison error values are high, compared to previous studies (Vaz et al. , 2015), because of the transitional nature of the flow ($Re(R) = 8.18 \cdot 10^5$) and of systematic errors in the experiments (thrust correction measured solely for the highest inlet speeds). The values of advance ratios close to zero-thrust condition were omitted in Figure 4 for clarity.

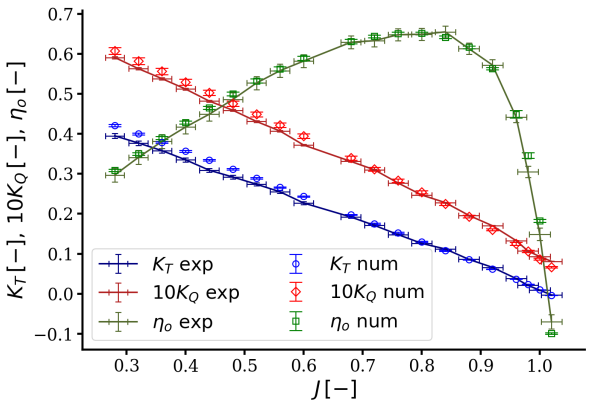

Fig. 2: Comparison between experimental results and uncertainties, Golf (2018), and numerical results and uncertainties of the open water diagram for 2000 RPM.

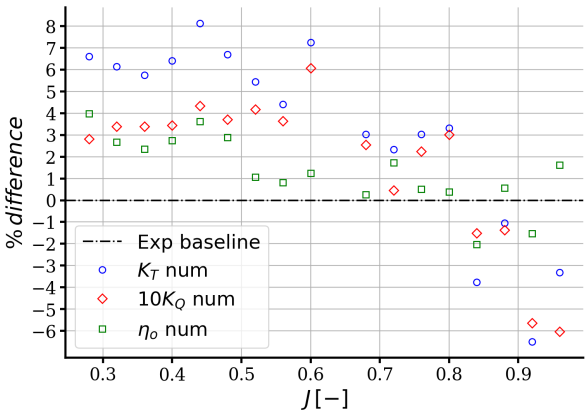

Fig. 3: Percentage difference between experimental results, Golf (2018), and numerical results of the open water coefficients for 2000 RPM not taking into account uncertainties.

4.2 Cavitating flow

The inception diagram constructed using the experimental tests by Golf (2018) is shown in Figure 5. It indicates that the two simulated operating points 1 and 2 fall in regions where multiple cavitation topologies are present: hub vortex, tip vortex and sheet cavitation. Comparison between experimental

Table 2: Verification study using Eça and Hoekstra (2014) for the three different intervals of advance ratios J dictated by the different flow regimes: for $0.28 \leq J \leq 0.68$ flow separation is present, for $0.72 \leq J \leq 0.92$ separation is not visible anymore, and the interval $0.96 \leq J \leq 1.02$ is close to the zero-thrust condition.

J interval	$u_{num}(K_T)$	$u_{num}(10K_Q)$	$u_{num}(\eta_O)$
$0.28 \leq J \leq 0.68$	0.6%	1.4%	0.9%
$0.72 \leq J \leq 0.92$	1.0%	1.5%	0.5%
$0.96 \leq J \leq 1.02$	1.1%	2.9%	2.1%

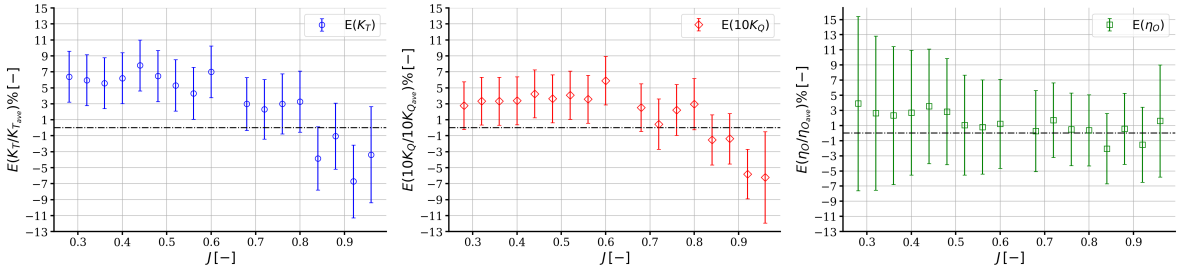

(a) Thrust coefficient K_T. (b) Torque coefficient $10K_Q$. (c) Open water efficiency η_O.

Fig. 4: Validation study following (ASME , 2009) procedure. Values of advance ratios J close to zero-thrust condition were omitted for clarity.

observations and numerical predictions of cavitation for these points shows that the area over which the cavity extends on the blade is comparable between the predictions and measurements (Figures 6 and 7). The inception of cavitation at the leading edge for Point 1 starts, for the experiments (Figure 6a), between 55 and 60 mm along the blade radius, while for the simulations (Figure 6b), onset of cavitation occurs between 50 mm and 55 mm along the radius; at the trailing edge, the cavity extends from circa 65 mm of the propeller radius to its tip in both cases. For Point 2 (Figures 7a and 7b), the inception at the leading edge is found between 50 mm and 55 mm of the propeller's radius for both experimental and numerical visualizations; at the trailing edge where the cavity extends from 70 mm of the radius to the tip of the blade in experimental photographs and simulations alike. In Figures 6 and 7 cavitation iso-surfaces were defined by a vapour volume fraction equal to 0.1. For both operating points, a slight under-prediction of the cavity volume and a steady-state is visible in the numerical solutions. Furthermore, the propagation of the cavity into tip vortex was not captured due to the use of RANS and the limited grid density (Lloyd et al. , 2017).

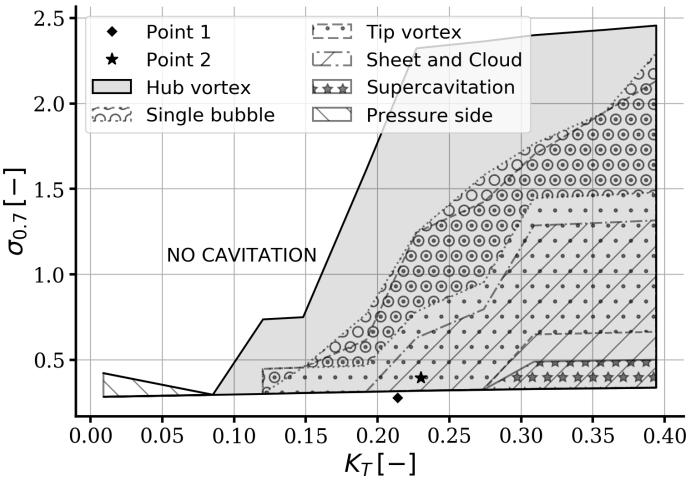

Figure 5: Representation of the cavitation inception diagram obtained via the experimental tests (Golf , 2018) and the location of the simulated operating points.

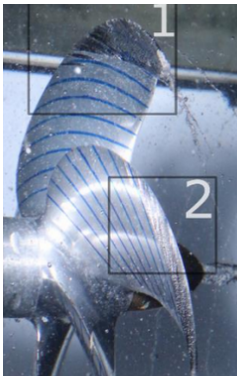

(a) Experiments

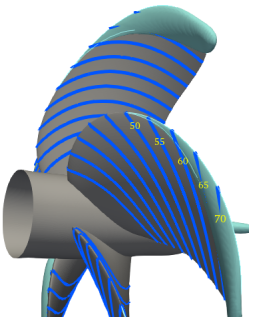

(b) Simulations

Fig. 6: Comparison of the cavitation pattern at operating Point 1.

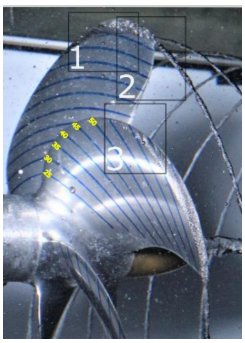

(a) Experiments

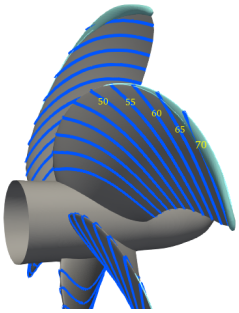

(b) Simulations

Fig. 7: Comparison of the cavitation pattern at operating Point 2.

5 Conclusions

The numerical study of the DPTC showed good agreement with the experimental work, both for wetted and cavitating conditions, with a maximum difference in wetted flow force coefficients of 8%, not considering experimental nor numerical uncertainties. This difference is caused by the transitional character of the flow due to low Reynolds numbers and systematic errors in the experiments. Comparable cavity extents for cavitating flow were also presented. To improve the quality of the results of both methodologies, the following suggestions can be taken into consideration: a more in depth analysis of the possible errors and uncertainties due to the measuring systems of the experimental setup due to the age of the apparatus; measurements of the inlet velocity during the cavitation tests to better define operating points tested (current velocity data were not reliable due to a malfunction of the measuring system while the tunnel was pressurized); application of transitional models (due to the limited dimensions of the propeller and intermediate Reynolds numbers), and investigation of different turbulence models to analyse the possibility to achieve higher quality results for the wetted flow; variation of time step to study the uncertainties of the temporal discretisation, local grid refinement should also be considered to better capture flow structures, such as tip vortex, important for the prediction of cavitating flow. Additionally, bubble, cloud and pressure side cavitation topology, as well as dynamic cavitation, could be explored by overcoming the limits imposed by the Volume of Fluid (VoF) methodology, known to have limitations in keeping a sharp interface, not offering detailed information on the cavity interface, nor allowing modeling of single bubbles.

Acknowledgements

The authors gratefully acknowledge the computing time granted by the Center for Computational Sciences and Simulation (CCSS) of the University of Duisburg-Essen and provided on the supercomputer magnitUDE (DFG grants INST 20876/209-1 FUGG, INST 20876/243-1 FUGG) at the Zentrum für Informations- und Mediendienste (ZIM). Additionally, the authors would like to acknowledge the Institute of Marine Technology, Maritime Engineering and Transport System (ISMT) for granting the use of the cavitation tunnel and Arjan Lampe from MARIN for generating the geometry of the propeller used for the numerical study.

References

R. Golf (2018). Kavitationsuntersuchung am DTC Propeller. B.Sc. Thesis, ISMT, University of Duisburg-Essen, Germany.

O. el Moctar, V. Shigunov, and T. Zorn (2012). Duisburg Test Case: Post-Panamax Container Ship for Benchmarking. *Sh Technol Res*, **59**(3), 50–64.

R. Dinter (2011). Fehlerrechnung für Einsteiger. Lecture notes TUHH.

F. R. Menter, Y. Egorov and D. Rusch (2006). Steady and unsteady flow modelling using the k-$\sqrt{k}$L model. Proceedings of the 5th International Symposium on Turbulence, Heat and Mass Transfer, Dubrovnik, Croatia.

D. R. Rijpkema, J. Baltazar and J. Falcão de Campos (2015). Viscous flow simulations of propellers in different Reynolds number regimes. Proceedings of the 4th International Symposium on Marine Propulsors, Austin, Texas, United States.

J. Sauer, and G.H. Schnerr (2001). Development of a new cavitation model based on bubble dynamics. *Zeitschrift für Angewandte Mathematik und Mechanik*, **81**(S3), 561–562.

G. Vaz, D. Hally, T. Huuva, N. Bulten, P. Muller, P. Becchi, J.L.R. Herrer, S. Whitworth, R. Macé and A. Korsström (2015). Cavitating flow calculations for the E779A propeller in open water and behind conditions: code comparison and solution validation. Proceedings of the 4th International Symposium on Marine Propulsors, Austin, Texas, United States.

L. Eça, and M. Hoekstra (2014). A procedure for the estimation of the numerical uncertainty of CFD calculations based on grid refinement studies. *J Comput Phys*, **262**, 104–130.

L. Eça, and M. Hoekstra (2009). Evaluation of numerical error estimation based on grid refinement studies with the method of the manufactured solutions. *Journal of Computers and Fluids*, **38**, 1580–1591.

ASME (2009). *Standard for Verification and Validation in Computational Fluid Dynamics and Heat Transfer: ASME V&V 20-2009.* American Society of Mechanical Engineers.

T. Lloyd, G. Vaz, D. Rijpkema and A. Reverberi (2017). Computational fluid dynamics prediction of marine propeller cavitation including solution verification. Proceedings of the 5th International Symposium on Marine Propulsors, Espoo, Finland.

Numerical Study on Wave Drift Force of Advancing Ship in Bow Seas

Kyung-Kyu Yang, Yoo-Chul Kim, Kwang-Soo Kim, Jin Kim, Bo Woo Nam, Min-Guk Seo
Korea Research Institute of Ships & Ocean Engineering, Republic of Korea
kkyang@kriso.re.kr

1 Introduction

Wave drift forces and moments are the time averaged forces and moments acting on a floating body in waves. When a ship is advancing in waves, the wave drift force in the longitudinal direction of the ship is called the added resistance in waves. The added resistance in waves is related to the speed loss in actual sea conditions and it is an important issue for reducing greenhouse gas emission to satisfy the energy efficiency design index (EEDI) regulated by International Maritime Organization (IMO). The sway drift forces and yaw drift moments are also important quantities to estimate the ship maneuverability in waves. Recently, many studies regarding the ship maneuvering in waves have been conducted using different methods of computing wave drift forces and moments (Skejic and Faltinsen, 2008; Seo and Kim, 2011; Yasukawa et al., 2019). In this study, wave drift forces and moments acting on an advancing ship in bow waves are investigated using an in-house numerical code that can solve highly nonlinear wave-body interaction problems. The program is called wave and viscous flow analysis system for hull form development (WAVIS) that has been developed by Korea Research Institute of Ships and Ocean engineering (KRISO). Basically, the finite volume method with block-structured mesh and non-staggered allocation is used to discretize unsteady RANS equations. The SIMPLEC method is adapted for velocity pressure coupling and a level-set method is used for free-surface capturing. The overset technique which is implemented in Suggar++ library is adapted for moving body problems. The realizable k-ε model with wall function is applied to model turbulent flows (Kim et al., 2017). Recently, generating oblique waves and solving six degree-of-freedom equations of motion have been implemented to WAVIS code for the present research.

2 Test Case

The target ship in this study is KVLCC2 with Froude number $Fn = U/(gL)^{0.5}$ is equal to 0.142, where U is the ship speed, g is the gravitational acceleration, and L is the ship length. The main particulars of KVLCC2 are summarized in Table 1. In the present numerical method, a non-dimensional form of the governing equation is considered and the Reynolds number for the model scale with 1/100 ratio is used in the following computations. The wave steepness of incident wave is H/L = 0.02 where H means the wave height and the wavelength over the ship length λ/L is varying from 0.5 to 1.5. The incident wave angle β is 150°, which means the incident wave is coming from the bow direction.
To solve the wave-body interaction problems, the overset technique is adapted in this study. The inner domain which is body-fitted structured mesh is moving with the ship motion, whereas the background mesh which has Cartesian grid topology is fixed in time. The background mesh is generated as the incident wave direction and the normal vector at cell faces are aligned. This is one of critical factors to generate the oblique incident waves correctly. The time step is fixed as $T_e/800$ throughout the computations, where T_e means the encounter wave period.

Table 1: Main particulars of KVLCC2.

L	B	D	T	Δ	C_B	Fn
320 m	58 m	30 m	20.8 m	312,622 m^3	0.8098	0.412

3 Results and Discussions

3.1 Convergence tests

To calculate the grid convergence index (GCI; Celik et al., 2008), three different grids were generated – subscript '1' is the finest grid, '3' is coarsest grid, and '2' is in between them and the grid system near the ship surface is shown in Fig. 1, while the background mesh was identical for different inner domain meshes. The total number of grids is varying from 260,000 to 1,410,000 and Table 2 summarizes the ratio of average grid spacing h and the resultant GCI values for the magnitudes of heave, pitch, and yaw motions, added resistance, and yaw drift moment. The ratio of grid spacing is about 1.8, which is larger than that of recommendation value 1.414. The apparent order is about 1.7 which is smaller than 2.0 that is the formal order of accuracy of the present numerical method. The GCIs of motion amplitudes are less than 1.0 %, whereas the added resistance and yaw drift moment are sensitive to the grid spacing. However, the GCIs of added resistance and yaw drift moment lie in the acceptable level compared to the uncertainty of experiment.

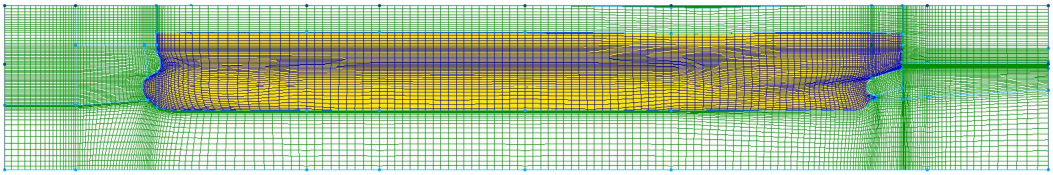

(a) Coarse grid, h_3

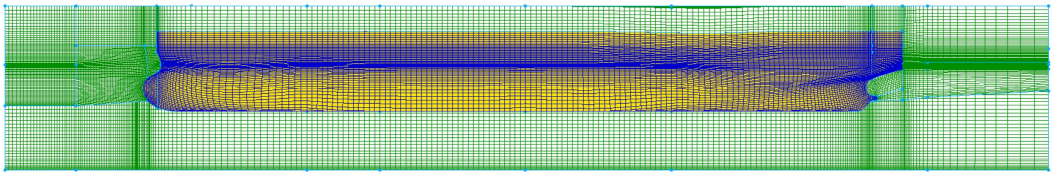

(b) Medium grid, h_2

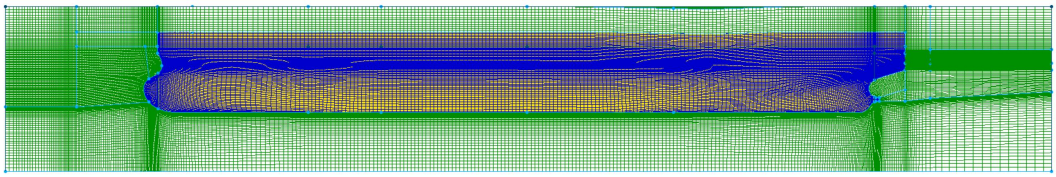

(c) Fine grid, h_1

Fig. 1: Side view of inner domain grids.

Table 2: Grid convergence index of motion responses and drift forces.

	$\lambda/L = 1.1$
h_3 / h_2	1.8486
h_2 / h_1	1.8524
Apparent order	1.753
GCI of heave amplitude (%)	0.782
GCI of pitch amplitude (%)	0.964
GCI of yaw amplitude (%)	0.703
GCI of added resistance (%)	15.33
GCI of yaw drift moment (%)	25.06

3.2 Motion responses and wave drift forces

The snapshots of wave contour and distribution of hydrodynamic pressure on the ship surface are shown in Figs. 2 and 3 for λ/L = 0.5 and 1.1, respectively. The time interval is $T_e/4$ and the hydrodynamic pressure is normalized with linear dynamic pressure ρgA, where ρ is the fluid density and A is the wave amplitude. The wave elevation η is also normalized with the wave amplitude. The black solid line on the ship surface indicates the position at which the level-set function is equal to zero. This iso-surface can be considered as the instantaneous position of free surface.

In the case of short wave (λ/L = 0.5), the ship motion is negligible and thus the ship surface in the weather side is acting like a rigid wall. Consequently, there exist partial standing waves in the weather side, while the incident wave is partially shaded by the ship in the lee side. On the other hand, there exist both diffraction and radiation waves for the resonance condition (λ/L = 1.1). The radiation waves are propagating in both weather and lee sides, while the similar diffraction wave pattern that observed in the short wave case can be seen. However, the amplitude of radiation waves is larger than that of diffraction waves and thus the wave elevation at the ship surface is similar in both weather and lee sides.

The magnitude of six degree-of-freedom ship motions and the wave drift force/moment are summarized in Fig. 4 with respect to the wavelength of incident wave. The diamond symbol represents the result of experiment (Seo et al., 2018) and the rectangular symbol means the result of present numerical method. The added resistance and wave drift force/moment are normalized as follows:

$$Cx = \left(\overline{Fx} - F_0\right) / \left(\rho g A^2 B^2 L\right); \qquad Cy = \overline{Fy} / \left(\rho g A^2 B^2 L\right); \quad Cn = \overline{Mz} / \left(\rho g A^2 B^2\right) \tag{1}$$

where Fx and Fy indicate the hydrodynamic forces in the longitudinal and transverse directions, respectively. Mz means the hydrodynamic moment in the vertical direction and the upper bar indicates the time averaged quantity. F_0 is the total drag in calm water condition, which can be obtained from a separated computation. The figure shows that the present numerical method predicts the motion amplitudes and wave drift force/moment with reasonable accuracy compared to the experimental data. The added resistance shows similar tendency compared to the well-known tendency of added resistance in head waves. In other words, there are mainly two components – diffraction and radiation – of added resistance and only the diffraction wave component exists in short wave region, whereas radiation component also exist as the ship motion becomes large. As the wavelength becomes longer, relative wave elevation along the ship surface becomes zero and thus the added resistance decreases. Further studies with different wave heading angles are required to investigate the effect of heading angles on wave drift force/moment.

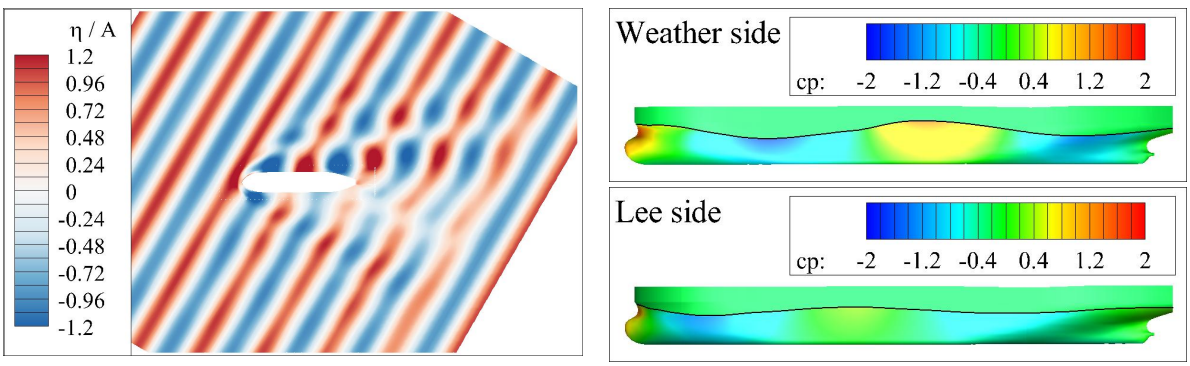

(a) $t = T_0$

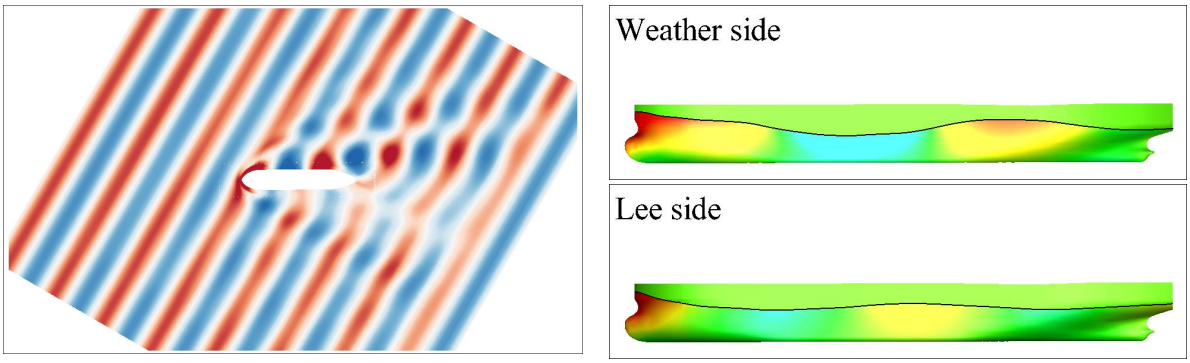

(b) $t = T_0 + T_e / 4$

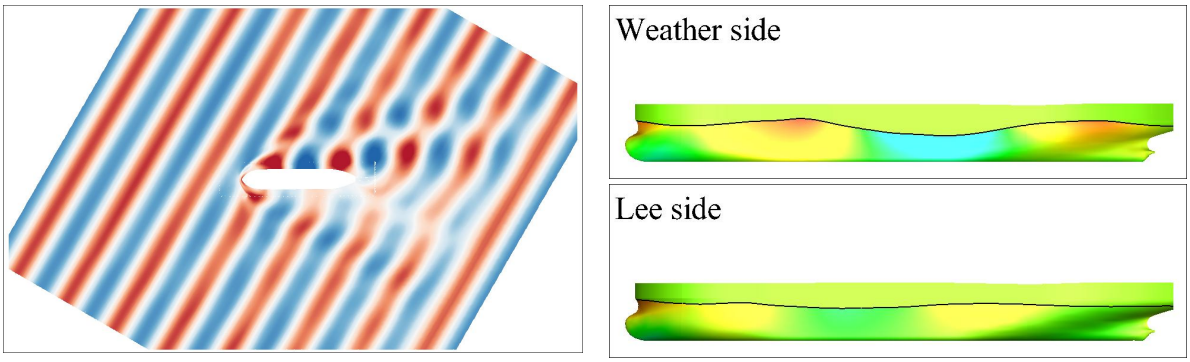

(c) $t = T_0 + 2T_e / 4$

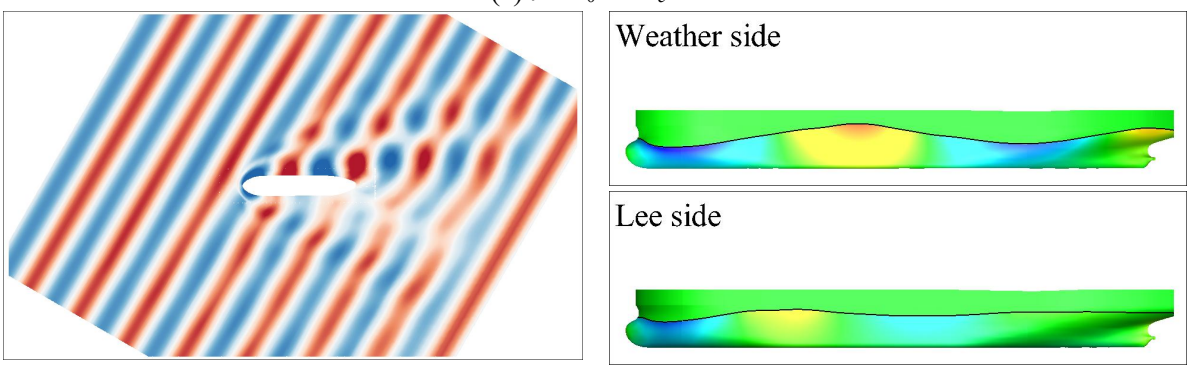

(d) $t = T_0 + 3T_e / 4$

Fig. 2 Snapshots of wave contour (left) and hydrodynamic pressure (right), $\lambda/L = 0.5$, $\beta = 150°$

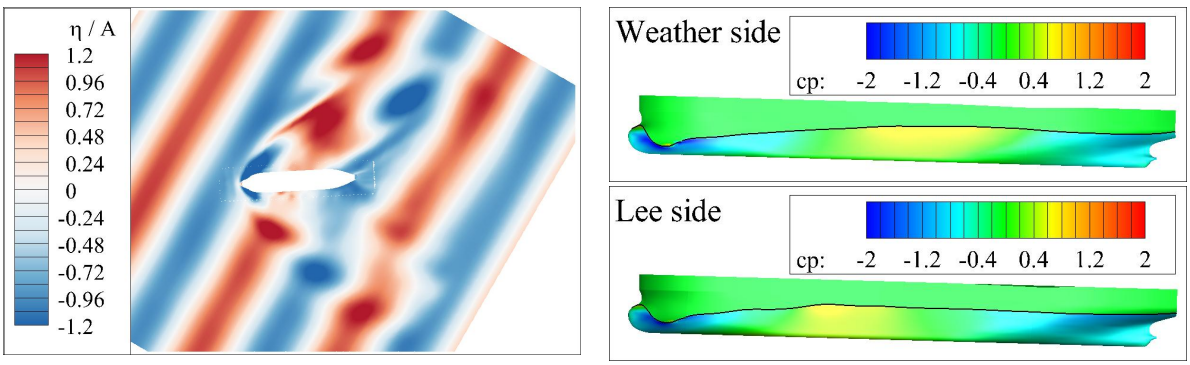

(a) $t = T_0$

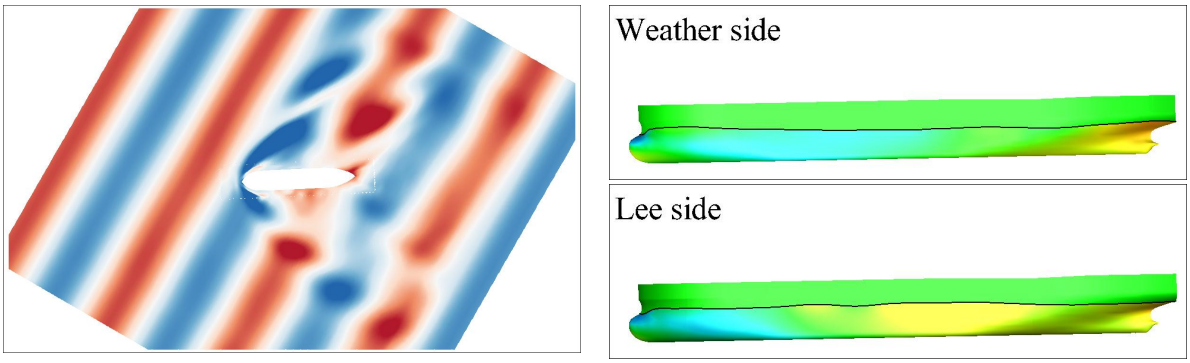

(b) $t = T_0 + T_e / 4$

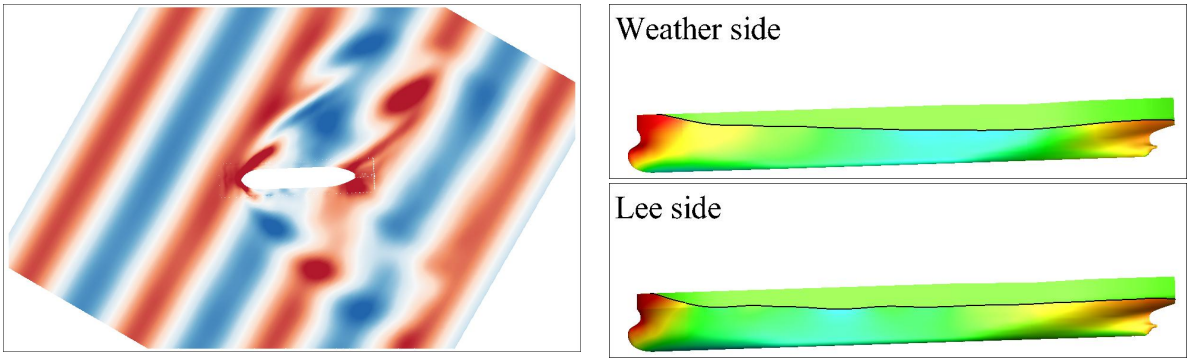

(c) $t = T_0 + 2T_e / 4$

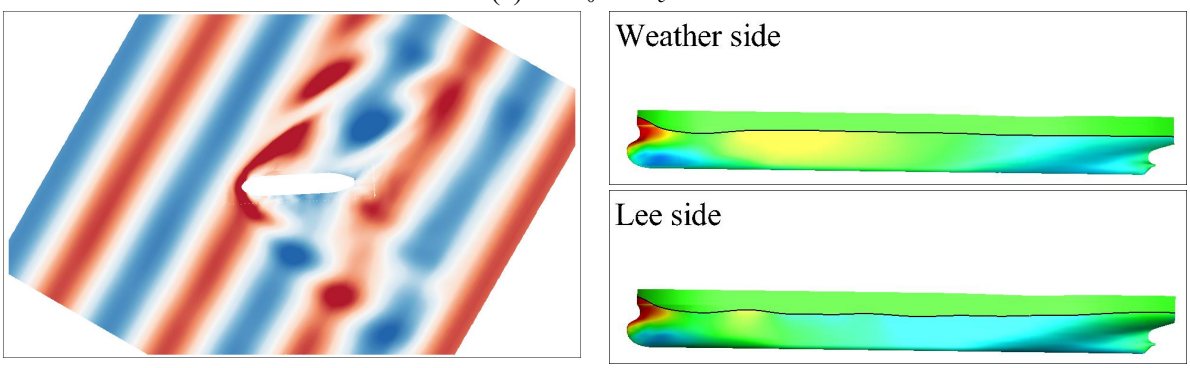

(d) $t = T_0 + 3T_e / 4$

Fig. 3 Snapshots of wave contour (left) and hydrodynamic pressure (right), $\lambda/L = 1.1$, $\beta = 150°$

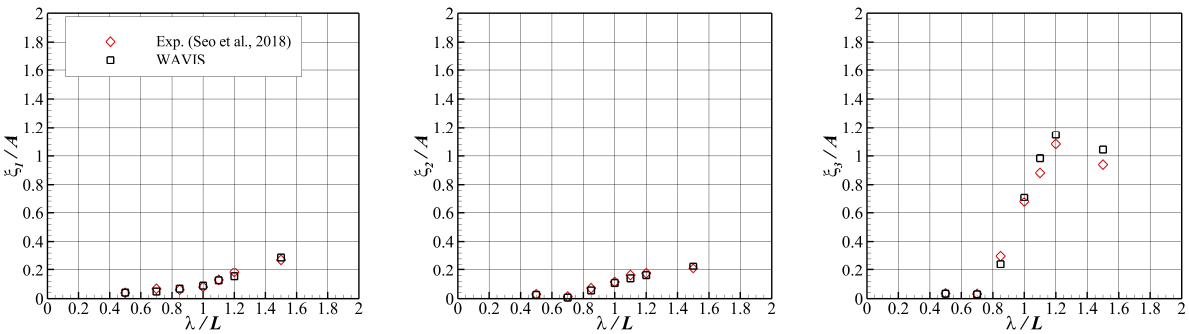

(a) Magnitude of surge motion (b) Magnitude of sway motion (c) Magnitude of heave motion

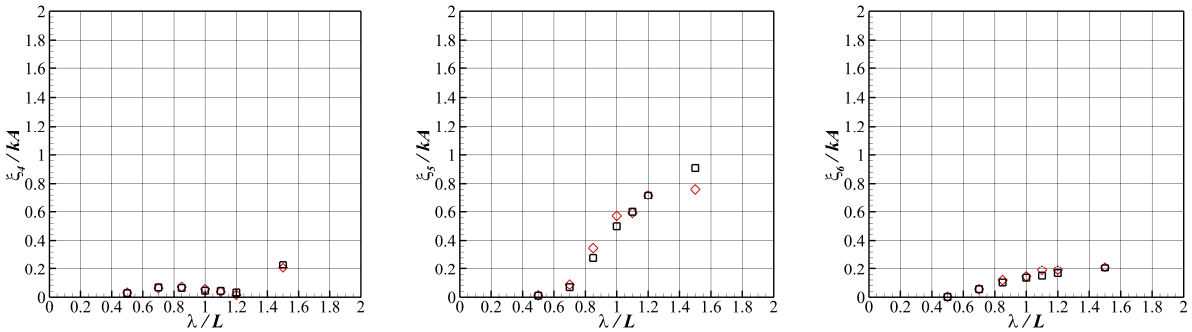

(d) Magnitude of roll motion (e) Magnitude of pitch motion (f) Magnitude of yaw motion

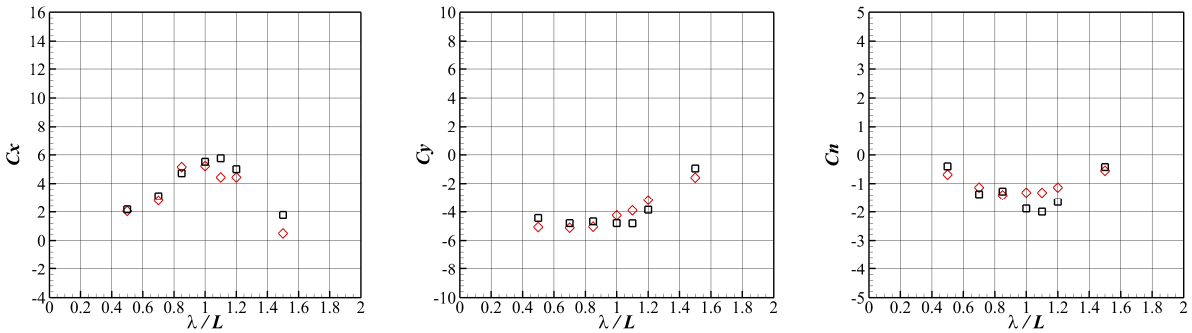

(g) Added resistance (h) Sway drift force (i) Yaw drift moment

Fig. 4 Transfer function of six degree-of-freedom motions and wave drift force/moment, $\beta = 150°$

4 Conclusion

In this study, the wave drift forces and moments acting on the ship advancing in bow waves were investigated using the numerical method that is based on the finite volume method with level-set approach and overset grid technique. The present numerical method showed good agreement with the available experimental data of motion responses and wave drift forces and moments. The results for other heading angles will be shown at the Symposium.

Acknowledgements

This research was supported by a grant from Endowment Projects – PES3010 and PES3030 – funded by Korea Research Institute of Ships and Ocean engineering. The authors appreciate all of the support received.

References

R. Skejic and O.M. Faltinsen (2008). A unified seakeeping and maneuvering analysis of ships in regular waves. *J Mar Sci Technol*, **13**(4), 371-394.

M.G. Seo and Y. Kim (2011). Numerical analysis on ship maneuvering coupled with ship motion in waves. *Ocean Eng*, **38**, 1934-1945.

H. Yasukawa, N. Hirata, A. Matsumoto, R. Kuroiwa, and S. Mizokami (2019). Evaluations of wave-induced steady forces and turning motion of a full hull ship in waves. *J Mar Sci Technol*, **24**(1), 1-15.

Y.C. Kim, K.S. Kim, J. Kim, Y. Kim, I.R. Park, and Y.H. Jang (2017). Analysis of added resistance and seakeeping responses in head sea conditions for low-speed full ships using URANS approach. *Int J Nav Archit Ocean Eng*, **9**(6), 641-654.

I.B. Celik, U. Ghia, P.J. Roache, C.J. Freitas, H. Coleman, and P.E. Raad (2008). Procedure for estimation and reporting of uncertainty due to discretization in CFD applications. *J Fluids Eng*, **130**, 078007-078004.

M.G. Seo, B.W. Nam, D.J. Yeo, K. Yun, D.J. Kim, J.Y. Park, and Y. Kim (2018). Numerical analysis of turning performance of KVLCC2 in regular waves. Proceedings of the Annual Autumn Conference, SNAK, Changwon, Korea.